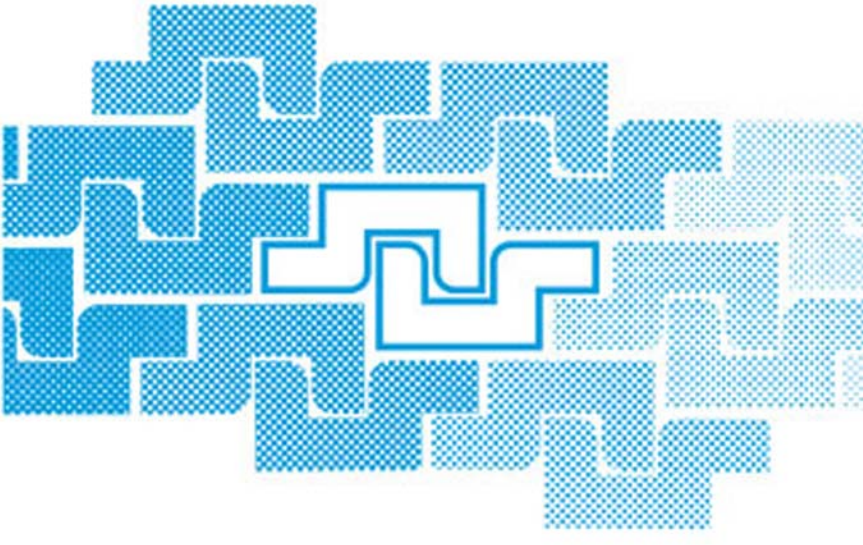

Photon-based Nanoscience and Nanobiotechnology

Edited by

Jan J. Dubowski and
Stoyan Tanev

NATO Science Series

II. Mathematics, Physics and Chemistry – Vol. 239

Photon-based Nanoscience and Nanobiotechnology

NATO Science Series

A Series presenting the results of scientific meetings supported under the NATO Science Programme.

The Series is published by IOS Press, Amsterdam, and Springer in conjunction with the NATO Public Diplomacy Division

Sub-Series

I. Life and Behavioural Sciences	IOS Press
II. Mathematics, Physics and Chemistry	Springer
III. Computer and Systems Science	IOS Press
IV. Earth and Environmental Sciences	Springer

The NATO Science Series continues the series of books published formerly as the NATO ASI Series.

The NATO Science Programme offers support for collaboration in civil science between scientists of countries of the Euro-Atlantic Partnership Council. The types of scientific meeting generally supported are “Advanced Study Institutes” and “Advanced Research Workshops”, and the NATO Science Series collects together the results of these meetings. The meetings are co-organized bij scientists from NATO countries and scientists from NATO’s Partner countries – countries of the CIS and Central and Eastern Europe.

Advanced Study Institutes are high-level tutorial courses offering in-depth study of latest advances in a field.
Advanced Research Workshops are expert meetings aimed at critical assessment of a field, and identification of directions for future action.

As a consequence of the restructuring of the NATO Science Programme in 1999, the NATO Science Series was re-organised to the four sub-series noted above. Please consult the following web sites for information on previous volumes published in the Series.

http://www.nato.int/science
http://www.springer.com
http://www.iospress.nl

Series II: Mathematics, Physics and Chemistry – Vol. 239

Photon-based Nanoscience and Nanobiotechnology

edited by

Jan J. Dubowski
Université de Sherbrooke, Sherbrooke, QC,
Canada

and

Stoyan Tanev
Carleton University, Ottawa, ON,
Canada

Published in cooperation with NATO Public Diplomacy Division

Proceedings of the NATO Advanced Study Institute on
Photon-based Nanoscience and Technology: from Atomic Level
Manipulation to Materials Synthesis and Nano-Biodevice Manufacturing
(Photon-NST'2005), Sherbrooke,
Quebec, Canada,
19–29 September 2005

A C.I.P. Catalogue record for this book is available from the Library of Congress.

ISBN-10 1-4020-5522-6 (PB)
ISBN-13 978-1-4020-5522-5 (PB)
ISBN-10 1-4020-5521-8 (HB)
ISBN-13 978-1-4020-5521-8 (HB)
ISBN-10 1-4020-5523-4 (e-book)
ISBN-13 978-1-4020-5523-2 (e-book)

Published by Springer,
P.O. Box 17, 3300 AA Dordrecht, The Netherlands.

www.springer.com

Printed on acid-free paper

Table of Contents

Preface

Jan J. DUBOWSKI
Center of Excellence for Information Engineering
Université de Sherbrooke, Sherbrooke, Québec J1K 2R1, Canada
and
Stoyan TANEV
Department of Systems and Computer Engineering
Faculty of Engineering and Design
Carleton University, Ottawa, Ontario K1S 5B6, Canada

The content of this book is based on peer reviewed invited articles corresponding to the tutorial presentations that were delivered in the frame of a NATO Advanced Study Institute (ASI) *'Photon-based Nanoscience and Technology: From Atomic Level Manipulation to Materials Synthesis and Nanobiodevice Manufacturing (Photon-NST'2005)'* held in Orford-Sherbrooke, Québec, Canada, September 19-29, 2005. The ASI was opened by John Polanyi, the 1986 Nobel Prize winner in chemistry, whose lecture on 'The Atomic Patterning of Surface by Chemical Reactions' set the stage for this frontier research and advanced technology forum.

Light has always played a significant role in the synthesis of materials and formation of small-scale solid structures. Until recently, the wavelength of photons has been the key factor limiting the minimum possible dimensions of two-dimensional or three-dimensional structures that they could produce. The invention of holographic and phase mask projection has enabled engineers to fabricate devices with characteristic features much smaller than the wavelength of the light used for processing. A further reduction of device dimensions has been achieved by implementing the processes that rely strongly on the non-linear effects of light-matter interaction. Photon-based nanoscience and technologies (Photon-NST) have created exciting opportunities and enabled new solutions with both documented and potential impact in such areas as communications, consumer electronics, automotive and aerospace industry. In addition, the accumulated to-date results of photon-based synthesis, deposition, etching, surface modification and particle manipulation demonstrate that the laser has the potential to offer enabling solutions for various needs of nano-scale processing, including fabrication and characterization of nano(bio)material devices and systems, and it is expected to significantly contribute to the development of Nanobiophotonics and Nanomedicine. The Photon-NST advancements have brought exciting nanoengineering tools for biomedical sciences, environmental monitoring, security and defense. The intention of this book was to provide the Reader, primarily graduate students and young researchers in materials engineering, bio(chem)physics, medical physics and biophysics, with a set of articles reviewing state-of-the art research and recent advancements in the field of photon-matter interaction for micro/nanomaterials synthesis and manipulation of properties of biological and inorganic materials at the atomic level.

An understanding of the physical and chemical aspects of the laser-matter interaction is very important for a deeper appreciation of the advances in photon-based nanoscience and technology. The chapter by Dickinson (‘*Physical and chemical aspects…*’) is a suitable reference addressing this problem. For a Reader specializing in the theory of laser-matter interactions, we recommend the chapter by Bandrauk et al. (‘*Attosecond control of electrons…*’), which discuses the concept of an ‘attosecond science’. The principles of nanoscale control of optical functions in solids and excited state dynamics of biomedical nanostructures are discussed by Prasad (‘*Fundamentals of Nanobiophotonics*’), while Wilson presents an exhaustive review of the potential uses of nanoparticles in oncology, as well as a discussion of photonic-based techniques for both therapeutic and diagnostic applications (‘*Photonic and non-photonics based nanoparticles…*’). A discussion of the definition of nanomedicine and the strategic Canadian initiative in the area of regenerative medicine is found in the chapter written by Marcotte and Quirion (‘*A summary of Canadian nanomedicine research…*’). The application of the finite-difference time-domain modeling technique to study the effect of optical immersion based enhancing of phase microscope imaging of single and multiple gold nanoparticles in biological cells is discussed by Tanev et al. (‘*Finite-difference time-domain modeling…*’). The fundamentals of plasmonics and the application of planar composite materials comprising metal nanocrystals for photonic sensor applications are discussed by Haglund (‘*Nonlinear optical physics…*’). In another chapter (‘*Applications of free-electron laser…*’) Haglund discusses the status of current research concerning the use of the free-electron laser in medicine, biochemical analysis and organic thin-film deposition. A novel biosensor approach, based on the application of arrays of epitaxial quantum dots that have previously been known for their applications in advanced communication devices such as quantum dot lasers, is discussed by Dubowski (‘*Quantum dot bio-template…*’). Laser synthesis of single-walled carbon nanotubes and nanohorns is discussed by Geohegan et al. (‘*Laser-based synthesis…*’) and Lippert (‘*Molecular design of polymers…*’) reviews the current status of designing polyimides and polymers dedicated for processing with lasers. Livingston and Helvajian (‘*Photophysical properties that activate selective changes…*’) investigate the fundamental effects of photoactivated changes in photostructurable glass ceramic materials and the application of this technology for manufacturing of so called ‘nanosatellite class space vehicles’. The photostructurable glass has also been used for the fabrication of 3D microstructures of some lab-on-a-chip devices using a femtosecond laser technology. This field is reviewed in the chapter by Sugioka et al. (‘*Three-dimensional micro and nanochips…*’). The design, operation, parametric monitoring and theory underlying the liquid phase photodeposition processes of nanosize colloid systems, such as a-Se, ZnS and Au, is discussed in the chapter by Peled and Mirchin (‘*Photo-assisted processes…*’) and the concept and results of using surface plasmon resonance for the fabrication of gold nanoparticles with a well-defined shape is discussed by Ouacha and Träger (‘*Controlling the surface plasmon resonances…*’).

This book is not to be read from the first to the last chapter but, rather, it has been intended as a reference to photon-based nanoscience and related technological

problems concerning the growing field of nanobiophotonics. We hope that it will be of use not only to a young generation of researchers entering this field, but also to some of the seasoned scientists as well.

Acknowledgements

The editors are grateful to all supporting organizations and people that made this ASI possible. Our special thanks are directed towards the NATO Security through Science Program (Brussels, Belgium), US Air Force Office of Scientific Research, Canadian Institutes of Health Research, and Canadian Institute for Photonic Innovations. We thank Vitesse Re-Skilling™ Canada for partnering in setting the initial vision of the ASI and for providing the organizational infrastructure during the meeting; the Canadian Department of Foreign Affairs and its Global Partnership Program that together with the International Science and Technology Center in Moscow (Russia) supported the participation of Russian scientists; the Canadian International Development Agency that together with the Science and Technology Center in Kiev (Ukraine) supported the participation of Ukrainian scientists. We also thank the Holon Academic Institute of Technology (Israel), the State University of New York at Buffalo (USA) and the Université de Sherbrooke (Canada) for supporting the participation of their students in this event.

PHYSICAL AND CHEMICAL ASPECTS OF LASER-MATERIALS INTERACTIONS

J.T. DICKINSON
Surface Dynamics Laboratory, Physics/Astronomy Department and Materials Science Program, Washington State University, Pullman, WA USA 99164-2814

Abstract. The use of lasers in to modify and characterize materials is an increasingly attractive choice for high technology manufacturing as well as analytical and medical applications. As we push for more demanding tasks and for smaller dimensions, an understanding of the underlying physical and chemical aspects of problems becomes important. Here we discuss some of these issues relevant to most applications involving laser materials interactions.

Keywords: laser processing of materials, physical and chemical properties, laser-materials interactions, micromachining

1. Introduction

Soon after the development of the first laser it was suggested that it would have uses as a manufacturing tool due to many of the advantages of radiation sources over conventional mechanical and thermal techniques. Furthermore, a number of biological and medical applications were considered such as surgery. Today, lasers are used for a number of laser processing tasks in advanced applications in industry. As the commercial boom in microelectronic and optoelectronic devices and the trend toward miniaturization continues, industrial use of lasers will play an increasingly important role. Materials ranging from ceramics/glasses, metals, semiconductors, polymers, natural and manmade fibers and composites have all been shown to interact with one or more laser types in useful ways. A number of biotechnical applications requiring precision and highly reproducible techniques rely heavily on laser processing. The arsenal of lasers of current or future interest includes both CW and pulsed lasers. The

J.J. Dubowski and S. Tanev (eds.), Photon-based Nanoscience and Nanobiotechnology, 1–30.

commonly used lasers include the CO_2 laser, Excimer Lasers, Solid State Lasers (including diode pumped YAG and Ti:Sapphire lasers), Metal Vapor Lasers, and for some applications, Diode (semiconductor) lasers. The microfabrication and processing applications that are potentially well matched to using lasers include:

- etching
- cutting
- stripping
- cleaning
- drilling
- surface modification
- dry patterning
- scribing
- deposition (PLD)
- diagnostics
- trimming
- welding/soldering
- bonding
- marking/printing
- annealing
- photolithography
- mask fabrication
- 3D microstructures
- laser recrystallization.

Microhole drilling and trimming of components and laser recrystallization are certainly the most successful applications of lasers in microelectronics. The “advantages” of using lasers in processing and biomedical applications always must be weighed against disadvantages. A typical list of advantages of using lasers includes:

- close tolerance (resolution; feature size-usually wavelength dependent)
- repeatability (often excellent)
- zone of modification can be near-surface (i.e., for strong absorption) and in the bulk for transparent materials (using multiphoton absorption techniques)
- potential unit cost reductions, cost effectiveness
- material versatility (including fragile, ultrathin, highly reflective materials)
- roughness of Surfaces (Sometimes < nm)
- minimal distortion in heat affected zones

- no tooling to wear out or change over – no contact with surface
- non-contact processing eliminates unwanted stress on materials; contamination eliminated
- clean processing: minimal debris, burrs, uplifted recast
- flexibility - fast setups achieved with computer controls.

However, in evaluating these "advantages" one must weigh the extent or degree of each, thus the quotation marks around the word advantages. For example, is the resulting roughness tolerable, is a small amount of re-deposited particulates acceptable, is the process truly competitive with traditional methods cost-wise. Regarding costs, always lurking in the background are the expenses for operator training and addressing safety concerns. The "complaints" of a fabrication manager might include:

- it doesn't work (it breaks it, instead of makes it)
- it's unpredictable (e.g., no software package to model the entire process)
- it's too slow
- it's too big (the modified area) or
- it's too small
- it's only one at a time
- it messes up (harms, degrades, contaminates) the 'neighborhood'
- it's too expensive
- it's only line of sight
- the laser and/or optics need too much maintenance.

Basic physics and chemistry can help address only a few of these issues. Of course, we note that the university academics state in every research proposal they submit: "*We need to understand the underlying mechanisms so that we can advance the technology*." In truth, most of the advancements in fabrication and processing are occurring ahead of the science and can't wait. The same is true in biomedical applications. It is often only when a particular process is very promising yet is not quite working, or not optimized, or has too many uncontrolled parameters that fundamental understanding would be a benefit. If the value-added by performing some manufacturing or biomedical step using lasers is high, this further motivates more basic research on mechanisms and understanding. In general, we want to understand the physical processes accompanying laser interactions with matter under conditions typical for laser-materials modification, removal, etching, etc. We certainly need to explore the relevant interactions of laser beams interaction with metals, dielectrics,

semiconductors, polymers and biological tissue. Such physical processes as heat transfer, phase transitions, material removal, plasma formation, and synthesis of nanoclusters and nanocrystalline films are very important.

2. Physical and Chemical Aspects

So let us explore a few of the major questions and issues involved in laser materials interactions, particularly those that involve material removal and heat driven processes. Some of the important aspects (much more than we can discuss) of laser materials interactions are as follows:

- light absorption processes (linear; nonlinear – multiphoton, multiple-photon; defects)
- absorbed energy density vs. position and time
- emission mechanisms (e-, ions, neutrals, clusters, "chunks")
- factors influencing rates of material removal and/or material modification
- photothermal vs. photoelectronic (fs, ps, ns)
- role of thermal-mechanical phenomena (∇T, shock) including
  - melting/Resolidification
  - fracture, spallation (particles)
  - diffusion or segregation
  - vaporization
  - condensation of vapors in gas phase (particles)
- role of external environment (reactive gases, liquids, pressure)
- equilibrium thermodynamics vs. non-equilibrium
- role of laser-plume interactions
- role of laser parameters (λ, t_{pulse}, I_{peak}, θ, spot size, rep. Rate, no. of pulses)
- understanding dependence on target parameters (e.g., optical & thermal properties, defects, morphology, spatial distributions, interfaces)
- generating predictive models (grand challenge to theorists)

All of these facets are addressable with today's knowledge and understanding of the underlying physics and chemistry. We want to emphasize that much of what is happening in the use of lasers involves either bond breaking or bond making. Usually it is desired to do this locally (precisely), quickly (to be cost effective; to avoid too much heating), and with "no" collateral damage. The use of lasers in fabrication is similar to the use of lasers in medicine – just like the medical doctor, the fabricator

must abide by the constraint: "*Above All, Do No Harm*". Minimizing this surrounding "damage" is often the biggest challenge.

2.1. BASIC BOND BREAKING

Often the types of bonds being broken (or made) influences the choice of laser parameters which include wavelength, pulse width/CW, peak irradiance, angle of incidence, spot size, repetition rate, and number of pulses. We usually consider four fundamental types of bonding:

- covalent bonding (diamond, Si, Ge, GaAs, GaN, BN, SiO_2)
- ionic bonding (alkali halides, alkaline earth halides, metal oxides such as MgO)
- metallic bonding (metals in general)
- intermolecular forces (Hydrogen Bonding - strongest)
- dipole-dipole forces
- London dispersion forces (non-polar structures interacting - weakest).

An example of where intermolecular forces would be important are interfaces which will be (making bonds) or are (breaking bonds)connected via adhesive bonds; another example is the entire range of interactions involving unwanted 'pesky' particles adhering to substrates which need to be removed. Using laser cleaning to remove a particle thus requires that these intermolecular forces be overcome in order to detach the particle. Electrostatic charge, if present, can of course increase the bonding of particles to surfaces considerably. The use of water ("steam cleaning") in laser cleaning would assist in neutralizing this charge along with the advantages of nucleating bubbles to assist lifting particles.[1-3] Of course all glassy polymers consist of covalently bonded polymer chains with intermolecular forces interacting between the chains. Thus, the properties of common polymers, such as polymethylmetha-crylate (PMMA), polycarbonate (PC), and polystyrene (PS), are strongly dependent on these intermolecular forces. These lead to inter-chain friction, entanglements, and free-volume dependent attributes (e.g., thermal properties; gas diffusivity).

Figure 1 shows schematically the interaction of a laser beam with a structure of some complexity. Assuming a reasonable degree of absorption (so we can ignore transmission), the incident photons are absorbed either due to excitation of electrons or for longer wavelengths, excitation of vibrational modes. The reflectivity of the material then dictates how much

of the incident beam is absorbed. The 3D distribution of absorption centers exposed to the incident beam and their optical properties in relation to the laser light dictate the energy density distribution in the near surface region. In metals, absorption takes place very near the surface and can occur by excitation of both conduction band (free electron-like) and valance band (interband absorption) electrons are the absorbing entities. These electrons transfer their increased kinetic energy to the lattice via phonon scattering on time scales of ps, resulting in a temperature increase. For long pulses (> ps) heating is occurring during the pulse and so in general one can treat light energy to heat in one step.

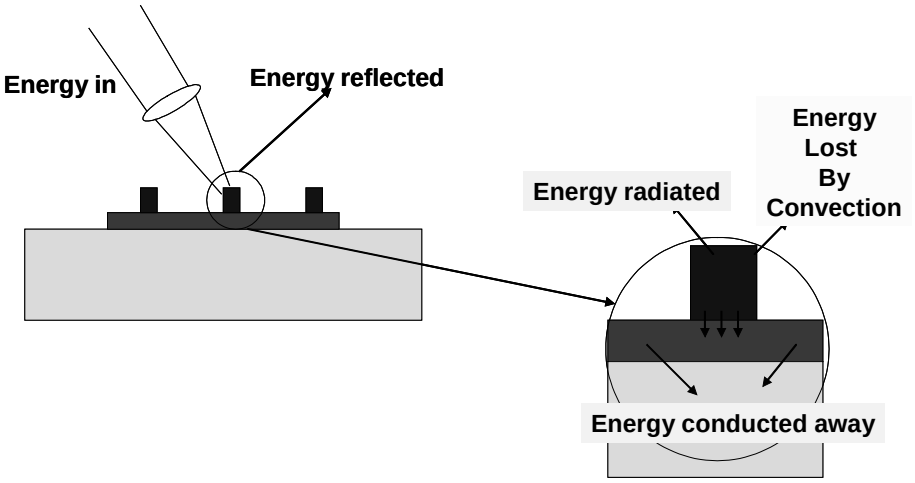

Figure 1. Schematic of relevant interactions and consequences of energy absorption.

For semiconductors and insulators, absorption is either through vibrational excitation (requiring infrared light matching allowed vibrational transitions of the material) or electronic excitations (e.g., via chromophores, defects, or band-to-band transitions). The electronic energy tends to be more localized than in metals, but in "real materials", the electronic energy is again quickly transformed into thermal energy. Atomic dimension energy localization can assist in the breakdown of materials, particularly in crystalline ceramics and silica-based glasses. For example, electron-hole pairs in an insulator are trapped at a lattice site which then may lead to motion of nuclei – the beginnings of decomposition of the material, all non-thermal in nature. Numerous examples of such phenomena are presented in the book by Itoh and Stoneham.[4] However, many of the rates of material removal using lasers, even those initiated by electronic processes, are still

thermally enhanced or thermally controlled; thus, in general, the practical use of lasers in fabrication is dominated by thermal processes--thus arguing over "photoelectronic" vs. "photothermal" is moot.

2.2. COMMENTS ON THERMAL MODELING

In seeking precision in processing, the fate of this deposited energy is highly significant. As seen in Fig. 1, the dispersion of the thermal energy away from the region where it was absorbed can involve radiative, convective, and conductive transport. By far the most important for practical applications is the heat transport by diffusion/conduction away from the higher temperature irradiated region into the cooler surrounding material. The rates and dimensions involved determine the spatial region that reaches high temperatures - the so-called Heat Affected Zone. Many modeling efforts have been focused on predicting the spatial and temporal distribution, T(**r**,t), during and following the laser pulse.[5] One can readily write down the appropriate time and space dependent heat conduction equation:

$$\rho C_p \frac{\partial T(\mathbf{r},t)}{\partial t} = \frac{H}{C_p} + \nabla \bullet [\kappa(\mathbf{r},T)\nabla T(\mathbf{r},t)]$$

where $k \equiv \rho C_p \kappa$ is the thermal conductivity with units of Joules and k is the thermal conductivity (with units of Joule/(mKs), κ is thermal diffusivity in m^2/s, H is the Heat Input per unit mass in Joule/(Kg.s)$*\alpha I(\mathbf{r},t)$ (linear absorption), α is the absorption coefficient, I is the instantaneous power density of laser radiation. Note that many of these "constants" are actually temperature dependent and must be treated as such.

The methods commonly used to solve the heat conduction equation analytically or numerically are:

Laplace transforms Green's functions Fourier transforms	Analytic
Stochastic/Monte Carlo Finite Differences	Numerical

Computer models suffer from two potential difficulties:

- Poor physical description. (The system has been idealized to the point where it no longer describes reality - similar to the physicist's "Spherical Cow").
- Poor algorithm. (The algorithm is not adequate to describe the behavior of the model, let alone reality.) Finite element models of laser absorption and heating generally involve good algorithms, but the computational overhead is high and again only simple models can be studied.

One approach that seems promising is the use of stochastic models. Stochastic models of laser absorption utilize a 'lean and mean' algorithm, allowing for more complex, realistic physical models. The main limitation to the physical models it can describe is that the temperature in each little cell is considered to be uniform. There are tricks to minimize the impact of this assumption (smaller cells, extrapolation etc.). Algorithmically, the output of these models always displays stochastic noise, which can be minimized by raising the number of heat packets and cells. Stochastic models provide an important check on the more well behaved output of finite element and Monte Carlo codes. If simplified physical models employed by these more sophisticated algorithms are adequate, their results will be consistent with properly executed stochastic models (to within the noise limits). An impressive example of a simulation of laser heating of silicon and silver surfaces using a stochastic/Monte Carlo method is described by Houle and Hinsberg,[6] where peak temperatures reached at the center of a Gaussian shaped laser spot vs. laser power and temperature vs. time were compared with experimental data. Fig. 2 shows Houle and Hinsberg's results results for Si and Ag. Note that even for a well known material such as Ag, the optical parameters were not sufficiently known to nail the experimental data although the overall time dependence looks very promising.

Which again raises the difficulty in modeling and simulation has do to again with complexity—namely, obtaining the appropriate physical constants. For simple homogeneous materials such as many pure metals and semiconductors, the optical and thermal constants are often available. Si, being the most studied element in the history of science, is very well characterized. As an example of T dependent thermal constants, we show data taken from the web for crystalline Si in Fig. 3. For more complex materials of use in packaging and fabrication, such information is very difficult if not impossible to obtain. In addition, optical constants may be fluence and time dependent; spatial dependence is often critical, and the influence of scattering cannot be ignored. Thus, surface roughness, the presence of interfaces, and the evolution of sub-micron structures in the

irradiated region further complicates quantitative modeling. The temperature dependence of both optical and thermal constants is often needed over large ranges, including through phase transitions (e.g., melting).

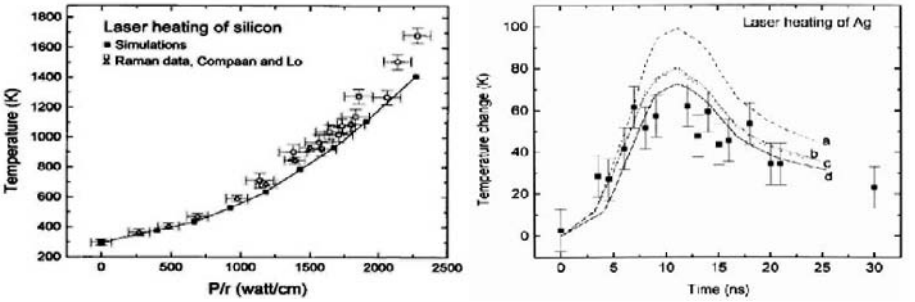

(a) (b)

Figure 2. (a) Simulations and Raman measurements of Si surface temperature at the center of the laser spot under CW laser irradiation as a function of P/r, where P is the laser power and r is the 1/e radius of the laser beam. (b) Simulations of the temperature and 2nd harmonic generation in a silver surface under pulsed IR irradiation (8 ns FWHM, 125 MW/cm^2). Traces are simulations assuming various optical parameters to determine their effect on the result.[6]

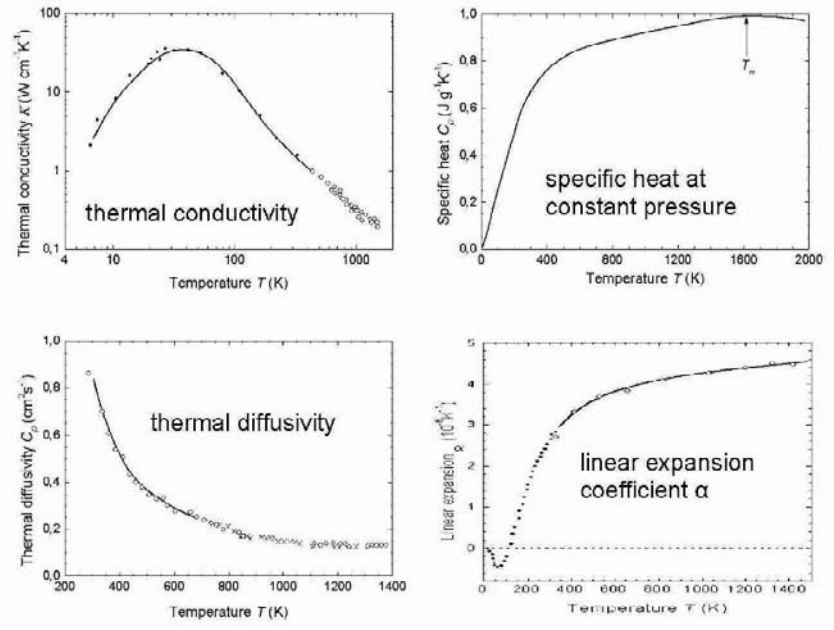

Figure 3. Temperature dependence of the thermal constants for crystalline silicon.

Similar issues are relevant to heating nanoparticles which can often perform very useful functions. Recently, Richardson, et. al. have shown that gold nanoparticles are extremely effective in generating localized heating when irradiated with laser light.[7]

3. The Potential of Ultrafast Laser

A number of studies have shown that femtosecond lasers are capable of producing machined features with a much smaller heat affected zone or re-solidified layer compared to ns pulses.[8-12] Most commercial ultrafast lasers are based on a Ti:Sapphire mode-locked oscillator pumped with a diode laser such as a doubled Nd:YVO_4 (at 532 nm). The oscillator output is tunable from 700 nm to 1000 nm and pulse energies are on the order of tens of nanojoules and a pulse repetition rate of tens of MHz. Much higher pulse energies (and therefore peak power) can be achieved using a regenerative amplifier, with typical outputs of a few mJ/pulse and frequencies up to a few kHz at pulse widths around 100 fs. Focusing the output of such a laser often makes possible exceptionally high quality machining for a wide variety of materials including transparent solids (e.g., silica based glasses), as well as sintered ceramics, metals, and polymers. At low irradiance on transparent materials, for sub bandgap photon energies the absorption behavior shows strong similarity to longer (ns) pulses, namely single photon defect-dominated absorption.[13-15] For strong absorbers (e.g., metals), again, single photon absorption occurs just as it does with longer, lower irradiance pulses. For short pulses, a two temperature model works well in describing the energy density vs. position and time, where only the electrons are heated (to very high $T_{electron}$) during the laser pulse, followed by ps time scale transfer of the energy to the lattice, resulting in a lagging and lower $T_{lattice}$ at a rate determined by the electron-lattice coupling constant usually denoted by γ.[16]

At higher irradiance in all materials, the high peak power of an amplified ultrafast laser can result in multiphoton ionization (MPI) which can lead directly to breakdown of the material. MPI also provides free electrons which can act as “seeds”; if the pulse is greater than ~ 40 fs, these seed electrons can absorb laser energy via inverse bremsstrahlung. If the energy of these “heated” electrons reaches sufficient energy to impact ionize atoms in the solid, avalanche ionization develops and the material breaks down. The thresholds in irradiance for breakdown in either regime are highly stable and give very predictable, reproducible behavior.

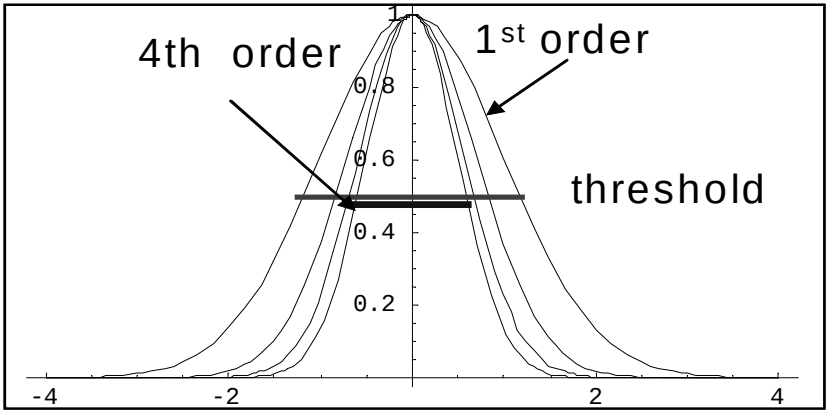

Figure 4. Energy density distributions vs. position for a Gaussian laser profile where we have normalized the distributions for 1st through 4th order. For a process with a threshold for each order the width of the active beam decreases. Using FWHM as the relevant distance, a 4th order process has ~ half the width.

Most processing studies to date have been carried out above the threshold for plasma formation. Because of the short interaction time, heat diffusion from the focus region of the laser beam into the surrounding area is very limited, thereby minimizing collateral damage. Due to the non-linearity, higher order absorption with for Gaussian beam profiles results in only the central portion of the beam being absorbed. 4th order absorption, for example, has a width less than 1/2 the Full Width at Half Maximum (FWHM) of the 1st order absorption, as shown in Fig. 4. Thus, ultrafast materials processing allows the machining of sub-wavelength feature size, which is not normally feasible with nanosecond lasers. Furthermore, because the multiphoton interaction with the material does not require direct absorption, ultrafast amplifiers can be used to process a wide spectrum of materials as mentioned above. The amount of material removed/pulse is very constant with ultrafast lasers, although because the energy/pulse is so low, the amount removed can be small. So if one is concerned with precision and small feature size, pulse to pulse reproducibility, and an extremely high degree of control, ultrafast lasers are very attractive. Brute force tasks requiring a few to watts of average energy require falling back on the traditional longer pulse or CW laser sources.

The high instantaneous powers associated with femtosecond lasers can lead to modification of materials including the coloration of otherwise transparent materials. Although the excitations responsible for this defect formation occur on subpicosecond time scales, subsequent interactions between the resulting electronic and lattice defects complicate the evolution

of color center formation and decay. These interactions must be understood in order to account for the long term behavior of coloration. Here we present some of our studies where we probe the evolution of color centers produced by femtosecond laser radiation in soda lime glass and single crystal sodium chloride on time scales from microseconds to hundreds of seconds. By using an appropriately chosen probe laser focused through the femtosecond laser spot, we can follow the changes in coloration due to individual or multiple femtosecond pulses, and follow the evolution of that coloration for long times after femtosecond laser radiation is terminated. For the soda lime glass, the decay of color centers is well described in terms of bimolecular annihilation reactions between electron and hole centers. Similar processes are also occurring in single crystal sodium chloride.

The extremely high power densities associated with femtosecond laser pulses allows for strong nonlinear interactions in nominally transparent materials. Defect production can be exploited to pattern these materials, often with feature sizes smaller than the nominal diffraction limit. Femtosecond lasers have long been exploited to study the kinetics of defect formation on subpicosecond time regimes.[17] If these lasers are to be exploited to modify and pattern transparent materials, the fate of these defects on time scales of nanoseconds to years soon becomes an important issue.

We can monitor the formation and fate of these defects measuring the intensity of a CW probe laser of the appropriate wavelength, focused through the center of a spot of material modified by a femtosecond laser. In our laboratory we use a Spectra Physics Hurricane laser system. The laser source is seeded with a Spectra Physics Mai Tai diode-pumped, mode-locked, Ti:Sapphire laser. After stretching, the pulse is amplified with a Ti:Sapphire regenerative amplifier, pumped with a Spectra-Physics Evolution diode-pumped, Q-switched, Nd:$LiYF_4$ laser. Subsequent recompression yields ~1 mJ pulses at 800 nm with a pulse width of 120 fs and a repetition rate of 1 kHz. Frequency doubled and tripled radiation was obtained by directing the 800-nm pulses through appropriately phase matched KDP crystals.

The output of the femtosecond laser source was focused with a 1-m focal length lens to form a 0.5 mm diameter spot on the sample. The output of a number of CW lasers was directed obliquely to the femtosecond laser and focused to a 0.1 mm diameter spot at the center of the femtosecond laser spot. This allowed transient, time resolved measurements of defect densities to be determined by use of a high speed photodiode. For maximum sensitivity, an input impedance of 1 MΩ was used in most experiments. Under these conditions, the RC time constant of the detection electronics was 130 μs. For fast time scale measurements at reduced

sensitivity, RC time constants of 10 ns could be obtained with an input impedance of 50 Ω.

3.1. SODA LIME GLASS

Absorption spectrum. The absorption spectrum of soda lime glass darkened with femtosecond laser radiation is similar to the absorption spectra of glass darkened with x- and γ-rays. Figure 5 displays the absorbance [$\log_{10}(I/I_0)$] of an as-received, 1-mm thick soda lime glass slide prior to irradiation, along with glass slides darkened with 800-nm femtosecond laser pulses and Cu Kα x-ray radiation from an x-ray diffraction unit. The spectral features in both darkened materials are stable on time scales of months. The broad absorption peaks centered at 460 and 620 nm are quite similar to absorption peaks observed in pure, x-irradiated soda silicate glasses[18,19] and soda aluminosilicate glasses.[20] Both femtosecond- and x-irradiated glasses also show enhanced absorption in the near UV due to trapped electron centers.[18,19] Color center formation in alkali silicates by exposure to ultrafast laser pulses at 850 nm has been previously reported and attributed to the response of the glass to the short wavelength component of supercontinuum light.[21] We find coloration occurring at laser intensities well below any white light formation and are able to explain defect formation as being initiated by multiphoton excitation.

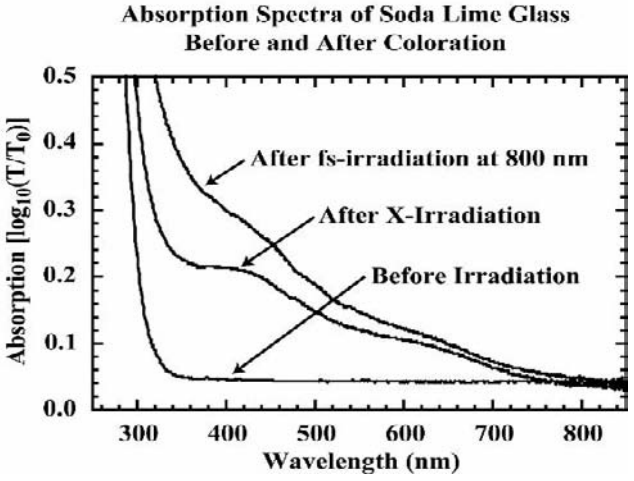

Figure 5. UV-VIS absorption spectra of untreated soda lime glass, of glass exposed to femtosecond 800-nm radiation, and glass exposed to Cu Kα x-rays. The broad peaks at 420 nm and 620 nm are attributed to H_2^+ and H_3^+ trapped-hole centers, respectively.

The broad absorption at 460 nm is conveniently probed with commercial CW diode lasers. In this work, the beam from a 473 nm diode laser was focusing through the center of the femtosecond laser spot. The transmitted intensity was measured with a fast photodiode.

Evolution of color center formation during fs irradiation. The coloration produced by femtosecond laser radiation is a strong function of pulse energy.[22] The transmission of 473-nm probe signal through an initially clear soda lime glass slide during exposure to 400-nm pulses (1 kHz repetition rate) appears in Fig. 6 for five pulse energies. Irradiation started at time $t = 0$ and continued for the duration of data collection. As one might expect, the transmission drops rapidly at high pulse energies and slowly at low pulse energies.

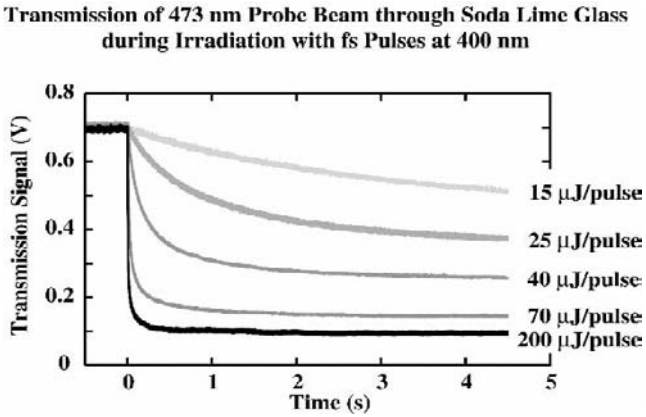

Figure 6. Transmission at 473 nm through soda lime glass during exposure to 400-nm femtosecond laser pulses at five selected pulse energies. One thousand femtosecond pulses per second were directed at the sample starting at time $t = 0$.

On the time scale of seconds, the transmission changes smoothly with time. High time-resolution measurements show clear, step-like drops with each laser pulse, especially at high pulse energies. Transmission measurements during the first five high-intensity femtosecond pulses incident on a soda lime glass slide on millisecond time scales (1 MΩ input resistance) are reported in Fig. 7(a). A nanosecond time scale measurement of the transmission signal during the first femtosecond pulse is shown in Fig. 7(b) (50 Ω input resistance). On both time scales, the initial drop in the transmission signal is rate limited by the time constant of the detection electronics. The nanosecond-scale transmission measurements show that the initial transmission drop is faster than about 10 ns. This is comparable to the 10 ns response of the electronics to a femtosecond pulse, shown in the inset of Fig. 7(b).

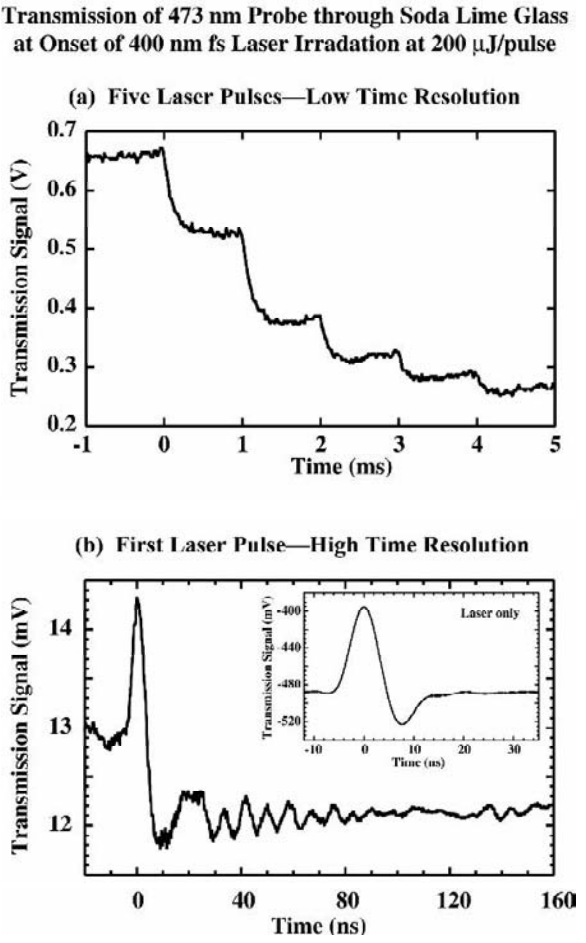

Figure 7. Transmission at 473 nm during exposure to 400-nm femtosecond pulses at 200 μJ/pulse. (a) Transmission during the first five laser pulses acquired with 1 MΩ input impedance (time resolution about 130 μs). (b) Average transmission signal acquired with an input impedance of 50 Ω (time resolution about 10 ns). The inset in (b) shows the signal due to scattered laser femtosecond laser light (no probe); scattered light is responsible for the peak in the transmission signal coincident with the laser pulse in (b).

Although defect creation is instantaneous on the time scale of these measurements, the transmission signal shows interesting kinetics between femtosecond pulses - provided that the total defect density is sufficiently high. The transmission drop following the first laser pulse in Fig. 7(a) is essentially permanent on the millisecond time scale. However, the transmission accompanying subsequent pulses drops immediately after the femtosecond pulse, then gradually rises until the next femtosecond pulse. Eventually an equilibrium is reached where the transmission drop produced

by a femtosecond pulse has entirely recovered just prior to the next femtosecond pulse.

The transmission rise between femtosecond pulses is especially evident in the microsecond time scale measurements of Fig. 8. After a few microseconds, transmission increases almost half-way back to its value before the femtosecond pulse. Significantly, the transmission rise or recovery is subsequently proportional to $t^{1/2}$, where t is the time since the most recent femtosecond pulse. This functional behavior is characteristic of bimolecular annihilation, where two defects (one mobile) annihilate when the mobile defect encounters its immobile partner. The $t^{1/2}$ time behavior in particular suggests that the mobile defect executes a random walk along a line or linear structure. As discussed below, this behavior is reasonable in light of the structure of alkali silicate glasses.

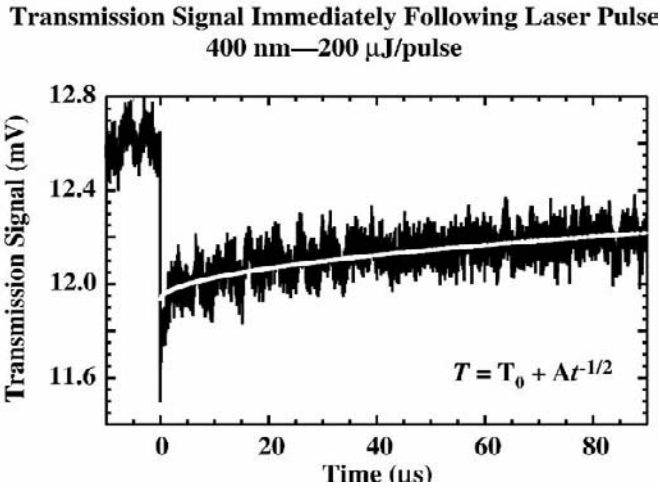

Figure 8. Average transmission signal acquired with an input impedance of 50 Ω (time resolution about 10 ns), showing the initial stages of transmission recovery following each pulse. The light line through the data shows a least squares fit of the data to a square-root decay.

Modeling transmission recovery. Transmission recovery continues for hundreds of seconds, as shown in Fig. 9. This particular sample was colored with 80,000 pulses of 800-nm femtosecond light, and was probed in the 620 nm absorption band with a 633-nm He:Ne laser. Here, time $t = 0$ corresponds to the onset of recovery, when the femtosecond laser beam was blocked. In contrast with the

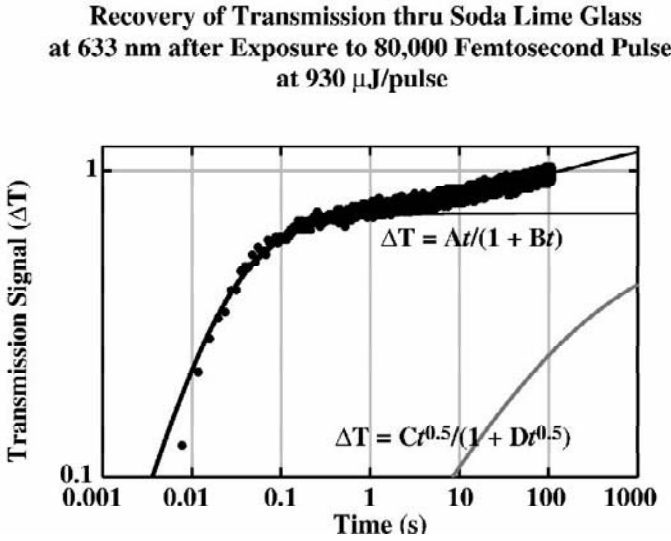

Figure 9. Recovery of the transmission signal after a darkening experiment plotted on a log-log scale. Darkening was achieved by exposure to 800-nm femtosecond laser radiation for 80 s with 1000 pulses per second at 930 μJ per pulse. The femtosecond laser beam was blocked at time $t = 0$ and remained blocked for the remainder of data collection. The signal at time $t = 0$ has been subtracted from each data point to emphasize the initially rapid recovery of the signal. The broad gray line shows the best fit of the data to a model incorporating Eqs. (2) and (5). This model represent the sum of two bimolecular annihilation processes, one where the mobile species is free to move in three dimensions and the other where the mobile species is confined to one dimensional structures.

transmission recovery on microsecond time scales, the recovery between 10 ms and 1 s is well described by bimolecular annihilation on a three dimensional lattice: the mobile defect is free to move in all three dimensions. We assume reactions of the form $A + B \rightarrow 0$, where the concentration of species A equals the concentration of species B. Typically, one assumes that one defect is mobile and performs a random walk on a lattice of L distinct sites, where some of the sites are occupied stationary recombination centers B. The probability (per unit time) of a walker encountering a recombination center is the product of the fraction of sites occupied by recombination centers (N/L), the average number of distinct sites visited by the walker per unit time S, and the total number of walkers (N). For uniform lattices (for example, cubic lattices where the jumping probability is identical for all pairs of adjacent sites) the average number of distinct sites visited by a walker per unit time is constant for all lattice dimensions $D > 2$. Then

$$\frac{dN}{dt} = -\left(\frac{N}{L}\right) S N = -\frac{S}{L} N^2 \quad (1)$$

The solution of this equation takes the form:

$$N(t) = \frac{N_0}{1 + C N_0 t} \quad (2)$$

If the mobile species is confined to structures of dimension *less* than two, the average number of sites per unit time visited by a walker is not constant. For instance, the average number of sites visited in a random walk along a 1-D line is proportional to $t^{1/2}$, because the walker spends much of its time visiting previously visited sites. Since the walker must have survived its passage through these previously visited sites, it is safe during subsequent visits to the same sites. In soda lime glass, some mobile defects may be confined to linear channels of sodium ions and their associated nonbonding oxygen centers. The existence of such channels is predicted by molecular dynamics simulations[23-27] and has been verified by x-ray diffraction[28] and magnetic resonance studies.[29]

Under these conditions, the probability of encountering new sites is proportional to the derivative of the total number of distinct sites visited, so $S = (S'/2)\, t^{-1/2}$, with S' a constant. The probability S can vary in similar ways if the mobile species encounters electron traps with a distribution of trap depths, where the mobile species spends a disproportionate time at sites with deep traps. If S(t) scales with the inverse square root of time, Eq. (1) becomes

$$\frac{dN}{dt} = \frac{-S' t^{-1/2}}{2L} N^2 \quad (3)$$

Equation (3) is readily solved by changing the variable of integration to $f = t^{1/2}$. Expressing N in terms of *f* yields:

$$\frac{dN}{df} = -\frac{S'}{L} N^2 \quad (4)$$

The solution of Eq. (4) is formally the same as the solution of Eq. (1), with $t^{1/2}$ replacing *t*. More generally, for dimensions less than two, the average total number of sites visited by a walker is proportional to $t^{D/2}$,[30] and

$$N(t) = \frac{N_0}{1 + C N_0 t^{D/2}} \quad (5)$$

where C = S'/L. This non-integral time behavior is often described as "fractal time."

The kinetics of transmission recovery in soda lime glass are well described in terms of recombination on 1-D and 3-D lattices, corresponding to terms with t^1 from Eq. (2) and $t^{1/2}$ in Eq. (5) (with D = 1). Extrapolating these equations to long times, using best fit parameters, suggests that approximately 30% of the defects present at the end of femtosecond irradiation are permanently stable. Physically, these defects constitute a separate population of defects that do not participate in the annihilation reactions described above. For instance, these defects may be physically isolated from mobile species.

In the short time limit, the $t^{1/2}$ term in Eq. (5) (for $D = 1$) dominates the t^1 term in Eq. (2). The curve fit parameters obtained from the data of Fig. 9 indicate that the $t^{1/2}$ term dominates at times less than a few microseconds. This is consistent with the early time behavior of the transmission recovery in Fig. 8, especially considering the vastly different experimental conditions employed in the two experiments.

3.2. SODIUM CHLORIDE

Darkening kinetics. Femtosecond pulses also color the alkali halides at modest pulse energies. The absorbance of a typical sodium chloride crystal before and after darkening by 400 nm femtosecond radiation is shown in Fig. 10. The broad F-center peak at 460 nm is well situated for probing at the 473 nm wavelength of the blue diode laser. The F-center consists of a alkali vacancy associated with a trapped electron. Thus the F-center site has the same nominal charge as the same site without the defect. F-center formation in the alkali halides has been extensively studied,[4,31-34] providing a wealth of information to use in the interpretation of new results. The other peaks in the absorption spectrum of Fig. 10 are attributed to M-centers (formed by two F-centers on adjacent sites) and V-centers (miscellaneous hole traps, often associated with impurities).

The progress of darkening during irradiation with 400-nm femtosecond pulses at four distinct pulse energies in illustrated in Fig. 11. As with soda lime glass, the rate of darkening is a strong function of pulse energy. At high pulse energies, the transmission at 473 nm quickly reaches an apparent minimum.

Model of transmission change during darkening. A model of the darkening process can be constructed by incorporating a defect source term into the equations for bimolecular annihilation. If the number of defects produced per laser pulse is the same for each laser pulse (= A), then N = N + A immediately after each pulse. The bimolecular annihilation reaction of

Eq. (1) operates between femtosecond pulses. In practice, it is convenient to work with more continuous functions, for example:

$$\frac{dN}{dt} = A - CN^2 \tag{6}$$

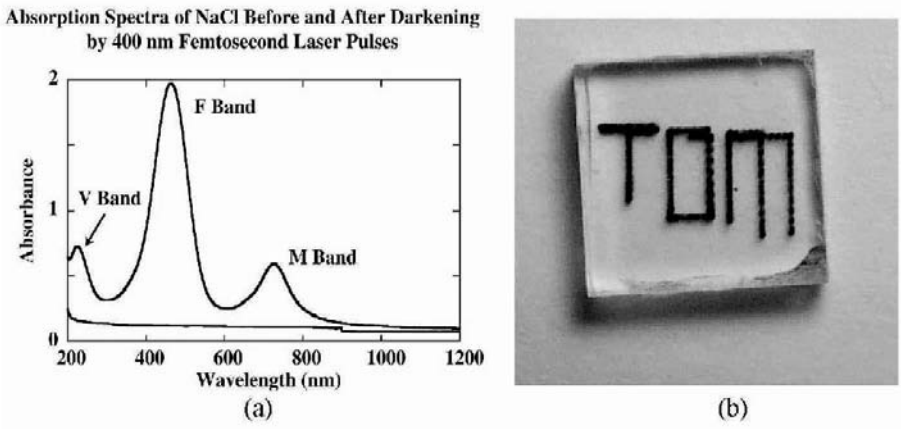

Figure 10. (a) Absorption spectra of a sodium chloride sample before and after darkening by 400-nm, femtosecond laser irradiation. (b) A *Professor Made* coloration of NaCl (the dots are single pulses) by scanning the laser beam by hand.

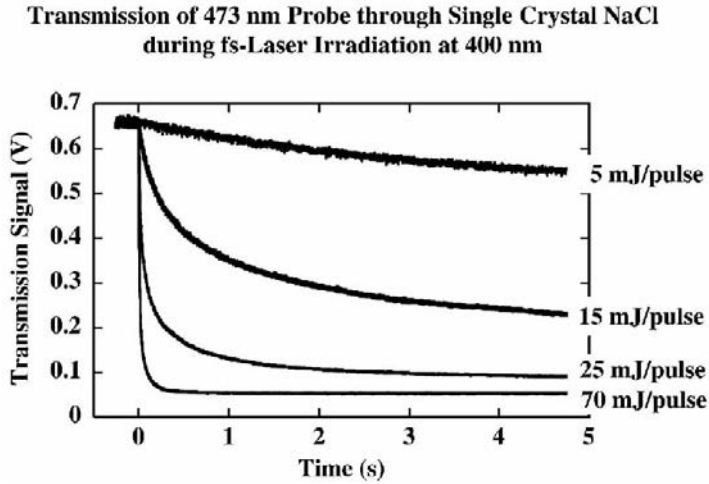

Figure 11. Transmission at 473-nm through single crystal sodium chloride during femtosecond laser irradiation at 400-nm at four different pulse energies.

The interpretation of the constants A and C in Eq. (8) is not straightforward due to the nature of the averaging process. Incorporating initial conditions [$N(t=0) = 0$], the solution can be expressed as:

$$N(t) = \sqrt{\frac{A}{C}}\tanh(\sqrt{AC}\,t) \tag{7}$$

Although this solution displays the correct behavior in the long time limit, the predicted initial rate of darkening is much faster than that the observed rate. A good fit to the experimental data is obtained by raising the time to a fractional power:

$$N(t) = \sqrt{\frac{A}{C}}\tanh(\sqrt{AC}\,t^{M}) \tag{8}$$

where M ≠ 1, i.e., fractal time. The need for fractal time in this continuum model may result treating discrete defect creation events (with each femtosecond pulse) as a continuous process. Models that incorporate defect creation and annihilation with each laser pulse are under construction and we hope to resolve this point soon.

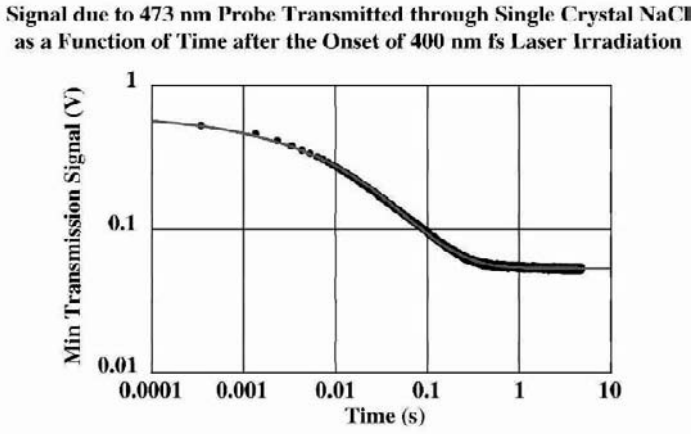

Figure 12. Log-log plot of the 473-nm transmission signal through single crystal sodium chloride during exposure to 400-nm, 70 μJ femtosecond pulses. The curve represents a least squares fit of Eq. (8) to the data, representing bimolecular annihilation where the mobile species is free to move in all three dimensions.

A log-log plot of a least squares fit of Eq. (8) to 473-nm transmission data acquired at a femtosecond pulse energy of 70 μJ is shown in Fig. 12. Equation 10 provides a good fit to the data over five orders of magnitude in time. Similar fits were obtained for pulse energies from 10 to 200 μJ.

Although the data are limited, the parameters corresponding to $(A/C)^{1/2}$ and $(AC)^{1/2}$ are consistent with defect production by a multiphoton process, where the defect production parameter A scales as a power of the pulse energy of at least two and C remains approximately constant. The power M in Eq. (8) is approximately 0.3 over this range of pulse energies. If this interpretation of A and C is correct, we should be able to fit data acquired at other pulse energies with the same C parameter; A should scale with the pulse energy to the third power (the expected pulse energy dependence).

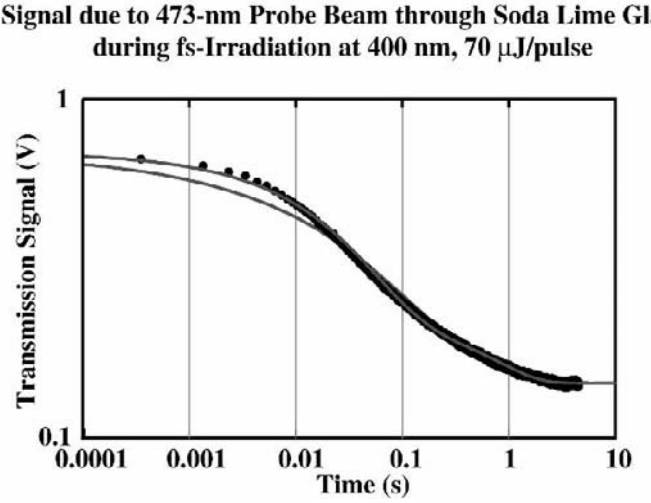

Figure 13. Log-log plot of the transmission at 473-nm through soda lime glass during exposure to 400-nm, 70-μJ, femtosecond pulses. The lower light line shows a least squares fit of Eq. (8) to the data. The upper light line shows a least squares fit of two terms corresponding to Eqs. (8) and (9), for the case M = 1.

Equation (8) is less successful at describing the darkening process in soda lime glass. A log-log plot of a least squares fit of Eq. (8) to typical transmission data during darkening is shown by the lower gray line in Fig. 13. The fits falls well below the data at times below 100 ms. If defect recombination evolves independently on 1-D and 3-D lattices, as suggested by the recovery of transmission after femtosecond irradiation, one might expect the darkening process to involve two independent processes as well. This would involve two defect densities, each with its own absorption and time evolution described by Eq. (8). Dimensionally, one expects the time exponent for a 3-D lattice to be twice the exponent for a 1-D lattice; that is, the time evolution of the defect density on the 1-D lattice would take the form:

$$N(t) = \sqrt{\frac{A'}{C'}}\tanh(\sqrt{A'C'}\,t^{M/2}) \quad (9)$$

Curve fits employing independent terms combining Eqs. (8) and (9) suggest that M is very close to one. A combined curve fit with M set to 1 is plotted in Fig. 13 (upper light curve, four free parameters) and provides good fit to the data at short times.

Although full understanding of defect production and annihilation in these materials during femtosecond irradiation is still lacking, a consistent picture is emerging in the case of soda lime glass. Models that treat defect annihilation in terms of bimolecular recombination operating independently on 3-D and 1-D sublattices provide a good description of the data. Physically, the 1-D sublattice would correspond to sodium-rich channels in this material. The situation is less clear in the case of sodium chloride. Preliminary data suggests that we may need to account for charge exchange among defects during femtosecond radiation to fully account for the darkening and recovery processes.

3.3. GRATING FORMATION

Creation of gratings inside the transparent materials by multiphoton nonlinear effects could have potential applications in integrated optics and photonics [20-22]. Highly nonlinear effects similar to the darkening in soda lime glass are often useful for pattering transparent materials. We can pattern a grating using this darkening mechanism with femtosecond, 800 nm laser pulses by splitting the beam into two equal intensity beams that are allowed to interfere at angle θ. Figure 14 shows the center and higher order spots out to fourth order produced when the 633 nm beam from a He:Ne laser is diffracted by a grating produced by the interference of two femtosecond, 800 nm laser beams converging at an angle θ=1.3˚. This geometry is expected to produce dark strips with spacing $\Lambda=\lambda/2\sin(\theta/2)$, where λ is the wavelength used to write the pattern. The predicted grating spacing is therefore Λ=35 μm. The diffraction pattern displayed in Fig.14 is consistent with Λ=36 μm, in agreement with the predicted value. The radiant intensity in the diffracted beams makes up 10.5% of the total intensity transmitted.

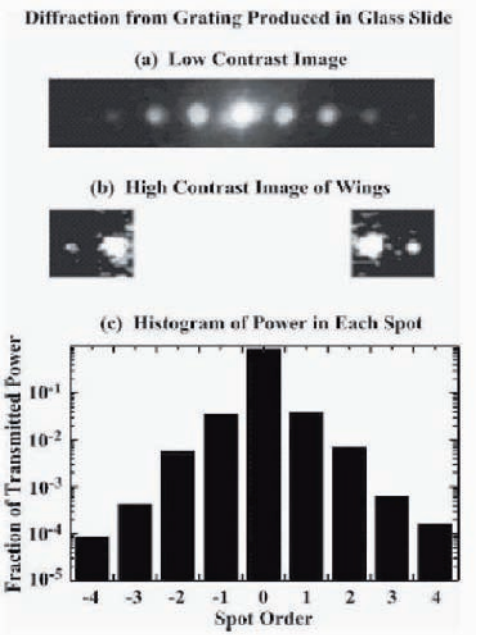

Figure 14. (a) Low contrast image of a diffraction pattern produced by the diffraction of a cw He:Ne beam from a grating produced in a soda lime glass slide by femtosecond pulses of 800 nm radiation. (b) High contrast image showing higher order spots. (c) Histogram of the fraction of the total transmitted power found in each spot of the diffraction pattern.

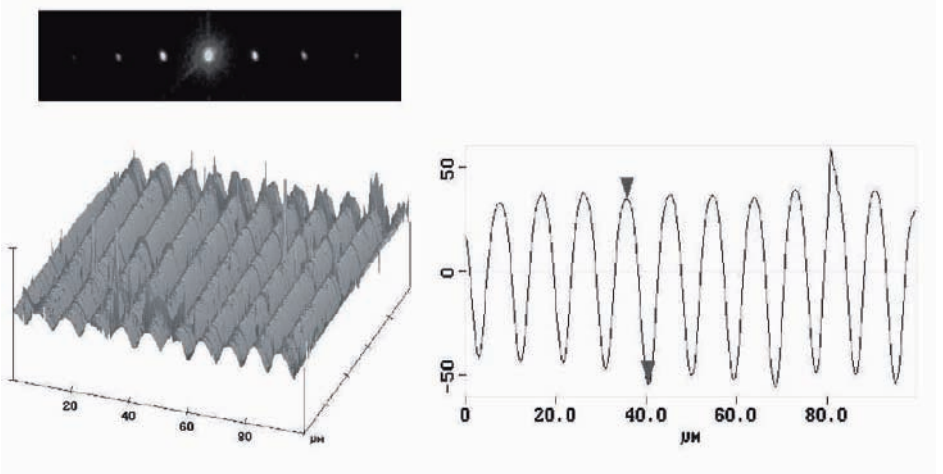

Figure 15. Grating structure formed on a DMP doped PMMA thick film exposed for ~ 1 second at 1kHz with 100 fs pulses at a wavelength of 400 nm. An image of the diffraction pattern generated by an incident He-Ne laser beam onto this surface at λ = 632 nm is also shown.

Nonlinear coupling to organic polymers can also be exploited to generate gratings with the two superimposed femtosecond laser beams. By doping PMMA (Poly(methyl methacrylate)) with an appropriate dye to enhance absorption at n photons, the grating formation is greatly enhanced. Fig. 15 shows an Atomic Force Micrograph of the PMMA topography showing a periodic structure with a peak to valley distance of ~85 nm. This particular grating was formed in less than a second of exposure at 400 nm light with a single photon absorbing dye, DMP --dicyanomethylene)-2-methyl-6-(4-dimethylaminostyryl)-4H-pyran; a similar grating (with corresponding larger spacing) was formed by two photon absorption at 800 nm incident wavelength.

4. Other Areas of Interest

Fundamental studies that focus on improvement, optimization, and extension of the use of lasers for processing are wide ranging and it is impossible to cover them all. I simply want to list a few general areas and examples for the packaging and laser processing community to consider. References given in the cited articles are extensive.

Type of Study	Goal	Example
Wavelength dependence of laser materials interactions.	Determine the mechanisms and understand why different wavelengths behave as they do.	Defects vs. intrinsic absorption; [35]Direct coupling into vibrational modes of polymers, crystalline solids;[36] near surface absorption vs. bulk absorption—mechanical consequences (melting vs. fracture);[37] particulate formation.[38]
Role of Chemical Environment on Material Removal rates; surface modification	Seeking synergisms and understanding of how surrounding reactive gases and liquids can cause enhanced interactions.	The role of water on laser decomposition and desorption;[39] surface microstructuring,[40] reactive etching in liquids.[41]

Continued:

Type of Study	Goal	Example
Adding absorbers to materials	Addition of strong absorption centers and understanding the absorbed energy enhances the sensitivity of the laser material interaction.	Increasing defect densities;[42] adding dyes to polymers to inhance absorption;[43] improved patterning.[44]
Adding exothermicity to solids	Using chemistry to design exothermic decomposing solids to improve rates and quality of ablation.	Use of polymers with functional groups tailored for rapid and energetic decomposition.[45-47]
Interesting simulations and mechanistic studies.	Using basic physics and chemistry to understand processes of interest to ablation and fabrication.	Molecular dynamics studies of ablation;[48] ablation mechanisms;[49] laser cleaning.[50-52]

Another consideration in the use of lasers for processing has to do with analysis and diagnostics. As more sophistication in terms of characterization and monitoring what is happening during a laser materials process, we point out that there are a number of techniques where (primarily) lasers can be used to probe the material and near surface region, even in real time. These Analysis techniques include:

- real time LIBS (Laser Induced Breakdown Spectroscopy)
- photothermal deflection
- black-body analysis
- interferometry
- ellipsometry
- non-linear optical spectroscopy
- plasma resonance spectroscopy
- roughness (laser scattering)
- confocal microscopy
- spectroscopy (Raman, Reflection, Electron/X-ray, EDAX).

Often such signals can be used to determine end-points on various material removal applications.

Finally, we point out that the use of lasers in biology and medicine is expanding at an enormous rate. One of the major reasons is that health

issues are highly valued by society so that funds for any potential diagnostic tool or cure finds support. The developments in the use of lasers in medicine have relied strongly on previous work on ceramics, polymers, and metals that fall into the traditional laser materials interactions domain. Nevertheless, because of the intensity of their activity, it would be wise to watch developments in the bio-areas and when appropriate, take back any good ideas. Some of the areas where biological and medical interests meet materials that may be relevant include the following:

- surgery - cellular; sub-cellular level; ultrafast; MUST minimize damage
- use of laser tweezers - particle manipulation
- fluorescent tags (perhaps in polymer composites)
- laser formation of nanoparticles; micromachining
- water (bubbles, jets, shockwaves) - use of other fluids
- optical diagnostics (non-invasive photodiagnostics)
- use of cryogens (sprays that cool while laser heats)
- tissue welding (bonding at buried interfaces)
- reshaping tissue (e.g., cartilage can be molded and shaped at 60 C)
- modeling of complex systems (skin, eye, blood vessels)
- field enhancement techniques (use of metal nanotips to enhance E fields)
- cauterizing
- photothermolysis
- photodynamic therapy
- removal of tumors, e.g., on skin, in bronchi, and esophagus
- fluorescence microscopy; two photon microscopy; second harmonic generation imaging
- medical diagnostics
- optical coherence tomography

Other areas of technology that are places to watch for new ideas relevant to are the Micro-Electro-Mechanical Structures (MEMS) and Nanotechnology arenas. In a variety of applications, processing and packaging will necessarily follow the trends to go to smaller and smaller dimensions. Thus, fabrication in several domains will clearly point in the direction of manipulating and generating features that eventually will challenge our usual approaches involving refractive optics that are limited by the wavelength of light.

5. Conclusions

The use of lasers will continue to be increased for processing and biomedical applications and of course in biological research. As the requirements for precision, quality, and processing/diagnostic speeds intensify, physical and chemical understanding will aid in making desired progress. As usual, practical needs are leading our understanding, simulation, and modeling capability. The reason is primarily the complexity of the structures, mix of materials, surface and bulk heterogeneities, and the presence of interfaces that make it challenging. Obtaining all of the needed optical, thermal, and mechanical constants for these models can also be difficult. Motivation is highest (as seen, for example in the use of lasers in medicine) where high value processes are involved. Where high value arises, "the experimentalists and simulators will come."

Acknowledgments

The author would like to thank Steve Langford and Sergei Avanesyan Washington State University, and Stefano Orlando, CNR-IMIP/PZ, Tito Scalo, Italy for their assistance. This work was supported in part by the U.S. Department of Energy under Grant DE-FG03-98ER14864 and by the National Science Foundation KDI Grant DMR-9980015.

References

1. Tam, A. C.; Do, N.; Klees, L.; Leung, P. T.; Leung, P. W., *Optics Lett.* 1992, *17*, 1809.
2. Tam, A. C.; Leung, W. P.; Zapka, W.; Ziemlich, W., *J. Appl. Phys.* 1992, *71*, 3515-3523.
3. Tam, A. C.; Park, H. K.; Grigoropoulos, C. P., *Appl. Surf. Sci.* 1998, *127-129*, 721-725.
4. Itoh, N.; Stoneham, A. M., *Materials Modifications by Electronic Excitation*. Cambridge University Press: New York, 2001.
5. Bäuerle, D., *Laser Processing and Chemistry*. 3rd ed.; Springer: Berlin, 2000.
6. Houle, F. H.; Hinsberg, W. D., *Appl. Phys. A* 1998, *66*, 143.
7. Richardson, H. H.; Hickman, Z. N.; Govorov, A. O.; Thomas, A. C.; Zhang, W.; Kordesch, M. E., *Nano Lett.* 2006, *6*, 783-788.
8. Krüger, J.; Kautek, W., *Appl. Surf. Sci.* 1996, *96-98*, 430-438.
9. Liu, X.; Du, D.; Mourou, G., *IEEE J. Quantum Electron.* 1997, *33*, 1706-1716.
10. Feit, M. D.; Rubenchik, A. M.; Kim, B.-M.; Silva, L. B. D.; Perry, M. D., *submitted to Appl. Surf. Sci.* 1998.
11. Rudolph, P.; Bonse, J.; Krüger, J.; Kautek, W., *Appl. Phys. A* 1999, *69*, S763.
12. Bonse, J.; Baudach, S.; Kruger, J.; Kautek, W.; Lenzner, M., *Appl. Phys. A* 2002, *74*, 19.

13. Williams, R. M.; Beck, K. M.; Joly, A. G.; Dickinson, J. T.; Hess, W. P. In *Pulse-width influence on laser induced desorption of positive ions from ionic solids*, Proc. SPIE Laser Applications in Microelectronic and Optoelectronic Manufacturing IV, San Jose, CA, 1999; Sugioka, J. J. D. H. H. E. W. K. K., Ed. SPIE: San Jose, CA, 1999; pp 37-44.
14. Beck, K. M.; Joly, A. G.; Hess, W. P., *Surf. Sci.* 2000, *451*, 166-173.
15. Hess, W. P.; Joly, A. G.; Beck, K. M.; Williams, R. M.; Dickinson, J. T., *Proceedings of the Fifth International Conference on Laser Ablation (COLA '99), Göettingen, July 19-23, 1999, edited by J. S. Horowitz, H.-U. Krebs, K. Murakami, and M. Stuke* 2000, *69*, S389-S393.
16. Chichkov, B. N.; Momma, C.; Nolte, S.; Alvensleben, F. v.; Tünnermann, A., *Proceedings of the Fifth International Conference on Laser Ablation (COLA '99), Göettingen, July 19-23, 1999, edited by J. S. Horowitz, H.-U. Krebs, K. Murakami, and M. Stuke* 1996, *63*, 109-115.
17. Bloembergen, N., *Rev. Mod. Phys.* 1999, *71*, S283-S287.
18. Mackey, J. H.; Smith, H. L.; Halperin, A., *J. Phys. Chem. Solids* 1966, *27*, 1759-1772.
19. Cohen, A. J.; Janezic, G. G., *Phys. Status Solidi A* 1983, *77*, 619-624.
20. Sigel, G. H., Jr., *J. Non-Cryst. Solids* 1973/74, *13*, 372-398.
21. Efimov, O. M.; Glebov, L. B.; Grantham, S.; Richardson, M., *J. Non-Cryst. Solids* 1999, *253*, 58-67.
22. Lonzaga, J. B.; Avanesyan, S. M.; Langford, S. C.; Dickinson, J. T., *J. Appl. Phys.* 2003, *94*, 4332-4340.
23. Soules, T. F., *J. Chem. Phys.* 1979, *71*, 4570-4578.
24. Mitra, S. K.; Hockney, R. W., *Philos. Mag. B* 1983, *48*, 151-167.
25. Murray, R. A.; Ching, W. Y., *J. Non-Cryst. Solids* 1987, *94*, 144-159.
26. Newell, R. G.; Feuston, B. P.; Garofalini, S. H., *J. Mater. Res.* 1989, *4*, 434-439.
27. Huang, C.; Cormack, A. N., *J. Chem. Phys.* 1990, *93*, 8180-8186.
28. Greaves, G. N.; Fontaine, A.; Lagarde, P.; Raoux, D.; Gurman, S. J., *Nature* 1981, *293*, 611-616.
29. Dupree, R.; Holland, D.; Williams, D. S., *J. Non-Cryst. Solids* 1986, *81*, 185-200.
30. Zumofen, G.; Blumen, A.; Klafter, J., *J. Chem. Phys.* 1986, *84*, 6679-6686.
31. Seitz, F., *Rev. Mod. Phys.* 1954, *26*, 7-94.
32. Fowler, W. B., *Physics of Color Centers*. Academic Press: Boston, 1968.
33. Sonder, E.; Sibley, W. A., Defect creation by radiation in polar crystals, In *Point Defects in Solids*, Crawford, J., James H.; Slifkin, L. M., Eds. Plenum: New York, 1972; pp 201-290.
34. Itoh, N., *Adv. Phys.* 1982, *31*, 491-551.
35. Lippert, T.; Nakamura, T.; Niino, H.; Yabe, A., *Appl. Surf. Sci.* 1997, *109-110*, 227.
36. Bubb, D. M.; Papantonakis, M. R.; Horwitz, J. S.; Haglund, R. F.; Toftmann, B.; Mcgill, R. A.; Chrisey, D. B., *Chem. Phys. Lett.* 2002, *352*, 135.
37. Langford, S. C.; Alexander, M. L.; Young, J. S.; Dickinson, J. T., *manuscript in preparation* 2006.
38. Webb, R. L.; Dickinson, J. T.; Exarhos, G., *Appl. Spectrosc.* 1997, *51*, 707-717.
39. Langford, S. C.; Dawes, M. L.; Dickinson, J. T., *Appl. Surf. Sci.* 1998, *127-129*, 81-87.
40. Pedraza, A. J.; Fowlkes, J. D.; Jesse, S.; Mao, C.; Lowndes, D. H., *Appl. Surf. Sci.* 2001, *168*, 251.
41. Wang, J.; Niino, H.; Yabe, A., *Appl. Phys. A* 1999, *69*, S271.
42. Dickinson, J. T., Low fluence laser desorption and plume formation from wide bandgap crystalline materials, In *Experimental Methods in Physical Sciences*, Miller, J. C.; Haglund, R. F., Eds. Academic Press: New York, 1998; Vol. 30, pp 139-172.

43. Lippert, T.; Webb, R. L.; Langford, S. C.; Dickinson, J. T., *J. Appl. Phys.* 1999, *85*, 1838-1847.
44. Preuss, S.; Stuke, M., *Appl. Surf. Sci.* 1993, *69*, 253.
45. Lippert, T.; Stebani, J.; Ihlemann, J.; Nuyken, O.; Wokaun, A., *J. Phys. Chem.* 1993, *97*, 12296-12301.
46. Lippert, T.; Langford, S. C.; Wokaun, A.; Savas, G.; Dickinson, J. T., *J. Appl. Phys.* 1999, *86*, 7116-7122.
47. Lippert, T.; Dickinson, J. T., *Chem. Rev.* 2003, *103*, 453-486.
48. Zhigilei, L. V.; Garrison, B. J., *Proceedings of the Fifth International Conference on Laser Ablation (COLA '99), Göettingen, July 19-23, 1999, edited by J. S. Horowitz, H.-U. Krebs, K. Murakami, and M. Stuke* 1999, *69*, S75.
49. Gamaly, E. G.; Rode, A. V.; Perrone, A.; Zocco, A., *Proceedings of the Fifth International Conference on Laser Ablation (COLA '99), Göettingen, July 19-23, 1999, edited by J. S. Horowitz, H.-U. Krebs, K. Murakami, and M. Stuke* 2001, *73*, 143.
50. Zhou, X.; Imasaki, K.; Furukawa, H.; Umino, H.; Sakagish, K.; Nakai, S.; Yamanaka, C., *Optics and laser technology* 2001, *33*, 189-194.
51. Wang, X., *Journal of physics. D, applied physics* 2005, *38*, 1805-1823.
52. Zheng, L.; Lambropoulos, J. C.; Schmid, A., *J. Non-Cryst. Solids 351*, 3271-3278.

ATTOSECOND CONTROL OF ELECTRONS – THE BASIS OF ATTOSECOND SCIENCE

ANDRÉ D. BANDRAUK*, SZCZEPAN CHELKOWSKI, GENNADY L. YUDIN
Laboratoire de Chimie Théorique, Faculté des Sciences, Université de Sherbrooke, Sherbrooke, Québec, J1K 2R1, Canada

Abstract. Numerical solutions of the time-dependent Schrödinger equation for a 1D model non-Born-Oppenheimer H_2^+ are used to illustrate the nonlinear nonperturbative response of molecules to intense $(I \geq 10^{13} W/cm^2)$, ultrashort $(t < 10\, fs)$ laser pulses. Molecular high-order harmonic generation (MHOHG) is shown to be an example of such response and the resulting nonlinear photon emission spectrum is shown to lead to the synthesis of single *attosecond* (10^{-18}s) pulses. Application of such ultrashort pulses to the H_2^+ system results in localized electron wave packets whose motion can be detected by asymmetry in the photoelectron spectrum generated by a subsequent probe attosecond pulse, thus leading to measurement of electron motion in molecules on the attosecond time scale. Such attosecond evolution of electron motion is shown to be observable and controllable by using "chirped" attosecond pulses thus leading to a new science: "Attosecond science".

Keywords: Time-dependent Schrödinger equation, ultrashort laser pulses, molecular high-order harmonic generation, attosecond pulses, attosecond science

* *Correspondence to:* A. Bandrauk; e-mail: andre.bandrauk@usherbrooke.ca
Canada Research Chair in Computational Chemistry and Photonics

J.J. Dubowski and S. Tanev (eds.), Photon-based Nanoscience and Nanobiotechnology, 31–54.

1. Introduction

Advances in current laser technology allow experimentalists access to new laser sources for examining molecular structure and dynamics on the natural time scales for atomic (vibrational) motion, femtosecond (fs = 10^{-15}s). These new sources are ultrashort ($t_p \leq$ 10 fs) and intense ($I \geq 10^{14} W/cm^2$).[1] Such pulses lead to a new regime of laser matter interaction, the nonlinear, nonperturbative regime. Thus, because the atomic unit (au) of electric field strength $E_0 = e/a_0^2$ = 5 X 10^9 V/cm (a_0 = 1 au = 0.0529 nm) corresponds to an au of intensity $I_0 = cE_0^2/8\pi$ = 3.5 X 10^{16} W/cm^2, laser intensities approaching I_0 have led to the discovery of new nonlinear phenomena in laser-atom experimental and theoretical studies,[2] such as ATI (above threshold ionization) the multiphoton equivalent of single-photon photoionization; and HOHg (high-order harmonic generation).[3]

The study of interactions of intense ultrashort laser pulses with molecules is a relatively new science,[4-7] with the first discovery of nonlinear nonperturbative laser-molecule interaction leading to a new concept, laser-induced molecular potentials (LIMPs)-predicted as early as 1981.[5] At the very high intensities now available, $I \geq 10^{14}$ W/cm^2, one now must consider dissociative ionization so that one must deal with bound-continuum transitions both in the electronic and nuclear Hilbert space. Multiphoton nonperturbative transitions in the nonlinear Hilbert space describing photodissociation only via LIMPs can be treated adequately, using a coupled equations approach based on the dressed molecule representation.[4] Inclusion of ionization involves treating numerically the complete field-electron-nuclear non-Born-Oppenheimer problem. This has been exactly solved recently for the 1D H_2^+ system,[8] leading to the first calculation of nonlinear molecular photo electronic spectra or ATI[9] and the concomitant Coulomb explosion (CE) spectra.[10,11] This benchmark calculation has led to a new method of measuring nuclear wave functions by laser Coulombs explosion imaging (LCEI).[10,11]

Electronic interaction with radiation in molecules differs from that of atoms because of the large delocalization of electrons in the former. As early as 1939, Mulliken[12] explained intense absorption bands due to large transition moments in molecules. Thus, in H_2^+, the electronic transition moment between the HOMO, $1\sigma_g$, and LUMO, $1\sigma_u$, $\mu(R) = \langle 1\sigma_g | z | 1\sigma_u \rangle = R/2$, which leads to large nonperturbative radiative interactions at large distances, $V(R) = RE/2$, in a field of strength E. As an example, 1 au of field strength leads to 1 au = 27.2 eV of. radiative interaction at the equilibrium distance R $\cong$ 2 au in H_2^+. Thus the combination of large electronic transition moments in symmetric molecules and current high laser intensities result

readily in nonperturbative radiation-molecule interactions. Such effects lead to LIMPs[5-7] and charge resonant enhanced ionization (CREI), whereby molecular ionization rates can exceed that of atomic fragments by orders of magnitude at large critical internuclear distance $R_c \cong 2R_e$, where R_e is the equilibrium distance.[13-15] Quasistatic models of atom-laser field interaction[2] have been extended to nonperturbative laser-molecule inter-actions with the tunneling ionization of Stark-displaced LUMOs leading to a simple consistent explanation of CREI and CE in molecules for one- or odd-electron molecular systems.[13-15]

Exact numerical solution of tow-electron molecules H_2[16,17] and H_3^+[18], in intense laser fields in the Born-Oppenheimer approximation (static nuclei) have shown the importance of the *ionic* state, e.g., H^+H^- in H_2, predicted by Hertzberg to exist in the UV spectral region[19] , as *doorway* states for CREI in these systems. Recently the ionic state of O_2, O^+O^-, has been identified by ZEKE experiments.[20] Such states have large dipole moments equal to the internuclear distance *R*, and thus can lead to large radiative interactions, *V(R) = ER*, exceeding molecular dissociation energies at current laser intensities. Studies of molecules in the nonlinear nonperturbative regime of molecule –radiation interaction is thus a new science requiring nonperturbative theories and numerical methods to treat laser control and manipulation of molecules in this regime.[21]

A seminal idea emanating from simple quasistatic models of electron ionization in atoms is the possibility of *recollision* of the ionized electron with its parent ion.[3,23] The returning energy of the electron at the nuclei can be shown to satisfy a simple law that explains the maximum energy of harmonics emitted by such a recolliding electron,

$$N_m \hbar\omega = I_p + 3.17U_p\,, \tag{1}$$

where N_m is the maximum harmonic order, I_p is the ionization potential,and U_p is the ponderomotive or oscillatory energy of an electron of mass *m* in a pulse of frequency ω and intensity *I:*

$$U_p(au) = I/4m\omega'^2 = 3.4x10^{21} I(W/cm^2\lambda^2(nm) \tag{2}$$

The corresponding field-induced displacement of such an ionized electron is given by the expression

$$\alpha(au) = eE/m\omega^2 = 2.4x10^{-12}\left[I(W/cm^2)\right]^{1/2}\lambda^2(nm).$$

Thus at an intensity $I = 10^{14}$ W/cm^2 and wavelength λ =1064 nm, U_p = 10.5 eV and α = 1.2 nm. We have shown that collision of ionized electrons with neighboring ions in molecules can lead to even larger harmonic orders

with photon energies of $6U_p$ up to $12U_p$, thus extending the recollision energy, cut-off law (1).[24]

Using ultrashort pulses, $t \leq 5$ fs, results in continuum HOHG in the region of the cut-off law (1) from which, by selecting a slice of the spectrum, one can synthetize *attosecond* (asec) pulses. First experimental results on the production and measuremnts of a 650 asec soft X-ray pulse from high intensity ionization of Ar atoms was reported in Refs.[25,26] This opens new possibilities for studying and controlling electron dynamics in atoms and molecules on asec times scales. We have recently shown that asec pulses can be used to measure the absolute electric field of few-cycle laser pulses[27] and asec *control* of ionization and HOHG in molecules to increase HOHG intensities and thus create a new single X-ray, UV pulse as short as 250 asec.[28] We illustrate in the present paper from numerical solutions of the time-dependent Schrödinger equation (TDSE) for a 1D H_2^+ model with full electron-nuclear dynamics, i.e., from non-Born-Oppenheimer simulations, our proposed methodology for producing asec pulses from a molecular medium. Finally, we demonstrate from solutions of the TDSE how a pump-probe experiment of the photoionization of H_2^+ using asec pulses can allow one to study the evolution of the movement of localized electron wavepackets, thus leading to a new attosecond molecular spectroscopy. A pump-probe excitation of atomic states in the asec time regime has been recently demonstrated.[29]

2. Classical Recollision Model

Before presenting quantum mechanical results on the one-electron H_2^+ molecule, we present an analysis of the simple recollision model in the presence of the electromagnetic field[23] which predicts the maximum energy, equation 1), for HOHG in atoms.

We solve the classical equation of motion of an electron in a laser field E(t):

$$\frac{d^2z}{dt^2} = \frac{dv}{dt} = -E_0 \cos(\omega t) \ , \quad v(t_0) = v_0 , \quad z(t_0) = z_0 = 0$$

Its solution is:

$$v(t_f) = v_0 + X \sin(\varphi_0) - X \sin(\varphi_f) \ ,$$

$$z(t_f) = (v_0 + X \sin(\varphi_0))(\varphi_f - \varphi_0)/\omega + \frac{X}{\omega}[\cos(\varphi_f) - \cos(\varphi_0)] \qquad (3ab)$$

$$\text{where } X = E_0/\omega \ , \ \varphi_0 = \omega t_0 \ , \ \varphi_f = \omega t_f$$

The final velocity is maximum (for $v_0>0$) when $\varphi_0=\pi/2$ and $\varphi_f=3\pi/2$, then it is equal to $v_f=v_0+2$ X. If $v_0=0$ the maximum energy is:

$$v_f^2/2 = 2*X^2 = 8\,U_p$$

where $U_p=X^2/4$ is the ponderomotive energy. This maximum energy can be reached only at $z\neq 0$,[24] when

$$|z(t_f)| = \frac{E_0}{\omega^2}(2n-1)\pi \quad , \text{with } n=1,2,..$$

It was shown by Corkum[23] that if the electron initial velocity is $v_0=0$, then the maximum energy that the electron can acquire at its return (i.e. when $z(t_f)=0$) is $E_f = v_f^2/2 = 3.17314U_p$. We show below that this result is also valid for the nonzero initial velocity v_0, i.e. we show that allowing a nonzero initial velocity v_0 leads to the same maximum energy of the electron at its return, i.e. to $E_f=3.17314U_p$, which occurs at $v_0=0$.

We impose the condition of the electron return $z(t_f)=0$; thus using eq.(3b) we can express v_0 as function of φ_0 and φ_f , or (as it appears to be more convenient), as function of φ_0 and $\Delta=\varphi_0-\varphi_f$ (which is the relative phase between the initial and final times):

$$\begin{aligned} &\frac{v_0}{X} = \beta_1\cos(\varphi_0)+\beta_2\sin(\varphi_0) \ , \\ &\beta_1 = \frac{1-\cos(\Delta)}{\Delta} \ , \ \beta_2 = \frac{\sin(\Delta)}{\Delta}-1 \ . \end{aligned} \tag{4}$$

After inserting (4) into (3a) we get the following expression for the electron velocity at the return time:

$$\begin{aligned} &\frac{v_f}{X} = f(\Delta,\varphi_0) = \alpha_1\cos(\varphi_0)+\alpha_2\sin(\varphi_0), \\ &\alpha_1 = \frac{1-\cos(\Delta)}{\Delta} - \sin(\Delta) \ , \ \alpha_2 = \frac{\sin(\Delta)}{\Delta}-\cos(\Delta) \end{aligned} \tag{5}$$

Eq. (5) gives are all possible return velocity with **Non-zero v_0.** For any value of Δ, φ_f v_0 can be calculated from (4). We note that $v_f/X=f(\Delta,\varphi_f)$ is the function of 2 independent variables Δ, φ_f. We find extrema of $f(\Delta,\varphi_f)$ by requiring its partial derivatives to be zero, which leads us to the two equations determining the coordinates of the extrema of the function $f(\Delta,\varphi_f)$:

$$\frac{\partial f}{\partial \Delta} = \alpha_1' \cos(\varphi_0) + \alpha_2' \sin(\varphi_0) = 0 \ , \qquad \frac{\partial f}{\partial \varphi_0} = -\alpha_1 \sin(\varphi_0) + \alpha_2 \cos(\varphi_0) = 0 \ , \tag{6-7}$$

where α_1' and α_2' are derivatives of $\alpha_1(\Delta)$ and of $\alpha_2(\Delta)$. After elimination of φ_0 from (7) we get from (6) the following equation determining Δ :

$$F(\Delta) = 2 - 2\Delta \sin(\Delta) + \cos(\Delta)\,(\Delta^2 - 2) = 0 \tag{8}$$

The function $F(\Delta)$ has following zero's: Δ_1=1.30048 π, Δ_2=2.4265 π, Δ_3=3.435 π ,Δ_4 =4.458 π, Δ_5 =5.461 π, etc. To each of these values , using (7) , we find following φ_0's (using the relation: $\varphi_0 = \mathrm{atan}(\alpha_2(\Delta)/\alpha_1(\Delta))$:

0.097607 π, 0.0367498 π, 0.032395 π, 0.02079 π, 0.0193425 π .

The first corresponds the maximum value of v_f =1.2595905 X, i.e. to the kinetic energy at the electron return: v_f^2 /2=3.1731365668 Up , all next extrema correspond to lower energies: E_f= 1.5423 Up , 2.4043 Up , 1.734 Up ,2.246 Up. At all of them, v_0 is zero, as we show below.

For large Δ the final velocity simplifies to:

$$\frac{v_f}{X} = f(\Delta, \varphi_0) \cong -\sin(\Delta + \varphi_0) = -\sin(\varphi_f) \ , \quad \text{for} \quad \Delta >> 1 \tag{9}$$

This means that for large delays $\Delta >> 1$ the final kinetic energy at the electron return to z=0 never exceeds 2Up . Thus we have proved that the electron final energy at the electron return never exceeds 3.173137 Up, even when one allows the non-zero initial velocity v_0. This proof is supported by 3-D graphs of the function v_f shown in Fig.2 in Ref.[30] This Figure shows all possible return velocities v_f with non-zero v_0 and we clearly see that the final velocity never exceeds 1.2586 X value which leads to the energy 3. 173137 U_p at the electron return.

Next, we show that v_0 is 0 at any extremum of the function v_f /X= $f(\Delta,\varphi 0)$, defined by $\partial f / \partial \varphi_0 = \partial f / \partial \Delta = 0$. First we find from (7) that $\tan(\varphi_0)=\alpha_2/\alpha_1$, next we insert it into (4), and thus we get:

$$\frac{v_0}{X} = \cos(\varphi_0)\left[\frac{1-\cos(\Delta)}{\Delta} + \left(\frac{\sin(\Delta)}{\Delta} - 1\right)\frac{\alpha_2}{\alpha_1}\right] = \frac{\cos(\varphi_0)}{\alpha_1 \Delta^2} F(\Delta) \ . \tag{10}$$

Note that v_0 is proportional $F(\Delta)$, therefore we conclude from (8) that at any extremum of the function $f(\Delta,\varphi_0)$ v_0 is zero. In other words we have proven that highest energies at the electron return occurs when v_0=0.

Similarly, to find maximum possible initial velocity v_0 , we seek extrema of function $h(\Delta,\varphi_0)= v_0 / X$:

$$\frac{\partial h}{\partial \Delta} = \beta_1' \cos(\varphi_0) + \beta_2' \sin(\varphi_0) = 0 ,$$
$$\frac{\partial h}{\partial \varphi_0} = -\beta_1 \sin(\varphi_0) + \beta_2 \cos(\varphi_0) = 0 , \qquad (11\text{-}12)$$

These conditions lead to $F(\Delta) = 0$ (see eq. (8)), i.e. to the same condition as in the case of the extrema of v_f / X . Thus extrema of the function $h(\Delta,\varphi_0)$ occur at same values of delta: Δ_1 , Δ_2 , etc., as in the case of v_f , but at different φ_0 values, which can be calculated from (12):

$$\varphi_0 = \mathrm{atan}(\beta_2(\Delta)/ \beta_1(\Delta)). \qquad (13)$$

We list below the value of Δ_i obtained from (8) and in the next line the corresponding values of φ_0 obtained with the help of (13), followed by the corresponding values of v_0' :
Δ_i: 1.30048 π, 2.4265 π, 3.435 π, 4.458 π, 5.461 π,
φ_0's: - 0.40024 π , -0.46325 π , -0.4676 π, -0.4788 π , -0.4803 π,
v_0 /X: 1.25959, 0.87815 , 1.09642, 0.931285, 1.05987.

We conclude that we have always:

$$|v_0| < v_{max} = 1.2595905 \ X = 1.2595905 \ E_0/\omega. \qquad (14)$$

In other words, if one initializes the classical trajectory with the initial velocity exceeding v_{max} the electron will never return to its starting point z=0 (this is true for all possible initial phases φ_0), and consequently, no harmonic generation occurs for high initial velocities $|v_0|$. Note that v_{max} coincides with the maximum return velocity found by Corkum (1993) and derived here from (6), (7). However, the initial and final phases φ_0, φ_f differ. We explain the above coincidence and difference in the following way: we know that the electron initialized with $v_0=0$ at $\varphi_0 \approx 0.1\ \pi$ returns to the initial z=0 at $\varphi_f \approx 1.4\ \pi$ with the velocity $v_f = 1.2596X$. Similarly, because of symmetry (consisting in replacing φ_0 by $\varphi_0+\pi$, and φ_f by $\varphi_f+\pi$) the electron initialized at $\varphi_0 \approx -0.9\ \pi$ (i.e. 0.1 π after the field minimum) returns to the initial z=0 at $\varphi_f \approx 0.4\ \pi$ (i.e. 0.4 π after the pulse maximum) with the velocity $v_f = -1.2596X$. Since Newton equations have time-reversal symmetry, we know that by just inverting the direction of the final velocity and by inverting the time flow we can move back this trajectory to z=0, where the final velocity will be equal to zero. Thus we conclude that by

initializing a trajectory at $\varphi_0 \approx -0.4\ \pi$ (i.e. $\approx -0.4\ \pi$ before the field maximum), with $v_0 = 1.2596X$ we will reach z=0 with final velocity $v_f = 0$. Since we know that the trajectory moving forward in time yielded maximum final velocity, we conclude that the trajectory initialized at $\varphi_0 \approx -0.4$ with $v_0 = 1.2596X$ corresponds to the maximal possible initial velocity. More details regarding the effects of the non-zero initial velocity in the classical model of HOHG and comparison with quantum calculations can be found in.[30]

3. A Non-Born-Oppenheimer 1D TDSE for H_2^+ in Intense Laser Fields

The exact 1D TDSE for H_2^+ is solved numerically describing both coupled electron (z-coordinate) and internuclear (R-coordinate) proton coordinate by the following equation in a.u. $\left(\hbar = m_e = e = 1, m_p / m_e = 1837, c = 137\right)$,

$$i\frac{\partial \Psi(z,R,t)}{\partial t} = \hat{H}(z,R,t)\Psi(z,R,t), \tag{15}$$

where

$$\hat{H}(z,R,t) = \hat{H}_R(R) + V_c(z,R) + \hat{H}_z(z), \tag{16}$$

$$\hat{H}_z(z) = -\beta\frac{\partial^2}{\partial z^2} - \kappa E(t), \hat{H}_R(R) = -\frac{1}{m_p}\frac{\partial^2}{\partial R^2} + \frac{1}{R}, \tag{17}$$

$$\beta = \frac{2m_p + m_e}{4m_p + m_e}, \kappa = 1 + \frac{m_e}{2m_p + m_e}, \tag{18}$$

$$V_c(z,R) = -\frac{1}{[a + (z \pm R/2)^2]^{1/2}}, \tag{19}$$

and m_e and m_p are electron and proton masses. The Hamiltonian (16) is the exact three-body Hamiltonian obtained after separation of the center-of-mass motion, because we are working in the dipole approximation, $r/\lambda << 1$, where the electric field is time-dependent only.[4] The Coulomb potential is now a 1D potential requiring a softening parameter *a*, which is set $a = 1$ to obtain the correct I_p for H_2^+ near equilibrium. The corresponding I_p of a 1D H atom with $a = 1$ is 0.67 a.u.

The softened V_c now contains no singularity so a high-order split-operator metho[31] is used to propagate the total TDSE (15) for a pulse length t_p. The integration step in space is $\delta z = 0.25 a.u. \sim 10^{-2}$ nm, which means that grids with $3000^2 \cong 10^7$ points are used. The temporal time step δt =

0.03 a.u. = 0.7 asec so that over 1000 time steps are required for a 10-fs pulse. The electric field, *E(t)*, needs special care since such fields have total area zero.[1] Thus *E(t)* is defined from the vector potential.

$$A(t) = -cE_0(t)\sin\left[\omega(t-t_m)+\Phi\right]/\omega, \tag{20}$$

$$E(t) = -(1/c)\partial A(t)\partial t, \tag{21}$$

where $t_m = \tau/2$, i.e. half the pulse length. We generally used the pulse envelope $E_0(t)$ in the following form

$$E_0(t) = E_0\sin^2(\pi t/\tau), 0 \le t \le \tau\,. \tag{22}$$

With t_p = 4 cycles – 10.6 fs for a 800-nm Ti:Saph laser, the pulse half-width (FWHM) is then given by t_p = 0.3641 ≅ 4 fs. Our definition of *E(t)* via *A(t)* guarantees that $A(0) = A(\tau) = E(0) = E(\tau) = 0$.

The emitted radiation spectra, constituting the HOHG spectrum in the presence of an intense laser field, polarized along the z-axis can be obtained from the time-dependent acceleration for an electron in a potential *V(r)*,[31]

$$a(t) = \frac{d^2}{dt^2}\langle z\rangle = \langle\psi(t)|-\partial V/\partial z|\psi(t)\rangle. \tag{23}$$

The wave function $\psi(t)$ is the solution of TDSE (15). The Fourier transform of *a(t)*, $a(\omega)$ from which one obtains the power spectrum of HOHG $|a(\omega)|^2$, is given by

$$a(\omega) = i(2\pi)^{-1/2}e^{-i\omega t}d(\tau) + i\omega e^{i\varpi e}d(\tau) - \omega^2\int_0^\tau e^{-i\omega t}d(t)dt. \tag{24}$$

The final integral in (24) is the HOHG power spectrum using the dipole form $d(t) = \langle\psi(t)|z|\psi(t)\rangle$. Clearly, this is only valid if the transients $d(\tau) = (d/dt)(d(t))|_{t=\tau}$ and $d(\tau)$ vanish at the end of the pulse. The acceleration form emphasizes maximum acceleration, as in the case of a recolliding electron.[23,24]

This is the form we have used. Because the energy *E* of such an electron is $3U_p \le E \le 10U_p$, where U_p is the ponderomotive energy [Eq. (2)], at high intensities one has highly oscillatory electron wave functions so that the TDSE (15) requires highly accurate numerical procedure.[8,31]

4. Attosecond Pulse Synthesis

As hinted in the Introduction, one of the great advances, if not breakthroughs, emanating from research in the nonperturbative response of atoms to short intense laser pulses has been the synthesis of asec pulses.[25,26]

The source of asec radiation is HOHG by recollision of the ionized electron with its parent[23] or neighboring ions.[24] Unfortunately, the efficiency of such spectra is low, as illustrated in Figure 1. The dotted line represents the HOHG of H_2^+ with *moving* nuclei, i.e., non-Born-Oppenheimer, exposed in a single 10-fs 800-nm pulse with peak intensity I = 6 x 10^{13} W/cm^2. Perusal of the spectrum shows the high inefficiency of the radiation coherently emitted due to low ionization from tunneling and the uncontrolled spreading of the ionized but returning (recolliding) electron wave packet.[23,24]

To enhance such low HOHG efficiencies we originally suggested two-color excitation to pre-ionize the electron by a high-frequency (3ω) field with subsequent control by an intense fundamental field (ω).[32] We have recently reformulated this idea by proposing a combination of an asec VUV pulse and an intense, short 800-nm pulse.[27] The advantage of this new approach are that the *pump* asec pulse, because of its large energy bandwidth, now produces an initially narrow spatial electron wave-packet that is subsequently *controlled* by intense short (fs) low-frequency pulses.

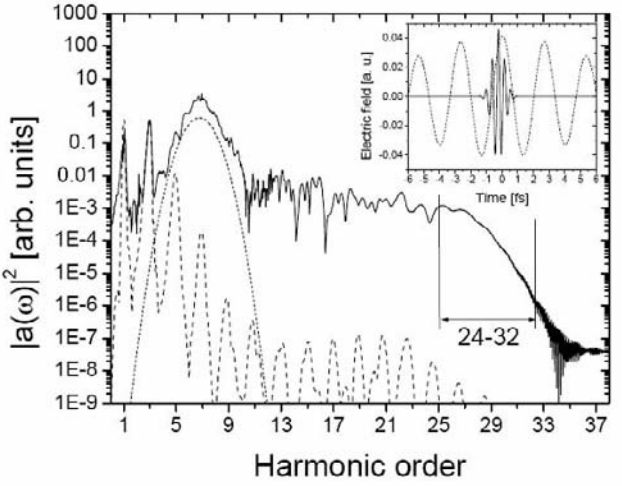

Figure 1. HOHG power spectrum $|a(\omega)|^2$ for non-Born-Oppenheimer H_2^+ excited by an 800 nm 10 -fs, 6x10^{13}W/cm^2 laser pulse in combination with a 600 asec (0.6-fs) probe ate 2x10^{13} W/cm^2. The phase difference $\Phi = \omega t = 0.1\pi$ (see inset). Solid-line: fs+asec pulse excitation. Dashed-line:single fs-pulse excitation.

As seen in Figure 1, the HOHG spectrum is now enhanced by several orders of magnitude. The spectrum is broad and quasi-continuous near the maximum order cut-off, N_m, predicted by Eq. (1).

Such a spectrum can be used to synthesize new single UV pulses as short as 250 asec, as illustrated in Figure 2. This is obtained by combining continuous coherent radiation as an example for the order $24 \le N \le 32$, i.e.,

$$a(t) = \int_{24_\omega}^{32_\omega} a(\omega) e^{i\omega t} d\omega \,. \tag{25}$$

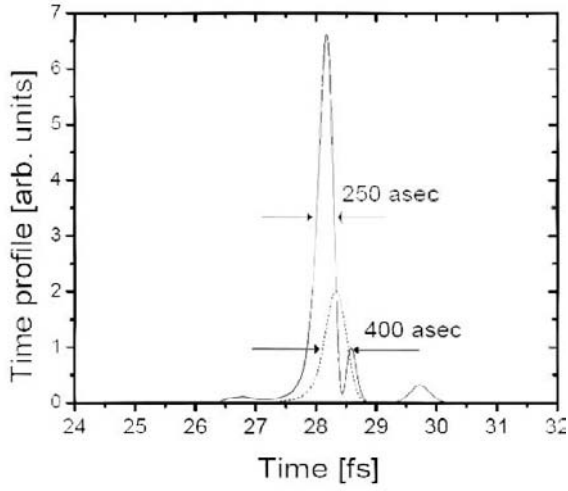

Figure 2. Attosecond (asec) pulses obtained from the continuous harmonics at relative phase , Φ= ωt=0.2π (inset Fig 1). 400 asec from 24 <N < 32; 250 asec from 21 < N < 32.

The end result is more intense asec pulses that are sensitive to the relative phase of the two colors (see inset, Fig. 1). Maximum enhancement of the new asec pulses is obtained at the relative phase $\phi = \omega t = -0.2\pi$ in contradiction to the atomic recollision model, which predicts the maximum order N_m for ionization at phase $\omega t = +0.1\pi$ with zero initial velocity due to tunneling ionization,[23,24] as discussed in Section 2. This phase sensitivity is an extension of *coherent control* of multiphoton processes[33] into the nonlinear, nonperturbative regime of laser-molecule interaction studied in the present article.

As shown in section 2 from simple classical mechanical considerations, zero velocity v_0=0, electrons have maximum return energy $3.17U_p$ when ionized at phase $\phi = 0.1\pi$. It is further proved there that the electron return energy never exceeds $3.17U_p$ even when one allows for nonzero initial velocity v_0. This simple picture neglects the structure (potential) of the ion core with which the electron recollides. In particular for H_2^+ (Fig. 3) one sees that the electron ionized at 115 nm is different from that at 70-nm wavelength. Thus, at 115 nm, the electron must tunnel out to ionize via the static Coulomb barrier, $V_c(Z,R) + EZ$, and thus leave with zero velocity, $v_0 =$

0, at the outer turning point. However, the presence of the intense (6 x 10^{13} W/cm^2) 800-nm pre-pulse traps the initial (Σ_g) electron wave packet in the lower left well. The 115-nm asec pulse thus creates an electron wave-packet localized near the maximum on the left of the distorted double well. This wave packet can re-cross the whole molecule from left to right and ionize after reflection from the right well. It will exit and produce maximum ionization when the barrier on the left is minimum. This is achieved by the electron wave packet being prepared at initial lower field phase, $\omega t = 0.2\pi$, so that on re-crossing the whole molecule and then exiting the barrier is lowest at , i.e., at the maximum of the field. This simple explanation emphasizes the importance of the potential of the ion core on the phase sensitivity of harmonic generation in H_2^+.

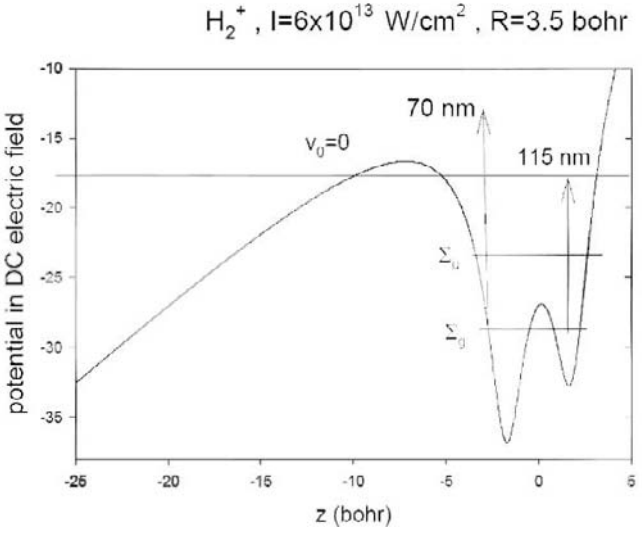

Figure 3. Quasistatic electronic potential V_C(z,R)+Ez at an intensity I=cE^2/8π = 6 x 10^{13} W/cm^2, R=3.5 au for H_2^+.

5. Electron Localization

In the previous section we showed how the molecular ion H_2^+ can be used to create intense sub-fs or equivalently asec pulses in the VUV frequency (wavelength) region. Thus, as shown in Figures 1 and 2,combining harmonics by filtering techniques[25] between the 24th and 32nd will create sub-fs pulses with considerable bandwidth. Here we examine the broadband electronic excitation of H_2^+ at fixed internuclear distance R = 8 au, which is excited by an 800-asec (0.8-fs) 115-nm *pump* pulse followed by a 100-asec (0.1-fs) 20-nm *probe* pulse (Fig. 4). The latter induces direct one-photon

ionization, and we use the corresponding photoelectron spectrum to monitor the subsequent electron motion. All calculations were performed using the numerical code to solve the TDSE equation (4) buy with nuclei fixed at R = 8 au, because the pulses are much shorter than the typical H atom motion time of ~ 10 fs. The TDSE thus yields the exact electronic wave function $\psi(z,t)$, from which one can calculate the induce dipole moment $d(t) = \langle \psi(z,t) | z | \psi(z,t) \rangle$.

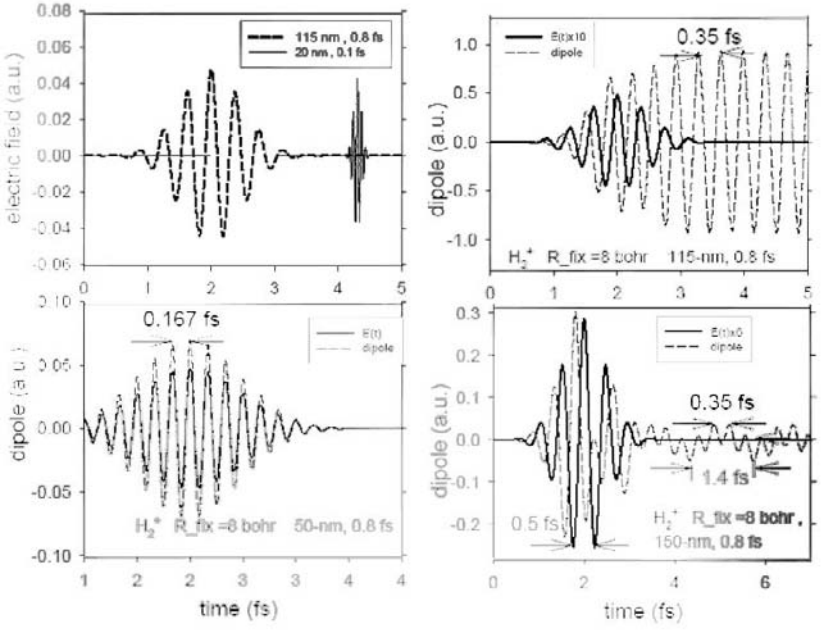

Figure 4. Resulting induced dipoles in a.u for H_2^+ at R=8 au excited by 50nm, 115nm, 150nm, 0.8fs (800 asec) pulses.

Excitation at 50 nm shows that the induced dipole (Fig. 4) is completely in phase with the field *E(t)*, since such short wavelengths ionize the electron which then follows the field. At 115 nm, which corresponds nearly to the H atom 1s-2p_0 transition, one observes that the dipole is out of phase with *E(t)* but shows a periodic oscillation of 0.35 fs or equivalently a photon energy at 105 nm ($\lambda = \tau c$). The dipole oscillations resulting from 150-nm, 800-asec excitations are much more reduced in intensity. The obvious explanation is that, at 115-nm excitation, one is exciting electronic states by transition to $2\sigma_u$ orbitals and others formed from 2s and/or $2p_0$ atomic orbitals of H, whereas at 150 nm one is below such resonances and the induced dipole is much reduced. Thus, the resulting electronic wave function can be represented as the combination

$$\psi(t) = c_1(t)\psi_{1\sigma_g} + c_2(t)\psi_{2\sigma_u}. \tag{26}$$

The corresponding induced dipole can be readily calculated to be

$$d(t) = \langle \psi(t) \,|\, z \,|\, \psi(t) \rangle = c_1(t)c_2^*(t)\langle 1\sigma_u \rangle e^{i(E_1 - E_2)t} + c.c., \tag{27}$$

which oscillates at the frequency corresponding to the energy difference $E_1 - E_2$ between the ground $1\sigma_g$ and excited $2\sigma_u$ molecular orbitals at R = 8 au. Furthermore, since $1\sigma_g \cong (1/\sqrt{2})[1s_a + 1s_b]$ and $2\sigma_u \cong (1/\sqrt{2}) \times [2p_a - 2p_b]$ have the largest dipole $\langle 1\sigma_g \,|\, z \,|\, 2\sigma_u \rangle \cong \langle 1s_a \,|\, z \,|\, 2p_a \rangle$, then the resulting time-dependent wave function $\psi(t)$ is a sp hybrid $(1s \pm 2p)$ situated on each proton. This laser-induced hybridization is clearly evident in Figure 5 where we illustrate the electron density $|\psi(z,t)|^2$ as a function of time. One see initially that the electron is delocalized equally between the two protons at Z = ± 4 au. After excitation with an 0.8-fs, 115-nm pulse one sees the electron density polarized inside the molecular bond, toward z = 0 corresponding to a single sp hybrid, i.e., *s* + *p*, which oscillates between the two nuclei with the period of the energy difference E1 – E2 = 0.35 fs or 350 asec.

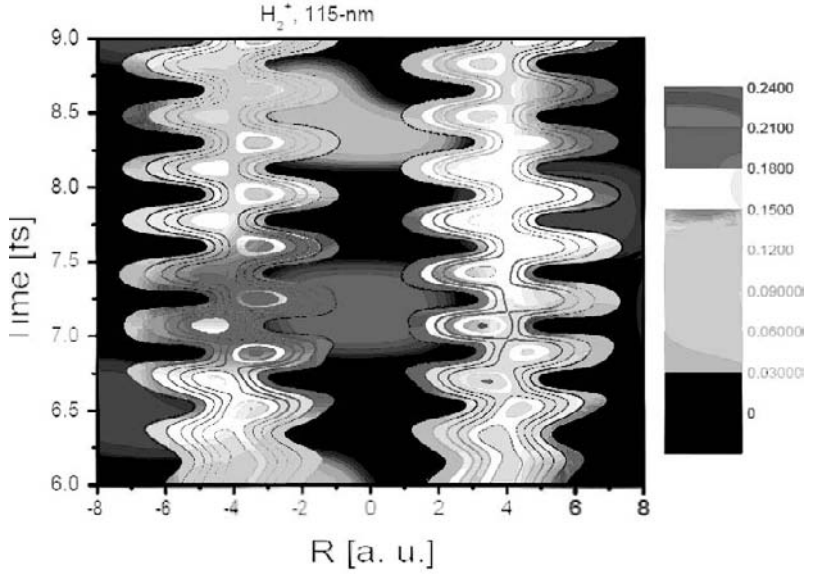

Figure 5. Electron probability psi $|\psi(z,t)|^2$ at R=8 au following excitation at 115 nm with 0.8fs pulse (see Fig 4).

This leads us to propose a spectroscopic method of spatially locating the electron. This is based on the resulting ionization asymmetry predicted

from ionization by intense ultrashort pulses and used to measure the electric field phase profile of such pulses by asec probe pulses[27]. Thus, as shown in Figure 4, a 20-nm, 100-asec pulse is used to ionize the sp hybrids prepared by the 115-nm, 800-asec prepulse. The resulting ionization asymmetry, defined as:

$$P_2 / P_1 = \frac{P_- - P_+}{P_- + P_+}, \tag{28}$$

where $P_{-(+)}$ is the left (right) ionization probability collected at opposing directions, is shown in Fig. 6. This asymmetry pulsates precisely with the frequency corresponding to the energy difference, E_1-E_2, between the ground and excited states that are coherently excited by the first (115-nm) asec pulse. Comparison with Fig. 5 shows that the asymmetry oscillations seen in Fig.6 are indeed correlated to a transfer of a localized electron between the different protons, as discussed in more detail in[34] . Importance of photoelectron asymmetries was emphasized by us earlier in[35] where we proposed a method for experimental determination of the laser absolute phase using such asymmetries.

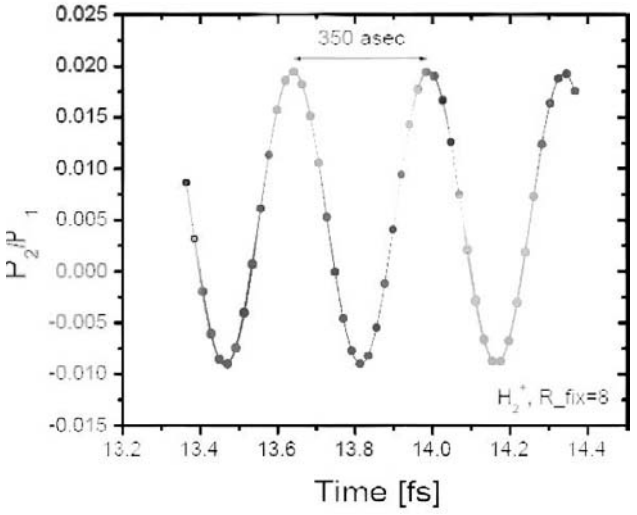

Figure 6. Normalized forward/backward asymmetry in the photoionization, P_2/P_1 , see eq.(28), as a function of time delay between a 20nm, 0.1fs and a 115nm, 0.8 fs pulse.

6. Chirped Attosecond Pulses

In this section we study analytically the photoionization of a coherent superposition of atomic and molecular electronic states by a chirped

ultrashort, attosecond x-ray pulse. Two kinds of phase interference between interfering photoionization amplitudes are found.

The main results from chirped attosecond pulses are:

- the time-dependent part of the phase shift corresponds to electron "*hopping"* with the time period $T = 2\pi / \Delta I_p$, where ΔI_p is the diference in ionization potentials;
- a new chirp effect: oscillations in photoelectron spectrum with the period in energy $W = 2\pi / \xi \Delta I_p \tau^2$ where τ_p is the pulse width and ξ is the spectral chirp rate;
- one can measure a linear chirp, ionization potentials I_p, populations, and pulse duration τ;
- long chirped attosecond pulses are much more sensitive tools in an experiment than ultrashort unchirped pulses which are absent today.

As theoretically tractable examples that capture the essence of our approach, we consider the hydrogen atom with a coherent superposition of 1*s* (atomic state$|1\rangle$) and $2p_0$ (atomic state $|2\rangle$) bound states. We also investigate a H_2^+ molecular ion in a coherent superposition of two electronic states: σ_g1s (molecular state |1>) + $\sigma_u 2p_0$ (molecular state $|2\rangle$). We assume that the molecule is aligned, a currently available experimental technique.

We use a pump pulse that starts at *t*_(<0), its envelope peaks at t_p and the pulse is terminated prior to *t*_<0

$$E_p(t) = E_0(t)\cos\left[\omega_p(t - t_p) + \varphi_{ce}\right]. \tag{29}$$

$E_0(t)$ is a slowly varying envelope and φ_{ce} is the carrier-envelope phase. At resonance $\omega_p = \Delta I_p = I_p^{(1,2)}$ are the ionization potentials of the states $|1\rangle$ and $|2\rangle$ (unless stated otherwise, we use atomic units $e = m_e = \hbar = 1$. The pulse prepares a coherent superposition of two bound states,

$$\Psi_i(r,t) = \alpha_1\psi_1(r,t) + \alpha_2 \exp(i\varphi_p)\psi_2(r,t) \tag{30}$$

where $\alpha_{1,2}^2$ are their populations $(\alpha_1^2 + \alpha_2^2 = 1)$ and α_p is an adjustable phase that depends on the laser excitation scheme. In the rotating wave approximation, the phase φ_p in Eq. (30) is : $\varphi_p = \omega_p t - \varphi_{ce} - \pi/2$. It is the carrier phase. At any moment $t \geq 0$ the probe attosecond pulse is turned-on.

In the general molecular case, the excitation by the pump pulse generates a nuclear wave packet on the repulsive state potential. The electron wave packet time scale is given by the level separation (~300 asec). The relative nuclear motion is given by the relative slopes of the

curves involved (~100 fs). These time scales remain well separated so the nuclei are considered fixed.

Each bound state of the H_2^+ ion is a molecular orbital that we approximate as a linear combination of atomic orbitals $\psi_{at}(\mathbf{r})$

$$\psi_b(\mathbf{r}) = N_b\left[c_1\psi_{at}^{(1)}(\mathbf{r}_1) + c_2\psi_{at}^{(2)}(\mathbf{r}_2)\right]. \tag{31}$$

The vectors $\mathbf{r}_{1,2}= \mathbf{r} \pm \mathbf{R}/2$, where $\mathbf{R}$ is directed from the nucleus 1 to the nucleus 2. In our case, $\psi_{at}^{(1)}(\mathbf{r})$ and $\psi_{at}^{(2)}(\mathbf{r})$ are the hydrogen-like 1*s*- and $2p_0$- wave functions with the variational Slater parameters a_1 and a_2 which are functions of the *R*.

The time-dependent phase shift

$$\delta(t) = \Delta I_p t - \varphi_p = \Delta I_p (t - t_p) + \varphi_{ce} + \pi/2, \tag{32}$$

parameterizes the electron motion via ΔI_p, which depends on *R* in molecular case.

Now we consider single photon photoionization induced by a probe attosecond x-ray pulse. We define the vector potential of such pulse as a linearly chirped Gaussian with dimensionless chirp ξ:

$$A(t) = e(A_0/2)\exp\left[-i\Omega t - (t - t_0{}^2/2\beta\tau^2\right], \tag{33}$$

where Ω is the central frequency of the attosecond pulse, e, A_0, and t_0 are the linear polarization vector, amplitude, and time at pulse peak . The parameter β =1 - $i\xi$. Positive chirp ξ > 0 corresponds to the instantaneous frequency increasing with time. The pulse duration is proportional to $\tau\sqrt{1+\xi^2}$.

We calculate the photoionization amplitude using the final two-center Coulomb wave function. For photoelectron momenta $p >> 1$ and $|pR \pm \mathbf{pR}| >1$ the direct molecular ionization transition amplitudes are determined by atomic amplitudes:

$$M_{mol}^{(1,2)} = N_{1,2}\chi M_{at}^{(1,2)}, \tag{34}$$

where the molecular interference factor is

$$\chi = N_p\left[\exp(i\mathbf{pR}/2)\phi(-R) + \exp(-i\mathbf{pR}/2)\phi(R)\right], \tag{35}$$

$Np = \exp(\pi/2p)\Gamma(1+i/p)$ is the normalization factor and Φ(R) is the hypergeometric function,

$\Phi(R) = F(i/p;\ 1;\ i(pR + \mathbf{pR}))$.

In the plane wave approximation the factor χ becomes $\chi_{pw} = 2\cos(\mathbf{pR}/2)$. The atomic (molecular) attosecond photoionization amplitude from the coherent superposition (32) is given by

$$M^{coh}_{at(mol)} = A_o \tau(\pi\beta/2)^{1/2}\ \varepsilon\ [\gamma_1 M^{(1)}_{at(mol)} + \gamma_2 \exp(-i\Lambda)\ M^{(2)}_{at(mol)}\ ]\ , \qquad (36)$$

where $\gamma_k = \alpha_k \exp(-\omega_k^2 \beta\tau^2/2)$ and $\omega_k = p^2/2 + I_p^{(k)} - \Omega,\ k = 1,2.$ The triple differential momentum spectrum is

$$d^3P^{coh}_{mol}(p,\theta,\varphi) = M^{coh}_{mol}|^2\ p^2 dp d\Omega_e \qquad (37)$$

where $d\Omega_e = \sin\theta d\theta d\varphi$ is the solid angle. Eq.(37) and Fig.7 show that there are two contribution to the photoelectron spectrum. The bandwidths $\Delta_{1,2}$ of electron wave packets in Fig. 7 are defined by functions in the amplitude (36).. It is of importance that both $\Delta_{1,2}$ and $\gamma_{1,2}$ do not depend on linear chirp of the x-ray pulse (for example, the transform-limited τ_{FWHM} =24.19 as (i.e., 1 a.u.) pulse and chirped τ_{FWHM} =250 as pulse at ξ=10 generate electron wave packets with the same bandwidths). For a broad-bandwidth pulses a photoelectron wave packets overlap and this overlapping is the same for a given transform-limited pulse (ξ=0) and its chirped modifications.

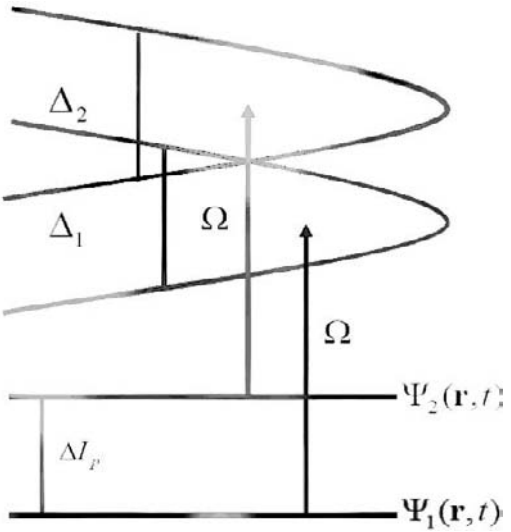

Figure 7. A sketch of an electron wave packet generated by photoionization of a coherent superposition of electronic states. The bandwidths $\Delta_{1,2}$ and spectral overlapping of wave packets do not depend on linear chirp of x-ray pulse.

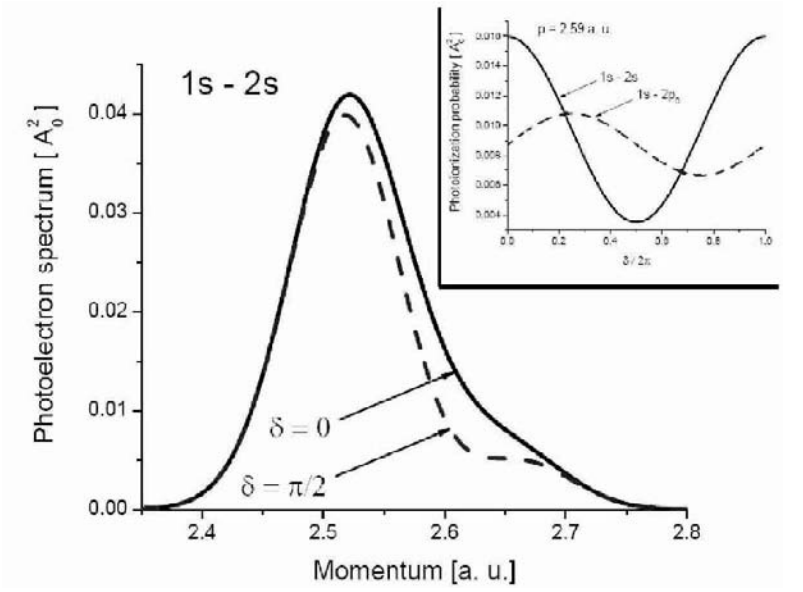

Figure 8. The time-dependent atomic photoelectron spectra generated by the transform-limited τ_{FWHM} =250 as pulse. The insert shows the interference signals as functions of time delay.

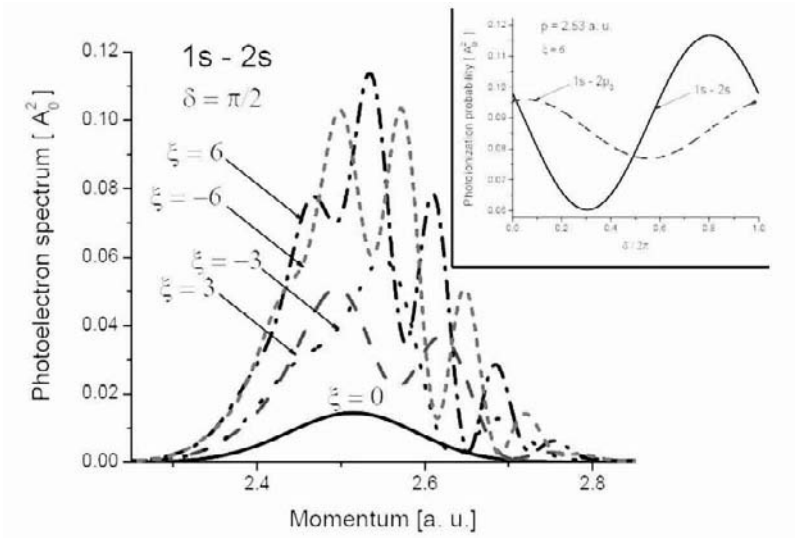

Figure 9. The time- and chirp-dependent atomic photoelectron spectra generated by the transform-limited and chirped pulses. The insert shows the interference signals asfunctions of time delay.

Equation (37) describes the angle resolved photoelectron spectrum. For a given attosecond pulse it contains all spatial and temporal information about the wave packet. Full phase shift between the second and first amplitudes in (9) is

$$\Lambda(t_0, \varepsilon, p) = \phi(\varepsilon, p) + \delta(t_0), \tag{38}$$

where

$$\phi(\varepsilon, p) = \xi \Delta I_p \left[p^2 + I_p^{(1)} + I_p^{(2)} - 2\Omega \right] \tau^2 / 2. \tag{39}$$

The time-dependent part $\delta(t_0)$ in the phase shift $\Lambda(t_0, \xi, p)$ corresponds to the electron "hopping" and the part $\phi(\xi, p)$ describes the chirped interference inside the photoelectron spectrum. Both functions in (38) are periodic: $\exp\left[-i\delta(t_0)\right]$ is the periodic function of time with the period $T = 2\pi / \Delta I_p$ and $\exp\left[-i\phi(\varepsilon, p)\right]$ is the periodic function of the photoelectron energy $E_p = p^2 / 2$ with the period $W = 2\pi / \varepsilon \Delta I_p \tau^2$.

We examine the photoelectron spectrum in the hydrogen atom case for the $1s + 2p_0$ superposition. The appropriate dipole photoionization amplitudes M_{1s} and M_{20} are given by

$$M_{ls} = 2\sqrt{2} a_1^{3/2} N_p G_1 \frac{(ep)(p - i)}{\pi p D_1^2} \tag{40}$$

$$M_{2p0} = 4i a_2^{1/2} N_p G_2 \frac{(ep)^2 8a_2^2 (p - i)(2P - i) + pD_2 (i - 2pa_2) - ip(1 + 2pa_2)^2}{\pi p^2 D_2^3} \tag{41}$$

where

$G_k = \exp\left[-(2/p)\arctan(kpa_k)\right]$ *and* $D_k = 1 + (kpa_k)^2$, $k = 1, 2.$

Figures 8 and 9 show atomic photoelectron spectra $d^3 P_{mol}^{coh}(p, \theta, \varphi) / dp d\Omega_e$, for the case of equal population of 1*s* and 2s hydrogen states, $\alpha_1^2 = \alpha_2^2 = 1/2$. The FWHM duration of the transform-limited unchirped x-ray pulse is 250 and150 asec, respectively and the FWHM duration of the chirped pulses are $\sqrt{1 + \xi^2}$ longer. In pump=probe spectroscopy dynamics is measured by delaying the probe pulse. The changes of the photoionization signal at fixed momentum at the value corresponding to strongest interference are shown in the insets in Figs. 8 and 9 for 1s-2 and $1s\_2p_0$ coherent superpositions.

The real factors of γ_1 and γ_2 factors in the coherent amplitude 9 restrict the effective momenta by some width δp near the peaks p_0 in the transform-limited cases. 1s momentum distribution is characterized by $p_0 \approx$ 2.52 a. u. and $\delta p \approx -0.205$ a. u., while in the 2*p* case we have $p_0 \approx 0.195$ a. u. (we define the effective boundaries as $\omega_{1,2}^2 \beta \tau^2 \approx 4$). Thus one can expect

the effective interval of the amplitude interference as $2.47 \le p \le 2.73$. The results presented in Figs. 8,9 confirm our conclusion. One can verify also the period in photoelectron energy spectrum $W = 2\pi / \varepsilon \Delta I_p \tau^2$. Note that in non-coherent transform-limited case the ratio between maximum 1*s* and $2p_0$ photoionization probabilities in approximately 324. The coherent coupling "enhances" the 2*p* contribution due to usual mathematical reason: if A >> a, the ratios a^2/A^2 and $\left[(A+a)^2 - A^2 \right] / A^2 = 2a/A$ are quite different.

To make attosecond wave packet measurements experimentally feasible we introduce the asymmetry parameter

$$\Delta(p,\phi,\varphi) = \frac{d^3P(p,\phi,\varphi)}{dpd\Omega e} - \frac{d^3P(p,\pi-\theta,\varphi)}{dpd\Omega e}. \tag{42}$$

In molecular case (as in atomic case) the asymmetry (42) is independent of the azimuthal angle φ since the molecule is aligned along z-axis.

From Eq. (9) we obtain:

$$\Delta_{at}(p,\theta) = 2\pi (A_0\tau)^2 \mid \beta \mid N_1 N_2 \alpha_1 \alpha_2 p^2 \mid X \mid^2 \mathrm{Re}\left\{ e^{-i\delta(t_o)-(\omega_1^2\beta^* + \omega_2^2\beta\tau^2/2} M_{1s}^* M_{2po} \right\}, \tag{43}$$

$$\Delta_{mol}(p,\theta) = \mid X \mid^2 \Delta_{at}(p,\theta). \tag{44}$$

In the case of high x-ray frequency (p>>1) we have approximately

$$\Delta_{at/mol}(p,\theta) = -\sin\left[\Lambda(t_0,\xi,p)\right]\cos\theta(2\cos^2\theta - a_2) \tag{45}$$

reflecting the time-dependence and chirped interference (via the factor $\sin\left[\Lambda(t_0,\xi,p)\right]$, 1*s* (via the factor $\cos\theta$), and $2p_0$ (via the factor $(2\cos^2\theta - a_2)$) interfering photoionization amplitudes.

Figure 10 shows the atomic differential photoelectron asymmetries as functions of the electron momentum p at different chirps and delays δ. The parameters of x-ray attosecond pulse are the same as in the case of Fig. 9. We find that for some values of momenta all electrons go in one direction. The figure also shows how the modulation of the photoelectron spectrum moves as the pump-probe delay changes.

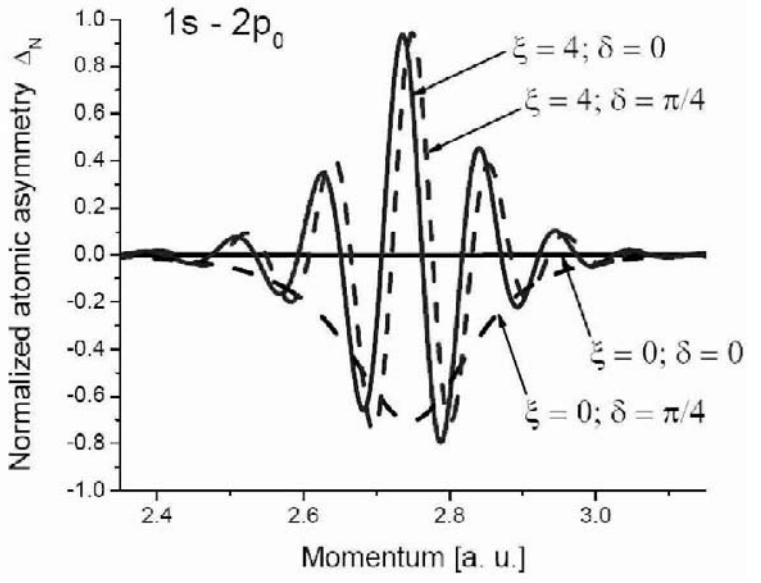

Figure 10. The normalized time- and chirp-dependent atomic photoelectron asymmetries in photoelectron spectra generated by the transform-limited and chirped pulses.

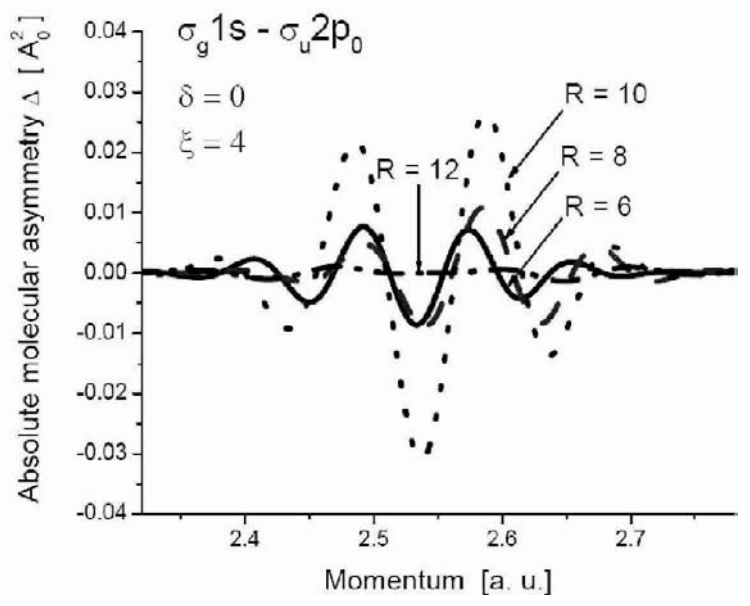

Figure 11. Molecular interference in the absolute photoelectron asymmetry at ξ =4 and different internuclear distances.

Analogous molecular asymmetries are displayed in Fig. 11 at different internuclear distances. The suppression of the asymmetry in R=12a. u. case is explained by Fig. 11: the interference factor has a minima in the region of maximum of atomic asymmetry. So far, we have shown how chirped pulses can be used to observe atomic wave packet motion. A diatomic molecule adds a two-centre interference. The absolute molecular asymmetries are displayed in Fig. 11 at large different internuclear distances. With changing of R the level separation slightly changes, but interference patterns is defined mostly by the values of pR and **pR** in the interferences factor introduced in eq. (35). The photoelectron signal and, therefore, the absolute asymmetry at R=12 is suppressed due to destructive molecular interference. The minimum value of $|\chi|^2$ in Fig. 11 is in the range of the photoelectron momenta.

In conclusion, we show that long chirped attosecond pulses can measure attosecond time scale electron dynamics. The dynamics can be measured just as effectively as if the pulses were transform-limited. Pump-probe time delay spectroscopy is possible, but not necessary if chirped pulses are used. We also show that the oscillations in the photoelectron spectra are described by the universal phase shift between the interfering photoionization amplitudes. The phase shift allows us to read the dynamics at a single time delay.

Acknowledgments

We are grateful to M. Yu. Ivanov for valuable discussions.

References

1. T. Brabec, F. Krausz, Rev. Mod. Phys. 545 (2000).
2. M. Gavrila, *Atoms in Intense Laser Fields*, (Academic Press, New York , 1992).
3. J. L. Krause, K.J. Schafer, K. Kulander, Phys. Rev. Lett. *68*, 3535 (1992).
4. A.D. Bandrauk, *Molecules in Laser Fields* (M. Dekker, New York , 1994).
5. A.D. Bandrauk, M.L. Sink, J. Chem. Phys. *74*, 1110 (1981); Chem. Phys. Lett. *57*, 569 (1978).
6. C. Wunderlich, E. Kohler, H. Figger, T. Hansch, Phys. Rev. Lett. *78*, 2333 (1997).
7. D. Pavicic, H. Figger, T. Hansch, Eur. Phys. J., *D26*, 39 (2003).
8. S. Chelkowski, C. Foisy, A.D. Bandrauk, Phys. Rev. *A57*, 1156 (1998).
9. I. Kawata, A.D. Bandrauk, Phys. Rev. *A67*, 013407 (2003).
10. S. Chelkowski, P.B. Corkum, A.D. Bandrauk, Phys. Rev. Lett. *82*, 3416 (1999).
11. A.D. Bandrauk, S. Chelkowski, Phys. Rev. Lett. *87*, 273004 (2002).
12. R.S. Mulliken, J. Chem. Phys. *7*, 20 (1939).
13. T. Zuo, A.D. Bandrauk, Phys. Rev. *A52*, 2511 (1995); Phys. Rev. A54, 3254 (1996).

14. T. Seideman, M. Ivanov, P.B. Corkum, Phys. Rev. Lett. *75*, 2819 (1995).

15. S. Chelkowski, A.D. Bandrauk, Phys. Rev. *B28*, L723 (1995).
16. I. Kawata, H. Kono, A.D. Bandrauk, Phys. Rev. *A62*, 031401 (2000).
17. K. Harumiya, H. Kono, A.D. Bandrauk, Phys. Rev. *A66*, 043403 (2002).
18. K. Kawata, H. Kono, A. D. Bandrauk, Phys. Rev. *A64*, 043911 (2001).
19. G. Herzberg, *Spectra of Diatomic Molecules* (Van Norstrand, New York, 1951).
20. J. D. Martin, J.W. Hepburn, Phys. Rev. Lett. *79*, 3154 (1997).
21. A. D. Bandrauk, Y. Fujimura, Gordon, R.J., *Laser Control and Manipulation of Molecules*; Eds, ACS Symposium Series 821; American Chemical Society: Washington, DC (2002).
22. A.D. Bandrauk, M. Delfour, C. Lebris Eds, *Quantum Control; CRM Proceedings and Lecture Notes*, Vol. 33; *American Mathematical Society*: Providence, RI (1994).
23. P. B. Corkum, Phys. Rev. Lett. *71*, 1993 (1994).
24. A.D. Bandrauk, H. Yu, Phys. Rev. *A59*, 539 (1999); J. Phys. *B31*, 4243 (1998).
25. M. Hentschel, R. Kienberger, C. Spielmann, G. Reider, N. Milosevic, T. Brabec, P.B. Corkum, U. Heinzmann, M. Drescher, F. Krausz, *Nature* 414,509 London (2001).
26. U. Kleineberg, U. Heinzmann, M. Drescher, F. Krausz, *Science* 297, 1144 (2002).
27. A.D. Bandrauk, S. Chelkowski, H.S. Nguyen, Phys. Rev. Lett. *89*, 283903 (2002).
28. A.D. Bandrauk, H.S. Nguyen, Phys. Rev *A66*, 031401 (2002).
29. R. Kienberger, V. Yakolev, A. Scrinzi, M. Drescher, F. Krausz, *Nature* 427, 817 (2004).
30. A. D. Bandrauk,, S.Chelkowski, S. Goudreau, J.Mod.Opt. 52, 411 (2005).
31. A. D. Bandrauk, H. Shen, J. Chem. Phys. *99*, 1185 (1993).
32. A.D. Bandrauk, S. Chelkowski, H. Yu, E. Constant, Phys. Rev. *A56*, 2357 (1997).
33. M. Shapiro, P. Brumer, *Principles of the Quantum Control of Molecular Processes* (Wiley Interscience, New York, 2002).
34. G.L.Yudin, S. Chelkowski, J. Itatani, A.D. Bandrauk, P.B.Corkum, Phys. Rev. *A*72, 051401 (2005).
35. S. Chelkowski, A.D. Bandrauk, A. Apolonski, Phys. Rev. *A*70, 013815 (2004).
36. G.L. Yudin, A.D. Bandrauk, P.B. Corkum, Phys.Rev.Lett. submitted.

FUNDAMENTALS OF NANOBIOPHOTONICS

PARAS N. PRASAD
Departments of Chemistry, Physics, Electrical Engineering and Medicine, Institute for Lasers, Photonics and Biophotonics
University at Buffalo, The State University of New York
Buffalo, NY 14260-3000

Abstract. Nanobiophotonics is an emerging field created by the fusion of photonics, nanotechnology and biomedical science. It provides multidisciplinary opportunities for biological sensing, imaging, and new form of optical diagnostics as well as light guided and activated therapies. This article describes some basic aspects of nanobiophotonics and illustrates applications to nanomedicine, a field receiving considerable attention world wide. The basic principles of nanoscale control of optical functions and excited state dynamics are discussed. Examples of nanoscale control of optical functions for biomedical applications are size dependence of optical transitions in quantum dots, useful for bioimaging. Examples of nanocontrol of excitation dynamics for bioapplication presented here are (i) manipulations of phonon induced relaxation to produce highly efficient up-converting rare-earth ions containing nanophors; ii) nanocontrol of non-radiative intersystem crossing from an excited singlet to a lower level triplet state involved in photodynamic therapy; and (iii) nanoscopic fluorescence resonance energy transfer (FRET) to monitor DNA delivery for gene therapy.

Keywords: nanophototonics, biophototonic, nanomedicine, bioimaging, nanotechnology, FRET, quantum dots, nano-scale control of optical functions

J.J. Dubowski and S. Tanev (eds.), Photon-based Nanoscience and Nanobiotechnology, 55–65.

1. Introduction

This is the age of multidisplinary frontiers in science and technology where major breakthroughs are likely to occur at the interfaces of disciplines. Photonics, the science and technology involving light-matter interactions, has already impacted our daily life, from the use that ranges from high bandwidth fiber-optics telecommunications to high capacity DVD's. Biomedical sciences are producing new approaches that may provide customized medicine based on genomics and proteomics. Nanotechnology utilizing nanomaterials and nanofabrications hold numerous promises to produce new, highly efficient and compact technologies.

The interface of these disciples as shown in Figure 1 has given rise to new frontiers which provide challenges for basic understanding of processes as well as for new technological inventions.

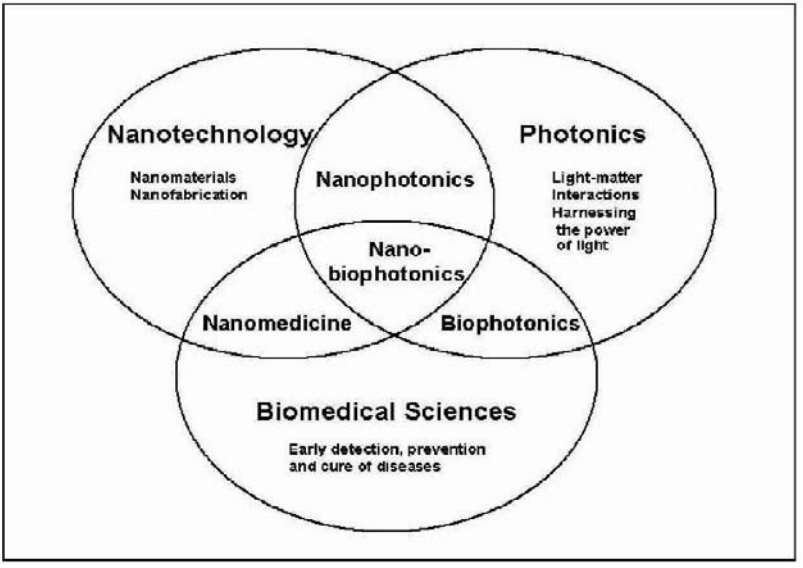

Figure 1. Interfaces of photonics, nanotechnology and biomedical sciences.

The interface of photonics with nanotechnology has produced the field of nanophotonics which deals with light-matter interactions on nanoscale. Nanophotonics covers a diverse range of topics dealing with near field microscopy, nanoscale optical materials, and nanofabrications, as presented in my recent monograph "Nanophotonics."[1]

The interface of photonics with biomedical sciences has produced yet another emerging field, "Biophotonics", which deals with interactions of light with biological matter or biologically relevant matter such as exogenous fluorescence probes. The field of biophotonics has received a great deal of attention worldwide, providing opportunities to use optical probes to study cellular interactions and dynamics as well as to effect new modalities of bioimaging, sensing and therapies, as discussed in my other monograph "Introduction to Biophotonics"[2] The entry of nanotechnology in biomedical sciences has give rise to the new field of "nanomedicine" where nanostructures can be used to produce new probes for diagnostics and more effective, targeted therapy. The vision offered by nanomedicine and its scope are depicted in Figure 2.

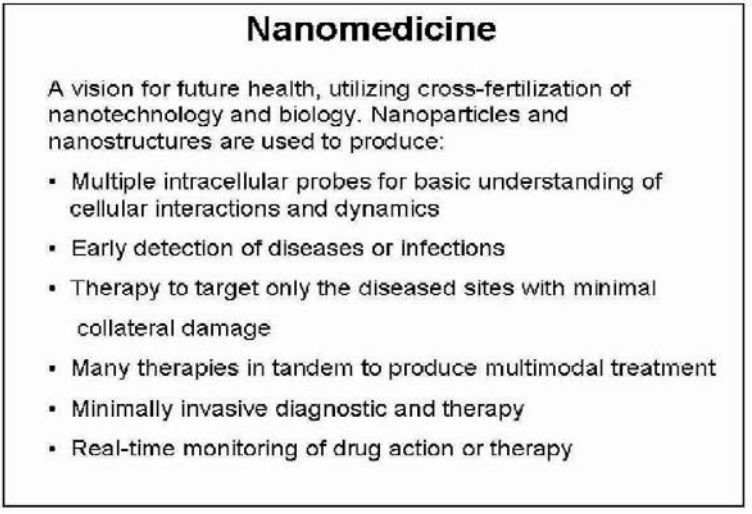

Figure 2. Nanomedicine, a vision and its scope.

This article focuses on nanobiophotonics, which is at the interface of all these disciplines, as depicted in Figure 1. Specifically, it deals with nanoscale control of optical functions to produce new modalities of bioimaging as well as light-activated and optically monitored therapies. Figure 3 illustrates the focus of this article. For the sake of convenience, examples provided are from our work at the Institute for Lasers, Photonics and Biophotonics which has a multidisciplinary program covering nanophotonics, biophotonics and nanomedicine. To accomplish this comprehensive multidisciplinary coverage, the Institute involves chemists, physicists, engineers and biomedical researchers.

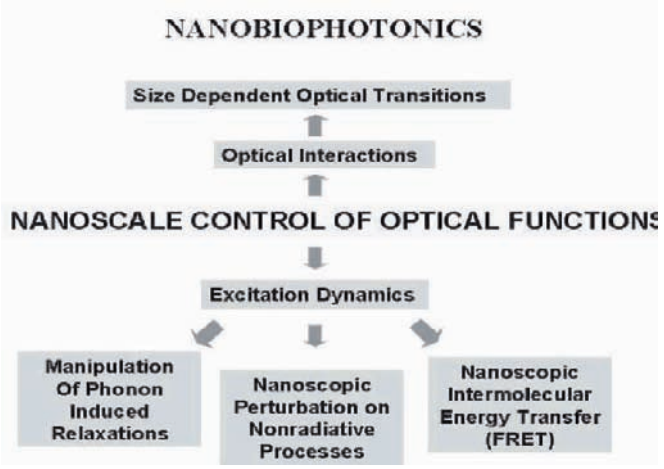

Figure 3. Nanoscale control of the optical functions for nanobiophotonics.

First, quantum dots which exhibit size dependent optical properties such as optical absorption and luminescence are discussed, together with their applications for bioimaging.

Second, we cover nanophosphors containing rare earth ions which up-convert 980 nm radiation to visible emission useful for bioimaging. Here nano-control of excitation dynamics produces efficient up-conversion in nanoparticles. Then the nanocontrol of excitation dynamics in relations to therapies is discussed. The first example is produced by photodynamic therapy which is a light-activated therapy. Here nano-control is used to enhance, intersystem crossing from a photoexcited singlet state to a metastable triplet which is a key intermediate in photodynamic therapy. The second example is nanoscale control of excitation energy transfer, also known as fluorescence(or Forster) resonance energy transfer and abbreviated as FRET, to optically monitor DNA delivery by using a nanoparticle.

2. Quantum Dots for Bioimaging

Quantum dots are nanoparticles of semiconductors which exhibit size dependent optical properties derived from quantum confinement of electrons and holes, once the size of the nanoparticle becomes comparable to or less than the Bohr radius of the semiconductor[1]. Under such confinement conditions, the smaller the size of the quantum dots, the shorter is the wavelength of the optical transition. Thus, the absorption and

the emission maxima of quantum dots of a specific semiconductor (e.g. CdSe) shift toward blue when the size reduces. Compared to organic dyes (also called fluorophores or flurochromes) which have been extensively used for fluorescence imaging[2], these quantum dots offer some specific advantages for bioimaging. Some of these relative advantages are: (i) quantum dots do not readily bleach where as it is a common problem with organic dyes; (ii) quantum dots have narrow (< 30 nm) and symmetric emission spectra compared to organic dyes (>100nm). Thus, quantum dots can conveniently be used in multiple resolvable colors (multiple imaging) that can be excited simultaneously using a single excitation wavelength.

For bioimaging, the quantum dots are surface functionalized by attaching appropriate ligands to make them water dispersible. Also, for selective imaging of targeted biological cells (e.g. a specific type of cancer cells), the quantum dots have been attached to targeting carriers (e.g. antibodies). CdSe quantum dots prepared through colloidal chemistry approaches[3,4] have extensively been used for bioimaging. Recently, there have been concerns about their toxicity derived from both Cd^{2+} and Se^{2-} ions. For this reason, there is a great deal of interest in other quantum dots such as InP. However, these III-V semiconductor quantum dots are difficult to prepare by colloidal solution chemistry routes. Our group recently developed a new precursor based colloidal synthesis which produces InP quantum dots rapidly and in monodisperse form[5]. These quantum dots were coated by a shell of wider band gap semiconductors, ZnS, by changing the reaction conditions. The shell structure confines the carriers in the core quantum dot (InP) and also passivates the surface to increase the luminescence quantum yield of these quantum dots. Then the quantum dot core-shell structure was chemically conjugated with a folic acid carrier which targets specific cell lines (such as KB cells) which have folate positive receptors[6]. The chemically conjugated quantum dot structure is shown in Figure 4 here. These quantum dots then are readily taken up by folate receptor positive cells (e.g. KB cells) by a process called receptor mediated endocytocis to produce selective bioimaging of these cells.

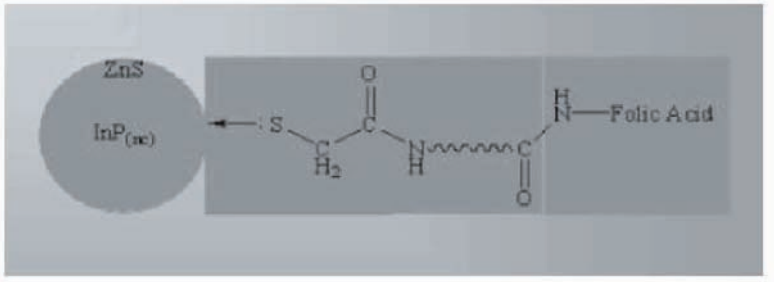

Figure 4. InP/ZnS quantum dots core-shell structure conjugated with Folic Acid.

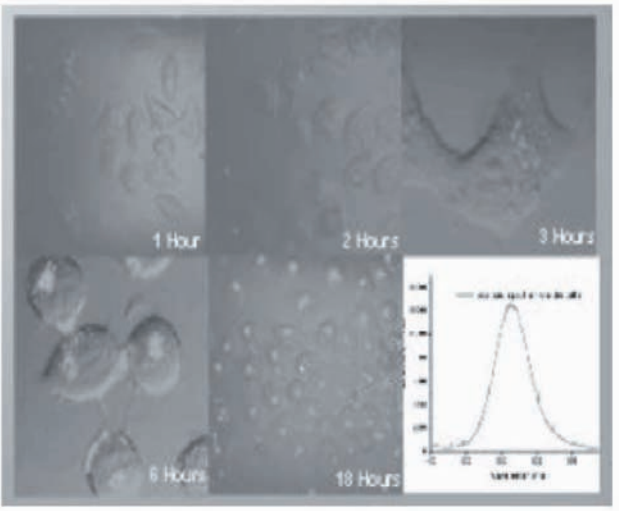

Figure 5. Receptor mediated endocytocis in InP core/shell nanoparticles imaged using confocal microscopy. Particles were targeted using folic acid to KB cells which are known to be folate receptor positive.

Figure 5 shows bioimaging of KB cells.[6] The insert shows luminenence spectrum of the InP/Zns core-shell quantum dots within the cell[6]. The InP/ZnS quantum dots also exhibit significant direct two-photon absorption whereby excitation with 800nm femto second (high intensity) pulses from a mode-locked Ti-sapphire laser produces up-converted (higher energy) emission in the visible. This type of two-photon excited emission from cell staining organic dyes is now routinely used in two-photon laser scanning microscopy to obtain high contrast (very little autofluorescence from the intrinsic constituents of the cell) 3 dimensional images of the cells. We successfully demonstrated two-photon laser scanning microscopic images of cells using ZnS coated InP quantum dots which has been the conjugated with folic acid. Figure 6 shows the uptake of these quantum dots by KB cells that are known to be folate receptor positive.

3. Nanoparticle Up-converters for Bioimaging

The second example for bioimaging is using nanophosphors containing rare-earth ions in an Y_2O_3 nanoparticle. The rare-earth ions exhibit up-conversion by a variety of mechanisms, some of which are represented in Figure 7 and are discussed in detail in reference [1].

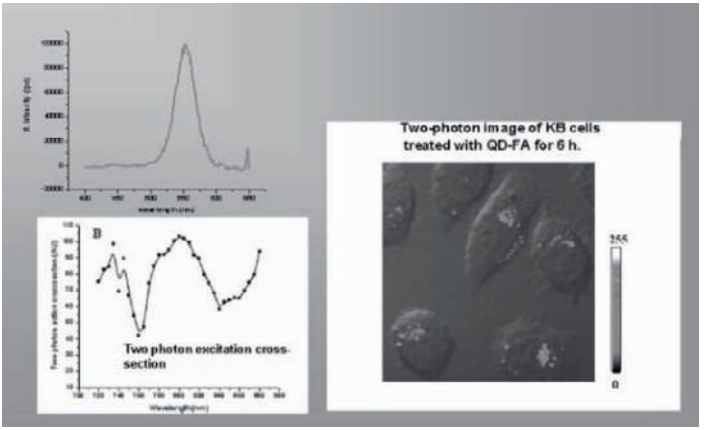

Figure 6. Two-photon properties of InP/ZnS quantum dot core-shells and two-photon imaging.

The challenge has been to prepare the rare-earth ions doped nanoparticles with good up-conversion efficiency. This requires nanocontrol of excitation dynamics whereby a specific up-conversion channel is preferentially manifested over other radiative and non-radiative channels. As shown in Figure 8, we have successfully prepared nanoparticles which exhibit blue, green or red up-conversion when excited at 975 nm using a CW diode laser.[1] The key step is the control of phonon induced relaxation to minimize it. We have chosen a host of low phonon frequency to accomplish this goal. Another challenge has been to functionalize the surfaces of these nanoparticles so that they can be dispersed in water, without aggregation.

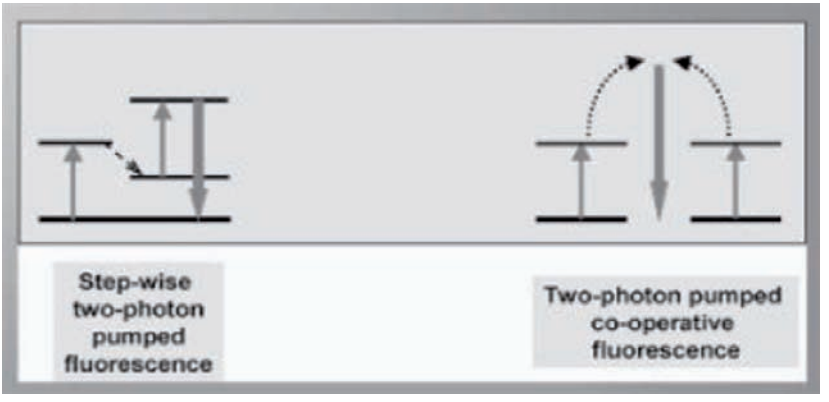

Figure 7. Various up-conversion processes exhibited by rare-earth ions.

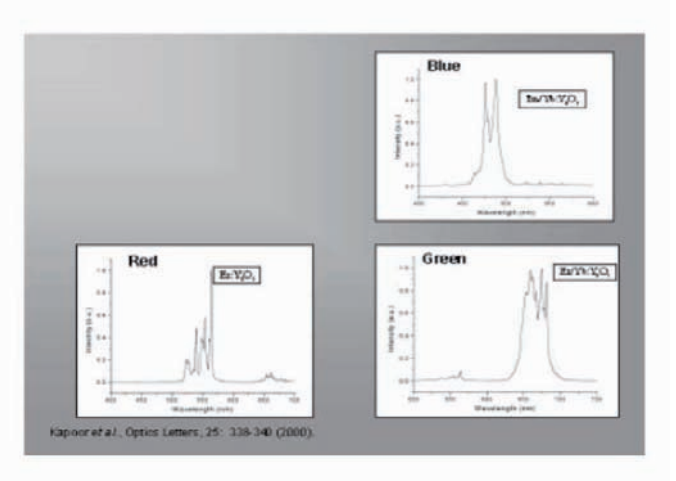

Figure 8. Up-conversion emission by rare-earth nanophosphors.

4. Photodynamic Therapy Using Nanobiophtonics

Another example of nanocontrol of excitation dynamics for biophotonics is in enhancing the efficiency of photosensitizers for photodynamic therapy[2]. Photodynamic therapy is an effective way of treating cancer using light irradiation. Photosensitizes exhibit the property that they are preferably retained by the cancer cells for a longer time. Hence after waiting for an appropriate time length, when a photosensitizer is cleared of normal cells and only held by the cancer cells, light irradiation is used to excite the photosensitizer to the singlet state from where intersystem crossing generates the excited metastable triplet state in the photosensitizer. The photosensenitizer in the triplet state then generates reactive oxygen species (such as singlet oxygen by transferring its excitation energy to triplet oxygen) which is highly cytotoxic, thus destroying the cancer cell. Hence, a key step is efficient generation of triplet state by manipulation of excitation dynamics in the photosensitizer. We have used nanocontrol by creating nanoparticles co-doped with heavy atoms, such as Iodine, and a photosensitizer. Here the presence of a heavy atom enhances intersystem crossing in the photosensitizer through increased spin-orbit coupling. We have demonstrated increased singlet oxygen generation using such nanocontrol of excitation dynamics.

5. Optical Tracking of DNA Delivery

Nanoscopic intermolecular energy transfer has been used efficiently to monitor DNA delivery for gene therapy. For this purpose, an organically modified silica (ORMOSIL) nanoparticle was used. The chemical composition of this nanoparticle is controlled so that the amino group on the surface becomes positively charged under appropriate pH. It can then electrostatically bind negatively charged DNA to transport it to the cell. For optical tracking of DNA binding and subsequent release, an organic dye, HPPH, was encapsulated within 20 nm ORMOSIL nanoparticles which acts as an energy acceptor for FRET energy transfer. Another dye, an energy donor, was intercalated in the DNA.

Figure 9 shows a schematic representation of this structure. When DNA is bound to the nanoparticle, excitation of the donor results in the fluorescence of the acceptor dye. When the DNA is released, no FRET can occur, as the donor and the acceptor are not within nanoscopic range. In such a case, acceptor emission is not observed when the donor is excited; only donor emission is observed. We successfully demonstrated optical tracking in our in-vitro study.[8]

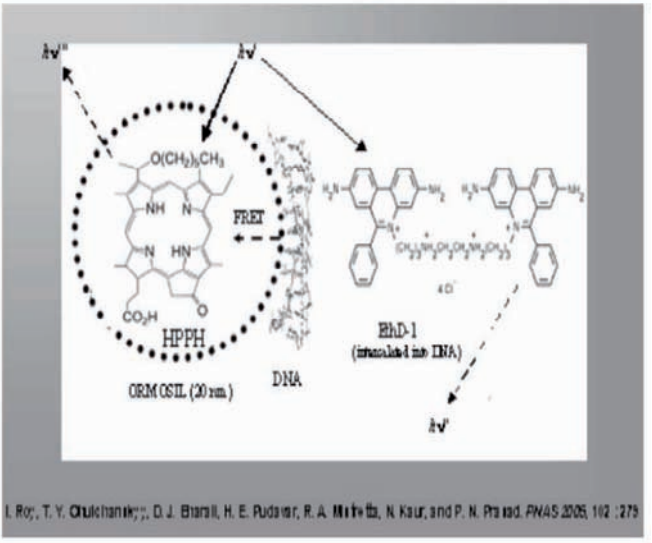

Figure 9. Optically trackable ORMOSIL nanoparticles for gene delivery.

6. Future Opportunities

Some future opportunities in nanobiophotonics research are listed below.

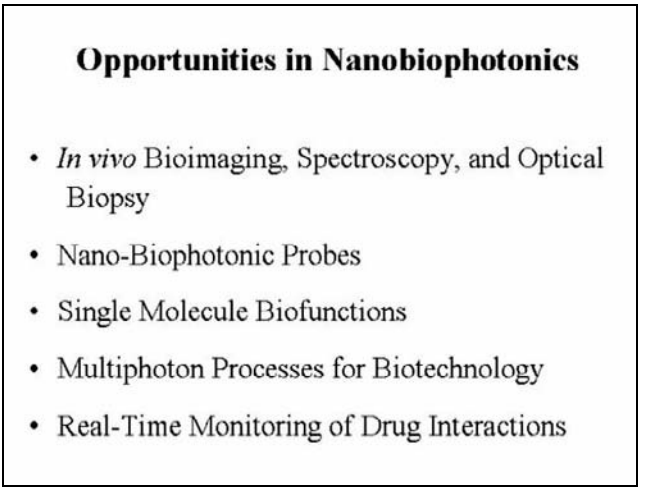

Figure 10. Opportunities in Nanobiophotonics.

Acknowledgements

The work reported here is supported in part by a DURINT Grant from the Chemistry and Life Sciences Directorate of the Air Force Office of Scientific Research and in part by a grant from the John R. Oishei Foundation of Buffalo. Partial support from the Center of Excellence in Bioinformatics and Life Sciences of the University at Buffalo is also acknowledged.

References

1. P.N. Prasad, "Nanophotonics", John Wiley & Sons, New York (2004).
2. P.N. Prasad, "Introduction to Biophotonics", John Wiley & Sons, New York (2003).
3. M. Bruchez, Jr., M. Moronne, P. Gin, S. Weiss, and A.P. Alivisatos, *Science* **281**, (1998) 2013-2016.
4. W. C. Chan and S. Nie, *Science* **281**, (1998) 2016-2018.

5. D. W. Lucey, D. J. MacRae, M. Furnis, Y. Sahoo, A. N. Cartwright and P.N. Prasad, *Chemistry of Materials* **17**, (2005) 3754-3762.
6. D.J. Bharali, D.W. Lucey, H. Jayakumar, H. E. Pudavar and P. N. Prasad, *Journal of the American Chemical Society* **127**, (2005) 11364-11371.
7. Unpublished results from our Institute.
8. I. Roy, T. Y. Ohulchansky, D. J. Bharali, R. A. Mistretta, N. Kaur, and P. N. Prasad, *Proceedings of the National Academy of Sciences* **102**, (2005) 270-284.

NONLINEAR OPTICAL PHYSICS AND APPLICATIONS OF THE PLASMONIC RESPONSE IN METAL NANOPARTICLES

RICHARD F. HAGLUND, JR.*
Department of Physics and Astronomy and
Vanderbilt Institute for Nanoscale Science and Engineering
Vanderbilt University, Nashville TN 37235-1807 U.S.A.

Abstract. The optics of the surface plasmon resonance in the linear regime have been extensively studied and applied for almost a century. The explosive growth of interest in plasmonics, however, is focusing attention on novel plasmonic structures and nonlinear optical applications. In this paper, the fundamental nonlinear optical physics of the surface plasmon resonance is reviewed. Methods for preparing metal nanoparticle composites with well-define optical properties are described. Recent experiments and applications of second- and third-order nonlinearities from metal nanoparticles and ordered arrays of metal nanoparticles are described.

Keywords: Surface plasmon resonance, second-order nonlinear nanoparticle optics, second-harmonic generation, third-order nonlinear nanoparticle optics, nonlinear refraction and absorption.

1. Introduction: Light Scattering from Metallic Nanoparticles

Ever since Gustav Mie successfully explained light scattering by metal nanoparticles in what is said to be the most-cited scientific paper of the 20th century,[1] the enhanced electromagnetic fields generated at the surface plasmon resonance (SPR) of metal nanoparticles have been exploited as probes of condensed-phase kinetics and dynamics. However, electromagnetic coupling between a metal nanoparticle and atoms, molecules and clusters in its environment depends critically on microscopic structural

* To whom correspondence should be addressed. Department of Physics and Astronomy, Vanderbilt University, Nashville TN 37235-1807. E-mail: Richard.Haglund@vanderbilt.edu.

J.J. Dubowski and S. Tanev (eds.), Photon-based Nanoscience and Nanobiotechnology, 67–96.

details of the metal-dielectric interface that are poorly understood. For example, nanoscale surface roughness directly affects the radiative *vs* non-radiative relaxation rates of the SPR; such effects almost certainly correlate with huge variations of sensitivity observed in surface-enhanced Raman scattering (SERS) and plasmon-exciton coupling between metal nanoparticles and adjacent fluorophores.[2]

The goal of much current research in this explosively growing field focuses on controlling electromagnetic fields at the nanoparticle interface with its surroundings, and is grounded in precise nanoparticle fabrication and characterization techniques, as well as the growing sophistication of the computational approaches to complex plasmonic geometries, most notably using finite-difference time-domain electrodynamics. By examining the optical responses of bare metal-nanoparticle composites and adsorbed molecular emitters at varying distances from the interface, it is increasingly possible to compute these electromagnetic field effects across the boundary from near-field to far-field regions, and to measure their effects at the nanoscale.

The current interest in photon-nanoparticle interactions both drives and is enabled by the capacity to fabricate ordered arrays of uniform metal nanoparticles, either on, or embedded in, linear and nonlinear media that can enhance the nanoparticle optical response. By combining "bottom-up" and "top-down" approaches to fabricating nanoparticle composites, metal-nanoparticle structures and arrays are available to provide a practical workbench for studying near- and far-field electromagnetic-field effects at nanoscale metal-dielectric interfaces. Apart from the inherent signal-to-noise enhancement achievable in an array configuration, large ensembles of identical nanoparticles can also be used to study the statistical properties of the individual nanoparticles and to highlight coherent interactions between nanoparticles. We have also developed linear and nonlinear optics experiments that make possible measurements of higher than usual sensitivity, for example by doing confocal microscopy of harmonic radiation from nanoparticle arrays in a scattering geometry. In this geometry, we can adapt in a straightforward way nonlinear optical techniques, such as surface second-harmonic generation, to molecular spectroscopy on nanoparticles.

In this paper, we describe interactions of laser light with metal nanoparticles in terms that make it possible to see how specific properties of MNPs relate to linear and nonlinear (second and third-order) phenomena, such as harmonic generation and nonlinear refraction. We present three examples that illustrate how fabrication of nanostructures can make it possible to observe specific nonlinear phenomena, and how the

computational tools developed from theory also make it possible to understand the physics underlying the phenomena.

2. Optical Physics of the Surface Plasmonic Response

A schematic depicting the effects of electromagnetic excitation of a metal nanoparticle is shown in Figure 1. The MNP is assumed large enough that the crystal structure is bulk-like. Classical local-field effects enhance the multipole response of the MNP to optical fields; quantum effects produce additional enhancement for MNPs smaller than 10-15 nm. At low concentrations, the electronic structure and optical properties of MNP composites can be treated in the Maxwell-Garnett limit.[3, 4] However, the high-concentration limit, described by Bruggemann theory, can also be reached by some synthesis techniques.[5]

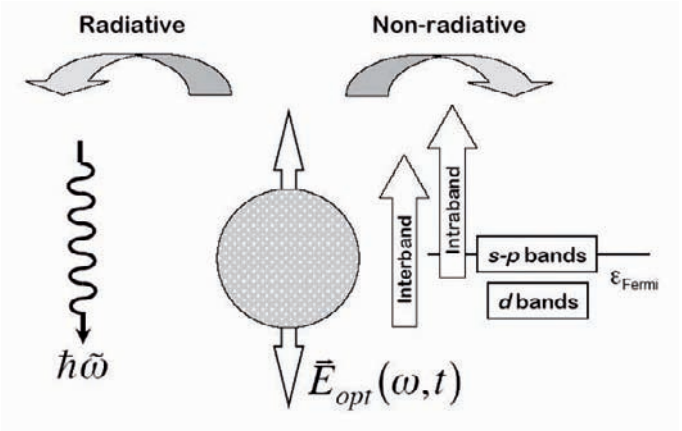

Figure 1. Schematic showing electromagnetic excitation of a metal nanoparticle and the radiative and non-radiative decay channels.

The first of the following sections presents a synopsis of the linear and nonlinear optical physics of the plasmonic excitations in MNPs. The interaction of an optical field with the MNP produces a collective oscillation of the electron gas, the elementary excitation called a *plasmon*. This excitation can decay non-radiatively into electron-hole pairs through intraband or interband excitations; the plasmon can also decay radiatively by photon emission. As with any dynamical excitation, the questions that can be asked include excitation and relaxation dynamics (*e.g.*, decay and dephasing times T_1 and T_2) and branching ratios, and the effects of various interactions (*e.g.*, such as interface damping) with the nanoparticle. Another set of questions, those primarily to be dealt with here, focuses on

the relationship of materials properties to the interaction of light with the nanoparticle. These are described by frequency-dependent linear and nonlinear susceptibilities that incorporate both classical and quantum effects.

2.1. ELECTRONIC STRUCTURE OF METAL NANOCRYSTALS

In semiconductor nanocrystals, differing effective electron and hole masses and a size-dependent bandgap energy make optical properties famously sensitive to size inhomogeneities.[6] In metals, on the other hand, the valence and conduction bands overlap, and the effective masses of electrons and holes are roughly equal (except for *d*-band electrons). Large optical nonlinearities observed in MNPs are due instead to the extreme anharmonicity of the potential in which the electrons move, and thus has high harmonic components. In fact, for metal NPs embedded in a dielectric, the Fermi energy of the metal particles lies near the midpoint of the insulator bandgap and the electrons behave as particles trapped in a three-dimensional box. However, at the metal-insulator interface, both physical (*e.g.*, interface roughness) and chemical (*e.g.*, tunneling between metal states and affinity levels) effects alter the plasmon response and lifetime.[7]

The density of states, roughly the number of conduction-band electrons divided by the Fermi energy, is[8]

$$D(E_F) = \delta^{-1} = \frac{V m_e k_F}{2\hbar^2\pi^2} = \frac{2\pi a^3 \left(3\pi^2 n_e\right)^{1/3}}{2\hbar^2\pi^2} \Rightarrow$$
$$\delta = 3.6215\cdot 10^{-2}\,\frac{1}{a^3\cdot \tilde{k}_F}\ eV \qquad (1)$$

where the Fermi momentum $\tilde{k}_F$ is in units of 10^8 cm^{-1} and NP radius a is in nm. For gold NPs, the level spacing reaches 1 eV at a diameter of ~2 nm.

The polarization induced in MNP composites by optical fields $\mathrm{E} = \mathrm{E}_o e^{i\omega t}$ is

$$P_i(\omega_i) = \sum_j \chi^{(1)}_{ij} E_j(\omega_j) + \sum_{j,k} \chi^{(2)}_{ijk} E_j(\omega_j) E_k(\omega k) + \sum_{j,k,\ell} \chi^{(3)}_{ijk\ell} E_j(\omega_j) E_k(\omega_k) E_\ell(\omega_\ell) + \ \ldots \qquad (2)$$

where the *j*, *k*, *l* refer to Cartesian coordinates and the electric-field polarization. In general $\chi^{(2)}$ vanishes in centrosymmetric materials;[9] however, plasmon-enhanced second-order nonlinearities have been observed in MNP arrays.[10]

Assuming that $\chi^{(2)}$ vanishes, an effective susceptibility $\tilde{\chi}$ can be written

$$\tilde{\chi}_{i\ell} = \chi^{(1)}_{i\ell} + \sum_{jk} \chi^{(3)}_{ijk\ell}\left(\omega_i = \omega_j + \omega_k + \omega_\ell\right) \times \left[E^*_j\left(-\omega_j\right)E_k\left(\omega_k\right) + E_j\left(\omega_j\right)E^*_k\left(-\omega_k\right)\right]E_\ell\left(\omega_\ell\right) \tag{3}$$

where the $\chi^{(q)}$ are functions of the optical frequency ω and of materials parameters defined both by classical and quantum effects.

2.2. EFFECTS OF CLASSICAL CONFINEMENT

In a mean-field approximation, the effective dielectric constant $\tilde{\varepsilon} \equiv \varepsilon_0\left(1+\tilde{\chi}\right)$ of a MNP with dielectric function $\varepsilon_{NP}(\omega) = \varepsilon_1(\omega) + i\varepsilon_2(\omega)$ occupying a volume fraction $p << 1$ in a transparent host with a dielectric constant ε_h satisfies

$$\frac{\tilde{\varepsilon} - \varepsilon_h}{\tilde{\varepsilon} + 2\varepsilon_h} = p \cdot \frac{\varepsilon_{NP} - \varepsilon_h}{\varepsilon_{NP} + 2\varepsilon_h} \tag{4}$$

Expanding this expression to first order in *p*, one finds

$$\tilde{\varepsilon} = 1 + \chi^{(1)} = \left[1 + 3p\varepsilon_h \frac{\left(\varepsilon_1^2 + \varepsilon_2^2 + \varepsilon_1\varepsilon_h - 2\varepsilon_h^2\right) + 3i\varepsilon_2\varepsilon_h}{\left(\varepsilon_1 + 2\varepsilon_h\right)^2 + \varepsilon_2^2}\right] \tag{5}$$

The complex-valued function $f_c(\omega) \equiv 3\varepsilon_h / \left[\varepsilon_{NP}(\omega) + 2\varepsilon_h\right]$ is called the *local-field enhancement factor*, and measures the enhanced susceptibility due to the effect of spatial confinement on the local dipole moment. It is resonant at the surface plasmon frequency ω_r for which $\varepsilon_1(\omega_r) + 2\varepsilon_h(\omega_r) = 0$. About 85% of the total oscillator strength comes from the surface plasmon polariton.[11]

The first-order susceptibility is related to the linear index of refraction n_0 and the linear absorption coefficient α_0 by:

$$\alpha_0 = \frac{\omega}{n_0 c}\ \Im m\left[\chi^{(1)}\right] \qquad n_0 = \Re e\left[1 + \chi^{(1)}\right] \tag{6}$$

In terms of $\chi^{(1)}$, the linear absorption coefficient for the composite is thus

$$\alpha_0(\omega) = p\frac{9\varepsilon_h^2}{\left|\varepsilon_{qd} + 2\varepsilon_h\right|^2}\varepsilon_2 \equiv p\left|f_c^2(\omega)\right|\varepsilon_2 \tag{7}$$

The resonant contribution to the absorption in MNP composites diminishes linearly with MNP radius, until for MNPs smaller than approximately 2 nm diameter a band gap opens up in the MNP electronic structure.[12]

For a free-electron metal, the lineshape of the plasmon resonance is a modified Lorentzian,[13] with a central frequency given by

$$\Omega_{SPR} = \frac{4\pi n_e e^2 / m_e}{\sqrt{\varepsilon_{lattice} + \varepsilon_{\text{inter}} + 2\varepsilon_{\text{intra}}}} \equiv \frac{\omega_p}{\sqrt{\varepsilon_\infty + 2\varepsilon_{\text{intra}}}} \tag{8}$$

where ω_p is the bulk plasmon frequency of the metal, and $\varepsilon_{lattice}$ and $\varepsilon_{\text{inter}}$ are respectively the lattice and interband contributions. The width of the surface-plasmon resonance is the inverse of the electron scattering time; semi-classically, this width is composed of the intrinsic electron-phonon and *Umklapp* scattering which contribute to τ_0, and the surface collision time:

$$\gamma = \frac{1}{\tau_e} = \frac{1}{\tau_0} + g\frac{v_F}{a} \tag{9}$$

where γ is a constant of order 0.7, v_F is the Fermi velocity, and a is the radius of the MNP. Measurements of plasmon linewidth in single Au nanocrystals with radii ranging from 16 to 24 nm yielded values in the range 150-200 meV, corresponding to a relaxation time around 8 fs [14].

For a material without a symmetry axis, the third-order susceptibility is related to the nonlinear index of refraction and absorption coefficient by[15]

$$\beta = \frac{96\pi^2\omega}{n_0^2 c^2}\ \Im m\ [\chi^{(3)}] \qquad n_2 = \frac{12\pi}{n_0}\ \Re e[\chi^{(3)}] \tag{10}$$

The third-order susceptibility, a fourth-rank tensor, has eighty-one components; however, this number is often reduced by symmetry. For example, NPs with cubic symmetry have only four independent components of $\chi^{(3)}$.

To find an explicit expression for $\chi^{(3)}$, one applies Maxwell's equations to first order in the electric field for a cubic nonlinearity;[16] the dielectric function is $\varepsilon_{qd} = \varepsilon + \chi^{(3)} \cdot \left|\vec{\mathrm{E}}\right|^2$, and the electric displacement is:

$$\vec{\mathrm{D}} = \varepsilon\vec{\mathrm{E}} + \chi^{(3)}\left|\vec{\mathrm{E}}\right|^2\ \vec{\mathrm{E}} \tag{11}$$

where contraction over the tensor product of the electric fields **E** with the $\chi^{(3)}$ is implied. For a charge-free medium in the quasistatic approximation, $\vec{\nabla} \bullet \vec{\mathrm{D}} = \mathbf{0}$; and $\vec{\nabla} \times \vec{\mathrm{E}} = \mathbf{0}$ as well. The composite nonlinear optical susceptibility is[17]

$$\chi_{eff}^{(3)} = p \cdot \chi_{NP}^{(3)} \frac{\left\langle \left|\vec{E}\right|^2 \vec{E}^2 \right\rangle}{\left|\vec{E}_0\right|^4} \tag{12}$$

where the brackets denote spatial and temporal averages. For spherical MNPs, the field **E** inside the particle is related to the electric far field by

$$\vec{E} = \vec{E}_0 \frac{3\varepsilon_h}{\varepsilon_{NP} + 2\varepsilon_h} \tag{13}$$

Substituting Eq. (13) into Eq. (12), the effective third-order susceptibility is:

$$\chi_{eff}^{(3)} = p \cdot \chi_{NP}^{(3)} \left| \frac{3\varepsilon_h}{\varepsilon_{NP} + 2\varepsilon_h} \right|^2 \cdot \left(\frac{3\varepsilon_h}{\varepsilon_{NP} + 2\varepsilon_h} \right)^2 \equiv p \cdot \chi_{NP}^{(3)} \left| f_c \right|^2 \cdot \left(f_c \right)^2 \tag{14}$$

Self-consistent treatments of a jellium metal[18] yield the same result.[19] This local-field enhancement in $\chi^{(3)}$ was first observed in filter glasses[20] and has since been verified in numerous experiments.[21,22]

2.3. EFFECTS OF QUANTUM CONFINEMENT

The third-order susceptibility of MNPs can be calculated from the quantum mechanics of the intraband and interband transitions, as well as from the hot-electron effects that change the thermodynamical state of the nanoparticles.[23]

Intraband transitions originate and terminate in conduction-band states and show strong quantum-confinement effects, since both initial and final electronic states are constrained to a length scale much smaller than the bulk-metal mean-free path. For an absorptive nonlinearity, a phemenological treatment yields

$$\chi_{\text{intra}}^{(3)} = -i \frac{64}{45\pi^2} T_1 T_2 \frac{1}{a^3} \frac{e^4}{m^2 \hbar^5 \omega^7} E_F^4 \, g_1(\nu) \left(1 - \frac{a}{a_o}\right), \; a \le a_o \tag{15}$$

where T_1 and T_2 are energy lifetime and dephasing time, respectively; g is a function with a magnitude near unity; and a_0 ~ 10-15 nm depending on the metal. Note the inverse a^3 dependence.

Interband transitions originate in the spatially localized *d*-bands and terminate in conduction-band states; they are only weakly confined by quantum effects because the initial state is already localized. The third-order susceptibility for dipole-allowed interband transitions is

$$\chi^{(3)}_{\text{inter}} = -i\frac{e^4}{m_e^2\hbar^2\omega^2}\frac{2\pi A(\Omega)}{3}\tilde{T}_1\tilde{T}_2 J(\omega)\cdot\left|P_{if}\right|^4 \qquad (16)$$

where $A(\Omega)$ is an angular form factor, $\tilde{T}_1$ and $\tilde{T}_2$ are the energy lifetime and dephasing time for the interband transition, respectively; $J(\omega)$ is the joint density of states; and P_{if} is a dipole matrix element. For gold nanoparticles in the 5-15 nm diameter range, the interband nonlinearity near the SPR is approximately 50-100 times as large as the intraband contribution.

Absorption of photons in a MNP creates a population of hot electrons that reach thermal equilibrium with the lattice only after several ps. The temperature-broadened Fermi-Dirac distribution contributes an additional hot-electron (*he*) term to the third-order nonlinear susceptibility:

$$\chi^{(3)}_{he} = i\frac{\omega\varepsilon_{D2}\tau_o}{24\pi^2\gamma T}\frac{\partial\varepsilon_{2L}}{\partial T} \qquad (17)$$

where γT is the electronic specific heat; ε_{D2} and ε_{2L} are, respectively, the imaginary parts of the free-electron-gas (Drude) and interband contributions to the dielectric function ε; and τ_0 is an electron cooling time. This size-independent hot-electron susceptibility can be 10-10^3 times as large as the third-order *intra*band susceptibility, and by reducing the electronic population near the Fermi level, may make possible otherwise forbidden interband transitions, thus shifting the center frequency of the SPR.[24]

3. Fabrication Techniques for Plasmonic Nanostructures

Metal NP composite materials have been fabricated as thin NP films made by ion implantation;[21] two-dimensional layered stacks of NPs made by sequential, multitarget pulsed laser deposition (PLD);[25] and fractal colloidal assemblies of NPs.[26, 27] Lithographic techniques have been used to make arrays of relatively larger metal nanoislands.[28] PLD of Cu and Al_2O_3 and low-energy (10 keV) ion implantation of Sn into fused silica produce thin layers of nanoparticles in the quantum confinement range of NP sizes.[29] These latter approaches produce better results than blanket ion implantation, but size and spacing are still determined by diffusion and aggregation kinetics.

Bulk nanocomposite films have been used to study kinetics and dynamics of NPs, adsorbate effects, and nonlinear refraction and absorption ($\chi^{(3)}$ effects). However, interest is shifting to NP structures designed to isolate and control specific optical effects. For instance, plasmon-photon coupling was studied using an Au NP array fabricated lithographically atop a waveguide.[30] The study of anomalous transmission effects in nanoscale

hole arrays relies on FIB fabrication or electron-beam lithography of sub-wavelength-scale arrays.[31]

Hence there is an emerging consensus that the nanosynthesis techniques will eventually combine "bottom up" self-assembly strategies with "top-down" lithographic patterning to produce useful devices. In this section, we examine some physics-based approaches that illustrate both the promise and the problems with this dual approach. In particular, the experiments described in Sections 3.1 and 3.2 show clearly how surface energies and diffusion rates at interfaces affect nucleation and growth of NPs at prepared sites. While these techniques generate small nanoparticles, there is still a stochastic dispersion in size and location that is characteristic of self-assembly.

In all cases, a focused ion beam (FIB) was used either to create at which metal NPs nucleate and grow, or for lithographic patterning. The FIB is a commercial tool used in the semiconductor industry for mask repair and similar tasks. The principles of material removal via sputter erosion using the FIB are well known. In the FIB ion source, liquid gallium is drawn to a very sharp tip (Taylor cone) from which individual ions are extracted. The ions are accelerated through 30kV potential and focused onto the substrate, where material is sputtered from the surface. The FIB is computer-controlled, and patterns of arbitrary complexity can be written to the substrate with user-defined pixel-addressable pattern files. The smallest feature size that we obtain in practice is 10 nm. The experimental approach is to create ordered damage sites in Si/SiO_2, a photoresist or other suitable material. Subsequently, standard deposition techniques can be used to form nanoparticles by nucleation and growth, or through lithographic patterning and lift-off.

3.1. COUPLING SELF-ASSEMBLY TO LITHOGRAPHIC PATTERNING

Electroless deposition has been used both to produce linear nanostructures and to encapsulate core-shell nanoparticles. However, in these cases, there is no control over the spatial distribution of the nanoparticles thus produced. One experiment undertaken at Vanderbilt used the focused ion beam (FIB) — a device widely used for stripline and mask repair in the semiconductor industry — to etch through the thin SiO_2 layer on a Si wafer. The FIB has a Ga^+ beam with a nominal diameter of 10 nm, and uses pixel-by-pixel computer control to provide nanometer-scale precision in the location of small holes or other patterns over lateral dimensions as large as 200 μm.

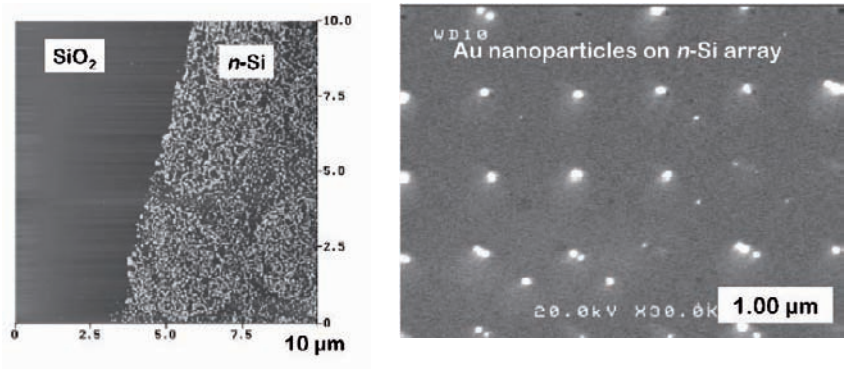

Figure 2. (Left) AFM scan of Au nanoparticles deposited by electroless deposition on an Si substrate; the nanoparticles are absent on the left portion of the substrate covered by a thermal oxide. (Right) Section of the FIB-machined array showing preferential nucleation and attachment of Au nanoparticles at the machined sites. Energy-dispersive X-ray analysis of the samples (not shown) showed only Au spectral lines and a large Si peak due to the substrate.

Electroless deposition of Au and self-assembly of Au nanoparticles was attempted on a Si surface patterned by a FIB.[32] Highly doped Si wafers were purchased commercially and immersed in a solution of colloidal Au. The wafers as delivered were covered with a 20 nm thick layer of furnace-grown SiO_2. Using a beam current of 11 pA from the FIB, arrays of holes with 50 nm diameter at half depth, located on 300 nm centers, were drilled through the oxide into the Si. The drilling of each hole required a few seconds of exposure to the Ga^+ beam. Following the patterning step, the wafer was etched in dilute (5%) HF to remove about half the oxide layer, rinsed with deionized water, and placed in a commercial electroless gold-plating solution for a few minutes at a temperature of 60 C. The size of the nanoparticles plated in this procedure depends primarily on the immersion time in the plating solution; one can expect some size dispersion due to statistical variations in this growth process.

AFM scans of the surface (Figure 2, left image) showed that the Au would nucleate and grow into nanocrystallites on the *n*-type Si, but not on that portion of the wafer with a 20 nm oxide layer. Energy-dispersive X-ray analysis of the electroless material showed that the patterned area contained Au and Si without other impurities. The Au also appeared to migrate and nucleate preferentially at predrilled holes in the Si substrate, as shown in the right panel of figure 2.

However, nucleation of multiple nanoparticles occurred some fraction of the time, as one can see in the array; there was also some variability in the size of the nanoparticles. These are typical problems with self-

assembling nanoscale systems, because of the inherent variability in processes ruled by chemical kinetics. However, a solution at least to the first problem has been described in a recent paper describing the use of capillary forces during the "drying down" of a solution of colloidal nanoparticles to control adhesion at predetermined, lithographically fabricated nucleation sites.[33] It should also be noted that this technique could, in principle, be used to fabricate arrays over large areas. However, most FIBs do not have the kind of interferometrically driven stages that would allow precise stitching of patterns any larger than 200x200 μm^2.

3.2. SELF-ASSEMBLING SILVER NANOBRACELETS

The second experiment[34] was also carried out with a nanomachined array of holes in a Si substrate, but this time Ag vapor was deposited by pulsed laser deposition. Once again, the goal was to have a maskless procedure that would avoid the challenges associated with deposition, patterning and lift-off of a photoresist. This configuration produced circular formations of nearly spherical Ag nanoparticles of average diameter, arranged in a "nanobracelet" formation around the 20 nm diameter holes in the substrate. That experiment demonstrated that "dry" deposition could also result in preferential nucleation and growth of the nanoparticles at sites machined by the focused ion beam. It also provides important insight into the problems posed by the stochastic nature of the self-assembly process.

The substrate was highly conductive, "metallic" *n*-type Si wafer, etched in a standard dilute solution of hydrofluoric acid and then re-oxidized in a controlled furnace environment to produce a layer of SiO_2 37 nm thick. The oxide thickness was verified by ellipsometry. Heteroepitaxial deposition of the metal - in this case, silver - was made by pulsed laser deposition (PLD), a versatile technique for depositing and growing nanoparticles and thin films of metals, semiconductors and insulators. In PLD, an excimer laser is used to ablate material from a target; atoms and ions from the resulting ablation plume of target material are deposited on a substrate. The laser parameters, deposition rate, and substrate temperature govern nucleation and growth of nanocrystals.

The FIB was used to prepare a nanoscale hole array prepared in the oxidized Si substrate, prior to PLD deposition. The array was prepared at 80 kX magnification using a 1 pA Ga^+ ion beam with an effective spot diameter of 8 nm. Hole-depth was controlled by adjusting the dwell time for the Ga beam at each lattice location. The array in Figure 3 shows 30 nm diameter holes spaced in a square pattern on 120 nm centers. This represents a limit of the current technique in the sense that collateral

sputtering attributable to the wings of the Ga beam intensity distribution can significantly erode the substrate at interstitial locations between lattice sites for spacings less than 120 nm. This effect degrades the quality of nanoparticles arrays we were able to achieve at that time. Then Ag was deposited on the substrates using the PLD at room temperature to a thickness of 1 nm. Nanoparticle formation was observed and characterized using SEM and AFM techniques.

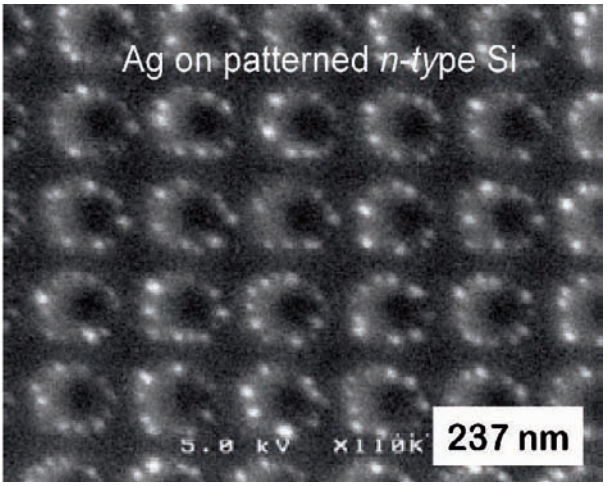

Figure 3. Schematic showing possible adhesion sites for Au or Ag nanoparticles on an oxidized Si substrate micromachined by a focused ion beam.

Substrates prepared with shallow holes that did not penetrate the oxide layer (that is, less than 37nm) did not display preferential growth sites for Ag islands, which formed irrespective of the presence of pits in the oxide surface layer, as confirmed by SEM and AFM observations. This same result was seen in experiments on bulk amorphous SiO_2 drilled by FIB. These observations rule out Ga-induced Ag clustering, simple SiO defects, or SiO_2 sidewall/surface interactions as mechanisms for the preferential nucleation at FIB damage sites.

SEM analysis of the nano-bracelet structure reveals that there is an average of 10 clusters per lattice point, each averaging 20 nm in diameter, and randomly distributed around the periphery of each lattice point. There are no detectable Ag clusters in the interstitial zones between lattice sites, showing that each FIB-drilled hole is an effective sink for Ag adatoms. Assuming each 20 nm diameter cluster is a cylinder with a thickness equal to the deposited Ag layer (1 nm) each bracelet accounts for a total of 19.4 x 10^6 Ag atoms. This compares reasonably with the 12.9 x 10^6 deposited

adatoms available to each lattice site, and well within the margin of error used in this estimate.

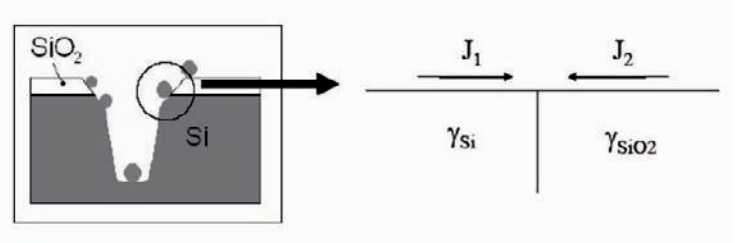

Figure 4. Schematic of the Si-SiO_2 interface near a FIB-drilled hole. (Right) Diffusion coefficients for Ag on Si and SiO_2 near the interface.

The self-assembly of the Ag nanoparticles can be understood as the result of differing surface energies γ of the Si *vs* the SiO_2 phases, respectively. Figure 4 depicts a one-dimensional model of the two phases separated by a sharp interface. Formation of clusters is mediated through the surface diffusion of adatoms. The flux of the diffusing species (Fick's first law) can be written as

$$J_1 = -D_{Ag(Si)} \frac{\partial C_{Ag(Si)}}{\partial x} - \frac{D_{Ag(Si)} C_{Ag(Si)}}{RT} \frac{\partial E}{\partial x} \tag{18}$$

where J_1 is the flux of Ag adatoms on the Si phase, $D_{Ag(Si)}$ the surface diffusion coefficient for Ag on Si, $C_{Ag(Si)}$ the interfacial concentration of Ag species on Si, T the temperature, and $\partial E/\partial x$ the surface-energy gradient between the two phases. A similar equation describes the flux of Ag atoms on the SiO_2 phase.

$$J_2 = -D_{Ag(SiO2)} \frac{\partial C_{Ag(SiO2)}}{\partial x} - \frac{D_{Ag(SiO2)} C_{Ag(SiO2)}}{RT} \frac{\partial E}{\partial x} \tag{19}$$

A "local" thermodynamic equilibrium must prevail [5] at the junction of the free surface and the interface. Since Ag is uniformly applied over the substrate during the PLD process, at least in the early stages of deposition, concentration gradients vanish, so terms of the form $\partial C/\partial x$ are negligible. At equilibrium, $J_1 = J_2$, and Ag redistributes according to the interfacial gradient in surface energy.

$$\frac{D_{Ag(Si)} C_{Ag(Si)}}{RT} \frac{\partial E}{\partial x} = -\frac{D_{Ag(SiO2)} C_{Ag(SiO2)}}{RT} \frac{\partial E}{\partial x} \tag{20}$$

Since the interface is sharp, the value of $\partial E/\partial x$ differs only in sign from right to left. Canceling common factors, the condition of local equilibrium is:

$$\frac{D_{Ag(Si)}}{D_{Ag(SiO2)}} = \frac{C_{Ag(SiO2)}}{C_{Ag(Si)}} \tag{21}$$

Thus this simple model predicts a redistribution and aggregation of Ag at the interface, driven by minimization of the chemical potential of Ag at the interface. Accumulation of Ag at the interface should depend on the difference between the activation energies for surface diffusion of Ag in either phase. Figure 3 shows that following deposition of Ag at the interface, stable clusters self-organize via a thermodynamically driven self-assembly mechanism.

3.3. FABRICATION OF METAL NANODISK ARRAYS

To circumvent the problem of variable nanoparticle size in self-assembly, we have also used the FIB in a lithographic process to generate nanoparticle "superlattices" designed to achieve particular optical effects. It should be noted, however, that the penalty is increased nanoparticle size.

As illustrated in Figure 5, a solution of PMMA (MW 950 K) in anisole (1.7% by weight), was spin-coated on an ITO-covered glass substrate, or onto a conductive silicon substrate. The spin coating is done in two stages: at 500 rpm for 5 seconds, then at 4000 rpm for 45 s; a hot bake at 180 ºC for 3 minutes follows. This produces a uniform layer 50-60 nm thick, matching the range of the Ga^+ ions at 30 keV. The Ga^+ beam is focused to a nominal diameter of 10 nm to pattern single-pixel dot arrays on the PMMA; typical ion current is 1 pA, and dwell time per dot is 80 µs. The exposed PMMA was developed in a 1:3 methyl isobutyl ketone and isopropyl alcohol mixture.

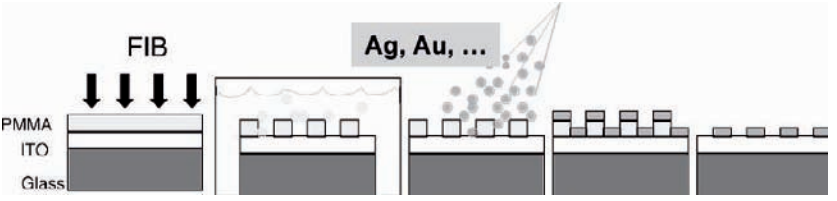

Figure 5. Schematic of the focused ion-beam lithography process used to fabricate arrays of noble-metal nanoparticles. From left to right: A spun-on PMMA film is irradiated by the focused ion beam (FIB) according to a pre-programmed pattern. The exposed sample is then developed and the FIB-irradiated portion of the mask washed away. Pulsed laser deposition is then used to deposit a layer of a noble metal (Ag, Au, Cu) on the masked surface, leaving the film covering the entire sample. Lift-off of the PMMA leaves an array of metal nanoparticles.

The developed samples are coated by a metal layer 20-60 nm thick either by pulsed laser deposition from commercial sputtering targets or, more commonly, by thermal evaporation. The laser deposition chamber was a commercial unit (Epion PLD3000). In the lift-off step, the remaining PMMA layer together with the PLD film deposited on it is removed by a stock resist remover (Microposit 1165) leaving the nanoparticles resting on the substrate. The stoichiometrically correct crystalline oxides are obtained by an additional step involving 30 minutes of thermal annealing at 450 ºC in 250 mTorr of O_2 background pressure. On insulating substrates where ion bombardment could charge the sample, a thin overlayer of silver is deposited on the PMMA, as the Ga^+ ions will easily penetrate a conductive overlayer 10 nm or so thick.

For optical experiments, the substrate is typically 0.5-mm Corning 1737 aluminosilicate glass coated with a 15-30 nm layer of indium tin oxide (ITO); the lithographic pattern was made in a ~50 nm poly(methyl) methacrylate (PMMA) spin-coated resist layer. A scanning electron microscope (SEM) was used to examine array integrity and nanoparticle structure. The lattice sites in the arrays have occupation factors that range from 0% in the case of very thin nanoparticles (3-4 nm) to 35% for 20-nm thick NPs. Even for the thicker NPs, however, the periodicity of the arrays is sufficient to observe strong diffraction. Once the technique of this lithography is mastered, arrays of NPs in a variety of configurations can be made, as shown in Figure 6 for Ag NPs. These NP super-lattices have a variety of different configurations and symmetries that can be used to test the understanding of various nonlinear optical responses.

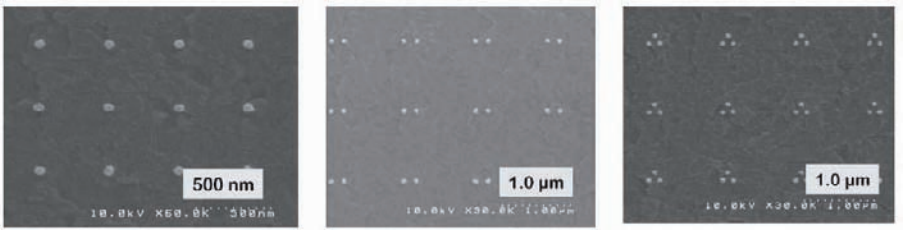

Figure 6. Sample of Ag nanoparticle monomer, dimmer and trimer arrays made by FIB lithography, for use in optical physics experiments on linear and nonlinear phenomena.

To sum up these discussions about "top-down" *vs* "bottom up" fabrication methods for nanoparticles, one can observe that self-assembly methods still produce the smallest nanoparticles, while lithographic techniques provide a way of gaining the advantage of optical coherence over the entire area of a sample by means of diffraction. It remains to be seen whether reported techniques for "sizing" nanoparticles after self-

assembly[35] can be combined with lithography to produce large arrays of nanoparticles in the quantum size-effect regime.

4. Plasmonics with Lithographically Fabricated Nanostructures

This section explores examples of optical physics studied using metal NPs and NP arrays fabricated by techniques described in Section 3. Three examples are considered: sensitive detection of sulfur pollution using the linear SPR response of a Ag nanoparticle array; second-harmonic generation from an array of ellipsoidal Au nanoparticles; and the size dependence of the nonlinear refractive index of refraction of Cu NPs in the quantum size-effect regime.

4.1. SURFACE-PLASMON RESONANCE SHIFTS AS SENSORS

The extraordinary sensitivity of the surface-plasmon resonance peak has been exploited in a galaxy of sensor applications. Silver, for example, famously tarnishes in air;[36-40] this sensitivity to gas exposure[41] has been used in sensors.[42] Until recently there had been no systematic study of corrosion effects on silver nanoparticles (Ag NPs) in the laboratory environment — despite the frequent use of Ag NPs in nonlinear optical experiments. By combining scanning Auger spectroscopy with measurements of the SPR peak and with calculations of the effect of corrosion, sensitivity was documented below the ppb level and the rate of corrosion of Ag NPs could be estimated using optical data, optical constants of silver sulfide from the literature[36] and reasonable physics assumptions.[43]

4.1.1. *Preparation of the nanoparticle array samples*

Arrays of Ag NPs arranged as dimers on a square lattice were fabricated on indium-tin-oxide (ITO) coated glass substrates using FIB lithography (IBL).[44, 45] The ITO is conductive enough to prevent charging during exposure and enable secondary-electron imaging. The Ag film was deposited by pulsed laser deposition (PLD) using a KrF excimer laser (248 nm), with a pulse energy of 400 mJ and a repetition rate of 25 Hz. The typical fluence in the elliptical target spot was approximately 2 ± 1 J/cm^2.

Optical scattering measurements were performed with a dark-field confocal microscope interfaced to a spectrometer with a CCD array detector for spectral analysis; complete spectra, normalized to the lamp output of the lamp, could be acquired at quarter hour intervals for time spans as long as days. Some arrays were analyzed at the Oak Ridge National Laboratory, using a scanning Auger nanoprobe with a spot diameter of order 20 nm.

Scanning electron micrographs of the nanoparticles were obtained as needed using a microscope equipped with a field emission gun. A scanning electron micrograph showing one such dimer can be seen in Figure 7 (left).

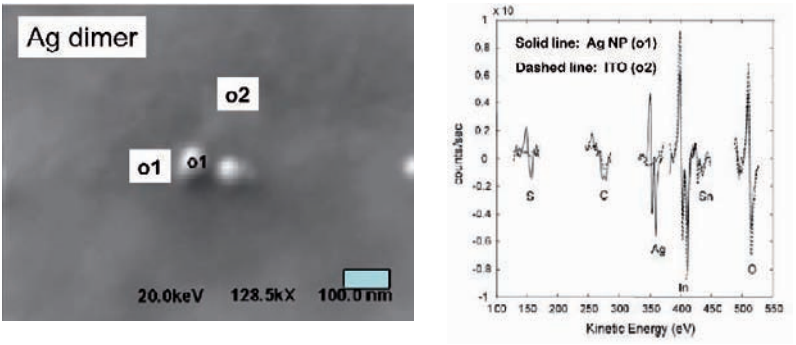

Figure 7. (Left) Electron micrograph of a Ag NP dimer used in Auger analysis; the scale bar at lower right is 100 nm long. (Right) Auger spectra of an Ag nanoparticle (location o1) and on the ITO-glass substrate (location o2) after thirty-six hours exposure to laboratory air.

4.1.2. *Optical Response as a Function of Environmental Exposure*

Auger spectra of Ag NPs exposed to ambient are shown in Figure 7 (right). The nanoparticle "dimer" in Fig. 7 (left) is one element of the 2D lattice structure fabricated by IBL. The Auger spectrum reveals the presence of sulfur on the silver NP. Signals from indium, tin and oxygen fall at the NP locations because Auger spectroscopy is so surface-sensitive. However, there is a slight increase in the impurity carbon peak at the NP.

4.1.3. *Chemisorption Effects on the Plasmon Spectrum*

Silver corrodes in air by reacting with ambient levels of hydrogen sulfide gas (H_2S, 0.03-5 ppb) and carbonyl sulfide (OCS, 0.5 ppb) to form silver sulfide (Ag_2S);[40] both processes are enhanced by high relative humidity (RH). As the background concentration of H_2S is only one tenth that of OCS, and there were no H_2S sources in the laboratory, it is probable that OCS plays a larger role than H_2S.[39] Corrosion in the Ag NPs will occur more rapidly than in thin films due to the much larger surface/volume ratio. The scanning Auger results also show that the nanoparticles were preferential sites for sulfur accumulation.

Figure 8 (left) shows the measured change in the optical response as a function of exposure to laboratory air for a square array of annealed silver nanodisks (20 nm high, 60 nm in diameter) with grating constant 162 nm. The peak amplitude decreases nearly one order of magnitude over the thirty-six hour observation period, while the resonance peak redshifted

65 nm at a rate of ~1.8 nm/hr. Electron microscopy shows that the nanoparticles do not change their shape significantly during this long exposure time.

The conjecture of NP sulfidation was confirmed by Mie scattering calculations, modeling the NPs as oblate spheroids, which in general exhibit two resonances. An oblate spheroid 20 nm high and 60 nm in diameter, embedded in an effective medium having $\varepsilon = 2.3$[46] has a strong surface-parallel mode at ~500 nm. Changing the nanoparticle interface from Ag/air to Ag/Ag_2S "scale" of increasing thickness redshifts and damps the SPR spectrum.

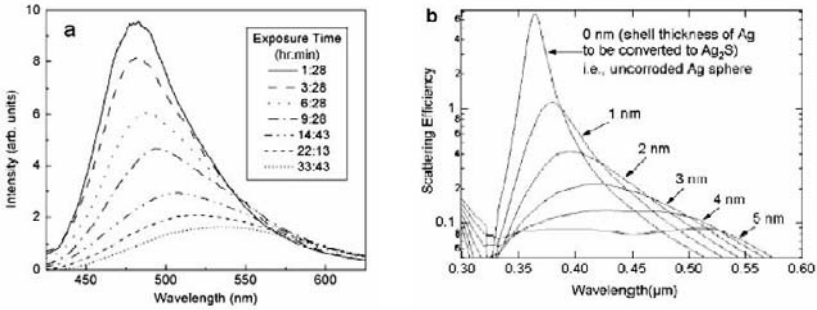

Figure 8. Comparison of experimental (a) and calculated (b) plasmon resonance spectra at various exposure times. Assumptions for the calculation are found in the text.

Figure 8(b) shows the calculated scattering efficiency for Ag spheres of 25 nm initial radius, assuming that the outer shell of Ag reacts completely to form Ag_2S scale. With optical constants for Ag[47] and for Ag_2S[36], and the density of Ag (10.5 g/cm^3) and its sulfide (7.2 g/cm^3),[48] the scale thickness is half again as large as the thickness of Ag that reacted to form the scale. Comparison of the calculated and observed spectral features suggests an upper limit of order 6 nm of scale growth on the Ag NPs.[37]

4.1.4. *Comparison of Theory with Experiment*

A linear increase of sulfide thickness with exposure is consistent with a flux-limited growth that extends up to ten equivalent monolayers (ML) of scale.[39] Due to the high surface-to-volume ratio, and the high curvature of the nanoparticle surface, the reaction rate should be higher for NPs than for bulk samples.[38,40] Since the scale growth is in the linear growth regime, these data can be used to estimate the increase in reactivity for the nanoparticles relative to the bulk. Since the resonance of Ag spheres blueshifts with decreasing radius, the redshift due to the increased dielectric function of the surroundings is partly compensated by shrinking of the Ag core. A 3-nm-thick shell of Ag converted to scale (4.7 nm Ag_2S) would

give an SPR shift of 54 nm, quite congruent with our data. Differences in the corrosion rate measured under conditions of differing relative humidity provide a consistency check, allowing us to conclude that this detailed picture of the corrosion mechanism is indeed accurate.

4.2. SECOND-HARMONIC GENERATION FROM METAL NANOPARTICLES

Second harmonic generation (SHG) has been widely used to probe electron dynamics and surface structure in metal films and nanoparticles, in solution and on substrates.[49-54] These studies have been motivated by the need to understand metallic behavior as a function of particle or film dimensions, the role of the metal plasmonic response in surface spectroscopy, and plasmonic applications such as all-optical switching and photon-plasmon interactions.[55-57]

Symmetry forbids even-order harmonic generation in centrosymmetric material systems.[58] Even when non-centrosymmetric particles are in an array that has inversion symmetry with respect to the illuminating beam, the "real-surface" SHG is quenched along the illumination direction.[28] Likewise, the SHG from within the optical skin depth vanishes in the illumination direction for pump light normally incident on a centrosymmetric NP sample.[51] Thus, SHG has not been widely used to probe electron dynamics in nanoparticles.[59] However, a Bragg diffraction grating can spatially isolate NP-generated SH light from both the pump beam and interface SH contributions, thus facilitating the measurement of small SHG signals.[60] The SHG can be resonantly enhanced by tuning the particle plasmon mode to the frequency of the excitation laser.

4.2.1. *Experimental Geometry*

We have detected plasmon-enhanced, Bragg-diffracted SHG from Au nanorods with an aspect ratio of 1.2, prepared lithographically in a symmetric grating geometry.[61] Nanoparticle arrays, typically 60 μm square, were fabricated by focused-ion-beam lithography and thermal evaporation. As depicted in Figure 9 (left), they were illuminated by a passively mode-locked Ti:sapphire oscillator producing 50-fs pulses centered at 800 nm at 93 MHz pulse-repetition frequency; average power was ~250 mW. The pump beam was focused to a 50 μm spot. Residual pump beam was blocked with a color filter. Fluctuations in incident power were monitored by a silicon photodiode, and pulse duration was measured with an autocorrelator. The fluence is low enough that significant SHG output was achieved without modifying the NP morphology. The extinction coefficients for different axes of the nanorods were determined separately by using a white-light source and rotatable linear polarizer.

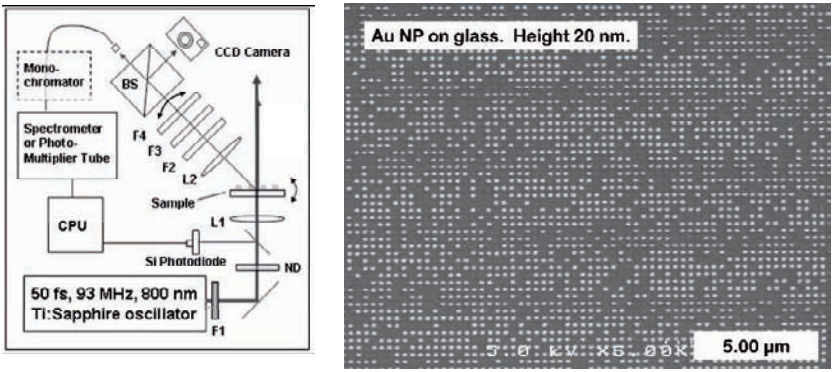

Figure 9. (Left) Experimental scheme for measuring second-harmonic generation from metal nanoparticle arrays. (Right) Typical array used to generate Bragg-diffracted second-harmonic light.

The sample and the detector arm are mounted on independent translation and rotation stages that maintain precise relative alignment of the laser beam, sample and microscope stage. The pump beam is normally incident from the rear (substrate) side of the sample,[60] and the arrays and the NPs are aligned with the polarization of the pump beam. The observation angle is varied, by rotating the detector arm in the plane defined by the pump-beam direction and polarization direction.

The detector optical train comprises a microscope objective (NA 0.25), removable filters, a beamsplitter cube for camera viewing, and an optical fiber to direct the light either to a spectrometer or a photomultiplier tube (PMT) connected to a photon counting module. For PMT measurements, the SHG light is filtered by a monochromator that passes only 400 nm light.

4.2.2. *Experimental Results*

Figure 10 shows the angular distribution of SH light from a grating of Au nanorods aligned along the grating axes. As seen in Fig. 10 the different axes of the nanorods have different associated plasmon modes. At 800 nm, the transmission for the short-axis mode is 95%, whereas for the long axis it is 85%. In Figure 10 (right) the SH signal is plotted for both in-plane particle axes as a function of observation angle from the normal. The long-axis excitation gives a strong SH response, while the signal is almost undetectable for short-axis excitation.

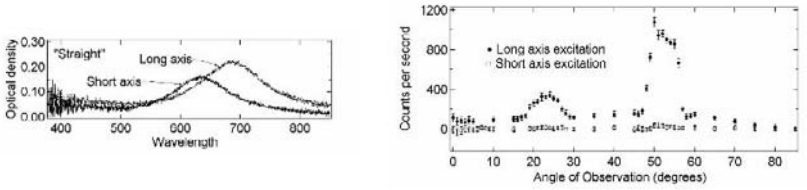

Figure 10. (Left) Extinction spectra for a Au NP array, measured with light polarized parallel (long axis) and perpendicular (short axis) to the long axis of the NP. (Right) Angular dependence of the second harmonic signal generated from this array along the same directions.

4.2.3. *Discussion*

These nanoparticles are symmetric in the plane of the sample. Out-of-plane, however, they are asymmetric, because the dielectric above the particle (air) differs from that beneath the particle (ITO). Hence the particles have a nonzero component of the second-order nonlinear susceptibility, $\chi^{(2)}{}_{\perp\parallel\parallel}$, corresponding to an out-of-plane dipole moment induced by a local in-plane excitation.[62] It is the change in *observation* angle, rather than incident angle, which reveals the effect under s-polarized illumination. Symmetry requires that there be virtually *no zero-order peak*, and the SHG intensity *increases* with diffracted order and with increasing angle of observation from the normal.

In principle, SH light produced by this mechanism cannot be experimentally distinguished from that produced by nonlocal or bulklike excitations.[58] The nonlinear polarization in a isotropic centrosymmetric medium is[63]

$$\vec{P}^{(2)}(2\omega) = (\delta - \beta - 2\gamma)(\vec{E}(\omega)\cdot\nabla)\vec{E}(\omega) + \beta\vec{E}(\omega)(\nabla\cdot\vec{E}(\omega)) + \gamma\nabla(\vec{E}(\omega)\cdot\vec{E}(\omega)) \quad (22)$$

where δ, β, γ are prefactors that contain material parameters and laser frequency. For a plane wave $\vec{E} = E_1 e^{i(kz-\omega t)}\hat{x}$, where $\hat{z}$ is the surface normal, the first two terms vanish and the third term (neglecting spatial variation) reduces to $\vec{P}^{(2)}(2\omega) = 2\gamma ikE_1^2 e^{-2i\omega t}\hat{z}$, with a prefactor $\gamma = n_0 e^3/8m_{eff}^2\omega^4$, where n_0 is the electron density, e the electronic charge, and m_{eff} the effective electron mass. This represents an out-of-plane second-order polarization induced in the particle, which will act as a source of SH light. Although this is a bulk effect, the nanoscale optical properties of the metal are included through the electric field inside the NP.

The angular distribution in a given measurement is the superposition of the radiation pattern from an individual NP with the diffraction pattern

dictated by the array geometry. The SHG emission angle is determined by the pitch of the NP array; this makes it possible to measure the angular distribution from the individual NPs with the high sensitivity gained from constructive interference.

4.3. NONLINEAR INDEX OF REFRACTION IN METAL NANOPARTICLES

The effects of the nonlinear susceptibility $\chi^{(3)}$ include nonlinear refraction, nonlinear absorption, phase conjugation and optical bistability.[64] These are the kinds of phenomena that make it possible to carry out all-optical switching, manipulation of the relative phase and amplitude of optical signals, and so on. One can use either resonant or non-resonant third-order optical nonlinearities in optical devices at ultrafast time scales, to achieve the long-sought dream of switching light by light. The speed and energy, power requirements required for all-optical switching, parameters are well-described in textbooks.[65]

4.3.1. *All-optical switching*

The third-order nonlinear effects described above can be used to construct optical switches. For example, consider the schematic optical switches shown in Figure 11, both based on a Mach-Zehnder interferometer geometry. At left, an electro-optic switch operates by inducing an index change - and hence a phase shift - between the two arms of the interferometer. Thus an input signal, evenly divided between the two arms, can give either a 0 or a 1 output depending on the phase shift. The same effect can be implemented in an all-optical configuration using a material with an intensity-dependent index of refraction n_2 in one arm of the interferometer; here the switching effect is set by the size of the nonlinear index and the size of the input signal.

Optical switching devices should typically have the following operating parameters: switching energy ~ 1 fJ; switching time ~1 ps; repetition frequency ~10 GHz; and average power ~10 μW. For a nonlinear switching device requiring a phase shift up to 2π, in a waveguide geometry 1 μm in cross section and 1 cm long, the nonlinear index of refraction must be:

$$P = \frac{10^{-15}\,\mathrm{J}}{10^{-12}\,\mathrm{s}} = 10^{-3}\,\mathrm{W} \Rightarrow I = 10^{5}\,\mathrm{W}\cdot\mathrm{cm}^{-2}$$
$$\Delta\phi = \frac{2\pi}{\lambda}(n_2 I)L \Rightarrow n_2 = \frac{\lambda}{LI} \approx 10^{-9}\,\mathrm{cm}^2\cdot\mathrm{W}^{-1} \qquad (23)$$

The largest measured values of n_2 at present are within one order of magnitude of this number; the switching energy can probably be lowered

by a factor 10^2 based on demonstrated enhancements of third-order processes in metal metal nanocrystals. However, the expected sensitivities have yet to be demonstrated in waveguide geometries, and there are additional performance figures-of-merit that must be demonstrated for practical implementation of device structures.[66, 67]

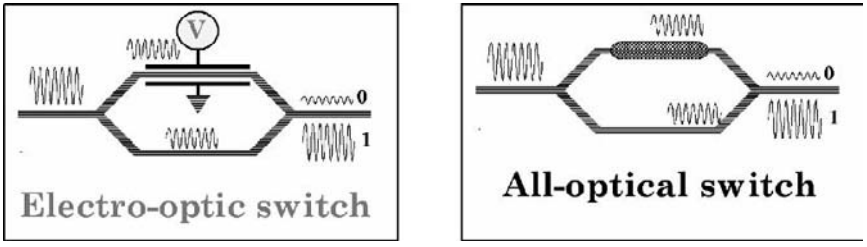

Figure 11. (Left) An electro-optic switch, in the Mach-Zehnder geometry. The phase shift between the two arms of the interferometer is induced by the electro-optic effect on the material in the upper arm. (Right) The same configuration, in which the phase shift is introduced through the nonlinear (intensity-dependent) index of refraction in the upper arm.

4.3.2. *Quantum size effect on the third-order susceptibility*

One possibility for implementing all-optical plasmonic switches is to capitalize on the quantum size effect on the third-order intraband susceptibility. (See Equation (15).) The quantum-confinement effect is manifested in the intraband transition in which electrons from occupied conduction bands near the Fermi edge are excited to unoccupied states higher up in the conduction band. According to Equation (15), the third-order susceptibility for these transitions should increase with the inverse third power of the dot radius below a critical value which is of the order of 11-14 nm for the noble metals.

In the case of Cu, the intraband and surface-plasmon resonances are closer to 565 nm, so that one could hope to see the quantum-size effect with a picosecond laser operating at 532 nm. Using four Cu:silica nanocomposites with Cu NP diameters of 5, 7.5, 10 and 13 nm,[68] the electronic intraband component of $\chi^{(3)}$ was measured using a mode-locked, Q-switched frequency-doubled Nd:YAG laser (532 nm) with a pulse duration of 30 ps, in a forward, phase-matched degenerate four-wave mixing configuration.[69] This measures the *xyxy* component of $\chi^{(3)}$, where the subscripts on the electric field vectors and susceptibilities indicate the polarization direction of the optical field.

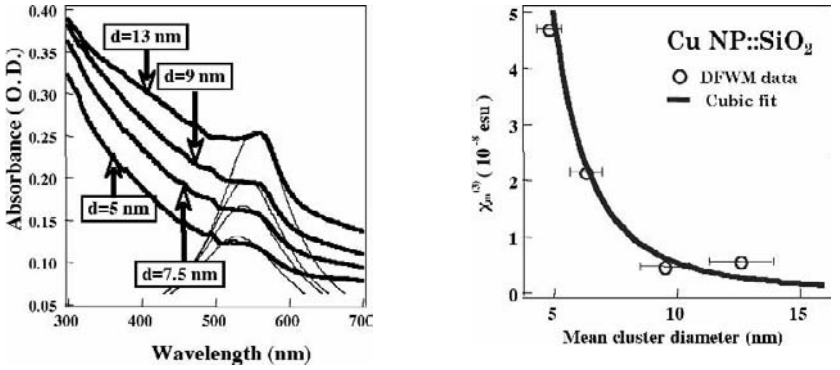

Figure 12. (Left) absorption spectrum for Cu nanoparticles of varying diameters. The Cu NPs were made by ion implantation and annealing. Note the decreasing amplitude of the first-order resonance. (Right) Plot of as a function of particle size for two differ.

By using cross-polarized pumps, it is possible to avoid the formation of a thermal population grating in the sample, eliminating the hot-electron contribution and isolating the intraband, electronic transition. The results are shown in Figure 12 give the results. At the left are the absorption spectra of the four Cu:SiO_2 samples; note that the plasmon resonance amplitude decreases with size, as noted in Section 2. Figure 12 (Right) shows the measured values for the metal component of $\chi^{(3)}$, together with a fit using a cubic curve. Even though the standard deviations of the mean radius distributions are relatively large, it is clear that the data fit the inverse cube dependence on radius or diameter rather well. Similar results have been obtained on even smaller nanocrystals by Afonso and co-workers using the Z-scan technique with shorter pulses.[70] On the other hand, measurements of the third-order interband nonlinearities of Cu and Ag nanoclusters in melt glass showed no quantum-size effects for the absorptive nonlinearity in the vicinity of the surface plasmon resonance,[71] as would be expected for the interband transition.

The quantum size effect offers potentially the greatest promise for practical implementation of photonic devices based on metal nanoparticles, because in a metal NP embedded in a dielectric, the absorption of the nanoparticles is proportional to their volume, while the third-order susceptibility in the quantum size regime increases inversely with volume, thus in some sense canceling the unwanted effects of linear absorption.[72] Thus the most important challenge as far as the technology of third-order photonics is concerned is to find useful ways of processing large-area methods for modifying the size distributions of the NPs. Some progress has been made in this area, using laser-sizing techniques,[73] two-stage

(nucleation and development) synthesis of nanoparticles,[74] and combined ion-exchange and ion-implantation effects to create nanoparticle waveguides with appropriately sized nanoparticles.[75]

5. Summary and Conclusions

Planar composite materials comprising metal nanocrystals embedded in linear or nonlinear dielectrics are attracting growing interest for applications in photonics and sensors. Long known for their useful linear optical properties, these materials also have interesting nonlinear optical properties which are the result of both classical and quantum effects, as we have seen. The classical effects arise from the time-dependent dipole field induced by an electromagnetic wave acting on the electrons in the immediate vicinity of the metal nanocrystal. The quantum-mechanical effects arise from the extreme spatial constriction of the electron mean-free-path relative to its magnitude in bulk materials.

Metal-nanocrystal composites can be fabricated by a number of different chemical and physical techniques, in thin-film geometries suitable for waveguides and other optical or electro-optical structures. Recently, it has also become possible to fabricate these composites with reasonably well-controlled size, size distribution and spatial configurations by a combination of self-assembly and lithography. The nonlinear optical response exhibits ultrafast switching speeds, large nonlinearity and modest switching energies. Recent experiments have explored relaxation and dephasing times, coupling between electrons and phonons, and surface/interface effects. There appear to be potentially interesting possibilities for the deployment of these materials in photonic devices for optical switching and computing. For some applications, it will be necessary to further develop the materials to satisfy figures-of-merit that reflect function, performance specifications and materials properties.

Acknowledgements

It is a pleasure to acknowledge financial support from a Senior Scientist Award of the Alexander von Humboldt Foundation during the writing of this review paper, and Prof. Dr. Paul Leiderer, University of Konstanz, for the hospitality of his research group during this time. Vanderbilt research on the nonlinear optical properties of metal nanoparticle materials is supported by the United States Department of Energy, Office of Science (DE-FG02-01ER45916), as well as by Major Research Instrumentation grants from the National Science Foundation (DMR-9871234, DMR-0321171).

References

1. G. Mie, "Beiträge zur Optik trüber Lösungen, speziell kolloidaler Metallösungen," Annalen der Physik **25**(3), 377-445 (1908).
2. H. R. Stuart and D. G. Hall, "Island size effects in nanoparticle-enhanced photodetectors," Applied Physics Letters **73**(26), 3815-3817 (1998).
3. J. C. Maxwell Garnett, "Colours in Metal Glasses, in Metallic Films, and in Metallic Solutions - II," Philosophical Transactions of the Royal Society of London A **205**, 237-288 (1906).
4. J. C. Maxwell Garnett, "Colours in Metal Glasses and in Metallic Films," Philosophical Transactions of the Royal Society of London A **203**, 385-420 (1906).
5. R. J. Gehr and R. W. Boyd, "Optical properties of nanostructured optical materials," Chemistry of Materials **8**(8), 1807-1819 (1996).
6. M. G. Bawendi, M. L. Steigerwald, and L. E. Brus, "The Quantum-Mechanics of Larger Semiconductor Clusters (Quantum Dots)," Annual Review of Physical Chemistry **41**, 477-496 (1990).
7. B. N. J. Persson, "Polarizability of Small Spherical Metal Particles - Influence of the Matrix Environment," Surface Science **281**(1-2), 153-162 (1993).
8. W. P. Halperin, "Quantum size effects in metal particles," Reviews of Modern Physics **58**(3), 533-606 (1986).
9. Y. R. Shen, *Nonlinear Optics* (John Wiley and Sons, New York, 1984).
10. R. Antoine, M. Pellarin, B. Palpant, M. Broyer, B. Prevel, P. Galletto, P. F. Brevet, and H. H. Girault, "Surface plasmon enhanced second harmonic response from gold clusters embedded in an alumina matrix," Journal of Applied Physics **84**(8), 4532-4536 (1998).
11. M. Brack, "The Physics of Simple Metal-Clusters - Self-Consistent Jellium Model and Semiclassical Approaches," Reviews of Modern Physics **65**(3), 677-732 (1993).
12. H. Hovel, S. Fritz, A. Hilger, U. Kreibig, and M. Vollmer, "Width of Cluster Plasmon Resonances - Bulk Dielectric Functions and Chemical Interface Damping," Physical Review B **48**(24), 18178-18188 (1993).
13. A. Kawabata and R. Kubo, "Electronic Properties of Fine Metallic Particles.2. Plasma Resonance Absorption," Journal of the Physical Society of Japan **21**(9), 1765-& (1966).
14. T. Klar, M. Perner, S. Grosse, G. von Plessen, W. Spirkl, and J. Feldmann, "Surface-plasmon resonances in single metallic nanoparticles," Physical Review Letters **80**(19), 4249-4252 (1998).
15. M. J. Weber, D. Milam, and W. L. Smith, "Non-Linear Refractive-Index of Glasses and Crystals," Optical Engineering **17**(5), 463-469 (1978).
16. D. Stroud and V. E. Wood, "Decoupling approximation for the nonlinear optical response of composite media," Journal of the Optical Society of America B-Optical Physics **6**(4), 778-786 (1989).
17. D. Stroud and P. M. Hui, "Nonlinear susceptibilities of granular matter," Physical Review B **37**(15), 8719-8724 (1988).
18. F. Hache, D. Ricard, and C. Flytzanis, "Optical Nonlinearities of Small Metal Particles - Surface- Mediated Resonance and Quantum Size Effects," Journal of the Optical Society of America B-Optical Physics **3**(12), 1647-1655 (1986).
19. F. Hache, D. Ricard, C. Flytzanis, and U. Kreibig, "The Optical Kerr Effect in Small Metal Particles and Metal Colloids - the Case of Gold," Applied Physics A-Materials Science & Processing **47**(4), 347-357 (1988).

20. C. Flytzanis, F. Hache, D. Ricard, and P. Roussignol, "Nonlinear Optics in Composite-Materials," Journal of the Optical Society of America B-Optical Physics **3**(8), P93-& (1986).
21. R. H. Magruder, L. Yang, R. F. Haglund, C. W. White, R. Dorsinville, and R. R. Alfano, "Optical-Properties of Gold Nanocluster Composites Formed by Deep Ion-Implantation in Silica," Applied Physics Letters **62**(15), 1730-1732 (1993).
22. K. Fukumi, A. Chayahara, K. Kadono, T. Sakaguchi, Y. Horino, M. Miya, K. Fujii, J. Hayakawa, and M. Satou, "Gold Nanoparticles Ion-Implanted in Glass with Enhanced Nonlinear-Optical Properties," Journal of Applied Physics **75**(6), 3075-3080 (1994).
23. R. Rosei, "Temperature Modulation of Optical-Transitions Involving Fermi- Surface in Ag - Theory," Physical Review B **10**(2), 474-483 (1974).
24. N. Del Fatti, F. Vallee, C. Flytzanis, Y. Hamanaka, and A. Nakamura, "Electron dynamics and surface plasmon resonance nonlinearities in metal nanoparticles," Chemical Physics **251**(1-3), 215-226 (2000).
25. R. Serna, C. N. Afonso, J. M. Ballesteros, A. Naudon, D. Babonneau, and A. K. Petford-Long, "Size, shape anisotropy, and distribution of Cu nanocrystals prepared by pulsed laser deposition," Applied Surface Science **139**, 1-5 (1999).
26. P. Meakin and F. Family, "Structure And Kinetics Of Reaction-Limited Aggregation," Physical Review A **38**(4), 2110-2123 (1988).
27. F. Family and P. Meakin, "Kinetics Of Droplet Growth-Processes - Simulations, Theory, And Experiments," Physical Review A **40**(7), 3836-3854 (1989).
28. B. Lamprecht, A. Leitner, and F. R. Aussenegg, "SHG studies of plasmon dephasing in nanoparticles," Applied Physics B-Lasers and Optics **68**(3), 419-423 (1999).
29. A. Nakajima, T. Futatsugi, N. Horiguchi, and N. Yokoyama, "Formation of Sn nanocrystals in thin SiO2 film using low-energy ion implantation," Applied Physics Letters **71**(25), 3652-3654 (1997).
30. S. Linden, J. Kuhl, and H. Giessen, "Controlling the interaction between light and gold nanoparticles: Selective suppression of extinction," Physical Review Letters **86**(20), 4688-4691 (2001).
31. W. L. Barnes, A. Dereux, and T. W. Ebbesen, "Surface plasmon subwavelength optics," Nature **424**(6950), 824-830 (2003).
32. R. A. Weller, W. T. Ryle, A. T. Newton, M. D. McMahon, T. M. Miller, and R. H. Magruder, "A technique for producing ordered arrays of metallic nanoclusters by electroless deposition in focused ion beam patterns," IEEE Transactions On Nanotechnology **2**(3), 154-157 (2003).
33. Y. Cui, M. T. Bjork, J. A. Liddle, C. Sonnichsen, B. Boussert, and A. P. Alivisatos, "Integration of colloidal nanocrystals into lithographically patterned devices," Nano Letters **4**(6), 1093-1098 (2004).
34. A. B. Hmelo, M. D. McMahon, R. Lopez, R. H. I. Magruder, R. A. Weller, R. F. Haglund, Jr., and L. C. Feldman, "Ceramic Nanomaterials and nanotechnology II," presented at the American Ceramic Society Annual Meeting, Nashville, TN, 2003. Published in *Ceramic Nanomaterials and Nanotechnology II*, eds. M. R. DeGuire, M. Hu, Y. Gogotsi and S. Lu, Ceramic Transactions **148**, 68 (2003)..
35. J. Bosbach, D. Martin, F. Stietz, T. Wenzel, and F. Trager, "Laser-based method for fabricating monodisperse metallic nanoparticles," Applied Physics Letters **74**(18), 2605-2607 (1999).
36. J. M. Bennett, J. L. Stanford, and E. J. Ashley, "Optical constants of silver sulfide tarnish films," Journal of the Optical Society of America **60**(2), 224-232 (1970).

37. J. L. Stanford, "Determination of surface-film thickness from shift of optically excited surface plasma resonance," Journal of the Optical Society of America **60**(1), 49-53 (1970).
38. B. T. Reagor and J. D. Sinclair, "Tarnishing of silver by sulfur vapor: film characteristics and humidity effects," Journal of the Electrochemical Society **128**(3), 701-705 (1981).
39. J. P. Franey, G. W. Kammlott, and T. E. Graedel, "The corrosion of silver by atmospheric sulfurous gases," Corrosion Science **25**(2), 133-143 (1985).
40. T. E. Graedel, J. P. Franey, G. J. Gaultieri, G. W. Kammlott, and D. L. Malm, "On the mechanism of silver and copper sulfidation by atmospheric H_2S and OCS," Corrosion Science **25**(12), 1163-1180 (1985).
41. T. Brandt, W. Hoheisel, A. Iline, F. Stietz, and F. Träger, "Influence of molecular adsorbate layers on the optical spectra of small metal particles," Applied Physics B-Lasers and Optics **65**(6), 793-798 (1997).
42. U. Kreibig, M. Gartz, and A. Hilger, "Mie resonances: Sensors for physical and chemical cluster interface properties," Berichte der Bunsen-Gesellschaft fuer Physikalische Chemie **101**(11), 1593-1604 (1997).
43. M. McMahon, R. Lopez, H. M. Meyer, L. C. Feldman, and R. F. Haglund, "Rapid tarnishing of silver nanoparticles in ambient laboratory air," Applied Physics B-Lasers And Optics **80**(7), 915-921 (2005).
44. R. L. Seliger, R. L. Kubena, R. D. Olney, J. W. Ward, and V. Wang, "High-resolution, ion-beam processes for microstructure fabrication," Journal of Vacuum Science and Technology **16**(6), 1610-1612 (1979).
45. N. W. Liu, A. Datta, C. Y. Liu, and Y. L. Wang, "High-speed focused-ion-beam patterning for guiding the growth of anodic alumina nanochannel arrays," Applied Physics Letters **82**(8), 1281-1283 (2003).
46. W. Gotschy, K. Vonmetz, A. Leitner, and F. R. Aussenegg, "Thin films by regular patterns of metal nanoparticles: tailoring the optical properties by nanodesign," Applied Physics B (Lasers and Optics) **63**(4), 381-384 (1996).
47. P. B. Johnson and R. W. Christy, "Optical constants of the noble metals," Physical Review B (Solid State) **6**(12), 4370-4379 (1972).
48. *Handbook of Chemistry and Physics* (CRC Press, Boca Raton, FL, 2003-2004).
49. T. Götz, M. Buck, C. Dressler, F. Eisert, and F. Träger, "Optical Second-Harmonic Generation by Supported Metal-Clusters - Size and Shape Effects," Applied Physics A-Materials Science & Processing **60**(6), 607-612 (1995).
50. A. Wokaun, J. G. Bergman, J. P. Heritage, A. M. Glass, P. F. Liao, and D. H. Olson, "Surface 2nd-Harmonic Generation From Metal Island Films And Microlithographic Structures," Physical Review B **24**(2), 849-856 (1981).
51. F. R. Aussenegg, A. Leitner, and H. Gold, "Optical 2nd-Harmonic Generation of Metal-Island Films," Applied Physics A-Materials Science & Processing **60**(2), 97-101 (1995).
52. B. Lamprecht, A. Leitner, and F. R. Aussenegg, "Femtosecond decay-time measurement of electron-plasma oscillation in nanolithographically designed silver particles," Applied Physics B-Lasers and Optics **64**(2), 269-272 (1997).
53. E. C. Hao, G. C. Schatz, R. C. Johnson, and J. T. Hupp, "Hyper-Rayleigh scattering from silver nanoparticles," Journal of Chemical Physics **117**(13), 5963-5966 (2002).
54. R. C. Johnson, J. T. Li, J. T. Hupp, and G. C. Schatz, "Hyper-Rayleigh scattering studies of silver, copper, and platinum nanoparticle suspensions," Chemical Physics Letters **356**(5-6), 534-540 (2002).
55. U. Kreibig and M. Vollmer, *Optical Properties of Metal Clusters*, Springer Series in Materials Science (Springer Verlag, Berlin-Heidelberg, 1995), Vol. 25.

56. R. F. Haglund, L. Yang, R. H. Magruder, J. E. Wittig, K. Becker, and R. A. Zuhr, "Picosecond Nonlinear Optical-Response of a Cu-Silica Nanocluster Composite," Optics Letters **18**(5), 373-375 (1993).
57. Y. R. Shen, *The Principles of Nonlinear Optics* (John Wiley and Sons, New York, 1984).
58. T. F. Heinz, "Second-order nonlinear optical effects at surfaces and interfaces," in *Nonlinear Surface Electromagnetic Phenomena*, H.-E. Ponath and G. I. Stegeman, eds. (North-Holland, Amsterdam, 1991), pp. 353-416.
59. B. Lamprecht, J. R. Krenn, A. Leitner, and F. R. Aussenegg, "Resonant and off-resonant light-driven plasmons in metal nanoparticles studied by femtosecond-resolution third-harmonic generation," Physical Review Letters **83**(21), 4421-4424 (1999).
60. N. I. Zheludev and V. I. Emel'yanov, "Phase matched second harmonic generation from nanostructured metallic surfaces," Journal Of Optics A-Pure And Applied Optics **6**(1), 26-28 (2004).
61. M. D. McMahon, R. Lopez, R. F. Haglund, E. A. Ray, and P. H. Bunton, "Second-harmonic generation from arrays of symmetric gold nanoparticles," Physical Review B **73**(4), 041401 (2006).
62. J. I. Dadap, J. Shan, K. B. Eisenthal, and T. F. Heinz, "Second-harmonic Rayleigh scattering from a sphere of centrosymmetric material," Physical Review Letters **83**(20), 4045-4048 (1999).
63. N. Bloembergen, R. K. Chang, S. S. Jha, and C. H. Lee, "Optical Second-Harmonic Generation in Reflection from Media with Inversion Symmetry," Physical Review **174**(3), 813-822 (1968).
64. J. W. Haus, N. Kalyaniwalla, R. Inguva, and C. M. Bowden, "Optical bistability in small metallic particle composites," Journal of Applied Physics **65**(4), 1420-1423 (1988).
65. B. E. A. Saleh and M. C. Teich, *Fundamentals of Photonics* (John Wiley and Sons, New York, 1991).
66. P. W. Smith and W. J. Tomlinson, "Nonlinear Optical Interfaces - Switching Behavior," Ieee Journal of Quantum Electronics **20**(1), 30-36 (1984).
67. P. W. E. Smith and S. D. Benjamin, "Materials for All-Optical Devices," Optical Engineering **34**(1), 189-194 (1995).
68. R. H. Magruder, R. F. Haglund, L. Yang, J. E. Wittig, and R. A. Zuhr, "Physical and Optical-Properties of Cu Nanoclusters Fabricated by Ion-Implantation in Fused-Silica," Journal of Applied Physics **76**(2), 708-715 (1994).
69. L. Yang, K. Becker, F. M. Smith, R. H. Magruder, R. F. Haglund, R. Dorsinville, R. R. Alfano, and R. A. Zuhr, "Size Dependence of the 3rd-Order Susceptibility of Copper Nanoclusters Investigated by Four-Wave-Mixing," Journal of the Optical Society of America B-Optical Physics **11**(3), 457-461 (1994).
70. J. M. Ballesteros, J. Solis, R. Serna, and C. N. Afonso, "Nanocrystal size dependence of the third-order nonlinear optical response of Cu: Al_2O_3 thin films," Applied Physics Letters **74**(19), 2791-2793 (1999).
71. K. Uchida, S. Kendko, S. Omi, C. Hata, H. Tanji, Y. Asahara, A. J. Ikushima, T. Tokizaki, and A. Nakamura, "Optical nonlinearities of a high concentration of small metal particles dispersed in glass: copper and silver particles," Journal of the Optical Society of America B-Optical Physics **11**(7), 1236-1243 (1994).
72. J. M. Ballesteros, R. Serna, J. Solis, C. N. Afonso, A. K. PetfordLong, D. H. Osborne, and R. F. Haglund, "Pulsed laser deposition of Cu:Al_2O_3 nanocrystal thin films with high third-order optical susceptibility," Applied Physics Letters **71**(17), 2445-2447 (1997).

73. F. Gonella, G. Mattei, P. Mazzoldi, E. Cattaruzza, G. W. Arnold, G. Battaglin, P. Calvelli, R. Polloni, R. Bertoncello, and R. F. Haglund, "Interaction of high-power laser light with silver nanocluster composite glasses," Applied Physics Letters **69**(20), 3101-3103 (1996).
74. E. Valentin, H. Bernas, C. Ricolleau, and F. Creuzet, "Ion beam "photography": Decoupling nucleation and growth of metal clusters in glass," Physical Review Letters **86**(1), 99-102 (2001).
75. G. W. Arnold, G. DeMarchi, F. Gonella, P. Mazzoldi, A. Quaranta, G. Battaglin, M. Catalano, F. Garrido, and R. F. Haglund, "Formation of nonlinear optical waveguides by using ion-exchange and implantation techniques," Nuclear Instruments & Methods in Physics Research Section B- Beam Interactions with Materials and Atoms **116**(1-4), 507-510 (1996).

FINITE-DIFFERENCE TIME-DOMAIN MODELING OF LIGHT SCATTERING FROM BIOLOGICAL CELLS CONTAINING GOLD NANOPARTICLES

STOYAN TANEV
Systems and Computer Engineering Department, Faculty of Engineering and Design, Carleton University, 1125 Colonel By, Ottawa, ON K1S 5B6, Canada; E-mail: tanev@sce.carleton.ca

VALERY V. TUCHIN
Institute of Optics and Biophotonics, Saratov State University, Saratov, Russia

PAUL PADDON
Lumerical Solutions, Inc., Vancouver, British Columbia, Canada

Abstract. The Finite-Difference Time-Domain (FDTD) modeling technique is applied to study the effect of the cell membrane thickness in optical immersion enhanced phase contrast microscope imaging. The FDTD approach is also applied for studying the implementation of the optical immersion technique for the visualization of single and multiple gold nanoparticles in biological cells. Three different scenarios of biological cells are considered *i)* with cytoplasm and membrane, *ii)* with cytoplasm, nucleus and membrane, and iii) with cytoplasm, nucleus, gold nanoparticle(s) and membrane. To the best of our knowledge, this is the first research study using numerical simulations to analyze the effect of cell membrane thickness and single gold nanoparticles on the forward scattered light from biological cells. The results demonstrate the potential of the FDTD modelling approach for biomedical research and extend its applicability to optical immersion technique enhanced nanobiophotonics imaging.

Keywords: finite-difference time-domain (FDTD) modeling, biophotonics simulations, light scattering from biological cells, gold nanoparticles, cancer diagnostics

J.J. Dubowski and S. Tanev (eds.), Photon-based Nanoscience and Nanobiotechnology, 97–119.

1. Introduction

The development of non-invasive optical methods for biomedical diagnostics requires a fundamental understanding of how light scatters from normal and pathological structures within biological tissue. It is very important to understand from what micro-biological structures light scatters, how sensitive are light scattering parameters to the dynamic pathological changes of these structures as well as, if possible, to quantitatively relate these changes to corresponding variations of the measured light scattering parameters. Unfortunately, the biological origins of the differences in the light scattering patterns from normal and pathological (i.e. pre-cancerous) cells and tissues are not fully understood. The major difficulty comes from the fact that most of the optical biodiagnostics techniques have a resolution comparable to the dimensions of the cellular and sub-cellular light scattering structures [1-2].

In many biomedical and photonics micro- and nano-structure research studies optical software simulation and modeling tools are the only means to get a deeper understanding, or any understanding at all, of the underlying physical and biochemical processes. In particular, the numerical modeling of light scattering from biological cells is usually approached from a single particle electromagnetic wave scattering perspective. The nature of this scattering perspective is defined by two major factors. First, this is the fact that the wavelength of light is larger than or comparable to the size of the scattering sub-cellular structures. Second, this is the fact that biological cells have irregular shapes and inhomogeneous refractive index distributions which makes it impossible to use analytical modeling approaches. Both factors necessitate the use of numerical modeling approaches derived from rigorous electromagnetic theory. Some of these approaches have been recently summarized [3] and include: the method of separation of variables, the finite element method, the method of lines, the point matching method, the method of moments, the discrete dipole approximation method the null-field (extended boundary condition) method, the T-matrix electromagnetic scattering approach, the surface Green's function electromagnetic scattering approach and the finite-difference time domain (FDTD) method.

FDTD simulation and modeling of the light scattering patterns from single and multiple, normal and pathological biological cells and sub-cellular structures has been attracting the attention of researchers since 1996 [4-16]. The FDTD approach was first adopted as a better alternative of Mie theory [17,18] and has been now acknowledged as a powerful tool for studying the nature of the light scattering mechanisms from biological cells during the detection of early changes associated with the dysplasia-to-

carcinoma sequence including increased nuclear size, nuclear pleomorphism and nuclear-to-cytoplasmic ratio [12].

In a previous research study we have applied the FDTD approach for the first time to numerically study the effect of the optical immersion technique for a significant enhancement of the quality of light scattering imaging of biological cells [16]. In this article, we apply the FDTD modeling technique to provide additional insight on the effect of the cell membrane thickness in optical immersion enhanced phase contrast microscope imaging. We are also providing initial results on the application of the FDTD approach for studying the implementation of the optical immersion technique for the visualization of single and multiple gold nanoparticles in biological cells. We will focus on three different scenarios considering single biological cells containing i) cytoplasm and membrane, ii) cytoplasm, nucleus and membrane, and iii) cytoplasm, nucleus, gold nanoparticle(s) and membrane. To the best of our knowledge, this is the first research study discussing the cell membrane thickness and single gold nanoparticle effects on the forward scattered light from biological cells. The results also demonstrate the potential of the FDTD modelling approach and extends its applicability to new and promising biomedical optics research areas such as the study of optical immersion technique enhanced bio-imaging.

2. The Optical Immersion Method

The optical immersion technique is based on the so called “optical clearing” effect consisting in the increased light transmission through microbiological objects due to the matching of the refractive indices of some of their morphological components to that of the extra-cellular medium. It was first applied in the 50s to cell and micro-organism phase contrast microscopy studies [19-21]. In the last decade it has greatly regained its popularity and can be now considered as a promising tool in biomedical optics research [22-26]. The optical immersion technique can be most easily demonstrated by analyzing phase microscope images of bacterial cells containing only a cytoplasm and a membrane [21].

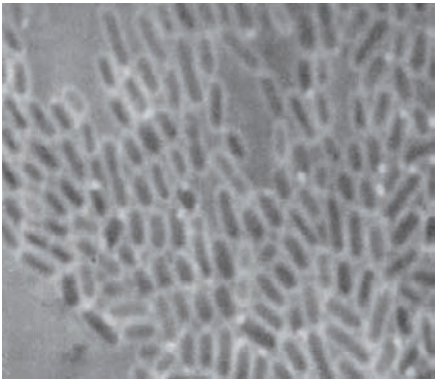

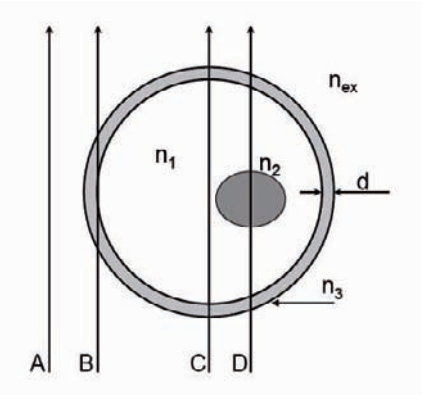

a) b)

Figure 1. Effect of the extra-cellular fluid to cytoplasm refractive index matching on the microscope image of dysentery bacteria cells. a) There is a sharp enhancement of the membrane brightness (Ref. 21, p. 70). b) A simplified picture of the physical mechanism explaining the brightness of the cell membrane. In the case where $n_1 = n_{ex}$, and due to the extremely small thickness of the cell membrane, the optical path accumulated by the light rays A and C is almost the same and much smaller than the optical path of the light ray B. Light ray D accumulates an additional phase shift due to the refractive index difference of the organelle.

In a case where the refractive index of the extra-cellular fluid is externally controlled by the administration of an appropriate chemical agent, the visual disappearing of the cytoplasm and the sharp enhancement of the membrane brightness can be used as a way for measuring the refractive index of the cytoplasm. Figure 1 illustrates the optical clearing effect. If a biological object is homogenous, matching of its refractive index value with that of the host medium will make it optically invisible. In the case of bacteria containing only a cytoplasm and a membrane, matching of the refractive index of the cytoplasm with that of the extra-cellular fluid will make the image of the cytoplasm disappear and sharply enhance the brightness of the membrane. The scattering cross-section of single biological cells depends on the refractive index mismatch between cellular tissue components such as the cell membrane, cytoplasm, nucleus, organelles, melanin granules, and the extra-cellular fluid. The marked reduction of scattering by optical immersion of bulk tissue by means of intra-tissue administration of the appropriate chemical agent has been successfully demonstrated. This and other applications of the optical immersion method were recently summarized in a detailed review by Tuchin [26].

3. The FDTD Method

The FDTD technique is a numerical solution of Maxwell's equations. The FDTD numerical scheme is applied on a finite in space and time numerical equivalent of the physical reality under investigation which, in the present case, is a biological cell immersed in a host material. The finite dimensions of the computational domain require the application of appropriate absorbing boundary conditions (ABC). The ABCs are used to truncate the computational domain and absorb any simulated wave reaching its boundaries as if it were to potentially propagate to infinity according to the particular physical properties of the host medium. Here we describe and use, to the best of our knowledge, the most advanced version of ABCs which are presently used by the scientific and engineering community – the so called Uniaxial Perfectly Matched Layer (UPML) ABC. It was first introduced by Sacks et al. [23] as a physically present layer of diagonally anisotropic material located at the edges of the computational domain. The UPML material properties can be chosen in such a way that the interface between the absorbing material and the host medium is reflection-less for all frequencies, polarizations, and angles of incidence. This approach does not involve a split-field modification of Maxwell's equations [24] and is suitable for the truncation of both free space and lossy or lossless dielectric medium space.

The explicit finite-difference approximation of Maxwell's equations can be derived following Sun et al. [27]. In a source free dielectric medium Maxwell's equations have the form:

$$\nabla \times \mathbf{E} = -\mu_0 \frac{\partial \mathbf{H}}{\partial t}, \tag{1a}$$

$$\nabla \times \mathbf{H} = \varepsilon_0 \varepsilon \frac{\partial \mathbf{E}}{\partial t}, \tag{1b}$$

where E and H are the electric and magnetic fields, respectively, μ_0 is the vacuum permeability and $\varepsilon_0\varepsilon$ is the permittivity of the medium. Assuming a harmonic ($\propto \exp(-i\omega t)$) time dependence of the electric and magnetic fields and a complex value of the relative permittivity $\varepsilon = \varepsilon_r + i\varepsilon_i$ transforms equation (1b) in the following way:

$$\nabla \times \mathbf{H} = \varepsilon_0 \varepsilon \frac{\partial \mathbf{E}}{\partial t} \Leftrightarrow \nabla \times \mathbf{H} = \omega \varepsilon_0 \varepsilon_i \mathbf{E} + \varepsilon_0 \varepsilon_r \frac{\partial \mathbf{E}}{\partial t} \Leftrightarrow$$
$$\frac{\partial(\exp(\pi t)\mathbf{E})}{\partial t} = \frac{\exp(\pi t)}{\varepsilon_0 \varepsilon_r} \nabla \times \mathbf{H} \tag{2}$$

where $\tau=\omega\varepsilon_i/\varepsilon_r$ and ω is the angular frequency of the light wave. The continuous coordinates (x, y, z, t) are replaced by discrete spatial and temporal points: $x_i = i\Delta s$, $y_j = j\Delta s$, $z_k = k\Delta s$, $t_n = n\Delta t$, where i = 0, 1, 2, …, I; j = 0, 1, 2, …, J; k = 0, 1, 2, …, K; n = 0, 1, 2, …, N. Δs and Δt denote the cubic cell size and time increment, respectively. Using central difference approximations for the temporal derivatives over the time interval [$n\Delta t$, $(n+1)\Delta t$] gives

$$\vec{E}^{n+1} = \exp(-\tau\Delta t)\vec{E}^{n} + \exp(-\tau\Delta t/2)\frac{\Delta t}{\varepsilon_0\varepsilon_r}\nabla\times\vec{H}^{n+1/2} \tag{3}$$

where the electric and the magnetic fields are calculated at alternating half-time steps. The discretization of Eq. (1a) over the time interval [$(n\text{-}1/2)\Delta t$, $(n+1/2)\Delta t$] (one half time step earlier than the electric field) ensures second-order accuracy of the numerical scheme. In three dimensions, equations (1-3) involve all six electromagnetic field components: E_x, E_y, E_z and H_x, H_y, and H_z. If one of the spatial dimensions is dropped out the 2D Maxwell's equations split into two independent sets of equations composed of three vector quantities each. If the propagation is considered in the x-y plane, the two sets of equations are as follows: TE - transverse electric, with non-zero field components E_x, E_y, H_z, and TM - transverse magnetic, with field components H_x, H_y, E_z. In a Cartesian grid system the TE equations for the x components of the electric and magnetic fields take the form

$$H_z^{n+1/2}(i,j) = H_z^{n-1/2}(i,j) - \frac{\Delta t}{\mu_0\Delta s} \tag{4a}$$
$$\times[E_y^n(i+1/2,j) - E_y^n(i-1/2,j) + E_x^n(i,j-1/2,k) - E_x^n(i,j+1/2)],$$

$$E_x^{n+1}(i,\,j+1/2) = \exp[-\frac{\varepsilon_i(i,\,j+1/2)}{\varepsilon_r(i,\,j+1/2)}\omega\Delta t]E_x^n(i,\,j+1/2) +$$
$$\exp[-\frac{\varepsilon_i(i,\,j+1/2)}{\varepsilon_r(i,\,j+1/2)}\omega\Delta t/2]\frac{\Delta t}{\varepsilon_0\varepsilon_r(i,\,j+1/2)\Delta s}$$
$$\times[H_z^{n+1/2}(i,\,j+1) - H_z^{n+1/2}(i,\,j)], \tag{4b}$$

$$E_y^{n+1}(i+1/2,\,j) = \exp[-\frac{\varepsilon_i(i+1/2,\,j)}{\varepsilon_r(i+1/2,\,j)}\omega\Delta t]E_y^n(i+1/2,\,j) -$$
$$\exp[-\frac{\varepsilon_i(i+1/2,\,j)}{\varepsilon_r(i+1/2,\,j)}\omega\Delta t/2]\frac{\Delta t}{\varepsilon_0\varepsilon_r(i+1/2,\,j)\Delta s}$$
$$\times[H_z^{n+1/2}(i+1,\,j) - H_z^{n+1/2}(i,\,j)], \tag{4c}$$

where E_x, E_y and H_z denote the electric and magnetic field components, respectively. The numerical stability of the FDTD scheme [28] is ensured through the Courant-Friedrichs-Levy condition: $c\Delta t \le \left(1/\Delta x^2 + 1/\Delta y^2\right)^{-1/2}$, where c is the light speed in the host medium and Δx and Δy are the spatial steps in the x and y, respectively. In our case $\Delta x = \Delta y = \Delta s$. In this study, we use $\Delta t = \Delta s/(2c\sqrt{2})$. The schematic positions of the magnetic and electric field components in a TE FDTD cubic cell are shown in Fig. 2.

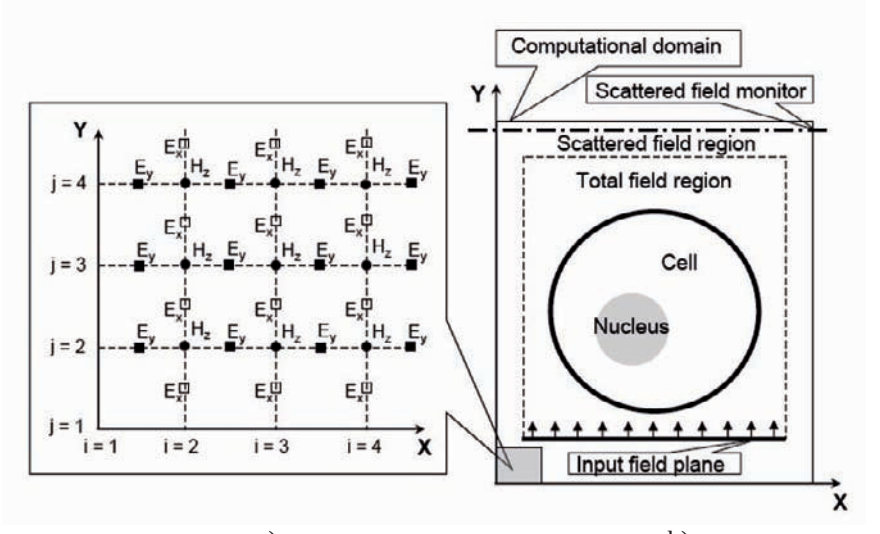

a) b)

Figure 2. a) Positions of the electric- and the magnetic-field components in an elementary cubic cell of the 2D TE FDTD lattice. b) Schematic representation of the FDTD computational domain.

In light scattering simulation experiments one uses the so-called total-field/scattered-field formulation [28] to excite the magnetic and electric fields and simulate a linearly polarized plane wave propagating in a finite region of a homogeneous absorptive dielectric medium. A schematic representation of the FDTD computational domain is shown in Fig. 2b illustrating the scattering object (the cell), the total field (the space internal to the dashed line) the scattered field (the space external of the dashed line) region. At the edges of the total field region the incident field is subtracted from the total field to ensure propagation of only scattered fields in the scattered field region. Based on the equivalence theorem [28], the existence of wave-excitation in the spatial domain enclosed by the total field region can be replaced by the equivalent electric and magnetic currents on its edges. If there is a scatterer inside the closed surface, the interior fields will be the total fields (incident plus scattered) and the exterior fields are just the

scattered fields. At the edges of the FDTD computational domain is truncated by the UPML boundary conditions that were briefly discussed above. More details about the "physics" of the UPML boundary conditions can be found in [16, 27, 28]. The simulation results presented here were performed by the FDTD Solutions™ software [29] where all the features of the FDTD scheme described above are implemented in a user-friendly way.

The FDTD simulations provide the transverse distribution of the forward scattered light field from the scattering object. The forward scattered light field from single biological cells is of particular interest here since it is its phase - the phase accumulated by a plane wave propagating due to the refractive index variations of the cell - that is mostly relevant for phase contrast microscope imaging. The phase contrast technique translates small variations in phase into corresponding changes in amplitude, which can be visualized as differences in image contrast. This article will focus on studying the enhancement of the phase contrast accumulation of plane waves propagating through biological cells due to the optical clearing effect without going into the details of the optical phase contrast microscope imaging technique. The development of a realistic phase microscope simulation model will be the subject of future studies. What is important for us here is the fact that the optical phase accumulation of the forward scattered light wave is the source of the phase contrast microscope efficiency, i.e. its enhancement will significantly improve the image quality. One of the major advantages of phase contrast microscopy is that living cells can be examined in their natural state without previously being killed, fixed, and stained. As a result, the dynamics of ongoing biological processes can be observed and recorded in high contrast with sharp clarity of minute specimen detail.

4. Cell Membrane Effect on Light Scattering Based Cell Imaging

In a previous research study we have demonstrated the applicability of the FDTD approach to numerically study the effect of the optical immersion technique for enhancing the light scattering images of biological cells. [16] We have demonstrated that taking into account the finite thickness of the cell membrane is critically important for the correct modeling of the optical clearing effect. The numerical results have indicated the need to further study the effect of the cell membrane thickness on the efficiency of the optical immersion technique for bio-imaging. Since the cell membrane thickness is of the order of 10 nm, any 3D FDTD simulation will require very fine numerical resolution (much below the limit ensuring the numerical stability of the algorithm) leading to heavy, computationally intensive and time consuming numerical experiments. This

has motivated us to proceed with a series of 2D TE FDTD simulations to analyze the transverse distribution of the forward scattered light phase and intensity as a function of cell membrane thickness.

4.1. CELL WITH CYTOPLASM AND MEMBRANE (NO NUCLEUS)

The 2D TE FDTD modeling of this particular case has three main purposes: i) to demonstrate the optical clearing effect in a 2D cell geometry; ii) to study the "pure" effect of the cell membrane thickness on the phase and intensity of the forward scattered light; and iii) to provide a reference case for the other simulations scenarios including a nucleus and gold nanoparticles. The geometry of the cell is shown on Fig. 3 together with the specific values of the refractive indices of its components. In all the simulation scenarios described in this article the FDTD computational domain has dimensions 3x3 μm. The resolution in both x and y directions is 2 nm. The time step is 0.00235865 fs. The simulation time is 500 fs. The total field region (please see Fig. 2b) is 2.8 μm to 2.8 μm large and located right in the middle of the computational domain. A plane wave is launched at one of the edges of the total field region and propagates in the +y direction. The forward scattered major electric field component E_x (both intensity and phase) is saved at the end of the simulation in the scattered field region by means of a scattered field monitor (please see Fig. 2b) located at y = 1.448 μm.

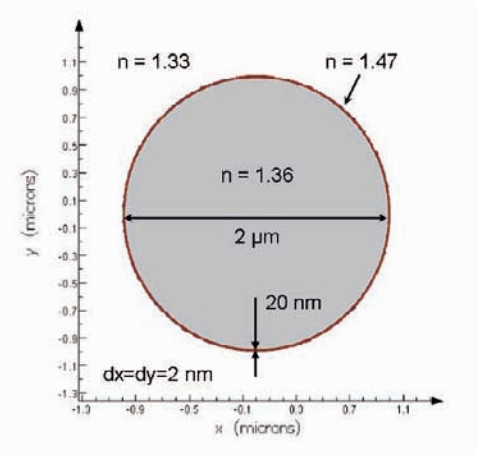

Figure 3. 2D cell geometry and refractive index distribution. The computational domain is 3 μm to 3 μm large. The cell is centered in the middle of the computational domain at x=0 μm and y=0 μm. The cell diameter is 2 μm. The FDTD space resolution is dx=dy=2 nm.

The simulation results are shown on Figure 4. The graphs on the left side correspond to no refractive index matching (refractive index of the extra-cellular matrix equal to 1.33, refractive index of the cytoplasm equal to 1.36). The graphs on the right side correspond to refractive index matching (refractive index of both, the extra-cellular matrix and the cytoplasm, equal to 1.36).

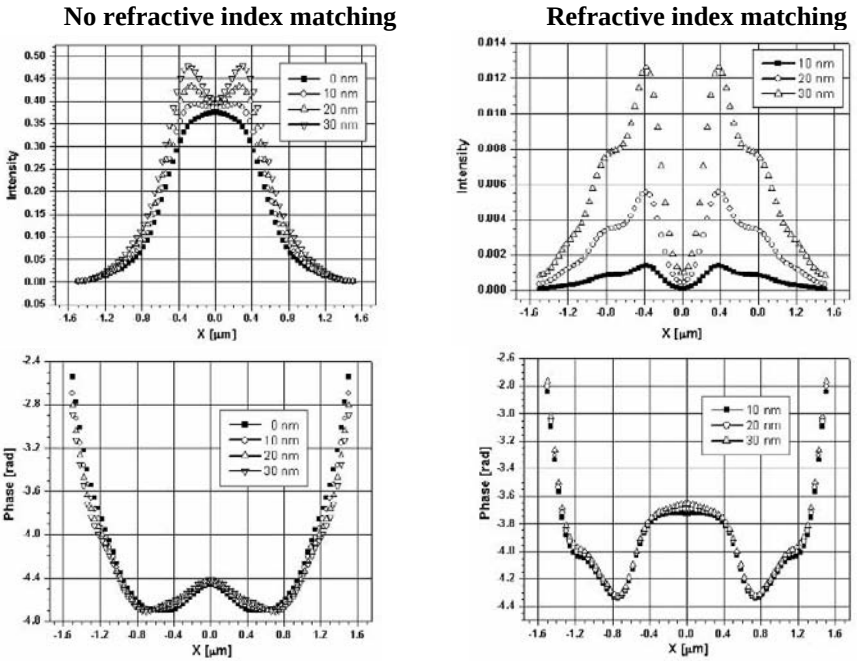

Figure 4. Effect of membrane thickness on the intensity and phase of the forward scattered light from the cell shown on Fig. 3. Refractive index matching (right column) corresponds to the case when the refractive index of the cytoplasm equals that of the extra-cellular matrix. The light wavelength is 632.8 nm.

Three different values of the cell membrane thickness are considered: 10 nm, 20 nm and 30 nm. In the case of no refractive index matching it is also possible to model the situation (labeled on the left side of Fig. 4 as “0 nm” thickness) where the cell membrane thickness is not taken into account – a simulation scenario that is very tempting in FDTD simulations especially in the 3D case where computer power and CPU time are particularly precious. This situation is impossible in the case of refractive index matching since it makes the cell completely disappear. The analysis of the results shown in Fig. 4 can be used to draw several conclusions. First, neglecting the thickness of the cell membrane removes the possibility to observe the optical clearing effect the transverse distribution of the forward

scattered intensity (top left graph on Fig. 4, no refractive index matching case) corresponding to 0 nm thickness (no membrane) is completely different from the rest of the curves corresponding to a finite membrane thickness. Second, small changes in the phase of the forward scattered light lead to significant changes in its intensity. Third, the optical clearing effect (top right graph on Fig. 4, refractive index matching case) significantly enhances the effect of the finite membrane thickness on the intensity of the forward scattered light. It should be pointed out that the ratio between the maximum forward scattered light intensities corresponding to cell membrane thicknesses 30 and 10 nm increases approximately 8.69 times only due to the refractive index matching associated with the optical clearing effect. This example shows the potential of the optical clearing effect associated with the immersion technique for the development of more sensitive optical bio-imaging methods.

4.2. CELL WITH CYTOPLASM, MEMBRANE AND NUCLEUS

The geometry and the refractive index distribution of a cell with a membrane and a nucleus are shown on Fig. 5. The FDTD simulation results for the forward scattered light from this cell are shown on Fig. 6.

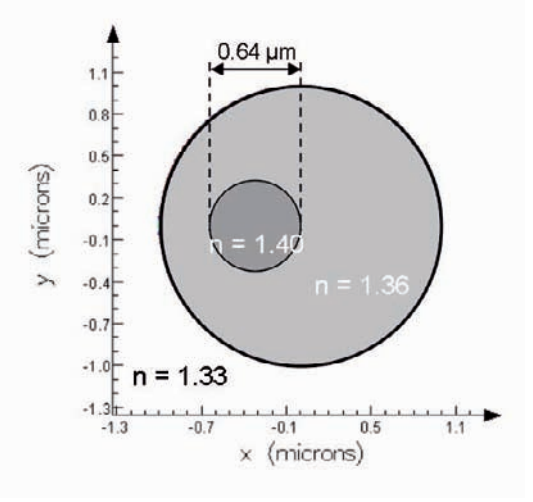

Figure 5. 2D geometry and refractive index distribution of a cell containing a membrane (n=1.47) and a nucleus (n=1.40). The computational domain is 3 μm x 3 μm large. The cell (diameter 2 μm) is centered at y=0 μm, x=0 μm. The nucleus (diameter of 0.64 μm) is centered at y=0 μm, x=-0.32 μm.

The incident plane wave propagation is along the +y axe. This specific choice of the propagation direction will obviously induce an asymmetry in the transverse distribution of the forward scattered light wave (please see sketch on Fig. 1b) and was intentionally chosen in order to better visualize the optical clearing effect. The membrane of the nucleus is not taken into account. The simulation results are shown on Figure 6. The graphs on the left side correspond to no refractive index matching (refractive index of the extra-cellular matrix equal to 1.33, refractive index of the cytoplasm equal to 1.36). The graphs on the right side correspond to refractive index matching (refractive index of both, the extra-cellular matrix and the cytoplasm, equal to 1.36).

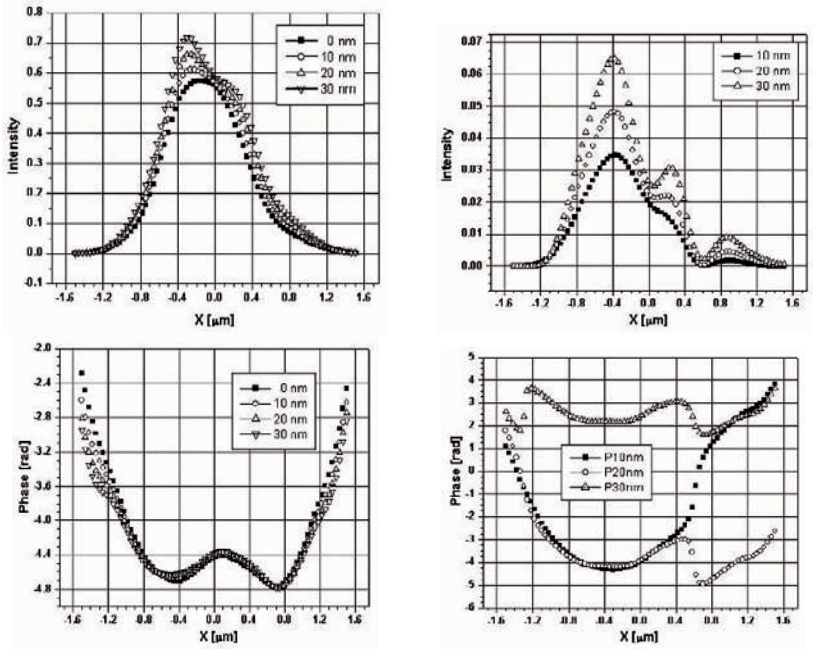

Figure 6. Effect of membrane thickness on the intensity and phase of the forward scattered light from the cell shown on Fig. 5. Refractive index matching (right column) corresponds to the case when the refractive index of the cytoplasm equals that of the extra-cellular matrix. The light wavelength is 632.8 nm.

The analysis of the results shown in Fig. 6 can be used to draw several conclusions. The presence of the nucleus introduces an additional optical phase accumulation of the forward scattered plane wave leading to an asymmetric transverse distribution of its intensity. Again, tiny phase changes lead to visible changes in the wave intensity. The correct interpretation of the transverse phase distributions on the right bottom graph (refractive index matching) should take into account that fact that phase

changes of 2π do not lead to changes in the intensity values. This will explain the smooth behaviour of the intensity curves on the top right graph where, as in the previous case of a cell without a nucleus, the optical clearing effect enhances the effect of the finite membrane thickness on the intensity of the forward scattered light. In this case the ratio between the maximum forward scattered light intensities corresponding to cell membrane thicknesses 30 and 10 nm increases approximately 1.6 times due to the refractive index matching associated with the optical clearing effect. It is worth noting that efficiency of optical clearing effect is approximately 5 times lower than the previous case. This can be explained by the fact that the transverse phase and intensity distributions are dominated the presence and size of the nucleus and the associated high refractive index contrast: 1.40 (nucleus) to 1.36 (cytoplasm). The presence of the finite membrane thickness leads to small relative changes of the transverse phase and intensity distributions on top of the contributions due to the nucleus.

5. Optical Clearing Effect on Single Gold Nanoparticle Imaging

Gold nanoparticles exhibit the ability to resonantly scatter visible and near infrared light. This property is the result of the excitation of surface plasmon resonances (SPR) and is extremely sensitive to the size, shape, and aggregation state of the particles. The ability to resonantly scatter visible and near infrared light is currently being explored for vital microscopy and treatment in living specimens. [30-34] Gold nanoparticles scatter light of many colors when illuminated with white light at appropriate angles. This color scattering property offers the potential for cellular imaging and detection labeling studies with a white light source.

In a recent research study El-Sayed et al. [31] used a very simple and inexpensive conventional microscope with proper rearrangement of the illumination system and the light collection system to image cells that were incubated with colloidal gold or with anti-epidermal growth factor receptor (anti-EGFR) antibody conjugated gold nanoparticles. It was found that the scattering images and the absorption spectra recorded from anti-EGFR antibody conjugated 35 nm gold nanoparticles incubated with cancerous and noncancerous cells are different and offer potential techniques for cancer diagnostics. When incubated in the presence of nanoparticles, the cells grow at a normal rate and the nanoparticles are accumulated inside the cells. The incorporated gold nanoparticles scatter strong yellowish light and make individual cells easily identifiable. Gold nanoparticles are predominantly accumulated inside the cytoplasm of the cells. In most noncancerous cells the gold nanoparticles demonstrate a spotted pattern inside the cytoplasm while the nanoparticles are homogeneously distributed

in the cytoplasm of cancerous cells. The light scattering pattern of gold nanoparticles were found to be significantly different when anti-EGFR antibodies were conjugated to gold nanoparticles before incubation with the cells. Noncancerous cells are poorly labeled by the nanoparticles and the cells could not be identified individually. When the conjugates are incubated with cancerous cells for the same amount of time, the nanoparticles were found predominantly located on the membranes of the cells. This contrast difference was explained by the specific binding of over-expressed EGFR on the cancer cells with the anti-EGFR antibodies on the gold surface.

The research studies mentioned above [30, 31] have provided a motivation for studying the possibility to adequately model the presence of gold nanoparticles in single biological cells including the imaging relevant effects due to surface plasmon resonances (SPR).

5.1. OPTICAL MATERIAL PROPERTIES OF GOLD NANOPARTICLES

We have used the dispersion model for gold derived from the experimental data provided by Johnson and Christy. [35] The total, complex-valued permittivity of the gold is given by the following formula,

$$\varepsilon(\omega) = \varepsilon_{REAL} + \varepsilon_L(\omega) + \varepsilon_P(\omega), \tag{5}$$

where each contribution arises from the a different material model. The first term represents the contribution due to the basic, background permittivity. The second and third terms represent Lorentz and plasma contributions:

$$\varepsilon_L(\omega) = \varepsilon_{LORENTZ}\omega_0^2/(\omega_0^2 - 2i\delta_0\omega - \omega^2) \tag{6}$$

$$\varepsilon_P(\omega) = \omega_P^2/(i\omega\nu_C + \omega^2), \tag{7}$$

where all material constants are summarized in the table below.

Background permittivity	Lorentz dispersion	Plasma dispersion
ε_{REAL} = 7.076500096493071	$\varepsilon_{LORENTZ}$ = 2.323056371040549 ω_0 = 4.634629996925336 x10^{+015} δ_0 = 9.267097992234386 x10^{+014}	ω_P = 1.390688491193091 x10^{+016} ν_C = 1.410836620968578 x10^{+007}

It is worth noting that the gold nanoparticle optical properties described above are the bulk material ones and do not take into account confinement effects due to nano-scale size of the gold particles. This, however, is not a limitation to our study since the resonant material dispersion properties are properly taken into account. The accounting for the confinement effects

will lead to a slight shift of the resonant frequencies but will not change the nature of the optical phenomena under examination. The optical resonant properties will be also slightly modified by the fact that we are using a 2D simulation model approximating the spherical shape nanoparticles with a circular 2D object having the same diameter and the optical material parameters. This, again, is not a limitation of our model since it will lead to a mere shift of the optical resonance. What is of importance for us here is to be able to model two different cases – forward light scattering from a single cell corresponding to on and off SPR of the gold nanoparticles. The ability to model both these cases together with the effect of optical clearing effect gives us the opportunity to study the possibility for imaging of a single gold nanoparticle uptake – a scenario which, to the best of our knowledge, was not studied before.

5.2. CELL WITH CYTOPLASM, MEMBRANE, NUCLEUS AND SINGLE NANOPARTICLE

In this section we discuss the effect of the presence of a gold nanoparticle on the forward scattered light from the biological cell shown on Fig. 7.

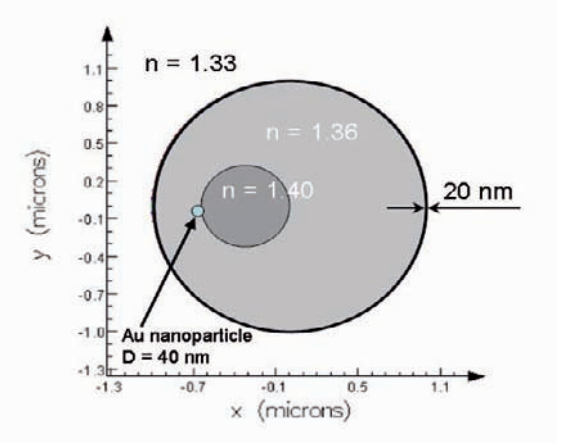

Figure 7. Geometry and refractive index distribution of a cell containing a gold nanoparticle (diameter 40 nm) attached to the the nucleus at y=0 μm, x=-0.34 μm.

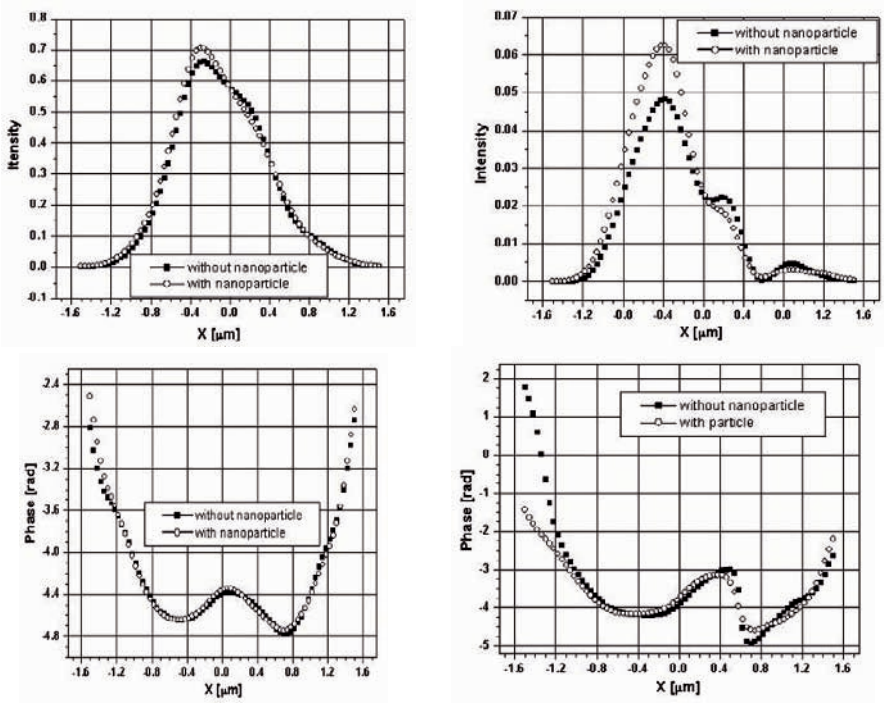

Figure 8. Effect of the presence of a gold nanoparticle on the intensity and phase of the forward scattered light from the cell shown on Fig. 7 The optical properties of the gold nanoparticle are described by Eqs. 5-7. The light wavelength is 632.8 nm.

The simulation results are given in Figure 8. The analysis of the results shows that in the refractive index matching case the ratio between the maximum forward scattering intensity from a cell with a without gold nanoparticle increases only 1.21 times. Again, this can be explained by the fact that the transverse phase and intensity distributions are dominated the presence and size of the nucleus. The presence of the nanoparticle leads to small relative changes of the transverse phase and intensity distributions on top of the contributions due to the nucleus. The low imaging efficiency of the optical clearing effect in this case necessitates the use of the SPR properties of the nanoparticle to further enhance its imaging.

5.3. CELL WITH CYTOPLASM, MEMBRANE, NUCLEUS AND SINGLE GOLD NANOPARTICLE AT SPR

We used the FDTD technique to calculate and plot the scattering and absorption cross-sections for a two dimensional gold nanoparticle immersed in a materials having the properties of the cytoplasm (n=1.36) over a

400-750 nm wavelength range. The wavelength dependence of the above cross sections is shown on Fig. 9.

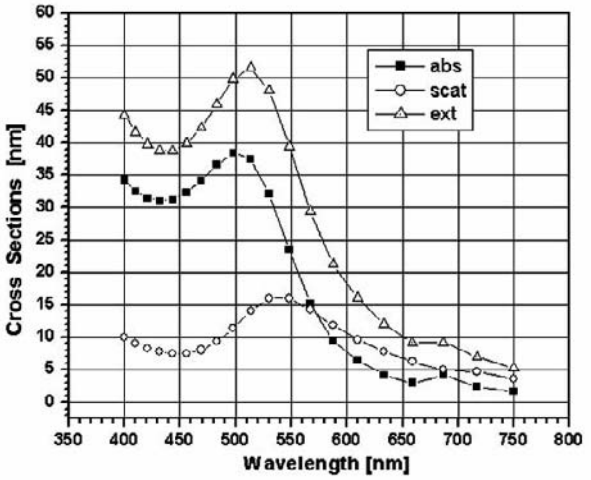

Figure 9. Scattering, absorption and extinction cross-section of a 40 nm gold nanoparticle immersed in material having the optical properties of the cytoplasm – n=1.36. The optical properties of the gold nanoparticle are described by Eqs. (5-7).

The scattering cross-section is defined as

$$\sigma_{scat} = P_{scat}(\omega) / I_{inc}(\omega), \tag{8}$$

where P_{scat} is the total scattered power and I_{inc} is the incident intensity in [W/m^2]. In 2D, the scattered power is usually described per unit length [W/m], and thus the scattering cross-section has dimensions of length (i.e. nm in our case). The total scattered power can be calculated by summing the power flowing outward through four scattered field power monitors located in the scattered field region on all sides of the computational domain (see Fig. 2b). The absorption cross-section is similarly defined as

$$\sigma_{abs} = P_{abs}(\omega) / I_{inc}(\omega), \tag{9}$$

where P_{abs} is the total power absorbed by the particle. The power absorbed by the particle can be calculated by calculating the net power flowing inward through the four total field power monitors located in the total field region of the computational domain. The extinction cross-section is the sum of the absorption and scattering cross-sections

$$\sigma_{ext} = \sigma_{scat} + \sigma_{abs}. \tag{10}$$

The results shown in Fig. 9 show that the extinction ratio has a maximum at around 515 nm (corresponding to the SPR of the gold nanoparticle) which is approximately equal to the Argon laser wavelength 514.8 nm. This means that the simulation results presented so far (at the Helium-Neon laser wavelength 632.8 nm) correspond to an off-SPR case.

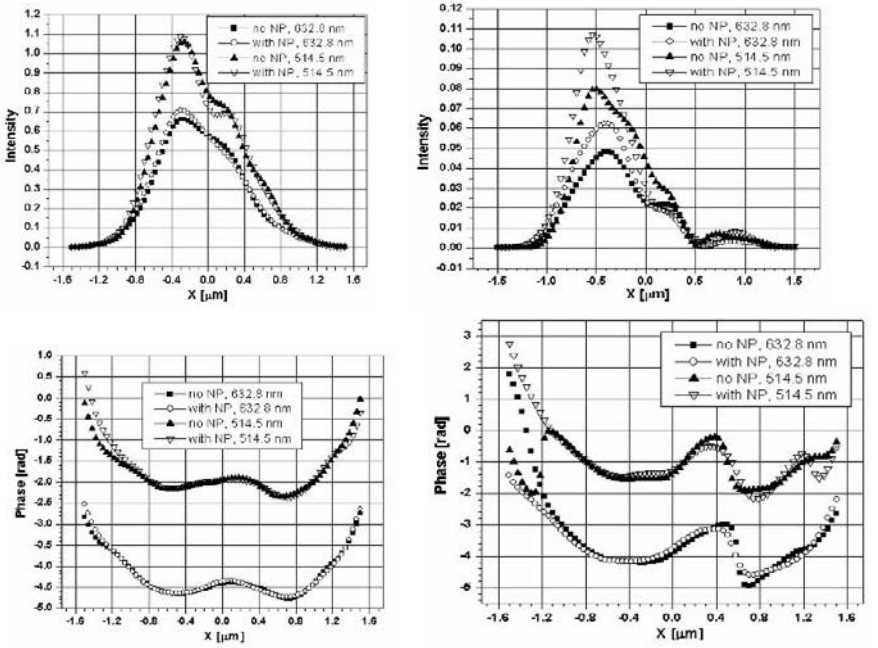

Figure 10. Effect of SPR (632.8 vs 514.5 nm) on single gold nanoparticle imaging - intensity and phase of the forward scattered light from the cell shown on Fig. 7 The optical properties of the gold nanoparticle are described by Eqs. (5-7).

Figure 10 shows the FDTD simulation results for the transverse distribution of forward scattered light from a cell containing a membrane, a nucleus and a gold nanoparticle (Fig. 7). Each graph shows four curves corresponding to a cell with and without nanoparticle at both light wavelengths – 638.8 nm (off SPR) and 514.5 nm (on SPR). The graphs on the left side correspond to no refractive index matching (refractive index of the extra-cellular matrix equal to 1.33, refractive index of the cytoplasm equal to 1.36). The graphs on the right side correspond to refractive index matching (refractive index of both, the extra-cellular matrix and the cytoplasm, equal to 1.36). The analysis of the results shows that in both, refractive index and no refractive index matching, cases the SPR condition visibly increases the intensity of the forward scattered light wave due to the presence of the gold nanoparticle. Since there are numerous simulation

scenarios (with or without nanoparticle, on or off SPR, with or without refractive index matching) it is worth comparing the ratio between the maximum scattered wave intensities corresponding to two particular cases: i) (no nanoparticle, no SPR) and ii) (with nanoparticle, at SPR). In the case of no refractive index matching this ratio is 1.65. In the case of refractive index matching the ratio is 2.18. Again, we can clearly see the role of the optical clearing effect for enhanced imaging of gold nanoparticle.

5.4. CELL WITH CYTOPLASM, NUCLEUS AND MULTIPLE NANOPARTICLES

As a final simulation example demonstrating the power of the FDTD approach for biomedical imaging research studies we consider two scenarios inspired by the work of El-Sayed et al. discussed above. [31] El-Sayed et al. have found that nanoparticles are homogeneously distributed in the cytoplasm of cancerous cells. Anti-EGFR antibodies conjugated to the gold nanoparticles before incubation with the cells made the nanoparticles to predominantly locate on the cell membranes. These two cases are schematically show on Fig. 11. The FDTD simulation results are shown on Fig. 12.

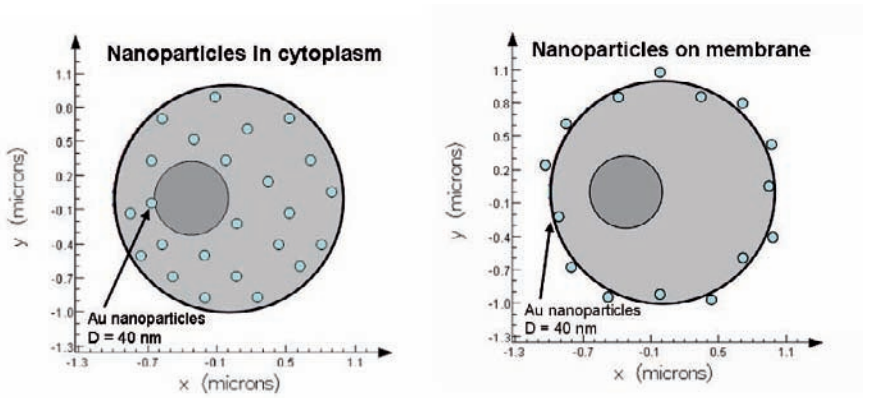

a) b)

Figure 11. Examples of cell geometry and refractive index distribution of biological cells containing multiple gold nanoparticles with a diameter of 40 nm: a) randomly distributed in the cytoplasm; b) randomly distributed on the membrane.

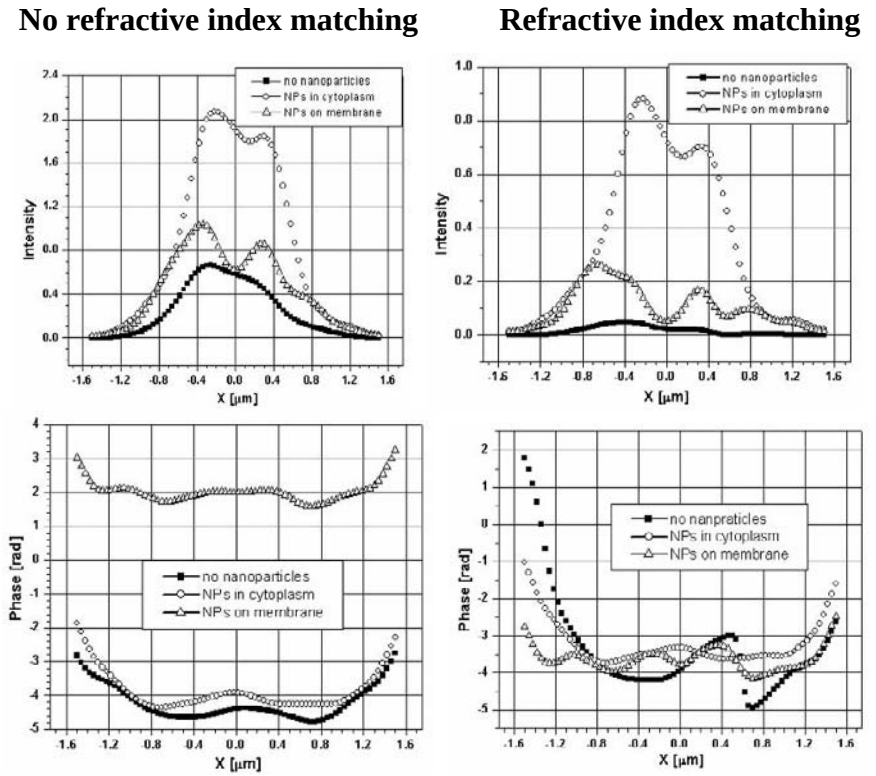

Figure 12. Intensity and phase of the forward scattered light from biological cells containing multiple nanoparticles as shown on Fig. 11.

The analysis of the simulation results shown on Fig. 12 demonstrates the role of the optical clearing effect for the enhancement of cell imaging containing nanoparticles. These results have a preliminary character and need to be further studied. Their purpose is, again, to show the potential of the FDTD approach for nanobiophotonics research.

6. Conclusions

We have applied the FDTD modeling technique to study the effect of the cell membrane thickness in optical immersion enhanced phase contrast microscope imaging. We have also provided initial results on the application of the FDTD approach for studying the implementation of the optical immersion technique for the visualization of single and multiple gold nanoparticles in biological cells. We have considered three different scenarios involving biological cells containing *i)* cytoplasm and membrane, *ii)* cytoplasm, nucleus and membrane, and iii) cytoplasm, nucleus, gold nanoparticle(s) and membrane. To the best of our knowledge, this is the first research study discussing the cell membrane thickness and single gold

nanoparticle effects on the forward scattered light from biological cells. The results also demonstrate the potential of the FDTD modelling approach and extends its applicability to new and promising biomedical optics research areas such as the study of optical immersion technique enhanced nanobiophotonics imaging.

References

1. P. N. Prasad, Bioimaging: principles and techniques, Chap. 7 in Introduction to biophotonics, John Wiley & Sons, New Jersey (2003), pp. 203-249.
2. V. V. Tuchin, Introduction to optical biomedical diagnostics, in Handbook of optical biomedical diagnostics, Valery V. Tuchin, Editor, SPIE Press, Bellingham, Washington (2002), pp. 1-25.
3. F. M. Kahnert, Numerical methods in electromagnetic scattering theory, Journal of Quantitative Spectroscopy and Radiative Transfer 73 (2003), pp. 775-824.
4. A. Dunn, C. Smithpeter, A. J. Welch and R. Richards-Kortum, Light scattering from cells, OSA Technical Digest – Biomedical Optical Spectroscopy and Diagnostics, Washington, Optical Society of America (1996), pp. 50-52.
5. A. Dunn, and R. Richards-Kortum, Three-dimensional computation of light scattering from cells, IEEE Journal of Selected Topics in Quantum Electronics 2 (1996), pp. 898-894.
6. A. Dunn, Light Scattering Properties of Cells, PhD Dissertation, Biomedical Engineering, University of Texas at Austin, Austin TX (1997): http://www.nmr.mgh.harvard.edu/%7Eadunn/papers/dissertation/index.html
7. A. Dunn, C. Smithpeter, A. J. Welch and R. Richards-Kortum, Finite-difference time-domain simulation of light scattering from single cells, Journal of Biomedical Optics 2 (1997), pp. 262-266.
8. R. Drezek, A. Dunn and R. Richards-Kortum, Light scattering from cells: finite-difference time-domain simulations and goniometric measurements, Applied Optics 38 (1999), pp. 3651-3661.
9. R. Drezek, A. Dunn and R. Richards-Kortum, A pulsed finite-difference time-domain (FDTD) method for calculating light scattering from biological cells over broad wavelength ranges, Optics Express 6 (2000), pp. 147-157.
10. A. V. Myakov, A. M. Sergeev, L.S. Dolin, R. Richards-Kortum, Finite-dfference time-domain simulation of light scattering from multiple cells, Technical Digest, Conference on Lasers and Electro-Optics (CLEO) (1999), pp. 81-82.
11. T. Tanifuji, N. Chiba and M. Hijikata, FDTD (finite difference time domain) analysis of optical pulse responses in biological tissues for spectroscopic diffused optical tomography, Technical Digest, The 4th Pacific RIM Conference on Lasers and Electro-Optics 1 (2001), pp. I-376 – I-377.
12. T. Tanifuji and M. Hijikata, Finite difference time domain (FDTD) analysis of optical pulse responses in biological tissues for spectroscopic diffused optical tomography, IEEE Transactions on medical imaging 21, No. 2, (2002), pp. 181-184.
13. R. Drezek, M. Guillaud, T. Collier, I. Boiko, A. Malpica, C. Macaulay, M. Follen, R. R. Richards-Kortum, Light scattering from cervical cells throughout neoplastic

progression: influence of nuclear morphology, DNA content, and chromatin texture, Journal of Biomedical Optics 8 (2003), pp. 7-16.
14. D. Arifler, M. Guillaud, A. Carraro, A. Malpica, M. Follen, R. Richards-Kortum, Light scattering from normal and dysplastic cervical cells at different epithelial depths: finite-difference time domain modeling with a perfectly matched layer boundary condition, Journal of Biomedical Optics 8 (2003), pp. 484–494.
15. S. Tanev, W. Sun, R. Zhang and A. Ridsdale, The FDTD approach applied to light scattering from single biological cells, Proceedings of SPIE, Vol. 5474, Saratov Fall Meeting 2003, Optical Technologies in Biophysics and Medicine V (2004), pp. 162-168.
16. S. Tanev, W. Sun, R. Zhang and A. Ridsdale, Simulation tools solve light-scattering problems from biological cells, Laser Focus World (January 2004), pp. 67-70.
17. S. Tanev, W. Sun, N. Loeb, P. Paddon and V. V. Tuchin, The Finite-Difference Time-Domain Method in the Biosciences: Modelling of Light Scattering by Biological Cells in Absorptive and Controlled Extra-cellular Media, in Advances in Biophotonics, Ed. B. C. Wilson, V. V. Tuchin and S. Tanev, NATO Science Series I, vol. 369, IOS Press, Amsterdam, 2005, pp. 45-78.
18. G. Mie, Beigrade zur optic truber medien, speziell kolloidaler metallsungen, Ann. Phys. (Leipzig) 25 (1908), pp. 377-455.
19. W. Sun, N. G. Loeb and Q. Fu, Light scattering by coated sphere immersed in absorbing medium: a comparison between the FDTD and analytic solutions, Journal of Quantitative Spectroscopy & Radiative Transfer 83 (2004), pp. 483–492.
20. R. Barer, K. F. A. Ross, and S. Tkaczyk, Refractometry of living cells, Nature 171 (1953), pp. 720-724.
21. R. Barer and S. Joseph, Refractometry of living cells, Q. J. Microsc. Sci. 95 (1954), pp. 399-406.
22. B. A. Fikhman, Microbiological Refractometry, Medicine, Moscow (1967).
23. H. Liu, B. Beauvoit, M. Kimura, and B. Chance, Dependence of tissue optical properties on solute – induced changes in refractive index and osmolarity, Journal of Biomedical Optics 1 (1996), pp. 200–211.
24. V. V. Tuchin, I. L. Maksimova, D. A. Zimnyakov, I. L. Kon, A. H. Mavlutov, and A. A. Mishin, Light propagation in tissues with controlled optical properties, Journal of Biomedical Optics 2 (1997), pp. 401-417.
25. D. A. Zimnyakov, V. V. Tuchin, and A. A. Mishin, Spatial speckle correlometry in applications to tissue structure monitoring, Applied Optics 36 (1997), pp. 5594–5607.
26. G. Vargas, E. K. Chan, J. K. Barton, H. G. Rylander III, and A. J. Welch, Use of an agent to reduce scattering in skin, Laser Surg. Med. 24 (1999), pp. 133-141.
27. V. V. Tuchin, Control of tissue and blood optical properties, in Advances in Biophotonics, Ed. B. C. Wilson, V. V. Tuchin and S. Tanev, NATO Science Series I, vol. 369, IOS Press, Amsterdam, 2005, pp. 79-122.
28. W. Sun, N. G. Loeb, S. Tanev, and G. Videen, Finite-difference time-domain solution of light scattering by an infinite dielectric column immersed in an absorbing medium, Applied Optics 44, No. 10 (2005), pp. 1977-1983.
29. A. Taflove and S. Hagness, Computational Electrodynamics: The Finite-Difference Time Domain Method, Artech House, Boston, 2000.
30. The FDTD Solutions™ was developed by Lumerical Solutions Inc., Vancouver, BC, Canada: www.lumerical.com

31. K. Sokolov, M. Follen, J. Aaron, I. Pavlova, A. Malpica, R. Lotan and R. Richards-Kortum, Real-time vital optical imaging of precancer using anti-epidermal growth
32. I. H. El-Sayed, X. Huang, and M. A. El-Sayed, Surface plasmon resonance scattering and absorption of anti-EGFR antibody conjugated gold nanoparticles in cancer diagnostics: applications in oral cancer, Nano Letters 5, No. 5 (2005), pp. 829-834.
33. N. G. Khlebtsov, A. G. Melnikov, L. A. Dykman and V. A. Bogatyrev, Optical properties and biomedical applications of nanostructures based on gold and silver bioconjugates, in Photopolarimetry in Remote Sensing, G. Videen, Ya. S. Yatskiv and M. I. Mishchenko (Eds.), NATO Science Series, II. Mathematics, Physics, and Chemistry, vol. 161, Kluwer, Dordrecht, 2004, pp. 265–308.
34. Vladimir P. Zharov, Jin-Woo Kim, David T. Curiel, Maaike Everts, Self-assembling nanoclusters in living systems: application for integrated photothermal nanodiagnostics and nanotherapy, Review article in Nanomedicine: Nanotechnology, Biology, and Medicine 1 (2005), pp. 326– 345.
35. Vladimir P. Zharov, Kelly E. Mercer,y Elena N. Galitovskaya, and Mark S. Smeltzer, Photothermal nanotherapeutics and nanodiagnostics for selective killing of bacteria targeted with gold nanoparticles, Biophysical Journal 90 (2006), pp. 619–627.
36. P. B. Johnson and R. W. Christy, Optical constants of noble metals, Physical Review B 6 (1972), pp. 4370-4379.

PHOTONIC AND NON-PHOTONIC BASED NANOPARTICLES IN CANCER IMAGING AND THERAPEUTICS

BRIAN C. WILSON*
Ontario Cancer Institute/University of Toronto, Canada

Abstract. This chapter presents an overview of the potential uses of nanoparticles in oncology. This includes the principles underlying the use of nanoparticles, firstly to enhance established treatment techniques such as radiation therapy, chemotherapy and surgery, as well as emerging treatment modalities, and secondly as contrast-enhancing agents to improve established tumor imaging methods, including X-ray, magnetic resonance, ultrasound and radionuclide techniques. In addition, photonic-based techniques will be emphasized, both therapeutic (photothermal, photomechanical and photodynamic therapies and fluorescence image-guided surgery) and diagnostic (fluorescence imaging, optoacoustic tomography and optical coherence tomography).

Keywords: Cancer, nanoparticles, imaging, diagnostics, therapeutics

1. Introduction

As in many other fields, nanotechnologies hold great promise for application in oncology, both as a research tool and to improve clinical diagnostics and therapeutics. Nano-scale devices, such as intra-cellular or interstitial biosensors (e.g. Zheng et al., 2005b), and many different types of nanoparticle are being investigated, as summarized in Figure 1, which shows both the major /needs in oncology and how nanotechnologies might contribute towards solutions.

* *To whom correspondence should be addressed: Dr. Brian C. Wilson, Division of Biophysics and Bioimaging, Ontario Cancer Institute, 610 University Avenue, Toronto, Ontario M5G 2M9, Canada; E-mail: wilson@uhnres.utoronto.ca*

J.J. Dubowski and S. Tanev (eds.), Photon-based Nanoscience and Nanobiotechnology, 121–157.

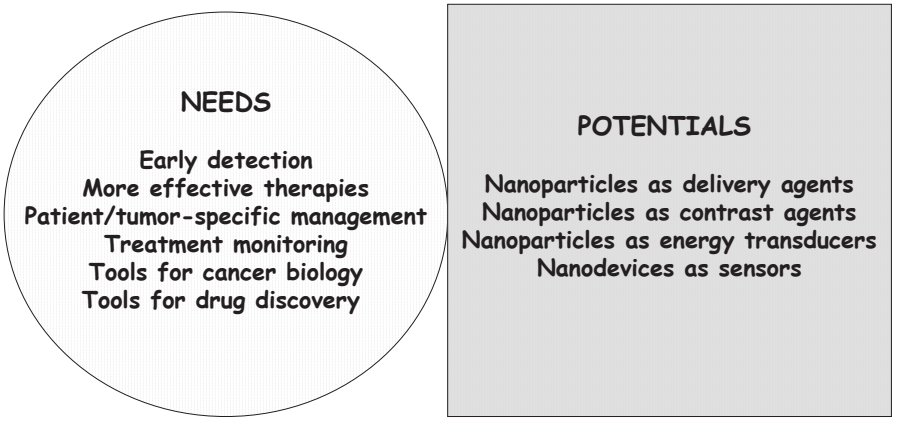

Figure 1. The convergence of oncology and nanotechnology.

A very useful source of information on the evolving applications of nanotechnologies in cancer can be found through the Alliance for Nanotechnology <www.nano.cancer.gov> of the US National Cancer Institute, which has committed a significant level of research funding to this field.

This chapter will be restricted to the use of nanoparticles in cancer imaging and treatment, and the reader is referred to other chapters for discussion of nanodevices. Excellent review articles on nanoparticles and nanotechnology in cancer are those of Brannon-Peppas and Blanchette (2004), Brigger et al. (2002), Ferrari (2005), Moghimi et al. (2005), Prow et al. (2004), Salata (2004), while the books by Prasad (2004) and Malsch (2005) provide broad overviews of different aspects of bionanotechnologies.

1.1. THE CANCER CHALLENGE

Cancer remains one of the leading causes of death and suffering. In the US, cancer accounts for nearly ¼ of all deaths, second only to cardiovascular disease. Further, while death rates for heart and cerebrovascular diseases (e.g. stroke) have fallen significantly in the last 50 years, that for cancer has remained essentially static (Am. Cancer Soc., 2006). This is not to say that there has been no progress, since morbidity and mortality for certain types of cancer have decreased substantially. However, the diverse group of diseases known as cancer continues to challenge our best minds and technologies. In part, this is because of its diversity, which goes beyond the historic recognition of different sites

(organ locations) and classes (pathologies) of cancer to the underlying genetic and molecular heterogeneity that exists, even between patients with the same types of cancer or within patients between, say, primary and secondary tumors.

Major potential roles for nanotechnology, and in particular nanoparticles used diagnostically or therapeutically, include (in temporal order of the cancer management process):

- prediction of cancer risk in individuals,
- early detection before the tumor has spread throughout the body or even at the pre-malignant stage: for most tumors the treatment response rates fall precipitously as the tumor becomes locally, regionally or systemically invasive (metastatic),
- tumor localization and staging to determine the best therapeutic strategy,
- targeted therapies, with greater tumor killing and reduced local or systemic side effects,
- guidance of therapy, including surgery, and
- patient follow-up and monitoring of treatment responses.

These clinical roles are in addition to the applications of nanotechnologies, including nanoparticles, as tools for discovery in the underlying causes and biology of cancer and in pre-clinical research and development of new anti-cancer drugs and other therapeutic agents.

1.2. NANOPARTICLES

According to the National Institutes of Health (US), nanoparticles (NP) are defined as being in the 10-100 nm diameter range and most of the examples presented below meet this criteria. However, there are a few cases where we will also show examples outside this strict range, e.g. the use of ultrasound micro-bubbles as contrast agents. It should be emphasized that, at this time, NPs for cancer treatment and diagnosis are still largely at the research and development phases, involving cell or animal model studies. However, it can be anticipated that some of these will eventually reach the clinic.

In diagnostics, the primary development of NPs has been as contrast agents for cancer imaging, in order to improve the detection of early-stage cancer or to detect metastatic spread of the disease. These NPs can be split into 2 main classes (see table 1). In the first the NPs themselves serve as the source of image contrast. Examples are the use of iron oxide

NP in X-ray imaging and quantum dots for fluorescence imaging. The NPs then either 'amplify' a pre-existing signal or generate a new signal. In the 2nd category the NPs serve as carriers of the contrast agent, as for example the use of polymers to carry a radionuclide for nuclear imaging or gadolinium for magnetic resonance imaging. In all cases, a means to 'target' the NPs to the tumor is required, such as tumor-specific antibodies, peptides, aptamers or antisense constructs (exploiting specific metabolic, molecular or genetic characteristics of the tumor cells or of the tumor microvasculature), in order to achieve tumor-specific contrast enhancement relative to the surrounding tissues and to minimize the total NP dose administered. This requires some physico-chemical binding of the targeting moiety to the NPs. For NP-carrier methods, there must also be a means to link or incorporate the active contrast agent onto or into the NP without destroying the NP signal or the targeting properties. It may also be possible to link more than 1 contrast agent to each nanoparticle to achieve image multiplexing, such as combined magnetic resonance and optical 'reporters'.

Table 1. Classes of NP-based applications in imaging diagnostics with specific examples and key references.

CATEGORY	*EXAMPLES*	*REFERENCES*
NPs as contrast agents	*Quantum dots (Qdots) for fluorescence imaging*	*Gao et al., 2004; Bharali et al., 2005; Larson et al., 2003*
	Qdot molecular beacons	*Chang et al., 2005*
	Gold NPs for OCT	*Lee et al., 2003; Chen et al., 2005*
	Iron oxide NPs for magnetomotive contrast in OCT	*Oldenberg et al., 2005*
	Melanin, gold or carbon NPs for optical coherence tomography (OCT)	*Lee et al., 2003*
	Iron oxide NPs for MRI	*Harisinghani et al., 2003; Neuwelt et al., 2004*
	2-plexes of iron oxide NPs for MRI plus Cy5.5 for fluorescence imaging[1]	*Veiseh et al., 2005*
	Gadolinium NPs for MRI	*Schmieder et al., 2005*
	Microbubbles for ultrasound imaging[2]	*Chomas et al., 2003*
NPs as carriers of contrast agents	*^{99m}Tc-polymer conjugates for radionuclide imaging*	*Mitra et al., 2005*

[1] In this case the MRI component belongs to the first class, whereas the same NP serves as a carrier for the optical agent.

[2] These may not be strictly considered as NP, due to their large size.

Table 2. Classes of NP-based applications in therapeutics with specific examples and key references.

NPs as therapeutic 'energy transducers'	*Somatostatin-photosensitizer dyads and triads for 2-photon PDT*[1]	*Spangler et al., 2005*
	Carbon-60 derivatives for PDT[1]	*Chi et al., 2006*
	Nanoporous silicon for PDT	*Kovalev and Fujii, 2005*
	Iron oxide NPs or gold nanospheres or nanoshells for photothermal therapy	*Pitsillides et al., 2003; Hirsch et al., 2003*
	Carbon nanotubes for photothermomechanical therapy	*Panchapakesan et al., 2005*
	Qdots for lymph node detection at surgery	*Kim et al., 2005; Soltesz et al., 2005*
	Gold NPs as X-ray absorbers	*Hainfield et al., 2004*
	Polystryrene NPs to increase ultrasound-enhanced drug delivery	*Larina et al., 2005*
NPs as carriers of therapeutic agents	*Polymeric or silica NPs for PDT sensitizer delivery*[3]	*McArthy et al., 2005; Yan and Kopelman, 2003*
	Dendritic polymers in micelles for PDT sensitizer delivery	*Ideta et al., 2005*
	Ceramic NPs encapsulating PDT sensitizers	*Roy et al., 2003*
	Co-polymer NPs carrying therapeutic radioisotopes	*Li et al., 2004*
	Liposomes containing boron-rich compounds for BNCT	*Thomas and Hawthorne, 2001*
	Carbon nanotubes with attached boron agents for BNCT	*Yinghuai et al., 2005*
	Polysaccharide (chitosan) NPs with gadolinium compounds for NCT	*Shikata et al., 2002*
	NPs for chemotherapeutic drug delivery: *- polymers* *- iron oxide* *- gelatin*[2] *- lipoproteins*	 *Farohkzad et al., 2004* *Jain et al., 2005* *Lu et al., 2004* *Zheng et al., 2005a*
	Gold NPs conjugated with tumor necrosis factor (TNF)	*Paciotti et al., 2004*
	Silica NPs for gene delivery	*Roy et al., 2005*
	Liposome-encapsulated magnetite NPs for hyperthermia	*Ito et al., 2005*

[1]These are likely molecular rather than true NP constructs but are included for completeness.

[2]These NP may also be direct PDT enhancers as well as photosensitizer carriers.

[3] These may not be strictly considered as NP, due to their large size.

Similar general conditions apply with respect to targeting the NPs to the tumor for therapeutic applications. Again, in some applications, the NPs serve effectively as 'energy transducers' to increase the therapeutic dose to the tumor. One example is in the use of gold NPs for local enhancement of the radiation dose in X-ray therapy, while another is the use of C-60 or quantum dots as photodynamic sensitizers. The other class of therapeutics, analogous to diagnostics, is to use the NPs as carriers of therapeutic drugs, biologics or therapeutic genes. One type of generic of NP structure is shown schematically in Figure 2.

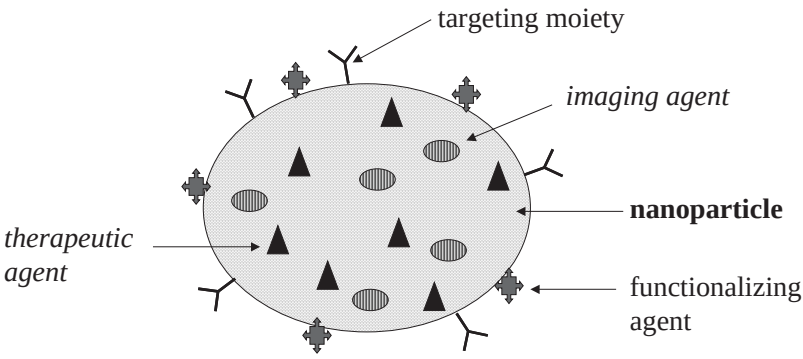

Figure 2. Schematic of a NP with a surface-bound functionalizing agent to facilitate delivery, a surface-bound tumor-targeting agent (e.g. antibody), and both imaging and therapeutic molecules in or on the NP. This is just one example of many different arrangements of these key components.

The desirable characteristics required of NPs for clinical imaging or treatment are listed in Table 3.

Table3. Desirable characteristics of clinical NPs.

CHARACTERISTIC	*(A): as active agent* *(B): as carrier of active agent*
Simple chemistry	***A , B***
"Tunable' physical properties	***A***
Strong 'signal'	***A***
Biocompatibility	***A , B***
Stability prior to and during use	***A , B***
Common platform for multiple applications	***A , B***
Low toxicity	***A , B***
Affordable (in production scale)	***A , B***
Manufacturable as a pharmaceutical	***A , B***

Clearly, for an NP-based agent to reach clinical use, it must be commercialized and produced as a pharmaceutical that is government approved for specific applications. This involves additional challenges. In general, the simpler the fundamental chemistry involved, both to synthesize the NP and to coat it and link it to the targeting and/or diagnostically- or

therapeutically-active agents, the cheaper it is likely to be and the easier to scale-up to production quantities of the required purity and stability. Biocompatibility and toxicity are major issues and vary between different forms of NP. For example, quantum dots are composed of heavy metals, such as Cd and Te, that are highly toxic if the Qdots disintegrate in the body. Hence, physico-chemical stability is critical, as are the means to shield the Qdots with a biocompatible and highly stable coating. Conversely, gold NPs are generally chemically inert and so could be used in relatively large doses. The idea of 'tunable' physical properties will be discuss in more detail later, particularly in the context of Qdots. The basic concept is to be able to adjust the NP parameters to optimize the signal and contrast between the tumor containing the NP and the background tissue, whether this is for diagnostic imaging purposes or to deliver enhanced therapeutic dose.

2. Diagnostic Imaging

The focus of this section is on the use of NPs to enhance the contrast in tumor imaging. This is distinct from nanotechnology-based devices for in vivo sensing or analysis of cells, tissues or body fluids. There are a number of well-established medical imaging techniques, which may be divided into 2 main classes: radiological and endoscopic, as illustrated in Figure 3. (Ophthalmology also relies heavily on imaging, particularly optical techniques, and many specialized instruments have been developed for this. However, these will not be discussed here, since ocular tumors are relatively rare and the same NP imaging principles largely apply as for other body sites.) Radiological imaging includes:

- X-ray techniques, comprising planar X-radiography (analogue or digital), fluoroscopy (real-time planar or multi-planar imaging) and computed tomography (cross-sectional imaging in which the image is computed from projection images at many different angles around the body),
- radionuclide imaging, which can be either planar or tomographic, with the latter including positron emission tomography,
- magnetic resonance imaging (MRI), which is usually volumetric with display of the images through any computed body section, and
- ultrasound imaging, applied either through the skin to image deep organs or endoscopically.

Endoscopy involves imaging the surfaces of internal hollow organs, such as the gastrointestinal tract (esophagus, stomach, colon), lungs, throat and oral cavity, bladder and cervix. Standard optical endoscopy is based on imaging the diffuse reflectance from the mucosal tissue surface, using broad-band (white) light. This is most commonly done using a flexible and maneuverable imaging probe, comprising either a coherent fiber-optic bundle to carry the image to one or more cameras outside the body or a video chip camera on the tip of the flexible endoscope. (Rigid endoscopes may be used for more accessible sites.) Endoscopy is particularly important in early cancer detection, since a large fraction of solid tumors originate as small, thin lesions (dysplasias) on the surface of hollow organs before developing into mass tumors that may obstruct the organ and/or spread beyond the site of origin.

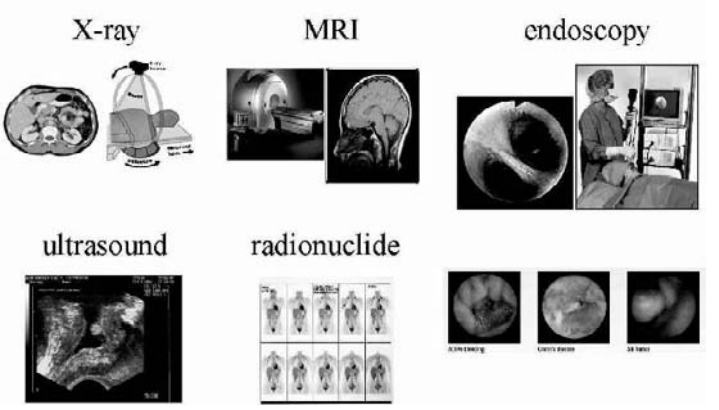

Figure 3. Major medical imaging techniques used for cancer diagnostics, showing: an X-ray CT cross-sectional image and the concept of computed tomography; a sectional MRI image through the brain and a typical high-field superconducting-magnet MRI unit; an ultrasound cross-section through the abdomen; multiple planar gamma-ray images of the whole body; a fiber-optic endoscope imaging the upper bronchus and; the 'camera pill' comprising a miniature white-light source and camera that are swallowed by the patient to image the GI tract.

These various techniques rely on either 1) the intrinsic differences in some physical property between the normal (or benign) tissues and the tumor (e.g. electron density in the case of X-rays, water spin relaxation times in MRI, density and elasticity in ultrasound, light absorption in endoscopy), or 2) concentration differences (uptake and/or clearance) of an administered (exogenous) contrast agent that provides a new physical signal (e.g. gamma-ray emission from a radioactive isotope) or enhances an intrinsic (endogenous) signal (e.g. changes the water relaxation times in

MRI). The latter is then the basis for developing NP-based contrast agents as a means to further increase the difference in signal between normal and malignant tissues. This can be achieved either by providing a new physical parameter (e.g. fluorescence in the case of quantum dots) or to increase the concentration of an existing contrast agent through improved tumor targeting. The examples that follow below will serve to illustrate these concepts.

In addition to these established imaging techniques there are several new techniques under development, particularly light-based. Those illustrated below, for which studies have been reported using NP contrast, are a) optical coherence tomography (OCT), b) optoacoustic tomography and c) fluorescence endoscopy. The principles on which these are based are, respectively, a) sub-surface imaging with near-infrared light that is analogous to (high frequency) ultrasound imaging, b) cross-sectional imaging using pulsed light to induce local generation of ultrasound waves through absorption of the optical energy and consequent rapid tissue expansion, and c) the use of fluorescence (emission of longer wavelength light by specific molecules upon absorption of shorter wavelength photons) as an adjunct to white-light diffuse reflectance imaging in endoscopy.

NP-based imaging may be considered as a sub-set of the evolving field of molecular imaging (Jaffer and Weissleder, 2005), in which new knowledge of the molecular-genetic basis of cancer (and other diseases) is exploited by developing contrast agents and mechanisms that target specific pathways or expression.

2.1. PHOTONIC-BASED IMAGING

In this section, we will illustrate the potential uses of NPs for each of the optical imaging techniques indicated above. As elsewhere in this chapter, the purpose is not to give a comprehensive survey of the rapidly expanding literature on NPs for medical imaging, but rather to present the basic concepts, to provide illustrative, state-of-the-art examples and to indicate possible future developments.

2.1.1. *Fluorescence Imaging*

Fluorescence imaging is under development for use in endoscopy and also as a means to guide tumor surgery (see below). Endoscopy based on the natural fluorescence of tissues (autofluorescence from tissue components such as collagen) has been investigated over the past 20 years and, recently, one system (OncoLIFE, Xillix Technologies Corp., BC, Canada) has been approved in the US and other countries for use in the lung to improve the sensitivity to detect early cancer/dysplasia (Lam et al.,

2000). This uses blue light excitation of the tissue surface, with imaging of the green fluorescence emission that is normalized to the red diffuse reflectance, which corrects for variables such as the different tissue distances and angles that can also affect the intensity of the fluorescence signal. This instrument is currently undergoing clinical trials in the esophagus and colon (results with an earlier prototype that used red fluorescence rather than reflectance to normalize the green collagen fluorescence intensity) are presented in Tytgat et al., 2001).

One of the limitations of autofluorescence imaging is that there tends to be a high 'false positive' rate, i.e. loss of specificity due to factors such as inflammation causing similar changes in the tissue fluorescence as early tumors. One strategy to overcome this is to use a targeted fluorescent dye, as illustrated in Figure 4 in a pre-clinical tumor model, in which the dye is linked to an antibody that recognizes molecules (antigens) on the tumor cell surface. There are, however, also limitations in the use of standard organic dye fluorophores, which may be overcome by the use of quantum dot (Qdot) nanoparticles (Jiang et al., 2004; Michelet et al., 2005).

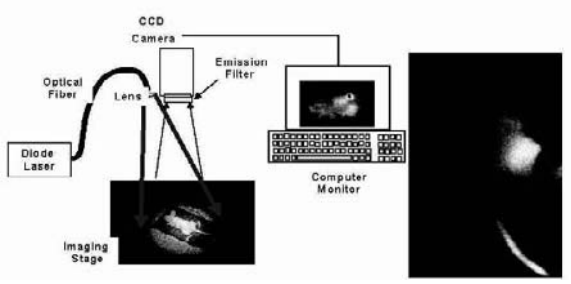

Figure 4. Fluorescence imaging using an antibody-organic fluorophore contrast agent. The set-up for the imaging is shown in the left, while the image on the right shows specific targeting of the Ab-dye conjugate to the (human colon) tumor in the mouse flank. The fluorescence along the tail is an artifact due to injection of the contrast agent via a tail vein. RH image from DaCosta et al,, 2002, with permission.

Qdots are NPs fabricated from one or more semiconductor materials, such as CdSe, ZnTe or InP. As illustrated in Figure 5, these typically have sizes in the 5-50 nm range. The properties that make Qdots potentially more useful than organic fluorophores for in vivo imaging (and other biomedical applications such as Qdot-based histopathological stains and for tracking of single cells or cell populations in tissue) are listed in Table 4. A further advantage is that near-infrared emitting Qdots are possible, which facilitates imaging more deeply into tissues (see section 3.1.3 on surgical guidance below). The current limitations of Qdots for clinical imaging clinically are their potential toxicity, high cost, complexity of bioconjugation and

relatively large effective size (which depends on the size of the semiconductor particles and on how these are coated and then 'decorated'

Table 4. Potential advantages of Qdots over organic fluorophores.

Property	Implications for Imaging
Low photobleaching	Signal stable throughout imaging Use high excitation intensity
High brightness	Low concentration of agent
Broad excitation spectra	Single excitation wavelength for multiplexing
Narrow, size-dependent emission spectra	Spectral multiplexing
large Stokes shift (gap between the excitation and emission wavelengths)	Easy separation of fluorescence from diffusely scattered excitation light

with the targeting moieties, e.g. antibodies). As mentioned above, the toxicity derives from the use of heavy metals in the semiconductor materials. Indium-based Qdots have been reported that may have acceptable toxicity if they can be used a low enough doses: note that the high brightness and low photobleaching of Qdots are important in minimizing the doses required. The toxicity also means that the coating of the Qdots has to be very stable so that the NPs do not disintegrate in vivo. The coating is also critical to reduce the sequestering of the Qdots by organs such as the liver and spleen before they can accumulate in the tumor. The coating and attachment of the targeting moities (bioconjugation) is intrinsically difficult for Qdots, since it involves linking of organic and inorganic materials.

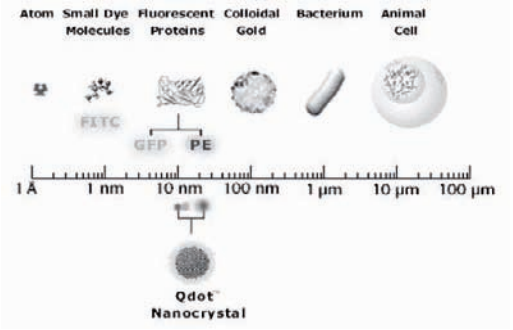

Figure 5. Qdots on size scale with other structures. (from website of Quantum Dot Corp., with permission).

One of the most promising characteristics of Qdots is that their narrow emission spectra may allow spectral multiplexing to be achieved, as illustrated in Figure 6, which shows the concept of administering a 'cocktail' of bioconjugated Qdots, each of a different emission wavelength linked to a different antibody (or other targeting agent). Simultaneous imaging of all Qdots would then improve the diagnostic sensitivity and specificity due to the multiple targeting to different pathologic characteristics of the tissues. It should be noted that, in order to make full use of the high-order multiplexing of Qdots, corresponding hyperspectral imaging technology is required that is suitable for the intended clinical application, e.g. endoscopy (Martin et al., 2006).

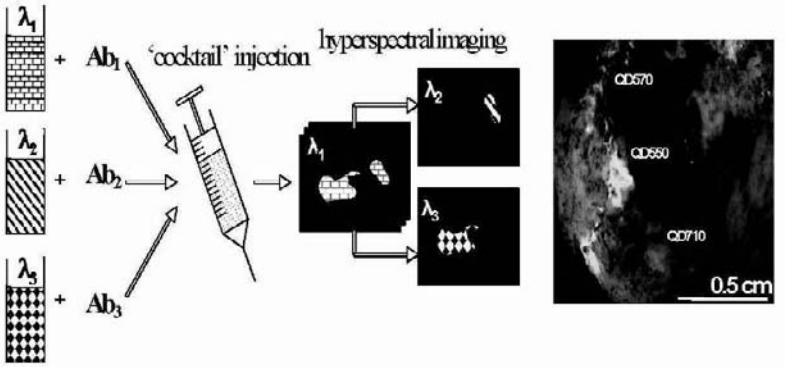

Figure 6. The concept of spectral multiplexing is shown on the left, with 3 different antibody-Qdot conjugates, each Ab having different specificity for each of the 3 tissue 'lesions'. The image on the right was taken in vivo after injection of 3 different colors of CdSe/ZnS Qdots at 3 sites into a human colon tumor in a mouse, to simulate the hyperspectral image that might be obtained if each was linked to a different Ab that was taken up at the different tissue locations. (Courtesy W. Chan and R. daCosta, University of Toronto, supported by the Canadian Institutes of Heath Research and the Ontario Research and Development Research Fund.)

There have also been a number of developments using special targeting or activation of Qdots. For example, Bharali et al. (2005) used Qdots comprised of an InP core and ZnS shell that were targeted to the folate receptor expressed on the surface of many cancer cells, and demonstrated both 1-photon and 2-photon confocal microscopy images of tumor cells in vitro. Chang et al. (2005) have demonstrated the Qdot analogue of 'molecular beacons', in which the Qdot emission is quenched by the proximity of conjugated gold NPs. Upon contacting the target, the gold NPs become separated, allowing the Qdots to fluoresce upon light activation. The unquenching can be achieved, for example, by linking the fluorophore (F) and quencher (Q) by a linker that can be cleaved by an

enzyme, or by attaching F and Q on the opposite end of an antisense molecule which, while in the circulation, is in folded ('hairpin') quenched conformation but that opens up to become unquenched by hybridizing with complementary mRNA in the target tumor cells. Figure 7 shows an example of enzymatic unquenching of Qdots fluorescence.

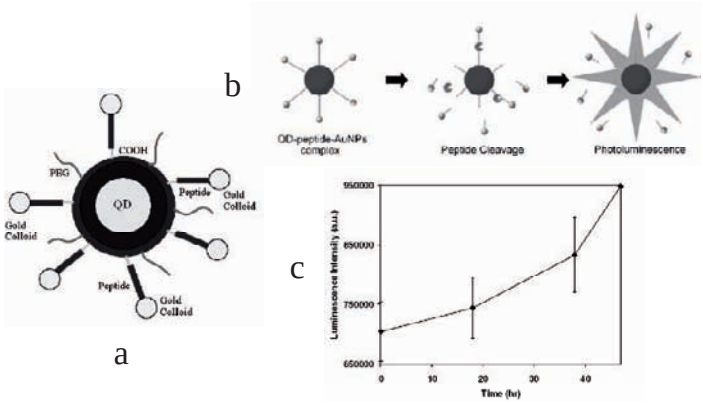

Figure 7. The concept of Qdot unquenching, after Chang et al. (2005), with permission: a) Au-quenched Qdot structure, b) steps in unquenching by peptide enzymatic cleavage, c) increase in Qdot luminescence with time of peptide exposure as the Qdots become unquenched.

2.1.2. *Optical Coherence Tomography*

Optical coherence tomography (OCT) uses near-infrared optical interferometry to form sub-surface cross-sectional images in tissue with high spatial resolution (Brouma and Tearney, 2001). A typical fiberoptic OCT scheme is shown in Figure 8a. It comprises a light source with a short coherence length. The light is split by a 50:50 coupler, with one arm going to the tissue and one to a scanning reference mirror (or, in practice, to an optical phase delay line in order to achieve high scanning speed). Light reflected by tissue microstructures at an optical depth corresponding to the optical path length in the reference arm undergoes constructive interference upon recombination with the reference beam in the splitter. The axial resolution is determined by the coherence length of the light source (inversely proportional to the spectral band-width). The interferogram signal is then sampled by a fast detector. As the mirror is scanned, the tissue is sampled along a line (A-scan) perpendicular to the surface. A 2-D image (B-scan) is then formed by sweeping the beam (or fiber) laterally along the tissue surface. Conceptually, this process is analogous to ultrasound echographic imaging, except that interferometry is used to perform the

depth ranging, rather than direct echo timing, which is impractical because of the high speed of light. OCT is in common use (in open-beam configuration) for retinal imaging and a variety of fiber-optic systems are under development for endoscopic, intravascular and interstitial imaging. Typically, OCT can image to a depth of about 2 mm below the tissue surface (or fiber tip) and current systems have spatial resolutions of about 10 μM. Doppler OCT has also be demonstrated, including endoscopically (Yang et al., 2005) for visualizing microvascular blood flow in near real-time.

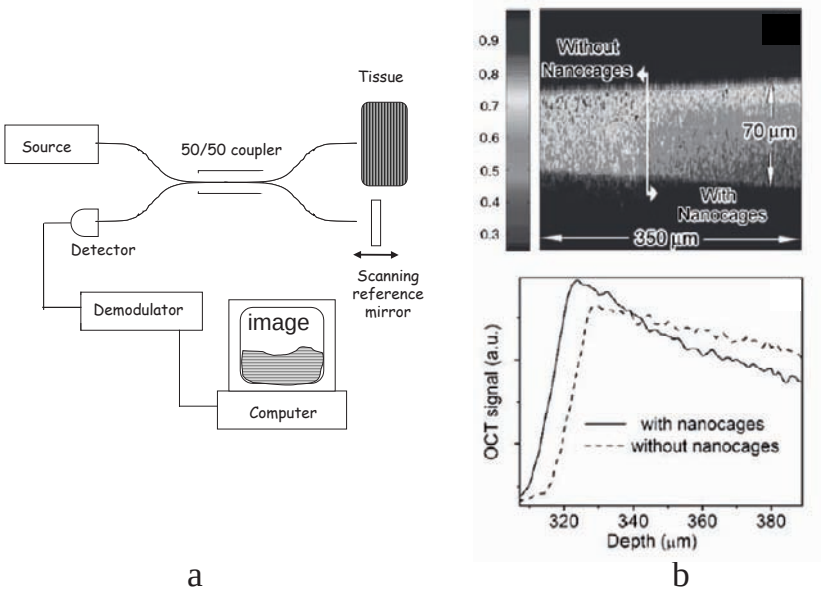

Figure 8. OCT imaging. a) principle of fiberoptic-based OCT, b) example of imaging through a region of a tissue phantom with and without gold nanocage NP contrast (Chen et al., 2005, with permission).

A critical feature of NP-enhanced OCT is the increase in light backscattering that can be achieved. This depends on the concentration of NPs and their optical properties, which vary with the NP size, geometry (e.g. solid sphere, shell, rod, etc) and material(s). For example, Chen et al. (2005) have investigated gold nanocages that are cuboidal shells about 30 nm in diameter and 3 nm thick. These have near-infrared (NIR) scattering and absorption cross-sections ~10^{-16}-10^{-15} m^2, which is 4 or 5 orders of magnitude larger than the absorption cross-section of indocyanine green, a widely-used NIR dye. These NPs could then be conjugated with, for example, thiol-polyethylene glycol (for biocompatibility) and then linked to

antibodies for targeting to tumor cells. In addition to having high cross-sections, the optical spectra are relatively narrow (~ 100 nm FWHM for scattering) due to the plasmon resonance conditions, and can be selected to have good overlap with the OCT source spectrum. The effect of using such NPs is shown in Figure 8b. This figure shows a significant trade-off in the use of NPs for OCT, in that the high scattering cross-section (and absorption) reduces the depth of imaging that can be achieved.

Lee et al. (2003) have demonstrated enhanced contrast in OCT imaging in vivo using melanin, gold and carbon-shell NPs. An interesting twist on the use of metal NPs for OCT has been demonstrated by Oldenberg and colleagues (2005), using 20-30 nm diameter magnetite ($Fe_3^{(II,III)}O_4$) NPs. A modulated (1kHz) external magnetic field then causes translation or rotation of the NP in the field gradient. This causes elastic deformation of the tissue, resulting in modulation of the optical scattering. OCT contrast is then achieved in this magnetomotive scheme by synchronizing the applied field with the optical A-scanning. This was demonstrated in phantoms and in vivo using a tadpole model in which the NPs were placed into their water tank at a non-toxic concentration for 24 h before imaging. Enhancement of the intestinal track was observed relative to the standard structural OCT images. This illustrates the use of two independent NP properties -magnetic and optical- to obtain image signal enhancement.

2.1.3. *OptoAcoustic Tomography*

In optoacoustic tomography the objective is to generate volumetric images in vivo through substantial thicknesses of tissue, for example to detect tumors in the breast. It is based on the propagation of photons that undergo multiple elastic scattering to 'fill' the tissue volume with a diffuse distribution of light. This is similar to diffuse optical tomography (DOT) (Hawrysz and Sevick-Muraca, 2000; Gibson et al., 2005)), except that in DOT the light that is eventually scattered out of the tissue volume is detected directly and the distribution of optical absorption and scattering are then reconstructed from the spatial and/or temporal distribution of the detected photons using a model of light propagation in a highly-scattering medium. The limitations of DOT are that the images have low spatial resolution and contrast: one could envisage NPs being used also as absorbing or scattering contrast agents in this case, but this has not been reported to date.

Rather than detecting the diffuse light exiting the tissue volume, optoacoustic tomography relies on the conversion of local absorption of light within the tissue, followed by detection of the acoustic wave pattern generated by the resulting thermal expansion. A short (~10 ns) laser pulse is required to generate ultrasound waves in the useful (MHz) frequency range

for volume imaging. The ultrasound image is then a direct image of the distribution of optical absorbers, weighted by the non-uniform distribution of light intensity throughout the tissue. As with DOT, the intrinsic absorption contrast of tumors relative to their host tissue background is limited (and is primarily due to differences in blood content, and/or the hemoglobin-to-oxyhemoglobin ratio, exploiting the fact that Hb and HbO_2 have different absorption spectra in the red-NIR range). Hence, NPs that are targeted to tumor could locally enhance the light absorption, as illustrated by the spectrum of gold nanospheres and nanorods in Figure 9a, and so increase the tumor image contrast.

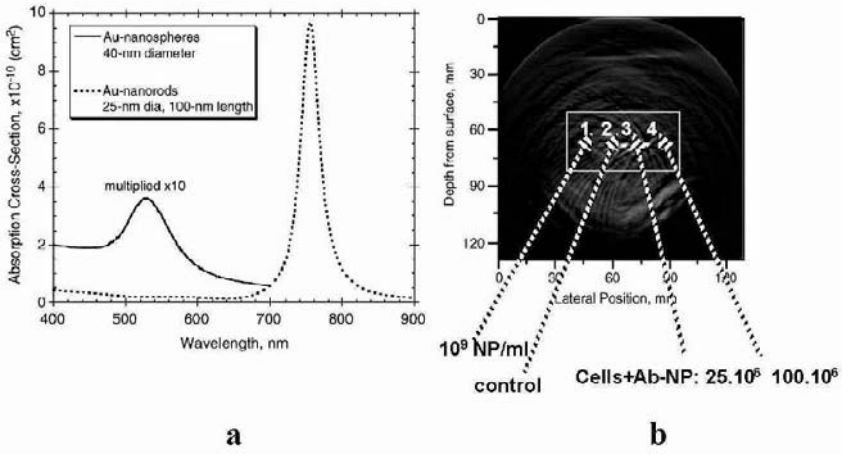

Figure 9. Optoacoustic imaging with NP enhancement. a) absorption spectra of gold nanospheres and nanorods, b) imaging of small 'tumors' in tissue-simulating phantoms with increasing concentrations of cells labeled with gold nanosphere-Ab conjugates. after Copland et al. (2004), with permission.

This has been demonstrated in tissue-simulating phantoms by Copland et al. (2004) using 40 nm diameter gold spheres, where concentrations of ~10^9-10^{10} NP/cm^3 (conjugated to herceptin antibody and attached to tumor cells) provided detectable optoacoustic signals in large tissue volumes (comparable, say, to breast imaging): see Figure 9b.

2.2. NON PHOTONIC-BASED IMAGING

NP studies have been reported for most of the established radiological imaging modalities, as follows.

2.2.1. *Magnetic Resonance Imaging*

In MRI the signal is due to radio-frequency excitation and subsequent relaxation of water molecules in a strong (few Tesla) magnetic field. A known field gradient is applied that spatially encodes the resonant frequency in order to form the image. The intrinsic contrast comes from variations in the tissue water content and relaxation times, the latter depending on the local physico-chemical microenvironment. Gadolinium is used commonly as an MRI contrast agent: being paramagnetic, it alters the relaxation times of the water molecules in the applied magnetic field.

To date, most studies of NPs as MRI contrast agents have used superparamagnetic iron oxide. For example, Harisinghani *et al.* (2003) used commercially-available NPs (Combidex: Advanced Magnetics, USA or Sinerem: Guerbet, the Netherlands), comprising 2-3 nm monocrystalline iron oxide and bound to dextrans to prolong their time in the circulation (overall particle size ~30 nm). These were injected intravenously at a dose of 3.6 mg of iron per kg body weight in a series of prostate cancer patients. The objective was to detect, by subsequent imaging, tumor involvement of pelvic lymph nodes. A standard 1.5T MRI system was used. In normal lymph nodes, the MRI signal decreased with the administration of the NP, associated with uptake by nodal macrophages, whereas in tumor-involved nodes the signal remained high or was non-uniform: this is illustrated in Figure 10. In a series of 80 patients, the sensitivity for detecting involved lymph nodes on MRI increased from 35 to 90% and the specificity from 90 to 98% when the NP contrast agent was used: the improvement was even more striking with nodes less than 10 mm diameter.

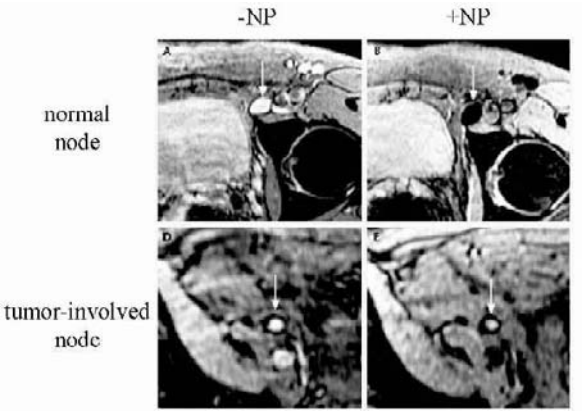

Figure 10. MRI images of pelvic lymph nodes (indicated by white arrows). Adapted from Harisinghani et al. (2003), with permission.

Neuwelt et al. (2004) demonstrated MRI enhancement in primary and metastatic brain tumors in a small series of patients using dextran-coated iron oxide NPs. On subsequent histopathology, the NPs localized in reactive cells (astrocytes and macrophages) rather than in the tumor cells themselves. This suggests further improvement might be gained by tumor cell-specific targeting of the NPs. Tumor targeting NPs was tested in a different approach by Schmieder et al. (2005), using an integrin antagonist ($\alpha_v\beta_3$: targeted to tumor vasculature) to label paramagnetic gadolinium NPs (270 nm diameter, 90K Gd^{3+} atoms per NP, 300 integrin ligands per NP). Detection of angiogenesis in early melanoma tumors was demonstrated in a mouse model.

As a final example, Sitharaman et al. (2005) have recently reported the fabrication and use of thin-walled carbon nanotubes (20-80 nm long, 1.4 nm diameter) loaded with Gd^{3+} ion clusters that have significantly higher efficiency as an MRI contrast agent than conventional gadolinium-based compounds.

2.2.2. *Radionuclide Imaging*

In radionuclide imaging, using either gamma-ray or positron isotopes, there are a large number of different molecules to target tumor or other pathologies (Jaffar and Weissleder, 2005). The applications are in tumor detection/localization, staging and in monitoring response to therapies. The role of NPs in nuclear imaging will be primarily in improving targeting/delivery of the radionuclides. To date, relatively few studies have been reported, possibly because of the extra complications of dealing with the bioconjugation of novel nanoparticles and radioactive materials. Figure 11 shows an example of radionuclide imaging of tumor using a large co-polymer targeting moiety carrying the gamma-emitting radionuclide ^{99m}Tc. While not strictly in the nanoparticle regime, this does illustrate the potential of using NP-type delivery systems in radionuclide imaging. The challenges in developing NP delivery systems for nuclear imaging will be similar to those for drug delivery, with the added constraints of 1) dealing with radioactive materials, 2) ensuring that the delivery kinetics are compatible with the physical half-life of the isotope and 3) biocongugating the radioactive atoms, which are often heavy metals in the case of gamma emitters. Another option is to use radiolabeling of NPs themselves in order to follow their biodistribution, for example in tracking therapeutic NPs.

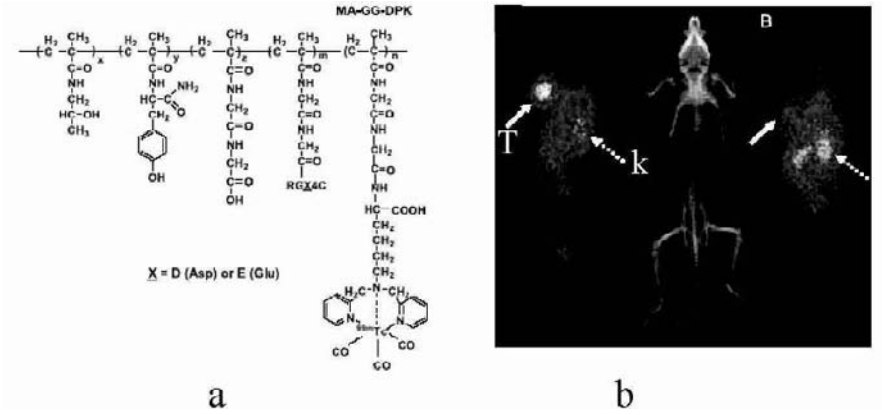

Figure 11. Technecium-99m labeled copolymer conjugates for scintigraphic imaging in a mouse tumor model. The structure of the conjugate in shown in (a), while (b) shows an image of the tumor (T) and kidney (K). after Mitra et al., 2005, with permission.

2.2.3. *Ultrasound Imaging*

To date, the main means of obtaining increased contrast in ultrasound imaging has been to use microbubbles. The resonant frequency of the bubble vibration is then matched to the frequency of the ultrasound source in order to increase the back-scattered echo signal. For typical medical ultrasound in the MHz range, the bubble sizes are of the order of a few microns diameter and so do not rigorously fit the definition of nanoparticles as being in the 10-100 nm size range. Nevertheless, many of the same opportunities and challenges pertain, including means to target the microbubbles specifically to tumor tissue, either through markers on the tumor cell surface or altered microvascularity. An interesting variation on the use of ultrasound microbubbles is to use a high-intensity ultrasound pulse to burst the bubbles within a specified image plane and then to follow the recovery of the contrast as new bubbles flow into the plane, thereby effectively imaging the blood flow rate (Chomas et al., 2003).

2.2.4. *Multi-Modality Imaging*

One of the most compelling attributes of NPs as image contrast agents is the potential to fabricate agents that can be used simultaneously (or sequentially) for more than one imaging modality. A recent example, combining MR and optical imaging, was demonstrated by Veiseh et al. (2005), who fabricated iron oxide NPs, which provided MRI contrast, linked to a fluorescent dye (Cy5.5) for optical imaging and to a tumor-specific peptide for targeting, as shown in Figure 12. In this case the MRI

contrast was demonstrated in phantoms, while tumor targeting was shown by fluorescence microscopy of cells after incubation with the agent. The potential value of such bi-modality agents for surgical guidance is discussed below.

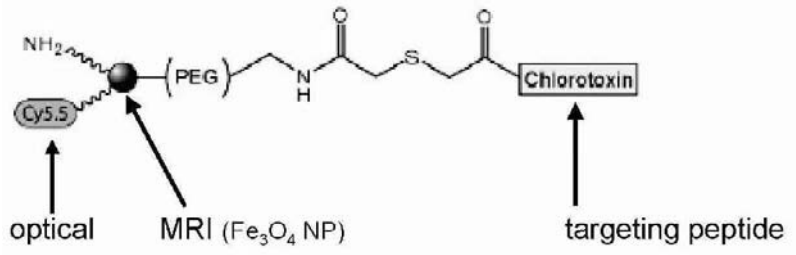

Figure 12. Tumor-targeted NP construct with both MR and optical imaging properties. Adapted from Veiseh et al. (2005), with permission.

3. Therapeutics

There are 3 main forms of cancer therapy that are used universally, either alone or in combination, for a wide variety of tumor types and stages. These are radiation therapy, chemotherapy and surgery. In addition, there are a number of other modalities that are used to a more limited extend and/or are still under development. These include hormone therapy, immunotherapy (or other 'biologics'), photodynamic therapy, hyperthermia/thermal therapy and gene therapy. An alternative way to categorize these various modalities is to consider them as either physical (radiation, surgery, thermal), chemical (cytotoxins) or biological (hormones, cytokines, immunotherapy, gene therapy), although this is an over-simplification, since, for example, ionizing radiation therapy works through the generation of active chemical intermediates, while photodynamic therapy involves both a chemical (photosensitizer) and a physical energy source (light).

As indicated in Table 1 above, NPs may play a role in enhancing the therapeutic efficacy of each of these modalities, either through improved targeting/delivery of the therapeutic agent or through serving to enhance the local deposition of 'dose' in the tumor. The greatest experience with the former is in the delivery of anti-cancer drugs (chemotherapeutics), for which a multiplicity of different agents has been developed, some of which may also find application in the other treatment modalities.

3.1. PHOTONIC-BASED THERAPIES

Historically, the main therapeutic uses of light have been 1) in dermatology for treatment of psoriasis using PUVA therapy (the combination of UV-A light and a DNA-intercalating drug psoralen that slows the abnormal proliferation of skin cells) and 2) in laser surgery, using a variety of different wavelengths, pulse lengths and powers to coagulate, cut or ablate tumor tissue (Puliafito, 1996). In addition, over the past 20 years there has been considerable development of photodynamic therapy for destruction of solid tumors and pre-malignant lesions, as well as a variety of non-cancer conditions, such as age-related macular degeneration, which causes blindness in the elderly and is caused by abnormal growth of blood vessels in the retina, and infections, for which PDT may be particularly effective against multi-drug-resistant bacteria. Photothermal techniques, in which (laser) light is used to destroy tumor tissue through heating, without ablation or mass removal of tissue, are less widespread but may be useful where the tumor is deep seated and adjacent to critical normal structures.

3.1.1. *Photodynamic Therapy*

The principle of photodynamic therapy (PDT) is that certain molecules (photosensitizers) that are not in themselves cytotoxic may be activated by absorption of light (visible or near-infrared) to generate cytotoxic photoproducts, particularly excited-state singlet oxygen (Patrice, 2003). In treating solid tumors, there is then a double targeting or selectivity, through the differential uptake and/or clearance of the photosensitizer in the tumor and the delivery of the activating light to the target tumor volume, for example through placement of optical fibers into the tumor mass or confinement of the light beam to the tumor area. There is considerable effort in developing new photosensitizers with high absorption and singlet oxygen quantum yield at NIR wavelengths (up to about 850 nm: beyond this the efficiency of singlet oxygen generation drops) where light penetration in tissue is greatest. Since the photosensitizer is non-toxic except when light activated, the requirement for tumor specific targeting is not as great as in the case of chemotherapeutic drugs that can kill cells, including normal cells, anywhere in the body. Nevertheless, delivering more photosensitizer to tumor tissue and cells is still highly desirable.

Roy et al. (2003) synthesized, by hydrolysis in a micellar medium (see Figure 13a), high-porosity silica-based NPs (diameter ~ 30 nm) for this purpose and showed active uptake into the cytosol of tumor cells (Figure 13b) and subsequent photodynamic killing (Figure 13c). It should be possible also to target these NPs by modifying their surface with different

functional groups and then labeling with targeting agents such as anti-tumor antibodies.

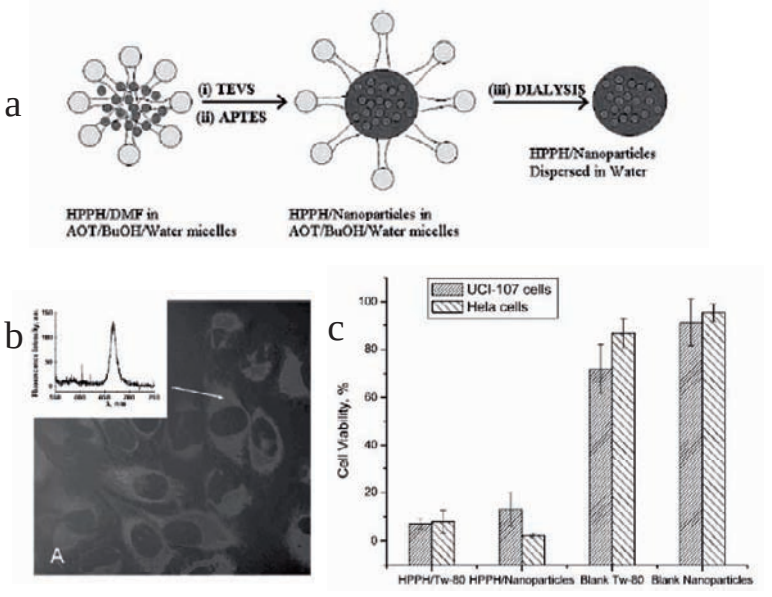

Figure 13. Ceramic-based NPs for delivery of PDT photosensitizer. a) procedure for synthesizing the NPs by first mixing the photosensitizer (HPPH) in the non-polar core of micelles, adding silanes to form the silica NPs and then purifying by dialysis, b) fluorescence of the HPPH in tumor cells (HeLa) after 2h incubation with the NPs, and c) cell viability after light exposure of 2 different tumor cell types incubated (L to R columns) in HPPH alone, HPPH-NP, no drug (control) and NP without HPPH (control). Adapted from Roy et al. (2003), with permission.

In terms of using NPs as the PDT-active agent, there have been a number of proposals. One example is the use of molecular triads containing a targeting agent, a separate reporter molecule to image the biodistribution and the photosensitizer (Spangler et al., 2005). A second is the use of C-60 modified to have high light absorption at long visible wavelengths and conjugated with a targeting molecule (Chi el al., 2006). At this stage of development it is not clear if these agents can be classified as true NP constructs or are simply large single molecules or aggregates. Recently, McCarthy et al. (2005) incorporated the photosensitizer mTHPC (which has been used clinically as a free drug) into 100 nm diameter polymeric nanoparticles. The drug was released and could be photoactivated upon uptake into cells, resulting in tumor cell killing in vitro and tumor destruction in vivo. A further example of NP-based PDT, in this case for neovascular disease, is that reported by Ideta et al. (2005), who developed a dendritic photosensitizer comprising a porphyrin molecule surrounded by

poly(benzylether) dendrons. These prevent loss of photoactivation due to the aggregation that often occurs with porphyrins and so allowed high drug loading in micelles for delivery, resulting in good photodynamic effect in a rat model of choroidal neovascularization.

The alternative approach, to generate singlet oxygen (or other reactive oxygen species) by photo-irradiation of NPs directly, has been demonstrated by the work of Kovalev and Fujii (2005) using NPs made of porous silicon, in which singlet oxygen was generated by dipole-dipole or direct electron exchange due to coupling between the excitons confined in the silicon nanostructure and molecular oxygen.

One of the driving forces for NP-based photosensitizers is to try to obtain agents with high cross-section for 2-photon activation. The energy diagrams for 1-γ activation (which is the usual way in which PDT is administered) and for simultaneous absorption of 2, long-wavelength photons are shown in Figure 14.

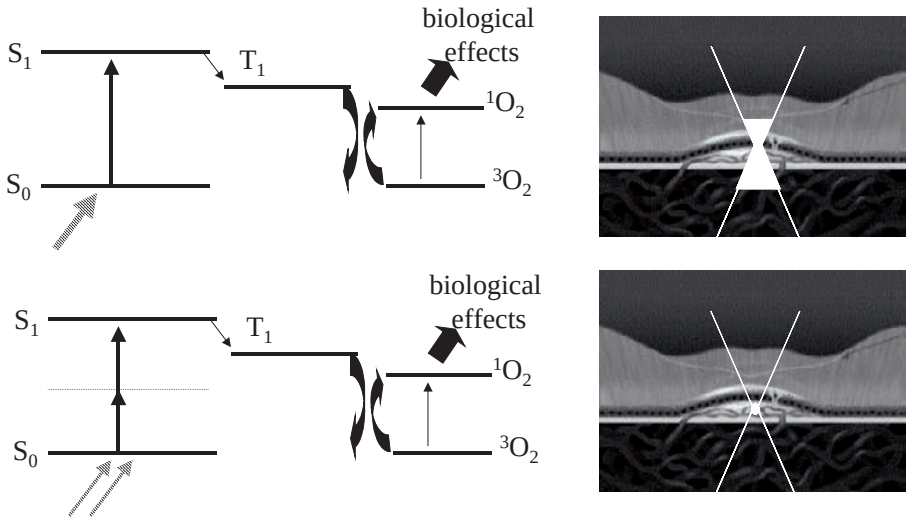

Figure14. Concept of 2-photon PDT. The upper charts show the energy-level diagram for 1-γ PDT and the effective volume of photo-activation in the retinal layers of the eye, while the lower charts show the equivalent situation for simultaneous absorption of 2 photons, each of half the energy (double the wavelength) of the 1-γ case. (S_0 photosensitizer ground state; S_1 photosensitizer singlet excited state that undergoes intersystem crossing to the triplet T_1 state; $^3O_2$ ground-state oxygen; $^1O_2$ singlet oxygen). Supported by the Canadian Institute for Photonic Innovations.

The potential advantages of 2-γ activation are 1) that the longer wavelength light has greater tissue penetration and 2) that, since the

probability of 2-γ absorption is proportional to the square of the local light intensity (I^2) rather than to I, focusing the light to a point in the tissue can result in tight spatial confinement of the volume of 2-photon activation. Point (1) may be useful in, for example, melanoma where the high melanin concentration prevents adequate light penetration in 1-γ PDT, while point (2) may be exploited for precise targeting abnormal blood vessels in the retina. Photosensitizers developed for 1-γ activation generally have low 2-γ cross sections (Karotki et al., 2006). One possible solution is to use Qdots, which have been reported by Larson et al. (2003) for 2-γ fluorescence imaging of blood vessels.

Finally, it should be noted that recent work (Chen et al., 2004) has demonstrated the PDT analogue of molecular beacons. In this case the photosensitizer was linked to a quencher molecule until these were separated by enzyme cleavage or hybridization to a biosubstrate, whereupon the photosensitizer generated singlet oxygen upon light activation. Hence, the same considerations could apply for NP-based PDT drug delivery as for delivery of optical imaging agents (fluorophores), as discussed in section 2.1.1 above.

3.1.2. *Photothermal Therapy*

Rather than being converted to chemical energy as in PDT, light can be applied therapeutically in order to raise the temperature of tumor tissue to above about 55°C at which lethal necrosis is produced. Other means to produce deep tissue heating in a minimally-invasive way are radiofrequency or microwave energy or high-power ultrasound. A general limitation is that the heating from energy sources is not specific, and relies on the spatial targeting of the energy to the tumor volume. Hence, the role of NPs is to increase the rate of local light absorption in order to increase the tumor temperature for the same power delivered and to limit heating of adjacent normal tissues. Hence, one requires NPs that have high absorption at optical wavelengths where there is adequate light penetration in tissue, namely in the near-IR range between about 800 and 1300 nm.

Metal NPs that have a size-tunable resonant absorption band are possible candidates. Hirsch et al. (2003) have reported the use of nanoshells with a 110 nm diameter silica core and with a 10 nm thick gold shell. The optical absorption spectrum of these NPs is shown in Figure 15a and peaks around 820 nm. The resulting increase in the local heating as a function of depth in human breast tumors transplanted in mice is demonstrated in Figure 15b, where it is compared with the temperature profile without the NPs: the average temperature increase (above the basal level) achieved in the 10 mm diameter tumors was 37.4 ± 6.6°C, which is well above the threshold for irreversible tissue damage. This was achieved with an incident

820 nm laser power of 4Wcm^{-2} for 4-6 min at 5-30 min following intra-tumoral injection of 20-50 μl of NP colloid (at 1.5x10^{10} NP/ml). This light exposure was an order of magnitude less than that required with indocyanine green as the thermal enhancement agent. Enhanced thermal killing of tumor cells in vitro was also demonstrated (Figure 15c).

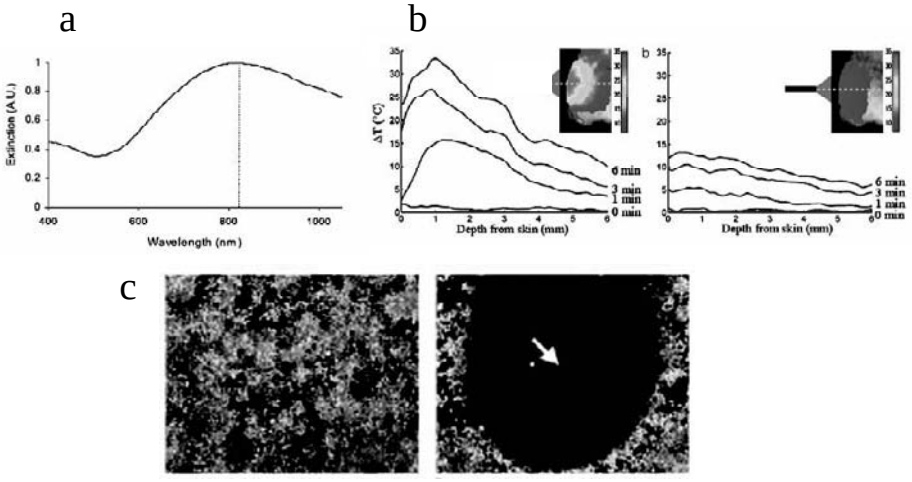

Figure 15. NP-enhanced photothermal therapy. a) optical absorption spectrum of gold nanoshells, b) temperature-depth profiles with increasing light exposure in tumors in vivo: left +NP, right –NP, c) tumor cell cultures in vitro irradiated with laser light: left –NP, right +NP (showing area of non-viable cells corresponding to the laser beam). adapted from Hirsch et al. (2003) with permission.

Cell death was demonstrated by Pittsilides et al. (2003) using antibody-targeted NPs irradiated with laser pulses that are short compared to the thermal relaxation of the NPs ('thermal confinement'). This induces rapid thermal expansion, resulting in creation of a vapor bubble around the NPs, as shown in Figure 16, and consequent damage due to cavitation. That is, this method operates through a photo-thermo-mechanical mechanism of action, similar to some short-pulse laser treatments targeted to naturally-occurring tissue absorbers such as melanin granules. Both iron oxide microparticles (~800 nm diameter) and 20 nm diameter gold NPs were investigated and it was shown that the effect is highly dependent on the particle size. With the smallest NPs (20 nm diameter) NPs transient permeabilization of the plasma membrane could also be achieved without killing the cells, which offers the opportunity to use this approach to tranfect tumor cells with genes or other therapeutic agents. Analogously, Larina et al. (2005) have reported the use of low-frequency ultrasound to permeabilize cells by cavitation in order to enhance uptake of therapeutic NPs.

Panchapakesan et al. (2005) have also reported photothero-mechanical disruption of cells using single-wall carbon nanotubes as the energy transducer. Confinement of the energy in the 1.5 nm diameter nanotubes causes explosive evaporation of the water content, leading to mechanical killing of the cells, as demonstrated in vitro in a breast cancer model.

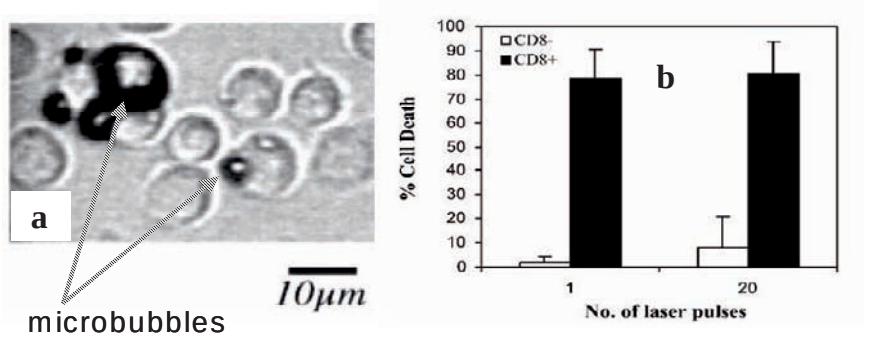

Figure 16. Photothermomechanical cell killing. a) microbubble formation in lymphocytes 100 ns after exposure to a 565nm, 20 ns pulse at a fluence of 35 Jcm^{-2}, using iron oxide microspheres (4 per cell), and b) cytotoxicity as a function of number of gold NPs per cell with (■) or without (□) or NP targeting to the cells by CD8 antibodies. after Pitsillides et al., (2003), with permission.

3.1.3. *Fluorescence-Guided Surgery*

Many solid tumors are surgically removed prior to giving either radiation and/or chemotherapy to kill tumor that is not completely resected (and also to destroy tumor that has spread beyond the primary site). In cancer surgery a compromise often has to be struck between aggressive resection to minimize the risk of residual tumor tissue and conservative resection in order to avoid unacceptable damage to adjacent normal structures. Since it may be difficult to see the residual tumor once the bulk of tumor has been removed, there is interest in extending the surgeon's vision, in particular through the addition of fluorescence imaging as an adjunct to standard white-light viewing. As with endoscopy, the options are to use autofluorescence imaging or a systemically- or locally-applied fluorescent contrast agent. For example, Stummer and colleagues (2003) have shown that the survival of patients with malignant brain tumors is significantly increased by using fluorescence image guidance during surgery. In this case the selective fluorescence in tumor tissue comes from protoporphyrin IX that is synthesized in the tumor cells after administration of aminolevulinic acid, a precursor in the heme biosynthetic pathway. (This

ALA-PpIX technique has also been used widely in PDT, since PpIX is also a photosensitizer (Kelty et al., 2002).)

Qdots have been investigated for surgical guidance, with the same intent of more clearly delineating residual tumor. In this case the high brightness and potential for greater tumor-cell selectivity through molecular targeting are the main properties of value, although the low photobleaching of Qdots compared to organic fluorophores may also be important since the exposed tissue may be illuminated by the operating-room lights for extended periods. One example is the use of Qdots to highlight tumor-involved lymph nodes during surgery. NIR-emitting Qdots are of particular interest for this purpose, because of the deeper light penetration. This has been demonstrated in pre-clinical rat (Kim et al., 2005) and pig (Soltesz et al., 2005) models: an example is shown in Figure 17, using injection of dots with a hydrodynamic diameter (effective diameter in tissue) of 20-30 nm, emitting in the 840-860 nm wavelength range. The light source for fluorescence excitation comprised two 150W halogen lamps filtered to give 5 $mWcm^{-2}$ on the tissue surface at 725-775 nm: fluorescence imaging was done using a CCD camera. Recently, the author's group has developed multi-spectral CCD camera systems for intra-operative fluorescence imaging (Yang et al., 2003; Bogaards et al., 2005) as a first step towards the future possibility of using spectral multiplexing with Qdot imaging at surgery.

The possibility of multi-modality NP-based surgical image-guidance is particularly exciting. For example, using the type of NPs described in section 2.2.4 above, it could be possible to perform pre- or intra-operative NP contrast-enhanced MRI imaging to guide the de-bulking phase of tumor surgery, followed by fluorescence image guidance to resect residual tumor that is below the resolution or contrast limit of MRI.

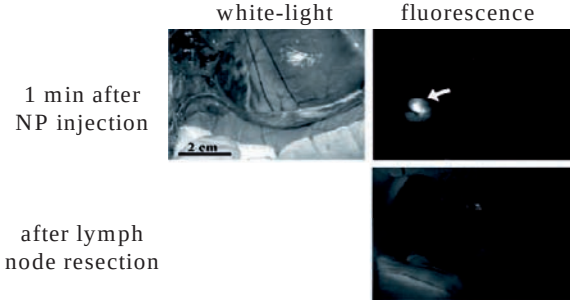

Figure 17. Qdot-based fluorescence guided lymph node resection in a pig lung model. The Qdot fluorescence in the lymph node can be seen clearly following intravenous injection of 100 μl of 2 μmol/L of NIR Qdots intraparenchymally adapted from Soltesz et al. (2005) with permission.

3.2. NON PHOTONIC-BASED THERAPIES

The above applications make use of the specific optical properties of different NPS. In this section, the use of NPS to enhance other forms of cancer treatment will be illustrated.

3.2.1. *Radiation Therapy*

Radiation treatment can be delivered using either externally-applied X-ray beams (and occasionally electron, neutron or proton beams) or implanted (or in some cases ingested or injected) radioactive materials. Taking the example of external beam therapy (teletherapy), a major challenge is to deposit a high enough radiation dose to the tumor volume (typically ~50 Gy total, in 20-30 fractions over a period of several weeks), while keeping the dose to the surrounding normal tissues low enough to minimize acute and long-term toxicity. In modern radiotherapy this is achieved by precise targeting of the radiation beams and shaping of the field to the tumor outline as seen from different angles around the body (conformal therapy). Despite the sophistication of this approach, normal dose toxicity often remains the limiting factor in achieving complete tumor destruction, so that means to enhance the tumor dose would be of major value. Historically, radiation sensitizers have been investigated for this purpose. These work, for example, by altering the chemical reactions that are induced on exposure of the tissues to ionizing radiation or by modifying the capacity of the tumor to repair the radiation damage: however, these are not advantageous enough to have entered clinical practice. Other options are to change the pattern of radiation dose deposition, for example by using high-energy protons that deposit energy preferentially near the end of their range in tissue, thereby increasing the tumor-to-normal tissue dose ratio. However, this requires large expensive proton accelerators and so is available in only a few centers. A further option, also not widespread, is neutron capture therapy (NCT), in which the reactions of epithermal neutrons (n) with specific atoms, administered essentially as contrast agents, cause nuclear reactions that result in short-range particles with high linear energy transfer, for example alpha particles in the reaction $^{10}B(n,\alpha)7Li$, for which boron is the administered material.

There are several pre-clinical reports investigating NP-enhanced radiation therapy. Hainfeld et al. (2004) intravenously injected gold NPs (diameter 1.9 nm) into tumor-bearing mice at a dose of up to 2.7 mg per kg body wt (resulting in a tumor tissue concentration at the time of treatment of 7 mg/g and an 8:1 tumor-to-normal tissue NP concentration ratio) and then irradiated the tumors with 250kVp X-rays. Since the K-edge for Au is 80.7 keV, this increased the local X-ray absorption and resulted in a

significant delay in tumor growth (Figure 18a) and increased survival (Figure 18b) compared with untreated tumors, radiation alone or lower dose of NPs.

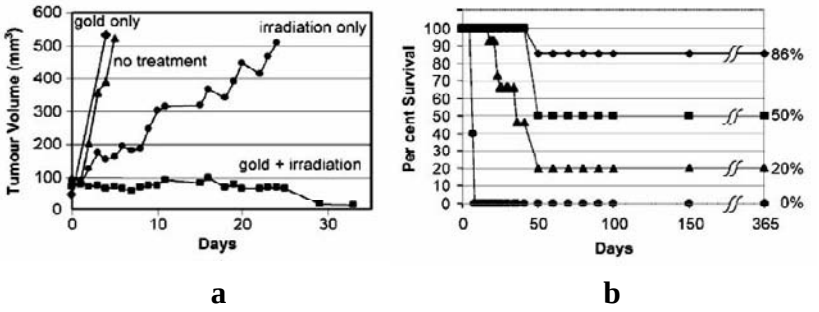

Figure 18. Response of EMT-6 breast tumors in mice as a function of time after X-ray therapy with or without gold NP. A) tumor volume vs time with 2.7 g/kg NPs compared with controls, b) percent survival. adapted from Hainfeld et al.(2004) with permission.

This study raises a number of issues. Firstly, the gold NPs were administered without any specific tumor targeting. Hence, the high tumor-to-normal tissue ratio was achieved simply by irradiating at a short time after injection (2 min), presumably while the NP were still in the circulation. Targeting could be expected to improve this further. Secondly, the use of relatively low energy X-rays (250 kVp) would give greater dose enhancement, because the spectrum overlaps the photoelectric K-edge of the gold, than would be obtained with the higher (MV) range used in most of radiotherapy treatments. Hence, it may be necessary to use NPs of other metals to give enhancement of high-energy X-rays. Thirdly, except in some cases of palliation, radiotherapy is always delivered over many fractions (to allow normal tissue healing), so that it would be necessary either to re-inject the patient for each fraction or the NPs would need to have a long residency time (days or weeks) in the tumor tissue. Finally, one might expect that the use of NPs in this way would simply result in high radiation dose to the NP themselves. However, it should be noted that most of the radiation dose to tissues comes not directly from the X-rays themselves but from the secondary electrons generated by the X-rays, so that presumably the small size of the NPs allows the secondary electrons that are produced in the gold to escape into the tissue.

A second approach is to use NPs as carriers of therapeutic radioisotopes. This is exemplified by the study of Li et al. (2004), who used copolymer-based NPs that were targeted either to a specific tumor-associated integrin or to a vascular endothelial growth factor receptor (expressed in tumor neovasculature) and that carried the beta-emitting isotope ^{90}Y. Significant

growth tumor growth delay was achieved in an animal model with this approach.

In neuron capture therapy several different forms of NP have been investigated for enhanced delivery of the neuron-target atoms to the tumor. For example, Thomas and Hawthorne (2001) used liposomes encapsulating hydrophilic boron compounds, while Yinghuai et al. (2005) attached substituted C_2B_{10} carborane cages to the side walls of single-wall carbon nanotubes, as illustrated in Figure 19. Both groups showed high concentrations of boron in breast tumors in mice relative to other tissues, peaking at 10-30 h after systemic injection.

Shikata et al. (2002) used gadolinium loaded into polysaccharide (chitosan) NPs to enhance the tumor uptake for the reaction $^{157}Gd(n,\gamma)^{158}Gd$. These NPs had a mean diameter of 428 (±28) nm and a Gd content of about 9%. They were found to have high cellular uptake (2 orders of magnitude higher than that of the standard MRI gadolinium contrast agent), mainly due to endocytosis of the NPs (see figure 20), and also had a long retention time in tumor tissue in vivo.

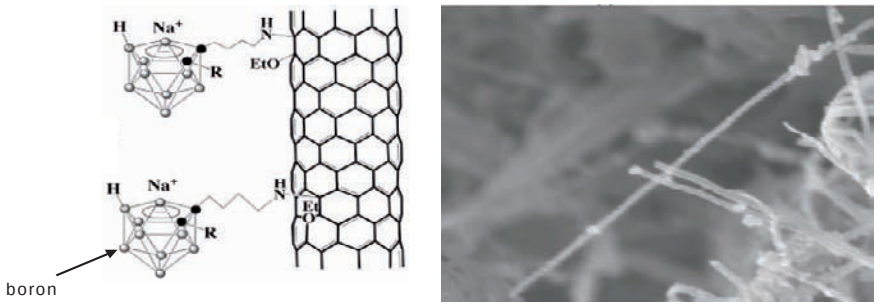

Figure 19. Carbon nanotubes with attached carborane cages. The B atoms in the cages are indicated: ● represents C atoms, R represents different side groups. The image on the right is a scanning electron micrograph of the nanotubes. adapted from Yinghuai et al. (2005) with permission.

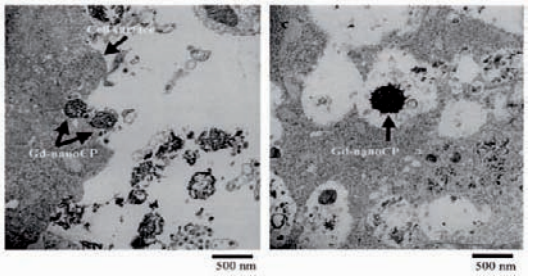

Figure 20. Transmission electron micrographs of fibroblast cells showing internalization of the Gd-loaded Chitosan NP after 12 h incubation. Shikata et al. (2002) with permission.

3.2.2. *Drug and Biologic Therapies*

Chemotherapy, using drugs that are toxic to tumor cells, is widely used in cancer management, often in combination with radiation and/or surgery in the case of solid tumors. Likewise, other biologic agents, such as hormones or cytokines, are in use for specific cancers, while gene therapy and the use of oncolytic viruses are under development. As reviewed by Jain (2005), there are a wide variety of current and potential delivery vehicles to enhance the tumor selectivity of these drugs and biologic agents. A primary driver is to increase the selectivity to the tumor tissues (cells and/or vasculature), since systemic toxicity is a major limiting dose factor. Carriers and targeting moieties have included microspheres, liposomes, polymers, emulsions, peptides and vitamins for drugs, while viruses are used for delivery of genes into target cells. Micelles and liposomes are already widely used for drug delivery. In some cases the purpose is to be able to deliver drugs systemically that are not water soluble. Strategies to improve targeting of anti-neoplastics are, therefore, very important, and nanoparticles may play a particularly valuable role in this. In general terms, the options are to have the drug encapsulated within the NPs, dispersed throughout the NPs or adsorbed onto the NP surface. Parameters such as particle size and morphology, surface charge and surface hydophobicity are important determinants of their effectiveness as delivery vehicles in vivo, while the surface chemistry is critical for bioconjugation.

One example is the use of 200 nm diameter iron oxide NPs with a hydrophilic coating to facilitate dispersion in aqueous media for long-term release of hydrophobic drugs (Jain et al., 2005). Using doxyrubicin as a model (non water-soluble) antineoplastic drug, uptake of the NPs and release of the doxyrubicin in tumors cells was demonstrated. As further examples, Farokhzad et al. (2004) synthesized polymer NPs bioconjugated with aptamers and demonstrated targeting to prostate cancer cells in vitro, while Lu et al. (2004) fabricated enzyme-degradable gelatin nano/microparticles (600-1000 nm diameter) loaded with the drug Paclitaxel and showed rapid release of this drug when it was administered intravesically into the bladder (in a dog model). Paciotti et al. (2004) demonstrated the use of colloidal gold NPs (approx. 30 nm diameter) to deliver tumor necrosis factor (TNF) and showed anti-tumor responses at lower total doses than when TNF was administered alone. Each NP was estimated to bind about 400 molecules of TNF. The uptake in the reticuloendothelial system (liver, spleen), which might be expected to trap the NPs, was also encouragingly low. These authors proposed to pursue this approach also for other anti-cancer drugs and to assess whether more than one active agent could be delivered by the same NPs. Zheng et al. (2005a)

have used lipoprotein NPs that have the advantages of being fabricated from natural materials, and are fully biodegradable and non-immunogenic. These do not have an intrinsic specificity for tumor cells, but can be targeted by various strategies. They have also been used for other applications, such as delivery of photodynamic sensitizers, gadolinium for MRI contrast and near-infrared fluorophores for optical imaging.

For gene delivery, Roy et al. (2005) used 80 nm diameter monodispersed calcium phosphate NPs doped with DNA and demonstrated surface modification of the NPs to facilitate targeting and delivery of the DNA to a specific organ. This may applicable to gene therapy of tumors using an appropriate cancer-targeting moiety.

In a different, combined-modality approach Larina et al. (2005) used polystyrene NPs (100 or 280 nm diameter) to increase the enhancement, by low-frequency (20kHz) ultrasound, of the uptake of the chemotherapeutic drug 5-fluorouracil into human colon cancer cells. This resulted in improved tumor response also in vivo in an animal model.

3.2.3. *Hyperthermia*

Hyperthermia involves heating tumor tissue to around 42-44^{o}C, typically for tens of minutes or longer. Unlike thermal therapy discussed above, in which the temperature is raised above the acute tissue damage threshold of around 55^{o}C, hyperthermia is not a stand-alone therapy but rather is used to enhance other treatments, particularly radiation therapy. As reviewed by Ito et al. (2005), magnetic NPs have been investigated as a means to heat tumor cells and tissues by application of an alternating magnetic field. Magnetite NPs behave as a super-paramagnetic rather than ferromagnetic material, because of the small size, so that the hysteresis loss is low. Liposomal encapsulation of these NPs (multiple 10 nm diameter NPs within the hollow core of 150 nm diameter liposomes, decorated with tumor-targeting antibodies) has been used to enhance delivery to tumor, and antibody conjugation has also been investigated for the same purpose. The same NPs also can serve simultaneously as MRI contrast agents.

4. Conclusions

As illustrated by the examples shown above, the use of nanoparticles in cancer diagnosis and treatment is richly diverse and growing rapidly. A few agents have reached clinical use or clinical trials, most notably iron oxide-based NPs as MRI contrast agents. Most others are still at the developmental stage. Which of these will progress to clinical trials and subsequent clinical use will depend on the balance between advantages and

costs, both financial and in terms of complexity of use and, particularly, toxicity (Hoet et al., 2004). Fundamentally, many of the potential advantages arise from the fact that the physical and/or chemical properties of materials can change markedly compared with the bulk material when fabricated at the nanometer scale. This can give rise to new or enhanced optical, electrical and mechanical signals for detection (imaging) or energy transduction (therapies). The large surface-to-volume ratio of NPs also enables them to carry many targeting and active molecules, thereby increasing the tumor concentration of other imaging agents or therapeutic drugs.

One of the most important characteristics of many NPs is their ability to deliver more than one diagnostic and/or therapeutic moiety at a time. This was illustrated by the case of combined MRI and optical imaging. This is still at a very early stage, with only a few examples yet in the open literature, but such multiplexing is likely to prove a powerful new paradigm in cancer control in the coming decades.

References

American Cancer Society, 2006, Cancer Facts and Figures; https://www.cancer.org.

Bagwe, R. P., Zhao, X. and Tan, W., 2003, Bioconjugated luminescent nanoparticles for biological applications, J. Disp. Sci. Tech. 24:453-464.

Bharali, T. J., Lucey, D. W., Jayakumar, H., Pudavar, H.E. and Prasad, P.N, 2005, Folate receptor-mediated delivery of InP quantum dots for bioimaging using confocal and two-photon microscopy, J. Am. Chem. Soc. 127:11347-11371.

Bogaards, A., Varma, A., Zhang, K., Zach, D., Bisland, S.K., Moriyama, E. H., Lilge, L., Muller, P. J. and Wilson, B.C., 2005, Fluorescence image-guided brain tumour resection with adjuvant metronomic photodynamic therapy: Pre-clinical model and technology development, Photochem. Photobiol. Sci. 4: 438-442.

Brigger, I., Dubernet, C. and Couvreur, P., 2002, Nanoparticles in cancer therapy and diagnosis, Adv. Drug Deliv. Rev. 54:631-651.

Brannon-Peppas, L. and Blanchtte, J.O., 2004, Nanoparticle and targeted systems for cancer therapy, Adv. Drug Deliv. Rev. 56:1649-1659.

Brouma, B. E. and Tearney, G. J., 2001, Handbook of Optical Coherence Tomography. Dekker, NY.

Chang, E., Miller, J. S., Sun, J., Yu, W. W., Colvin, V. L., Drezek, R. and West, J. L., 2005, Protease-activated quantum dot probes, Biochem. Biophys. Res. Comm. 334:137-1321.

Chen, J., Stefflova, K., Niedre, M. J., Wilson, B. C., Chance, B., Glickson, J. D. and Zheng, G., 2004, Protease-triggered photosensitizing beacon based on singlet oxygen quenching and activation, J. Am. Chem. Soc. 126:11450-11451.

Chen, J., Saeki, S., Wiley, B. J., Cang, H., Cobb, M. J., Li, Z.-Y., Au, L., Kimmey, M. B., Li, X. and Xia, Y., 2005, Gold nanocages: Bioconjugation and their potential use as optical imaging contrast agents, Nanolett. 5:473-377.

Chi, Y., Canteenwala, T., El-ourly, M. E., Akari, Y., Pritzker, K., Ito, O., Wilson, B. C. and Chiang, L. Y., 2006, Efficiency of singlet oxygen production from self-assembled nanospheres of molecular micelle-like photosensitizers FC_4S. J. Med. Chem., in press.

Chomas, J. E., Pollard, R. E., Sadlowski, A. R., Griffey, S. M., Wisner, E. R. and Ferrara, K. W., 2003, Contrast-enhanced US of microcirculation of superficially implanted tumors in rats, Radiology 229:439-446.

Copland, J. A. Eghtedari, M., Popov, V. L., Kotov, N., Mamedova, M, Motamedi, M. and Oraevsky, A.A., 2004, Bioconjugated gold nanoparticles as a molecular based contrast agent: Implications for imaging of deep tumors using optoacoustic tomography, Mol. Imag. Biol. 6:341-349.

DaCosta, R. A., Wilson, B. C. and Marcon, N. E., 2002, New optical technologies for earlier endoscopic diagnosis of premalignant gastrointestinal lesions, J. Gastroenterol. Hepatol. 17:S85-104.

DaCosta, R. A., Wilson, B. C. and Marcon, N. E., 2003, Photodiagnostic techniques for the endsoscopic detection of premalignant gastrointestinal lesions, Digest. Endosc. 15:153-173.

Farokhzad, O. C., Jon, S., Khademhosseini, A., Tran, T.-N., LaVan, D. A. and Langer, R, 2004, Nanoparticle-aptamer bioconjugates: A new approach for targeting prostate cancer cells, Cancer Res. 64:7668-7672.

Ferrari, M., 2005, Cancer nanotechnology: opportunities and challenges, Nature Reviews-Cancer 5:161-171.

Gao, X. and Nie, S., 2003, Molecular profiling of single cells and tissue specimens with quantum dots, Trends Biotechol. 21:371-373, 2003. (review)

Gao, X., Cui, Y., Levenson, R. M., Chung, L. W. K. and Xie, S., 2004, In vivo cancer targeting and imaging with semiconductor quantum dots, Nature Biotech 22:969-976.

Gibson, A. P., Hebden., J. C. and Arridge, S. R., 2005, Recent advances in diffuse optical imaging, Phys. Med. Biol. 50:R1-43.

Hainfeld, J. F., Slatkin, D. N. and Smilowitz, H. M., 2004, The use of gold nanoparticles to enhance radiotherapy in mice, Phys. Med. Biol. 49:N309-315.

Harisinghani, M. G., Barentsz, J., Hahn, P. F., Deserno, W. M., Tabatabaei, S., Hulsbergen van de Kaa, C., de la Rosette, J. and Weissleder, R., 2003, Non-invasive detection of clinically occult lymph-node metastases in prostate cancer, New Eng. J. Med. 248:2491-2499.

Hawrysz, D. J. and Sevick-Muraca, E. M., 2000, Developments towards diagnostic breast cancer imaging using near-infrared optical measurements and fluorescent contrast agents, Neoplasia 2:388-417.

Hirsch, L. R., Stafford, R. J., Bankson, J. A., Sershen, S. R., Rivera, B., Price, R. E., Hazle, J. D., Halas, N. J. and West, J. L., 2003, Nanoshell-mediated near-infrared thermal therapy of tumors under magnetic resonance guidance, Proc. Nat. Acad. Sci. 100:13549-13554.

Hoet, P. H. M., Bruske-Hohlfeld, I. And Salata, O. V., 2004, Nanoparticles-known and unknown health risks, J. Nanobiotechnol. 2:12,1-15.

Ideta, R., Taska, S., Jang, W.-D., Nishiyama, N., Zhang, G.-D., Harada, A., Yanagi, Y., Tamaki, Y., Aida, T. and Kataoka, K, 2005, Nanotechnology-based photodynamic therapy for neovascular disease using a supramolecular nanocarrier loaded with a dendritic photosensitizer, Nanolett. 5:2426-2431.

Ito, A., Shinkai, M., Honda, H. and Kobayashi, T., 2005, Medical application of functionalized magnetic nanoparticles, J. Biosci. Bioeng. 100:1-11.

Jaffar, F. A. and Weissleder, R., 2005, Molecular imaging in the clinical arena, J. Am. Med. Assoc. 293:855-862.

Jain, K. K., 2005, Nanotechnology-based drug delivery for cancer, and editorial Targeted drug delivery for cancer, Tech. Cancer Res. Treat. 4:407-416 and 311-313.

Jain, T. K., Morales, M.A., Sahoo, S.K., Leslie-Pelecky, D.L. and Labhasetwar, V., 2005, Iron oxide nanoparticles for sustained delivery of anticancer agents, Mol. Pharm. 2:194-205.

Jiang, W., Papa, E., Fischer, H., Mardyani, S. and Chan, W. C. W., 2004, Semiconductor quantum dots as contrast agents for whole animal imaging, Trends Biotechnol. 22:607-609.

Karotki, A., Khurana, M., Lepock, J. R. and Wilson, B. C., 2006, Simultaneous two-photon excitation of Photofrin and its application to photodynamic therapy, Photochem. Photobiol., in press.

Kelty, C. J., Brown, N. J., reed, M. W. and Ackroyd, R., 2002, the use of 5-aminolaevulinic acid as a photosensitizer in photodynamic therapy and photodiagnosis, Photochem. Photobiol. Sci. 1:158-168.

Kim, S.-W., Zimmer, J. P., Ohnishi, S., Tracy, J. B., Frangioni, J. B. and Bawendi, M. G, 2005, Engineering $InAs_xP_{1-x}$/InP/ZnSe III-V alloyed core/shell quantum dots for the near infrared, J. Am. Chem. Soc. 127:10526-10532.

Kovalev, D. and Fujii, M., 2005, Silicon nanocrystals:Photosensitizers for oxygen molecules, Adv. Mater. 17:2531-2544.

Lam, S., MacAulay, C., leRichie, J. C. and Palcic, B., 2000, Detection and localization of early lung cancer by fluorescence bronchoscopy, Cancer 89:2468-2473.

Larina, M.S., Evers, B.M., Ashitkov,T. V., Bartels,C., Larin, K. V. and Esenaliev, R. O., 2005, Enhancement of Drug Delivery in Tumors by Using Interaction of Nanoparticles with Ultrasound Radiation, Tech. Cancer Res. Treat. 2: 217-226.

Larson, D. R., Zipfel, W. R., Williams, R. M., Clark, S. W., Bruchez, M. P., Wise, F. W. and Webb, W.W., 2003, Water-soluble quantum dots for multiphoton fluorescence imaging in vivo, Science 300:1434-1436.

Lee, T. M., Oldenberg, A.L., Sitafalwalla, S., Marks, D.L., Luo, W., Toublan, F.J., Suslick, K.S. and Boppart, S.A., 2003, Engineered microsphere contrast agents for optical coherence tomography, Opt. Lett. 28:1546-1548.

Li, L., Wartchow, C. A., Danthi, N., Shen, Z., Dechene, N., Pease, J., Choi, H. S., Doede, T., Chu, P., Ning, S., Lee, D. Y., Bednarski, M. D. and Knox, S. J., 2004, A novel antiangiogenesis therapy using an integrin antagonist of anti-Flk-1 antibody coated ^{90}Y-labelled nanoparticles, Int. J. Rad. Oncol. Biol. Phys. 58, 1215-1227.

Loo, C. Lin, A. Hirsch, L., Lee, M.-H., Barton, J., Halas, N., West, J. and Drezek, R., 2004, Nanoshell-enabled, photonics-based imaging and therapy of cancer, Tech. Cancer Res. Treat. 3:33-40.

Lu. Z., Yeh, T.-K., Tsai, M., Au, J., L.-S. and Wientjes, M. G., 2004, Paclitaxel-loaded gelatin nanoparticles for intravesical bladder cancer therapy, Clin. Cancer Res. 10:7677-7684.

Malsch, N. H. (ed.), 2005, Biomedical Nanotechnology, CRC/Taylor & Francis, NY.

Martin, M. E., Wabuyele, B., Pahnjepour, M., Overholt, B., DeNovo, R., Kennel, S., Cunningham, G. and Vo-Dinh, T., 2006, An AOTF-based dual-modality hyperspectral imaging system (DMHIS) capable of simultaneous fluorescence and reflectance imaging, Med. Eng. Phys. 28:149-155.

McArthy, J. R., Perez, J. M., Brückner, C. and Weissleder, R., 2005, Polymeric nanoparticle preparation that eradicates tumors, Nanolett. 12:2552-2556.

Michalet, X., Pinaud, F.F., Bentolinla, L. A., Tsay, J.M., Doose, S., Li, J. J., Sundaresan, G, Wu, A. M., Gambhir, S. S. and Weiss, S., 2005, Quantum dots for live cells, in vivo imaging and diagnostics, Science 307:538-544.

Mitra, A. Mulholland, J., Nan, A., McNeill, E., Ghandehari, H. and Line, B. R., 2005, Targeting tumor angiogenic vasculature using polymer-RGD conjugates, J. Control. Release 102:192-202.

Moghimi, S. M., Hunter, A. C. and Murray, J. C., 2005, Nanomedicine- current status and future prospects, FASEB J. 19:31-330.

Neuwelt, E. A., Varallyay, P., Bago, A. G., Muldoon, L. L., Nesbit, G and Nixon, R., 2004, Imaging of iron oxide nanoparticles by MR and light microscopy in patients with malignant brain tumors, Neuropath. Appl. Neurobio. 30:456-471.

Oldenberg, A.L., Toublan, F. J.-J., Suslick, K. S., Wei, A. and Boppart, S. A., 2005, Magnetomotive contrast for in vivo optical coherence tomography, Opt. Expr. 13:6597-6614.

Paciotti, G. F., Myer, L., Weinreich, D., Goia, D., Pavel, N., McLauglin, R. E. and Tamarkin, L., 2004, Colloidal gold: a novel nanoparticle vector for tumor directed drug delivery, Drug Deliv. 11:160-183.

Panchapakesan, B., Lu, S., Sivakumar, K. Cesarone, G. and Wickstrom, E., 2005, Single-wall carbon nanotube nanobomb agents for killing breast cancer celle, Nanobiotech. 1:2:133.

Patrice, T. (ed.), 2003, Photodynamic Therapy, Royal Soc Chemistry, UK.

Pitsillides, C.M., Joe, E. K., Wei, X., Anderson R. R. and Lin, C. P., 2003, Selective cell targeting with light-absorbing microparticles and nanoparticles, Biophys. J. 84:4023-4032.

Prasad. P., 2004, Nanophotonics, Wiley, N.Y.

Prow, T. W., Salazar, T. H., Rose, W. A., Smith, J. N., Reece, L., Fontenot, A. A., Wang, N. A., Lloyd, R. S., and Leary, J. S., 2004, Nanomedicine- nanoparticles, molecular biosensors, and targeted gene/ drug delivery for combined single-cell diagnostics and therapeutics, Proc. Soc. Photo-Opt. Instr. Eng. 5318:1-11.

Puliafito, C. A. (ed.), 1996, Laser Surgery and Medicine: Principles and Practice, J. Wiley, NJ, USA.

Roy, I., Mitra, S., Maitra, A. and Mozumdar, S., 2003, calcium phosphate nanoparticles as novel non-viral vectors for targeted gene delivery, Int. J. Pharm. 250:25-33.

Roy, I., Ohulchanskyy, T. Y., Pudavar, H. E., Bergey, E. J., Oseroff, A. R., Morgan, J., Dougherty, T. J. and Prasad, P. N., 2003, Ceramic-based nanoparticles entrapping water insoluble photosensitizing anticancer drugs: A novel drug-carrier system for photodynamic therapy, J. Am. Chem. Soc. 125:7860-7865.

Salata, O. V., 2004, Applications of nanoparticles in biology and medicine, J. Nanobiotechnol. 2:3.

Schmieder, A. H., Winter, P. M., Caruthers, S. D., Harris, T. D., Williams, T. A., Allen, J. S., Lacy, E. K., Zhang, H., Scott, M. J., Hu, G., Robertson, J. D., Wickline, S. A. and Lanza, G. M., 2005, Molecular MR imaging of melanoma angiogenesis with $\alpha_\upsilon\beta_3$-targeted paramagnetic nanoparticles, Mag. Res. Med. 53: 621-627.

Shikata, F., Tokumitsu, H., Ichikawa, H. and Fukumori, Y., 2002, In vitro cellular accumulation of gadolinium incorporated into chitosan nanoparticles designed for neutron capture therapy of cancer , Eur. J. Pharmaceut. Biopharmaceut. 53:57-63.

Sitharaman, B., Kissel, K. R., Hartman, K. B., Tran, L. A., Baikalov, A., Rusakova, I., Sun, Y., Khant, H. A., Ludtke, S. J., Chiu, W., Laus, S., Toth, E., Helm, L., Merbach, A. E. and Wilson, L. J., 2005, Superparamagmetic gadonanotubes are high-performance MRI contrast agents, Chem. Commun. (Camb.) 31: 3915-3917.

Soltesz, E. G., Kim, S., Laurence, R. G., De Grand, A.M., Parungo, C. P., Dor, D. M., Cohn, L. H., Bawendi, M. G. and Frangioni, J. V., 2005, Intraoperative sentinel lymph node mapping of the lung using near-infrared quantum dots, Ann. Thorac. Surg. 79:269-277.

Spangler, C. W., Meg, F., Gong, A., Drobizhev, M., Karotki, A. and Rebane, A., 2005, Nanophotonic ensembles for targeted multi-photon photodynamic therapy, Proc. Soc. Photo-Opt. Instr. Eng. 5331:85-92.

Stummer, W., Reulen, H. J., Novotny, A., Stepp, H. and Tonn, J. C., 2003, Fluorescence-guided resections of malignant gliomas -- an overview, Acta Neurochir. Suppl. 88:9-12.

Tannock, I., Hill, R.P., Bristow, R. G. and Harrington, L., 2004, The Basic Science of Oncology, Pergamon Press, NY.

Thomas, J. and Hawthorne, M.E., 2001, Dodeca(carbolyl)-substituted closomers: towards unimolecular nanoparticles as delivery vehicles for BNCT, Chem Commun. (Camb.) 18:1884-1185.

Tytgat, G. N. J., Yano, H., Iishi, H., Tatsuta, M., Ogihara, T., Watanabe, H., Sato, N., Marcon, N., Wilson, B. C. and Cline, R., 2001, Autofluorescence endoscopy: Feasibility of detection of GI neoplasms unapparent to white light endoscopy with an evolving technology, Gastrointest. Endosc. 53:642-650.

Veiseh, O., Sun, C., Gunn, J., Kohler, N., Gabikian, P., Lee, D., Bhattarai, N., Ellenbogen, R., Sze, R., Hallahan, A., Olsen, J. and Zhang, M., 2005, Optical and MRI multifunctional nanoprobe for targeting giomas, Nanolett. 5:1003-1008.

Yan, F. and Kopelman, R. 2003, The embedding of meta-tetra(hdroxyphenyl)-chlorin into silica nanoparticle platforms for photodynamic therapy and their singlet oxygen production and pH-dependent optical properties, Photochem. Photobiol. 78:587-591.

Yang, V., Muller, P. J., Herman, P. and Wilson, B. C., 2003, A multispectral fluorescence imaging system: Design and initial clinical tests in intra-operative Photofrin-photodynamic therapy of brain tumors, Lasers Surg. Med. 32:224-232.

Yang, V. X. D, Tang, S. J., Gordon, M. L., Qi, B., Gardinar, G., Kortan, P., Haber, G. B., Kandel, G., Vitkin, I. A., Wilson, B. C. and Marcon, N. E., 2005, Endoscopic Doppler optical coherence tomography in the human GI tract: Initial experience, Gastrointest. Endosc. 61: 879-890.

Yinghuai, Z., Peng, A. T., Carpenter, K., Maguire, J. A., Hosmane, N. S., Takagaki, M., 2005, Substituted carborane-appended water-soluble single-wall carbon nanotubes: New approach to boron neutron capture therapy drug delivery, J. Am. Chem. Soc. 127:9875-9880.

Zheng, G., Chen J., Li, H. and Glickson, J. D., 2005a, Rerouting lipoprotein nanoparticles to selected alternate receptors for the targeted delivery of cancer diagnostic and therapeutic agents, Proc. Nat. Acad. Sci. 102:17757-17762.

Zheng, G., Patolsky, F., Cui, Y., Wang, W. U. and Lieber, C. M., 2005b, Multiplexed electrical detection of cancer markers with nanowire sensor arrays, Nature Biotechnol. 23:1294-1301.

QUANTUM DOT BIO-TEMPLATE FOR RAPID DETECTION OF PATHOGENIC SUBSTANCES

JAN J. DUBOWSKI*
Laboratory for Quantum Semiconductors and Laser-based Nanotechnology, Center of Excellence for Information Engineering, Université de Sherbrooke
Sherbrooke, QC J1K 2R1, Canada

Abstract. To address some of the technological problems related to the application of colloidal semiconductor nanocrystals for biosensing, we have proposed a novel approach based on the application of arrays of epitaxial quantum dots (eQD) that have been known for their applications in advanced communication devices such as quantum dot lasers.

Keywords: biosensors, epitaxial quantum dots, laser-induced bio-functionalization

1. Introduction

Semiconductor nanocrystals, also known as colloidal quantum dots (cQD), have unique properties that made them attractive for developing new bio-imaging technologies and a new generation of devices for biosensing. The driving force behind this interest is their bright photoluminescence (PL), small diameter (< 10 nm) and the ability of cQD, in contrast to fluorescent dyes, to yield theoretically unbleachable PL. Different wavelength emitting cQD could be excited with a single wavelength excitation source, which would greatly simplify the measuring schemes of cQD-based biosensing. Commercially available colloidal CdSe QDs emit in the 500 to 650 nm range,[1,2] thus, they are attractive for inspection in the visible range of the human eye. However, for *in-vivo* investigation of human organs and tissues, it would be advantageous to have material emitting in the 800 – 1100 nm range, which falls in the range of the minimum optical absorption (bio-diagnostics window) of combined human blood, tissue, skin and water.[3] Efficient and cost-effective cQD's for such applications have yet to be developed. Also, development of cQD's compatible with different bio-environments or functionalized for chemisorption of specific biomolecules has challenged the efforts of researchers involved in this domain of

* Canada Research Chair in Quantum Semiconductors; E-mail: jan.j.dubowski@usherbrooke.ca

J.J. Dubowski and S. Tanev (eds.), Photon-based Nanoscience and Nanobiotechnology, 159–173.

nanoscience and biotechnology. For instance, critical to the bright and stable PL of cQD's is the ability to minimize the role of surface defects (traps), which are the source of the PL quenching signal through non-radiative recombination centers (NRRC). Surface trap related intermittence in PL emission, also known as blinking, has been commonly observed from cQD's.[4] Such behaviour could impose significant limitations on the successful use of cQD's for biosensing or single biomolecule imaging. The neutralization of surface defects requires the development of ever elusive surface passivation methods. In addition, the free-standing nature of cQD's makes it difficult to implement otherwise powerful dry methods of processing such as laser-assisted etching and surface functionalization.

To address some of the problems related to the technology of cQD's, we have proposed an alternative method of using quantum dots for bio-detection based on the application of arrays of epitaxially grown quantum dots (eQD's). It is known that eQD's do not suffer from the blinking effect, although the ability to process surfaces of eQD's is as important as that of cQD's. Furthermore, eQD's can be processed with specialty tools that would be impractical for cQD's, allowing to tune the emission wavelength of an individual eQD or groups of eQD's and to carry out selective area surface passivation/functionalization for the immobilization of different antibodies.

In this paper we discuss the basic concept of the proposed device and technologies that are expected to facilitate reaching the ultimate goal of this approach.

2. Epitaxial Quantum Dots (eQD's) – an Innovative Approach for Biosensing

2.1. BASIC DEVICE STRUCTURE

The proposed sensor basic architecture is schematically shown in Figure 1. The surface of a wafer with eQD's emitting at a specific wavelength, or with pixels of eQD's emitting at λ_0, λ_1, λ_2, etc., is functionalized with biotinylated antibodies of different analytes. Upon excitation, each eQD, which typically is 20 - 40 nm in diameter at its base, will emit radiation in a rapidly expanding cone. This radiation is expected to be modified in the presence of nano-objects, such as trapped viruses, located 2 - 8 nm above the biofunctionalized surface (cap) of eQD.

A device with eQD's pixels (ensembles) of dimensions comparable with or smaller than the cross-section area of an analyte, or with eQD's which can be probed individually, has the potential to offer single analyte (biomolecule) level detection. Such a device could include specially

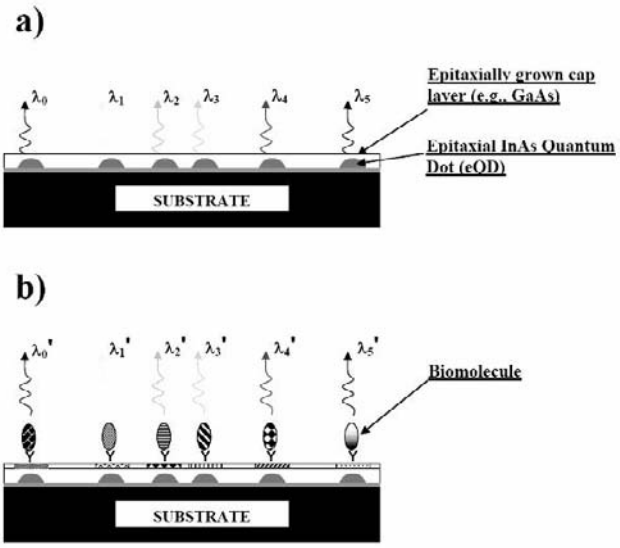

Figure 1. (a) Multicolor array of eQD's fabricated, e.g., by Laser-induced Quantum Dot Intermixing; (b) Detection of different biomolecules trapped at the bio-functionalized surface of GaAs is monitored by measuring the photoluminescence signal from eQD's.

designed microstructures for the realization of a fluorescence resonance energy transfer (FRET) between eQD and various dye labelled biomolecules.[5]

2.2. ENABLING TECHNOLOGY

The widespread method of preparing semiconductor wafers with two-dimensional (2D) arrays of immobilized eQDs is based on self-assembled growth, which is triggered by the temporal reduction of the wafer temperature in the growth chamber. Arrays of InAs eQD's fabricated by this technique could consist of 20-60 nm diameter semi-spheres emitting at near 1.5 μm wavelength at room temperature if their height is about 15 nm.[6] Smaller eQD's of the same material have been reported to emit at 1.1-1.3 μm.[7] The self-assembly growth makes it possible to fabricate wafers with eQD's of densities up to 100s per μm^2. Advanced methods of eQD fabrication are based on self-assembled growth on patterned wafers.[8] An individual eQD, or group of eQD's could be fabricated by such technology on top of pyramids dispersed at distances exceeding the spot size of the laser probing beam (typically, 30 μm or more). The irradiation of each pyramid with the PL exciting laser beam guarantee that the optical signal

would originate exclusively from the well known eQD (or group of eQD's). It is interesting to mention that PL spectra of eQD's are typically narrower than those of cQD's, and even at room temperature they exhibit details that can be directly linked to electronic states in eQD's.[9] Generally, the position, spectral shape and intensity of ground and excited states in eQD's are expected to be influenced by external fields induced by biomolecules attached to their surface.

In addition to PL measurements, cathodoluminescence (CL) measurements could be carried out with a relatively high spatial resolution to characterize the process of biomolecule immobilization. Although it is less attractive due to the requirement of a vacuum, the CL technique offers the possibility to carry out fundamental research aimed at understanding the mechanisms of the non-linear interaction of electromagnetic radiation with an eQD located in the vicinity of a nanoparticle. Also, an electrically biased eQD wafer would make it possible to carry out both electroluminescence and photocurrent measurements.

Optimized performance of the biosensor will depend on the ability to establish a robust and reproducible process of eQD surface functionalization as well as to control the eQD-analyte distance. While the application of thiols with different length CH_2 chains and different bio-linkers offers potential precision in the location of targeted analytes above the bio-functionalized surface, the depth at which eQD is buried below the cap surface (GaAs in case of InAs eQD) is not easily controllable by conventional means. Due to the formation of non-radiative recombination centers (NRRC), which are additionally promoted by the structural defects at the lattice mismatched InAs/GaAs interface (same problem concerns the CdSe/ZnS interface), the minimum thickness of the epitaxially grown GaAs cap layer is typically kept at 20 nm or more. Not satisfying this condition leads to a drastically reduced eQD PL signal. However, it has been demonstrated that an almost 2-fold increase of the InAs QD PL signal could be achieved if a 10 nm thick GaAs cap layer over the InAs eQD was thiolated (passivated) with a monolayer of octadecythiol.[10] Our experiments (see Sec. 3.1) have demonstrated that a 19-fold enhancement of the PL signal could be achieved form thiolated bulk GaAs samples.[11] Thus, the successful fabrication of InAs eQD bio-templates (and other eQD bio-templates), which would require that the eQD-analyte distance was less than, say 10 nm, will need the application of special thickness tuning procedures and *in-situ* passivation with a self-assembled monolayer (SAM) of a suitable thiol. Among various technologies that could be applied for that purpose, one that appears especially attractive is the laser-assisted dry etching method (LADE), which has proven to be capable of etching GaAs and InP materials with precision better than a fraction of a monolayer per laser pulse[12] and without generating defects typical for wet etching or

reactive-ion etching.[13] The LADE method is compatible with controlled atmosphere experiments, therefore it should allow for the carrying out of thiolation of the etched surfaces without exposing them to a deteriorating atmospheric environment.

Construction of an integrated device capable of multi-analyte detection will require pixels of eQD's functionalized with specific antibodies. In that context, different colour emitting eQD's will play an important role in maximizing sensitivity of the device to the presence of specific biomolecules, e.g., by precise matching of the eQD emission energy with the absorption energy of various dyes (acceptors) applied to realize the FRET process. Thus, the proposed approach has the potential to carry out rapid and error-free multi-analyte detection. Arrays or pixels of eQD's emitting at different wavelengths could be fabricated by the application of the quantum well intermixing (QWI) technique, such as laser-based QWI that we develop for processing of epitaxially grown QW and QD wafers.[14,15] Figure 2 illustrates that the 1078 nm emission (ground state

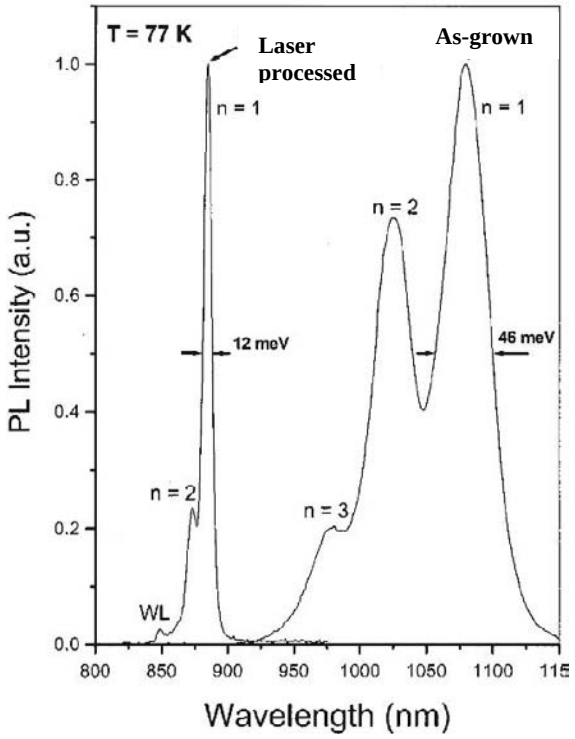

Figure 2. Photoluminescence spectra measured at two sites (4 mm apart) on same sample corresponding to the as-grown InAs/GaAs eQD material (long-wavelength spectrum) and the laser-QDI material blueshifted by 251 meV.[15]

transition, n = 1) of the InAs eQD material could be shifted to 885 nm using the laser-QD intermixing technology.[15] This 193 nm (250 meV) blueshift has been achieved over the 4 mm distance between the as-grown material and the centre of the laser processed site. An array of lines of eQD's emitting minimum 10 of distinctly different colours over the same distance should be achievable with the currently available laser-QD intermixing technology. Clearly, laser-based eQD and QW intermixing technologies along with the laser nano-etching procedure have the potential to yield nanostructures for biosensing not easily attainable with conventional methods of semiconductor device fabrication.

The choice of InAs eQD's that emit photons at near 1 μm wavelength, i.e., inside of the bio-diagnostics window, has been dictated by our long-term interest in exploring the feasibility of this sensor for bio-diagnostics *in-vivo*. Of paramount importance for such an approach is an understanding of the conditions leading to the controllable/repeatable bio-functionalization of GaAs – the material of choice for capping InAs eQD's.

3. Device Fabrication Processes

Biomolecules of interest could be directly immobilized on solid substrates by covalent linkage using carbodiimide chemistry.[16,17] However, the direct immobilization approach cannot control the molecule orientation. It has been reported that randomly oriented streptavidin films bind with biotin-DNA less efficiently when compared to the biotin-DNA assembled on the molecularly ordered streptavidin films.[17] The consequence is lower efficiency of the target DNA capture and lower sensitivity in the hybridization analysis achieved with randomly oriented streptavidin films. To maximize probe biomolecules uptake and consequently capture more target moieties for detection, the most often employed configuration consists of the substrate/biotin/avidin/biotinylated probe/target architecture.[17,18,19,20] We choose to investigate a GaAs-thiol-biotin-avidin architecture to provide conditions for trapping targeted biomolecules. It has been known that deposition of SAMs of various thiols on InP and GaAs could lead to an enhanced PL signal from such materials, which is indirect evidence of at least a partial 'repairing' of the defective surface of these materials.[21,22] The mechanism responsible for this behaviour is related to the role that the thiol-provided sulphur plays in the passivation of III-V surfaces.[23] For example, our *ab-initio* calculations have shown that As dimers at the surface of (001) GaAs are responsible for the formation of surface states with their energy greater than the Fermi level, and that these states could be removed following thiol adsorption.[24]

The interest in thiol is driven by the need to create an 'ohmic' contact between a trapped pathogenic molecule (analyte) and the surface of GaAs, and to achieve conditions that would provide a robust architecture for efficient (specific) attachment of a targeted analyte. We anticipate that a biomolecule (virus) trapped at the surface above eQD would induce measurable changes in its PL intensity and/or emission wavelength. Ultimately, the measurements of PL emission from individual eQD should make it possible to carry out 'zero background' detection of a trapped single biomolecule.

3.1. THIOLATION (PASSIVATION) OF GAAS

We have investigated thiols ($SH(CH_2)_nT$) with various lengths of their methylene chain: $2 \leq n \leq 15$, and with hydrophilic (T = COOH, OH, NH_2) or hydrophobic (T = CH_3) terminal groups.[11,23] Deposition of thiols was achieved by immersing the cleaned and freshly etched wafer in a 5 mM thiol solution in ethanol and 5% aqueous ammonia. The up to 18-hour immersion in the solution, which was continuously purged with nitrogen and heated to 55 ºC, led to the formation of SAMs of the investigated thiols. After thiol deposition, the wafers were rinsed with hot isopropanol, methanol and water, and finally blown dried with nitrogen.

Based on the results of x-ray photoelectron spectroscopy, attenuated total reflection Fourier-transform infrared spectroscopy (ATR-FTIR) and PL measurements, we have established that long-methylene-chain thiols with $n \geq 10$ provide superior conditions for passivation of the surface of GaAs when compared to thiols with shorter methylene chains.[23] Figure 3

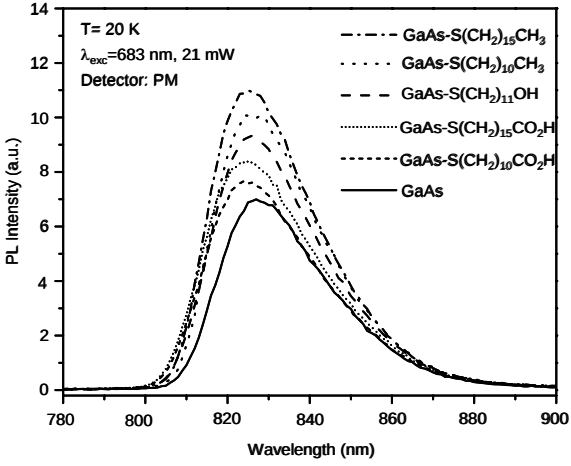

Figure 3. Photoluminescence spectra of freshly etched (001) GaAs and samples covered with self-assembled monolayers of different thiols.[23]

shows low-temperature (20 K) PL spectra measured from a freshly etched (001) GaAs and samples that were coated with SAMs of long-chain thiols. It can be seen that the PL signal from SAMs coated samples clearly exceeds that from the etched only wafers. The PL enhancement, from the weakest of ~10% to the strongest of ~50%, follows the sequence of thiols from $S(CH_2)_{10}CO_2H$, $S(CH_2)_{15}CO_2H$, $S(CH_2)_{11}OH$, $S(CH_2)_{10}CH_3$ to $S(CH_2)_{15}CH_3$. As suggested by the ATR-FTIR measurements, the hydrophobic terminated SAMs, such as GaAs-$S(CH_2)_{15}CH_3$ and GaAs-$S(CH_2)_{10}CH_3$ tend to be relatively highly organized and closely packed. Thus, they provide a higher concentration of sulphur atoms capable of neutralizing the greater concentration of NRRC at the surface of (001) GaAs. Clearly, the strongest enhancement of the PL signal from the sample coated with SAM of a long-chain hydrophobic terminated thiol has been linked to the increased density of a passivation layer,

The stability of the GaAs-$S(CH_2)_{15}CH_3$ interface was investigated at room-temperature as a function of time, up to 1000 hours.[11] Both thiolated (001) GaAs that was solvent cleaned and etched using standard procedures, and thiolated (110) GaAs that was obtained by cleaving in air have been investigated. Additionally, we have investigated the influence of washing the samples with a commercially available detergent solution (Roche Diagnostics) that is commonly applied for the preparation of various clinical specimens, on cleaning and aging of the GaAs surface. We have observed that the detergent treatment significantly influences (enhances) the PL signal from (001) GaAs. The results shown in Figure 4 illustrate this effect. Initially, the PL signal from a non-detergent treated sample is I(0) ≈ 1.6, but it decays relatively quickly and after 400 hours becomes comparable to that of a freshly etched sample (Fig. 4a). A significantly enhanced PL signal, with I(0) ≈ 2.3, is observed for the 18 h thiolated

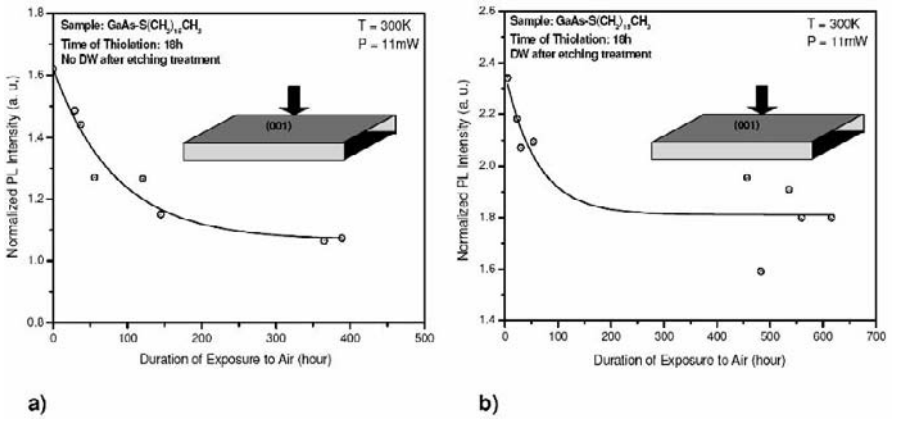

Figure 4. Time dependence of the normalized photoluminescence intensity for (001) GaAs passivated with HS(CH2)15CH3 without detergent washing (a) and with detergent washing that followed the HCl deoxidation treatment (b). The time of thiolation was 18 hours.[11]

sample that, following the HCl treatment, was exposed to detergent washing (Fig. 4b). The PL signal from that sample, even after 600 h is about 1.8 times stronger than that from a freshly etched and detergent treated sample. In contrast, detergent washing practically does not affect the PL signal from cleaved (110) GaAs. The absence of such an effect suggests that the concentration of NRRC in this case was minimal or that the efficiency of removing defects from (110) GaAs was low.

It is worth of mentioning that the cleaning and HCl etching procedure of investigated (001) GaAs samples (undoped material) leads to an increase of the PL signal by up to 8 times. Thus, the 2.34 PL increase following the detergent treatment (Fig. 4b) indicates that we were able to achieve a total of 19-times enhancement of the PL signal with respect to the initial signal from the highly oxidized (001) GaAs sample. The XPS measurements have indicated a significant reduction in the oxygen content related to the presence of As_2O_3 or As_2O_5 on the detergent washed surface of (001) GaAs.[25] Thus, it is reasonable to expect that the defects in question are related to the presence of various arsenic oxides. It has been reported that detergent treatment could be efficient in reducing the surface roughness of chemically modified mica.[26] We expect that such a treatment could also reduce the concentration of oxide-rich surface precipitates.

The mechanism of GaAs surface passivation and related changes of physical properties of this material, such as PL intensity and ability to link with inorganic materials, are expected to depend not only on the crystallographic orientation of the wafers as discussed in this paragraph, but also on the type and doping level of impurities in this material. Nevertheless, the data acquired to date allowed us to initiate the bio-functionalization experiments involving deposition of avidin on the thiolated surface of (001) GaAs.

3.2. BIO-FUNCTIONALIZED GAAS

3.2.1. *Immobilization of Avidin on (001) GaAs*

Avidin is a robust and well-studied protein that has a very strong affinity for biotin.[27] The immobilization of avidin was investigated with biotin, which was connected to the GaAs surface through commercially available long or short methylene chain amino group terminated alkanethiols (11-amino-1-undecanethiol (UDT): $HS(CH_2)_{11}NH_2$ or $HS(CH_2)_2NH_2$), or through a biotinylated thiol (BT) synthesized in our laboratory.[28] The chemical structure of long-chain thiols applied for that purpose is shown in Figure 5.

Biotinylated surfaces were obtained either directly by exposing GaAs to a solution of BT and thiol diluent (TD) with the molar ratio of 1:1, or by the

reaction between surface amino groups of thiols and NHS-biotin (200 μg/ml in DMSO). Exposure to avidin was carried out by immersing GaAs wafers in a 200 μg/ml solution of avidin in Tris buffer (pH 7.4) for 2 hours, which was followed by rinsing with Tris buffer and DI water and dried with

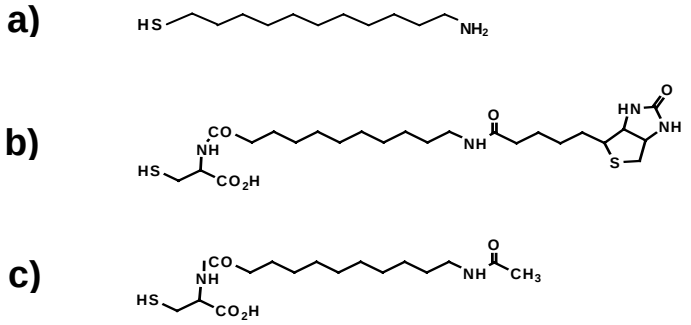

Figure 5. Chemical structure of a) the 11-amino-1-undecanethiol [$HS(CH_2)_{11}NH_2$], b) biotinylated thiol [2-(11-biotinylamino-undecanoylamino)-3-mercapto-propionic acid], and c) a thiol diluent [2-(11-acetylamino-undecanoylamino)-3-mercapto-propionic acid].

nitrogen flow. Each step of the exposure of GaAs to thiol, biotin and avidin was monitored by measuring the PL signal from GaAs (near 870 nm at 300 K).[28]

We have found that the exposure to long chain thiols resulted in a significant enhancement of the PL signal, while a short chain $HS(CH_2)_2NH_2$ thiol did not show such an effect at all. This confirmed our earlier observations concerning the efficiency of passivation of GaAs with thiols having various lengths of their methylene chains,[23] and it is in agreement with the chain-length dependence of the organization of various thiols on the surface of Au.[29] The deposition of avidin on surfaces provided by GaAs, GaAs-thiol-biotin and GaAs-biotinylated thiol has always resulted in an increased GaAs PL signal. The strongest PL signal enhancement was measured from avidin-exposed surfaces of GaAs-$S(CH_2)_{11}NH_2$-biotin and GaAs-BT+TD. Also, a comparable enhancement of the PL signal was observed for GaAs-BT+TD exposed to avidin that was stained with fluorescein emitting at 518-523 nm.

Fluorescence microscopy measurements showed a faint visible green fluorescence observed from the surface of GaAs that was directly coated with stained avidin. After washing this wafer with detergent, the fluorescence disappeared entirely, which confirmed that the avidin was not efficiently attached to the surface. Detergent washing also removed stained avidin from the GaAs-$S(CH_2)_{11}NH_2$-biotin surface, indicating that the

concentration and/or orientation of biotin available for the reaction with avidin was not optimized. In contrast, the fluorescence from stained avidin immobilized on the GaAs-BT+TD surface was relatively easy to detect, even following its washing with a standard detergent.[28] We argue that this is strong evidence of the efficient attachment of avidin molecules to the surface of (001) GaAs via specific biotin-avidin interaction. The increased efficiency of binding avidin in this case has been attributed to the organization of the architecture provided by long-chain thiols and diluted concentration of biotin headgroups.[30]

3.2.2. *Biotinylated nano-beads on (001) GaAs*

Further evidence concerning the robustness of the GaAs-thiol-biotin-avidin architecture has been provided by studying the attachment 200 nm diameter biotinylated nano-beads (*b*-NB) to the surface of (001) GaAs functionalized with avidin *via* UDT ($HS(CH_2)_{11}NH_2$) and biotin.[31] Although our initial experiments have indicated that UDT did not facilitate immobilization of a large (fluorescence measurable) concentration of avidin, we expected that a significantly larger contact area of the investigated *b*-NB could make the process of anchoring these nano-objects more feasible. The nano-beads were stained with an organic dye emitting at 515 nm (manufactured by Molecular Probes), which made it possible to detect their presence by fluorescence microscopy. The immobilization architecture for trapping *b*-NB on (001) GaAs is shown in Figure 6.

The strength of *b*-NB immobilization on GaAs surface was investigated by subjecting the samples to detergent washing and ultrasonic cleaning. A

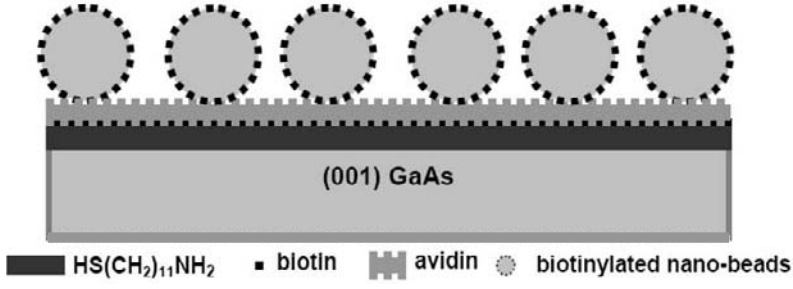

Figure 6. The architecture of biotinylated nano-beads immobilization on (001) GaAs surface via avidin, biotin and alkanethiol.[31]

sample with *b*-NB directly deposited on GaAs was used as a control. On both types of samples, the *b*-NB adhered to the GaAs surface after detergent washing, as confirmed by both fluorescence and atomic force microscopy (AFM) measurements. However, in contrast to the sample with

the thiol-biotin-avidin interface, no fluorescence could be detected from the sample coated directly with *b*-NB that was ultrasonicated for 1 min.

Figure 7 shows an AFM image taken from the avidin functionalized GaAs that was exposed to the *b*-NB solution. The density of coverage with *b*-NB is estimated as $\rho \approx 1.4 \times 10^7$ mm^{-2}, which corresponds to the surface

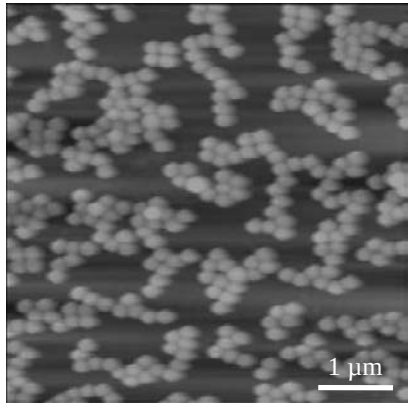

Figure 7. Atomic force microscopy image of the avidin functionalized surface of (001) GaAs following the exposure to a solution with 200 nm diameter biotinylated nano-beads. Qualitatively same image was observed following the ultrasonication procedure.[31]

coverage of approximately 44%. Similar coverage was also observed for non-functionalized surface of GaAs. However, with the exception of the avidin functionalized GaAs, no *b*-NB could be found on other surfaces following the ultrasonication procedure. These results demonstrate that GaAs functionalized with avidin via UDT ($HS(CH_2)_{11}NH_2$) and biotin provides an efficient link for the immobilization of *b*-NB on the surface of (001) GaAs. They also confirm that immobilization of avidin is feasible with UDT although the efficiency of this process may be very low as it was suggested earlier.[28]

Although non-specific binding of *b*-NBs to GaAs has been observed in this experiment, it is evident that the thiol-biotin-avidin link is crucial to anchor the investigated *b*-NB to (001) GaAs. Of interest for the development of a virus anchoring bio-architecture is that the diameter of the investigated nano-beads is comparable to that of some viruses (e.g., Influenza A virus). Thus, the immobilization of *b*-NB on functionalized surface of GaAs could serve as a tool in developing models of trapping various pathogenic substances on GaAs and in studying mechanisms of interaction between a semiconductor and various organic nano-objects.

4. Conclusions

A new concept of biosensing based on epitaxial quantum dots (eQD's) has been discussed to address some of the technological problems related to the application of colloidal semiconductor nanocrystals, known also as colloidal quantum dots (cQD's). The use of an eQD as a stable source of luminescence is particularly attractive for single molecule detection as eQD's do not suffer from the poisonous intermittent photoluminescence that characterises cQD's. Also, a 2-dimensional (2D) organization of eQD's on various substrates offers an excellent opportunity to carry out processing of individual or closely packed eQD's. Using laser-quantum-dot-intermixing technology, the emission wavelength of such eQD's could be tuned to fabricate arrays of multicolour pixels. Consequently, the bio-functionalization of 2D arrays of eQD's could be carried out not only with advanced wet chemistry, but also with dry methods developed for the semiconductor industry, including laser-assisted dry etching. The latter could be applied to tune the thickness of the cap layer to provide an optimized eQD-analyte distance as well as to functionalize *in-situ* the processed surface. Clearly, laser-based eQD intermixing and laser nano-etching have the potential to yield nanostructures for biosensing not easily attainable with conventional methods of semiconductor device fabrication.

We have investigated a GaAs-thiol-biotin-avidin architecture to provide conditions for trapping targeted biomolecules. Experiments involving attenuated total reflection Fourier transform spectroscopy, photoluminescence, x-ray photoelectron spectroscopy, atomic force microscopy and fluorescence microscopy have indicated that self assembled monolayers of long-chain thiols efficiently passivate the surface of (001) GaAs and provide conditions favourable for building a bio-architecture comprising biotin and avidin for the attachment of biotinylated antibodies or DNA. The strong binding energy of thiol-GaAs, which has been observed experimentally and confirmed by our theoretical calculations, places this material system at par with a well known thiol-Au system, and validates the potential of GaAs as an attractive material for binding different bio-moieties above the surface of InAs eQD's.

Acknowledgements

The Author acknowledges enlightening discussions with Dr. Dr. Eric Frost and Emanuel Escher from the Faculty of Medicine, Université de Sherbrooke. The assistance of Ximing Ding, Oleksandr Voznyy and Khalid

Moumanis is also acknowledged. This work was supported by the Canadian Institutes of Health Research (CIHR).

References

1. M. Bruchez, M. Moronne, P. Gin et al., "Semiconductor nanocrystals as fluorescent biological labels," Science **281** (5385), 2013-2016 (1998).
2. P. Mitchell, "Turning the spotlight on cellular imaging - Advances in imaging are enabling researchers to track more accurately the localization of macromolecules in cells," Nature Biotechnology **19** (11), 1013-1017 (2001).
3. Tuan Vo-Dinh, *Biomedical photonics handbook*, CRC Press, Boca Raton, Fla., 2003.
4. Sungchul Hohng and Taekjip Ha, "Near-Complete Suppression of Quantum Dot Blinking in Ambient Conditions," J. Am. Chem. Soc. **126** (5), 1324-1325 (2004).
5. I. L. Medintz, A. R. Clapp, H. Mattoussi et al., "Self-assembled nanoscale biosensors based on quantum dot FRET donors," Nature Materials **2** (9), 630-638 (2003).
6. P. J. Poole, R. L. Williams, J. Lefebvre et al., "Using As/P exchange processes to modify InAs/InP quantum dots," Journal of Crystal Growth **257** (1-2), 89-96 (2003).
7. R. L. Williams, G. C. Aers, J. Lefebvre et al., "Quantum dot site-selection using in situ prepared nano-templates," Physica E-Low-Dimensional Systems & Nanostructures **13** (2-4), 1200-1203 (2002).
8. J. Lefebvre, P. J. Poole, G. C. Aers et al., "Tunable emission from InAs quantum dots on InP nanotemplates," Journal of Vacuum Science & Technology B **20** (5), 2173-2176 (2002).
9. A. Passaseo, G. Maruccio, M. De Vittorio et al., "Dependence of the emission wavelength on the internal electric field in quantum-dot laser structures grown by metal-organic chemical-vapor deposition," Appl. Phys. Lett. **79** (10), 1435-1437 (2001).
10. Klaus Adlkofer, Eric F. Duijs, Frank Findeis et al., "Enhancement of photoluminescence from near-surface quantum dots by suppression of surface state density," Phys. Chem. Chem. Phys. **4**, 785-790 (2002).
11. Kh. Moumanis, X. Ding, J.J. Dubowski et al., "Aging and detergent wasing effects of the surface of (001) and (110) GaAs passivated with hexadecanethiol," J. Appl. Phys., in print (2006).
12. J.J. Dubowski, M. Julier, G.I. Sproule et al., "Laser-assisted dry etching ablation for microstructuring of III-V semiconductors," Mat. Res. Soc. Symp. Proc. **397**, 509-518 (1996).
13. J. J. Dubowski, B. E. Rosenquist, D. J. Lockwood et al., "Structure damage in reactive-ion and laser etched lnP/GalnAs microstructures," J. Appl. Phys. **78** (3), 1488-1491 (1995).
14. J. J. Dubowski, Y. Feng, P. J. Poole et al., "Monolithic multiple wavelength ridge waveguide laser array fabricated by Nd:YAG laser-induced quantum well intermixing," J. Vac. Sci. Technol. A. **20** (4), 1426-1429 (2002).

15. J. J. Dubowski, C. Nı. Allen, and S. Fafard, "Laser-induced InAs/GaAs quantum dot intermixing," Appl. Phys. Lett. **77** (22), 3583-3585 (2000).
16. Patrick Vermette, Thomas Gengenbach, Upulie Divisekera et al., "Immobilization and surface characterization of NeutrAvidin biotin-binding protein on different hydrogel interlayers," J. Coll. Int. Sci. **259**, 13-26 (2003).
17. Xiaodi Su, Ying-Ju Wu, Rudolf Robelek et al., "Surface Plasmon Resonance Spectroscopy and Quartz Crystal Microbalance Study of Streptavidin Film Structure Effects on Biotinylated DNA Assembly and Target DNA Hybridization," Langmuir **21** (1), 348-353 (2005).
18. J. Ladd, C. Boozer, Q. M. Yu et al., "DNA-directed protein immobilization on mixed self-assembled monolayers via a Streptavidin bridge," Langmuir **20** (19), 8090-8095 (2004).
19. Tom T. Huang, Jennifer Sturgis, Rafael Gomez et al., "Composite Surface for Blocking Bacterial Adsorption on Protein Biochips," Biotech. Bioeng. **81** (5), 618-624 (2003).
20. Reid N. Orth, T.G. Clark, and H.G. Craighead, "Avidin-biotin micropatterning methods for biosensor applications," Biomedical Microdevices **5:1**, 29-34 (2003).
21. Ting Hou, C. Michael Greenlief, Steven W. Keller et al., "Passivation of GaAs (100) with an Adhesion Promoting Self-Assembled Monolayer," Chem. Mater. **9** (12), 3181-3186 (1997).
22. Fazila Seker, Kathleen Meeker, Thomas F. Kuech et al., "Surface Chemistry of Prototypical Bulk II-VI and III-V Semiconductors and Implications for Chemical Sensing," Chem. Rev. **100**, 2505-2536 (2000).
23. Ximing Ding, Khalid Moumanis, Jan J. Dubowski et al., "Fourier-transform infrared and photoluminescence spectroscopies of self-assembled monolayers of long-chain thiols on (001) GaAs," J. Appl. Phys. **99(5)**, 54701 (2006).
24. O. Voznyy and J. J. Dubowski, "Structure, bonding nature and binding energy of alkanethiolate on As-rich GaAs (001) surface: a density functional theory study," J. Phys. Chem. B, submitted (2006).
25. G. Marshall, private communication, 2006.
26. Hong Xing You and Christopher R. Lowe, "AFM Studies of Protein Adsorption: 2. Characterization of Immunoglobulin G Adsorption by Detergent Washing," J. Coll. Int. Sci. **182**, 586-601 (1996).
27. William A. Goddard, Donald W. Brenner, Sergey E. Lyshevski et al., CRC Press, Boca Raton, Fla., 2003.
28. X. Ding, Kh. Moumanis, J.J. Dubowski et al., "Immobilization of avidin on (001) GaAs surface," Appl. Phys. A **83** (3), 357-360 (2006).
29. J. Christopher Love, Lara A. Estroff, Jennah K. Kriebel et al., "Self-Assembled Monolayers of Thiolates on Metals as a Form of Nanotechnology," Chem. Rev. **105** (4), 1103-1169 (2005).
30. Michael Riepl, Mattias Ostblom, Ingemar Lundstrom et al., "Molecular Gradients: An Efficient Approach for Optimizing the Surface Properties of Biomaterials and Biochips," Langmuir **21(3)**, 1042 (2005).
31. X. Ding, Kh. Moumanis, J.J. Dubowski et al., "A study of binding biotinylated nano-beads to the surface of (001) GaAs," SPIE Conf. Proc. **Vol. 6106**, L1-L7 (2006).

APPLICATIONS OF FREE-ELECTRON LASERS IN BIOLOGICAL SCIENCES, MEDICINE AND MATERIALS SCIENCE

RICHARD F. HAGLUND, JR.*
Department of Physics and Astronomy and
W. M. Keck Foundation Free-Electron Laser Center
Vanderbilt University, Nashville TN 37235-1807

Abstract. The advent of broadly tunable free-electron lasers with a combination of high irradiance, low-to-moderate pulse energy, high pulse repetition frequency and high average power has opened new opportunities in materials analysis, modification and processing. This paper describes several such areas, including laser surgery, infrared laser-assisted mass spectrometry, and resonant infrared pulsed laser deposition of polymer thin films.

Keywords: Wave-length-selective materials modification, picosecond mid-infrared laser, infrared laser surgery, infrared matrix-assisted laser desorption-ionization mass spectrometry, wavelength-selective pulsed laser deposition of polymer thin films.

1. Introduction: Laser-driven Materials Processing

In his address following acceptance of the Nobel Prize for Physics in 1964, Alexander Prokhorov proposed a bold vision of laser-initiated chemistry: "Construction of an oscillator for any given radiation frequency will greatly extend the region of application of lasers. It is clear that if we make a laser with a sweep frequency, we apparently shall be able to influence a molecule in such a way that definite bonds will be excited and, thus, chemical reactions will take place in certain directions. However, this problem will not be simple even after design of the appropriate lasers. But one thing is clear: the problem is extremely interesting and perhaps its

* To whom correspondence should be addressed. Richard F. Haglund, Jr., Department of Physics and Astronomy, Vanderbilt University, Nashville TN 37235-1807; E-mail: Richard.haglund@vanderbilt.edu.

J.J. Dubowski and S. Tanev (eds.), Photon-based Nanoscience and Nanobiotechnology, 175–203.

solution will be able to make a revolution in a series of branches of chemical industry."[1]

The kind of laser-initiated photochemistry that Academician Prokhorov had in mind has been substantially more difficult to achieve than was once believed. While there has been some progress in the development of femtosecond laser chemistry and the related coherent control schemes, there has been no large-scale industrial application of laser-driven chemistry other than laser isotope separation. More sophisticated laser photochemistry experiments, such as coherent control of branching ratios in bimolecular reactions, have remained in the realm of proof-of-concept demonstrations.

In this paper, we review a different class of laser-driven materials processing applications based on the use of wavelength-specific materials properties, primarily in the realm of organic materials. These applications are made possible by the recent development of powerful, broadly tunable free-electron lasers (FELs). These accelerator-based light sources are scalable, efficient, and bring a new flexibility to researchers who would like to use lasers for materials processing. By identifying and benchmarking particular processing regimes, FEL-based materials research also enables the confident design of conventional laser systems for specific applications.

The three applications considered here all rely on selective vibrational excitation of materials in the mid-infrared "fingerprint" region of the spectrum: laser surgery of soft and hard tissues, matrix-assisted laser desorption-ionization mass spectrometry, and laser vaporization of polymers for thin-film deposition. These applications capitalize on the tunability of the FEL to drive thermal or thermomechanical changes in the material being processed, and may properly be classified as using laser-driven phase transformations rather than laser chemistry. Nevertheless, the fact that these applications are dependent on wavelength-selective excitation suggests that they partake of the spirit, if not the letter, of Academician Prokhorov's Nobel Lecture.

2. Making the Case for the Free-electron Laser in Materials Processing

Historically, laser modification of materials has been practiced using whatever lasers were ready to hand, with mechanistic explanations constructed after the fact. However, one can argue that the FEL offers, in many cases, an unprecedented opportunity for choosing the laser parameters to fit the properties and desired modifications of the material. This is particularly true for materials with infrared-active modes in the mid-infrared region of the electromagnetic spectrum. The following paragraphs

consider in turn the case for the FEL as a paradigmatic driver for laser-based materials science using ultra-short pulses, high intensities pulse repetition frequencies, and tunability.

2.1. THE CASE FOR ULTRASHORT LASER PULSES

The burgeoning use of ultrashort laser pulses for materials processing stems from their impulsive mode of energy deposition. For example, femtosecond Ti:sapphire lasers modify and process materials by generating high densities of *electronic* excitation on a time scale short compared to electron-phonon coupling times — thus insuring that the laser energy is absorbed before thermal equilibrium is reached. Relatively little is known, however, about mechanisms of materials processing initiated by high spatio-temporal densities of *vibrational* excitation. Mode-selective infrared (IR) excitation produces anharmonic vibrations that have little overlap (in the perturbation-theoretic sense) with the harmonic vibrations constituting the phonon bath. Hence the localized anharmonic modes couple relatively slowly to the extended, harmonic wave functions of the phonon bath that define the material temperature. With relaxation times up to a few picoseconds, nuclear motion and bond-breaking can begin before the absorbed energy leaks out of the anharmonic mode, if the density of excitation is sufficiently high.

A necessary (though not sufficient) condition for bond-breaking to occur before the energy is dissipated into heat is that the laser energy be localized within the absorption volume for a time that is long compared to a characteristic harmonic vibrational period, say, the inverse Debye frequency. To avoid the formation of a heat-affected zone, laser energy also must be confined for a time scale short compared to thermal diffusion times; otherwise, energy will dissipate out of the absorption zone before the system begins to move along the desired configuration coordinate. Finally, to minimize photoacoustic and photomechanical effects, the laser pulse duration should be short compared to the time it takes for acoustic shock waves to "unload" from the absorption volume and propagate through the unirradiated material. These characteristic times are related to optical and mechanical materials properties; they are[2]

$$\tau_p << \tau_{thermal} \approx L_p^2 / D_{thermal}, \quad \tau_p \leq \tau_s \approx L_p / C_s$$

where τ_p is the laser pulse duration, $\tau_{thermal}$ and τ_s are, respectively, the thermal and stress confinement times. L_p is the optical penetration depth into the material, $D_{thermal}$ is the characteristic diffusion length, and C_s is the speed of sound in the material. Since sound speeds are of order 10^3 m·s^{-1} in solid materials, and with $D_{thermal}$ ranging from to , this pair of equations

indicates that pulse durations of 1 ps or less are always going to satisfy these conditions. On the other hand, for longer pulse durations - for example, the 4 μs macropulse "burst" from a free-electron laser - it is likely that the stress-confinement condition will *not* be fulfilled. The thermal-confinement condition may or may not be satisfied, depending on the thermal conductivity of the material.

2.2. THE CASE FOR TUNABLE MID-INFRARED LIGHT

The photon energies of lasers now used for materials modification range from 1.2 eV (Nd:YAG) and 1.55 eV (Ti:sapphire) to 7.9 eV (F_2 excimer). When materials are irradiated by photons in this energy range, the material response is a single-photon or multi-photon induced transition from the ground state to an excited electronic state. The absorbed energy is dissipated by phonon emission that heats the lattice, eventually leading to the lowest vibrational energy level of the excited state, and thence via photon emission to a lower energy state that is often *not* the original ground state. Continued cooling and relaxation then leads to a final modified material state, possibly one that has been photochemically altered. The intermediate relaxation paths are complex, not well characterized, and difficult to generalize. Hence it is difficult to reconstruct the energy budget for the materials modification and to develop robust processing protocols.

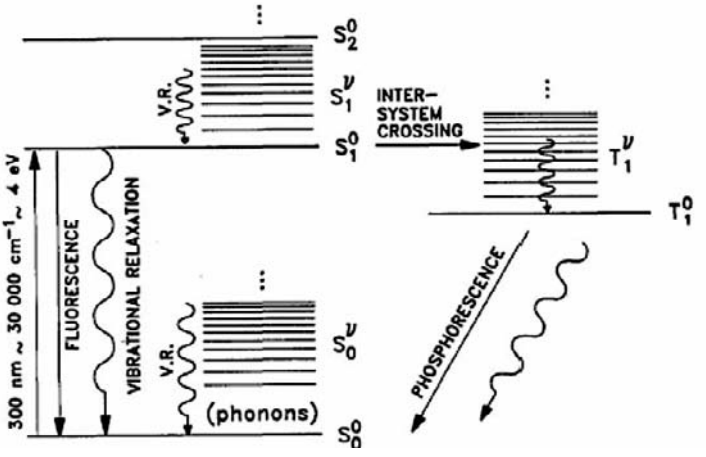

Figure 1. Schematic contrasting electronic *vs* vibrational excitation mechanisms in molecular solids. Vibrational relaxation occurs by phonon emission, electronic relaxation by radiative transitions.

The infrared spectra of materials, on the other hand, can almost always be identified in a straightforward way with specific molecular groupings and vibrations; the relaxation channels also are often well known. When infrared excitation does not lead to electronic transitions, the system remains in the electronic ground state and the analysis of the materials modification dynamics is correspondingly simpler. This suggests that it may be possible not only to make selective materials modifications by vibrational excitation, but also to understand in detail the mechanism through which the modifications occur.

2.3. THE CASE FOR HIGH PULSE REPETITION FREQUENCY

Recently attention has been drawn to the possibility of laser processing of materials using ultrashort pulses at high pulse-repetition frequency (PRF).[3] The *Ansatz* is that laser ablation dynamics can be optimized by a vaporization mechanism that employs modest pulse energies to ablate only a small amount of material with each pulse; relatively high intensity to enhance cross section; and high pulse repetition frequency to optimize material throughput or process yield. Low laser-pulse energy or fluence minimizes collateral damage, particulate emission, and undesirable thermal loading in the material. Since reaction *rates* are fundamentally proportional to intensities and cross sections, rather than to fluence, high laser intensity maximizes the probability of the desired laser-materials interaction; in addition, at high intensities, nonlinear effects may produce additional yield of desirable products. High PRF, which determines the average power and hence the yield of a laser-materials modification procedure, also mimics the effect of continuous laser irradiation, a situation optimal, for example, in thin-film deposition.

2.4. THE FREE-ELECTRON LASER AS A TEST BED

There have been few systematic tests of the high-PRF materials-processing paradigm described above. Mode-locked Nd:YAG lasers have 100-ps pulses during which the material reaches thermal equilibrium, and cannot deliver really high intensities, although high quality films of amorphous carbon with unusual magnetic properties have been made in this way.[4] Femtosecond mode-locked lasers have too little energy in each pulse for materials modification except in a few special cases, notably in subsurface structuring of dielectrics. Moreover, given fixed frequencies of these lasers, it is not possible to optimize the spatio-temporal density of electronic excitation in the ablation target.

Tunable, mid-IR picosecond free-electron lasers, on the other hand, provide an ideal testing ground for these concepts. With micropulse durations in the 0.5-2 picosecond range, these lasers deliver energy in a time scale comparable to or shorter than vibrational relaxation times. Because these lasers produce as much as tens of microjoules in these picosecond pulses, they achieve intensities in the $10^{10\text{-}11}$ W/cm^2 range, sufficient to initiate multiphoton processes if desired and to sustain high reaction rates. And with micropulse repetition frequencies in the 50 MHz-3 GHz range, and macropulse repetition rates ranging from 30 Hz to continuous, they can deliver average powers as high as kilowatts.[5] Finally, because FELs can be tuned to select the desired mode of material absorption, the spatial density of vibrational excitation can be controlled by the combination of wavelength, fluence and intensity.

3. A Free-electron Laser Primer

The free-electron laser (FEL) is a device in which light emitted by a relativistic electron beam moving through a spatially periodic magnet array or *wiggler* is amplified by classical electromagnetic-field effects rather than by stimulated emission as is typical of atomic and molecular lasers.[6] The essential components of an FEL are shown in Figure 2 below; they include an extremely high-brightness electron gun, an accelerator capable of producing an electron beam at relativistic energies, the wiggler (spatially periodic magnet array), and the optical cavity in which the amplification takes place.

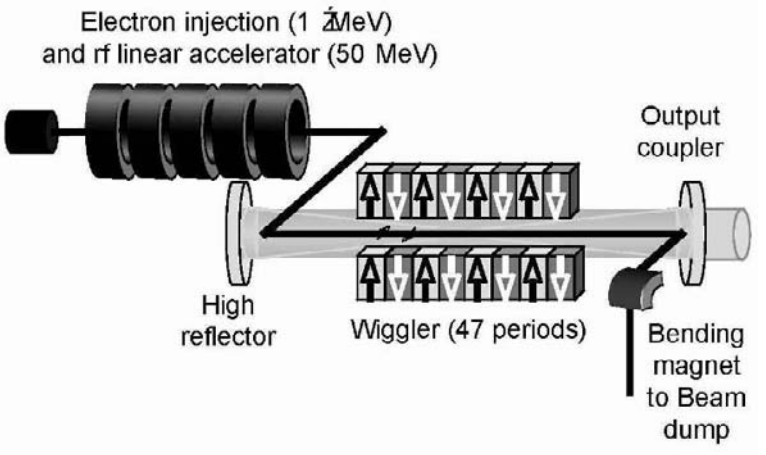

Figure 2. Schematic of an rf-linac driven free-electron laser.

3.1. GENERAL CHARACTERISTICS OF FREE-ELECTRON LASERS

In the reference frame of the moving electron, $\lambda_{wiggler}$, the wiggler wavelength, is foreshortened by the factor $\gamma \equiv E_{beam} / m_e c^2$; the wavelength of the light emitted by the oscillating electron is then shortened by another factor γ upon transformation back to the laboratory reference frame. In this approximate treatment, the wavelength λ_{FEL} of the FEL is then given by

$$\lambda_{FEL} = \frac{\lambda_{wiggler}}{2\gamma^2}\left[1 + \kappa^2(B)\right]$$

where B is the axial magnetic field and κ is function of near unit magnitude. The FEL wavelength can be varied continuously over a wide range by changing either the axial magnetic field or the electron-beam energy (and hence γ). For a 50 MeV electron beam and 2 cm wiggler-magnet spacing, an axial magnetic field of 0.5 T yields a FEL wavelength of 3 μm.[7] One might say that the FEL "converts" low-energy, wiggler-field photons into high-energy IR photons.

The temporal pulse structure and output wavelength of a free-electron laser are determined largely by the choice of electron accelerator. Currently operating free-electron lasers use electron beams produced by Van de Graaff generators to produce near-continuous beams of millimeter-wave photons; storage rings to generate picosecond pulses of visible and ultraviolet photons and even gamma rays, and radio-frequency linear accelerators to produce picosecond and femtosecond pulses of photons ranging from the far-infrared to X-ray regions of the electromagnetic spectrum.

3.2. THE VANDERBILT FREE-ELECTRON LASER

The examples of FEL materials processing and analysis described in Section 4 are all from experiments undertaken at Vanderbilt University's W. M. Keck Foundation Free-Electron Laser Center. The Vanderbilt free-electron laser is based on the Mark III rf-linac driven accelerator pioneered by Madey and his collaborators;[8] substantial modifications and upgrades have been made to improve both reliability and beam quality.[9] The FEL wavelength is continuously tunable from 2 to 10 μm, and the pulse structure is optimized for materials modification rather than for spectroscopic applications.

The electron gun is a LaB_6 thermionic emitter maintained in ultrahigh vacuum. The gun injects a beam of electrons accelerated to 1 MeV in a small rf cavity, through an analyzing magnet, and into an accelerator powered by an S-band klystron operated at 2.865 GHz. The klystron

produces 4 μs macropulses at an optimal repetition rate of 30 Hz. However, within each macropulse, the small phase-space acceptance angle of the rf accelerator produces some 10^4 optical micropulses of approximately 1 ps duration. Typical macropulse energies are of order 30-120 mJ. The optical bandwidth of the transform-limited micropulses is typically 1% of the center frequency (FWHM) with a micropulse energy of several μJ, yielding a peak unfocused irradiance of order 10^7 W/cm^2. The fluence for the experiments reported later is that of the macropulse; where the intensity is reported, it is that of the micropulse.

Because of the water absorption bands in the mid-infrared region of the spectrum, the beam is transported from the shielded accelerator vault in high-vacuum lines to user laboratories as well as clinical facilities located in the Center. Following extraction of the FEL beam from the evacuated beam-delivery system, the beam is delivered to end users. In the surgical suites, the delivery system may be either an articulated arm with mirrors located at the joints, or a fiber-optic type surgical handpiece based on broadband hollow waveguides whose interior surfaces are plated with silver. In general, for these applications, the entire FEL macropulse is used, as experience indicates that the ablation of hard and soft tissue is essentially thermal.

In the laboratory experiments described in Sections 4.2 and 4.3, it is often appropriate to use a "slice" of the full macropulse to minimize thermal loading of the target material. In such cases, the a spherical mirror telescope compresses the beam by a factor of 4 to fit the free aperture of a fast broadband electro-optic switch (Pockels cell).[10] A BaF_2 beam splitter is used to obtain a trigger signal for the Pockels cell driver electronics and to monitor pulse-to-pulse energy variations; Si or Ge windows filter out higher FEL harmonics ranging down to visible wavelengths, which could damage the CdTe crystal in the Pockels cell when the high voltage is applied. The electro-optic switch slices the desired micropulse train ($\tau \geq 50$ ns) out of the FEL macropulse. Because the interval between micropulses is so short, it is not possible in this machine to switch out single pulses.

After the Pockels cell, a polarization analyzer consisting of ZnSe Brewster plates suppresses the unwanted residual unpolarized beam with a typical contrast ratio of 1:160. A second rotatable ZnSe polarizer following the analyzer can be used as an attenuator. Infrared-transmissive lenses with focal lengths f = 85-250 mm lens are used to produce elliptical spots on material targets typically measuring approximately 150-300 μm in diameter.

Important operating parameters of the Vanderbilt FEL are given in Table 1. The final entries are especially important for understanding the mechanisms of resonant IR interactions with materials, as these indicate

areal and volumetric photon fluxes that enable nonlinear optical effects during laser irradiation.

Table 1. Optical characteristics of the Vanderbilt Mark-III Free-Electron Laser.

Optical characteristic	Best observed	Typical values
Wavelength tuning range	1.8-10.6 μm	2.3-8.5 μm
Linewidth $\Delta\nu/\nu$	0.7%	2–4%
Pulse-to-pulse timing jitter	0.1%	0.4%
Macropulse energy	360 mJ	30-150 mJ
Mactopulse energy stability	±5%	±10-15%
Macropulse duration	6 μs	3-5 μs
Micropulse duration	0.7 ps	1-2 ps
Micropulse peak power	2 MW	0.5-1 MW
Macropulse repetition frequency	30 Hz	30 Hz
Average power	11 W	2-3 W
Micropulse irradiance	$\sim 5 \cdot 10^{29}$ cm^{-2}·s^{-1}	
Volume photon density	$\sim 5 \cdot 10^{22}$ cm^{-3}	

4. Examples of Free-electron Laser Applications

In discussions of laser materials modification using infrared lasers (*e.g.*, the CO_2 laser at 10.6 μm), it is commonly stated that the modification is induced by thermal processes. Experience with wavelength-selective infrared excitations, on the other hand, clearly shows evidence of athermal or non-thermal processes.

For example, in early studies of inorganic molecular crystals, we irradiated the molecular crystal calcium carbonate and its isoelectronic cousin sodium nitrate.[11] Calcite, in the crystalline form of calcium carbonate ($CaCO_3$), occurs naturally in the mineral form used in these experiments. In its crystal structure, each CO_3 group forms a triangular cluster whose plane is perpendicular to the optic axis. Hence the crystal is anisotropic and birefringent. Transparent in the visible, calcite has a resonance absorption peak at around 7.1 μm (fundamental) and 3.5 μm (overtone) because of the asymmetric stretch of carbonate groups. Sodium nitrate ($NaNO_3$) has essentially the same electronic and vibronic structure and infrared absorption, with the asymmetric stretch of the nitrate group located at a wavelength of 7.2 μm. Both materials have an absorption depth of approximately 200 nm at the peak of this resonance.

Mass-selected, positive-ion emission was recorded from $NaNO_3$ and $CaCO_3$ at 3.5 μm, the overtone of the carbonate/nitrate group. The primary

cations detected from these two materials were Na^+ and Ca^+ respectively. Normalized TOF records for positive ion emission corresponds to a kinetic energy of 3.6 eV, over 10 times the incident photon energy of 0.354 eV! The peak in the Na^+ TOF corresponds to an higher kinetic energy of 4.2 eV. Further, the width of the trace is too narrow to be attributable to a Maxwell-Boltzmann energy distribution even if a surface temperature of over $3\text{-}4 \cdot 10^4$ K were reasonable.

Clearly, then, the high-energy component of the ion energy distribution is not thermal; indeed, this non-thermal mechanism of ion emission is dominant over the range of laser intensities employed in our experiments. In the following sections, we provide additional examples of wavelength-selective, non-thermal or athermal effects from tunable infrared laser radiation.

4.1. MEDICAL APPLICATIONS OF THE FREE-ELECTRON LASER

One of the primary motivations for the building of the free-electron laser was for the exploration of possible surgical applications in the mid-infrared region of the spectrum. The rationale for this is easily seen by looking at the optical absorption spectrum of water, the primary component of typical soft tissue. These absorption features coincide with the tuning range of the Mark III free-electron laser (FEL), and have made it possible to compare the comparative efficiency and collateral effects of various laser cutting protocols.

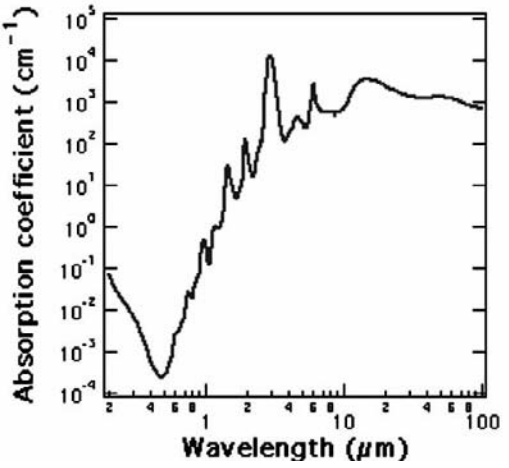

Figure 3. Absorption coefficient of liquid water as a function of wavelength.

However, unlike the case of inorganic materials, the requirement that tissue adjacent to the laser cut remain viable requires that the laser cutting procedure be relatively "cold," *i.e.*, that it not raise the temperature of the surrounding tissue much above 50 C, at which point proteins are denatured and lose functionality. Thus it is crucial that the pulse structure of the free-electron laser allow for thermal confinement. It is also often the case that applications limit the use of ultraviolet lasers, which can ablate organic materials by means of photochemical reactions.

The first demonstration of the efficacy of the FEL in tissue ablation was carried out by an interdisciplinary team at Vanderbilt University in 1994.[12] Brain, dermis and ocular tissue were ablated at 3 μm and 6.45 μm wavelengths corresponding to the absorption peaks of water and the protein amide II band. Based on thermal confinement arguments, the 3 μm irradiation should have produced the most effective ablation and the smallest heat-affected zone; however, the results of histopathological studies clearly showed that targeting the amide II protein band at 6.45 μm produced the better results (Figure 4).

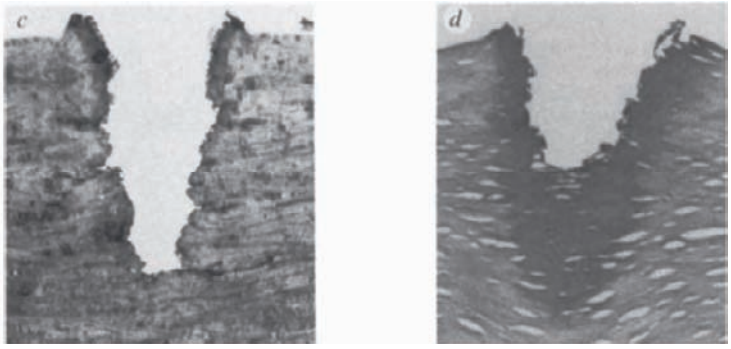

Figure 4. FEL incisions in cadaver corneal sclera made at 6.45 μm (left) and 3.00 μm (right), made by FEL irradiation using a sequence of ten macropulses. The collateral damage zones in the two cases were measured to be 40 μm and 150 μm, respectively.

The experimental evidence in favor of this wavelength, however, required a new explanation, since the popular optical-breakdown model for infrared laser ablation, developed by practitioners using 1.064 μm Nd:YAG lasers, clearly did not explain the data. Moreover, the sharply defined selectivity of the amide II cutting demanded a more detailed, microscopic model of the laser-tissue interaction than had been developed up to that time.

The primary argument advanced by Edwards and collaborators[13] connected the thermo-mechanical properties of collagen with the unusual macropulse-micropulse time structure produced by the FEL. Energetic arguments showed that neither pyrolytic fragmentation nor simple

vaporization of the biopolymers was likely; moreover, similar phenomenology was observed regardless of the type of tissue, suggesting that details such as water or collagen content were not crucial to the mechanism. Hence a picture of a cooperative mechanism was proposed, in which the laser irradiation induced structural changes in the biopolymers that contributed to a loss of mechanical integrity and enabled a photomechanical ejection of material. This process was assisted by the fact that the water in the tissue, which was also absorbing energy through the wings of the bending mode at 6.1 μm, reached the critical temperature at nearly the same point in the laser irradiation at which the protein became denatured. This model was further strengthened by computer calculations of the microscopic thermodynamic response of laminar, corneal tissue to FEL-like pulse trains.[14]

Since that first paper, a number of other experiments have been performed on other tissues,[15-17] cartilage[18] and cortical bone.[19, 20] All of these show that significant improvements in surgical efficiency can be realized by the mid-infrared laser ablation protocol, usually targeting the amide protein bands. The challenge for the future is twofold: to demonstrate that the mid-IR laser ablation technique opens up new areas for future clinical interventions, and to find an appropriate clinical laser sources that mimic the effects of the FEL.

One of the most promising of such areas is in ophthalmology, where the possibility of introducing laser light through hollow waveguide[21] makes opportunities for new clinical treatments. Consider one example: the operation called fenestration of the optic nerve sheath. A number of pathological conditions can lead to increased intracranial pressure on the optic nerve; these include obesity, middle-ear disease, pregnancy, steroid use, some antibiotics, and nutritional and immune disorders. Increased pressure on the optic nerves causes headaches, and also can produce edema of the optic disc.

The treatment aims to decrease the intracranial pressure around the optic nerve by cutting through the nerve sheath to provide a “safety valve” against the build-up of fluid pressure. Aside from the intrinsic delicacy of the surgery, there are complications that can arise from unnecessary mechanical manipulation of the optic nerve in the conventional surgical procedure, which requires enucleation of the eyeball.

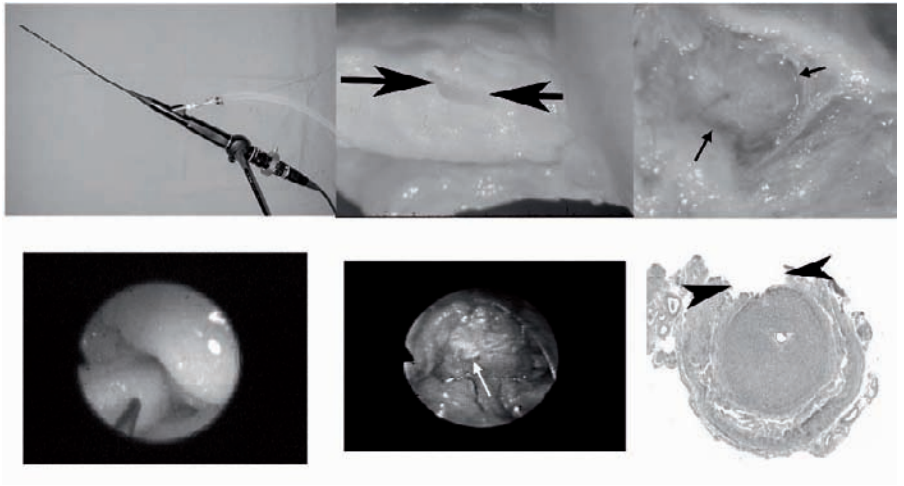

Figure 5. Photographs illustrating various features of the opthalmological studies on fenestration of the optic nerve to relieve intracranial pressure. Details are explained in the text. Photographs courtesy of Dr. Karen Joos, M.D., Ph.D., Department of Opthalmology, Vanderbilt University.

Figure 5 gives some insight into the complexity involved in the operations as well as demonstrating the details of the FEL procedure. At the top left, one sees a photograph of the endoscopic handpiece used by the surgeons in the early animal studies, designed and constructed by the biomedical engineering faculty at Vanderbilt University and based on a hollow waveguide fiber developed at Rutgers University. This handpiece must "feel" similar enough to a scalpel to permit effective use of the hand skills of the surgeon. The upper center and right photographs show the incision in the sheath that protects the optic nerve. The advantage of IR wavelengths used in FEL surgery is that the penetration depth can be precisely calibrated so that the surgeon can stop cutting before damaging the optic nerve itself. The photographs at the lower left and center show views through the operating microscope during the operation. Finally, the photograph at lower right shows the histological section that confirms the clean resection of the optic nerve sheath and the intact surface of the nerve itself. More details on this FEL surgical procedure have been reported elsewhere.[22-25] The procedure itself has moved through the phases of animal and human trials and is now being implemented in a minimally invasive endoscopic version.

At the present time, the Vanderbilt free-electron laser and a similar FEL in Osaka, Japan have been and are being used in a wide variety of biomedical and biophysical studies.[26] These include, but are by no means limited to:

- Studies of wound healing that compare recovery of animal models from incisions made with scalpels compared with those for FEL and conventional surgical incisions using inserted luciferase genes as reporters;[27]
- Measurements of the efficacy of dermatological treatments such as skin resurfacing comparing the FEL to conventional lasers, usually CO_2 lasers operating in the 9-10 μm region;[28]
- Cartilage reshaping as a part of plastic surgery (*e.g.*, rhinoplasty), where the superior ablation efficiency of mid-infrared wavelengths (6.1 and 6.45 μm) indicates a preference over wavelengths strongly absorbed by water;[29]
- Selective removal of the cholesteric esters in atherosclerotic plaques from the luminal walls of carotid arteries, using 5.75 μm light, apparently a quite different result from that achieved with conventional lasers;[15]
- Stimulation of nerves using low-fluence infrared light in the spectral regions away from the protein absorption bands (2.1 and 4.0 μm) as an alternative to conventional neurological methods such as electrical stimulation.[30]

While the Vanderbilt FEL has been used in Food and Drug Agency-approved experimental surgeries of human subjects, it seems unlikely that the FEL will ever be used in routine medical treatments. Even the compact FELs envisioned by some would be too large and complicated to be usable in clinical settings.

For this reason, efforts to develop alternative laser sources for amide-band ablation are underway, boosted by the discovery that the unique temporal pulse structure of the FEL does not seem to be crucial for the benefits achieved by 6.45 μm irradiation.[31] Leading candidates for this task are the strontium vapor laser and a tunable alexandrite laser based on stimulated Raman scattering.

4.2. INFRARED-LASER MASS SPECTROMETRY OF BIOMOLECULES

Matrix-assisted laser desorption-ionization (MALDI) mass spectrometry (MS), a "soft ionization" technique that makes possible mass identification of large biomolecules, was honored with the Nobel Prize for Chemistry in 2002. In conventional MALDI-MS, an analyte molecule at low concentrations (~10^{-4} or less) is co-crystallized at low concentration in a weak organic acid with strong ultraviolet (UV) absorption. A nanosecond UV laser, typically the inexpensive N_2 gas laser, ablates a thin layer of material from the surface of the substrate. During the ablation process, a small fraction (~10^{-6}) of the embedded analyte molecules are ionized, probably during collisions in the laser plume between ion donors from the matrix and appropriate acceptors on the analyte molecule. The sensitivity of MALDI-MS is now in the attomole regime.

MALDI with IR lasers broadens the class of possible matrix materials and leads to improved mass spectrometry of nucleic acids;[32] phosphorylated, glycosylated, and sulfated peptides;[33, 34] and proteins embedded in polymer membranes.[35] IR-MALDI at 2.94 μm clearly fragments large proteins and noncovalent complexes less than UV-MALDI in the same matrix [34, 36, 37]. Using the FEL, direct IR laser desorption and ionization of biomolecules embedded in frozen aqueous solutions[38] and in polyacrylamide gels[39] by selectively exciting vibrational modes of the ice or gel matrix has also been demonstrated.

4.2.1. *Two-Color Matrix-Assisted Laser Desorption and Ionization*

Because of the large laser penetration depths of IR compared to UV, IR-MALDI at 2.94 μm ejects approximately 10^3 times more material per laser shot than UV-MALDI under typical conditions; the total ion yield is less than 10^{-6} of the ejected material.[40] This can be an advantage in certain applications, and indeed, the greater quantity of ejected material is probably responsible for the higher ion yields of very large biomolecules in IR-MALDI, for instance. Here, one can also capitalize on the large volume of neutrals ejected to provide a higher number density of analytes that can be ionized at the optimum density of the ablation plume. We use two lasers, an IR laser to ablate a substantial quantity of material without electronically exciting it, and then at an appropriate time in the expansion of the ablation plume, a UV laser to ionize the matrix molecules and thereby enhance the fraction of ions that enter the mass spectrometer.

Figure 6 shows MALDI mass spectra of immunoglobulin G (IGG, mass 166 kDa) in sinapinic acid matrix. The UV (N_2, 337 nm) and IR (FEL, 5.9 μm) laser fluences were set just above threshold, yielding the spectra shown in the lower traces (intensities increased x10 for these spectra).

When both lasers were used, with ranging from 0 to 500 ns of the UV laser relative to the IR laser, the signal-to-noise was enhanced by a factor of up to 50. The spectrum shown in the uppermost trace of Figure 6 was taken at a 190 ns. The resulting two-color spectrum has many characteristics of typical IR-MALDI mass spectra: multiply charged monomers and oligomers of the analyte are observed without peak broadening on the low-mass side that is usually seen in UV-MALDI and indicates fragmentation.[41] At the same time, the spectra exhibit the shot-to-shot reproducibility normally associated with UV-MALDI. The ability to independently vary fluences, delay times, and mass spectrometer ion optics opens new windows onto the mechanism of ion formation in IR-MALDI by separating the ablation and ionization processes.[42] In particular, the existence of an optimum delay time between the ablation and ionization lasers, if coupled to a measurement of the expansion velocity of the plume, would indicate the the plume density at the time of maximum ionization.

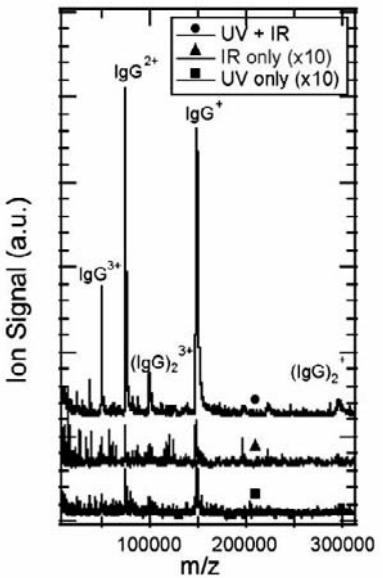

Figure 6. MALDI-MS spectra of immunoglobulin G (IGG) in a sinapinic acid. The three traces are described in detail in the text.

4.2.2. *Mass Spectrometry of Complex Environmental Materials*

The tunability of the FEL makes it possible to meet another MALDI-MS challenge, that of identifying metal-ligand complexes in poorly characterized or contaminated samples from the environment. Small metal-organic molecules, and especially carboxylic-alkali complexes, are important in biological processes[43] such as cation transport through

membranes;[44, 45] interface physics and chemistry;[46] and mass spectrometry.[47-49] However, alkali atoms such as potassium and sodium — ubiquitous especially in biological systems — tend to suppress positive ion signals in MALDI [50, 51] and, by forming multiple alkali adduct peaks, reduce signal/noise and broaden spectral lines.[52, 53]

An instructive example is furnished the need for analysis of mixed chemical, radioactive and flammable wastes stored primarily in enormous carbon-steel, underground tanks at several U. S. Department of Energy sites. Large quantities of chelating agents — including EDTA, HEDTA and citric acid, nitrates and nitrites — were originally added to the hazardous waste products to reduce acidity and thus preserve long-term tank integrity. However, the long storage time has inevitably led to leaks in the tanks. In the evolving tank environment, condensed-phase reactions between organic chelators (acting as the fuel) and nitrate/nitrite salts (serving as oxidizers) could lead to explosive release of toxic and radioactive materials to the environment [54].

As the tank waste ages, chemical and radiolytic degradation of the chelators reduces the organic fraction available as fuel. Mass spectrometric analysis of the organic fraction in real time is a key to the risk assessment required prior to treating or relocating these hazardous wastes. However, the harsh chemical and radioactive environment and presence of large amounts of sodium complicates MALDI-MS analyses. Unlike MALDI studies of tank waste simulants using exogenous matrices [50, 55], sodium nitrate, an intrinsic component of the waste composite, can be used as an IR-MALDI matrix by tuning the FEL to match its vibrational absorption modes. This eliminated the need for an exogenous matrix whose spectral signature might obscure the relatively low-mass analyte ions, as well as complicate matrix-analyte chemistry in UV-MALDI [56, 57].

With IR-MALDI, tuning the laser to the ν_2-ν_4 C=O stretching vibration of the sodium nitrate at 7.1 μm, it was possible to identify all of the organic species in tank-waste simulants, as shown in Figure 7.[56] In addition, the studies showed that the ion spectra are strongly dependent on the wavelength used for ablation; the ions are formed by gas-phase collisional processes; and the memory of cation complexes characteristic of the solid waste phase is lost. Because of the simple structures of the molecules involved, it was even possible to make reasonable conjectures about the specific binding sites of the sodium ions and the effect of ionization on the structure of the ion complexes observed, conclusions qualitatively confirmed by computational modeling. Importantly, because the initial laser excitation targeted only specific vibrational modes, these conclusions about the ionization mechanism remove the ambiguities that arise from

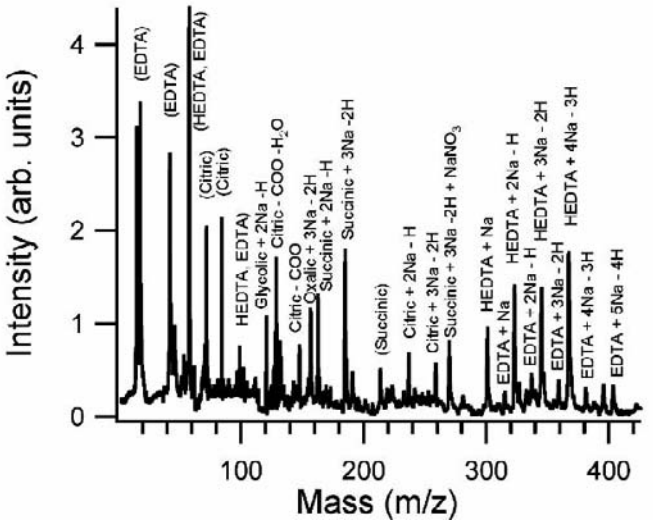

laser-induced photochemistry during ablation and MALDI with fixed-frequency ultraviolet lasers.

Figure 7. Mass spectrum of a tank-waste simulant using the $NaNO_3$ in the mixture as an endogenous matrix. The FEL wavelength was chosen to resonate with the nitrate stretching vibration of $NaNO_3$ at 7.1 μm.

4.2.3. *Direct Desorption of Insulin from a Polyacrylamide Gel*

A key problem in proteomics - sometimes known as functional genomics - is the rapid identification of proteins and characterization of their location, structure and function within the cell. This is a much more difficult problem than deciphering the human genome, because the "alphabet" of amino acids from which proteins are constructed has twenty components of very similar masses, not just the four amino-acid building blocks of nucleid acids. Moreover, many of the proteins of greatest biomedical interest are present only in small numbers in the cells. This leads to major issues of both sensitivity and mass discrimination that are extremely challenging.

Mass spectrometry (MS) is indispensable to solving the proteomics problem because the mass resolution of separation techniques — *e.g.*, liquid chromatography (LC), capillary electrophoresis (CE) and polyacrylamide gel electrophoresis (PAGE) - is limited by diffusion kinetics. A number of protocols exist for preparing separation products from GE for mass spectrometry, such as extraction of the protein from the gel, blotting the protein onto a membrane or drying the gel. In each of these methods, the

preparative step is followed by additional sample handling, including matrix addition, which may cause sample loss, adduct formation, and/or contamination.

The standard MALDI-MS technique in proteomics relies on an exogenous matrix, chosen to provide strong ultraviolet or infrared absorption for the fixed-frequency lasers available, which in turn imposes significant limitations on the usable matrix materials and requires tedious and time-consuming additional steps of dicing the gel, adding matrix, and drying. But by adjusting the parameters of the FEL to optimize ablation and ionization of the analytes based on the optical and vibrational properties of the material in which they are embedded during the separationg procedure, it is possible instead to avoid the introduction of the exogenous matrix and with it the extra steps.

Approximately 4 μL of a solution combining angiotensin II (1046.2 Da) and bovine insulin (5733.5 Da) in deionized water containing 0.1% triflouroacetic acid (TFA) at concentrations of 5 mM and 3mM respectively, were pipetted onto a native polyacrylamide gel (PAGE) with a total monomer concentration of 7.5%. After 10 minutes, the gel section was rinsed with deionized water and excess liquid was removed with an absorbent blotter.

Transmission spectra of the gel were acquired in Fourier-transform infrared (FTIR) spectrometer equipped with a liquid cell. The Fourier-transform infrared spectrum of the PAGE shows a broad peak centered around 3 μm (3330 cm^{-1}) containing the N-H and O-H stretching modes. This peak in the transmission is somewhat stronger than, but close to that of a transmission peak centered around 6 μm containing the C=O and C-N stretching modes, the N-H deformation mode and the O-H bending mode.

A broadband electro-optic switch was used to select a 100-ns portion of the macropulse with pulse energies around 100 μJ. The laser was focused to a spot approximately 150 μm in diameter at the sample surface, producing micropulse intensities as high as $8x10^9$ W/cm^2. The FEL was tuned to wavelengths corresponding to various room temperature absorption modes of the polyacrylamide gel and mass spectra were recorded under various conditions using a custom-built 3 m reflectron time-of-flight mass spectrometer in which the sample was mounted on a cryostage at a temperature of 105 ± 5 K.

Figure 3 shows the IR-MALDI mass spectra of angiotensin II and bovine insulin in a native polyacrylamide gel at 5.9 μm with no added matrix. Figure 3a shows a 25 shot average mass spectrum with each shot taken at a different spot on the gel, 1-on-N, in which angiotensin II and bovine insulin peaks are clearly visible. The FEL macropulse duration was 100 ns, with an energy of approximately 150 μJ; the micropulse intensity

was $3x10^9$ W/cm^2. We did not observe adduct formation on the analytes attributable to gel components. However, the peak at 371 Da — observable in a number of spectra — is apparently related to the polyacrylamide itself, as it is seen even when no analyte is present on the gel.

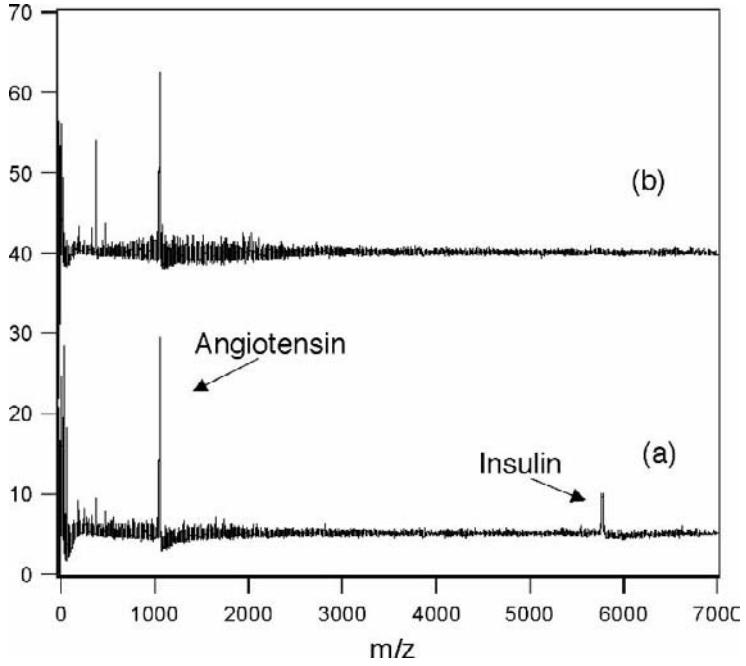

Figure 8. IR-MALDI mass spectra for angiotensin and insulin pipetted onto a polyacrylamide gel and irradiated at 5.9 μm. (a) shows an average of twenty-five single laser shots at different points on the gel, while (b) shows a twenty-five shot average taken at the same spot.

Figure 8b shows a mass spectrum of this same sample, averaged over 25 shots taken at the same spot, that is, an "N-on-1" average. The mass peak of angiotensin II is clearly visible while that of bovine insulin is not, indicating that the higher-mass insulin does not diffuse as far into the gel as angiotensin II. This procedure is motivated by the fact that polypeptides diffuse into the volume of the gel during electrophoresis; thus, multiple shots are required to ablate and ionize the analytes distributed throughout the thickness of the gel.

No analyte signal was observed at 2.9 μm under any conditions, consistent with a previous experiment in which it proved impossible to detect analyte signal from gels at 2.9 μm even when a matrix was added. Therefore, it appears that 5.9 μm is the optimal wavelength for desorbing and ionizing polypeptides. The clear discrepancy in the performance at the two wavelengths with roughly equal absorption strength also demonstrates

that the ionization process is not determined simply by thermal or pressure confinement, since these are material-dependent characteristics in which the wavelength enters only through the penetration depth of the laser light. Hence, recent discussions about the possible role of these energy-confinement mechanisms in MALDI may need some revision in light of these experimental data.

4.3. RESONANT INFRARED PULSED LASER DEPOSITION OF POLYMERS

The need for high-quality, carefully controlled films of organic materials is rapidly increasing as polymers and other organic molecules are employed in electronics, photonics, sensing and protective coatings. Polymer film deposition using aerosols, spin coating and dip coating is often bedeviled by solvent issues or coating uniformity, and only small organic molecules can be deposited by thermal evaporation. Polymer films can sometimes be created by plasma processing, chemical or photoactivation of a monomer layer on a substrate. However, this usually requires processing temperatures that are in many cases unacceptably high. Thus the defects of the standard techniques render them unacceptable for many applications in electronics, sensors and electro-optics that require high-precision but low-temperature processing.

Pulsed Laser Deposition (PLD) with ultraviolet (UV) lasers is extremely successful for depositing thin *inorganic* films of metals, semiconductors and dielectrics. The technique works because UV laser ablation is very efficient, and has the virtues of precise thickness control and stoichiometric reproducibility. While it is tempting to think about PLD as a route to organic thin-film deposition, UV laser ablation has the unfortunate tendency to "unzip" many polymers — *e.g.*, poly(methyl methacrylate), poly(tetrafluoroethylene), poly-*a*-methyl styrene — therefore necessitating high-temperature post-ablation processing to repolymerize the deposited monomeric material. There is an alternative — matrix-assisted pulsed laser evaporation (MAPLE) — in which a guest molecule to be deposited is dissolved at a concentration of 0.1 to 1% and frozen to form an ablation target. The solvent, like the matrix in MALDI mass spectrometry, transports the guest molecules toward the substrate and shields them from thermal and mechanical energy transfer during ablation. However, while MAPLE sometimes yields smooth uniform films, it is not always easy to find suitable solvents; the deposition rate is also much lower than in conventional PLD because of the low initial concentration of guest molecules.

Given the variety of infrared absorption bands of typical organic bonds shown in Table 2, it is easy to think of infrared lasers for PLD of small

organic molecules and polymers. This is especially so given the success of IR-MALDI in ablating large biomolecules intact, since the neutral fraction of ablated materials is typically 10^6 times the ion yield. Particularly if it turned out to be possible to keep the polymers in the ground electronic state (see Figure 2) during ablation, one could avoid the problem of photochemical alterations in the ablated material. Indeed, if the damage were limited to modest reductions in the molecular weight of the polymer, the process could still be useful, as long as the local structure of the functional groups, and hence the chemical functionality of the transferred material, remained undisturbed.

Table 2. Wavelengths and dissociation energies for organic molecular bonds.

Vibration	Wavelength (cm^{-1})	Dissociation Energy (kJ/mole)
C-C stretch	1000-1600	—
C-C bend	400-1000	—
C-H stretch	3000-3100	—
C-N	1180-1360	300
C=O	1690-1760	750
N-H	3300-3500	390
N-O	3610-3640	460

As of this writing, numerous polymers have been successfully deposited as thin films by resonant infrared pulsed laser deposition (RIR-PLD). Examples include: poly(ethylene glycol),[58, 59] polystyrene,[60] functionalized sensor polymers,[61] biocompatible polymers,[62] the light-emitting polymer MEH-PPV,[63] linear and super-coiled DNA, and large proteins with fluorescent labels.[64] The poly(amic acid) precursor to one of the most useful thermosetting polymers — polyimide — has been successfully deposited without cross-linking it, opening up the possibility of post-deposition patterning to set or "cure" the polymer.[65]

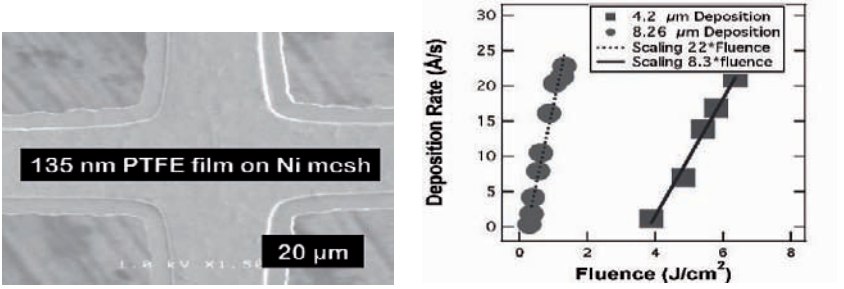

Figure 9. (Left) Scanning electron micrograph of PTFE film on Ni mesh. (Right) Deposition rate of PTFE as a function of fluence and wavelength, measured in vacuum with a quartz-crystal micro-balance.

Perhaps the most impressive accomplishment of RIR-PLD to date is the deposition of crystalline poly(tetrafluoroethylene) or PTFE — trade-name Teflon® — even at room temperature.[66] What makes this unusual is that PTFE is insoluble, and hence cannot be spin-coated; aerosol coating requires very high-temperature post-processing to generate smooth films, and even then it is hard to achieve the level of thickness control required for advanced technology applications. In Figure 9, at left there is a scanning electron micrograph of a 25-μm Ni mesh coated with 135 nm PTFE using the free-electron laser tuned to 8.26 μm. The target was neat PTFE in the form of commercially purchased rod stock; the time required for deposition was five minutes. The right-hand side of Figure 9 shows the measured deposition rate for PTFE as a function of macropulse fluence at 8.26 μm (the C-F_2 stretching vibration) and at 4.15 μm, at the first overtone of that vibrational mode. Tests of the deposited material using X-ray photoelectron spectroscopy, X-ray diffraction and Fourier-transform infrared spectroscopy, not shown here, confirm that the deposited material is indeed crystalline PTFE. The ablation threshold on resonance is an order of magnitude lower than at the overtone; moreover, even though intact PTFE is deposited at the overtone, the rate of increase with fluence is only about one-third of that on resonance.

The mechanism by which large, intact polymers are vaporized by resonant infrared laser irradiation remains a topic of active investigation. The most recent study of polystyrene ablation at the C-H stretching vibration near 3.4 μm suggests that the mechanism of vaporization, at least for polymers smaller than the entanglement limit, may be thermomechanical in origin, a combination of thermal and stress confinement effects. However, it is also likely that the mechanism differs for neat and guest-host matrix targets, and this will require more detailed studies of energy balance and plume dynamics than have been undertaken thus far.

4. Conclusions

Research using the free-electron laser in medicine, biochemical analysis and organic thin-film deposition has opened new avenues for advanced materials science and medical research in the mid-infrared. Nascent commercial interest in these possibilities is sufficient to suggest that "technology pull" can support more basic science in this area. In photonics and electro-optics, sensor technology and electronics, the use of tunable infrared radiation for the deposition of thin polymer and organic films looks especially interesting. Some of the areas now ripe for exploration are the following:

- *To what extent is the picosecond substructure in the free-electron laser a necessary element of its success in polymer thin-film deposition?* The evidence so far is mixed, with some applications in IR matrix-assisted laser vaporization seeming to work with nanosecond Er:YAG lasers and other applications, especially with biopolymers, not effective at all. On theoretical grounds, one expects picosecond and femtosecond pulses to have advantages over nanosecond pulses, but this has yet to be confirmed.
- *Can nonlinear optical materials be developed that will extend the tuning range and increase the average power of solid-state optical parametric oscillators and amplifiers?* At present the workhorse material for high-power tunable mid-infrared light is periodically poled $LiNbO_3$, and its tuning range extends only to approximately 4 μm. The research shows significant applications potential around 6 μm and 8 μm where there are presently no high-average power nonlinear IR materials.
- *Is it possible to produce entire devices — such as organic light-emitting diodes — in a single vacuum chamber using a tunable mid-IR laser?* Organic light-emitting diodes (OLED) are the future of display technologies that today are dominated by liquid-crystal materials. OLED fabrication still relies on a combination of thermal evaporation (for the organic light emitters) and liquid-phase processing (for the charge-transport and barrier layers) essential to OLED functionality. Demonstrating all-in-vacuum fabrication of the OLED might possibly be a game-changing breakthrough.

Finding answers to these questions will be challenging for both scientifically and technologically motivated investigations for some time to come.

Acknowledgements

It is a pleasure to acknowledge financial support from a Senior Scientist Award of the Alexander von Humboldt Foundation during the writing of this review paper, and Prof. Dr. Paul Leiderer, University of Konstanz, for the hospitality of his research group during this time. Special thanks are due to Dr. Karen Joos, M.D., Ph.D. of the Vanderbilt University Medical School for her help in understanding issues associated with the opthalmological surgical results shown in Section 4.1 of the paper.

References

1. A. M. Prokhorov, "Quantum Electronics," in *Nobel Lectures, Physics 1963-1970* (Elsevier Publishing Company, Amsterdam, 1972).
2. L. V. Zhigilei and B. J. Garrison, "Microscopic mechanisms of laser ablation of organic solids in the thermal and stress confinement irradiation regimes," Journal of Applied Physics **88**(3), 1281-1298 (2000).
3. E. G. Gamaly, A. V. Rode, and B. Luther-Davies, "Ultrafast ablation with high-pulse-rate lasers. Part I: Theoretical considerations," Journal of Applied Physics **85**(8), 4213-4221 (1999).
4. A. V. Rode, E. G. Gamaly, and B. Luther-Davies, "Formation of cluster-assembled carbon nano-foam by high-repetition-rate laser ablation," Applied Physics A-Materials Science & Processing **70**(2), 135-144 (2000).
5. G. R. Neil, C. L. Bohn, S. V. Benson, G. Biallas, D. Douglas, H. F. Dylla, R. Evans, J. Fugitt, A. Grippo, J. Gubeli, R. Hill, K. Jordan, G. A. Krafft, R. Li, L. Merminga, P. Piot, J. Preble, M. Shinn, T. Siggins, R. Walker, and B. Yunn, "Sustained kilowatt lasing in a free-electron laser with same-cell," Physical Review Letters **84**(22), 5238-5238 (2000).
6. C. A. Brau, "Free-Electron Lasers," Science **239**(4844), 1115-1121 (1988).
7. C. A. Brau, "The Vanderbilt-University Free-Electron Laser Center," Nuclear Instruments & Methods In Physics Research Section A-Accelerators Spectrometers Detectors And Associated Equipment **319**(1-3), 47-50 (1992).
8. D. A. G. Deacon, L. R. Elias, J. M. J. Madey, G. J. Ramian, H. A. Schwettman, and T. I. Smith, "1st Operation Of A Free-Electron Laser," Physical Review Letters **38**(16), 892-894 (1977).
9. G. S. Edwards, D. Evertson, W. Gabella, R. Grant, T. L. King, J. Kozub, M. Mendenhall, J. Shen, R. Shores, S. Storms, and R. H. Traeger, "Free-electron lasers: Reliability, performance, and beam delivery," IEEE Journal Of Selected Topics In Quantum Electronics **2**(4), 810-817 (1996).
10. K. Becker, J. B. Johnson, and G. Edwards, "Broad-Band Pockels Cell And Driver For A Mark Iii-Type Free-Electron Laser," Review Of Scientific Instruments **65**(5), 1496-1501 (1994).
11. D. R. Ermer, M. R. Papantonakis, M. Baltz-Knorr, D. Nakazawa, and R. F. Haglund, "Ablation of dielectric materials during laser irradiation involving strong vibrational coupling," Applied Physics A-Materials Science & Processing **70**(6), 633-635 (2000).
12. G. Edwards, R. Logan, M. Copeland, L. Reinisch, J. Davidson, B. Johnson, R. Maciunas, M. Mendenhall, R. Ossoff, J. Tribble, J. Werkhaven, and D. Oday, "Tissue Ablation By A Free-Electron Laser Tuned To The Amide-II Band," Nature **371**(6496), 416-419 (1994).
13. J. Tribble, D. C. Lamb, L. Reinisch, and G. Edwards, "Dynamics of gelatin ablation due to free-electron-laser irradiation," Physical Review E **55**(6), 7385-7389 (1997).
14. M. S. Hutson, S. A. Hauger, and G. Edwards, "Thermal diffusion and chemical kinetics in laminar biomaterial due to heating by a free-electron laser," Physical Review E **65**(6), 061906 (2002).
15. Y. Nakajima, K. Iwatsuki, K. Ishii, S. Suzuki, T. Fuitnaka, T. Yoshimine, and K. Awazu, "Medical application of an infrared free-electron laser: selective removal of

cholesterol ester in carotid artery atheromatous plaques," Journal Of Neurosurgery **104**(3), 426-428 (2006).

16. N. J. Wu, E. D. Jansen, and J. M. Davidson, "Comparison of mouse matrix metalloproteinase 13 expression in free-electron laser and scalpel incisions during wound healing," Journal Of Investigative Dermatology **121**(4), 926-932 (2003).
17. J. B. Robbins, L. Reinisch, and D. L. Ellis, "Wound healing of 6.45-mu m free electron laser skin incisions with heat-conducting templates," Journal Of Biomedical Optics **8**(4), 594-600 (2003).
18. J. I. Youn, G. M. Peavy, and V. Venugopalan, "Cartilage ablation at 2.79, 2.9, and 6.45 μm using free electron laser: Mass removal studies," Lasers In Surgery And Medicine, 9-9 (2005).
19. J. I. Youn, G. M. Peavy, and V. Venugopalan, "A comparison of mass removal and crater morphology produced in cortical bone by ablation using selected mid-infrared wavelengths of a free electron laser," Lasers In Surgery And Medicine, 14-14 (2006).
20. B. Ivanov, A. M. Hakimian, G. M. Peavy, and R. F. Haglund, "Mid-infrared laser ablation of a hard biocomposite material: mechanistic studies of pulse duration and interface effects," Applied Surface Science **208**, 77-84 (2003).
21. Y. Matsuura, K. Matsuura, and J. A. Harrington, "Power delivery of free electron laser light by hollow glass waveguides," Applied Optics **35**(27), 5395-5397 (1996).
22. K. M. Joos, L. A. Mawn, J. H. Shen, and V. A. Casagrande, "Chronic and acute analysis of optic nerve sheath fenestration with the free electron laser in monkeys," Lasers In Surgery And Medicine **32**(1), 32-41 (2003).
23. K. M. Joos, L. A. Mawn, J. H. Shen, E. D. Jansen, R. D. Robinson, M. A. Mackanos, J. Mavity-Hudson, and V. A. Casagrande, "Human optic nerve sheath fenestration with the free electron laser (FEL)," Lasers In Surgery And Medicine, 47-47 (2005).
24. K. M. Joos, R. D. Robinson, and J. H. Shen, "Optic nerve sheath fenestration with endoscopic accessory instruments versus the free electron laser (FEL)," Lasers In Surgery And Medicine, 42-42 (2006).
25. K. M. Joos, J. H. Shen, D. J. Shetlar, and V. A. Casagrande, "Optic nerve sheath fenestration with a novel wavelength produced by the free electron laser (FEL)," Lasers In Surgery And Medicine **27**(3), 191-205 (2000).
26. G. S. Edwards, R. H. Austin, F. E. Carroll, M. L. Copeland, M. E. Couprie, W. E. Gabella, R. F. Haglund, B. A. Hooper, M. S. Hutson, E. D. Jansen, K. M. Joos, D. P. Kiehart, I. Lindau, J. Miao, H. S. Pratisto, J. H. Shen, Y. Tokutake, A. F. G. van der Meer, and A. Xie, "Free-electron-laser-based biophysical and biomedical instrumentation," Review Of Scientific Instruments **74**(7), 3207-3245 (2003).
27. J. J. Wilmink, J. T. Beckham, S. Opalenik, A. Viehoever, and E. D. Jansen, "Using bioluminescent reporter genes in a novel skin model to temporally and noninvasively monitor gene expression," Lasers In Surgery And Medicine, 4-4 (2005).
28. J. S. Chen, B. Shack, L. Reinisch, N. Spector, J. W. Zinsser, N. K. Weisberg, G. P. Stricklin, and D. L. Ellis, "A comparison of scar revision with the free electron and carbon dioxide resurfacing lasers," Plastic And Reconstructive Surgery **108**(5), 1268-1275 (2001).
29. J. I. Youn, P. Sweet, G. M. Peavy, and V. Venugopalan, "Mid-IR laser ablation of articular and fibiro-cartilage: A wavelength dependence study of thermal injury and crater morphology," Lasers In Surgery And Medicine **38**(3), 218-228 (2006).

30. J. Wells, C. Kao, E. D. Jansen, P. Konrad, and A. Mahadevan-Jansen, "Application of infrared light for in vivo neural stimulation," Journal Of Biomedical Optics **10**(6)(2005).
31. M. A. Mackanos, J. A. Kozub, D. L. Hachey, K. M. Joos, D. L. Ellis, and E. D. Jansen, "The effect of free-electron laser pulse structure on mid-infrared soft-tissue ablation: biological effects," Physics In Medicine And Biology **50**(8), 1885-1899 (2005).
32. S. Berkenkamp, F. Kirpekar, and F. Hillenkamp, "Infrared MALDI mass spectrometry of large nucleic acids," Science **281**(5374), 260-262 (1998).
33. R. Cramer, W. J. Richter, E. Stimson, and A. L. Burlingame, "Analysis of phospho- and glycopolypeptides with infrared matrix-assisted laser desorption and ionization," Analytical Chemistry **70**(23), 4939-4944 (1998).
34. B. A. Budnik, K. B. Jensen, T. J. D. Jorgensen, A. Haase, and R. A. Zubarev, "Benefits of 2.94 mu m infrared matrix-assisted laser desorption/ionization for analysis of labile molecules by Fourier transform mass spectrometry," Rapid Communications in Mass Spectrometry **14**(7), 578-584 (2000).
35. K. Strupat, M. Karas, F. Hillenkamp, C. Eckerskorn, and F. Lottspeich, "Matrix-Assisted Laser-Desorption Ionization Mass-Spectrometry of Proteins Electroblotted after Polyacrylamide-Gel Electrophoresis," Analytical Chemistry **66**(4), 464-470 (1994).
36. T. Lippa, N. I. Taranenko, C. R. Prasad, and V. M. Doroshenko, "Infrared matrix-assisted laser desorption/ionization quadrupole ion trap mass spectrometry," European Journal of Mass Spectrometry **8**(3), 263-271 (2002).
37. R. Cramer and A. L. Burlingame, "IR-MALDI - Softer Ionization in MALDI-MS for Studies of Labile Macromolecules," in *Mass Spectrometry in Biology & Medicine*, A. L. Burlingame, S. A. Carr, and M. A. Baldwin, eds. (Humana Press, Totowa NJ, 2000), pp. 289-307.
38. M. L. Baltz-Knorr, K. E. Schriver, and R. F. Haglund, "Infrared laser ablation and ionization of water clusters and biomolecules from ice," Applied Surface Science **197-198**, 11-16 (2002).
39. M. Baltz-Knorr, D. R. Ermer, K. E. Schriver, and R. F. Haglund, "Infrared laser desorption and ionization of polypeptides from a polyacrylamide gel," Journal of Mass Spectrometry **37**(3), 254-258 (2002).
40. J. Gross and K. Strupat, "Matrix-assisted laser desorption/ionisation mass spectrometry applied to biological macromolecules," Trac-Trends in Analytical Chemistry **17**(8-9), 470-484 (1998).
41. S. Berkenkamp, C. Menzel, M. Karas, and F. Hillenkamp, "Performance of infrared matrix-assisted laser desorption/ionization mass spectrometry with lasers emitting in the 3 mu m wavelength range," Rapid Communications in Mass Spectrometry **11**(13), 1399-1406 (1997).
42. M. W. Little, J. K. Kim, and K. K. Murray, "Two-laser infrared and ultraviolet matrix-assisted laser desorption/ionization," Journal of Mass Spectrometry **38**(7), 772-777 (2003).
43. L. Stryer, *Biochemistry*, 4th ed. (W. H. Freeman, New York, 1995), p. 1064.
44. J. S. Klassen, S. G. Anderson, and A. T. Blades, "Reaction enthalpies for M+L = M+ + L, where M+ = Na+ and K+ and L = acetamide, n-methylacetamide, N,N-dimethylacetamide, glycine, and glycylglycine, from determinations of the collision-

induced dissociation thresholds," Journal of Physical Chemistry **100**, 14218-14227 (1996).

45. D. A. Griffith and A. M. Pajor, "Acidic residues involved in cation and substrate interactions in the Na+/dicarboxylate cotransporter, NaDC-1," Biochemistry **38**(23), 7524-7531 (1999).
46. B. C. Guo, B. J. Conklin, and A. W. Castleman, Jr., "Thermochemical properties of ion complexes Na+(M)n in the gas phase," Journal of the American Chemical Society **111**(17), 6506-6510 (1989).
47. J. Zhang, T.-K. Ha, R. Knochenmuss, and R. Zenobi, "Theoretical Calculation of Gas-Phase Sodium Binding Energies of Common MALDI Matrices," Journal of Physical Chemistry A **106**(28), 6610-6617 (2002).
48. J. Zhang, R. Knochenmuss, E. Stevenson, and R. Zenobi, "The gas-phase sodium basicities of common matrix-assisted laser desorption/ionization matrices," International Journal of Mass Spectrometry **213**(2-3), 237-250 (2002).
49. G. Ohanessian, "Interaction of MALDI matrix molecules with Na+ in the gas phase," International Journal of Mass Spectrometry **219**(3), 577-592 (2002).
50. S. C. Goheen, K. L. Wahl, J. A. Campbell, and W. P. Hess, "Mass spectrometry of low molecular mass solids by matrix-assisted laser desorption/ionization," Journal of Mass Spectrometry **32**(8), 820-828 (1997).
51. M. Karas, A. Ingendoh, U. Bahr, and F. Hillenkamp, "Ultraviolet-laser desorption/ionization mass spectrometry of femtomolar amounts of large proteins," Biomedical Environmental Mass Spectrometry **18**(9), 841-843 (1989).
52. F. Dubois, R. Knochenmuss, R. Steenvoorden, K. Breuker, and R. Zenobi, "On the mechanism and control of salt-induced resolution loss in matrix-assisted laser desorption/ionization," European Mass Spectrometry **2**(2-3), 167-172 (1996).
53. W. Z. Zhang, S. F. Niu, and B. T. Chait, "Exploring infrared wavelength matrix-assisted laser desorption/ionization of proteins with delayed-extraction time- of-flight mass spectrometry," Journal of the American Society for Mass Spectrometry **9**(9), 879-884 (1998).
54. J. E. Meacham, A. B. Webb, M. G. Plys, S. J. Lee, J. M. Grigsby, P. G. Heasler, J. L. Bryant, J. J. Toth, and P. M. Daling, "Safety Criteria for the Organic Watch List Tanks at the Hanford Site," WHC-SD-WM-SARR-033 (Westinghouse Hanford Company, Richland, WA, 1996).
55. W. P. Hess, H. K. Park, O. Yavas, and R. F. Haglund Jr., "IR-MALDI of low molecular weight compounds using a free electron laser," Applied Surface Science **127-129**, 235-241 (1998).
56. M. R. Papantonakis, D. R. Ermer, and R. F. Haglund Jr., "Picosecond infrared matrix-assisted laser desorption/ionization mass spectrometry of organic molecules on sodium nitrate crystallites," Applied Surface Science **197-198**, 213-216 (2002).
57. R. F. Haglund, M. Baltz-Knorr, D. R. Ermer, M. R. Papantonakis, and K. E. Schriver, "Laser mass spectrometry at high vibrational excitation density," Spectrochimica Acta, Submitted (2003).
58. D. M. Bubb, J. S. Horwitz, J. H. Callahan, R. A. McGill, E. J. Houser, D. B. Chrisey, M. R. Papantonakis, R. F. Haglund, M. C. Galicia, and A. Vertes, "Resonant infrared pulsed-laser deposition of polymer films using a free-electron laser," Journal Of

Vacuum Science & Technology A-An International Journal Devoted To Vacuum Surfaces And Films **19**(5), 2698-2702 (2001).

59. D. M. Bubb, M. R. Papantonakis, B. Toftmann, J. S. Horwitz, R. A. McGill, D. B. Chrisey, and R. F. Haglund, "Effect of ablation parameters on infrared pulsed laser deposition of poly(ethylene glycol) films," Journal Of Applied Physics **91**(12), 9809-9814 (2002).
60. D. M. Bubb, M. R. Papantonakis, J. S. Horwitz, R. F. Haglund, B. Toftmann, R. A. McGill, and D. B. Chrisey, "Vapor deposition of polystyrene thin films by intense laser vibrational excitation," Chemical Physics Letters **352**(3-4), 135-139 (2002).
61. D. M. Bubb, J. S. Horwitz, R. A. McGill, D. B. Chrisey, M. R. Papantonakis, R. F. Haglund, and B. Toftmann, "Resonant infrared pulsed-laser deposition of a sorbent chemoselective polymer," Applied Physics Letters **79**(17), 2847-2849 (2001).
62. D. M. Bubb, B. Toftmann, R. F. Haglund, J. S. Horwitz, M. R. Papantonakis, R. A. McGill, P. W. Wu, and D. B. Chrisey, "Resonant infrared pulsed laser deposition of thin biodegradable polymer films," Applied Physics A-Materials Science & Processing **74**(1), 123-125 (2002).
63. B. Toftmann, M. R. Papantonakis, R. C. Y. Auyeung, W. Kim, S. M. O'Malley, D. M. Bubb, J. S. Horwitz, J. Schou, P. M. Johansen, and R. E. Haglund, "UV and RIR matrix assisted pulsed laser deposition of organic MEH-PPV films," Thin Solid Films **453-54**, 177-181 (2004).
64. R. F. Haglund, Jr., D. M. Bubb, D. R. Ermer, J. S. Horwitz, E. J. Houser, G. K. Hubler, B. Ivanov, M. R. Papantonakis, B. R. Ringeisen, and K. E. Schriver, "Resonant Laser Materials Processing at High Vibrational Excitation Density: Applications and Mechanisms," presented at the Laser Precision Micromanufacturing, Munich, Germany, 2003.
65. N. L. Dygert, K. E. Schriver, and R. F. Haglund, Jr., "Vaporization and deposition of an intact polyimide precursor by resonant infrared laser ablation," presented at the Photonics West: Laser-Based Micropackaging, San Jose, CA, 2006.
66. M. R. Papantonakis and R. F. Haglund, "Picosecond pulsed laser deposition at high vibrational excitation density: the case of poly(tetrafluoroethylene)," Applied Physics A-Materials Science & Processing **79**(7), 1687-1694 (2004).

LASER-BASED SYNTHESIS, DIAGNOSTICS, AND CONTROL OF SINGLE-WALLED CARBON NANOTUBES AND NANOHORNS FOR COMPOSITES AND BIOLOGICAL NANOVECTORS

DAVID B. GEOHEGAN,* ALEX PURETZKY, ILIA IVANOV, GYULA ERES, ZUQIN LIU, DAVID STYERS-BARNETT, HUI HU, BIN ZHAO, HONGTAO CUI, CHRIS ROULEAU, STEPHEN JESSE, PHILLIP F. BRITT, HANS CHRISTEN, KAI XIAO, AND PAMELA FLEMING
Condensed Matter Sciences Division and the Center for Nanophase Materials Sciences, Oak Ridge National Laboratory, Oak Ridge, Tennessee, 37831-6056, USA

AL MELDRUM
Department of Physics, University of Alberta, Edmonton, Alberta, Canada

Abstract. The controlled synthesis of nanoparticles and nanotubes utilizing lasers is described with applications in multifunctional composites and biological nanovectors. Lasers offer unique advantages for the synthesis of novel nanomaterials such as single-walled carbon nanotubes and single-walled carbon nanohorns, which form naturally within the laser vaporization plume under certain conditions. Time-resolved, laser spectroscopy and imaging is described to characterize and control the laser vaporization synthesis process. The growth conditions of single-walled carbon nanotubes by laser vaporization is described, and compared with that for single-walled carbon nanohorns. Optimization of the growth conditions is essential to produce nanomaterials which may be highly purified. This is contrasted with chemical vapor deposition of carbon nanotubes which are grown oriented from predeposited metal catalyst on substrates. Laser diagnostics are described which permit the first direct kinetics measurements of nanotube growth by chemical vapor deposition, understanding of the growth process, and control of nanotube length and wall number. Through these diagnostic techniques, both highly-purified loose nanomaterials or oriented nanotubes on substrates may be obtained to

* To whom correspondence should be addressed. David B. Geohegan, CMSD, Oak Ridge National Laboratory, Oak Ridge, Tennessee 37831-6056; E-mail: geohegandb@ornl.gov

J.J. Dubowski and S. Tanev (eds.), Photon-based Nanoscience and Nanobiotechnology, 205–223.

take advantage of the unique properties of nanomaterials as multifunctional nanocomposites and biological nanovectors.

Keywords: Nanotube, nanohorn, laser vaporization, nanocomposite, nanovector, chemical vapor deposition, laser spectroscopy

1. Introduction

Nanomaterials hold great promise for biological applications in magnetic resonance imaging, drug delivery, fluorescent probes, and cancer treatment "nanovectors" which can be tailored to penetrate cells to simultaneously deliver therapeutic agents with response to external stimuli.[1] For example, some single-wall carbon nanotubes are highly absorptive in the infrared region of the spectrum. Through chemical functionalization with a folate moiety, they have been shown to selectively enter cancer cells and allow these cells to be selectively killed through infrared heating.[2]

With diameters variable from one to several nanometers, and lengths from nanometers to millimeters, carbon nanotubes appear poised to satisfy multiple functionalities by filling their internal spaces, decorating their external ends, and decorating their walls. As hollow carbon materials, they promise biocompatibility while protecting their inner payload. As schematically outlined in Figure 1, nanotubes naturally form bundles via their natural strong attraction via the van der Waals force, so combining nanotubes filled with quantum dots, drugs, or fluorophores should be chemically feasible with a variety of combinations. End-functionalized and sidewall-functionalized nanotubes offer mechanisms of tethering these assemblies to surfaces, or alternatively, penetrating cellular membranes.

However, as also indicated in Figure 1(d,e), building blocks consisting of well-characterized and purified nanotube segments need first be synthesized with controlled length, diameter, number of walls, and electronic properties. The type and quantity of wall defects is also crucial to their processability and chemical functionalization. Methods of purification and solubilization must be developed to prepare as-synthesized nanomaterials for use in biology.

Lasers are enabling tools in nanoscience, both for synthesis and for remote characterization of nanomaterials. Here we explore the use of lasers for both purposes simultaneously – to synthesize unique nanomaterials while remotely characterizing their growth environment and properties. Laser vaporization techniques are described to form nanoparticles, single-wall carbon nanotubes, and single-wall carbon nanohorns which have applications in biology. Laser spectroscopy and imaging techniques are

also described which provide real-time diagnostic information about their growth environment in order to understand how they grow – and how growth may be controlled for specified length, diameter, and properties. The first direct growth kinetics of carbon nanotubes grown by chemical vapor deposition using time-resolved laser interferometry are also described. These techniques are general, and may be applied to the growth of nanowires of many materials – growing both in the gas-phase within a tube furnace, or aligned vertically on substrates.

These measurements and techniques represent important first steps toward controllable laser synthesis of nanomaterials with pre-designed properties.

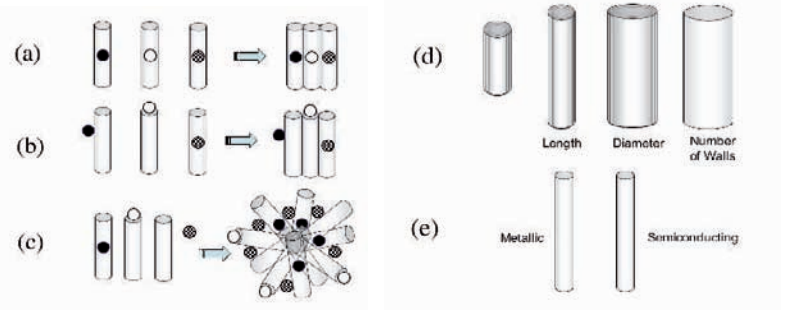

Figure 1. Concepts for biovectors from chemically-functionalized nanotube segments. (a) nanotubes filled with clusters or nanoparticles of different types may be combined in solution to form aggregates with multiple functionality (e.g. fluorescent tags, MRI contrast imaging agents, drugs, etc.). (b) Side-functionalized, end-functionalized, and filled nanotube segments may be similarly used. (c) Aggregates may also be decorated utilizing their interstitial sites. (d) Nanotubes with different lengths, diameters, number of walls are required as functional building blocks. (e) Metallic and semiconducting single-wall carbon nanotubes add additional opportunities and complexity to concepts for biovectors based upon their properties.

2. Laser Synthesis of Nanomaterials Utilizing in Situ Diagnostics

2.1. NANOPARTICLES

A great variety of nanoparticles may be synthesized by laser ablation of targets into background gases or liquids. The advantages are similar to those for pulsed laser deposition of thin films.[3] A solid target is laser vaporized using a pulse of light into atoms and molecules within a hot laser plasma. This material interacts with a background gas and condenses into

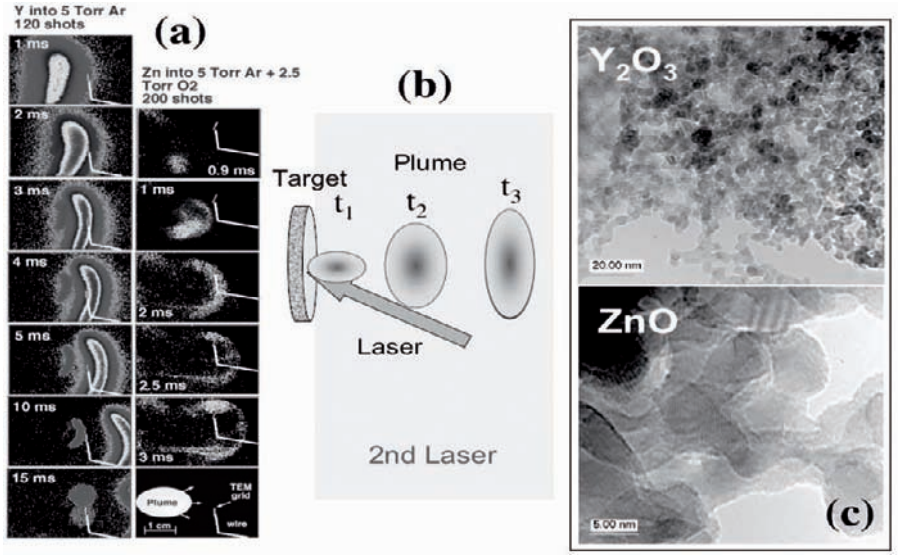

Figure 2. Nanoparticle synthesis by laser vaporization of solid targets into room-temperature background gases is captured via laser-induced fluorescence of oxide molecules and laser-induced photoluminescence of nanoparticles themselves utilizing a second, time-delayed 308-nm laser. A gated, intensified CCD-array camera records the intensity of the luminescence within typically 20 ns time intervals starting at the times indicated. As indicated in (a) and (b), laser ablation of a solid target results in an outwardly-expanding plume of atoms and molecules which condense into nanoparticles at a given position from the target and time after the laser pulse. As shown for zinc ablation into Ar/O_2 , the luminescence from ZnO nanoparticles can suddenly appear at a particular distance from the target and time after the laser pulse. A TEM grid positioned at different points in the chamber samples the plume as it passes. High resolution TEM micrographs confirms that the particles are crystalline, with lattice spacings corresponding to yttrium oxide and zinc oxide. Such *in situ* diagnostics are used to tune the synthesis conditions for nanoparticles to produce different size distributions.

nanoparticles. The virtues of this technique are that very high purity targets can be used, the nanoparticles which are formed typically reproduce the exact stoichiometry of the target, and the nanoparticle formation can occur within a highly-pure background gas. Thus, nanoparticles of complex stoichiometry can be formed without the need for chemical surfactants or solvents, which typically are very hard to completely purify. The interactions of laser plasmas with background gases are complex; however they can be understood through the use of *in situ* plasma diagnostic techniques.[4]

As shown in Figure 2, gated intensified-CCD array (ICCD) photography can be used to provide snapshots of the laser synthesis process. The images in Fig. 2(a) were obtained by first supplying a 2 J/cm^2

pulse of 248-nm laser light onto a solid target to create the plume of ejected material, then triggering a time-delayed pulse of 308-nm light from a 2nd laser which was formed into a sheet beam. The entire visible spectrum of light induced by this second laser pulse was then recorded utilizing the ICCD camera at different time delays. In the case of Y ablation into 5 Torr Ar, bright emission from YO dominates the images (the 5 ppm of oxygen within the argon responsible for its formation). A weaker region of luminescence is also observed, and appears to originate between 3 and 4 ms after laser ablation. This region appears to correspond to luminescence from Y_2O_3 nanoparticles.

A small grid used for TEM specimens was mounted in the chamber as shown in Figure 2(a) to sample material responsible for this region of luminescence. Crystalline nanoparticles of Y_2O_3 and ZnO are found. In the case of ZnO ablation into Ar/O_2 only the photoluminescence from nanoparticles of ZnO is observed in the images. Thus, synthesis of photoluminescent nanoparticles may be directly optimized *in situ* utilizing laser excitation, spectroscopy, and imaging in combination with *ex situ* electron microscopy. Similar measurements were performed to understand the synthesis of photoluminescent SiO_x nanoparticles by laser ablation of Si.[5,6]

2.2. SINGLE-WALL CARBON NANOTUBES

2.2.1. *Synthesis of Nanotubes and Nanowires*

Single-wall carbon nanotubes[7] and a great variety of nanowires[8,9] may be grown by laser vaporization techniques. In general, a composite target containing a primary constituent (e.g. carbon) and a small percentage of metal catalyst which is known to form an alloy with the primary constituent (e.g. Ni, Co, Y, Fe, etc.). Ablation is carried out within a tube furnace set at a temperature near the eutectic temperature of the metal-constituent alloy, and precipitation of nanowires is thought to occur by the vapor-liquid-solid (VLS) mechanism.[8,9]

The general method is diagrammed in Figure 3(a). As seen in time-resolved images of the laser vaporization process [Figure 3(b)], a laser pulse strikes a target resulting in a hot laser plasma which propagates away from the target. This material can be efficiently converted into carbon nanotubes which are found on the walls of the tube furnace downstream of the gas flow. Remarkably, and unlike the growth of nanowires, only single-wall carbon nanotubes (SWNTs) are formed in this process within a small

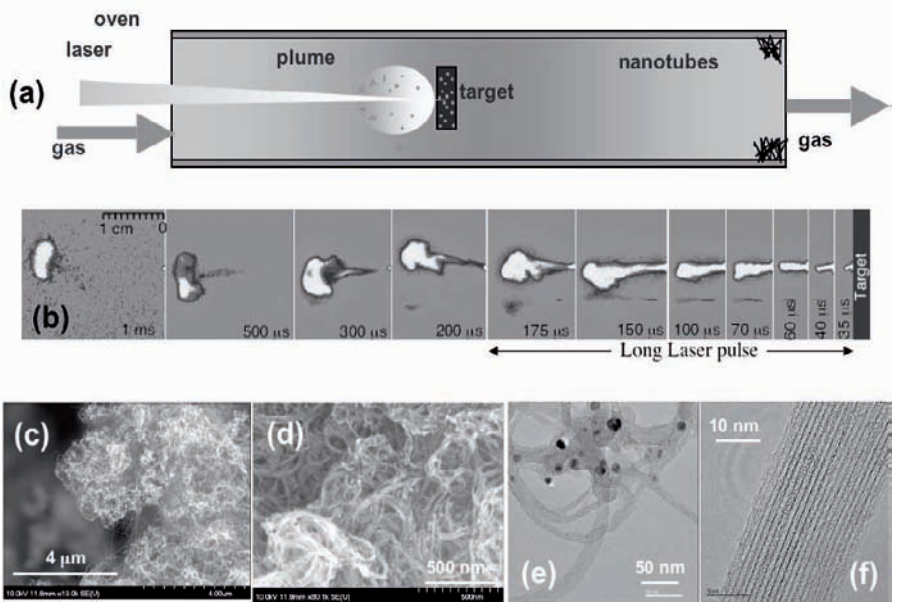

Figure 3. (a) Schematic of single-wall carbon nanotube synthesis by laser vaporization. Laser pulses from nanoseconds to milliseconds duration may be used to efficiently vaporize a target containing 98 at.% C, and 1 at.% Ni and Co. (b) Gated intensified CCD-array images of the laser plasma and subsequent plume propagation into the 1000°C background Ar (500 Torr) reveal that the ejected material is confined to a small volume. Nanotubes are found in dense bundles at the exit of the hot oven as shown in SEM pictures (c) and (d). Remarkably, only single-walled carbon nanotubes are formed. (e) and (f) Transmission electron microscope images show the 1.2-1.4 nm-diameter nanotubes bundled into ropes, consisting about 50% of the product, the remainder being amorphous carbon and metal catalyst nanoparticles of 2-20 nm diameters.

diameter range (1.2–1.4 nm) despite the variety in sizes of the metal nanoparticles observed [2–20 nm, as in Figure 3(e)]. Bundles of SWNTs in high yield may comprise up to 70 wt.% of the product, with amorphous carbon and metal accounting for the rest.

2.2.2. *Laser-Based Diagnostics of SWNT Synthesis*

In order to understand the growth process of single-wall carbon nanotubes by laser vaporization, laser-based imaging and spectroscopy of the plume of material ejected from the target was performed with a windowed tube furnace.

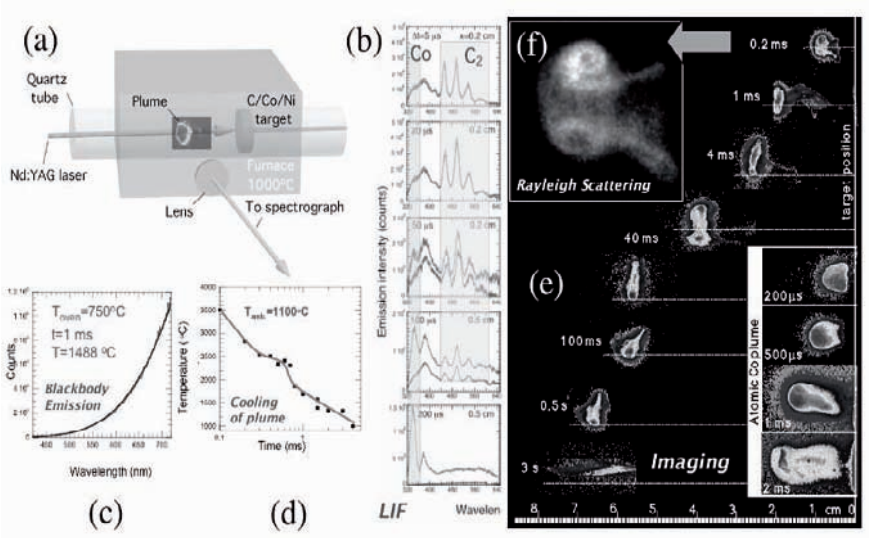

Figure 4. Time-resolved diagnostics of nanomaterials synthesis at high temperatures, applied to a 98% C target with 1% each Co and Ni ablated by an Nd:YAG laser. (a) A windowed tube furnace permits imaging and spectroscopy of the laser vaporized atoms, molecules, and clusters. (b) Emission spectra from excited atoms and molecules in the plume are collected without (lower traces) and with (upper traces) time-delayed excitation using a second laser to excite ground state neutrals in the plume. Here, C_2 is observed to disappear within 0.5 ms after laser ablation, and neutral Co atoms are observed to increase in population as the hot laser plasma recombines during the same period. (c) As clusters and nanoparticles form, blackbody radiation is observed, which can be used to estimate the temperature of the ejecta. (d) These temperature measurements are used to observe that the hot clusters cool to the 1000°C oven temperature within 4 ms after laser ablation. (e) Imaging of the plume at long times is accomplished using gated, intensified CCD-array imaging of the laser-excited clusters to reveal the plume dynamics. The inset shows a color-filtered image to observe laser-excited Co atoms, which confirm that they condense into clusters during 1 ms < t < 2 ms times, after the C in the plume has already converted to clusters. (f) Rayleigh scattering imaging of the plume records scattered light from clusters and nanoparticles induced by the second, time-delayed laser pulse, here revealing that the ejecta are trapped within vortices caused by the plume expansion.

A variety of techniques were used, for different purposes:

- Gated ICCD imaging using a time-delayed, second laser pulse
  Position and dynamics of the ejected material
- Laser-induced fluorescence spectroscopy
  Composition of the plume, excitation of ground state neutrals.

- Blackbody emission spectroscopy, laser induced incandescence
  Temperature of the ejecta, cooling rates
- Rayleigh scattering imaging, optical absorption spectroscopy
  Nanoparticle detection and size estimation

Typical data for such measurements is presented in Figure 4. These diagnostics permitted a comprehensive study of the SWNT growth environment to be performed by time-resolved growth experiments.[10–13]

For different laser fluences, gas flows, and background gas pressures, the dynamics of the plume vary considerably. First, gated imaging of the plume dynamics is performed on separate laser pulses. The process is highly repeatable, permitting assembly of a representative sequence of images from different laser shots as shown in Figure 4(e). Initially (for ~ 0.2 ms after ablation) a hot laser plasma emits light from excited atoms and molecules. After this time, a second laser is then required to induce luminescence from the plume—either laser-induced fluorescence (LIF) from ground-state atoms or molecules, or laser-induced incandescence (LII) from clusters or nanoparticles.

Laser-induced fluorescence is valuable to locate the *ground state* atoms and molecules in the plume. When combined with gated ICCD imaging, it can reveal the spatial profiles of the different constituents in the laser plume. For example, in Figure 4(e) a comparison of the 1 ms images for the overall plume and the atomic Co LIF-image (obtained by placing a spectral filter in front of the ICCD camera to selectively image light from excited Co* atoms) reveals that the majority of material in the plume has condensed into a vortex ring while the atomic Co has yet to condense, and remains within a uniform ball-shaped cloud. At $t = 2$ ms, both LIF spectroscopy and imaging reveal that the atomic Co is disappearing as Co atoms form Co clusters and nanoparticles.

As clusters grow into nanoparticles, Rayleigh scattering may be used to observe them directly, as shown in Figure 4(f). Here, the ICCD-camera is gated to overlap the second, time-delayed laser pulse and promptly-scattered light is captured at the wavelength of the second laser. The magnitude of the Rayleigh scattered signal can be used to estimate the size and density of nanoparticles in the plume.

Meanwhile, the temperature of the plume can be estimated using blackbody emission spectra from the hot clusters, as indicated in Figure 4(c). Glowing clusters radiating intensities greater than that of the glow of the oven can be discerned, and the plume can be followed in space and time using ICCD-imaging to measure its temperature by LII as it propagates. As shown in Figure 4(d), this yields a cooling rate for the plume.

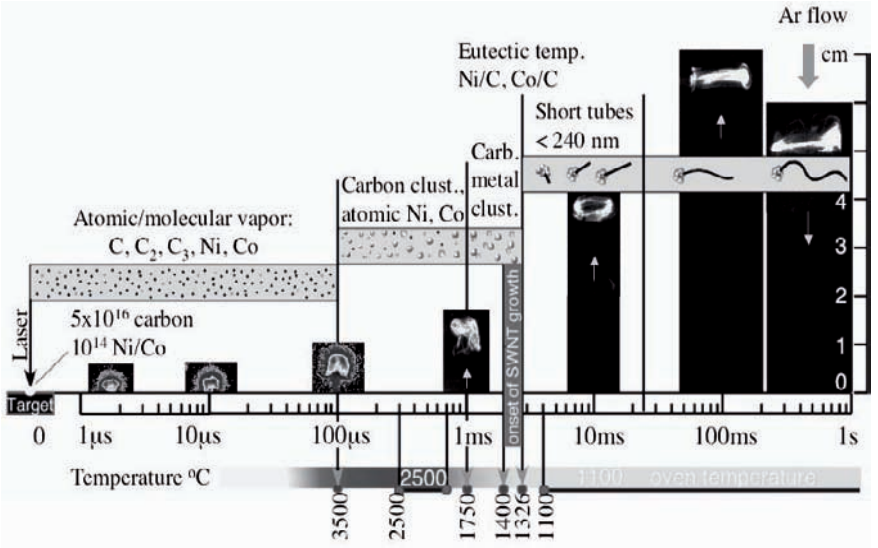

Figure 5. Summary of results from laser-based diagnostics of single-wall carbon nanotube synthesis by laser vaporization of C/Ni/Co (98:1:1) targets into 500 Torr Ar within a hot tube furnace, summarizing the data of the type shown in Figure 2 as well as HRTEM analyses of materials collected in time-resolved growth experiments. The laser strikes the target at t = 0, and images of the plume expanding away from the target are shown at the indicated times (see cm-scale at right). Emission and LIF spectroscopy indicate that only atoms and molecules are ejected from the target. The diagnostics reveal that condensation of C begins at ~ t = 100 μs, and the majority of C is in cluster form by t = 0.5 ms. However the metal atoms begin to condense much later, when plume temperatures of ~ 1750 °C are measured. Thus, metal nanoparticles form after carbon clusters. The onset of nanotube nucleation is inferred from these measurements, and from time-resolved growth collections (where plumes were ejected and collected from the hot oven after well-defined times at high temperatures). Only short nanotubes are collected after t = 20 ms growth times.[12,13] Growth rate estimations from these experiments indicate that the great majority of nanotube growth to microns lengths occurs over extended times at rates of 1-5 μm/s, from a feedstock of *condensed phase* clusters and nanoparticles.

In summary, the combination of ICCD-imaging, LIF-, blackbody-, and LII- spectroscopies, and Rayleigh scattering imaging can be combined to provide a comprehensive picture of the ejected material as it evolves from atoms and molecules into nanoparticles and nanotubes.

2.2.3. *Summary of SWNT Synthesis and Diagnostics*

The synthesis of single-wall carbon nanotubes by laser vaporization is summarized in Figure 5 which plots the temperature and composition of the plume deduced from the spectroscopic diagnostics on a logarithmic plot of

the time, along with representative ICCD-images of the plume position and shape. During the first 100 μs, the laser plasma is extremely hot (> 3500°C) and propagates approximately 1 cm from the target through 500 Torr Ar gas (at 1000°C).

Only atoms and molecules (C, C_2, C_3, Ni, and Co) are observed and no molten particulates are observed emanating from the target. During the next 100 μs, the C_2 and C_3 in the plume disappear and clusters become visible by Rayleigh scattering, indicating that the carbon has condensed into clusters. The trapping of the clusters into vortex rings is observed, consistent with these observations. During the period to Δt = 1 ms, the metal ground state population rises with the temperature of the plume too high to allow condensation of the metal vapor. After Δt = 1 ms, the metal atom populations are observed to decrease and the species-resolved images show a similar conversion from uniform clouds into vortex-trapped nanoparticles. At t ~ 2 ms, the material in the plume is apparently all condensed and the temperature of the plume is very close to the eutectic temperature for Ni/C and Co/C alloys – the natural temperature for SWNT nucleation according to expectations based upon the VLS mechanism. It is here that the onset of SWNT nucleation is thought to begin.

After this time, and for the next 20 milliseconds, the plume travels from d = 2 cm to d = 4 cm in the shape of a vortex ring with all the condensed clusters and nanoparticles confined by the vortex hydrodynamics to a small volume. Utilizing ICCD imaging and adjustment of the target position, it was possible to adjust the time spent by the plume inside the high temperature region of the tube furnace before. Following this time period the plume exited the furnace, rapidly quenched the temperature of the material within the vortex ring. HRTEM micrographs of the collected material revealed only very short (< 240 nm-long) SWNTs for 20 ms growth times. Further experiments with longer growth times followed the progression in length and allowed growth rates to be estimated in the range of 1–5 microns/s.[12,13]

The conclusions from these measurements are striking. First, the great majority of nanotube growth does not occur during the period of maximum plume density, but after the plume has expanded far from the target. At these positions, times, and temperatures, nearly all of the material is in the form of clusters and nanoparticles. Therefore, SWNT growth occurs from interactions between *condensed phase* materials. Lastly, growth occurs at microns/second rates.

These measurements and conclusions have implications for strategies involving doping of nanotubes during growth, for methods of production of short, size-selected nanotube seeds, and for manufacturing methods utilizing condensed phase conversion. In experiments designed to test these

implications, short SWNT 'seeds' were produced by laser vaporization and were collected, then laser-annealed at various temperatures. Much longer SWNTs were observed to grow from the annealed mixture of SWNT seeds and unconverted carbon, indicating that condensed phase growth was indeed a mechanism for SWNT synthesis.[12]

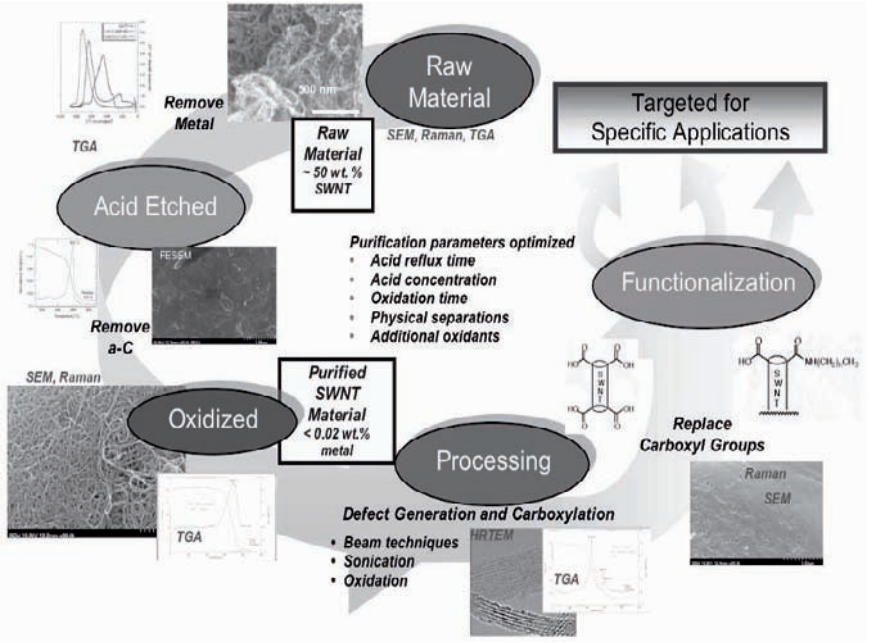

Figure 6. Purification and functionalization processes for loose single-wall carbon nanotubes synthesized by laser vaporization at Oak Ridge National Laboratory. Raw material containing ~50 wt.% SWNTs undergoes acid etching to remove metal impurities, and oxidative treatments to remove amorphous carbon. Extremely high SWNT purities may be obtained (<0.02 wt.% metal) through careful analysis by TGA, Raman, optical absorption spectroscopy, and SEM through repeated treatments. Defect generation processing and chemical functionalization reactions are used to introduce end or sidewall chemical groups in order to attach the nanotubes to specific materials for specific applications.

2.2.4. *Purification of Single-Wall Carbon Nanotubes*

Loose single-wall carbon nanotubes must be chemically purified and functionalized prior to use in applications. Figure 6 outlines the main processes utilized at Oak Ridge National Laboratory. It is important to note that the laser vaporization conditions during synthesis affect the treatments and ultimate purifiability of the material. The yield of SWNTs vs.

amorphous carbon in the laser-produced raw material is sensitive to the laser parameters, oven temperature, gas flow, and other processing parameters. An initial thermogravimetric analysis (TGA) is interpreted to understand the oxidative temperatures to burn amorphous carbon, isolated nanotubes, and nanotubes in the proximity of catalyst nanoparticles. Second, the raw material undergoes acid etching in refluxed nitric acid for 12–16 hours to remove the majority of metal nanoparticles.

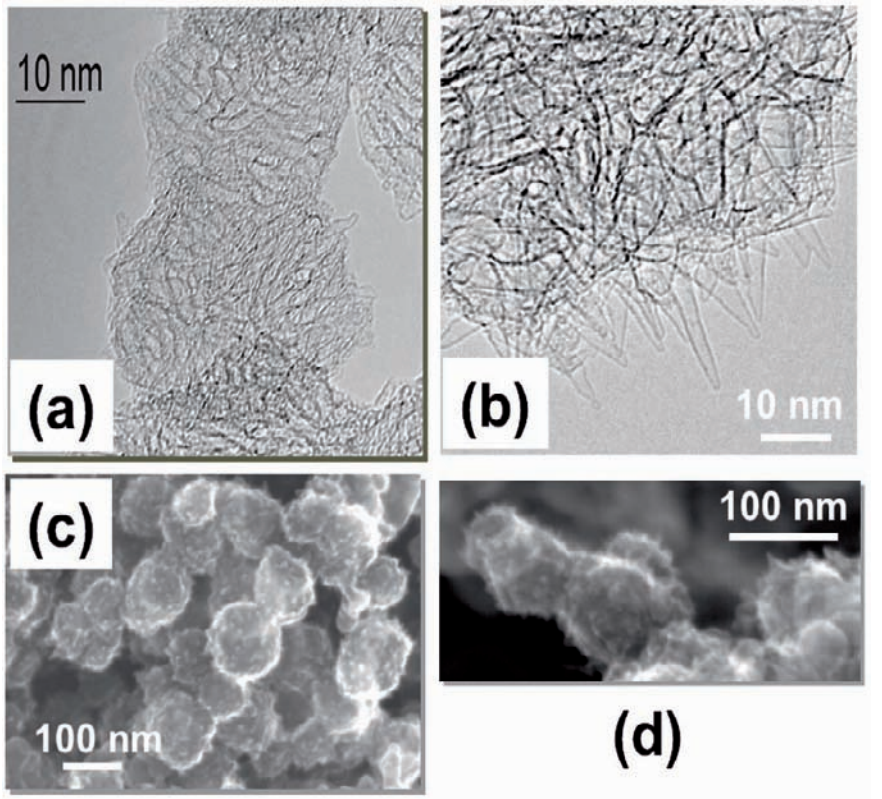

Figure 7. Single-wall carbon nanohorn aggregates produced by laser vaporization at ORNL. Nanohorns are closed, hollow, single-wall carbon nanostructures approximately 2.5 nm in diameter, and up to 20 nm long. Their aggregates form roughly spherical particles ranging up to 150 nm in diameter. (a) Smaller "bud-type" aggregates are comprised of short nanohorns, while (b) longer nanohorns protrude extended distances from longer aggregates. (c) and (d) SEM images of nanohorn aggregates reveal the sharp, protruding nanohorns.

Third, after another TGA analysis, the material is oxidized in air at a temperature chosen to selectively burn amorphous carbon while leaving the more robust (crystalline) carbon in the nanotubes. Optical absorption spectroscopy, Raman spectroscopy, TGA analysis, and ICP are used to

assess the purity of the material. Using these techniques, SWNTs have been purified to extremely high levels (< 0.02 wt.% metal). The assessment for purity vs. amorphous carbon is still a protocol which has not been agreed upon internationally.

The purification process tends to consume nanotubes which have wall defects. Hence, for chemical functionality, defects must be introduced in order to permit chemical groups to be attached to the ends or sidewalls for various applications.

2.3. SINGLE-WALL CARBON NANOHORNS

Single-wall carbon nanohorns are a remarkable example of the importance of laser conditions on nanomaterial production. Since the discovery of SWNTs, the desire to produce larger quantities by laser vaporization or electric arc production necessitated the use of higher power lasers. However, upgrading lasers with average powers of Watts to kiloWatts resulted in an unexpected finding, the discovery of single-wall carbon nanohorns (SWNHs).[14]

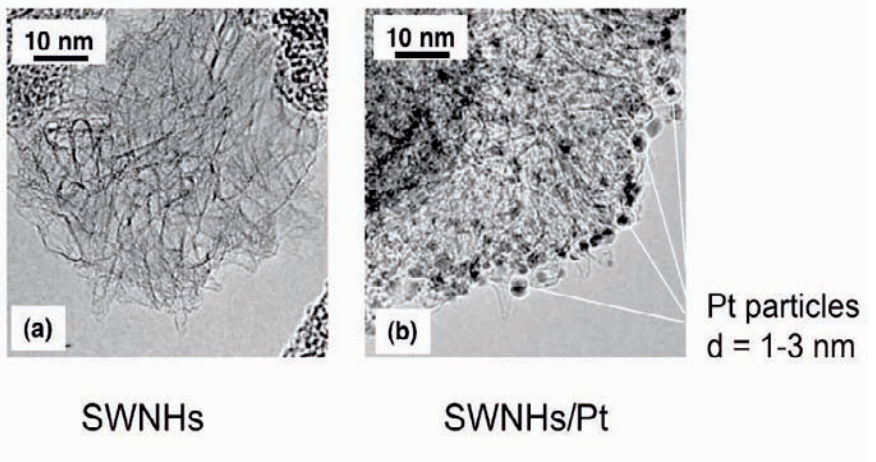

Figure 8. Single-wall carbon nanohorn aggregates (a) of pure carbon (b) decorated externally with platinum nanoparticles of average diameter 1 to 3 nanomaters in size. Nanohorns are closed single-wall carbon nanostructures approximately 2.5 nm in diameter, and up to 20 nm long. Their aggregates permit metallic nanoparticle decoration at high densities while limiting their aggregation.

SWNHs are single-wall carbon tubules like nanotubes, but are irregular in shape with closed conical ends. Their individual lengths are estimated at ~ 20 nm, their diameters are approximately 2.5 nm, and they are found in ball-shaped aggregates of roughly 50-100nm in diameter. Figure 7 shows

SWNHs formed by laser vaporization with a 600W Nd:YAG laser utilizing 20 ms pulses of ~ 90J/pulse at 5 Hz at an oven temperature of 1100°C.

SWNHs are synthesized *without* the use of a metal catalyst. They can be formed in very high yield (up to 95% pure).[15] How do they form? Their formation process is poorly understood; however extended times spent at high temperatures within the laser plume itself appear required to form these novel nanomaterials. Long laser pulse lengths in the milliseconds regime, coupled with high laser energies, supply enough time and temperature for the nanohorns to grow without the aid of a metal catalyst. Revised laser spectroscopic and imaging diagnostic techniques must be employed to probe within long laser pulses to ascertain the formation mechanisms of these and other nanomaterials formed rapidly at very high temperatures.

2.3.1. *Decoration of SWNHs with Nanoparticles*

In contrast to SWNTs, SWNHs exhibit a rich number of wall defects and interstitial sites to enable chemical decoration. Figure 8 shows as-produced SWNHs and SWNHs decorated with Pt nanoparticles. The rough morphology of the nanohorn surface limits aggregation of these nanoparticles and provides rich sites for connections between these nanoparticles and other moieties. For example, Zhu et al. coupled amine-functionalized iron oxide magnetic nanoparticles to SWNHs to selectively recognize different peptides.[16]

3. Chemical Vapor Deposition of Vertically-aligned Nanotube Arrays

Laser-based diagnostics have also recently been applied to understand and control the growth of carbon nanotubes by chemical vapor deposition (CVD), providing some of the first direct kinetics measurements and growth rates measured *in situ*.[17,18] During CVD of carbon nanotubes or other nanomaterials, metal catalyst nanoparticles are often predeposited onto substrates to serve as sites for nucleation and growth.

As shown in Figure 9(a), nanoparticles may be formed in high surface areal densities by the natural roughening of an evaporated metal film multilayer at high temperatures. Ideally, uniform particle sizes and high nucleation site density produce a uniform array of carbon nanotubes when a hot gas mixture containing hydrocarbons is passed over the substrate.

The nanotubes align perpendicular to the substrate by crowding. The metal film can be patterned into lines, dots, or functional structures (such as coil patterns) for sensor applications. Regions as small as 200 nm in diameter still result in aligned nanotube posts.

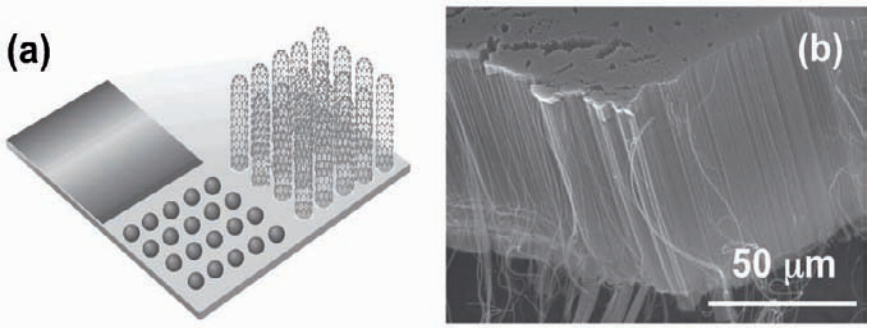

Figure 9. (a) Schematic of chemical vapor deposition (CVD) growth of aligned nanotube arrays. A thin film catalyst is deposited (usually 10 nm of Al as a buffer layer on Si, then ~ 1 nm of Fe as catalyst, and sometimes ~ 0.2 nm of Mo as a mixed catalyst). During heating in a tube furnace to 550–950°C in Ar/H_2 mixtures, the catalyst film roughens into nanoparticles. A mixture of hydrogen, argon and acetylene is then introduced (or another hydrocarbon such as methane, ethylene, etc.) and nanotubes nucleate and grow from the metal catalyst nanoparticles to form dense, self-aligned arrays. (b) SEM micrograph of a cleaved VANTA (vertically-aligned nanotube array). The Si wafer is at the bottom, and the top of the array indicates the porous nature of the block of continuous nanotubes. Most VANTAs are < 10 vol.% dense.

Detailed examination of SEM micrographs such as shown in Figure 9(b) imply that the nanotubes are continuous from top to bottom of the array and grow in a coordinated fashion, producing a flat top surface. In most cases for multiwall and single-wall carbon nanotube arrays, the catalyst particle remains attached to the substrate during growth. The mechanism(s) responsible for the coordinated growth of these structures is not completely understood.

In order to understand the growth of carbon nanotubes in vertically-aligned nanotube arrays (VANTAs) laser reflectometry was employed, as shown in Figure 10(a). A HeNe laser beam reflects from the metal-coated Si wafer and the intensity of the laser is monitored on a photodiode. During the ramp-up in oven temperature, the Al underlayer of the film (~10 nm) oxidizes along with the Fe metal catalyst. Partial reduction of the catalyst using hydrogen/argon mixtures is used to prepare the surface for nanotube growth, and the temperature is stabilized for several minutes before a hydrocarbon mixture (typically containing acetylene) is introduced. After a constant time delay for the hydrocarbon gas mixture to flow to the substrate, nanotubes nucleate and begin to grow as evidenced by the attenuation of the laser intensity. The photodiode signal then typically displays a series of fringes, which correspond to increments in length of the VANTA. As indicated in Figure 10(b), the growth may be stopped after different numbers of fringes to yield nanotube arrays of controlled length.[17]

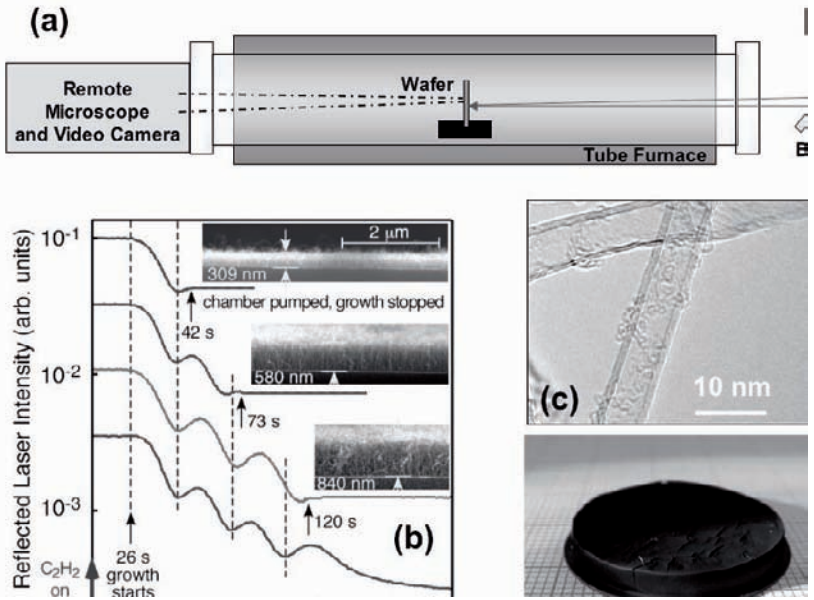

Figure 10. (a) Schematic of apparatus used for direct, *in situ* measurement of carbon nanotube growth kinetics. A CW-HeNe laser beam is reflected from a vertically-standing substrate through the end window of a tube furnace. A remote microscope and video camera may be used from the opposite window to record growth to millimeters lengths. (b) As the nanotubes begin to grow, the HeNe laser beam is reflected from both the metallized Si substrate and the top of the growing nanotube array, resulting in Fabry-Perot interference fringes measured at the detector (in addition to signal attenuation due to absorption). The fringes can be used to control the length of the nanotube arrays, as indicated in the 3 stop-growth experiments plotted. (c) A HRTEM of just one of the nanotubes in the array, showing 3-walls and a diameter of 8 nm for growth at 730°C. (d) 3-mm-tall VANTA array grown through optimization of the growth conditions.

The number of walls of the nanotubes within the arrays varies with growth temperature. Thus the optical properties of arrays grown at different temperatures are different, and must be calibrated to account for the different amount of carbon per nanotube. In general, the number of walls of the nanotubes in the VANTAs decreases with increasing growth rate (which maximizes at ~730°C for acetylene). Few-walled nanotube arrays comprising a very high fraction of SWNTs may be grown.

The kinetics of growth revealed by this technique are fascinating. For the first time, the initial growth rate, sustained growth rate, and termination of growth may be measured directly within a single growth run. As shown in Figure 11, VANTAs typically start growing at a high rate, then the growth slows and terminates. The mechanisms responsible for the

termination of growth include various catalyst poisoning processes which are the subject of much debate.

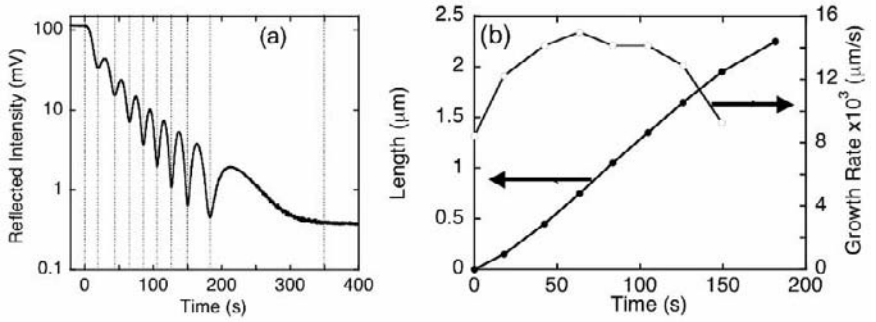

Figure 11. (a) Reflected light intensity during CVD. The fringe positions serve as fiducial markers to directly measure the length of the VANTA array throughout growth. (b) Length vs. time data, and calculated growth rate vs. time for each time interval, plotted for the data in (a). Absolute growth rates provide information on growth kinetics, catalyst poisoning, and optimization of flow and temperature conditions for rapid or sustained growth.

Through *in situ* kinetics measurement experiments in which the temperature, gas flow, and hydrocarbon concentration were varied, a kinetics model was developed to fit the measured growth rates and terminal lengths of the VANTAs. Activation energies for the different processes were determined, and the optimal growth conditions to produce long nanotube arrays were predicted.[18]

4. Summary and Conclusions

Methods to controllably synthesize nanomaterials and understand how they grow have been developed utilizing laser-based spectroscopy and imaging. Such understanding is crucial to prepare nanomaterials with well-specified length, diameter, and purity for biological and other applications. These tools are providing some of the only direct measurements of growth rates and kinetics, which are essential to understand growth mechanisms and current limitations, and paths forward to produce new nanomaterials with predictable properties.

This paper has concentrated upon carbon nanostructures grown by laser vaporization and chemical vapor deposition, where growth rates for each process have been measured. The growth mechanisms for the two processes appear quite different. For SWNTs synthesized by laser vaporization (LV), the plume cools from extremely high (~4000 K)

temperatures where metal vapors condense and metal nanoparticles pass through a liquid state. In this case, SWNTs grow from the conversion of condensed phase clusters and nanoparticles of carbon at an optimum temperature of ~1150°C. Remarkably, a very narrow range of nanotube diameters is produced (1.2 – 1.4 nm) and all nanotubes are single-wall. By contrast, during CVD growth of nanotube arrays, optimal growth proceeds at 700°C from a hydrocarbon gas where it is difficult to imagine a molten metal catalyst nanoparticle. In CVD, most nanotubes are multiwall and it is difficult to grow pure SWNTs or control their diameters to a narrow range. In both LV and CVD growth of nanotubes, we find ~ micron/second growth rates.

There is still much to learn about these two widely varying processes for nanotube synthesis. The high-yield, LV synthesis of single-wall carbon nanohorns (SWNHs) without the need of a metal catalyst illustrates this point since the synthesis conditions for LV-SWNT and LV-SWNH are so similar.

The techniques presented here apply to the synthesis of nanoparticles and nanowires of many other materials relevant to biological applications, where high-purity and well-specified properties must be delivered reproducibly.

Acknowledgements

Research sponsored by the Division of Materials Sciences and Engineering, Office of Basic Energy Sciences, U.S. Department of Energy, under contract DE-AC05-00OR22725 with Oak Ridge National Laboratory, managed and operated by UT-Battelle, LLC. Portions of this research were conducted by staff and postdoctoral scholars at the Center for Nanophase Materials Sciences, which is sponsored at Oak Ridge National Laboratory by the Division of Scientific User Facilities, U.S. Department of Energy. Funding for research on carbon nanohorn synthesis for hydrogen storage was provided by the US Department of Energy's Office of Energy Efficiency and Renewable Energy within the Center of Excellence on Carbon-based Hydrogen Storage Materials.

References

1. M. Ferrari, Cancer Nanotechnology: Opportunities and Challenges, *Nat. Rev. Cancer* 5(3), 161–171 (2005).

2. N. W. S. Kam, M. O'Connell, J. A. Wisdom, and H. Dai, Carbon Nanotubes as Multifunctional Biological Transporters and Near-Infrared Agents for Selective Cancer Cell Destruction, *PNAS* 102(33), 11600–11605 (2005).
3. D. B. Chrisey and G. K. Hubler (editors), Pulsed Laser Deposition of Thin Films (Wiley, New York, 1994).
4. D. B. Geohegan, Ch. 4, Ibid.
5. D. B. Geohegan, A. A. Puretzky, G. Duscher, and S. J. Pennycook, Time-Resolved Imaging of Gas Phase Nanoparticle Synthesis by Laser Ablation, *Appl. Phys. Lett.* 72, 2987–2989 (1998).
6. D. B. Geohegan, A. A. Puretzky, G. Duscher, and S. J. Pennycook, Photoluminescence from Gas-Suspended SiO_x Nanoparticles Synthesized by Laser Ablation, *Appl. Phys. Lett.*73, 438–440 (1998).
7. A. Thess, R. Lee, P. Nikolaev, H. Dai, P. Petit, J. Robert, C. Xu, Y. H. Lee, S. G. Kim, A. G. Rinzler, D. T. Colbert, G. E. Scuseria, D. Tomanek, J. E. Fischer, and R. E. Smalley, Crystalline Ropes of Metallic Carbon Nanotubes, *Science* 273(5274), 483–487 (1996).
8. A. M. Morales and C. M. Lieber, A Laser Ablation Method for the Synthesis of Crystalline Semiconductor Nanowires, *Science* 279(5348), 208–211 (1998).
9. X. Duan and C. M. Lieber, Synthesis of Compound Semiconductor Nanowires, *Adv. Mater.* 12(4) 298–302 (2000).
10. A. A. Puretzky, D. B. Geohegan, X. Fan, and S. J. Pennycook, In situ Imaging and Spectroscopy of Single-Wall Carbon Nanotube Synthesis by Laser Vaporization, *Appl. Phys. Lett.* 76, 182–184 (2000).
11. A. A. Puretzky, D. B. Geohegan, X. Fan, and S. J. Pennycook, Dynamics of Single-Wall Carbon Nanotube Synthesis by Laser Vaporization, *Appl. Phys. A* 70, 153–160 (2000).
12. D. B. Geohegan, H. Schittenhelm, X. Fan and S. J. Pennycook, Condensed Phase Growth of Single-Wall Carbon Nanotubes from Laser Annealed Nanoparticulates, *Appl. Phys. Lett.* 78(21), 3307–3309 (2001).
13. A. A. Puretzky, H. Schittenhelm, X. Fan, M. J. Lance, L. F. Allard, and D. B. Geohegan, Investigations of Single-Wall Carbon Nanotube Growth by Time-Restricted Laser Vaporization, *Phys. Rev. B, Condens. Matter Mater. Phys*. 65, 245425/1 (2002).
14. S. Iijima, M. Yudasaka, R. Yamada, S. Bandow, K. Suenaga, F. Kokai, and K. Takahashi, Nano-Aggregates of Single-Walled Graphitic Carbon Nano-Horns, *Chem. Phys. Lett.* 309, 165–170 (1999).
15. D. Kasuya, M. Yudasaka, K. Takahashi, F. Kokai, and S. Iijima, Selective Production of Single-Wall Carbon Nanohorn Aggregates and Their Formation Mechanism, *J. Phys. Chem. B* 106, 4947–4951 (2002).
16. J. Zhu, D. Kase, K. Shiba, D. Kasuya, M. Yudasaka, and S. Lijima, Binary Nanomaterials Based on Nanocarbons: A Case for Probing Carbon Nanohorns' Biorecognition Properties, *Nano Letters*, 3(8), 1033–1036 (2003).
17. D. B. Geohegan, A. A. Puretzky, I. N. Ivanov, S. Jesse, G. Eres, and J. Y. Howe, In situ Growth Rate Measurements and Length Control During Chemical Vapor Deposition of Vertically Aligned Multiwall Carbon Nanotubes, *Appl. Phys. Lett.* 83(9), 1851–1853 (2003).
18. A. A. Puretzky, D. B. Geohegan, S. Jesse, I. N. Ivanov, and G. Eres, In Situ Measurements and Modeling of Carbon Nanotube Array Growth Kinetics During Chemical Vapor Deposition, *Appl. Phys. A, Mater. Sci. Process.* 81(2), 223–240 (2005).

PHOTOPHYSICAL PROCESSES THAT ACTIVATE SELECTIVE CHANGES IN PHOTOSTRUCTURABLE GLASS CERAMIC MATERIAL PROPERTIES

F. E. LIVINGSTON AND H. HELVAJIAN*
Space Materials Laboratory, The Aerospace Corporation, Los Angeles, CA 90009, USA

Abstract. A series of experimental results are presented that investigate the photoactivated changes in photostructurable glass ceramic materials. The results show that by selectively controlling the incident photon irradiance and wavelength, it is possible to have a controllable effect on the material properties after the exposed material has undergone a specific thermal processing protocol. We present the results of optical transmission spectroscopy, X-ray diffraction spectroscopy, and chemical etching to demonstrate the ability to control the optical transmission, material strength and chemical solubility. These results have drawn attention to the need for developing a new methodology for material processing that has high fidelity in the delivery of a specified flux of photons during patterning. We have developed such a methodology and have implemented this approach with a new processing tool. The results are persuasive. Finally, we have applied our experimental results and the understanding of the critical photophysical processes to the development of a glass ceramic propulsion module for a nanosatellite class space vehicle.

Keywords: Photostructurable glass ceramics, photophysics, photo-activation, laser direct-write patterning.

1. Introduction

Novel micro/nanofabrication technologies will facilitate the next generation of integrated-package fabrication of devices in the meso, micro and nano domains. To achieve this next level of device integration, the base structural material must be "engineered" to serve a multifunctional purpose. By this we mean that the "package" must do more than just encapsulate the device: A channel, be it optical, fluidic or electrical must do more than act as a conduit. To enable this advancement, the development of new

* To whom correspondence should be addressed. H. Helvajian, Space Materials Laboratory, MS:M2-241, The Aerospace Corporation, PO Box 92957, Los Angeles, CA, USA.

J.J. Dubowski and S. Tanev (eds.), Photon-based Nanoscience and Nanobiotechnology, 225–265.

materials and processing techniques that can utilize the same base material in a multifunctional sense is required. By implementing photon-based processing and a better understanding of the photochemistry and physics of light-matter interaction, it may be possible to utilize one engineered *base material* but allow it to *express* different properties where it is desired, and thereby enable the co-fabrication of multiple functionalities. This logic lends to the promise of co-fabrication of many operational systems, where each draws function from a different property of the same material and the ensemble unit performs as an integrated system. Such an integrated system, designed around a common base material will further the integration of photonics (i.e., controlling light), bionics (i.e., controlling fluids), wireless communications (i.e., controlling radio frequency (RF) waves), microelectronics (i.e., controlling current) and microelectronmechanical systems, MEMS (i.e., controlling inertial motion).

We desire a class of structural materials where the material properties can be changed through activation via photolytic excitation. Some of the material properties that would be beneficial to alter selectively on a local scale include material strength, optical transmission and index, residual stress, and the chemical solubility and reactivity. A material class that retains some of these attributes is the glass ceramics (GCs), along with a subset class referred to as photostructurable glass ceramics (PSGCs). As a material class, glass is intrinsically metastable with the crystalline form representing the low energy state. Ingredients are added to the base glass ceramic to controllably induce the in situ crystallization in such a manner that the resulting system is nearly polycrystalline. The material properties of the polycrystalline material can differ from that of the amorphous glass, especially with regards to material strength (related to density), optical index (related to density) and chemical solubility (related to chemical order). In the case of the photostructurable glass ceramics, additional dopants are included to further refine the control of the in situ ceramization process. The ability to control the phase transformation process enables the local-scale tailoring of material properties. This can be accomplished by either arresting the crystallization process midstream (e.g., rapid cooling) or by establishing a set of initial conditions that alter the phase transformation pathway. As a processing tool, lasers and especially pulsed lasers are uniquely suited for inducing local transient excitation (thermal or non-thermal) and thereby enabling the tailoring of material properties patchwork-quilt style. Beyond their usefulness in applications that span a wide range of industries, glass and glass ceramics are also a convenient medium for fundamental studies in induced phase transformation since atomic rearrangements in viscous liquids occur relatively slowly and can potentially be investigated in a time-resolved manner.

In this chapter we present the concept of a multifunctional material and use the PSGC material class as a model system. In these systems, certain material properties can be *expressed* or altered by way of laser excitation and through the use of laser direct-write patterning we have been able to locally alter the material chemical solubility, the optical transmission and, over a small region, the material strength. This chapter is delineated into seven sections. Section 1 presents the motivation and the need for multifunctional materials. Section 2 presents an overview of glass ceramic and photostructurable glass ceramic materials. Section 3 presents the results of our measurements and the need for an approach to optimize the controlled delivery of photons regardless of patterning motion. Section 4 presents a process for the controlled delivery of photon-doses with high fidelity to a surface regardless of patterning velocity: Digitally-Scripted Genotype Sequencing and Electro-Optic Modulation. Section 5 presents a specific application in the use of photostructurable glass ceramics and laser direct-write patterning for the development of a small (<1kg) space nanosatellite propulsion system. Sections 6 and 7 represent the conclusions and acknowledgements, respectively.

2. Glass Ceramics and Photostructurable Glass Ceramics

Glass ceramics are a material class that can be controllably converted to the ceramic phase after molding or shaping. In the final state, the material is a composite of glass (amorphous) and ceramic (crystalline) phases. GC materials are unique material class that combines the special properties of sintered ceramics with the characteristics of glasses. Glass ceramics are manufactured in the amorphous homogenous glass state and can be transformed to a composite material via heat treatment and the subsequent controlled nucleation and crystallization of the glass ceramic constituents. One novelty of the GC material class is the ability to alter the material properties by altering the constituent ingredients and composition to suite a particular application. A common GC example are the pyrocerams that have been widely used in the production of kitchen flatware. Another example that has had wide technological applications is the development of GC materials for hermetic metal-insultor seals for use in electrical connectors and feedthroughs.[1] Other intrigiung GC applications include RF devices, medical technology and architectural features. An uncommon example are the photostructurable glass ceramics which comprise a small subset of the GC class. In the GC materials, the phase transformations occur via the thermal treatment step and the subsequent physical property changes are globally affected. In contrast, the material transformation

process in the PSGC material class can be *locally controlled*. This is accomplished by the addition of a photoexcitation step that permits lithographic techniques to be utilized for patterning. The photoexcitation process establishes the initial conditions that are required for the material transformation and conversion process that occur during the thermal treatment steps. This photochemical process is accomplished by the addition of photo-initiator compounds to the base glass ceramic matrix. The PSGC materials have some advantageous attributes that they share with the GC materials:

- Zero porosity and optical transparency
- Biocompatiblity
- High temperature stability
- Manufactured in a wide range of sizes
- Material can be preshaped and molded
- Lighter than most metals (e.g. Foturan^{TM} 2.4 g/cm^3, Al-2017 2.8 g/cm^3)
- High strength and toughness
- Adaptability to surface mounting of photonics, electronics and RF devices (e.g., ceramic interconnect technologies for multigigabit opto-electronic packaging).

The PSGC materials also have an additional unique attribute that corresponds to the ability to microfabricate two- and three-dimensional ($2D^2$ and $3D^3$) structures with high fidelity via optical lithographic patterning and a chemical etching process. The important fundamental discoveries that occurred in the late 1940s and early 1950s and lead to the development of GC and the PSGC materials are attributed to Donald Stookey of Corning Corporation in the United States.[4] However, significant work and invention, especially on the metallic phosphate GC systems, should be attributed to McMillan and co-workers in Great Britain.[5] Finally, a compilation of research and invention in the former Soviet Union can be found in the work of Berezhnoi.[6]

2.1. PROCESSING OF GLASS CERAMIC AND PHOTOSTRUCTURABLE GLASS CERAMIC MATERIALS

From a processing perspective, both the GC and the PSGC materials can be "engineered" for specific applications by changes in glass composition. In fact, GC materials have been applied beyond the cookware manufacturing

industry and the list includes the aerospace, medical and dental, electrical and electronic, automotive and architectural industries. These materials can be "engineered" for high precision instruments (e.g., optical telescopes) or for high temperature applications (e.g., turbines). Both materials can be molded to the desired shape prior to ceramization. Whereas for the GC material the bulk material properties are globally altered by the bulk ceramization step, in the case of the PSGC material the material properties are locally altered and depend on the photolytic initiation process. The extent of the photolytic activation influences the phase transformation processes occurring during the ceramization step. There is another subtle difference between the GC and PSGC materials that can be used to advantage. In the case of the GC materials, a single bake protocol step governs the in situ growth of the ceramic phase whereas for the PSGC material there are at least two bake protocols that define which ceramic phase is predominantly grown.

2.2. THE PHOTOSTRUCTURABLE GLASS CERAMIC FOTURAN™

The present study utilized a PSGC material obtained from the Schott Corporation under the trade name Foturan™. There have been two other PSGC trade names: Fotoform™ manufactured by Corning Corporation and PEG3™ manufactured by Hoya Corporation. Fotoform and PEG3 are no longer manufactured but have compositional similarity to Foturan. Foturan is an alkali-aluminosilicate glass and consists primarily of silica (SiO_2: 75-85 wt %) along with various stabilizing oxide admixtures, such as Li_2O (7-11 wt%), K_2O and Al_2O_3 (3-6 wt%), Na_2O (1-2 wt%), ZnO (<2 wt%) and Sb_2O_3 (0.2-0.4 wt %). The photoactive component is cerium (0.01-0.04 wt% admixture Ce_2O_3) and the nucleating agent is silver (0.05-0.15 wt% admixture Ag_2O). The photo-initiation process (latent image formation) and subsequent "fixing" of the exposure (permanent image formation) proceed via several generalized steps (Equations 1–3). Upon exposure to actinic radiation λ<~350 nm, the nascent cerium ions are photo-ionized resulting in the formation of trapped electrons with defect electronic state absorptions (Equation 1). These trapped (defect) states correspond to the latent image and have been associated with impurity hole centers and electron color centers. Thermal treatment is then used to convert the latent image into a fixed permanent image. The nucleation process is initiated by the scavenging of the trapped electrons by impurity silver ions as described by Equation 2. During thermal processing, the atomic silver atoms agglomerate to form nanometer-scale Ag clusters as shown in Equation 3. The formation of metallic clusters corresponds to "fixing" of the exposure and permanent image formation in the glass matrix. The formation of the

silver cluster is dictated by the concentration of trapped electrons and silver ions and the nucleation kinetics of both the neutral and ionic silver (Ag^o, Ag^+) species; these processes have been shown to be highly temperature dependent.[7]

$$Ce^{3+} + h\nu \rightarrow Ce^{4+} + e^- \quad (1)$$

$$Ag^+ + e^- + \Delta H \rightarrow Ag^0 \quad (2)$$

$$xAg^0 + \Delta H \rightarrow (Ag^0)_x \quad (3)$$

In Foturan, the intended photosensitizer compound is Ce_2O_3 and is added at concentrations of <0.04 wt%. Cerium has two valence states (3+ and 4+) and it is the Ce^{3+} oxidation state that is UV photoactive[8] and donates a photoelectron.[9] For the silver concentration found in Foturan, the "fixing" temperature is near 500°C and is below the temperature required for crystallization. At higher temperatures, a new crystalline ceramic phase "precipitates" on the silver clusters. This precipitation process is catalyzed when the neutral silver clusters reach a critical size of ~8 nm. There are at least two crystalline ceramic phases that have practical application. These two major ceramic phases can be grown via thermal treatment following a specific protocol. For a 75–85 wt% mixture of SiO_2 and a 7-11 wt% mixture of Li_2O, a lithium metasilicate crystalline phase (LMS; Li_2SiO_3) grows at temperatures near 600°C. The structure is a chain silicate and the crystallization of this compound proceeds dendritically. By reducing the fraction of the silicate to 60.8 mol% and increasing the fraction of Li_2O to 35.6 mol%, the metasilicate phase can be observed at temperatures as low as ~440-500°C. However, homogeneous metasilicate formation at these temperatures requires induction times of ~20 to 150 minutes.[10] At higher temperatures of ~700-800°C, a lithium disilicate (LDS; $Li_2Si_2O_5$) crystalline phase is observed. The LDS crystalline phase is a layered silicate structure[11] that retains a 75% degree of "polymerization" similar to that of Muscovite (mica; $KAl_2(AlSi_3O_{10})(OH)_2$).[12] This layered morphology facilitates mechanical impact machining. At temperatures above 850°C, the MDS phase dissolves and only the LDS phase remains.[13] The ceramicized material containing the LDS phase crystals also includes crystalline phases of silica (e.g., crystobalite and quartz). Another feature that might be exploited is the fact that by selecting the temperature during the material phase transformation process, it is possible to get mixed-phase (LMS:LDS) systems with a commensurate compositional change in the remaining glass matrix. The goal of our laboratory is developing an improved understanding of the relationships between processing, microstructure and properties of materials to develop "new" materials based on innovative approaches of

synthesis. The complex phase transformation processes that are evident in Foturan (and would likely be the case in Fotoform and PEG3) allow the potential for controlled patterning of materials properties from a single base material of complex composition.

S. D. Stookey was the first to recognize a unique attribute of the lithium metasilicate crystalline phase.[14] The LMS phase is soluble in dilute aqueous hydrofluoric (HF) acid, and the solubility ratio between exposed and unexposed material approaches 50:1 for some PSGC formulations.[15] Using chemical etching to remove the patterned material, all the disadvantages associated with mechanical machining are mitigated. For example, chemical etching is a batch parallel process, whereas mechanical machining is serial in nature. In a batch process, there is the advantage of process control to attain component uniformity. The processing of large areas becomes feasible which may reduce operational and manufacturing costs. In contrast to the LMS phase, the LDS phase is relatively inert to HF chemical etching, and if directly machined by traditional mechanical approaches will display stress and microfractures. However, it is not necessary to mechanically machine the LDS phase. All volume areas that are to be removed are first converted to the LMS crystalline phase. The part is chemically etched and then flood exposed and thermally processed a second time to convert all the areas to the LDS phase. The outcome is patterned structures made of the LDS crystalline phase that can operate under high temperature (~1000^{o}C) and chemically caustic conditions.

Equations 4-6 describe the predominant chemical steps in the etching of the LMS phase. Because the LMS phase is encapsulated in an amorphous glass, there are at least three competing chemical processes for the reagent molecule. Equation 4 describes the chemical reaction of HF with the crystalline LMS phase [Li_2SiO_3] with reaction rate $R_{crystal}$. Equations 5 and 6 describe the two competing reactions with rates R_1 and R_2. Equation 7 describes the etch rate contrast between exposed and unexposed material. The etch rate contrast depends on the processing protocol and the material doping density and can vary from 20:1 to 50:1.

$$Li_2SiO_3 + 8HF \rightarrow 2LiF + H_2SiF_6 + 3H_2O \quad (4)$$

$$SiO_2 + 4HF \rightarrow SiF_4 + 2H_2O \quad (5)$$

$$SiF_4 + 2HF \rightarrow H_2SiF_6 \quad (6)$$

$$R_{crystal} / (R_1 + R_2) \sim 20\text{-}50 \quad (7)$$

An analysis of the chemical etching process reveals the following relationships:

- The reaction rate $R_{crystal}$ is proportional to the density of $[Li_2SiO_3]$ crystals.
- But, the $[Li_2SiO_3]$ is proportional to the silver cluster density, $[(Ag^0)_x]$, through the fact the clusters catalyze the growth of the crystals.
- The $[(Ag^0)_x]$ density is proportional to the reduced silver atom density, $[Ag^0]$, through equation (3) and the $[Ag^0]$ density is proportional to the photoelectron density, $[e^-]$, through equation (2).
- Finally, as described by equation (1), the $[e^-]$ density is proportional to the number of incident photons ($I/h\nu$) where I represents the incident irradiance (W/cm^2) and $h\nu$ is the energy per photon.

The above relationships are consistent with the following conclusion: The chemical etching rate, $R_{crystal}$, should be proportional to the number of photons or incident irradiance. This conclusion has several implications beyond the obvious that the chemical etching rate should depend on the incident laser irradiance. First, for a particular thermal processing protocol the incident photon number is also related to the density of LMS crystals (i.e., $[Li_2SiO_3]$) and to the density of trapped electrons in defect states (i.e., $[e^-]$). The concentration of these two reagent species has a profound impact on the material strength and the optical transmission. Second, since the etch front can only proceed through physical connectivity between etchable crystals, there should be a minimum density of $[Li_2SiO_3]$ crystalline sites that can form a connected etchable network and this minimum density should be reflected in a minimum critical dose of light.

3. Photoactivated Changes in Photostructurable Glass Ceramic Materials

A series of experiments have been conducted to evaluate the change in material properties as a function of laser irradiance for the commercially available PSGC Foturan. An initial experiment was also devised to measure the necessary critical dose to establish a connected network of etchable sites.[16] Equation 1 by itself does not suggest the emergence of a threshold in photon dose. However, the requirement to form an interconnected network of etchable sites does entail mathematics that dictates a threshold. To prove the existence of a threshold an experiment was performed using a measured Gaussian spatial profile laser beam that

was kept at constant incident power (#pulses/sec x Energy-per-pulse/cm^2). A selected number of lenses were used to focus the laser energy onto a cleaned Foturan sample. The exposed and baked areas were etched and the critical fluence was derived from the boundary perimeter of the etched hole where the value of the etch rate is essentially that of the native unexposed glass. The data from the critical dose experiment were fit to a parametric model as given by equations 8 and 9, where ρ is the density of etchable nuclei sites, D_c is defined as the critical dose, F_c is the critical per pulse fluence (J/cm^2), *m* is the power dependence, K is a normalization constant, and N represents the number of applied laser pulses. This parametric model supports the notion that the threshold for exposure should depend on both the incident single pulse laser fluence (number of photons per unit area) and on the number of laser shots applied.

$$\rho = KF^mN \tag{8}$$

$$\rho/K = D_c = F_c^mN \tag{9}$$

Figure 1 shows the data for λ = 355 nm laser exposure along with a fit of the linearized form of the parametric Equation 9. The fit parameters for the data from both λ = 355 nm and λ = 266 nm pulsed laser irradiation are given in Table 1.

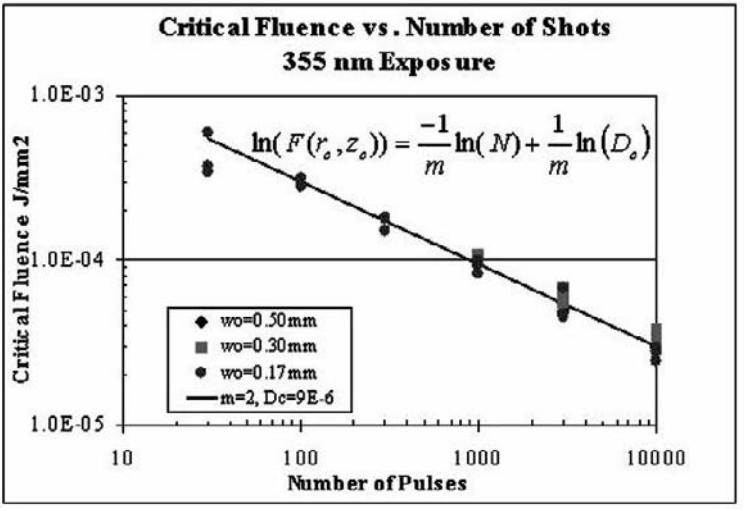

Figure 1. Measurement of the critical fluence versus number of laser shots.

Table 1. Critical dose and fluence dependence parameters for Equation 9 measured at threshold for inducing chemical etching.

Wavelength (nm)	D_c (J^2/mm^4)	*m*
355	9.0×10^{-6}	2
266	6.0×10^{-8}	2

The results in Table 1 show that a critical dose value can be defined and, more importantly, the threshold for exposing the material has a quadratic dependence on the single shot laser fluence (m=2). A simple calculation shows that only 9.4 nJ of photon energy is required to expose a 2μm diameter spot size in one laser shot (N=1) for a 6 ns pulse width at λ=355 nm. In the more commonly accepted units, the required incident critical fluence at the focal volume is 300 mJ/cm^2. These results suggest that it should be possible to fabricate undercut structures by setting the exposure conditions above D_c for the volume elements that are to be chemically etched. Furthermore, in comprehending equation 9 we realize that there are two means to attain a critical exposure dose. It is possible to reach D_c by setting the fluence (F) with the mathematical leveraging of the quadratic dependence or we can set the number of laser shots (N). Both of the "levers" can be used as controls in the generation of high fidelity exposures. From a laser processing perspective, it is generally easier to add an extra laser shot, at a given spot size, rather than to precisely increase the fluence to match the conditions. The required level of precision in the laser fluence to match the equivalence of adding an extra laser shot goes as $(N/N+1)^{1/2}$. For N=10, the laser fluence must be metered with a precision of 5%. Modern diode pumped solid-state lasers operating at the UV wavelengths still have shot-to-shot energy fluctuations on the order of 5%. Consequently, the use of the number of shots can be used as a powerful control "lever" to help mitigate laser shot-to-shot fluctuations in the cases where high fidelity exposures are desired.

Figure 2 shows a scanning electron microscope (SEM) photograph of an undercut structure that was fabricated at The Aerospace Corporation according to these principles. The figure shows an etched tunnel threaded with a human hair. The tunnel region was exposed from above and the exposure conditions were set so that only the volume comprising the tunnel satisfied the D_c condition. The proof-of-demonstration structure in Figure 2 is an example that permits the development of suspended structures. Suspended structures are used in numerous micro-device applications, including inertial and chemical sensors and mechanical structures that add compliance to a co-fabricated part.

Figure 2. Scanning electron microscope photograph of an embedded channel etched between two fluidic chambers. A human hair has been threaded between the chambers.

An experiment was assembled to measure the change in material properties as a function of laser irradiance for the commercially available PSGC Foturan. The hallmark of the apparatus is that a metered dose of laser photons could be applied to a sample during constant velocity motion. Two general approaches are possible in a laser direct-write exposure-patterning scheme: either the sample is placed in motion with the laser beam fixed or the laser beam is placed in motion with the sample fixed. The first scheme typically employs a XYZ motion stage and a microscope objective, while the second approach implements a galvanometer and an f-theta lens. We selected direct-write patterning using a XYZ motion stage since the sample motion velocity could be kept constant with higher precision. In addition, there is no need to compensate for the subtle changes in the focal spot size and shape that inevitably occur with galvanometer and f-theta lens motion systems. The experimental station consists of a computerized XYZ motion station that provides 3D motion of the sample with ~5 μm precision and can achieve patterning velocities of a few mm/sec. A computer workstation is used to control the XYZ motion system and a stepper motor that is attached to a circular variable transmission neutral density filter (CVI Laser Corp., CNDQ-2-2.00). The precision of the stepper motor is greater than 1^{o}. Using this approach, it is possible to control the incident laser irradiance to a resolution of $\pm$10 μW over a range of 1-22 mW for slow velocity motions (~1 mm/sec). Figure 3 shows a schematic of the experimental layout and Figure 4 shows the data of the measured indicated power as a function of the surface power.

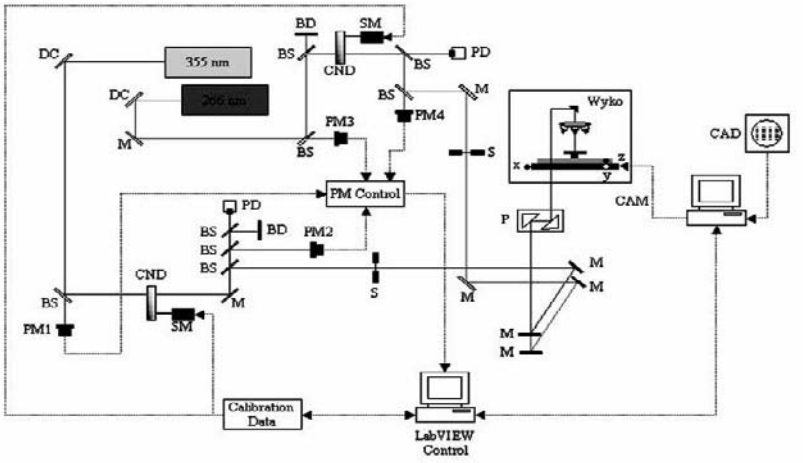

Figure 3. Schematic representation of the experimental setup used for the calibrated exposure studies. BD, beam dump; BS, beam splitter; CND, circular neutral density filter; DC, dichroic mirror; M, high-reflectance mirror; P, periscope assembly; PD, photodiode; PM, power meter; S, shutter; SM, stepper motor. The XYZ motion system is integrated into a non-contact, white light optical interferometer stage (WYKO/Veeco Corp.) and is controlled by computerized CADCAM software.

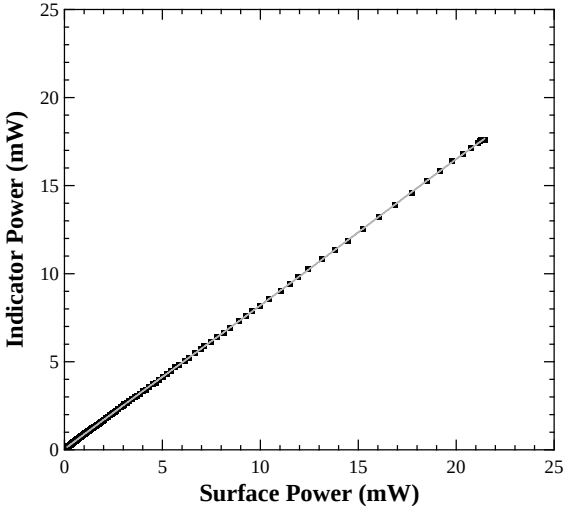

Figure 4. Calibration data that corresponds to the measured "indicator" power versus the power measured at the sample surface.

Although the approach to control the incident surface power provides a high level of precision for the dose experiments, it is not an optimal

approach when the sample velocity is non-uniform. In most XYZ motion systems, constant velocity can be guaranteed only in raster type patterning motions, and the raster scan time must exceed the time required for the motors to achieve the desired velocity by a factor of ≥ 4. For these laser exposure studies, a raster scan pattern was used to expose a 1.5 mm x 8.0 mm area with a laser spot diameter of 3.0 μm and a XY stage velocity of 1.0 mm/s. Two Q-switched and diode-pumped solid state lasers serve as the patterning light sources (Nd:YVO_4 systems manufactured by Spectra-Physics: OEM Models J40-BL6-266Q and J40-BL6-355Q). The lasers operate at λ=266nm and λ=355 nm wavelengths, respectively. The pulse-to-pulse stability of the lasers is $\pm$5% at a nominal pulse repetition rate of 10.0 kHz. Typical laser pulse durations of 6.0±0.5 ns (FWHM) were achieved in the Q-switched TEM_{00} operation mode.

During exposure patterning, the incident laser surface power was controlled in real time by a closed-loop LabVIEW software program that monitored the power at an indicator position in the optical train. This "indicated" power could be related to the incident surface power by applying the appropriate calibration factors.[17] A UV grade, achromatic 10x microscope objective (OFR, LMU-10x-U) was used as the focusing element. For the exposure tests, several Foturan wafers (100 mm dia, 1 mm thick) were cut into 1 cm x 1 cm square coupons and thinned to 200 μm and 500 μm thicknesses. The coupons were then polished to achieve an optically flat finish. The 200 μm and 500 μm coupons were used for the λ=266 nm (initial absorptivity=10.05/cm) and λ=355 nm (initial absorptivity=0.27/cm) studies, respectively. The thicknesses were selected to ensure that the laser penetration depth exceeded the glass sample thickness and to minimize gradients in the exposure volume. The samples were cleaned using a RCA cleaning protocol and were subsequently handled using gloves and clean room techniques. The exposed samples received thermal and chemical processing protocols that were commensurate with the desired phase transformation process. More than 150 samples were prepared to obtain valuable statistics. Finally, the exposed samples not undergoing analysis were stored in a refrigerator.

Several characterization techniques are used in the analysis of the exposed samples. Optical transmission spectroscopy (OTS) is used to measure changes in the absorption as a function of laser irradiance. X-ray diffraction (XRD) spectroscopy and transmission electron microscopy (TEM) are used to identify the phase transformations and the formation of crystalline matter. Time-monitored chemical etching and white-light interferometry are used for measuring the etch depth and the etch rate, which provide information on the chemical solubility and reactivity.

Piezoacoustic transmission spectroscopy is used to measure the mechanical properties of the sample. The latter technique is a non-destructive approach to measure changes in sample stiffness and the Young's modulus.

Initially, there is a measured change in the optical transmission as a function of laser irradiance for samples that have undergone thermal processing to form the LMS phase. This relationship can be gleaned from the Equations 1-3. There is also commensurate change in the material transmission properties following exposure, but prior to baking. In Foturan, the Ce^{3+} chromophore has a $4f^1$ electronic configuration and therefore a $^2F_{5/2}$ ground state. The only f-f transition is to the J=7/2 electronic state and this occurs in the infrared (~ 0.248 eV).[18] However, there are several bands in the UV that arise through transitions from the 4f level to the 5d level. The 5d orbitals, unlike the 4f, are impacted by chemical interactions with surrounding atoms and ions and result in a fall in the energy of the 5d levels. Therefore, the UV absorption spectrum of cerium containing glasses is influenced by the glass composition.[19]

In a silicate glass that contains Na_2O (like Foturan), the Ce^{3+} absorption is an asymmetrical band with a single maximum at 314.5 nm (3.94 eV) and a FWHM of ~ 0.5 eV.[20] Consequently, silicate-based PSGC materials that are doped with cerium are transparent in the visible wavelength region. However, Equation 1 shows that the photoexcitation process produces electrons that remain trapped in electronic defect states. These defect states have optical absorption features in the UV and the concentration of these defect states can be carefully controlled via the incident laser irradiance. Consequently, it is possible to vary the extent of absorption in the UV wavelength region as well. Control of the optical spectrum in the visible wavelength region could be accomplished by controlling the silver cluster particle size. This is the technique that is used in the development of polychromatic glass where a range of possible colors can be manufactured.[21] Figure 5 shows OTS data taken after the sample has been exposed and baked according to the normal protocol to form the LMS crystalline phase. The left panel in Figure 5 shows the measurement of the optical transmission as a function of laser irradiance in the IR wavelengths, and the right panel displays the average transmission within a narrow band (1700-2100 nm) in the IR as a function of laser irradiance.

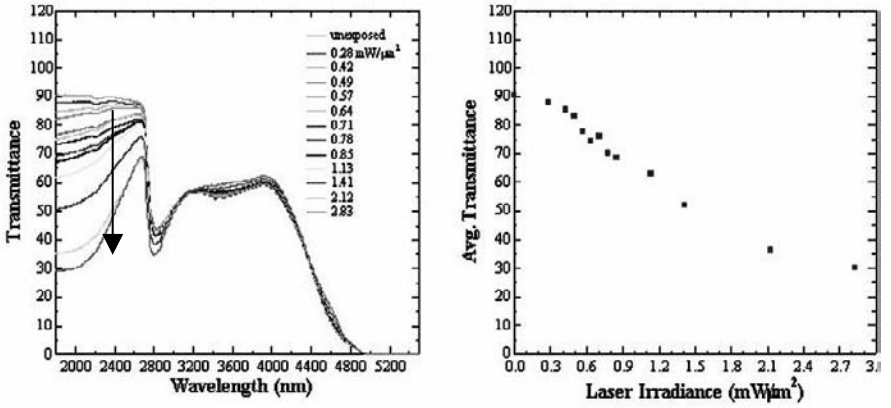

Figure 5. Left: Measurement of the optical transmission in the IR as a function of incident laser irradiance (λ=355 nm) for exposed and thermally-processed Foturan. Right: A plot of the change in the average transmission (λ = 1700–2100 nm) as a function of exposure laser irradiance.

The data presented in Figure 5 shows that it is possible to controllably meter the transmission in the IR wavelengths down to 2500 nm. The absorption profile below 2500 nm shows less dependence on the incident laser and is likely to be associated to water absorption bands. The data also shows that for a change in the laser exposure irradiance of a factor of 10, there is a corresponding absolute change in the transmission by a factor of 3 (90% down to nearly 30%). The practical consequence of this result is that it should be easy to fabricate a calibrated IR filter by metering the irradiation dose to get the desired transmission. A similar change in the UV edge of the optical transmission can be measured in PSGC for material that has been exposed but *not* baked. Figure 6 shows this data, where the plots in the left panel correspond to a series of OTS measurements as a function of incident laser irradiance, and the plots in the right panel represent the changes in the UV edge transmission as a function of incident laser irradiance. The cut-off wavelength is determined by an arbitrary transmission value of 10%. The lines in the plot are not fits but are to be used as general visual guides. The data shows that by metering the laser exposure dose it is possible to controllably move the UV edge from nearly 300 nm to 800 nm. Both IR and UV filters can be fabricated on the same sample, although IR filter formation requires thermal processing. For fabrication, the IR filter exposure is patterned first and, if required, the filter exposure pattern could be embedded below the surface using the technique described in Figure 2 to protect the filter from the environment (e.g., etch chemicals). The sample is then thermally processed to generate or develop

the IR filter. Following this initial heat treatment, the UV cutoff filter can be patterned in areas that have not received prior exposure. PSGC materials do not lose their photosensitivity upon normal thermal processing to form the LMS phase.

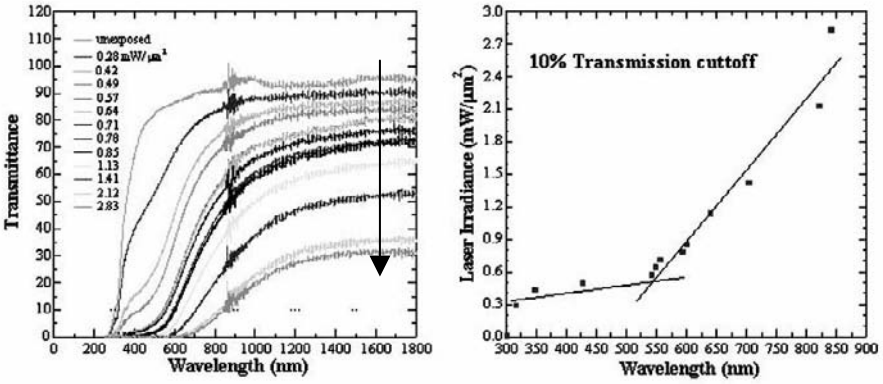

Figure 6. Left: Transmission spectrum of partially exposed PSGC as a function of incident laser irradiance at λ=355 nm. Right: A plot of the necessary laser irradiance to induce a specific cutoff wavelength. The cutoff wavelength is defined by the arbitrary value of 10% transmission.

Equations 1-3 and the results shown in Figure 5 suggest that the density of LMS crystals ($[Li_2SiO_3]$) should have a correlation with the laser exposure or laser irradiance. The material begins in the amorphous phase and at the highest exposure doses will contain a large fraction of crystalline material. In some PSGC materials up to 35 wt% crystalline concentration has been reported.[22] Figure 7 shows some results measured in our laboratory, where the exposed and thermally processed samples were analyzed using XRD spectroscopy. The left panel in Figure 7 shows three XRD spectra that correspond to λ=355 nm exposure (top), λ=266 nm exposure (middle), and a LMS reference material (bottom). The top and middle spectra correspond to an exposed sample that contains non-crystallinity (evidenced by the amorphous background signal) with some crystalline matter. Using the <111> crystalline peak near 27° for the exposure wavelength of λ=355 nm we plot, in the right panel of Figure 7, a series of XRD data that show the change in the peak height as a function of the laser exposure irradiance. The data shows that with irradiance 0.496 mW/μm^2 the peak height, in arbitrary units, is roughly 3000 counts and increases to over 15000 counts for a laser irradiance of 2.83 mW/μm^2. Except for the change in the incident laser irradiance, all the samples

underwent the same handling, thermal processing and XRD analysis protocols.

These results suggest that the mechanical properties of PSGC can be controlled, quite possibly only over a limited extent, by controlling the laser irradiance. The published values of the Young's modulus for Foturan are 78 GPa for the native unexposed glass and nearly 88 GPa at maximum exposure.[23] Recent experiments for the Young's Modulus for the native glass conducted at Aerospace agree with the reported value. We measure 79Gpa for the native glass and there is no change after thermal processing with the thermal protocol used at Aerospace. The modulus of rupture over the same range varies from 60-150 Mpa.[24] The ability to locally control the material strength also suggests that there exists a process to control the residual stress. Residual stress is the stress that remains in a body that is stationary with its surroundings. It can be detrimental to the performance of a material and the devices that are fabricated from the material. On the other hand, residual stresses can be introduced deliberately for a beneficial purpose. In the case of the data as presented, the residual stresses are a result of intergranular stresses. These stresses are termed micro stresses that can have some effect in microstructures but will have large compounding effects for a linked series of co-fabricated microstructures. We are now initiating experiments to exploit the ability to locally control the mechanical properties of Foturan for the development of novel complex microsystems.

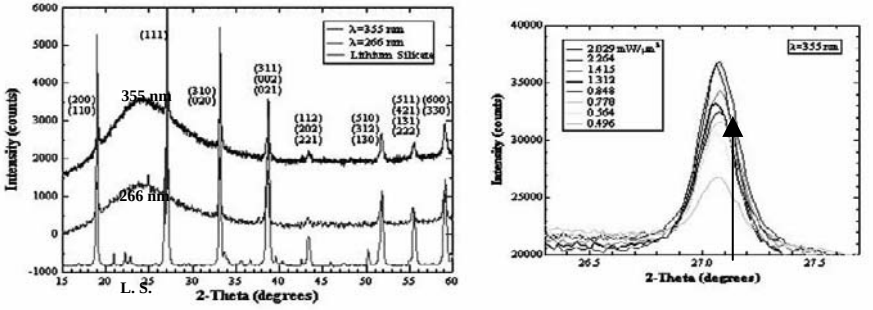

Figure 7. Left: XRD spectra measured following laser exposure and thermal processing; λ=355 nm (top) and λ=266 nm (middle). A XRD spectra acquired for a lithium metasilicate reference sample is also shown (bottom). Right: Plots of the <111> peak height at ~27.1° for various incident laser irradiances.

By far the most obvious correlation as outlined in Equations 1-7 is that the chemical solubility as defined by the etching rate should be dependent on the laser irradiance. To investigate the effect of the incident laser

irradiance and the chemical etching rate, a series of controlled experiments were conducted using the apparatus shown in Figure 3. For these studies, Foturan samples were initially irradiated at laser wavelengths of λ=266 nm and λ =355 nm, and then thermally processed to form the LMS crystalline phase. The samples then underwent a timed etch protocol process and the etch depth was measured using white-light interferometery techniques. Figure 8 shows the results from these experiments where the etch depth is plotted as a function of etch time for a family of laser irradiance values.[25] A linear dependence fit has been ascribed to each laser irradiance data set. The change in the fit slope as a function of laser irradiance supports the notion that the chemical etching rate is dependent on the laser irradiance.

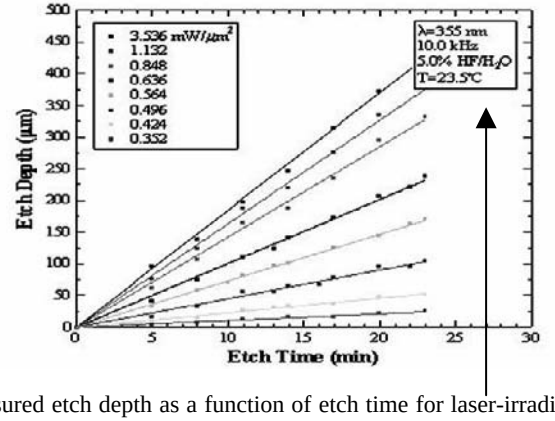

Figure 8. Measured etch depth as a function of etch time for laser-irradiated and thermally-processed Foturan at λ=355 nm.

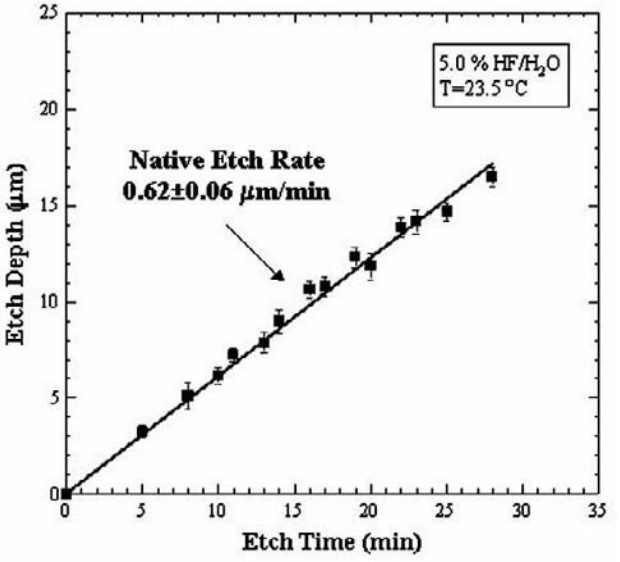

Figure 9. Measured etch depth as a function of time in chemical etchant solution for unexposed but thermally processed Foturan glass.

Figure 9 shows the corresponding data set for the chemical etching of unexposed, but thermally processed, Foturan. These measurements were acquired both at the periphery of the exposed samples (with the exposure pattern located in the center) and with unexposed coupons from the sample wafer. By utilizing this measurement approach material manufacturing non-uniformity can be minimized. The slope of the data shown in Figure 9 yields the etch rate of the native Foturan glass and is determined to be 0.62 $\pm$ 0.06 μm/min.

The data in Figure 8 can be recast to represent a more practical laser processing parameter, the etch contrast or etch rate ratio. This parameter represents the ratio of the etch rate of the exposed material divided by the etch rate of the unexposed but thermally processed material. The etch ratio or contrast is the desired parameter for a material processing expert as it defines the maximum possible aspect ratio that can be achieved for structures patterned in Foturan PSGC. Figure 10 shows the recast data of Figure 8, where the etch rate ratio is plotted as a function of laser irradiance for λ=266 nm λ=355 nm.

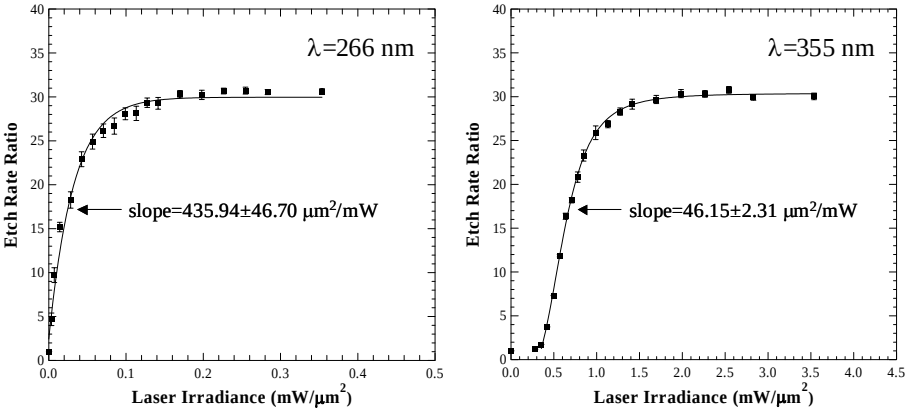

Figure 10. Measured etch rate ratios as a function of incident laser irradiance for λ=266 nm (left) and λ=355 nm (right). The solid squares correspond to the measured etch rate results and the solid lines represent optimized Hill equation fits to the experimental data.

Recast in this format, the etch rate data exhibits a number of interesting features. First, the etch rate ratio appears to saturate at a value near 30:1 regardless of exposure wavelength. Although this etch rate ratio is partially dependent on the thermal processing protocol, the fact that it is independent

of the two exposure wavelengths suggests that the "final state" etchable material comprising the Li_2SiO_3 crystalline phase does not depend on the wavelength of the laser exposure tool. Second, much less laser irradiance is required to achieve contrast saturation for λ=266 nm exposure compared with λ=355 nm exposure. The knee of the curve, where the etch contrast begins to saturate, occurs at a laser irradiance of ~1 mW/μm^2 for λ=355 nm, while only ~0.1 mW/μm^2 is required for exposure at λ=266 nm. These results suggest that although the density of the etchable crystalline phase (i.e., material final state) does not depend on the laser exposure wavelength, the reaction kinetics that proceed the laser exposure are wavelength dependent. Third, prior to reaching the contrast saturation condition, the etch rate ratio data show that there is a region of laser irradiances whereby the etch rate ratio is a monotonically increasing function and can be linearized to define a slope. Furthermore, the slope for λ=355 nm is approximately 10 times smaller compared with the slope for λ=266 nm. The fact that there is a region of laser irradiances where the etch contrast can be linearized suggests that it may be possible to vary the etch rate ratio to gain precise localized control of the etch contrast. The large difference between the two slope measurements suggests that the distribution of reagents as generated by λ=266 nm wavelength irradiation is more efficient in forming the final state species (i.e., Li_2SiO_3). The general conclusions that can be derived from this data set are that both the laser wavelength and the irradiance can be used to set an appropriate set of exposure conditions that affect the final state.

Although the final state of the material is the property that drives most of the practical applications, it is important to understand the role and dependence of the intermediate state "reagents" if there is to be any hope of developing novel photofunctional behavior in PSGC materials. In Figure 11 we present additional data that measures the concentration of two intermediate state "reagents" measured as a function of laser irradiance. The measurements were conducted at two common solid-state laser wavelengths (λ=266 nm and λ=355 nm) to ascertain the dependence on wavelength. These "reagent" species characterize two intermediate states of the PSGC material while undergoing thermal processing. Along with the etch rate ratio data (cf., Figure 10), the concentration of the photo-generated electrons (Equation 1) and the concentration of silver clusters produced by the redox process (Equation 3) are also co-plotted in Figure 11. The photo-generated electron and $(Ag^0)_x$ species data were measured via optical absorption spectroscopy.[26] The photo-generated electron is identified in the plot as the trapped defect state and is characterized by an absorption band at 265-280 nm. The measurement of the silver cluster species has a

characteristic spectroscopic signature at 410-420 nm.[27] Both wavelength exposure results are directly comparable as the absorption data has been reduced to integrated linear absorption coefficients and identified in the plot in units of peak area.

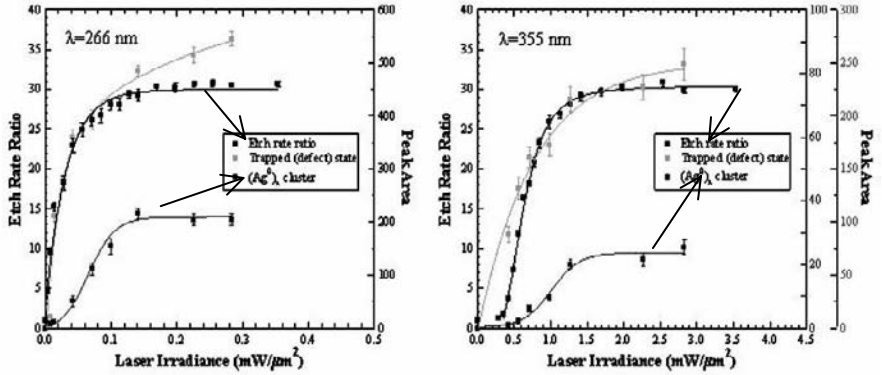

Figure 11. Comparison of the photophysical measurements (Peak Area; right axis) and the chemical etching data (Etch Rate Ratio; left axis) for laser exposure processing at λ=266 nm (left) and λ=355 nm (right). Plotted are the etch rate ratio, the trapped "defect" state and the silver cluster densities.

The results show that both the photoelectron defect state concentration and the silver cluster concentration mimic the etch rate ratio curve as it turns over toward saturation. The fact that these two precursor reagents show some saturation behavior could explain the saturation behavior measured in the etch contrast data. However, upon closer inspection, the data shows that although the silver cluster concentration saturates with increasing laser irradiance, there appears to be no similar saturation behavior, as ascertained from data outside the error bars, for the photoelectron defect state concentration. The reaction process follows the sequence of photoelectron generation with subsequent reduction of silver ions and the formation of silver clusters (450-500^{o}C). It is likely that the difference as noted is a consequence of the kinetic processes during the thermal processing phase. Since there appears to be an excess of photoelectrons at the higher laser irradiances, an experiment was performed to determine if more silver clusters could be formed. The experiment entailed increasing the available reaction time during which the silver clusters grow (500^{o}C). A number of equally dosed samples were prepared where all samples were exposed with equivalent laser irradiances. The normal thermal processing protocol was altered such that the samples were subjected to the 500^{o}C temperature plateau for various time durations, and then removed from the oven to quench the bake phase I thermal process.

This modification in the thermal processing protocol permits the silver ion redox process to proceed, but does not allow the formation of the LMS crystalline phase. Optical transmission spectroscopy was used to monitor the change in the photoelectron concentration and the silver cluster concentration.

Figure 12 shows the bake phase-I time duration test results for a laser exposure wavelength of λ=355 nm. The left panel in Figure 12 shows that with increasing bake phase I time, there is corresponding growth in the absorption at 420 nm. The 420 nm band has been previously associated with the silver cluster plasmon frequency[28]. The data also reveal that by increasing the bake phase-I time duration beyond 60 minutes (i.e., the normal bake protocol at 500^{o}C), there is a measurable increase in the silver cluster concentration. A more clear indication of this behavior is presented in the right panel of Figure 12, where the peak absorption values of the trapped photoelectron defect states and silver cluster bands are co-plotted as a function of bake phase-I duration at 500^{o}C. The results show that with increasing time duration at the 500^{o}C temperature plateau, there is a progressive diminishment of the electron defect concentration and a concomitant increase in the silver cluster concentration. The electron defect concentration appears to be fully titrated by 100 minutes. On the other hand, the cluster concentration continues to grow with further baking time but not at the loss of electron defect concentration. We attribute the continued increase in the silver cluster concentration to a second kinetic process that entails cluster formation as a result of the outlying silver atoms that have the requisite mobility and the time to find partners for cluster formation.

These results provide insight into the reaction kinetics associated with the baking phase and the possibility for altering the reaction process in "midstream" with the aim of altering the final state properties of the ceramicized material. The results of Figure 12 provide a method for increasing the silver cluster concentration. The issue of whether this increase in the silver cluster density has any appreciable effect on the properties of the composite glass ceramic with the LMS crystalline phase can be addressed by reviewing the data in Figure 11. Figure 11 shows that the concentration of silver clusters (identified by Peak Area units) are larger for laser irradiation at λ=266 nm compared with laser irradiation at λ=355 nm. However, in comparing the value of the maximum in the etch contrast for the two exposure wavelengths, we conclude that there is no difference. In both cases, the maximum etch contrast is ~30:1 despite the ratio of silver cluster concentrations for λ=266 nm and λ=355 nm is ~10:1. These results indicate that the higher concentration of silver clusters does not result in a higher number of LMS crystals and a larger chemical etching rate or etch

contrast. Although there appears to be no effect on the chemical etching rate of the glass ceramic, there will be an impact on the optical transmission properties. We are now conducting experiments in our laboratory to expose the material prior to the ceramization phase to alter the cluster size by resonant excitation in the plasmon band.[29]

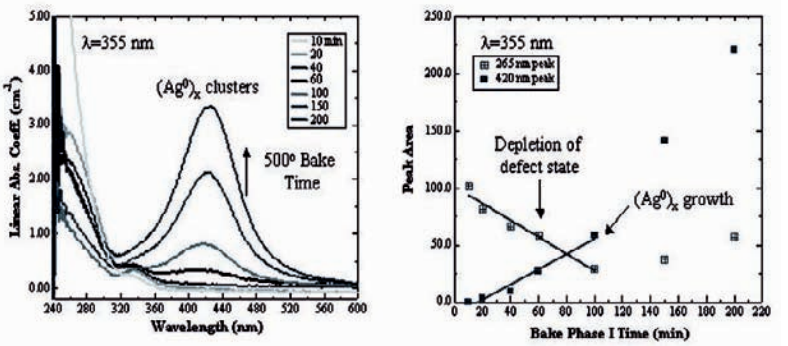

Figure 12. Left: Measured optical transmission spectra acquired for the optical band that is representative of the silver cluster density for different bake phase I time durations at 500°C. Right: Plot of the peak of the absorption bands for the photoelectron defects (open squares) and the silver clusters (closed squares) as a function of bake phase-I time at 500°C.

We have used the results shown in Figures 10 and 11 to develop a variable dose laser exposure tool that utilizes the direct-write patterning approach to fabricate microstructures in true three-dimensions. Figure 13 shows an example of the variable exposure dose as applied to the control of the local chemical solubility and the optical transmission. The optical photograph on the left shows an etched structure. A cross-cut of the design profile and the actual measured depth profile are presented in the middle panel, while the right panel showcases the variation of color or optical transmission in the orange-red region of the visible spectrum.

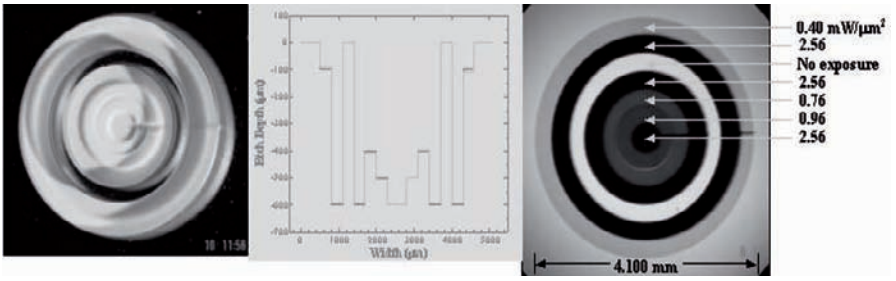

Figure 13. Structures fabricated by the variable dose laser direct-write fabrication technique. Left: A microfabricated structure that has been chemically etched. Middle: Profilometry results of the measured depth of the structure along with the design requirements. Right: The controlled local change of optical transmission in the PSGC material.

In this example, the same pattern is used to demonstrate the ability and precision regarding control of the solubility and the optical transmission. The example also helps to illustrate the power of the variable dose approach for microstructure fabrication. Using traditional photoresist and lithographic patterning techniques (e.g., single exposure) to microfabricate the simple structure in the left panel of Figure 13 would require four individual positive tone masks (i.e., to support the four depth levels shown) for the lithographic step alone and quite possibly another four negative tone masks to protect the complementary areas during the chemical etching phase. With the variable exposure dose method and the direct-write patterning technique, no masks were used in either the patterning or in the chemical etching phase to fabricate the structure shown in Figure 13. By controllably varying the dose during the patterned exposure, as defined by the fit slope of the data in Figure 10, *each local area etches at a different rate* so that a single timed-etch step produces all of the desired features. Using this technique, we have patterned complex 3D structures that would normally require over 30 masks and multiple etch times utilizing traditional lithography techniques (e.g., operations per masking step: apply photoresist, lithography exposure, bake, strip photoresist, etch, and repeat).

4. Digitally-Scripted Genotype Sequencing and Electro-optic Modulation

Over the past 5 years, commercial laser manufacturers have made significant progress regarding system reliability. For example, the mean time-to-failure (MTF) for most diode pumped solid-state lasers now exceeds one year. These improvements have been realized by the increasing quality of laser source materials, a conscious effort to make the materials that are integrated into laser systems more compatible and in the implementation of microelectronic clean room techniques during the assembly and test phases of the laser manufacturing. As a result of these technological improvements, modern lasers not only have better MTF figures but also show more shot-to-shot stability (especially those that implement low power lasers as seed-pump sources). Consequently, laser material processing techniques that would not have been viable a few years ago now become possible.

In laser material processing, the goal is to deposit, in metered fashion, a specific quantity of light on the target undergoing the processing. The quantity of light necessary to induce a particular material transformation event is fundamentally driven by the light-matter interaction and the underlying photochemical or photophysical processes. Typically, either

CW or pulsed laser systems are used to induce these processes. In the case of CW lasers, the processes are normally characterized by defining the exposure time duration. For repetitively pulsed lasers, the processes are defined by the laser repetition rate and per pulse energy. Traditionally, concepts such as average laser power (Watts/cm^2) and fluence (Joules/cm^2) have been used to characterize processes activated by both CW and pulsed lasers. For photophysical processes that are non-linear with respect to the incident light flux, the concept of peak laser power (Watts/cm^2) serves as a useful measure. These means of quantifying the amount of photons delivered to a substrate are valuable characterizations of the laser material interaction process. However, they represent a holdover from CW laser material processing methodology, where the intent was to maintain constant laser power and vary the exposure time during the irradiation step. This methodology has been inadvertently extended to the case of pulsed laser material processing applications by requiring that the incident laser fluence be maintained constant.

The use of average laser power or constant fluence as process control parameters characterizes the process only on a global scale and overlooks the more complex material interaction effects resulting from the fact that the exposure duration is extended in time or multiple laser pulses were applied. Material properties can change with laser exposure either for CW or with pulsed lasers, and this change will be significant for photolytically activated materials. For example, in the simple case of laser heating of metals for welding or other thermally initiated processing applications, the heat capacity of the metal is temperature dependent (e.g., low temperature dependence of $c_v \sim (T/T_D)^3$, where T is temperature and T_D is the Debye temperature of the material). If the desire is to controllably increase the temperature to a specific set point, the applied mode for laser processing should not be with constant fluence or average power. The repeated deposition of constant fluence laser pulses or a constant average power laser exposure only exacerbates the problem. Without compensating for the expected changes in heat capacity, the outcome will be a reduction of control during laser processing.

The laser processing community is aware of these issues. The concern is typically represented under the heading of incubation[30] or rep-pulse effects.[31] The technical approaches that have been implemented to investigate these effects have included experiments that show the changes in the material property as a function laser dose, number of laser pulses and laser repetition rate. The technical means to mitigate these effects have been to determine the optimum processing “window” within which the

constant laser power or constant fluence criteria can be applied to achieve the desired effect.

With modern laser systems and the advancements in electro- and acousto-optic shuttering technology, a better approach to laser material processing is now possible. The capability now exists to compensate for the dynamic changes that will occur in materials as a result of repeated pulses or extended exposures. Even for a material transformation process that is realized by a single laser shot, experiments with ultra fast femtosecond (fs) lasers and pulse shaping techniques have shown the distinct advantages that can be achieved in processing fidelity by altering the pulse temporal shape.[32] In these experiments, the concept of laser peak power is not meaningful. What is meaningful is the profile of the final realized pulse-shape, which can serve to provide information on the dynamical aspects of the actual photophysical process. Consequently, the process can be more meaningfully characterized by using the total incident photon density and the photon-distribution profile.

Laser material processing techniques must progress beyond the established techniques that were developed for lasers of generation past. The repetition rates of table top lasers have long since crossed the kHz (high power) barrier and are in now in the range of tens of MHz (low power). High average power (>1 KW) MHz repetition rate lasers have also been developed, but these are not table top class systems but are intended for large industrial applications.[33] Complementing these developments has been the technology for modulating laser light at high repetition rates. Currently, lasers can be readily amplitude modulated at MHz repetition rates. This capability has been made realized by the significant development of high voltage, high bandwidth electronics, along with materials that display large electro-optic and acousto/elasto-optic coefficients. Therefore, it is beneficial to consider an alternate approach to laser material processing. The desired approach should be one that refines the processing control to at least compensate for the known changes that occur in a material as a consequence of administering multiple laser pulses or extended duration exposures. This process control scheme could be realized for either CW or pulsed lasers by dynamically modulating the amplitude of the delivered photon density.

The scheme should result in a higher fidelity process since the pulsed or CW laser exposure "script" contains a photon distribution profile that attempts to compensate for the effects from prior irradiation. This methodology of an exposure script would have the advantage that it could be matched to a desired laser processing affect for a particular material. For example, if the desired effect were the scribing of a polished glass surface a photon flux profile or *script* could be specifically designed and tested for

the material and the desired outcome in question. There could be another script for ablative drilling in a specific metal, one for inducing crystallization in a particular amorphous material, etc. In all cases, one would describe the process for achieving the desired effect by the laser type, the total photons delivered and the applied script or the amplitude modulated irradiation profile. The experimental approach to defining the optimum script would entail finding an important measurand that correlates with the desired effect. For example, in the case of welding or a solid state phase transformation process the measurand could correspond to the temperature profile of the irradiated material. If a single paramount measurand does not exist, then it may be possible to utilize genetic algorithm[34] methodologies to identify a select set of key measurands. These techniques have proven useful in characterizing gas phase photochemical processes in small molecules.[35]

The proposed methodology initially suffers from the fact that a library of scripts would have to be developed for each material and the corresponding desired photophysical outcome. This is no different from the existing state of affairs where specific process windows are defined for each desired material processing application. However, the generation of a library or digest consisting of material processing scripts could help theoretical modeling efforts since the descriptive models could have built-in constraints that were experimentally defined. In return, the results of the theoretical analysis could not only be used to refine the pulse script but also to characterize the pulse script in terms of first principals. In the final examination and after the script profile has been fully refined through rigorous theoretical analysis and successful experimental testing, the script has attributes that are analogous to the biological genotype. In biology, a genotype has coded information that permits the expression of a particular biological functionality (i.e., a phenotype). In this analogue, the script has coded information in the form of a specific photon flux density distribution that enables a laser to induce or "express" the desired effect in a material.

The proposed methodology where a laser-material interaction process is characterized in the form of a script or "genotype" is useful for understanding fundamental investigations in laser-material interaction phenomena. However, to have practical use a tool must be developed that enables the delivery of a specific photon script or "genotype" at a prescribed location during patterning motion. The Aerospace Corporation has been developing such a tool that uses a specially designed laser direct-write patterning station.

In most laser patterning tools where direct-write techniques are employed, the motion control system computer utilizes a computer-assisted-manufacturing (CAM) operating system where a pattern,

comprised of motion sequences, is realized via the execution of a discrete series of commands (e.g., G-code command structures) that control the drive motors. In most complex motion sequences, the tangential velocity of the motion system is never constant but is continually varying in preparation for the upcoming motion maneuver. The motion control operating system implements these velocity modulations because it must compensate for the inertia of the stage or motion platform. As a consequence, patterned exposures from even the most stable laser system will be inconsistent and uneven as a result of the continual variation in the motion platform velocity.

The primary objective of a laser direct-write patterning tool is to ensure that each laser spot size along the direct-write pattern profile receives the same exposure dose (#photons/area). Realizing this objective is normally hindered by the continual variation in the motion platform velocities. An ideal laser exposure patterning system would not only provide constant exposure dose regardless of motion velocity, but each nominal spot size would receive a prescribed photon dose that is designed to induce a specific material property change. Using the genotype classification scheme as an analogy, the intent would be to "express" a particular functionality or property of the material. Therefore, the ideal exposure patterning system would utilize two "scripts". One script defines the motion pattern in Cartesian space. This is the tool-path "script" and it is generated by computer-assisted design (CAD) and CAM software. The second "script" contains information on the required laser dose in terms of the number of laser pulses and amplitudes that each laser spot area is destined to receive in Cartesian space. The second script is the "genotype" script and is generated with prior knowledge of the photochemical and photophysical properties of the material. Conceptually, these two scripts are not hard to realize. The first script is CNC (computer numerical control) code and is generated by commercially available CADCAM software, while the second script corresponds to a concatenated series of voltages for amplitude modulation of the output pulse train of the laser system. The missing key element is the means for synchronously integrating these two scripts and guaranteeing that every motion step on the order of the laser spot size receives the prescribed photon dose regardless of the motion control velocity.

We have developed a scheme for controlling the delivery of laser photons that not only mitigates the adverse effects of velocity variation, but also allows the capability to parse the laser dose based on a predefined and prescribed need.[36] In our technique, the "genotype" script is comprised of a concatenated series of amplitude-modulated voltages that drive an electro-optic (EO) Pockels cell. The inter-communication link between the laser and the motion control platform is based on a series of signal pulses

generated from the motion control platform that delineates the traversing of a prescribed distance along the tool path pattern. In the application, a trigger signal is generated after moving the equivalent distance of a laser spot size in 3D Cartesian space (e.g., laser spot size with a 10x objective, 3-5 μm). Because the technique does not rely on the duration of time spent traversing the defined distance, it is independent of the local velocity of the motion platform. The trigger signal drives an arbitrary waveform signal generator (AWSG), which synthesizes information that is stored in memory and includes the voltage profile that is prescribed for that specific laser spot size. The output pattern of the AWSG is connected to the EO Pockels cell modulator.

The result of this synchronization between the motion platform (tool path pattern) and the amplitude-modulated laser (laser pulse pattern) is that only the desired amount of light with the appropriate intensity profile is administered to each specific location. No additional light is administered until another trigger signal is received marking the transition to a new spot size. The consequence is that the motion control platform can move according to its natural inertia and the laser system can be left to run at its most effective operational mode. The two stable systems are linked in a common process mode that is defined by the external modulator (EO Pockels cell) and the AWSG. An appropriate analogy of this technique might be a computer system, where the operating system utilizes stable clocks to create functional bytes and words that act to control a particular event. In our technique, the pulsed laser system and the motion control platform signals represent the clocks, and the AWSG and the EO Pockels cell represent the operating system. We have demonstrated this technique by using an Aerotech Corp. XYZ motion stage (X; ABL80050, Y; ABL20030, Z; ALS130-150), a Tektronix Corp. arbitrary waveform signal generator (AWG 420), and an electro-optic Pockels cell modulator system manufactured by ConOptics, Inc. We have shown that it is possible to modulate a sequence of laser pulses while the motion platform is moving in excess of 400 mm/sec.[37]

Figure 14 shows the genotype pulse modulation technique applied to the femtosecond laser ablative scribing of Foturan glass. The results show two images that were acquired with the same optical microscope and under identical magnification and lighting conditions. The scribing pattern is an octagon structure and the magnified image corresponds to a region located near an apex where the motion velocity is expected to change. The image on the left was acquired following laser ablation without the scripted genotype control scheme, while the image on the right was acquired with this feature activated. The required average power of the femtosecond laser was defined through a series of test and analysis cycles until the scribe

could be judged as acceptable without the use of scripted genotype control scheme. The laser power level was not altered for either of the cuts shown in Figure 14.

The results of this simple demonstration are compelling. The image on the left is blurred due to spallation and debris formation, while the image on the right is clear and shows highly localized material removal. We have successfully applied this technique to control the laser dose during the patterning of photosensitive materials such as Foturan, and we believe the technique is applicable to most photoreaction control experiments. Power supply drivers for Pockels cells can now be acquired with bandwidths approaching tens to hundreds of MHz that facilitate light modulation with sub-100 ns transition times. For pulsed lasers operating at repetition rates of tens of MHz, the fidelity of the scripted genotype control scheme will be a strong function of the shot-to-shot power stability of the laser rather than the average power. The challenge to the laser manufacturers will be to reduce the fluctuations in the shot-to-shot peak power.

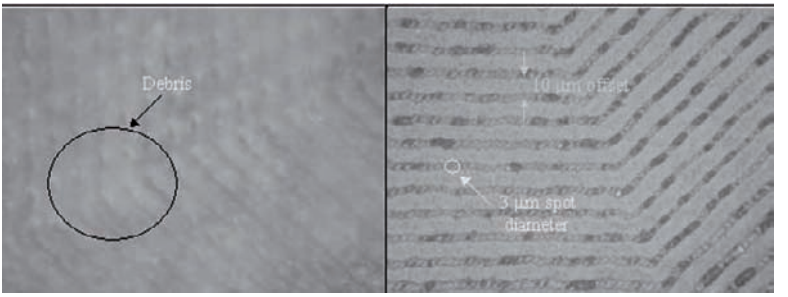

Figure 14. Optical microscope images acquired under the same microscope, magnification and lighting conditions. The images correspond to the femtosecond laser ablative scribing of Foturan. The image on the left is without laser pulse scripting control, while the image on the right has the feature activated.

The newly developed technique engenders the development of a laser material processing library consisting of specific "genotype" scripts. One of the goals of our laboratory is to begin developing these genotype scripts for common materials and the desired laser induced effects.

5. The Development of a Glass-Ceramic Propulsion Module for a Co-Orbiting Satellite Assistant Space Vehicle

In the Co-Orbiting Satellite Assistant (COSA) mission scenario, a small spacecraft is ejected from a mother ship in order to provide a mobile imaging system for high-resolution inspection of external surfaces for a few hours, days, or weeks.[38] Three-axis stabilization, orbit-adjust propulsion,

and an optical imaging system are typically required. Previous analyses had shown that a small COSA vehicle could operate using an average power level less than 2 W; a small solar array or primary battery could provide sufficient power for the mission.[39] In principle, the COSA mission can be accomplished using a ~1-kg mass vehicle, such as the The Aerospace Corporation's MEMS Pico-Satellite Inspector (MEPSI).[40] Our concept, the COSA, is a 1-kg mass inspector satellite fabricated out of photostructurable glass ceramic material. The goal is to demonstrate, for the first time, the utility of PSGC materials in space systems by fabricating, assembling, and testing a miniature cold-gas propulsion system that could be used on a miniature satellite. The propulsion system is sized for a kilogram-mass satellite inspector and carries enough propellant for a one-week inspection mission that includes ejection from a host satellite at 700 km altitude, transfer to a circular observation orbit at a range of 50 m from the host satellite, followed by a transfer to a second observation orbit. Figure 15 shows an example initial transfer (phasing) trajectory and two observation orbits for the COSA. The satellite in the center is the host ship.

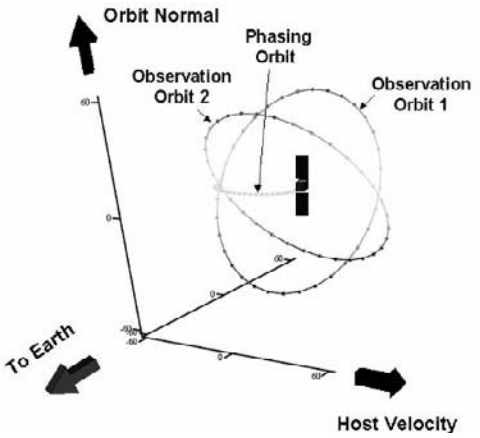

Figure 15. Orbit transfer and observation orbits for a satellite inspector as seen in the host satellite reference frame.

Small satellites can enable new space missions due to their reduced cost per platform. Microsatellites (10–100 kg mass spacecraft) typically cost between $1 and $20 million and nanosatellites (1–10 kg mass) are expected to cost about an order of magnitude less. With mass production of hundreds to thousands of identical units, the costs should drop further. Nanosatellites can be used as satellite assistants, low Earth orbit communication relays and on-orbit testing platforms. Groups of

nanosatellites with VPN-like (virtual private network) connectivity could be placed in specific locations to conduct space experiments with the results being communicated to the mother ship that can then transfer the data to monitoring stations on earth using a high-speed downlink. Most sensors that a nanosatellite mission might use have already been miniaturized by the use of microelectronics technology. The one satellite subsystem that has not been miniaturized is the propulsion system. The ideal propulsion system is a compact and inexpensive unit that requires few interfaces to the spacecraft and includes an inertial measurement unit (IMU) to sense orientation and position.

A project was initiated at The Aerospace Corporation with the goal to demonstrate the fabrication and assembly of a spacecraft propulsion system constructed of glass ceramic material. As a material class, glass ceramics have distinct advantages for space applications. First, because they can be molded or shaped allows for designing satellites that have non-cylindrical shapes. Second, these materials provide low thermal conductivity, low electrical conductivity, dimensional stability, and strength at high temperature. In space applications, dimensional stability is a desirable property and an issue for earth orbiting satellites that are not in sun synchronous orbit. These satellites undergo large fluctuations in temperature on every orbit. Materials with low thermal conductivity are also desirable and can be used to mitigate against the large temperature fluctuations. Third, glass ceramic materials are used in radio frequency (RF) applications. For example, the low-temperature, co-fired ceramics (LTCCs) are one class of glass ceramic materials that are used as substrates for many modern wireless electronics.[41] For the case of the nanosatellite, the advantage is the potential for integrating the RF communication system with the antenna. Fourth, there are glass ceramic materials that are resistant to chemicals and this capability is most useful for storing propulsion propellants such as hydrazine, nitrogen tetroxide, and hydrogen peroxide.

In a previous effort, we fabricated a first-generation propulsion module using direct-write laser-processing of Foturan.[42,43] This unit weighing nearly 100 grams had six independent thrusters and “flew” on an air table. For laboratory safety reasons, 1,1,1,3,3,3-hexafluoropropane (Dupont HFC-236fa; 30 PSIG at room temperature) was used as the propellant. The converging/diverging nozzles were designed for a 10 mN thrust level with a 200-μm effective throat diameter. Pulse-width modulation of the individual thrusters provided thrust level control; the minimum impulse bit was 0.1 mN. The 50-mm x 50-mm x 30-mm propulsion module had a limited propellant capacity for the COSA mission.

The first-generation COSA propulsion module performed several maneuvers on an air table. Thrust levels were adequate and the bi-

directional communications proved functional. Thrusting commands were sent to the module while telemetry (propellant temperature, propellant pressure, and rotation rate) was sent from the propulsion module. An Analog Devices MEMS gyro (ADXRLS150) provided rotation rate information with minimum impact on vehicle size or mass.[44]

Our current propulsion module is 10-cm in diameter and can store 30 cm^3 of propellant. Based on an estimated on-orbit specific impulse of 38 s for the 1,1,1,3,3,3-hexafluoropropane, this module could provide a 15 m/s ΔV for a 1-kg mass COSA. Figure 16 shows an exploded schematic view of this PSGC propulsion module. The propellant tank is formed by a 4-mm thick PSGC layer with integrated structural ribs that is bonded to a solid bottom layer and to a perforated vapor/liquid separator layer on the top. The bottom layer contains dual integrated propellant heaters (one is a spare) to maintain temperature, and hence vapor pressure. As gas is removed by thruster operation and the liquid undergoes evaporative cooling additional heat must be supplied. The heater layer was fabricated with a 700-micron deep trench to hold the heater element below the surface. A thin nickel layer was deposited on the surface and the surface was mechanically polished to remove conductor that was not in the trenches. Subsequent electroless nickel plating increased the conductor thickness to provide 5-Ohm coils. Each coil is designed to provide 3W of heat to support a continuous 20-mN thrust level. Additional traces were also included to provide electrical connections to temperature sensors.

In fabricating the COSA propulsion module, a manufacturing methodology was demonstrated that allows for the possibility to mass produce and customize nanosatellites. The methodology employed maintained all the design, test and fabrication phases in digital format. The approach is a form of digital-direct-development (D^3) in which solid modeling software is first used to design and form fit test subsystem modules and complete assemblies. The final approved design is then converted into machine tool path code using commercial CAM software. Finally, the machine tool path code is translated into code that is specific to the three-axis laser direct-write exposure tool at The Aerospace Corporation. The translator software, called a post-processor, is an in-house creation and integrates aspects of the laser shuttering with the motion stages. In the Aerospace direct-write tool, no masks are used and all processing is handled by digital data in the form of a 3D tool path code. Also, there is a defined tool path segment for each kind of material processing to be done by the direct-write tool. For example,

- Tool path segments were delineated for locations where the material is to be completely removed by a chemical etching operation.

- Tool path segments were defined for locations where there is to be metallization, for example by the use of laser induced plasma-assisted ablation (LIPAA)[45] or via laser direct-write chemical vapor deposition (CVD)[46] techniques.
- Tool path segments were defined for locations where epoxy material is to be dispensed by a glue-bonding robot.

In future COSA generations we intend to also include additional tool path segment types that will define where the material strength is to be slightly increased, segments where the material chemical solubility is to be decreased, segments where the material temperature shielding effectiveness is to be increased, and segments where the material optical and RF transmissions are to be altered in a controllable fashion. However, rather than maintaining numerous tool paths, in future generations the composite different tool paths will be integrated into a single concatenated series of genotype scripts that will define what is to occur at each volume pixel (voxel) element in the material.

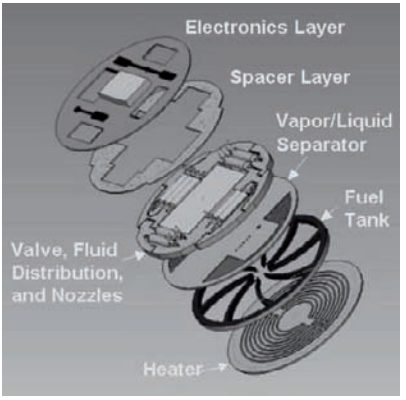

Figure 16. Exploded schematic view of the second-generation COSA design. All wafers are to be fabricated from PSGC material.

Figure 17 shows a photograph of the bottom-view of the assembled COSA excluding the valves. Note the temperature sensor pads in the center. Figure 18 shows a photograph of the partially-assembled layers with the valves installed. The miniature solenoid valves (LEE Corporation. INKA1222210H), have a maximum response rate of 1 kHz.[47] Our control system is being designed for a 5-10 millisecond valve open-close cycle, which should provide a minimum impulse bit of 0.1-0.2 mN-s. Ten valves are used in this propulsion module; 4 valves provide X-Y translation (+X, -

X, +Y, -Y), 4 valves provide one-axis rotation (one couple for CW rotation, one for CCW rotation), 1 valve is used for propellant fill, and 1 valve is used for propellant vent. For low earth orbit (LEO) missions, the last valve could be used to inflate a balloon for the end-of-life satellite deorbit maneuver. The high-drag coefficient of a 1 meter diameter inflated balloon retrieve the satellite into earth atmosphere for burn up. Unlike the earlier generation smaller module, this propulsion module is correctly sized for the LEO mission, and could be adapted to the geostationary orbit missions by decreasing the average thrust level to 1 mN.

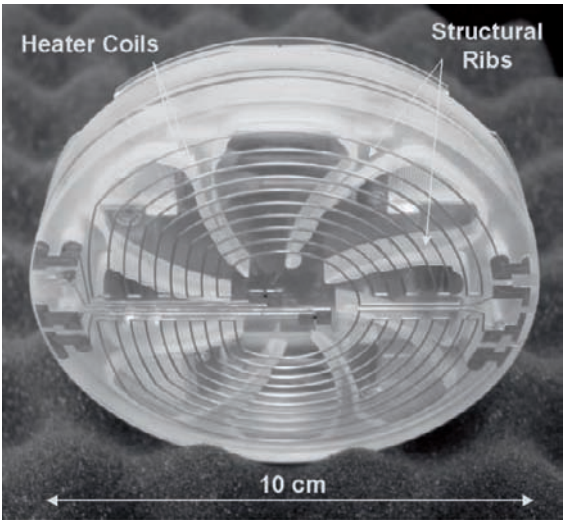

Figure 17. Optical photograph of the bottom view of an assembled PSGC sandwich representing the COSA unit. The shown heater coil is nickel and was fabricated using laser patterning of PSGC followed by chemical electroplating.

The glass ceramic COSA propulsion module is now undergoing testing on an air table. Motion-control algorithms have been written that coordinates rotation and translation motions by high speed repetitive thrusting. Figure 19 shows a photograph of the COSA vehicle on a weight

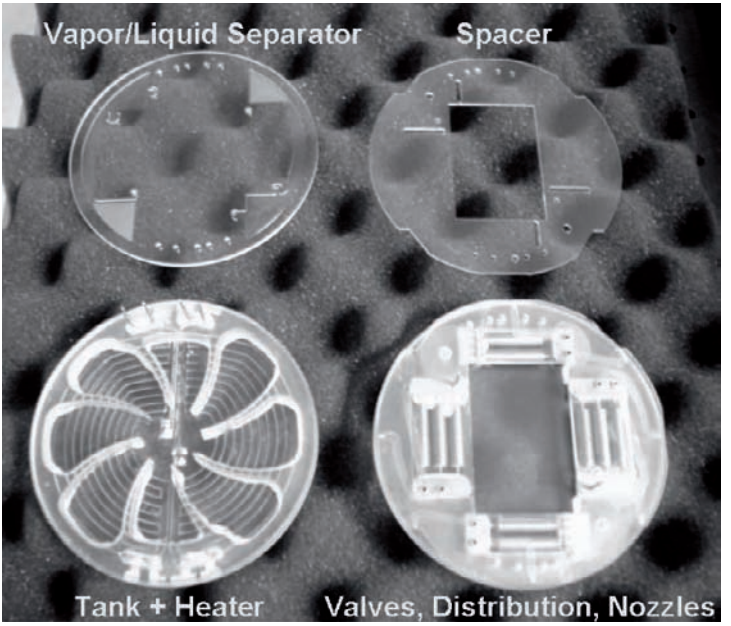

Figure 18. Optical photograph of patterned and processed PSGC wafers and partial wafer stack assemblies. The valves and fluid/gas distribution lines can be seen on the lower right image.

scale. Using direct-write patterning speeds of 1 mm/sec and an incident UV laser power <20 mW, the complete COSA vehicle was patterned, assembled and tested in 210 hours. The laser-patterning portion required over 55 hours of processing time. However, with a commensurate increase in the patterning speed and laser power the direct-write patterning operation can easily be reduced to 5 hours. Further reduction in manufacturing time can be achieved by implementing batch-processing techniques for the sample bake and chemical etching procedures. Consequently, fabrication and assembly a complete COSA propulsion unit can be realized in less than 50 hours.

Figure 19. Photograph of the completed COSA propulsion system with wireless telemetry, inertial measurement unit and thrust control electronics on a weight scale.

6. Conclusions

Material processing based on photolytic activity has a wide range of applications that not only permit the fabrication of high precision components but also the ability to place materials in phase "states" that could have novel properties. We believe that the development of metastable or protean materials to be a research area worth of pursuit, especially with materials that can be activated by light. Using the class of photostructurable glass ceramics as an example of a light activated protean material, we have conducted a series of experiments to better understand the underlying photophysical processes that initiate the phase transformation process. Our goal has been to investigate the outcome of the material in its "final state" as a result of an initial controlled laser excitation event. Using irradiance and wavelength as two control parameters, we have investigated the photophysical excitation processes of a commercially available PSGC, Foturan. The results show that it is possible to control over specific ranges the material final state, solubility, optical transmission and strength. To have any hope of utilizing this ability to control the material properties to some advantage and with some fidelity requires

developing the means to control the incident laser power to a high degree of precision.

In this regard, we have developed a laser modulation control scheme that not only enables high fidelity control of the incident laser power, but also opens a new approach to laser material processing. The developed methodology is characterized in the form of a script or "genotype". The script has coded information in the form of a specific photon flux density distribution that is designed to induce or "express" the desired effect in a material. We have developed a processing tool that implements this methodology on a three-axis high precision motion stage. The initial results are persuasive. Finally, we believe that photostructurable glass ceramics have important applications in widely differing industries. To prove this point we have developed and operated a glass ceramic propulsion system for a space vehicle of the 1 kg mass class, called a nanosatellite. Glass ceramic nanosatellites are possible and could usher in to the aerospace industry the concepts of mass-production and mass customization.

Acknowledgements

The authors would like to thank The Aerospace Corporation, Independent Research and Development Program and the Air Force Office of Scientific Research (Dr. Howard Schlossberg) for their generous support toward understanding the fundamental laser photophysical processes in PSGC materials. Furthermore, the authors would also like to thank the Defense Advance Research Project Agency (Dr. William Coblenz) for the generous support in the development of the first glass-ceramic propulsion system using PSGC materials and laser variable dose fabrication technology. Finally the authors are indebted to Bill Hansen, Lee Steffeney, Adam Huang, Paul Adams and Dr. Siegfried Janson for their help in acquiring the data and for enlightening discussions.

References

1. R. E. Loehman, "Glass-Ceramics for Hermetic Metal-Insulator Seals " J. Met. **38**, (1986) 42.
2. S.D. Stookey, "Chemical Machining of Photosensitive Glass," Ind. Eng. Chem., Vol. 45, (1953) 115.

3. W.W. Hansen, S.W. Janson, and H. Helvajian, "Direct-write UV Laser Microfabrication of 3D Structures in Lithium Aluminosilicate Glass", Proc. SPIE **2991** (1997) pg. 104.
4. W. Hölland and G. Beall, "Glass-Ceramic Technology" (Am. Ceram. Soc. Press, Westerville OH) 2002.
5. P. W. McMillan "Glass Ceramics", 2nd Edition (Academic Press, NY, NY) 1979.
6. A. Berezhnoi, "Glass-ceramics and Photositalls" English translation of Russian text, (Plenum Press, NY) 1970.
7. U. Kreibig, "Small Silver Particles in Photosensitive Glass: Their Nucleation and Growth," Appl. Phys. **10** (1976) pg. 255.
8. J.S. Stroud, "Photoionization of Ce^{3+} in Glass," J. Chem. Phys. **35** (1961) pg. 844.
9. M. Tashiro, N. Soga, and S. Sakka, "Behavior of Cerium Ions in Glasses Exposed to X-rays," J. Ceram. Assoc. Japan **87** (1960) pg. 169.
10. G.A. Sycheva, "Nucleation Kinetics of Lithium Metasilicate in Photosensitive Lithium Aluminosilicate Glass," Glass Phys. and Chem. **25** (1999) pg. 501.
11. F. Liebau, "Untersuchungen an Schicktsilikaten des Formeltyps $A_m(Si_2O_5)_n$. I. Die Kristallstruktur der Zimmertemperaturform des $Li_2Si_2O_5$," Acta Crystallogr. **14**, (1961) pg. 389; R. Dupree, D. Holland and M. G. Mortuza, "A MAS-NMR Investigation of Lithium Silicate Glasses and Glass-Ceramics," J. Non-Cryst. Solids **116** (1990) pg. 148.
12. W. Hölland and G. Beall, "Glass-Ceramic Technology" (Am. Ceram. Soc. Press, Westerville OH, 2002), pg.7.
13. M. P. Borom, A. M. Turkalo and R. H. Doremus, "Strength and Microstructure in Lithium Disilicate Glass-Ceramics", J. Am. Ceram. Soc. Vol. 58, (1975) 385.
14. S.D. Stookey, "Chemical Machining of Photosensitive Glass," Ind. Eng. Chem., Vol. 45, (1953) 115.
15. A. Berezhnoi, "Glass-Ceramics and Photo-Sitalls," (Plenum, New York, 1970).
16. P.D. Fuqua, D. P. Taylor, H. Helvajian, W. W. Hansen, and M. H. Abraham, " A UV Direct-Write Appraoch for Formation of Embedded Structures in Photostructurable Glass-Ceramics" Mat. Res. Soc. Symp. Proc. Vol 624 (2000) pg. 79.
17. F.E. Livingston and H. Helvajian, True 3D Volumetric Patterning of Photostructurable Glass Using UV Laser Irradiation and Variable Exposure Processing: Fabrication of Meso-Scale Devices", Proc. SPIE **4830** (2003) pg. 189.
18. R. Reisfeld, "Spectra and Energy Transfer of Rare Earths in Inorganic Glasses" in *Structure and Bonding*, Vol. 13, J.D. Dunitz, P. Hemmerich, J.A. Ibers, C.K. Jorgensen, J.B. Neilands, R.S. Nyholm, D. Reinen and J.P. Williams, Eds. (Spring-Verlag, New York, 1973) p.53.
19. J.A. Duffy and G.O. Kyd, "Ultraviolet Absorption and Fluorescence Spectra of Cerium and the Effect of Glass Composition," Phys. Chem. Glasses **37** (1996) pg. 45.
20. J.S. Stroud, "Photoionization of Ce^{3+} in Glass," J. Chem. Phys. **35**, (1961) pg. 844.
21. S. D. Stookey, G. H. Beall and J. E. Pierson, "Full-color Photosensitive Glass", J. Appl. Phys. **49**, (1978) pg. 5114.
22. S.D. Stookey, "Chemical Machining of Photosensitive Glass", Industrial & Eng. Chem. Jan. (1953), 115
23. Foturan specification information guide, Schott Corporation Technical Glass Division literature F10/1999.
24. Ibid.
25. F. E. Livingston and H. Helvajian, " Variable UV Laser-Exposure Processing of Photosensitive Glass-Ceramics: Maskless Micro- to Meso-Scale Structure Fabrication", Appl. Phys. A. **81** (2005) pg. 1569.

26. F. E. Livingston, P. M. Adams and H. Helvajian, " Influence of Cerium on the Pulsed UV Nanosecond Laser Processing of Photostructurable Glass Ceramic Materials", Appl. Surf. Sci. **247** (2005) pg. 526.
27. U. Kreibig, "Small Silver Particles in Photosensitive Glass: Their Nucleation and Growth", Appl. Phys. **10** (1976) pg. 255.
28. Ibid
29. J. Bosbach, C. Hendrich, F. Stietz, T. A. Vartanyan, T. Wenzel and F. Traeger, "Laser Manipulation of the Size and Shape of Supported Metal Nanoparticles", Proc. of SPIE 4274 (2001) pg. 1
30. S. Kuper and M. Stuke, "UV-Excimer-Laser Ablation of Polymethylmethacrylate at 248 nm: Characterization of Incubation Sites with Fourier Transform IR- and UV-Spectroscopy", Appl. Phys. A: Solids Surf. **49** (1989) 211.
31. S. Z. Shuja, A. F. M. Arif and B. S. Yilbas, "Laser Repetitive Pulse Heating of Steel Surface: A Material Response to Thermal Loading", J. Manufact. Sci. and Eng., Vol. 124 (2002) 595.
32. F. Verluise, V. Laude, Z.Cheng, Ch. Spielmann and P. Tournois, " Amplitude and Phase Control of Ultrashort Pulses by use of an Acousto-Optic Programmable Dispersive Filter : Pulse Compression and Shaping " Optics Letters, Vol. 25, n°8, (2000) p.575-577.
33. H. F. Dylla and S. T. Corneliussen, "Free-Electron Lasers Come of Age: A Quarter Century after their Invention, free-electron Lasers are Driving Worldwide Investigations", Photonics Spectra, August 2005.
34. Proceedings of the 5th International Conference on Parallel Problem Solving from Nature, A. E. Eiben, T. Back, M. Schoenauer and H-P Schwefel Eds. Lecture Notes in Computer Science Vol. 1498 (Springer Verlag, London, UK) 1998.
35. R. A. Bartels, T. C. Weinacht, S. R. Leone, H. C. Kapteyn and M. M. Murnane, "Nonresonant Control of Multimode Molecular Wave Packets at Room Temperature", Phys. Rev. Lett. Vol. 88 (2002) 033001
36. F.E. Livingston and H. Helvajian, "Development of New Laser Material Processing Technique Using Digitally-Scripted Genotype Sequencing and Electro-Optic Pulse Modulation" Proc. 6th Int. Conference on Laser Precision Microfabrication, LPM2005, Williamsburg, VA 2005.
37. Ibid
38. S. Janson, A. Huang, W. Hansen, and H. Helvajian, "Development of an Inspector Satellite Propulsion Module Using Photostructurable Glass/Ceramic Materials," AIAA paper 2004-6701, presented at CANEUS 2004: Conference on Micro-Nanotechnologies, Monterey, CA, Nov. 1-5, 2004.
39. D. Sutton, S. Janson and H. Helvajian, Workshop Reports, *Proceedings of the International Conference on Integrated Micro/Nanotechnology for Space Applications*, Houston, TX, Oct. 30 to Nov. 3, 1995, The Aerospace Press, El Segundo, CA, 1995.
40. D. Hinkley, D. Williamson and T. George, "MEPSI on STS-113 Post Flight Report," AIAA paper 2004-5847, Space 2004 conference, San Diego, CA, Sept. 28-30, 2004.
41. Ceramic Interconnect Initiative: http://www.imaps.org/cii
42. A. Huang, W. W. Hansen, S. W. Janson and H. Helvajian, "Development of a 100gm Class Inspector Satellite Using Photostructurable Glass/Ceramic Materials", in Photon Processing in Microelectronics and Photonics, K. Sugioka, M. C. Gower, R. F. Haglund, Jr., A. Piqué, F. Träger, J. J. Dubowski, W. Hoving Eds. Proc. SPIE Vol. 4637 (2002) pg. 297.

43. Henry Helvajian and Siegfried W. Janson, “The Fabrication of a 100 gm Co-Orbiting Satellite Assistant (COSA) Using Glass Ceramic Materials And 3-D Laser Processing Techniques,” Proceedings of the 9th International Micromachine/Nanotech Symposium, Tokyo, Japan, pp. 33-41, Nov. 13, 2003.
44. Analog Devices Datasheet “ADXRS150, ” Analog Devices, Norwood, MA, 2003. available online at http://www.analog.com/UploadedFiles/Data_Sheets/740673780ADXRS150_a.pdf
45. Hanada . K Sugioka. Y Gomi . H Yamaoka . O Otsuki . I Miyamoto and K Midorikawa. “Development of Practical System for Laser-Induced Plasma-Assisted Ablation (LIPAA) for Micromachining of Glass Materials” Applied Physics A (Materials Science Processing), Vol.A79, no.4-6, Sept.-Oct. 2004, pp.1001-3.
46. R.L. Jackson, T. H. Baum, T. T. Kodas, S. J. Ehrlich, P. B. Comita, “ Laser Deposition: Energetics and Chemical Kinetics” in Laser Microfabrication: Thin Film Processes and Lithography D. J. Ehrlich and J. Y. Tsao Eds., (Academic Press, NY, NY, 1989) pg. 385.
47. INKA1222210H data sheet, The Lee Company, Westbrook, CT, 2004, at: http://www.theleeco.com/PDF.nsf/bdb21d9b7952d46a85256a400071dc4c/fd40d7f2bf25608585256a9400546396/$FILE/inka1222210hb.pdf

MOLECULAR DESIGN OF POLYMERS FOR LASER STRUCTURING AND THIN OXIDE FILMS BY PULSED LASER DEPOSITION AS MODEL SYSTEM FOR ELECTROCHEMICAL APPLICATIONS

THOMAS LIPPERT
Paul Scherrer Institut, General Energy Research Department, 5232 Villigen PSI, Switzerland; E-mail: thomas.lippert@psi.ch

Abstract. This work reviews the interaction of photons with polymers with an emphasis on UV laser ablation. Polymethylmethacrylate, polyimides and special designed polymers are used as examples to show that the mechanism is a mixture of photochemical and photothermal features which are closely related to the polymer structure and properties. Different approaches to probe the ablation mechanisms and to improve ablation are discussed. A critical evaluation of the experimental procedures and analysis techniques is presented. In the second part the pulsed laser deposition of thin oxides films is considered. Perovskite films and Li-spinel films are analyzed in great details and used as examples of two model systems that are appropriate for application in re-chargeable batteries.

Keywords: Laser ablation, designed polymers, PLD, PRCLA, perovskite, Lithium Spinel, thin film

1. Introduction

1.1. ABLATION OF POLYMERS

The interactions of photons with a polymer can result in a large variety of reactions which range from the modification of the polymer surface to the complete decomposition. The latter usually results in the ablation and/or carbonization of the irradiated polymer area. The first reports about laser ablation of polymers were published in 1982[1,2] and since then numerous studies dealing with ablation of a wide variety of polymers and the ablation mechanism(s) have been published and are well summarized in various

J.J. Dubowski and S. Tanev (eds.), Photon-based Nanoscience and Nanobiotechnology, 267–306.

reviews.[3-9] The discussion about the mechanism of ablation started very soon after the discovery of ablation, and up to now no general agreement exists whether the mechanism is photochemical or photothermal. Recent papers[10] and reviews[11] favor a photothermal mechanism, but these studies are based on modeling of data for one polymer, i.e. Kapton™. This approach may be reasonable, but we should also not forget that there exists a long standing research topic, i.e. organic polymer photochemistry,[12] that has proven over many years that irradiation of organic molecules or polymers with UV photons will result in photochemical reactions. It is therefore very likely that also under ablation conditions, i.e. much higher fluences, photochemical reactions take place. The ablation products and the products of these photochemical reactions are related to the type of polymer and irradiation wavelength. Polymers may be classified for photon-induced reactions into polymers that depolymerize upon irradiation and into polymers that decompose into fragments. The assignment of the polymers to one of these two classes is closely related to the synthesis of the polymer: polymers that are formed by radical polymerization from monomers which contain double bonds are classical candidates for depolymerization upon irradiation, while polymers that are formed by reactions such as polycondensation will not decompose into the monomers upon irradiation. This means of course also that no films with the same chemical structure and/or molecular weight can be obtained by pulsed laser deposition from these polymers as targets. A possible exception may be a process termed resonant infrared pulsed laser deposition (RIR-PLD)[13] where a tunable IR laser, i.e. a free electron laser, is applied as irradiation source. Other processes, such as MAPLE (matrix-assisted pulsed laser evaporation)[14] or RIR-MAPLE[15] may be utilized to form polymer films with intact structures of the films and without any pronounced degradation of the polymer. More common than the deposition of organic or polymeric films is the laser deposition of metallic or ceramic films, which will be discussed for selected oxides films below.

1.2. PULSED LASER DEPOSITION OF METAL OXIDES

For the deposition of thin metal or ceramic films various methods can be applied, such as molecular beam epitaxy (MBE),[16] chemical vapor deposition (CVD),[17] sputtering (RF, Magnetron, and ion beam),[18] and pulsed laser deposition (PLD).[19-21] The advantages of PLD compared with other deposition techniques are well summarized by Chrisey and Hubler.[22] Briefly, the main advantage of PLD is the flexibility to control different parameters which allows an optimization of the deposition conditions. The arrival rates of atoms on the substrate and the possibility to work with

higher pressures of background gases are other important factors. PLD has been successfully used for the growth of many types of multicomponent thin films with a very high quality.[6,23] Nevertheless, some limitations exist, such as particulates, incongruent ablation and oxygen deficiency in oxide materials. To minimize these limitations some modifications to the traditional PLD method have been developed. Some examples for these modifications are Aurora-PLD,[24] RF plasma assisted pulsed laser deposition,[25,26] PLD with an electric field applied to the substrate,[27] UV assisted PLD,[28] off-axis PLD,[29] magnetic-field PLD,[30] and pulsed reactive crossed-beam laser ablation (PRCLA).[31]

The first report on the combination of a pulsed gas supply with PLD was published by Gupta and Hussey in 1991.[32] This setup allows the application of low background pressures, which enables the implementation of *in-situ* vacuum characterization techniques, e.g. reflection high-energy electron diffraction (RHEED). The main difference between this setup and the PRCLA setup used in our studies (Fig. 1) is the distance of the gas pulse to the ablation spot on the target.

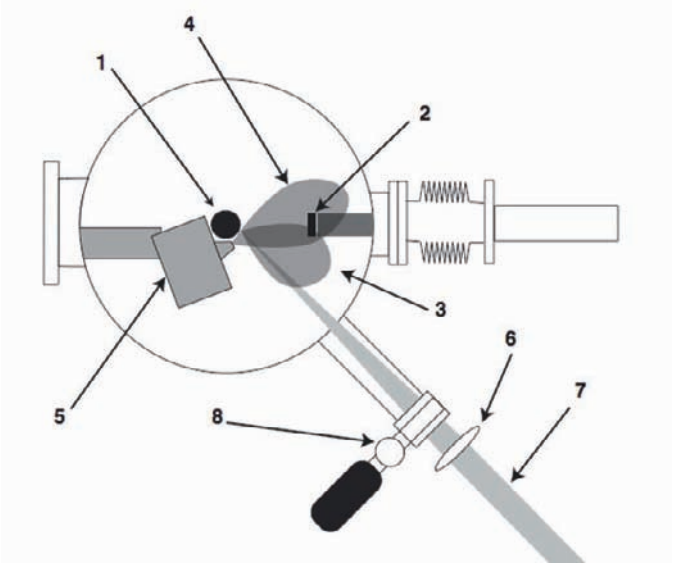

Figure 1. Pulsed reactive cross-beam laser deposition setup: 1) cylindrical target rod, 2), heated and rotating substrate 3) expanding plasma plume generated by the laser, 4) expanding pulsed gas, 5) nozzle of the gas pulse generator, 6) focusing lens, 7) laser beam, 8) inlet for oxygen.

For PRCLA the distance is smaller than 10 mm, which allows an increase of the gas phase interaction and the probability of reactive scattering between the gas pulse and plasma, while the resulting species

propagate freely away from the localized scattering region.[23] The advantages of PRCLA compared to PLD were demonstrated by Willmott and Antoni[33] for the growth of GaN films. PRCLA has also been applied successfully[34] for the growth of perovskite films. The films present the desired oxygen content without any post-annealing procedure.

The optimization of the different deposition parameters during the growth of $La_{0.6}Ca_{0.4}CoO_3$ thin films, and its influence on the electrochemical performance for the oxygen evolution/reduction reaction, are presented in this chapter. The specific material composition was selected due to its industrial application as bifunctional catalyst in electrically rechargeable Zn/air batteries.[35-37]

1.2.1. *Selected Oxides: Perovskites and Li-Spinels*

Metal oxides constitute a fascinating class of materials whose properties cover the entire range from metals to semiconductors and insulators. Their surfaces play a crucial role in several processes, i.e. passivation of metal surfaces against corrosion, catalysis for the partial oxidation of hydrocarbons, and the stability of electrode/electrolyte interfaces in fuel cells.

In spite of all their technological and scientific importance, our understanding of the basic physics and chemistry of metal-oxide surfaces lags a decade or more behind that of other metals and semiconductors. However, over the past twenty years, an increasing number of groups have begun to study the properties of transition metal oxides for novel applications. For example in catalysis stimulated by the discovery of TiO_2 as a catalytic electrode in a photoelectrolysis cell, which decomposes water into H_2 and O_2, without the application of an external voltage[38] or by the discovery of Cu-oxide-based high T_c superconductors.[39]

Metal oxides, with an empirical formula ABO_3, derive their name from the mineral “perovskite”, with the chemical structure $CaTiO_3$. The cubic form of this material is referred to as ideal perovskite, and has a unit cell edge of approximately 4Å. In reality, only a few perovskite-type materials have this ideal cubic structure at room temperature, but many reach it at higher temperatures.[40] Distortions from the cubic symmetry produce tetragonal, orthorhombic, and rhombohedral structures as shown in Fig. 2. In the face centred cubic (FCC) structure the *A cations* are located at the corners while the O atoms are on the faces. The *B cation* is in the centre of the unit cell.

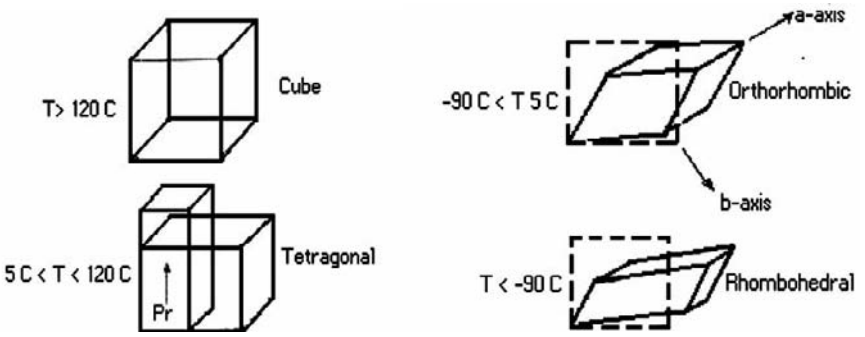

Figure 2. Different perovskite structures.

The perovskite structure possesses a very high degree of compositional flexibility, which allows to accommodate a wide variety of A and B cations, and is also tolerant for large concentrations of both oxygen and cation vacancies. In some complex composition the A and B sites can be occupied by more than one cation species ($A_{1-x}A'_xB_{1-y}B'_yO_3$). In the case of the B sites this can involve cations of more than one element (chemical variation), or different oxidation states of the same element (charge variation).

The physical properties of the perovskite-type materials, such as ferroelectric, dielectric, pyroelectric, and piezoelectric behaviour, will depend on the cation ordering, anion vacancies, and changes in the structural dimensionality. The ongoing research does not only cover the study of magnetic and electronic properties,[41] but also the development of new materials to optimize renewable energy sources, i.e. solid oxide fuel cells[42], direct methanol fuel cells, and metal/air batteries.[43]

The most important topic for the production of metal/air batteries (i.e. Zn/air) is the development of new materials for anodes and cathodes. These materials have to be stable under long term operation conditions (acidic or alkaline medium with an applied potential), and should be cheaper than the commonly used noble metal materials, i.e. Pt. The Zn/air battery is the battery that offers one of the highest storage densities, which is due to the fact that one of the components in the reaction comes from outside of the battery, i.e. atmospheric oxygen from the air as cathode reactant. The recent design of a re-chargeable Zn air battery consists of two electrodes, i.e. Zn paste and a bifunctional oxygen electrode with an integrated electrocatalyst for reduction and evolution of oxygen.[44,45] However, one major problem associated with the development of these secondary batteries is the limited lifetime of the bifunctional electrode (which catalyzes the reduction and the evolution of oxygen). The development of a stable catalyst is still a

challenging task. Only few catalysts are intrinsically bifunctional to act as catalysts for both oxygen reactions. Most of the catalysts exhibit either a low catalytic activity or they are unstable under operating conditions.[46,47] The perovskites containing Co, Fe, Mn and Ni are excellent catalysts for the oxygen evolution (OER) and oxygen reduction reaction (ORR).[48,49] The origin of the catalytic activity is not yet fully understood and the different preparation methods are one reason for conflicting results. The best method to overcome this influence is the preparation of electrodes on inactive substrates with well defined electrolyte/oxide interfaces, i.e. model systems. This will allow to study and compare the mechanism of the oxygen reduction/evolution reaction of different perovskite oxides without any interference from the carbon support material. Another advantage of the model system is the possibility to study the influence of the crystallographic orientation on the catalytic activity. The best model system will therefore be a dense crystalline films deposited on an inactive substrate, which can be prepared by pulsed laser deposition.

Another class of oxides that play a major role for batteries, but in the case of lithium-batteries, is the lithium spinels. The ideal spinel oxide structure is AB_2O_4 where the oxygen atoms form a face-centered cubic packing and occupy 32*e* sites of the space group Fd3m. The cations A and B occupy the tetrahedral 8*a* sites and the 16*d* sites respectively, whereas the octahedral site 16*c* remains empty. The spinel structure is illustrated in Figure 3.

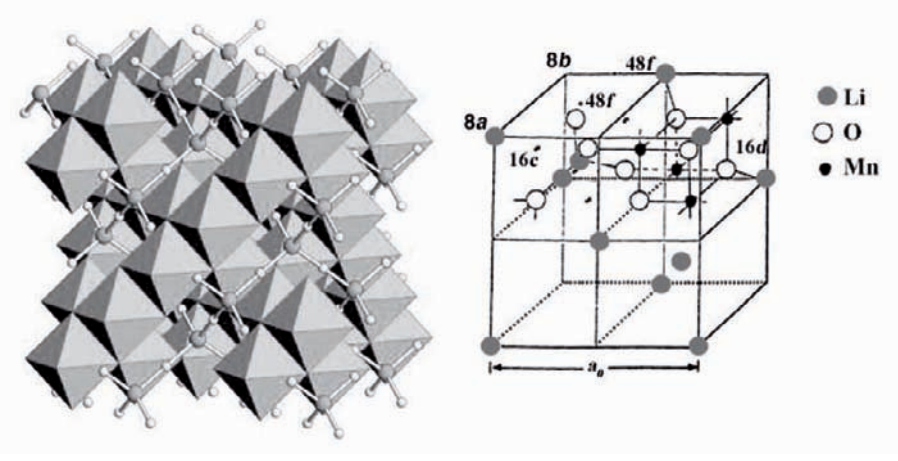

Figure 3. Crystal structure of spinel phase, general (left) and for $LiMn_2O_4$ (right). Adopted from [60].

For cathode electrode materials, suitable lithium spinels oxides are generally of the form LiM_2O_4 (with M: transition Metal such as Mn and

Co). The 8*a* tetrahedral and 16*c* octahedral sites of the Mn_2O_4 framework form a diamond type network. The empty sites are interconnected by common faces and edges to form a three-dimensional pathway for the lithium diffusion (see Fig. 3, right). The angles formed by the consecutive straight spokes, 8*a* - 16*c* - 8*a* measure about 107°. In the case of $LiMn_2O_4$, the lattice constant of the unit cell is 8.247 Å. However, in inverse spinels, where a part of the transition metal ions situated in the 16*d* sites displace the lithium ions in the 8*a* sites and prevent easier diffusion of lithium ions from 8*a* to other 8*a* sites via vacant octahedral 16*c* sites. The lithium intercalation has long been demonstrated for LiM_2O_4 (with M= Ti, V, Mn) with a capacity of one additional lithium atom per formula unit at room temperature.[50-55] In addition to that, some studies were carried out on more complex spinel type phases such as $Li_2Mn_4O_9$, $Li_4Mn_5O_{12}$, $Li_4Ti_5O_{12}$, $LiFe_5O_8$, etc.[56-59]

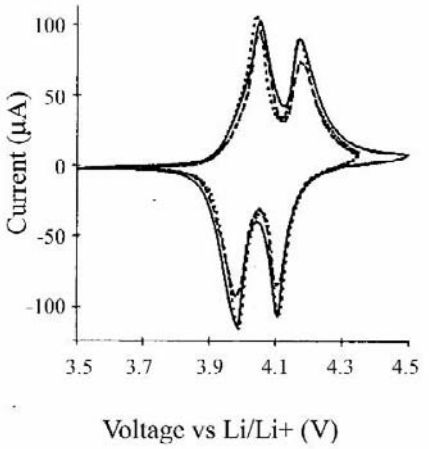

Figure 4. Cyclic voltammogram of three 0.3 μm thick $LiMn_2O_4$ in 1M $LiPF_6$/EC/DMC (1:2), 1 mV/s. Aadopted from [61].

During charge and discharge of the battery, the lithium ions are extracted and reintercalated respectively into the spinel framework. In Fig. 4 a typical cyclic voltammogram in the 3.4 to 4.5 V range of a $LiMn_2O_4$ film produced by PLD onto stainless steel substrates is shown. The four peaks correspond to the intercalation/deintercalation of the Li-ions into the spinel phase. The first step is usually located between 3.9 and 4.1 V (in this case at 4.03 V). It corresponds to the extraction of lithium from half of the tetrahedral sites during charging. The second peak is situated between at 4.17 V and corresponds to the extraction from the rest of the Li ions. The Li-Li interaction forces are much stronger after extraction of the first part of

the Li-ions due to the formation of Mn^{4+} sites. Extraction of Lithium from sites in the neighborhood of Mn^{4+} sites requires more energy, which is the reason for the pronounced two steps Li extraction. The two peaks at 3.99 and 4.1 V (at negative currents) correspond to the reintercalation of lithium upon discharge.

2. Results and Discussion

2.1. ABLATION OF POLYMERS

2.1.1. *Classification of Polymers for Laser Ablation*

A typical example for a polymer that depolymerizes, i.e. forming the monomer, is poly-methylmethacrylate (PMMA), while typical examples for polymers that decompose into fragments are polycarbonates and polyimides. These polymers are formed by the reaction of the monomers where HCl or H_2O are formed as products. These polymers will decompose upon irradiation with photons in some fragments that cannot be identical with the monomers.

In the case of PMMA decomposition into the monomer is possible, but a complete transformation is only possible for a pure thermal degradation with temperatures above the ceiling temperature, T_C (≈ 280 °C), of PMMA. The ceiling temperature is defined as the temperature where the equilibrium between the polymer and monomer is totally on the side of the monomer, but analysis of the ablation products upon irradiation with UV wavelengths reveals that only a small amount, i.e. ≈ 1% for 248 nm irradiation and ≈ 18% for 193 nm irradiation[62,63] of the products is the monomer. The detected products are at least partially compatible with the well-known products of the photolysis of PMMA. The photodecomposition starts with the excitation of monomer unit, where for 248 nm irradiation the $n \rightarrow \pi^*$ transition of the ester group is excited. The following steps are the side chain scission of the ester group which is followed by hydrogen abstraction by the radicals, and elimination of CO or CO_2. The initial reaction, i.e. the bond scission next to the carbonyl group is one of the most prominent photochemical reactions, known as Norrish type I reaction or α-cleavage. The successive steps are the main chain scission which is accompanied by the creation of double bonds (chain end and mid chain) which is also detected during UV laser irradiation of PMMA.[64] These reactions create a modified polymer and the process has been termed photo-yellowing for low photon fluxes, e.g. sunlight, and incubation for ablation conditions. Incubation describes the chemical and physical changes in the polymer prior to ablation, i.e. mainly an increase of the absorption at the irradiation

wavelength. The final step of the PMMA decomposition is the unzipping of the polymer, to yield the monomer. It is noteworthy to mention, that one chain end radical will yield around 6 monomers at room temperature and over 200 at temperatures above the glass transition temperature (T_g = 104 °C). This unzipping reaction is also observed for other polymers such as Teflon and polystyrene. The small fragments, i.e. CH_4, CO, and CH_3OH, the detection of the monomer, and of the double bonds (chain end or in-chain) upon incubation and laser ablation are again clear indications for the involvement of photochemical reactions in the laser ablation process of PMMA. One other important fact is the difference of the products for UV and IR laser irradiation of PMMA. The monomer is the exclusive product upon irradiation with a CO_2 laser,[65] which is a clear indication for a pure thermal process, i.e. heating of the polymer above the ceiling temperature, while UV irradiation yields a rather broad mixture of products. The pronounced differences of the ablation products between UV and mid-IR irradiation and the clear signs for photochemical reaction in PMMA suggest strongly that the clear division of the ablation mechanism into photothermal or photochemical is at least questionable for UV laser ablation.

2.1.2. *Laser Ablation of Selected Polymers*

In an attempt to study the ablation mechanism of PMMA and to apply longer irradiation wavelengths, i.e. 308 nm, which may be economically more interesting, various dopants to induce absorption at this wavelength have been tested. These dopants range from polyaromatic compounds, such as pyrene, to compounds which contain a photochemical active group.[66] The utilization of dopants allows also to decouple the absorption site, i.e. the dopant, from the polymer main chain. The polyaromatic compounds reveal a photothermal mechanism which has been modeled by a cyclic multiphoton absorption mechanism where the triplet states play a key role.[67] The photochemical active compounds have been selected to test whether the properties of the dopants have a pronounced influence on the ablation properties. For these studies various dopants, based on the triazene group (-N=N-N<), have been tested, which are photochemically well studied[68-70] and which release also a large amount of nitrogen during the photochemical decomposition. It has also been suggested that the nitrogen or other released gases may act a driving force of ablation, which carries larger ablation fragments away from the surface. A detailed study of the ablation properties of PMMA doped with these triazene compounds revealed that very high ablation rates of up to 80 µm per pulse could be reached at high laser fluences and low doping levels, i.e. 0.5 to 1 wt.-%. A weak relation between the photochemical activity, i.e. the quantum yield, and the ablation rates was suggested.[71] A clear sign for the release of the gaseous products,

i.e. mainly nitrogen, was detected. The quality of the ablation structures is not satisfying due to the high roughness in the ablation craters, the ill-defined rims, and the large amount of ablation products surrounding the structures. One reason for these features could be the low amount of dopants and the corresponding low absorption coefficients of the doped polymers. Doping of polymers with small molecules is unfortunately limited because it is only possible to dope polymers with up to ≈ 10 wt.-% which is already accompanied by a clear decrease of the glass transition temperatures of the polymers. Higher doping levels can also result in an agglomeration of the dopant, which may cause inhomogeneous ablation. Therefore, new polymers were developed which had the photolabile triazene group in the polymer main chain, with two triazene chromophores in each repetition unit. This approach has several distinct advantages:

- the possibility to evaluate the influence of photochemical reactions on the ablation properties by tailoring the polymer;
- the chance to overcome some of the drawbacks of laser ablation that are normally observed for standard polymers. These drawbacks are the pronounced carbonization of the ablated surface and the redeposition of ablation products in the vicinity and inside the ablation craters.

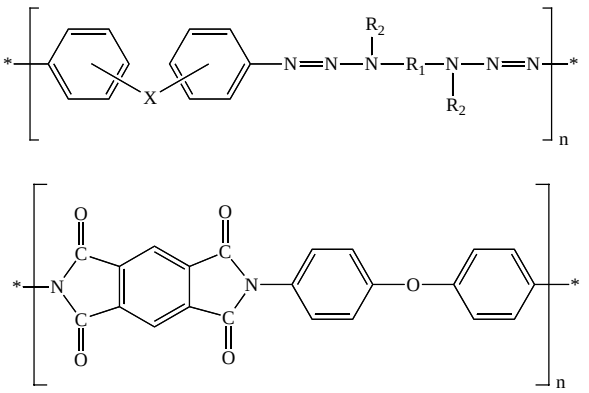

Figure 5. Chemical structures of the triazene polymers (TP) and of polyimide (Kapton™).

The designed triazene-polymers, TP, (general structural unit shown in Figure 5 top) reveal several unique features. The absorption maximum and absorption coefficient can be tuned to certain wavelengths by varying “X” in Figure 5.[69] This allows to match their absorption coefficients to other polymers that are used for comparison, e.g. polyimide, Kapton™ (structure shown in Figure 5 bottom). The absorption maximum of the TP can be tuned from 290 to 360 nm with maximum linear absorption coefficients,

α_{lin}, reaching almost 200 000 cm^{-1}. Typical absorption spectra of a triazene and a polyimide polymer are shown in Figure 6.

The spectrum reveals also one of the very interesting properties of the triazene polymers, i.e. the two absorption maxima that can be clearly assigned to the aromatic system (around 200 nm) and the triazene unit (around 330 nm).[72] This allows to selectively excite various chromophores of the polymer by switching from 193 to 248 and 308 nm irradiation.

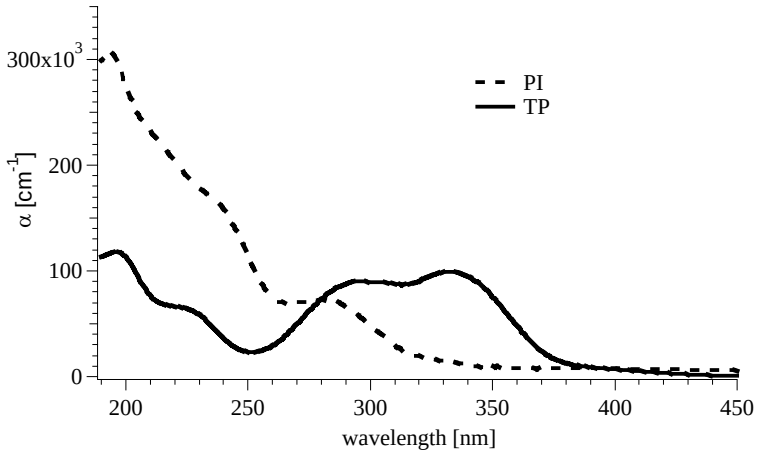

Figure 6. UV-Vis absorption spectra of thin films of a triazene polymer (structure shown in Figure 7) and of a soluble polyimide (similar in structure to Kapton™).

2.1.3. *Ablation of Polyimides and Triazene Polymers*

The detailed comparison of the ablation rates of a polyimide, PI (i.e. Kapton™ HN), and the triazene polymer (with the chemical structure shown in Figure 7) is shown in Figure 8 for irradiation at 308 nm where both polymers exhibit almost the same linear absorption coefficients. The data were analyzed from multi-pulse experiments using the slope of etch depths versus pulse number plots.

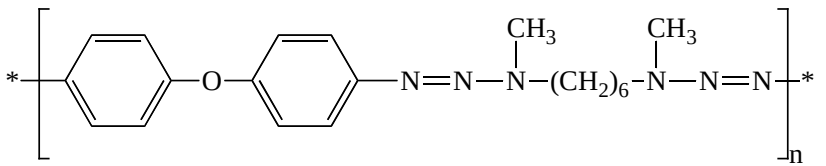

Figure 7. Chemical structure of the triazene polymer which has been used for the UV-Vis absorption spectra and most ablation experiments.

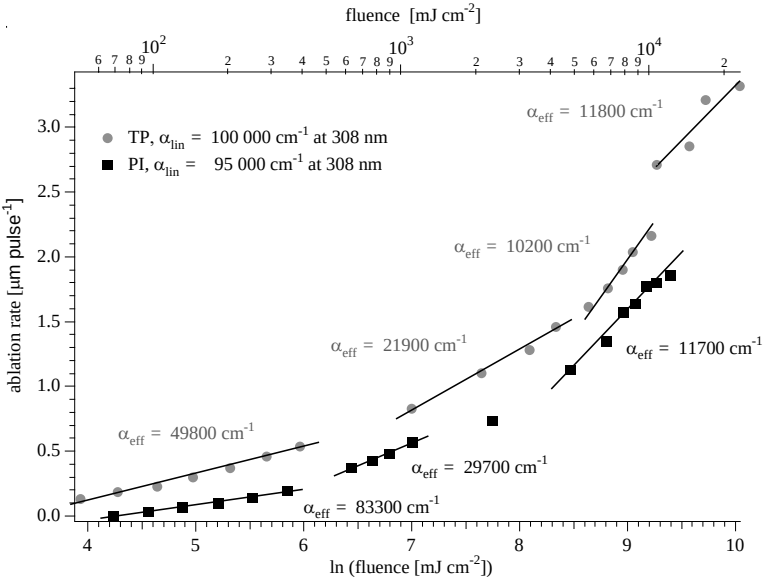

Figure 8. Ablation rates versus laser fluence for TP1 and Kapton™, including the linear fits according to equation 1 to obtain the effective absorption coefficients, α_{eff}.

The effective absorption coefficient, α_{eff} was calculated according to equation 1 (see below). Both polymers reveal a quite complex ablation behavior, which may be described by several linear relations which indicate changes of the ablation process or mechanisms. The linear ranges can be used to calculate α_{eff} which suggest in the case of TP and also for PI (Kapton™) that in the whole fluence range a pronounced bleaching is observed (lower α_{eff} than α_{lin}).[73-75] This results in larger laser penetration depths and therefore higher ablation rates than predicted by the absorption coefficients. This bleaching process is more pronounced for TP in the low fluence range than for PI, but increases for both polymers with increasing fluences. At the highest fluences this trend seem to change in the case of TP, where a slight increase of α_{eff} is observed, which is assigned to plasma absorption (plasma shielding).[74] The differences between the two polymers in the low fluence range are most probably due to the more efficient photochemical decomposition of the TP during the laser pulse. Another interesting difference between these polymers is the quality of the ablated structures. The TP can be structured at this irradiation wavelength with high quality and without any visible redeposited ablation product or modification of the abated polymer surface. The pictures in Figure 9 show the comparison of a test pattern ablated into TP (left) and Kapton™.

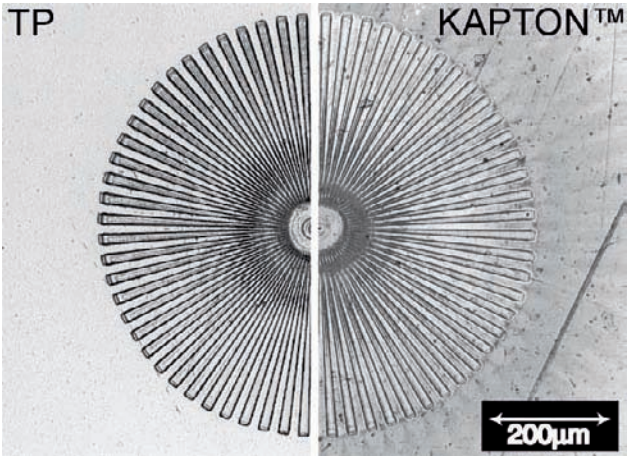

Figure 9. Ablation pattern in TP1 (left) and Kapton™ (right) created by 308 nm irradiation using a gray tone phase mask.

The structure in TP is much sharper and the re-deposited carbon material that is clearly visible for PI is absent. This modification of the surface has been studied for both materials using various analytical tools, such as X-ray photoelectron spectroscopy (XPS) and confocal Raman microscopy.[76, 77] In the case of TP no chemical and physical surface modification was detected for ablation at 308 nm with fluences above the threshold of ablation. The change of the surface composition of Kapton™ has been analyzed in detail by XPS[78] and confocal Raman microscopy.[79] The data show clearly that the ablation structures are surrounded by a carbon layer which is depending on the applied fluence and number of pulses, while inside the structures carbonization was also detected, but with a slightly higher degree of crystallinity for the carbon.[78]

It is noteworthy to mention in this context that "polyimide" (PI) is probably the most studied polymer in laser ablation. Polyimide is also the material for which most ablation models are applied, but great care has to be taken for which polyimide the data are obtained. Polyimide is not single polymer, but describes a class of polymers which contain at least one cyclic imide group (shown in Figure 11) per repetition unit. Even Kapton™ is not one polymer, but there are also many different types of Kapton™, which are defined with additional letters, e.g. HN.

In the context of comparing ablation data it is also very important to be very careful, as the usual ablation parameter, such as ablation rate, d(f), threshold fluence, F_0, and effective absorption coefficient, α_{eff}, are strongly influenced by the method that was applied for determining these values.

The usual way to obtain these values is by applying the following empirical equation[80,81] to the ablation rates:

$$d\ (F) = \frac{1}{\alpha_{eff}} \ln(\frac{F}{F_{th}})$$

The ablation rate per pulse, d(F), is plotted as function of the logarithm of the laser fluence, F, and from the linear fits the threshold fluence, F_0, and the effective absorption coefficient, α_{eff}, are obtained. The first fundamental issue is the ablation rate per pulse, and whether this is defined as an ablation rate for a single pulse, or as the slope of a plot where the ablation depth is plotted as function of the pulse numbers for a given fluence. These two different analytical methods can result in very different ablation rates, especially in the case of polymers which reveal incubation. Incubation is defined as the processes that are often accompanied by an increase of absorption, e.g. due to the double bonds in PMMA and which take place during irradiation or prior to the onset of ablation. This means for ablation that a certain number of pulses are not inducing ablation, but only chemical or physical modification of the polymer. If the ablation rates include these incubation pulses, then of course different ablation rates are obtained then for an analysis where only the pulses are used for which ablation is detected. Another problem in analyzing the ablation depth from multipulse experiments is the above described surface modification of the polymer which may alter the ablation rates with consecutive pulses. These difficulties can be overcome by utilizing only single pulse ablation rates, which are of course more difficult to measure, as very sensitive techniques are needed. Unfortunately even one problem may be encountered for single pulse experiments which originates from an experimental procedure where consecutive pulses are delivered to the same position of the polymer. In the case of polyimide[82,83] and several other polymers chemical modifications are detected, which corresponds very often to carbonization of the polymer. The polymer with this carbonized layer exhibits a different ablation rate, due to the different material properties of this composite material, which are not comparable to the original polymer. It is also necessary to consider that also physical changes of the polymer surface, i.e. an increase of roughness, can cause problems. An increase of roughness corresponds also to an increase of the surface area, which results in an decrease of laser fluence that can even terminate ablation when the fluence decreases below the ablation threshold.[84] True single pulse experiments may also encounter a problem originating from the sample preparation, if solvent based techniques are used. A dense skin layer may be formed, which can exhibit different ablation rates, i.e. lower rates, than the bulk material that contains also remaining solvent. The last point that has to be considered is the

method of measuring the ablation depth. This can be done my "mechanical" methods with a tip, e.g. profilometry or atomic force microscopy, where changes of the surface morphology are detected. Another method is a gravimetric method, i.e. quartz crystal microbalance (QMB), where the weight loss is measured. The latter can and will also detect reactions inside the polymer layer which are associated with a weight loss, e.g. loss of N_2 for the triazene polymer, but not with the creation of an ablation crater that is measured by the "mechanical" methods.

2.1.4. *Ablation Mechanisms*

Various approaches to obtain a better understanding of the ablation mechanisms were developed and may be divided into three different methods:

- Changing the polymer structure
- Time-resolved measurements during ablation and
- Varying the laser pulse lengths and wavelengths.

Various polymers have been designed to study the influence of the chemical structure on the ablation behavior.[85-88] The tested polymers included the triazene-polymers, polymers based on photoactive ester groups, and mixed polymers that contained both groups (ester and triazene). The polymers were compared considering the threshold fluence and ablation rate at low fluences. The lowest thresholds and highest ablation rates were found for the triazene group containing polymers. The linear absorption coefficients are within the tested range (10 000 to 100 000 cm^{-1}) only of minor importance. It is also noteworthy to mention that the triazene polymer with the highest density of the photochemical active triazene groups per repetition unit (TP) reveals the highest ablation rates. The order of the ablation rates also follows quite well the order of photochemical decomposition in solution using low fluences and low concentrations of the polymer in solution (in the range of 10^{-5} Mol l^{-1}).[85] Excimer lamps were also employed to study the effect of low fluence irradiation at 222 and 308 nm, where linear (no ablation) photochemistry is expected.[89] Excimer lamps emit incoherent, quasi-continuous radiation at the same wavelength as the excimer laser. At the low photon fluxes provided by the lamps, multi-photon processes can be neglected. Decomposition of the triazene chromophore was detected by UV-spectroscopy for 222 and 308 nm irradiation, while decomposition of the aromatic chromophore was detected only at 222 nm. This is consistent with the absence of surface carbonization for 308 nm irradiation and the detection of carbonization for 248 nm

irradiation. The triazene-chromophore decomposes at fluences well below the ablation threshold and is clearly the most sensitive chromophore in the triazene-polymer that decomposes directly during 308 nm irradiation. The ablation data suggest also that the photochemical activity and therefore also the possibility of a photochemical part in the ablation mechanism is at least likely.

Therefore one triazene polymer, i.e. TP (Figure 7) was selected for analysis by various time-resolved techniques during and directly after irradiation at 308 nm and 248 nm. The following techniques have been applied to probe the ablation mechanism:

- Time resolved transmission
- Ns shadowgraphy
- Ns surface interferometry and
- Time-of-flight mass spectrometry.

In an attempt to account for the different ablation behavior at 308 and 248 nm, i.e. the different surface modification[76,77] and the lower ablation rates for 248 nm irradiation,[73] time resolved transmission experiments were performed. An increase in transmission with increasing fluences was observed for 248 and 308 nm irradiation, suggesting the presence of a bleaching process at higher fluences.[72,90] In principle, this bleaching could be transient or permanent (=decomposition). A higher degree of bleaching was detected for 308 nm irradiation which can account for the higher ablation rates at this wavelength. To address the issue of a possible photothermal contribution to the ablation mechanism, a nanosecond imaging technique[91-94] was employed that produces a series of shadowgraphs of the air-polymer interface. Two different experimental techniques were employed, which have been described in detail elsewhere.[95] Only a very pronounced shockwave in air was detected which also confirms the absence of solid products for 308 nm irradiation. The advance of the supersonic shock waves can be modeled by a model of the blast wave which incorporates the mass of the ablated polymer and the decomposition enthalpy of the polymer. Shadowgraph imaging was supplemented by ns-surface interferometry.[93,96,97] Interferometric images (shown in Figure 10) can reveal changes in surface morphology on ns-timescales, both during and after the laser pulse. Some of these changes are potentially related to photochemical and photothermal ablation mechanisms: photothermal ablation is often associated with a pronounced surface swelling and delayed material ejection, while photochemical ablation is expected to yield instantaneous etching. Interferometric images of TP at 193, 308[98,99] and 351 nm[97] show that etching of the film begins and ends with the laser pulse (shown in Fig. 10 for 308 nm irradiation). In

contrast, corresponding images of polyimide for 351 nm irradiation reveal pronounced swelling, followed by material removal that persists for microseconds after the laser pulse.[100,101]

Significantly, surface reflectivity measurements (probed at 532 nm) during ablation at 308 nm show a decrease in reflectivity (darkening) during the laser pulse (included in Figure 10) which recovers completely after the laser pulse.[97]

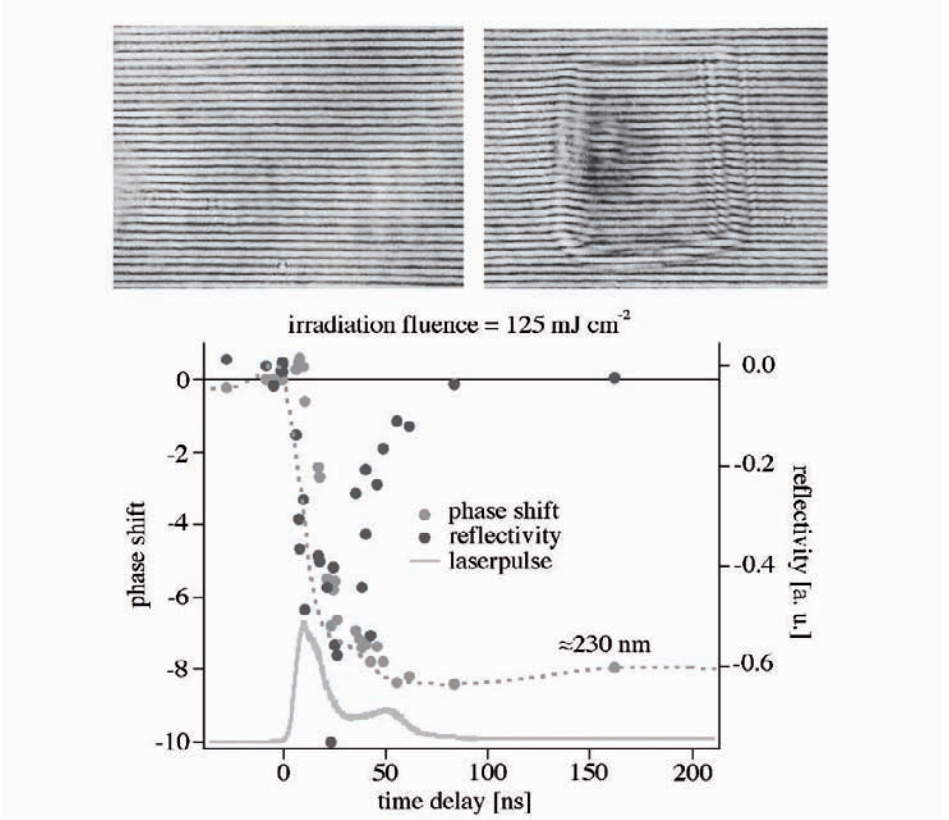

Figure 10. Surface interferometric analysis of the ablation process for TP1 and an irradiation wavelength of 308 nm. Top left: Interference image prior to irradiation; top right: interference image after a delay time of 160 ns. Bottom: analysis of a complete set of interferometric images using a FFT routine which yields the phase shift (depth) and reflectivity.

Insight into the ablation mechanisms is also provided by studying of the ablation products, e.g. by mass-spectrometry. It is noteworthy to mention that time-resolved mass spectrometry at 248 and 308 nm irradiation identified all the expected fragments of the decomposition of TP1 (shown

in Figure 11),[89,102,103] but it is also a fact that thermal decomposition yields similar products.[69]

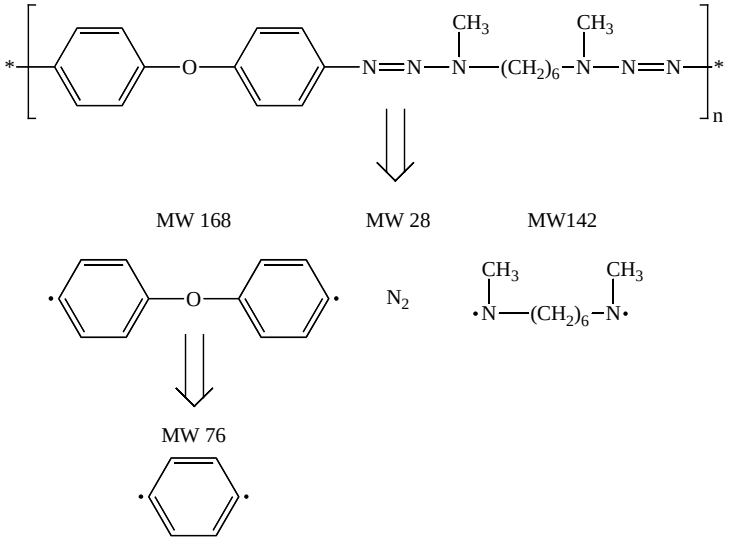

Figure 11. Decomposition pathway for TP1 and 308 nm irradiation with all fragments that were observed in TOF-MS measurements.

Importantly, three different species of nitrogen were detected in the TOF-signals (shown in Figure 12), including a very fast ground state neutral (up to 6 eV of kinetic energy), a slower neutral ground state species with a broad energy distribution (probably a thermal product), and possibly a metastable (excited) neutral N_2 species.[104] The latter can only be created by an electronic excitation. The time of flight curves for a commercial polymer, i.e. Teflon™, after irradiation at 248 nm reveals unzipping, where the main product of decomposition is the monomer (mass 100, C_2F_4). The TOF curve was modeled by a Maxwell-Boltzman distribution which yields a temperature of 710 °C that is at least compatible with the decomposition (> 400 °C) and ceiling temperature (≈ 930 °C) of Teflon.[105]

The data for the photochemical active triazene polymer (TP) suggest strongly that photochemistry can play an important role in the ablation mechanism of polymers, but it is also clear that photothermal induced reactions are also important. This is for example confirmed by the presence of a thermal N_2 product in the TOF curves. A photothermal mechanism will always be present, especially if the polymers decompose exothermically during photochemical decomposition and if the quantum yields of the photochemical reactions is not equal to 1.

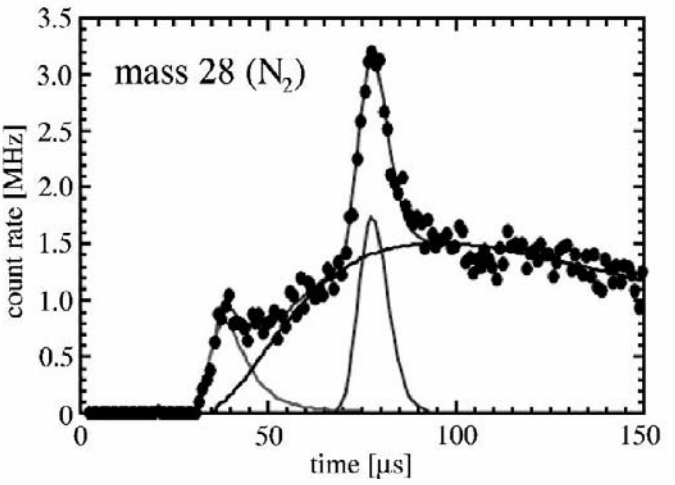

Figure 12. Time of flight curve for mass 28 obtained for 308 nm irradiation of the TP.

Ablation of polymers will therefore always be a mixture between photochemical and photothermal reactions, where the ratio between these two is influenced by the material, i.e. mainly thermal for polymers such as Teflon and with more pronounced photochemical features for photoactive polymers. The photochemical features are, e.g. the bleaching of the triazene chromophore during the pulse, the ablation starting and ending with the laser pulse, and the very fast or metastable ablation products.

2.2. PULSED LASER DEPOSITION OF THIN OXIDE FILMS

2.2.1. *Parameter which Influence Thin Film Growth of Perovskites*

When PLD is performed under vacuum conditions, two main aspects are different from sputtering or conventional thermal evaporation techniques. First, pulses of high vapour fluxes (~ 1 ms) are separated by periods of no vapour flux (~ 100 ms) and relatively high vapour arrival energies at the substrate. Second, there are ions with energies in the keV range and neutral atoms with energies of several eV. PLD can also be performed in the presence of a background gas, e.g. oxygen, two effects are expected during the film formation: the reduction of the kinetic energy of the vapour flux, and a high flux of background oxygen molecules bombarding the surface during deposition. This high flux could change the film and substrate surface energies and will increase the oxygen content (for oxide films). The first arriving pulse causes the nucleation of a high density of smaller

clusters. These subcritical clusters tend to dissociate into mobile species that will nucleate during the time of no vapour arrival into new clusters of a different size. The next pulse will initiate the same process again, with the difference that some of the mobile atoms will reach the previous formed clusters. There are a number of changes in the film growth mode that are readily observed as a function of the PLD parameters (wavelength, fluence, repetition rate, and pulse width). Table 1 presents a summary of different deposition parameters and the effect on the film growth.[22]

Table 1. Relationship between deposition parameters and film characteristics.

Category	Parameters	Effect on process	Possible effect on film
Primary	Laser Wavelength Laser Power Density	Thermal or nonthermal evaporation	Control of compositional variation and transfer ratio
	Laser Repetition Rate	Ratio of neutral to ionic species in the plasma Kinetic energy of the ejected species	Formation of metastable structures Particulates
Secondary	Substrate temperature	Mobility of ablated species on the substrate	Formation of metastable structures
	Oxygen partial pressure	Reactive oxygen species	Oxygen content of film, Epitaxial growth Control of crystal structure
Tertiary	Substrate-target distance	Plume density near the substrate	Film Thickness

2.2.2. *Effect of the Different Oxygen Sources*

The presence of an oxygen background during the film growth is one of the most important aspects to avoid oxygen deficient films. It has been suggested by Craciun et al.[106] that prolonged laser ablation of $La_{0.5}Sr_{0.5}CoO_3$ (LSCO) causes preferential oxygen evaporation in the target, which results in volume absorption and explosive volume boiling, causing the ejecting of droplets from the target[107]. This is not the case for the very similar LCCO compound ($La_{0.6}Ca_{0.4}CoO_3$) using PRCLA as deposition technique, where even after 2×10^6 pulses to the target no changes in the film quality and composition (also of the target) were observed. LCCO-Films grown in an O_2 background are dark and mirror like, independent of the cooling

conditions. The film thickness measured by a profilometer is around 500 nm (after 42000 pulses) with a roughness in the range of 4-5 nm for 21 000 pulses. The composition of the films, measured by RBS, is $La_{0.64\pm0.05}Ca_{0.35\pm0.05}Co_{0.95\pm0.05}O_{3\pm0.05}$, suggesting an almost perfectly congruent material transfer.

The effect of different oxygen sources during PRCLA on the oxygen content of the grown films was studied by applying only the oxygen background (8×10^{-4} mbar), or only the gas pulse (N_2O at 2 bar) or both together, during the deposition process. The compositions of the deposited films are presented in Table 2.

Table 2. Stoichiometry of the LCCO films produced with different oxygen sources.

Film	Deposition Condition	Stoichiometry
A	Gas pulse (2 bar)	$La_{0.68\pm0.05}Ca_{0.32\pm0.05}Co_{0.93\pm0.05}O_{2.6\pm0.05}$
B	Oxygen background (8×10^{-4} mbar)	$La_{0.6\pm0.05}Ca_{0.4\pm0.05}Co_{0.98\pm0.05}O_{2.75\pm0.05}$
C	Gas pulse (2 bar) + oxygen back.	$La_{0.68\pm0.05}Ca_{0.32\pm0.05}Co_{0.91\pm0.05}O_{2.91\pm0.05}$

The composition of the films changes with the different deposition conditions. When the films are grown in the presence of 8×10^{-4} mbar of oxygen background, lower amounts of La and Ca are observed, while the best oxygen stoichiometry is obtained when the films are deposited using the gas pulse and the oxygen background. The presence of only one oxidizing source always produces films with lower oxygen content. The effect of different gases during the formation of multicomponent metal-oxides has been investigated for a long time.[32,108] The oxygen requirements during the growth of oxides are controlled by the oxidation kinetics and the thermodynamic phase stability at the growth temperature.[32] When PLD is used as the film growing technique, a large amount of material is deposited in a very short time separated by periods with no vapor flux. This makes it necessary to have a high flux of oxygen available to oxidize the species that arrive at the substrate. In principle, the oxygen could originate exclusively from the oxide target, without the necessity of an additional oxidizing source. However, only a fraction of the oxygen is released as atoms (neutrals and ions), wile the remaining part is ejected as O_2[109]. The adsorption probability of O_2 is less than unity due to the inefficient adsorption at the surface[110] compared to the high sticking probability of atomic O. The fact that the oxygen molecules have a lower probability of remaining at the substrate surface makes it necessary to utilize an additional oxidizing source for the effective oxidation of the cations during the film growth. The flux of oxygen molecules is much lower in the case of the

$8x10^{-4}$ mbar background, as compared to the flux of liberated target atoms created by laser ablation. The kinetic requirement for stoichiometric oxide growth is therefore not fulfilled (to produce an effective oxidation of the cationic species), resulting in films with an oxygen deficiency. With the synchronized N_2O gas pulse, an excess of oxygen atoms (originating from the dissociation of N_2O by collisional fragmentation with the plasma species, or electron-impact[108]) is created, and the species from the LCCO target arrive simultaneously at the substrate, resulting also in films with oxygen deficiency. The films with the best oxygen stoichiometry are obtained when both oxidizing sources are applied. To understand these results we have to consider not only the arrival time of the particles at the substrate, but also the time between each pulse. There exists an oxygen diffusion equilibrium that influences the oxygen content of the growing film[111,112]. This equilibrium is partially shifted due to loss of oxygen from the film, when only the background is present ($8x10^{-4}$ mbar of oxygen). In the case of the N_2O pulse only, there is more reactive oxygen present leading to the desired oxygen partial pressure during the arrival of the atoms at the substrate. The low background of 2×10^{-6} mbar and the absence of additional oxygen between the pulses will shift the diffusion equilibrium even further in the direction of "out diffusion". When both the N_2O pulse and the additional oxygen background are applied, a large number of oxygen atoms will arrive together with the species originated from the target at the substrate. There is now more oxygen available between the pulses, which minimizes the loss of the volatile oxygen from the surface. Therefore the films with the highest oxygen content are obtained when a gas pulse and background pressure are applied.

2.2.3. *Influence of the Substrate Temperature – Distance Between Target-Substrate*

The substrate temperature not only determines the initial growth of a film, but its subsequent growing as well, and therefore determining its microstructure. In general, the best value of substrate temperature corresponds to the regime where there is sufficient surface diffusion to allow surface atoms to minimize their surface energy to reach thermodynamically stable sites.

The velocity and the kinetic energy of selected neutral and charged ablation species produced by PRCLA are compiled in Table 3. The data are obtained from time- and space-resolved emission spectroscopy. The low kinetic energy of these species arriving at the substrate compared to PLD[113] is due to the large number of collisions with the gas pulse molecules, which occur in the initial interaction zone (around 10 times more collisions than

for PLD)[114]. After the interaction zone the particles propagate freely in the direction of the substrate with almost no collisions with the oxygen molecules of the background gas (8×10^{-4} mbar). The analysis of time and space resolved emission spectra reveal several pronounced differences of PRCLA compared to PLD. First, lower kinetic energies are observed for the species arriving at the substrate. Second, a larger amount of excited states species and (excited) ionic species arrive at the substrate. It is of course important, that the film composition will not change, if the other deposition parameters are varied to optimize/analyze the film growth. A distance between substrate-target of 4.5 cm and a substrate temperature of 650 °C were chosen because epitaxial films could be obtained for these conditions. The results reveal that varying deposition parameters, (i.e. temperature and distance) do not affect the composition of the films, suggesting that the deposition condition can be varied over a wide range without changing the chemical composition of the films. These results can be explained by the fact that the kinetic energy of the ablated species arriving at the substrate (0.74 to 1.99 eV), is too small to cause re-sputtering (typically observed for kinetic energies of »10 eV) of the elements from the growing film.[115] No changes in the stoichiometry are also observed when the distance is kept constant (4.5 cm) and the temperature is varied from 550 °C to 700 °C. This suggests that there is no pronounced re-evaporation of the elements from the growing films at these temperatures.

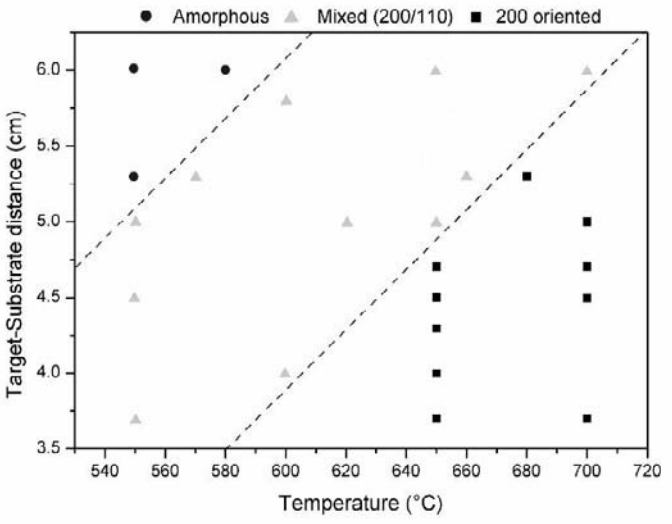

Figure 13. Structure type of LCCO thin film deposited under various conditions of target – to - substrate distance and substrate temperature.

The crystallographic orientations of the grown films as a function of target-substrate distance and substrate temperature are shown in Fig. 13. For a given temperature (e.g. 650 °C) and a variable target-substrate distance the films are only oriented in the (100) direction (same as the substrate) for distances up to approximately 4.7 cm; while for larger distances a mixture of (100/110) orientations is observed. A change in the orientation is also observed when the distance is kept at 4.5 cm and the temperature is increased from 550 to 700 °C. At lower temperatures a mixture of the (100/110) orientation is observed, while at higher temperatures only the (100) orientation is present. Amorphous films can be obtained at low temperatures and large distances. This control of crystallinity can be explained by the kinetic energy of the arriving particles at the substrate surface. Two energy sources are important during PLD film growth, i.e. the kinetic energy of the arriving particles and the substrate temperature, and influence therefore the crystallographic structure and film morphology. The substrate temperature is determining the crystallographic orientation when the distance (kinetic energy) is kept constant. An increase of the temperature improves the surface mobility of the clusters and atoms arriving at the substrate. In this case the number of defects is minimized (due to the surface mobility) and the film growth in the orientation of the substrate. The transition temperature from mixed orientation to epitaxial film growth is observed at higher temperatures when the target-substrate distance is increased (to e.g. 5 cm), yielding lower kinetic energies of the arriving species. This behaviour, i.e. the synergetic effect of the energy from substrate temperature and kinetic energy, is confirmed by the corresponding experiments where the temperature is kept constant while the distance is varied. The transition of mixed orientation to single crystalline is now observed when the distances are decreased. The variation of these two parameter (distance and temperature), gives the unique opportunity to prepare films with crystallographic features that vary from amorphous to epitaxial without changing the pressure of the background gas or the substrate.

2.2.4. *Electrochemical Characterization of Thin Films vs. Gas Diffusion Electrodes*

The comparison between gas diffusion and thin films will only be discussed briefly. An electrochemical process involves several steps, i.e. mass transfer, chemical reaction, adsorption/desorption, and electron transfer. The mass transfer of oxygen from the solution to the electrode surface is assumed to be the same for both electrode types. For the last two steps a pronounced difference exists between the gas diffusion and the thin film

electrodes. In the gas diffusion electrode the surface is porous and the real area of the electrode is extremely difficult to determine. Additionally, the reactive area consists of carbon and catalyst. Contrary to this, the thin film electrode consists of a compact structure with very few small pores. The surface area can be assumed to have a similar value as the geometrical area and only the catalyst is present on the surface. These differences suggest that different adsorption mechanisms are present on both surfaces. If we consider the electron transfer as well, the situation becomes even more complicated due to the fact that for thin films the electron transfer will be possible only through electron holes or oxygen vacancies and determination of their presence in the crystal lattice during the redox-reaction is nearly impossible. For the gas diffusion electrode the electron transfer will take place on different surfaces, i.e. on the perovskite (oxygen evolution) and on the carbon followed by the perovskite (oxygen reduction). Any attempt at a quantitative comparison between the systems will therefore be associated with a large systematic error. Polarization curves reveal that the model systems present a slightly smaller overpotential for the two oxygen reactions than the optimized gas diffusion electrode. The model system is more active for the oxygen evolution reaction while the gas diffusion electrode is more active for the oxygen reduction reaction. An important factor is that current density values are comparable to the ones obtained for the carbon-based perovskite gas diffusion electrodes, indicating that thin films can be used as model system to screen different perovskite electrodes.

2.2.5. *Effect of the Crystallinity on the Electrochemical Activity*

Most of the reported electrochemistry with solid electrodes involves polycrystalline materials. Such electrodes consist of a variety of small domains with different crystal faces and edges which will face the electrolyte. Different crystal faces exhibit different properties (e.g. work function) so that the behavior observed at a polycrystalline electrode represents an average of that for a number of different crystal planes and sites. One possible way to analyze solid electrode interfaces and their influence in a specific reaction can be performed by using single-crystal electrodes. The most common metals used as electrodes, i.e. Pt, Pd, Ag, Ni and Cu, form face-centered cubic crystal structures. Three low index faces (100), (110), and (111) are the surfaces most frequently used as electrodes, because they tend to be stable and can be polished to yield fairly smooth, uniform surfaces. Nevertheless, even the most carefully prepared surfaces are not atomically smooth over areas larger than a few square micrometers, and they inevitably show steps, edges, and defect sites. Catalytic and adsorptive properties of solid surfaces can depend upon the crystal face. An

example is the difference in cyclic voltammograms for the adsorption/desorption of hydrogen on the different surfaces of platinum.[116]

The importance of the crystallinity on several electrochemical reactions and the fact that until now the studies for the oxygen evolution/reduction on LCCO were only performed on polycrystalline gas diffusion electrodes were one of the driving forces to perform experiments using thin LCCO films with different crystallographic orientations. Only for dense films will the observed catalytic activity correspond to the catalyst and the active area of the electrode can be easily determined and compared to other electrodes.

The polarization curves for thin amorphous, mixed, and single crystalline LCCO films are compared in Fig. 14.

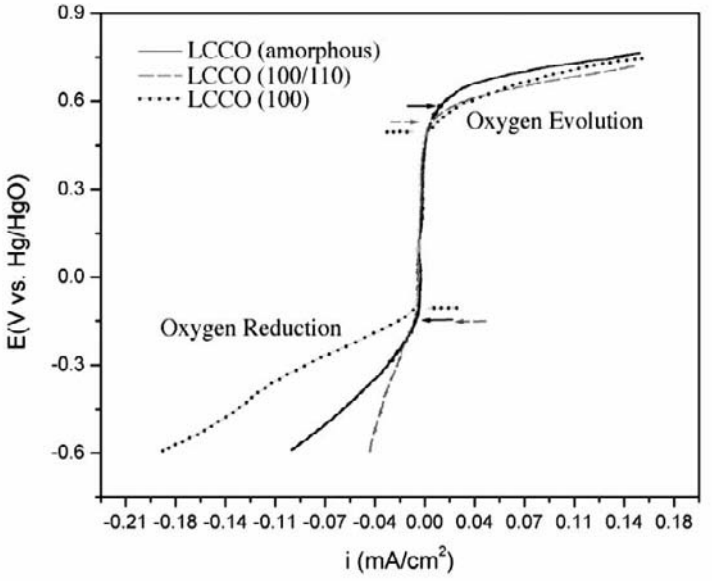

Figure 14. Polarization curves of amorphous, single- and polycrystalline LCCO thin films deposited on MgO(100) substrates.

The polarization curves show that the crystallinity influences directly the catalytic activity for oxygen reduction and evolution reactions (measured by the overpotential). The overpotential is the difference between the values indicated with the arrows in Fig. 14. The film with the smallest overpotential (597 mV) is the (100) oriented sample followed by the film with mixed 110 and 200 orientation (679 mV) and the amorphous film (738 mV). An electrochemical process, as discussed previously, involves several steps, i.e. mass transfer, chemical reaction, adsorption/desorption, and electron transfer. The result indicates that the only step that can influence the electrochemical behaviour of these three

electrodes, i.e. the adsorption of the oxygen molecules, is affected by the surface energy of the electrode surface, which depends on the exposed crystallographic orientation and grain boundaries. It can also be concluded that the phase with (100) orientation presents the best performance.

2.2.6. *Parameters Influencing the Deposition of Lithium Spinel Films*

In the case of Li-spinels different substrate materials can result in different preferred crystallographic orientation of the deposited film. Several authors[117, 118] have shown that the deposited films form a polycrystalline spinel with random orientation on substrates such as platinum, stainless steel and silicon. However, Rougier et al. have shown that the utilization of $Si(100)/Si_3N_4$ substrates yields to a preferred (111) orientation.[119] Another parameter that influences the crystallinity of the films is the substrate temperature.[120-122] At higher substrate temperatures the characteristic reflexes in the X-ray-diffraction patterns ((111) at 19.5° and (444) at ~ 45°,[122]) increases. These reflexes are associated with the degree of crystallinity of the films. This influence has previously been shown by various authors.[117,120,123,124] who also analyzed the influence of the oxygen background pressure and target composition. Julien et al.[120] revealed that films grown from a target with an excess of 5% of lithium shows very poor crystallinity. With an increasing excess of lithium in the target (up to 15%), the deposited films reach the regular spinel crystal structure, which can also be improved with increasing substrate temperatures. These experiments where carried out at relatively low substrate temperatures, ranging from 100 °C to 300 °C and at a very low background pressure of $6.7x10^{-5}$ mbar of O_2 and with non stoichiometric targets. The necessary experimental parameters may vary from theses values when using a stoichiometric target. As described earlier for the perovskite-type phases, Pulsed Reactive Cross-Beam Laser Deposition (PRCLA) is in principle a very suitable method for the deposition of complex oxides. However, in the case of spinels the utilization of the PRCLA set up is not applicable due to the crossed gas pulse, which significantly increases the scattering of light atoms, such as lithium. Only a minor amount of Li-spinel can be detected in the XRD spectra.

In Fig. 15 the X-ray diffraction (XRD) patterns of $LiMn_2O_4$ deposited on polished titanium using the classical PLD setup (without the gas pulse) at an oxygen pressure of 0.2 mbar and a substrate temperature of 510 °C is shown. A KrF excimer laser (248 nm) with a repetition rate of 10 Hz, a fluence of 3-4 J/cm^2 and 18000 pulses was used for the deposition. The diffraction patterns show clearly the reflexes that can be attributed to a spinel structure of the film which is in agreement with results reported by other groups[117,119,125].

Fig 16 shows the cyclic voltammogram of a $LiMn_2O_4$ film deposited on polished titanium foil under the same conditions. The film is roughly 0.7 μm thick.

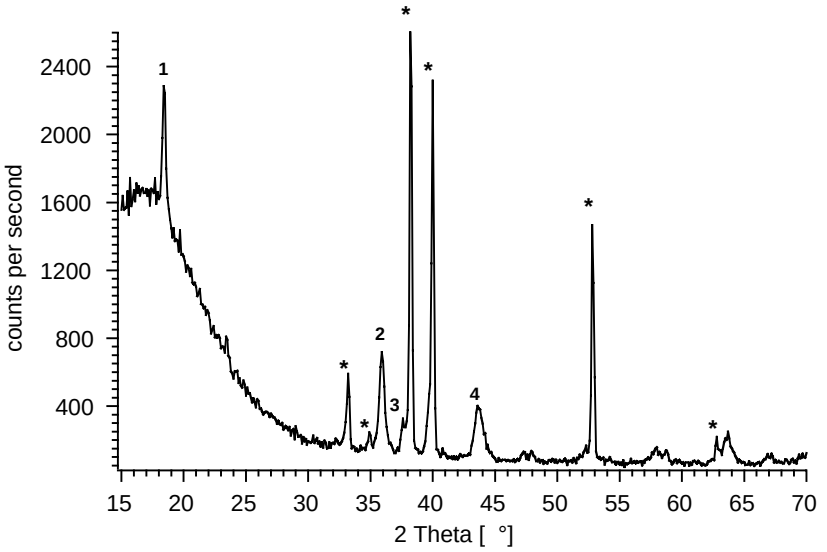

Figure 15. XRD spectrum of a $LiMn_2O_4$ (nominal composition) film deposited on a titanium substrate. The signals that can be attributed to a spinel structure are: 18.4° for the (111) (1), 35.6° for the (311) (2), 37.78° for the (222) (3) and 43.6° for the (004) (4) orientation. The peaks marked with an asterisk can be assigned to the titanium substrate.

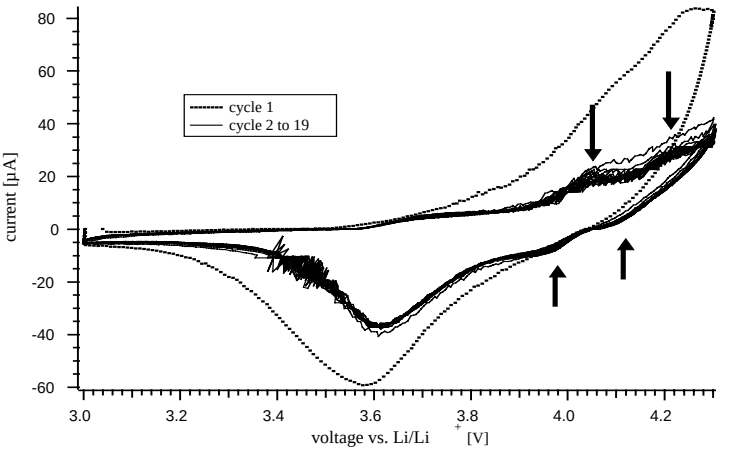

Figure 16. Cyclic Voltammogram of a $LiMn_2O_4$ (nominal composition) film deposited on a titanium substrate at a distance of 3 cm from the target.

In the first cycle an oxidation peak is observed around 3.6 V. However, this is most probably not related to the extraction of lithium from the lithium manganate spinel but is due to the titanium substrate. The peaks around 3.6 V in the negative current region and the increase of the current at 3.6 V in the positive current region correspond quite well with the peaks found for an uncoated Ti-foil sample (see Fig. 17). The extraction/insertion of lithium from the lithium spinel can be detected as very weak peaks in the voltammogram (see arrows in Fig. 16). These peaks occur in the expected region, i.e. two oxidation peaks between 4.05 V and 4.2 V in the positive current region and two reduction peaks between 3.9 V and 4.1 V in the negative current region. This leads to the conclusion that a spinel phase is present on the substrate. The difference between the first and the following cycles is most probably due to the expected formation of an solid electrolyte interphase (SEI) and, possibly, structural transformation. The pronounced noises in Fig. 16, e.g. between 3.4 and 3.5 V, are currents from the electrochemical reactions of the electrolyte in solution in contact with the non-coated surface of the titanium substrate.

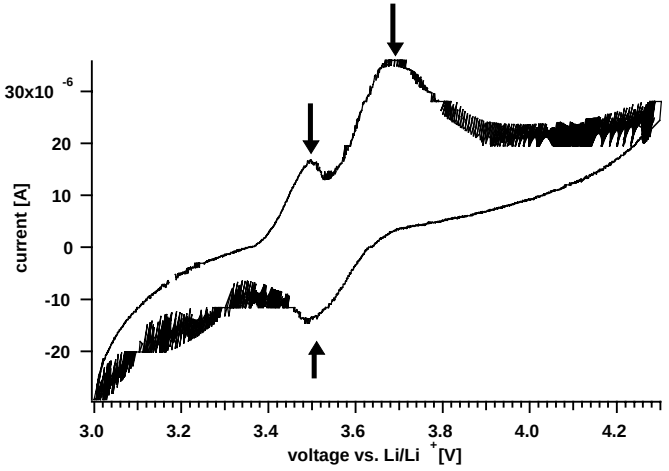

Figure 17. CV of an uncoated titanium foil sample. Arrows mark the extraction and reintercalation of lithium into the titanium-oxide layer.

The RBS/ERDA measurements reveal a strong lithium deficiency (Li/Mn ration between 0.4 and 0.5) for all films deposited under an oxygen background pressure between 0.1 and 0.3 mbar. Nevertheless, the X-ray diffraction patterns in Fig. 15 give clear evidence for the presence of a spinel phase but which may not be homogeneously distributed over the whole substrate. There are two possible ways to overcome this problem. One possibility is to utilize an excess of lithium in the target,[119,120,124] or to optimize the conditions for the classical PLD setup (without the gas pulse).

Morcrette et al.[117,123] have shown that there is a small window for the oxygen background pressure that can be used for the stoichiometric deposition of $LiMn_2O_4$. The group analyzed $LiMn_2O_4$ films deposited on polycrystalline platinum substrates by PLD from a stoichiometric target. The oxygen pressure was varied between 10^{-6} and 1 mbar while the temperature was varied between 300 and 700°C.[117,123] A quadrupled Nd:YAG laser with a wavelength of 266 nm, 5 Hz repetition rate and with a fluence of 2 J/cm^2 was applied for these experiments. No post-deposition annealing was performed to eliminate the possibility of compositional changes in the film. The results indicate that a low background pressure results in lithium deficient films. This is most probably due to the low vapor pressure of Lithium oxide which could evaporate at lower oxygen background pressure and higher substrate temperatures.

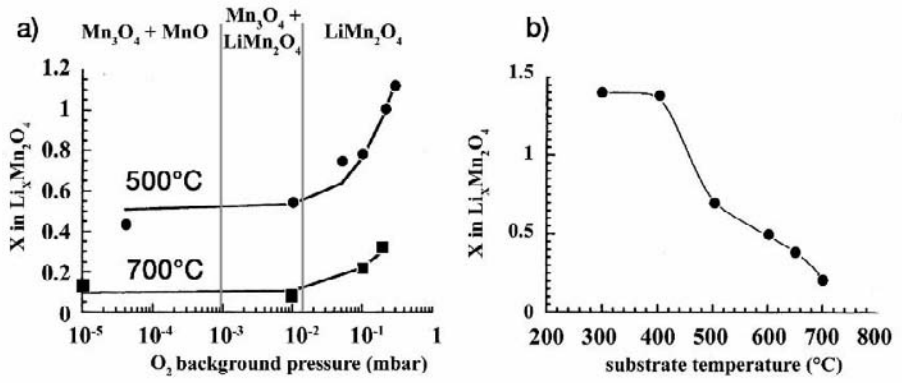

Figure 18. (a) RBS analysis of the Li stoichiometry coefficient as a function of the oxygen pressure for two temperatures 500°C (top curve) and 700°C (bottom curve), (b) RBS analysis of the Li stoichiometry coefficient as a function of temperature for the pressure of 0.1 mbar. Adopted from [117].

The higher oxidation states of manganese, such as Mn^{3+} in $Li_xMn_2O_4$ are not formed in the film since lower oxidation states, such as Mn^{2+} are favored.[117] In Fig. 18 the RBS analysis of the Li/Mn ratio as a function of oxygen pressure and substrate temperature is shown, which reveals a manganese deficiency due to high background pressure.[123] The optimized pressure for obtaining a $LiMn_2O_4$ spinel phase is 0.2 mbar while the optimum temperature for 0.1 mbar of pressure is 450 °C (Fig. 18b). The electrochemical characterization, i.e. cyclic voltammogram, of these films correspond to what is expected from $LiMn_2O_4$.[117,123] Experiments performed at different target/substrate distances between 3 and 7 cm and background pressures between 0.1 and 0.3 mbar support these results.[126] XRD

measurements revealed a spinel phase on all substrates deposited at these conditions, however, electrochemical activity in the expected voltage range was only obtained for films deposited at a background pressure of 0.2 mbar and at a distance between the target and the substrate of 3-4 cm (see Fig. 16). Furthermore, RBS/ERDA measurements revealed a strong deficiency in lithium and oxygen in these films. Whereas the oxygen content can be easily increased by cooling down the sample in pure oxygen atmosphere after deposition, the increase of the lithium content is much more difficult. Characterization of the laser-created plasma with a Langmuir Probe and Mass spectroscopy suggest the presence of high energetic ions (over 50 eV), mainly lithium and manganese, which can resputter the growing film from the substrate. An increase of the background pressure from $1 \cdot 10^{-4}$ mbar to 1 mbar strongly reduces the kinetic energy of these ions, especially of manganese which results in a lower sputtering yield of the ionic species in the plasma. The reduced sputtering yield can be observed by measuring the deposition rate with a Quartz Crystal Microbalance (QCM) for various laser energies and variable background pressures (see Fig. 19). Higher laser fluences result as expected from larger ablation rates in higher growth rates per pulse.

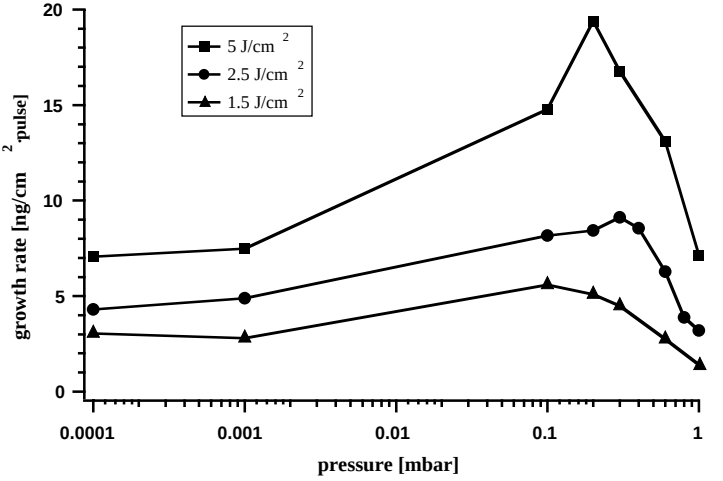

Figure 19. Pressure dependence of the growth rate at constant laser fluence of 1.5, 2.5 and 5 J/cm^2.

The deposition rate first increases with increasing background pressure, then decreases again after reaching a peak around 0.1-0.3 mbar. The position of this peak corresponds to the small window of 0.1 to 0.3 mbar for optimum deposition conditions. It might therefore be possible that the

lithium deficiency in the films is also a result of preferential resputtering of Li caused by the fast ionic species in the plasma which are sufficiently slowed down by the molecules of the background gas at higher pressures.

3. Conclusion

Laser ablation of polymers is an established technique in various industrial applications and the large number of studies published annually indicate that this is still an attractive area of research. Discussions above the ablation mechanisms are ongoing and will continue to be one of the topics in ablation of polymers. The development of polymers designed specifically for laser ablation is a unique tool for probing the ablation mechanisms as well as for improving ablation properties. New commercial applications will require improved ablation rates and control of undesirable surface effects, such as debris. The complexity of interactions between polymers and laser photons are illustrated by the various processes associated with different irradiation conditions, e.g for short pulses, high repetition rates, CW irradiation, etc.. The ongoing maturation of laser techniques will increase the number of applications of laser ablation in the future. In the last decade we have seen the development of several exciting laser ablation tools, including femtosecond lasers, VUV lasers, free electron lasers, and high repetition-rate lasers. All these new techniques are applied in ongoing research in conjunction with a variety of analytical techniques. Femtosecond lasers and VUV lasers in particular are expected to lead to important industrial applications. The simultaneous development of various VUV sources for large area irradiation, such as excimer or resonance lamps, will also result in a steady increase of applications and a better understanding of photon induced processes in polymers.

The application of PRCLA as deposition technique allows the preparation of thin films of perovskite-type oxide materials with a nearly completely filled oxygen sublattice and without additional processing steps (e.g. annealing). The low kinetic energy of the atoms/species arriving at the substrate surface prevents re-sputtering, which yields films with the same composition as the target material, for a variety of target-substrate distances. The crystallinity of the films can be controlled from amorphous to single crystalline, by varying the substrate temperature, the substrate and its orientation, and the distance between target and substrate. Our studies have revealed that the crystallinity has a pronounced influence on the catalytic activity. The films produced by PRCLA prove the possibility to apply thin films as model systems for electrochemical studies. Epitaxial films of LCCO reveal a higher activity than films with mixed orientation, followed by amorphous films.

For the Li-spinels, it can be concluded that the deposition of $LiMn_2O_4$ is most practicable with a standard PLD equipment, but physical constraints such as atom scattering and vapor pressure leave only a small window for the optimum experimental parameters. The optimum conditions are a background pressure around 0.2 mbar and a substrate temperature of 500 °C. However, the lithium deficiency in the deposited film is still an issue. This deficiency is most probably due to the evaporation of lithium from the film and to the sputtering effect of high energetic ions in the plasma at low background pressures. At higher background pressures, these ions are sufficiently slowed down to minimize the damage produced at the film surface. The deposition of stoichiometric $LiMn_2O_4$ from a stoichiometric target has been demonstrated by Morcrette et al.[117,123]. Nevertheless, the utilization of an excess of lithium in the target seems to be the easiest way to compensate for the loss of lithium during deposition. The extraction/insertion of lithium from the lithium spinel could be detected for the films deposited at the optimized conditions. Differences between the first and the following cycles can be assigned most probably to the expected formation of a solid electrolyte interphase (SEI) and, possibly, structural transformation. This proves that thin films are also in the case of Li-ion batteries very good model system to study the fundamental processes of Li intercalation and de-intercalation and of the corresponding interphase processes.

Acknowledgements

This work has been partially supported by the Swiss National Science Foundation.

References

1. R. Srinivasan and V. Mayne-Banton, Self-Developing Photoetching Of Poly(Ethylene-Terephthalate) Films By Far Ultraviolet Excimer Laser-Radiation, *Appl. Phys. Lett.* 41(6), 576-578 (1982).
2. Y. Kawamura, K. Toyoda and S. Namba, Effective Deep Ultraviolet Photoetching Of Poly(Methyl Methacrylate) By An Excimer Laser, *Appl. Phys. Lett.* 40(5), 374-375 (1982).
3. R. Srinivasan and B. Braren, Ultraviolet-Laser Ablation Of Organic Polymers, *Chem. Rev.* 89(6), 1303-1316 (1989).
4. P. E. Dyer, *Photochemical processing of materials*, (Academic Press, London, 1992).
5. S. Lazare and V. Granier, Ultraviolet-Laser Photoablation Of Polymers - A Review And Recent Results, *Laser Chem.* 10(1), 25-40 (1989).
6. D. Bäuerle, *Laser Processing and Chemistry*, (Springer Verlag, Berlin, 2000).

7. T. Lippert and J. T. Dickinson, Chemical and spectroscopic aspects of polymer ablation: Special features and novel directions, *Chem. Rev.* 103(2), 453-485 (2003).
8. T. Lippert, in: Polymers And Light, (Springer-Verlag Berlin, Berlin, 2004), pp. 51-246.
9. N. Bityurin, Studies on laser ablation of polymers, *Annu. Rep. Prog. Chem., Sect. C* 101, 216-247 (2005).
10. N. Arnold and N. Bityurin, Model for laser-induced thermal degradation and ablation of polymers, *Appl. Phys. A-Mater. Sci. Process.* 68(6), 615-625 (1999).
11. N. Bityurin, B. S. Luk'yanchuk, M. H. Hong and T. C. Chong, Models for laser ablation of polymers, *Chem. Rev.* 103(2), 519-552 (2003).
12. J. F. Rabek, *Mechanism of Photophysical Processes and Photochemical Reactions in Polymers*, (John Wiley & Sons, 1987).
13. D. B. Chrisey, A. Pique, R. A. McGill, J. S. Horwitz, B. R. Ringeisen, D. M. Bubb and P. K. Wu, Laser deposition of polymer and biomaterial films, *Chem. Rev.* 103(2), 553-576 (2003).
14. A. Pique, R. A. McGill, D. B. Chrisey, D. Leonhardt, T. E. Mslna, B. J. Spargo, J. H. Callahan, R. W. Vachet, R. Chung and M. A. Bucaro, Growth of organic thin films by the matrix assisted pulsed laser evaporation (MAPLE) technique, *Thin Solid Films* 356, 536-541 (1999).
15. B. Toftmann, M. R. Papantonakis, R. C. Y. Auyeung, W. Kim, S. M. O'Malley, D. M. Bubb, J. S. Horwitz, J. Schou, P. M. Johansen and R. E. Haglund, UV and RIR matrix assisted pulsed laser deposition of organic MEH-PPV films, *Thin Solid Films* 453-54, 177-181 (2004).
16. H. S. Wang, D. Eissler, Y. Kershaw, W. Dietsche, A. Fischer, K. Ploog and D. Brunner, New Crucible Made Of Y_2O_3 For Preparing Yttrium Based High-T_c Superconducting Films By Molecular-Beam Epitaxy, *Appl. Phys. Lett.* 60(6), 778-780 (1992).
17. C. Dubourdieu, M. Rosina, H. Roussel, F. Weiss, J. P. Senateur and J. L. Hodeau, Pulsed liquid-injection metalorganic chemical vapor deposition of $(La_{0.7}Sr_{0.3}MnO_3/SrTiO_3)(15)$ superlattices, *Appl. Phys. Lett.* 79(9), 1246-1248 (2001).
18. T. G. S. Cruz, M. U. Kleinke and A. Gorenstein, Evidence of local and global scaling regimes in thin films deposited by sputtering: An atomic force microscopy and electrochemical study, *Appl. Phys. Lett.* 81(26), 4922-4924 (2002).
19. V. G. Prokhorov, Y. P. Lee, K. W. Kim, V. M. Ishchuk and I. N. Chukanova, Long-aging effects on the properties of $La_{0.5}Sr_{0.5}CoO_3$-delta films, *Appl. Phys. Lett.* 80(13), 2353-2355 (2002).
20. F. J. Cadieu, L. Chen, B. Li and T. Theodoropoulos, Enhanced room temperature magnetoresistance response in textured $La_{0.7}Sr_{0.3}MnO_3$ strips made by pulsed laser deposition, *J. Appl. Phys.* 87(9), 6770-6772 (2000).
21. R. Rauer, J. Backstrom, D. Budelmann, M. Kurfiss, M. Schilling, M. Rubhausen, T. Walter, K. Dorr and S. L. Cooper, Thickness dependent phase separation in $La_{0.7}Ca_{0.3}MnO_3$ films, *Appl. Phys. Lett.* 81(20), 3777-3779 (2002).
22. D. B. Chrisey and G. K. Hubler (eds.), *Pulsed Laser Deposition of Thin Films*, (John Wiley & Son, New York, 1994).
23. P. R. Willmott and J. R. Huber, Pulsed laser vaporization and deposition, *Reviews Of Modern Physics* 72(1), 315-328 (2000).
24. T. Kobayashi, H. Akiyoshi and M. Tachiki, Development of prominent PLD (Aurora method) suitable for high-quality and low-temperature film growth, *Appl. Surf. Sci.* 197, 294-303 (2002).
25. A. Giardini, V. Marotta, A. Morone, S. Orlando and G. P. Parisi, Thin films deposition in RF generated plasma by reactive pulsed laser ablation, *Appl. Surf. Sci.* 197, 338-342 (2002).

26. C. Vivien, M. Dinescu, P. Meheust, C. Boulmer-Leborgne, A. P. Caricato and J. Perriere, Nitride-molecule synthesis in plasma produced by reactive laser ablation assisted by RF discharge for thin-film deposition, *Appl. Surf. Sci.* 129, 668-673 (1998).
27. A. Narazaki, T. Sato, Y. Kawaguchi, H. Niino, A. Yabe, T. Sasaki and N. Koshizaki, Pulsed laser deposition of semiconductor-ITO composite films on electric-field-applied substrates, *Appl. Surf. Sci.* 197, 438-441 (2002).
28. V. Craciun, D. Craciun, Z. Chen, J. Hwang and R. K. Singh, Room temperature growth of indium tin oxide thin films by ultraviolet-assisted pulsed laser deposition, *Appl. Surf. Sci.* 168(1-4), 118-122 (2000).
29. J. W. Yoon, T. Sasaki and N. Koshizaki, Pressure-controlled preparation of nanocrystalline complex oxides using pulsed-laser ablation at room temperature, *Appl. Phys. A-Mater. Sci. Process.* 76(4), 641-643 (2003).
30. G. Radhakrishnan and P. M. Adams, Pulsed-laser deposition of particulate-free TiC coatings for tribological applications, *Appl. Phys. A-Mater. Sci. Process.* 69, S33-S38 (1999).
31. M. J. Montenegro, M. Dobeli, T. Lippert, S. Muller, B. Schnyder, A. Weidenkaff, P. R. Willmott and A. Wokaun, Pulsed laser deposition of $La_{0.6}Ca_{0.4}CoO_3$ (LCCO) films. A promising metal-oxide catalyst for air based batteries, *Phys. Chem. Chem. Phys.* 4(12), 2799-2805 (2002).
32. A. Gupta and B. W. Hussey, Laser Deposition Of $YBa_2Cu_3O_7$-Delta Films Using A Pulsed Oxygen Source, *Appl. Phys. Lett.* 58(11), 1211-1213 (1991).
33. P. R. Willmott and F. Antoni, Growth of GaN(0001) thin films on Si(001) by pulsed reactive crossed-beam laser ablation using liquid Ga and N_2, *Appl. Phys. Lett.* 73(10), 1394-1396 (1998).
34. M. J. Montenegro, J. Lippert, S. Muller, A. Weidenkaff, P. R. Willmott and A. Wokaun, Pulsed laser deposition of electrochemically active perovskite films, *Appl. Surf. Sci.* 197, 505-511 (2002).
35. S. Müller, K. Striebel and O. Haas, $La_{0.6}Ca_{0.4}CoO_3$ - a Stable and Powerful Catalyst for Bifunctional Air Electrodes, *Electrochim. Acta* 39(11-12), 1661-1668 (1994).
36. S. Müller, F. Holzer, O. Haas, C. Schlatter and C. Comninellis, Development Of Rechargeable Monopolar And Bipolar Zinc Air Batteries, *Chimia* 49(1-2), 27-32 (1995).
37. S. Müller, O. Haas, C. Schlatter and C. Comninellis, Development of a 100 W rechargeable bipolar zinc/oxygen battery, *Journal Of Applied Electrochemistry* 28(3), 305-310 (1998).
38. T. Watanabe, A. Nakajima, R. Wang, M. Minabe, S. Koizumi, A. Fujishima and K. Hashimoto, Photocatalytic activity and photoinduced hydrophilicity of titanium dioxide coated glass, *Thin Solid Films* 351(1-2), 260-263 (1999).
39. J. G. Bednorz and K. A. Muller, Possible High-T_c Superconductivity In The Ba-La-Cu-O System, *Zeitschrift Fur Physik B-Condensed Matter* 64(2), 189-193 (1986).
40. F. S. Galasso, *Structure: Properties and Preparation of Perovskite-type Compounds*, (Pergamon Press, London, 1969).
41. H. Song, W. Kim, S. J. Kwon and J. Kang, Magnetic and electronic properties of transition-metal-substituted perovskite manganites-$La_{0.7}Ca_{0.3}Mn_{0.95}X_{0.05}O_3$ (X=Fe,Co,Ni), *J. Appl. Phys.* 89(6), 3398-3402 (2001).
42. J. T. Cheung, P. E. D. Morgan, D. H. Lowndes, X. Y. Zheng and J. Breen, Structural And Electrical-Properties Of $La_{0.5}Sr_{0.5}CoO_3$ Epitaxial-Films, *Appl. Phys. Lett.* 62(17), 2045-2047 (1993).

43. S. Müller, F. Holzer and O. Haas, Optimized zinc electrode for the rechargeable zinc-air battery, *Journal Of Applied Electrochemistry* 28(9), 895-898 (1998).
44. B. D. McNicol and A. A. J. Rand, *Power Sources for Electric Vehicles*, (Elsevier, Amsterdam, 1984).
45. I. Buchmann, *Batteries in a portable world*, (Cadex Electronics, Richmond, 2001).
46. J. Prakash, D. Tryk and E. Yeager, Electrocatalysis For Oxygen Electrodes In Fuel-Cells And Water Electrolyzers For Space Applications, *J. Power Sources* 29(3-4), 413-422 (1990).
47. J. Prakash, D. Tryl, W. Aldred and E. Yeager, *Electrochemistry in Transition*, (Plenum Press, New York, 1992).
48. R. N. Singh, N. K. Singh and J. P. Singh, Electrocatalytic properties of new active ternary ferrite film anodes for O_2 evolution in alkaline medium, *Electrochim. Acta* 47(24), 3873-3879 (2002).
49. T. Horita, K. Yamaji, N. Sakai, H. Yokokawa, A. Weber and E. Ivers-Tiffee, Oxygen reduction mechanism at porous $La_{1-x}Sr_xCoO_{3-d}$ cathodes/$La_{0.8}Sr_{0.2}Ga_{0.8}Mg_{0.2}O_{2.8}$ electrolyte interface for solid oxide fuel cells, *Electrochim. Acta* 46(12), 1837-1845 (2001).
50. J. B. Goodenough, A. Manthiram, A. C. W. P. James and P. Strobel, Lithium Insertion Compounds, Solid State Ionics (G. Nazri, R. A. Huggins and D. F. Shriver, Eds.), *Material Research Society Symposium Proceedings* 135, 391 (1989).
51. D. W. Murphy, R. J. Cava, S. M. Zahurak and A. Santoro, Ternary Li_xTiO_2 Phases From Insertion Reactions, *Solid State Ionics* 9-10(DEC), 413-417 (1983).
52. L. A. Depicciotto and M. M. Thackeray, Transformation Of Delithiated $LiVO_2$ To The Spinel Structure, *Materials Research Bulletin* 20(2), 187-195 (1985).
53. L. A. Depicciotto and M. M. Thackeray, Lithium Insertion Extraction Reactions With $LiVO_2$ And LiV_2O_4, *Solid State Ionics* 18-9, 773-777 (1986).
54. G. Pistoia, M. Pasquali, L. A. Depicciotto and M. M. Thackeray, Behavior Of The Spinel LiV_2O_4 As A Positive Electrode For Secondary Li Cells, *Solid State Ionics* 28, 879-885 (1988).
55. M. M. Thackeray, W. I. F. David, P. G. Bruce and J. B. Goodenough, Lithium Insertion Into Manganese Spinels, *Materials Research Bulletin* 18(4), 461-472 (1983).
56. M. H. Rossouw, A. Dekock, L. A. Depicciotto and M. M. Thackeray, Structural Aspects Of Lithium-Manganese-Oxide Electrodes For Rechargeable Lithium Batteries, *Materials Research Bulletin* 25(2), 173-182 (1990).
57. F. Lubin, A. Lecerf, M. Broussely and J. Labat, Chemical Lithium Extraction From Manganese Oxides For Lithium Rechargeable Batteries, *J. Power Sources* 34(2), 161-173 (1991).
58. K. M. Colbow, J. R. Dahn and R. R. Haering, Structure And Electrochemistry Of The Spinel Oxides $LiTi_2O_4$ And $Li_{4/3}Ti_{5/3}O_4$, *J. Power Sources* 26(3-4), 397-402 (1989).
59. L. A. Depicciotto and M. M. Thackeray, Lithium Insertion Into The Spinel $LiFe_5O_8$, *Materials Research Bulletin* 21(5), 583-592 (1986).
60. M. Wakihara and O. Yamanoto, *Lithium Ion Batteries*, (Wiley-VCH, New York, 1998).
61. K. A. Striebel, A. Rougier, C. R. Horne, R. P. Reade and E. J. Cairns, Electrochemical studies of substituted spinel thin films, *J. Electrochem. Soc.* 146(12), 4339-4347 (1999).
62. R. Srinivasan, B. Braren, D. E. Seeger and R. W. Dreyfus, Photochemical Cleavage Of A Polymeric Solid - Details Of The Ultraviolet-Laser Ablation Of Poly(Methyl Methacrylate) At 193-Nm And 248-Nm, *Macromolecules* 19(3), 916-921 (1986).

63. R. Srinivasan, Ablation Of Polymethyl Methacrylate Films By Pulsed (Ns) Ultraviolet And Infrared (9.17-Mu-M) Lasers - A Comparative-Study By Ultrafast Imaging, *J. Appl. Phys.* 73(6), 2743-2750 (1993).
64. T. Lippert, R. L. Webb, S. C. Langford and J. T. Dickinson, Dopant induced ablation of poly(methyl methacrylate) at 308 nm, *J. Appl. Phys.* 85(3), 1838-1847 (1999).
65. M. Hertzberg and I. A. Zlochower, Devolatilization Wave Structures And Temperatures For The Pyrolysis Of Polymethylmethacrylate, Ammonium-Perchlorate, And Coal At Combustion Level Heat Fluxes, *Combust. Flame* 84(1-2), 15-37 (1991).
66. T. Lippert, A. Yabe and A. Wokaun, Laser ablation of doped polymer systems, *Adv. Mater.* 9(2), 105-119 (1997).
67. H. Fukumura and H. Masuhara, The Mechanism Of Dopant-Induced Laser-Ablation - Possibility Of Cyclic Multiphotonic Absorption In Excited-States, *Chem. Phys. Lett.* 221(5-6), 373-378 (1994).
68. T. Lippert, J. Stebani, O. Nuyken, A. Stasko and A. Wokaun, Photolysis Of 1-Aryl-3,3-Dialkyltriazenes, *J. Photochem. Photobiol. A-Chem.* 78(2), 139-148 (1994).
69. O. Nuyken, J. Stebani, T. Lippert, A. Wokaun and A. Stasko, Photolysis, Thermolysis, And Protolytic Decomposition Of A Triazene Polymer In Solution, *Macromol. Chem. Phys.* 196(3), 751-761 (1995).
70. A. Stasko, V. Adamcik, T. Lippert, A. Wokaun, J. Dauth and O. Nuyken, Photochemical Decomposition Of Triazenes - (Electron-Paramagnetic-Resonance Study), *Makromolekulare Chemie-Macromolecular Chemistry And Physics* 194(12), 3385-3391 (1993).
71. T. Lippert, A. Wokaun, J. Stebani, O. Nuyken and J. Ihlemann, Dopant-Induced Laser-Ablation Of PMMA At 308-Nm - Influence Of The Molecular-Weight Of PMMA And Of The Photochemical Activity Of Added Chromophores, *Angew. Makromol. Chem.* 213, 127-155 (1993).
72. T. Lippert, L. S. Bennett, T. Nakamura, H. Niino, A. Ouchi and A. Yabe, Comparison of the transmission behavior of a triazeno-polymer with a theoretical model, *Appl. Phys. A-Mater. Sci. Process.* 63(3), 257-265 (1996).
73. T. Lippert, A. Wokaun, J. Stebani, O. Nuyken and J. Ihlemann, Triazene Polymers Designed For Excimer Laser Ablation, *Angew. Makromol. Chem.* 206, 97-110 (1993).
74. T. Lippert, J. Stebani, J. Ihlemann, O. Nuyken and A. Wokaun, Excimer-Laser Ablation Of Novel Triazene Polymers - Influence Of Structural Parameters On The Ablation Characteristics, *J. Phys. Chem.* 97(47), 12296-12301 (1993).
75. O. Nuyken, J. Stebani, T. Lippert, A. Wokaun and A. Stasko, Synthesis And Characterization Of Novel Triazeno-Group Containing Photopolymers, *Macromol. Chem. Phys.* 196(3), 739-749 (1995).
76. T. Lippert, T. Nakamura, H. Niino and A. Yabe, Irradiation wavelength selective surface modification of a triazeno polymer, *Macromolecules* 29(19), 6301-6309 (1996).
77. T. Lippert, T. Nakamura, H. Niino and A. Yabe, Laser induced chemical and physical modifications of polymer films: Dependence on the irradiation wavelength, *Appl. Surf. Sci.* 110, 227-231 (1997).
78. T. Lippert, E. Ortelli, J. C. Panitz, F. Raimondi, J. Wambach, J. Wei and A. Wokaun, Imaging-XPS/Raman investigation on the carbonization of polyimide after irradiation at 308 nm, *Appl. Phys. A-Mater. Sci. Process.* 69, S651-S654 (1999).
79. F. Raimondi, S. Abolhassani, R. Brutsch, F. Geiger, T. Lippert, J. Wambach, J. Wei and A. Wokaun, Quantification of polyimide carbonization after laser ablation, *J. Appl. Phys.* 88(6), 3659-3666 (2000).

80. J. E. Andrew, P. E. Dyer, D. Forster and P. H. Key, Direct Etching Of Polymeric Materials Using A XeCl Laser, *Appl. Phys. Lett.* 43(8), 717-719 (1983).
81. R. Srinivasan and B. Braren, Ablative Photodecomposition Of Polymer-Films By Pulsed Far-Ultraviolet (193 Nm) Laser-Radiation - Dependence Of Etch Depth On Experimental Conditions, *J. Polym. Sci. Pol. Chem.* 22(10), 2601-2609 (1984).
82. M. Schumann, R. Sauerbrey and M. C. Smayling, Permanent Increase Of The Electrical-Conductivity Of Polymers Induced By Ultraviolet-Laser Radiation, *Appl. Phys. Lett.* 58(4), 428-430 (1991).
83. T. Feurer, R. Sauerbrey, M. C. Smayling and B. J. Story, Ultraviolet-Laser-Induced Permanent Electrical-Conductivity In Polyimide, *Appl. Phys. A-Mater. Sci. Process.* 56(3), 275-281 (1993).
84. Z. Ball, T. Feurer, D. L. Callahan and R. Sauerbrey, Thermal and mechanical coupling between successive pulses in KrF-excimer-laser ablation of polyimide, *Appl. Phys. A-Mater. Sci. Process.* 62(3), 203-211 (1996).
85. J. Wei, N. Hoogen, T. Lippert, O. Nuyken and A. Wokaun, Novel laser ablation resists for excimer laser ablation lithography. Influence of photochemical properties on ablation, *J. Phys. Chem. B* 105(6), 1267-1275 (2001).
86. T. Lippert, J. Wei, A. Wokaun, N. Hoogen and O. Nuyken, Polymers designed for laser microstructuring, *Appl. Surf. Sci.* 168(1-4), 270-272 (2000).
87. T. Lippert, J. Wei, A. Wokaun, N. Hoogen and O. Nuyken, Development and structuring of combined positive-negative/negative-positive resists using laser ablation as positive dry etching technique, *Macromol. Mater. Eng.* 283(10), 140-143 (2000).
88. J. Wei, N. Hoogen, T. Lippert, C. Hahn, O. Nuyken and A. Wokaun, Characterisation of combined positive-negative photoresists by excimer laser ablation, *Appl. Phys. A-Mater. Sci. Process.* 69, S849-S853 (1999).
89. T. Lippert, C. David, J. T. Dickinson, M. Hauer, U. Kogelschatz, S. C. Langford, O. Nuyken, C. Phipps, J. Robert and A. Wokaun, Structure property relations of photoreactive polymers designed for laser ablation, *J. Photochem. Photobiol. A-Chem.* 145(3), 145-157 (2001).
90. T. Lippert, L. S. Bennett, T. Nakamura, H. Niino and A. Yabe, Single pulse threshold and transmission behaviour of a triazeno-polymer during pulsed UV-laser irradiation, *Appl. Surf. Sci.* 96-8, 601-604 (1996).
91. H. Fukumura, E. Takahashi and H. Masuhara, Time-Resolved Spectroscopic And Photographic Studies On Laser-Ablation Of Poly(Methyl Methacrylate) Film Doped With Biphenyl, *J. Phys. Chem.* 99(2), 750-757 (1995).
92. R. Srinivasan, K. G. Casey, B. Braren and M. Yeh, The Significance Of A Fluence Threshold For Ultraviolet-Laser Ablation And Etching Of Polymers, *J. Appl. Phys.* 67(3), 1604-1606 (1990).
93. H. Furutani, H. Fukumura and H. Masuhara, Photothermal transient expansion and contraction dynamics of polymer films by nanosecond interferometry, *J. Phys. Chem.* 100(17), 6871-6875 (1996).
94. H. Kim, J. C. Postlewaite, T. Zyung and D. D. Dlott, Ultrafast Imaging Of Optical-Damage Dynamics And Laser-Produced Wave-Propagation In Poly(Methyl Methacrylate, *J. Appl. Phys.* 64(6), 2955-2958 (1988).
95. M. Hauer, D. J. Funk, T. Lippert and A. Wokaun, Time resolved techniques as probes for the laser ablation process, *Optics and Laser Engineering* 43, 545 (2005).
96. H. Furutani, H. Fukumura and H. Masuhara, Nanosecond Time-Resolved Interferometric Study On Morphological Dynamics Of Doped Poly(Methyl Methacrylate) Film Upon Laser-Ablation, *Appl. Phys. Lett.* 65(26), 3413-3415 (1994).

97. H. Furutani, H. Fukumura, H. Masuhara, T. Lippert and A. Yabe, Laser-induced decomposition and ablation dynamics studied by nanosecond interferometry .1. A triazenopolymer film, *J. Phys. Chem. A* 101(32), 5742-5747 (1997).
98. M. Hauer, D. J. Funk, T. Lippert and A. Wokaun, Laser induced decomposition of a designed and a commercial polymer studied by ns-interferometry and shadowgraphy, *Appl. Phys. A-Mater. Sci. Process.* 77(2), 297-301 (2003).
99. M. Hauer, D. J. Funk, T. Lippert and A. Wokaun, *Proc. SPIE-Int. Soc. Opt. Eng.* 4760, 259 (2002).
100. T. Masubuchi, T. Tada, E. Nomura, K. Hatanaka, H. Fukumura and H. Masuhara, Laser-induced decomposition and ablation dynamics studied by nanosecond interferometry. 4. A polyimide film, *J. Phys. Chem. A* 106(10), 2180-2186 (2002).
101. T. Lippert, C. David, M. Hauer, T. Masubuchi, H. Masuhara, K. Nomura, O. Nuyken, C. Phipps, J. Robert, T. Tada, K. Tomita and A. Wokaun, Novel applications for laser ablation of photopolymers, *Appl. Surf. Sci.* 186(1-4), 14-23 (2002).
102. T. Lippert, A. Wokaun, S. C. Langford and J. T. Dickinson, Emission of neutral molecules during UV laser ablation of a photolabile triazeno polymer, *Appl. Phys. A-Mater. Sci. Process.* 69, S655-S658 (1999).
103. T. Lippert, S. C. Langford, A. Wokaun, G. Savas and J. T. Dickinson, Analysis of neutral fragments from ultraviolet laser irradiation of a photolabile triazeno polymer, *J. Appl. Phys.* 86(12), 7116-7122 (1999).
104. M. Hauer, T. Dickinson, S. Langford, T. Lippert and A. Wokaun, Influence of the irradiation wavelength on the ablation process of designed polymers, *Appl. Surf. Sci.* 197, 791-795 (2002).
105. J. T. Dickinson, J. J. Shin, W. Jiang and M. G. Norton, Neutral And Ion Emissions Accompanying Pulsed Excimer-Laser Irradiation Of Polytetrafluoroethylene, *J. Appl. Phys.* 74(7), 4729-4736 (1993).
106. G. P. Luo, Y. S. Wang, S. Y. Chen, A. K. Heilman, C. L. Chen, C. W. Chu, Y. Liou and N. B. Ming, Electrical and magnetic properties of $La_{0.5}Sr_{0.5}CoO_3$ thin films, *Appl. Phys. Lett.* 76(14), 1908-1910 (2000).
107. V. Craciun, D. Craciun, J. Perriere and I. W. Boyd, Droplet formation during extended time pulsed laser deposition of $La_{0.5}Sr_{0.5}CoO_3$ thin layers, *J. Appl. Phys.* 85(6), 3310-3313 (1999).
108. A. Gupta, B. W. Hussey and M. Y. Chern, Effect Of Different Oxidizing Gases On The Insitu Growth Of $YBa_2Cu_3O_7$-Delta Films By Pulsed Laser Deposition, *Physica C* 200(3-4), 263-270 (1992).
109. C. H. Chen, R. C. Phillips and M. P. McCann, Observation Of Trapped O_2 In High-T_c Metal-Oxide Superconductors, *Phys. Rev. B* 39(4), 2744-2747 (1989).
110. J. R. Engstrom and T. Engel, Atomic Versus Molecular Reactivity At The Gas-Solid Interface - The Adsorption And Reaction Of Atomic Oxygen On The Si(100) Surface, *Phys. Rev. B* 41(2), 1038-1041 (1990).
111. M. Cherry, M. S. Islam and C. R. A. Catlow, Oxygen-Ion Migration In Perovskite-Type Oxides, *Journal Of Solid State Chemistry* 118(1), 125-132 (1995).
112. Y. M. L. Yang, A. J. Jacobson, C. L. Chen, G. P. Luo, K. D. Ross and C. W. Chu, Oxygen exchange kinetics on a highly oriented $La_{0.5}Sr_{0.5}CoO_3$-delta thin film prepared by pulsed-laser deposition, *Appl. Phys. Lett.* 79(6), 776-778 (2001).
113. H. J. Dang and Q. Z. Qin, A thermal-controlling mechanism for laser ablation of a colossal magnetoresistant oxide target, *Chem. Phys. Lett.* 354(3-4), 210-216 (2002).

114. M. J. Montenegro, C. Clerc, T. Lippert, S. Muller, P. R. Willmott, A. Weidenkaff and A. Wokaun, Analysis of the plasma produced by pulsed reactive crossed-beam laser ablation of $La_{0.6}Ca_{0.4}CoO_3$, *Appl. Surf. Sci.* 208, 45-51 (2003).
115. T. Scharf and H. U. Krebs, Influence of inert gas pressure on deposition rate during pulsed laser deposition, *Appl. Phys. A-Mater. Sci. Process.* 75(5), 551-554 (2002).
116. J. A. Bard and L. R. Faulkner, *Electrochemical Methods*, (John Wiley & Sons, New York, 2000).
117. M. Morcrette, P. Barboux, J. Perriere and T. Brousse, $LiMn_2O_4$ thin films for lithium ion sensors, *Solid State Ionics* 112(3-4), 249-254 (1998).
118. A. Rougier, K. A. Striebel, S. J. Wen and E. J. Cairns, Cyclic voltammetry of pulsed laser deposited $Li_xMn_2O_4$ thin films, *J. Electrochem. Soc.* 145(9), 2975-2980 (1998).
119. A. Rougier, K. A. Striebel, S. J. Wen, T. J. Richardson, R. P. Reade and E. J. Cairns, Characterization of pulsed laser-deposited $LiMn_2O_4$ thin films for rechargeable lithium batteries, *Appl. Surf. Sci.* 134(1-4), 107-115 (1998).
120. C. Julien, E. Haro-Poniatowski, M. A. Camacho-Lopez, L. Escobar-Alarcon and J. Jimenez-Jarquin, Growth of $LiMn_2O_4$ thin films by pulsed-laser deposition and their electrochemical properties in lithium microbatteries, *Mater. Sci. Eng. B-Solid State Mater. Adv. Technol.* 72(1), 36-46 (2000).
121. D. Singh, W. S. Kim, V. Craciun, H. Hofmann and R. K. Singh, Microstructural and electrochemical properties of lithium manganese oxide thin films grown by pulsed laser deposition, *Appl. Surf. Sci.* 197, 516-521 (2002).
122. D. Singh, *Influence of microstructure on electrochemical properties of Li-Mn-O thin films*, Thesis at Ecole Polytechnique Fédéral de Lausanne (2001).
123. M. Morcrette, P. Barboux, J. Perriere, T. Brousse, A. Traverse and J. P. Boilot, Non-stoichiometry in $LiMn_2O_4$ thin films by laser ablation, *Solid State Ionics* 138(3-4), 213-219 (2001).
124. M. Inaba, T. Doi, Y. Iriyama, T. Abe and Z. Ogumi, Electrochemical STM observation of $LiMn_2O_4$ thin films prepared by pulsed laser deposition, *J. Power Sources* 81, 554-557 (1999).
125. C. M. Julien and M. Massot, Lattice vibrations of materials for lithium rechargeable batteries III. Lithium manganese oxides, *Mater. Sci. Eng. B-Solid State Mater. Adv. Technol.* 100(1), 69-78 (2003).
126. T. Dumont, T. Lippert, M. Döbeli, H. Grimmer, J. Ufheil, P. Novák, A. Würsig, U. Vogt and A. Wokaun, Influence of experimental parameter on the Li-content of $LiMn_2O_4$ electrodes produced by pulsed laser deposition, *Appl. Surf. Sci.* article in press, (2006).

THREE-DIMENSIONAL MICRO AND NANOCHIPS FABRICATED BY FEMTOSEDOND LASER FOR BIOMEDICAL APPLICATIONS

KOJI SUGIOKA*, YA CHENG AND KATSUMI MIDORIKAWA
RIKEN – The Institute of Physical and Chemical Research, Wako, Saiatma 351-0198, Japan

Abstract. Three-dimensional (3D) micromachining of photosensitive glass is demonstrated by a photochemical reaction using femtosecond (fs) laser for lab-on-a-chip application. True 3D hollow microstructures embedded in the glass are fabricated by fs laser direct writing followed by heat treatment and successive wet etching. The modification mechanism of the photosensitive glass by the fs laser and advantage of this process are discussed. Various microcomponents for the lab-on-a-chip devices such as microfluidics, microvalves, microoptics, microlasers, etc. are fabricated by using this technique and their performance is examined.

Keywords: microchip, nanochip, lab-on-a-chip, μ-TAS, 3D fabrication, laser micromachining; femtosecond laser

1. Introduction

Microchip and nanochip, in other words, lab-on-a-chip, open new avenues for chemical and biological applications, for example, genetic science, medical inspection, environmental monitoring, new drug development, synthesis of new materials, etc., since their performance is more efficient, more accurate and more cost-effective compared with conventional means. In some of these chips, microfluidic components and microoptical components are highly integrated for on-site analysis of samples and reactants, which is referred to as a micro-total analysis system (μ-TAS). （Burns et al., 1998. In μ-TAS, infusion and reaction of the samples and analysis of the reactants are successively conducted in a single chip with a size of the order of mm^2 ~ tenth cm^2. Consequently, μ-TAS is capable of measuring nano-liter or even pico-liter volumes of reagents

*To whom correspondence should be addressed. Koji Sugioka, Laser Technology Laboratory, RIKEN – The Institute of Physical and Chemical Research, Wako, Saiatma 351-0198, Japan; E-mail: ksugioka@riken.jp

J.J. Dubowski and S. Tanev (eds.), Photon-based Nanoscience and Nanobiotechnology, 307–332.

resulting in fast reaction, high speed and cost-effective analysis, minimized reagent consumption and waste product, and enhanced portability. Currently, fabrication of μ-TAS relies on planar microfabrication techniques like conventional semiconductor processing based on photolithography. Although these techniques have been well established and are suitable for surface microfabrication, multilayer and multistep processes including stacking and bonding substrates are required to form true three-dimensional (3D) microstructures for the high integration of microfluidics and microoptics.

The use of a femtosecond (fs) laser has facilitated the internal modification of transparent materials due to a multiphoton absorption process (Scaffer et al., 2001; Yamada et al., 2001). Therefore, fs laser micromachining is a promising and simple approach for embedding 3D microstructures inside the materials. Furthermore, direct writing using such a laser has several advantages over conventional semiconductor processing. Namely, it has great flexibility due to the fact that it is resistless and maskless, making it suitable for rapid prototyping.

Li et al. (2001) demonstrated direct drilling of 3D holes from the posterior surface of fused silica. In this process, the posterior surface of the sample is in contact with distilled water, and the fs laser is focused to the interface of the posterior sample surface and the water. Then, ablation takes place at the posterior surface and the water can flow into the drilled hole to reduce the effect of blocking and redeposition of ablated material in the small hole, resulting in the formation of 3D holes in fused silica. Three-dimensional nano holes were also fabricated in fused silica by the similar method (Ke et al., 2005).

Another way to fabricate a 3D hollow microchannel in glass is the two step process comprising fs laser direct write followed by chemical wet etching. This two-step process can produce more complicated 3D microstructures with more ease when compared with direct ablation. Marcinkevicius et al. (2001) have fabricated hollow microchannels inside fused silica by fs laser irradiation followed by post chemical etching with a hydrofluoric (HF) acid solution. In our experiment, it was revealed that this technique needed laser power of ~10 mW and scanning speed of ~10 μm/s at 1 kHz repetition rate of a laser pulse using an objective lens of numerical aperture (NA) of 0.46. In our case, photosensitive glass is used as a substrate instead of fused silica, since it may be a more attractive candidate for high efficiency and high throughput processing. This is due to its pure photochemical reaction which is responsible for much smaller laser power and much higher scanning speed employed for direct writing, as described later.

In the present paper, 3D microstructuring of the photosensitive glass is demonstrated by fs laser direct write process followed by a thermal treatment and successive chemical wet etching in a HF aqueous solution for lab-on-a-chip device manufacture (Masuda et al., 2003, 2004; Cheng et al., 2003a, 2003b, 2004, 2005a, 2005b; Sugioka et al., 2004; Sugioka, Cheng et al., 2005). Although the photoreaction mechanism of the photosensitive glass by the UV light has been well studied as described below, that of the fs laser is still unclear. Therefore, the photoreaction mechanism by the fs laser is discussed based on the determination of the critical dose and measurement of the absorption spectrum change after the laser irradiation (Hongo et al., 2005). Then, 3D microfluidic, micromechanical, and microoptical components are fabricated in the glass by this technique and these microcomponents are integrated to manufacture functional devices for biochemical applications.

2. Photosensitive Glass

The photosensitive glass has been developed by Stooky (1953) at Corning for surface microstructuring using an ultraviolet (UV) light. There are now over 5,000 varieties of these glasses and one of the most successfully commercialized is manufactured by Schott Glass Corporation and sold under a trade name of Foturan (see *http://www.mikroglas.com/-foturane.htm*). It comprises lithium aluminosilicate glass doped with trace amounts of silver and cerium. The cerium (Ce^{3+}) ion plays an important role as photosensitizer, which releases an electron by exposure of the UV light and then becomes Ce^{4+}. Some silver ions are reduced by the generated free electrons, and silver atoms are created. In a subsequent heat treatment, first the silver atoms diffuse and agglomerate to form silver nanoclusters with a size of 8 nm or larger at about 500 °C°; then the crystalline phase of lithium metasilicate grows in the amorphous glass matrix in the vicinity of the silver clusters, which act as a nucleus, at about 600 °C. As this crystalline phase of lithium metasilicate is much more soluble in a dilute solution of HF acid than the glass matrix, it can be preferentially etched away. Usually, a UV lamp is used for a two-dimensional (2D) microfabrication of the photosensitive glass. Although internal microstructuring of the photosensitive glass is possible even by a pulsed UV laser (Hansen et al., 1997; Fuqua et al., 1999, 2000; Helvajian et al., 2000), a higher order of multiphoton absorption by the fs laser irradiation makes it possible to fabricate true and more complicated 3D microstructures with a higher spatial resolution, in particular, in a vertical direction, i.e., the direction parallel to the laser beam propagation. This is the reason why we are using the fs laser in this study.

3. Experimental

The photosensitive glass used in this work was commercially available Foturan glass from Schott Glass Corporation. The experiments were carried out using a commercial fs laser micromachining workstation at HOYA CANDEO OPTRONICS. Figure 1 shows a schematic illustration of the workstation. The laser wavelength, pulse width and repetition rate were 775nm, 140±5fs and 1kHz, respectively. To guarantee a high beam quality, a 6mm diameter of the output laser beam was reduced to 3mm by an aperture in front of the focusing system. The focusing system was a 20x microscope objective with a numerical aperture (NA) of 0.46. Samples were translated by a PC controlled x-y-z stage with a resolution of 0.5μm during the fs laser direct write. The fabrication process was displayed on the PC monitor by a charge-coupled device (CCD). Three-dimensional latent images are written inside the photosensitive glass by the fs laser direct write. At this stage, silver atoms are precipitated, but no visible change occurs. After exposure of the fs laser, the samples are conducted to programmed heat treatment. The temperature is first ramped up to 500 °C at 5 °C/min and held at this temperature for 1h. Then it is raised to 605 °C at 3 °C/min and held for another hour. Here, the laser-exposed regions become a crystalline phase of lithium metasillicate and show dark color. After the sample is cooled to room temperature, it is soaked in a solution of 10% HF acid diluted with water in an ultrasonic bath. The formed lithium metasillicate is preferentially etched away with a contrast ratio of 43 in etching rate compared with the unmodified regions as described in *Sec. 4*, and finally, hollow microstructures were formed inside the glass. In principle, any arbitrary internal structure possesses one or more openings on the sample surface and such openings are always necessary for the lab-on-a-chip devices for the introduction of samples.

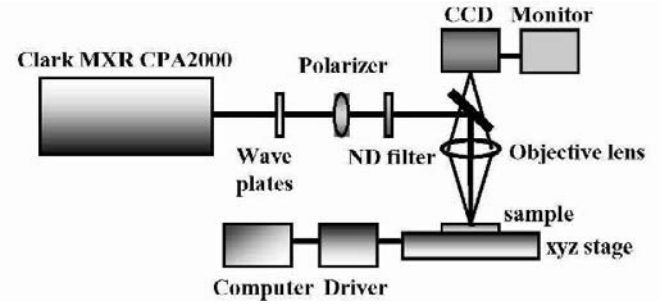

Figure 1. Schematic illustration of the fs laser micromachining workstation.

4. Determination of Process Parameters

The first step of this work is to check the critical dose for the photoreaction as the high precision machining is only performed at the condition just above this critical dose. The critical dose D_c is defined as the lowest dose necessary for achieving selective etching of the photosensitive glass at the exposed region. The model proposed by Fuqua et al. (2000) assumes that to make the photosensitive glass selectively soluble in a HF solution, the density of nuclei should reach a critical range to form an interconnected network of crystallites, which is defined as the critical density ρ_c. One can expect that the density of the nucleation site ρ should be proportional to the dose. Therefore, ρ would be fluence dependent, which could be mathematically given as follows:

$$\rho = KF^m N, \tag{1}$$

where F is the per-pulse fluence; m is the power dependence; N is the number of laser pulses; K is a proportionality constant. By defining an arbitrary dose D that is equal to ρ/K, Eq. (1) is represented by

$$D = F^m N. \tag{2}$$

For a given number of pulses, D_c corresponds to a critical fluence F_c, so that Eq. (2) becomes

$$D_c = F_c{}^m N. \tag{3}$$

In a regime above D_c, the laser exposed regions are selectively etched, while in a regime below D_c, the selective etching is not carried out. This critical dose is a constant, which merely depends on material composition and process parameters.

To determine the critical dose, we irradiated the photosensitive glass with the fs laser at different pulse energies and shot numbers, then baked the sample and etched it in a 10% HF acid solution. Under the microscope, it was clearly observed that for a given number of laser pulses, there existed a threshold of the pulse energy over which a visible etched mark could be formed on the glass sample. From this threshold and the spot size of the laser beam, the F_c can be determined. Figure 2 shows a log-log plot of the critical fluence versus the number of laser pulses. By fitting the data using Eq. (3), the slope discloses m = ~ 6, which means a six-photon process, and $D_c = 1.35 \times 10^{-5}$ J^6/cm^{12}.

According to the experimental results of the critical dose, the average laser fluence in the exposed regions for the 3D micromachining in this study was chosen to be 78mJ/cm^2, which was calculated by the assumption

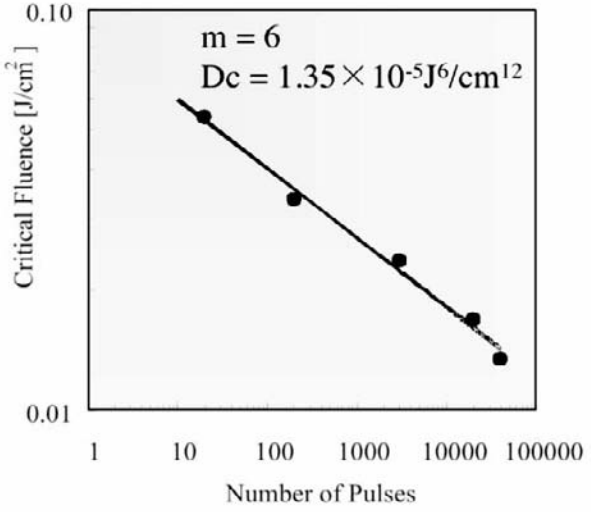

Figure 2. Dependence of critical fluence on the number of laser pulses for photosensitive glass microstructuring using the fs laser.

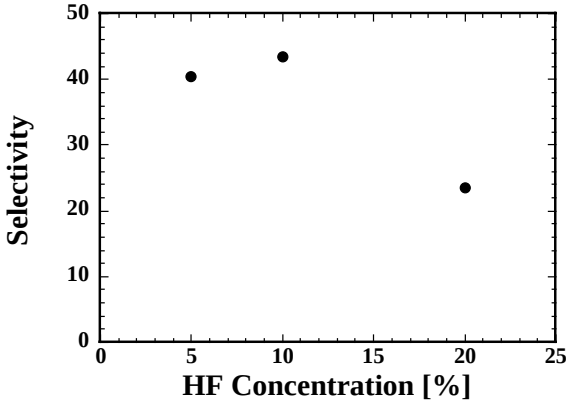

Figure 3. Dependence of the etching selectivity between the laser-exposed regions and un-exposed regions on concentration of HF solution.

of a Gaussian beam profile of 26 μm in diameter. The beam diameter was determined by the diameter of etched holes fabricated in the glass surface by fs laser ablation with fluence much larger than the critical fluence. The scanning speed for the whole processing was set at 510μm/s at which 50 pulses were overlapped at the same position. The 50-pulse irradiation at an average fluence of 78mJ/cm^2 could just reach the critical dose for the selective etching (see Fig. 2).

Another important parameter for high precision micromachining is etching selectivity between the exposed and unexposed regions. We directly measured this parameter by comparing the etching rates of exposed and unexposed regions on the same sample. Figure 3 shows the dependence of the etching selectivity on the concentration of HF solution. The selectivity was calculated by dividing the etching rates of the exposed samples by those of the unexposed samples, with the scanning speed of 510μm/s for laser fluence of 0.78 mJ/cm^2. In this experiment, the laser beam was scanned from the bottom to the top surface of samples along the laser beam propagation direction, i.e., z direction in Fig. 1. One can see the largest selectivity in the vicinity of 10 % , which is estimated to be approximately 43. Thus, 10 % HF solution is used for selective etching of the modified regions in this study.

5. Photoreaction Mechanism

Figure 4 shows an absorption spectrum of the photosensitive glass used in this study. Absorption edge is around 340 nm and the small peak around 315 nm is ascribed to resonant absorption by Ce^{3+}. Therefore, the fs laser of 775 nm wavelength used in this study is transparent to this glass and two-photon absorption is impossible, but three-photon absorption is likely. Three-photon absorption of the IR fs laser by this glass was experimentally confirmed by Kim et al. (2004). For reference, 355-nm wavelength of a 3rd harmonic of Nd:YAG laser has little absorption, while 266-nm wavelength of the 4th harmonic has strong absorption. Additionally, 308-nm wavelength of XeCl excimer laser is very close to the resonant absorption by Ce^{3+}.

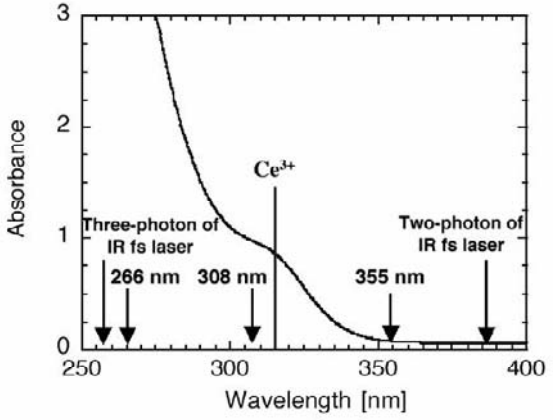

Figure 4. Absorption spectrum of the photosensitive glass in a UV region.

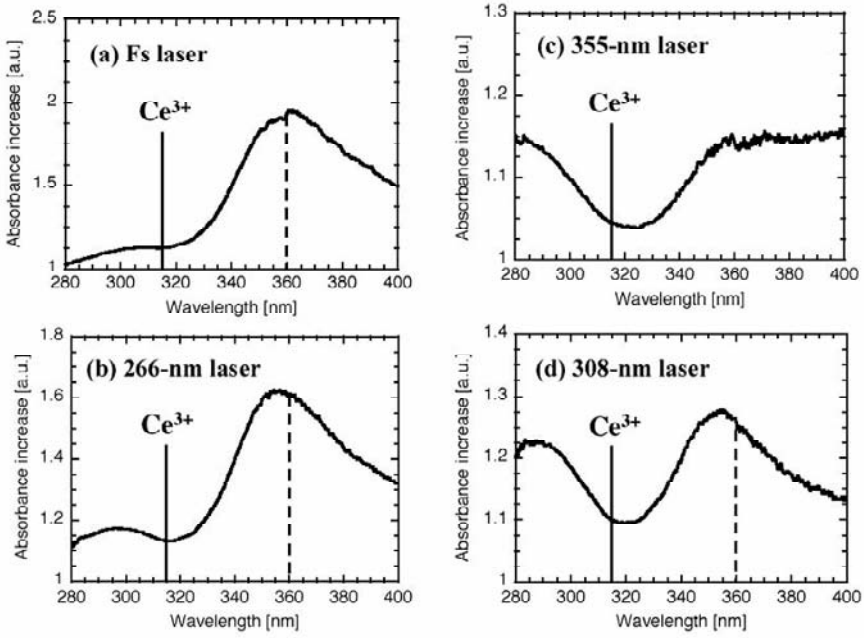

Figure 5. Absorbance increase spectra in photosensitive glass after exposure to (a) fs laser, (b) 266-nm laser, (c) 355-nm laser and (d) 308-nm laser, which are derived by dividing the absorbance spectrum of the exposed sample by that of the unexposed sample.

As discussed in *Sec. 4*, photoreaction of the photosensitive glass by the fs laser takes place by a six-photon process. Here, we investigate this process in comparison with the results obtained by other lasers. In an earlier investigation, a two-photon process was observed for both of 266-nm and 355-nm pulsed UV lasers (Fuqua et al., 2000), although the 266-nm laser has strong absorption by the photosensitive glass whereas the 355-nm laser has little absorption as shown in Fig. 4. If the laser beam is absorbed by Ce^{3+} whose resonant absorption is around 315 nm, two-photon process is reasonable for the 355 nm due to two-photon absorption. However, this process cannot explain the two-photon process of the 266-nm laser because the photosenstitive glass should be absorbed by a single-photon of the 266 nm laser. Then, we employed the XeCl excimer laser whose wavelength is very close to the resonant absorption by Ce^{3+}. The slope of log-log plot of the critical fluence versus the number of pulses for 308-nm laser suggested a 1.5-photon process (Hongo et al., 2005).

For further investigation, we measured absorption change in a UV-visible range after irradiation by each laser. Figure 5 shows spectra of absorbance increase in photosensitive glass after exposure to (a) fs laser, (b) 266-nm laser, (c) 355-nm laser and (d) 308-nm laser, which are derived by

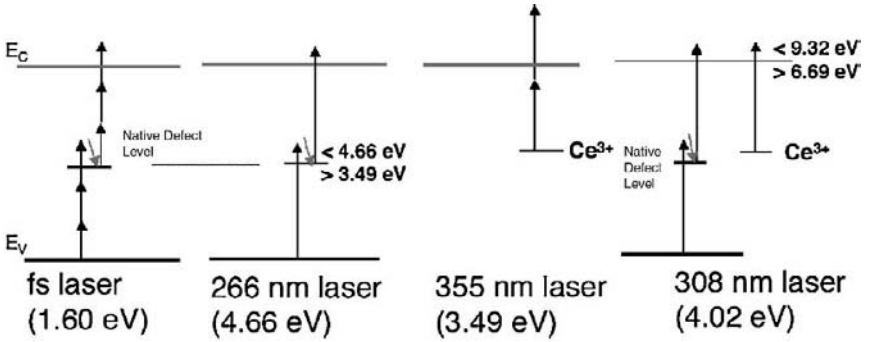

Figure 6. Electron excitation processes for free electron generation by (a) fs laser, (b) 266-nm laser, (c) 355-nm laser and (d) 308-nm laser.

dividing the absorbance spectrum of the exposed sample by the unexposed one. For the fs laser (Fig. 5 (a)), a significant increase in the vicinity of 360 nm corresponding to absorption arising from oxygen deficient centers (ODC) (Kondo et al., 1999) is observed, while one cannot see any significant change around 315 nm implying change of Ce^{3+} to Ce^{4+}. This means that Ce^{3+} hardly contributes to free electron generation for reducing Ag^{+} to Ag^{0} in the case of the fs laser irradiation. Preferably in this case, the free electrons should be generated by inter-band excitation. Namely, when the fs laser is irradiated to the photosensitive glass, free electrons are generated from valence band to conduction band, resulting in bond scission of Si and O in the glass and then the formation of ODC which pairs with the non-bridging oxygen hole center (NBOHC). The spectrum for the 266-nm laser (Fig. 5 (b)) looks similar to that of the fs laser, which means that the electron generation process by the 266-nm laser should be similar to the fs laser. On the other hand, the spectrum for 355-nm laser (Fig. 5 (c)) shows little change around 360 nm but significant change around 315 nm ascribing to Ce^{3+} absorption. This fact indicates that free electrons are generated from Ce^{3+} absorbing the 355 nm laser. In the meantime, both changes around 315 nm and 360 nm are observed for the 308 nm-laser whose wavelength is almost resonant at Ce^{3+} absorption (Fig. 5 (d)). In this case, free electrons would be generated by both Ce^{3+} absorption and the inter-band excitation.

Based on these results, free electron generation processes are summarized in Fig. 6. For the fs and 266-nm lasers, free electrons are generated by inter-band excitation. In these cases, single-photon absorption for the 266-nm laser and three-photon absorption for the fs laser are possible by taking into account the absorption edge (see Fig. 3) and literature (Kim et al., 2004). This absorption may be dominated by defect

levels ascribing to impurities and native defects rather than by Ce^{3+} (since absorption cross section of the defects seems to be much larger than that of Ce^{3+}). Therefore, electron excitation from the valence band to the conduction band through these defect levels is most likely, that means, a two-step excitation. This consideration is consistent with the two-photon process of the 266 nm laser for photoreaction as described above. Additionally, the six-photon process of the fs laser is also reasonable. In this case, the first excitation to the defect levels takes place by three photons (three-photon absorption) and successive excitation to the conduction band does by an additional three photons (another three-photon absorption). Consequently, six photons in total are required for photoreaction. For the 355-nm laser, free electrons are generated by two-photon absorption by Ce^{3+}. Meanwhile, for the 308-nm, both inter-band excitation through the defect levels and Ce^{3+} absorption simultaneously take place for free electron generation. The former process requests two photons in total due to two-step excitation, while the latter one takes place by single-photon absorption. As a result, we observed 1.5-photon process for the photoreaction. Thus, Ce^{3+} doping seems to be unnecessary for the modification of the photosensitive glass by the fs laser.

6. Advantages of the Present Technique

Such a higher order of three-photon absorption for the present technique is beneficial to the internal fabrication with high spatial resolution, because the effective beam width for *n*-photon absorption is equivalent to $\omega_0/\sqrt{n}$, where ω_0 is the actual beam width. In particular, vertical resolution, i.e., the resolution in the beam propagation direction, can be much improved.

Another important feature of this process is pure photochemical reaction based on the reducing reaction using free electrons generated by the inter-band excitation. Three-dimensional hollow microchannels can be fabricated even inside fused silica by fs laser irradiation followed by post chemical etching in a HF acid solution (Marcinkevicius et al., 2001). However, we revealed that when an objective lens with NA of 0.46 was used, this technique needed laser power of ~10 mW and scanning speed of ~1 μm/s at 1 kHz repetition rate of laser pulse (maybe due to photophysical or photothermal reaction). On the other hand, the typical irradiation condition of the present technique is 1 mW of laser power and ~500 μm/s of scanning speed. The simple estimation gives ~500 times larger throughput for manufacture using the present technique.

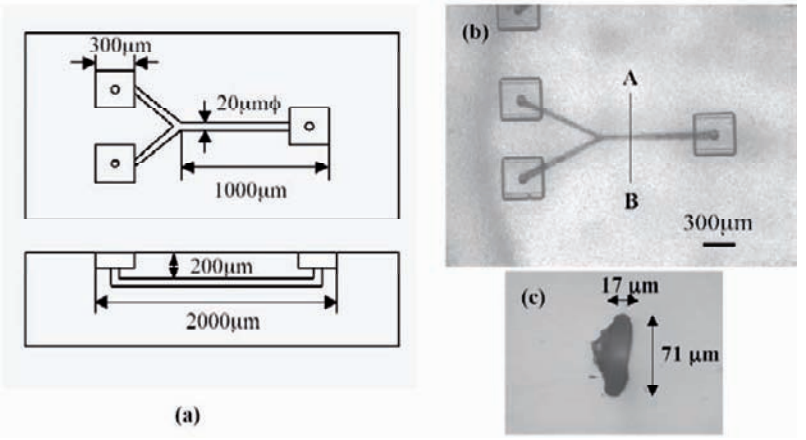

Figure 7. (a) Schematic configuration of the horizontal "Y" branched microchannel structure, photos of (b) the fabricated structure, and (c) cross-section of the microchannel that was mechanically cut along the A-B line in (b).

7. Fabrication of Microfluidic Components

Based on the process parameters obtained in *Sec. 4*, we fabricated a planer microfluidic structure with 3D Y-branched microchannel embedded in the photosensitive glass as shown in Fig. 7. Figure 7(a) shows a schematic configuration of the fabricated structures. Three open microreservoirs of 300 μmx300 μm, formed at the surface, were connected by a Y-branched hollow microchannel embedded 200 μm below the surface. Figure 7(b) shows an optical micrograph of the structure fabricated by programmed baking process and the successive etching for 55 min in 10 % HF solution after fs laser direct writing. The laser irradiation condition is set at 78 mJ/cm^2 with a scanning velocity of 510 μm/s as described in *Sec. 3*. For a more detailed examination of embedded microchannels, the coupon was mechanically cut along the A-B line indicated in Fig. 7(b). Figure 7(c) shows an optical micrograph of the cross-section of the embedded microchannel. One can see an elliptical form of a hollow channel, whose width and aspect ratio (ratio of the height to the width of channel) are 17 μm and 4.2 respectively. This elliptical shape is mainly derived from the mismatch between the focal radius and Rayleigh range at the focus when using an objective lens with a NA of 0.46. The large aspect ratio of the cross-sectional shape of the microchannel is not a disadvantage for μ-TAS, since such a shape creates a wider interface area between two kinds of liquid solutions for mixing, resulting in an enhancement of the chemical

reaction rate. Nevertheless, control of the cross-sectional shape is still an important issue for flexible μ-TAS fabrication. The use of higher NA lenses could reduce the aspect ratio, but the working distance would become very short (several hundred μm), which would make the fabrication of highly integrated 3D structures difficult. We developed a very simple method to control the aspect ratio by using a narrow slit (Cheng et al., 2003a). By using the slit with a width to 0.2 mm, the aspect ratio of the fabricated microchannel was greatly improved to ~1.3. A more specific method to realize the perfectly circular cross-sectional shape is crossed-beam irradiation of the fs laser beams, in which the foci of two fs laser beams are spatiotemporally overlapped inside the glass by two orthogonal objective lenses (Sugioka et al., 2006).

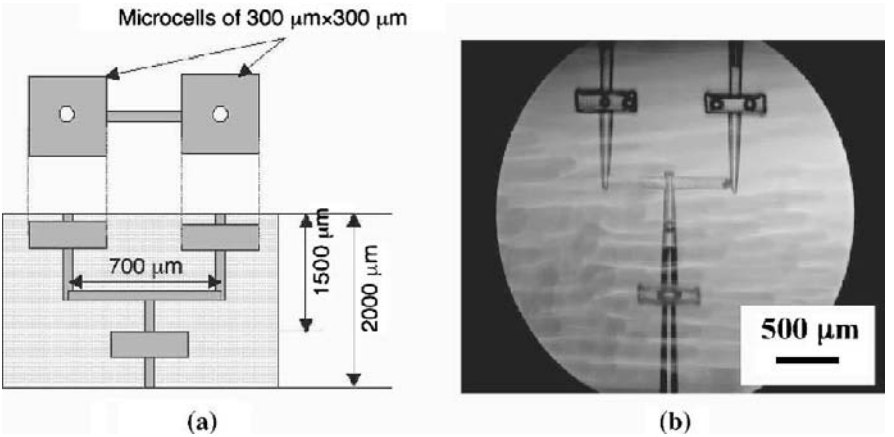

Figure 8. (a) Schematic illustration of vertical microfluidic structure and (b) optical micrograph of side view of the fabricated vertical microfluidic structure.

Fabrication of vertically arranged microfluidic structure inside the photosensitive glass as shown in Fig. 8 (a) was also attempted. In this structure, two microreservoirs of 300 μm 5300 μm with injection channels from the surface were completely embedded 200 μm below the surface, and another microreservoir of 300 μm 5300 μm with an ejection channel to the bottom was embedded 1500 μm below the surface. Each microreservoir was connected with microchannels at the center of each microreservoir. Figure 8 (b) shows an optical micrograph of side view of the 3D vertically arranged microfluidic structure fabricated inside the glass after programmed baking process followed by etching for 75 min in 10 % HF solution. For the fs laser direct writing, the slit with a width of 0.2 mm was used to reduce the aspect ratio of the cross-sectional shape of the horizontal channel

as well as the thickness of the microreservoirs. It is obvious that the very nice vertically arranged microfluidic structure is formed.

Mixing of two kinds of liquid solutions in the planer microfluidic structure as shown in Fig. 7 was successfully demonstrated (Cheng et al., 2005a). In this experiment, blue and red inks were injected from the upper and the lower open microreservoirs of the left side, respectively, and then they were drawn to the right side open microreservoir by a syringe pump. The two solutions were mixed in the channel after the junction and the color gradually changed into purple. Thus, it has been simulated that this structure can act as a microreactor.

8. Fabrication of Micromechanical Components

In μ-TAS, micromechanical components like a microvalve, a micromixer, and a micropump must be integrated into the glass chip with the microfluidic components to control flow and reaction of chemical reagents. The micromechanical components should be able to move in the microfluidics freely. The freely movable microcomponents can be also fabricated by the present technique. Figure 9 shows the experimental scheme for fabricating the freely movable microplate inside the photosensitive glass. First, dark color regions inside the glass are exposed with a scanning focused fs laser beam, and then baked to form the modified

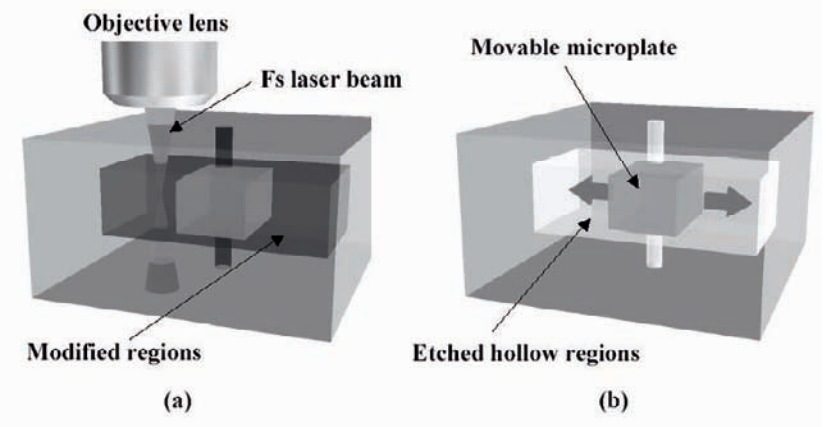

Figure 9. Experimental scheme for fabricating the freely movable microplate inside the photosensitive glass. (a) dark color regions inside the glass is exposed with a scanning focused fs laser beam, and then baked to form the modified regions. (b) After wet etching in a HF solution, the dark color regions in (a) can be completely removed and a glass microplate is left in a hollow chamber embedded in the glass. This glass microplate can move inside the hollow chamber freely.

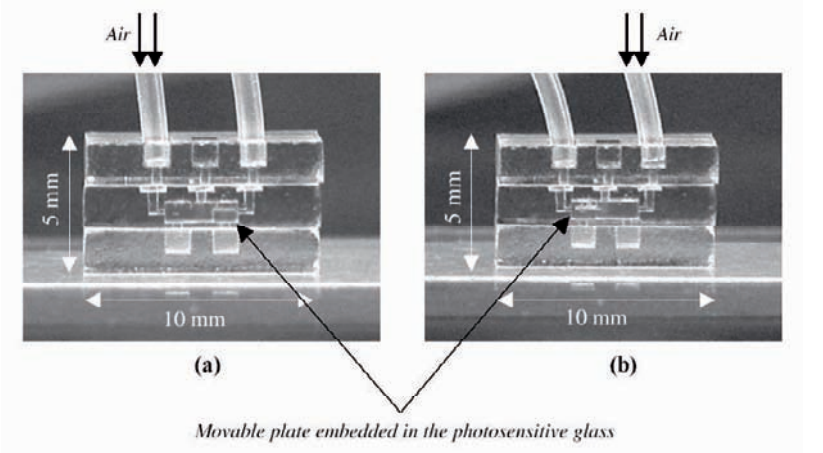

Figure 10. Prototype of a microfluidic device with a freely movable microplate which can switch the flow direction of reagents. (a) By infusing the compressed air from the left opening of the top part, the microplate moves to right side. (b) As the compressed air is infused from the right opening of the top part, the microplate moves to left side.

regions (Fig. 9 (a)). To fabricate this structure, large volume of the glass must be exposed with the fs laser. To shorten the writing time, the laser fluence was increased to 170 mJ/cm^2, so that the scanning speed could be increased to 2 mm/s. After wet etching in a HF solution, the dark color regions in Fig. 9 (a) can be completely removed and a glass microplate is left in a hollow chamber embedded in the glass. This glass microplate can move inside the hollow chamber freely (Fig. 9 (b)).

Figure 10 shows a fabricated prototype of a microfluidic device with a freely movable microplate that can switch the flow direction of reagents. The microplate indicated by the arrow in Fig. 10 can move inside the glass by compressed air. When the compressed air is infused from the left opening of the top part, the microplate moves to right side (Fig. 10 (a)). In this scheme, the reagent injected from the central opening of the top part flows into the left channel of the bottom part through the chamber of the middle part since the microplate blocks the right channel of the bottom part as shown in Fig. 11 (a). Meanwhile, as the compressed air is infused from the right opening of the top part, the microplate moves to left side (Fig. 10 (b)) and then the direction of reagent flow turns to the right channel of the bottom part (Fig. 11 (b)). Therefore, this microvalve can act as a stop valve to switch a stream of reagent in the microfluidics. We have already confirmed this function using this structure. The device was intentionally designed large for a clear demonstration of the function, however, there is no difficulty in fabrication of smaller devices. Besides the microvalve, other micromechanical components like a microturbine and a microgear could be also structured in this way.

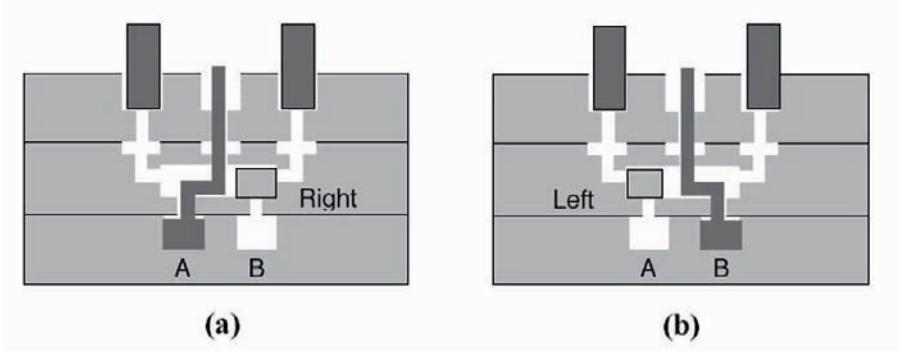

Figure 11. Schematic illustration of the function of the microfluidic device shown in Fig. 10. The flow direction of chemical reagents infused from the central opening of the top part can be controlled by the movable microplate.

In Fig. 9, movement of the micropalate was controlled by the compressed air; however, the electrical control of micromechanical components using electromagnetic force is more desirable for actual μ-TAS operation. Selective metallization of the micromechanical components and internal walls of microfluidic components is essential for this control. For this purpose, we developed a new technique for selective metallization of the glass by the photochemical reaction using the fs laser. In this technique, the photosensitive glass is placed in a fused silica cell filled with a Cu electroless plating solution.

The fs laser beam is focused to the rear surface of glass substrate at room temperature. Selective metallization of internal walls of hollow microstructures embedded in the glass was succeeded by this technique. The details are described elsewhere (Sugioka, Hongo et al., 2005). The mechanism of selective metallization is considered as follows. When the fs laser beam is focused at the rear surface of photosensitive glass, multiphoton absorption takes place only at the focused region. Free electrons are then generated by inter-band excitation through defect levels as discussed in Sec. 5. Generated free electrons reduce metal ions in the electroless plating solution near the laser irradiated regions, resulting in precipitation of metal atoms and finally in the formation of metal thin films on the rear surface of substrates.

9. Fabrication of Microoptical Components

In μ-TAS, analysis of reactants produced in the microfluidics is successively carried out in the same chip. For the analysis, optical means such as absorption spectroscopy and fluorescence measurement are employed. Therefore, microoptical components like a micromirror, a

microlens, a microbeam splitter, a microoptical sensor, a microlight source, etc. should be integrated in the glass chip.

The present technique is applied for fabrication of the micromirror and the microbeam splitter embedded in the glass. For example, a 45° micromicrror embedded in the photosemsitive glass is shown in Fig. 12 (a). To form this structure, we scanned parallel lines from the upper surface of the sample to the bottom of the sample. The interval between two adjacent lines in the photosensitive glass was 15 μm. Thus in consideration of the sample thickness of 2000 μm, we scanned 140 parallel lines in total to form a through structure. After laser irradiation, the sample was subjected to the heat treatment and the subsequent chemical etching. In this case, the time for the chemical etching was 1hr.

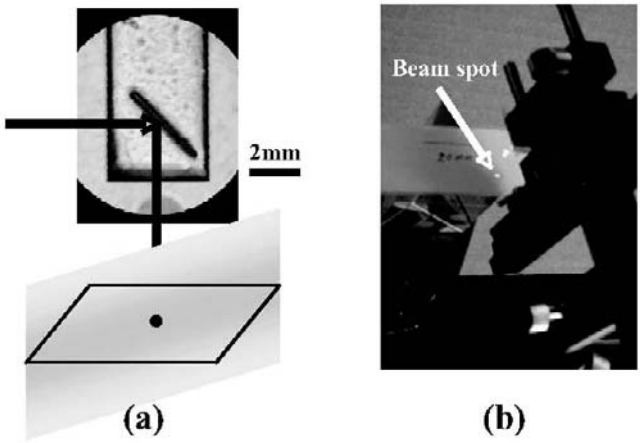

Figure 12. (a) Top view of the 3D micromirror fabricated inside the photosensitive glass with its optical path indicated by arrows, and (b) a beam spot reflected by the fabricated micromirror on a receiving screen placed at a distance of 10 mm from the end of the end of the photosensitive glass.

For higher performance of the fabricated microoptics, surface quality of the hollow structure is very important. Since the crystallites of lithium metasilicate developed by the heat treatment must be grown to a certain size (a few microns) to form an etchable network, etching of the crystallites leaves behind a rough surface. This large roughness causes strong scattering and consequently, the divergence and the loss of the light reflected by the fabricated micromirror, therefore, it must be improved for microoptics application.

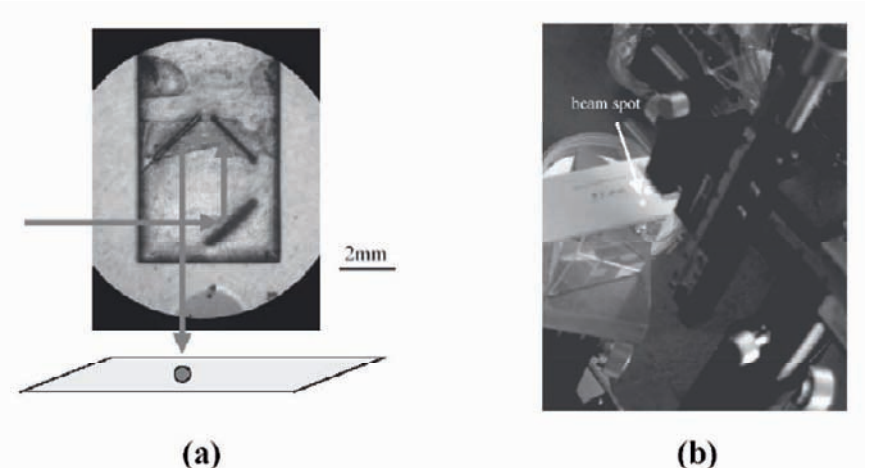

Figure 13. (a) Top view of the microoptical circuit fabricated inside the photosensitive glass with its optical path indicated by arrows, and (b) a beam spot reflected by the fabricated microoptical circuit on a receiving screen placed at a distance of 5 mm from the end of the photosensitive glass.

We solved this problem by an additional annealing process. After the chemical etching, we baked the photosensitive glass sample again. The temperature for this additional annealing is lower than that for the crystallization of lithium metasilicate. First, the temperature is ramped up to 570 °C at 5 °C/min and held at this temperture for 5 hours, then it is reduced to 370 °C at 1 °C/min. The average roughness of the surface before the additional annealing is 81 nm, whereas the average roughness is reduced to only 0.8 nm for the surface after the additional annealing.

To demonstrate the micromirror, we polished the sidewalls of the sample. We then used a He-Ne laser to examine the beam spot reflected from the internal etched surface. The 45° incident angle led to a total reflection. The optical path is indicated by the arrows in Fig. 12 (a). Figure 12 (b) shows a beam spot with a small divergence reflected by the fabricated micromirror on a receiving screen placed at a distance of 10 mm from the end of the photosensitive glass. The optical loss including the losses of two Fresnel reflections from the imput and output surfaces of 0.36 dB was evaluated to be 0.60 dB at 1.55 μm wavelength.

By the same procedures, we fabricated an optical circuit as shown in Fig. 13 (a). Three 45° micromirrors were structured within an area of only 4 mm x 5 mm, and this size can be further reduced without any difficulty. We chose this size just because the beam diameter of our He-Ne laser was larger than 1 mm. The direction of the input laser beam was turned 270° by

the three total reflections, then impinged on the receiving screen which was placed 5 mm away from the end of the sample, as shown in Fig.13 (b). The beam spot is also indicated by the arrow head. The optical loss of the microoptical was evaluated to be 1.6 dB at 1.55 μm wavelength.

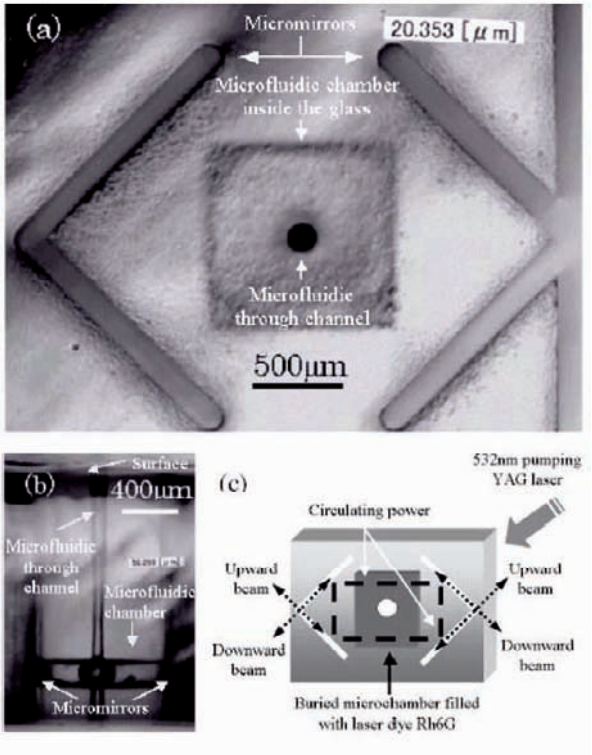

Figure 14. (a) Optical micrograph of the top view of the microfluidic laser, (b) optical micrograph of the side view of the microfluidic chamber and through channel, and (c) illustration of the light path of the microfluidic laser.

The 3D microoptics and the 3D microfluidics can be easily integrated into a single chip for fabricating hybrid devices, such as microfluidic dye lasers which are useful as light sources for applications like fluorescence detection or photoabsorption spectroscopy in the lab-on-a-chip devices (Burns et al., 1998). Figure 14 (a) shows the top view of the fabricated microfluidic laser which has an optical microcavity composed of four 45° micromirrors vertically buried in the glass, a horizontal microfluidic chamber embedded 400 μm below the glass surface, and a microfluidic through channel via the center of the microchamber. Figure 14 (b) shows a micrograph of the side view of the fabricated microfluidic laser, showing the microchannel with an average diameter of 80 μm and the microchamber with a thickness of 200 μm. Figure 14 (c) illustrates the optical path of the

microfluidic laser. The optical cavity is composed of a pair of corner mirrors that are formed by the two micromirrors on the left-hand side and the two on the right-hand side. Light bounces back and forth in the optical cavity by total internal reflections. Lasing action can occur if the microchamber is filled with a gain medium laser dye Rhodamine 6G (Rh6G), and then pumped by a frequency-doubled Nd:YAG laser. Since the surfaces of the micromirrors cannot be fabricated perfectly smooth without any roughness, and the angles between any two micromirrors cannot exactly be at right angles due to the limited precision of fabrication, a small amount of light will eventually leak out from the optical cavity and emit tangentially from the internal surfaces of the micromirrors. The light emission from the side of the cavity has been frequently observed in many experiments with microcavity lasers (Moon et al., 2000; Poon et al., 2001). The design of this microfluidic laser is similar to that of a square-shaped microcavity laser (Poon et al., 2001); however, for achieving high laser output for biophotonic applications, our microfluidic laser is larger thus the microchamber can be filled with more gain medium

We carried out lasing experiments to demonstrate the function of the microfluidic laser. By using a syringe needle, the microfluidic chamber was filled with laser dye Rh6G dissolved in ethanol (~0.02 mol/l). Then the sample was fixed on an optical alignment stage and pumped by a 2nd harmonic of pulsed Nd:YAG laser with a pulse duration of 5 ns and a repetition rate of 15Hz. After increasing the pumping power above a threshold, light emission was clearly seen from the output end of the microfluidic dye laser.

We measured the emission spectra of the microfluidic laser at different pumping energies. The detector head of the spectrometer (USB2000, Ocean Optics, Inc.) was placed near the output end of the microfluidic laser to collect the light from one beam that propagated downward. The obtained spectra are shown in Fig. 15. When a low pumping fluence of 0.46 mJ/cm^2 was applied, only spontaneous emission with wide spectrum are observed on the computer screen connected to the spectrometer, as shown in Fig.15 (a). Lasing action initiated near a pumping fluence of 1.66 mJ/cm^2, as shown in the emission spectrum in Fig. 15 (b). Further increasing pumping fluence induced rapidly increased output power of the microfluidic laser accompanied by narrowed bandwidth. A typical emission spectrum with center wavelength of 578 nm of the microfluidic laser under high pumping energy of 4.49 mJ/cm^2 was measured as shown in Fig. 15 (c). In addition, the output power of the microfluidic laser was evaluated at this pumping energy using a power meter (LASERMATE, Coherent, Inc.). Because we didn't use any focusing lens to collect the light, only one of the two laser beams, namely, the one propagating in the downward direction, was

coupled into the detector head of the power meter placed near the output end of the microfluidic laser. The measured average power reached ~10 μW at 15 Hz repetition rate. Considering that not all of the light of the microfluidic laser beam could be effectively coupled into the power meter, a conservative estimation of the pulse energy of the microfluidic laser is approximately 1 μJ for each laser beam. Because of the symmetry of the laser cavity, there would be four laser beams bi-directionally emitted from the four sides of the micromirrors, thus the total output energy would be even higher.

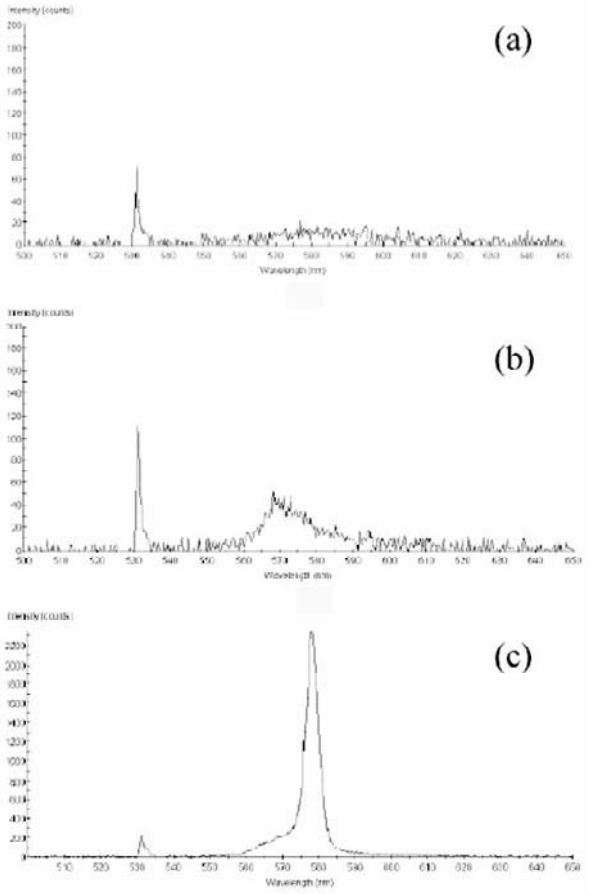

Figure 15. Spectra of emissions of the microfluidic laser at pumping powers of (a) 0.46mJ/cm^2, (b) 1.66mJ/cm^2, and (c) 4.49mJ/cm^2. The peaks centered at 532nm are from the scattered pumping light.

Furthermore, the use of such true 3D microprocessing also enables fabrication of a laser array with multi-layered configurations (Cheng et al., 2005a). By arranging two microfluidic chambers serially in the glass, we built a microfluidic dual-color laser that produces an array of two laser emissions with different wavelengths by only one pumping laser. Figure 16 shows a 3D schematic diagram of the dual-color laser, which has two individual microfluidic systems separated from each other. After the two chambers were filled with two different laser dyes of Rhodamine 640 and Rh6G, and pumped by the 2nd harmonic of Nd:YAG laser, two laser beams with different wavelengths were emitted simultaneously from different positions inside the glass. A measured spectrum of this dual-color laser is shown in Fig. 17, which presents two lasing wavelengths of Rh6G and Rhodamine 640 centered at 568 nm and 618 nm, respectively. Since it is possible to fabricate a microchamber array composed of more chambers, and each chamber can then be filled with different laser dyes, a tiny laser covering any wavelength in a visible range could be achieved for chemical or biological analysis in the lab-on-a-chip devices.

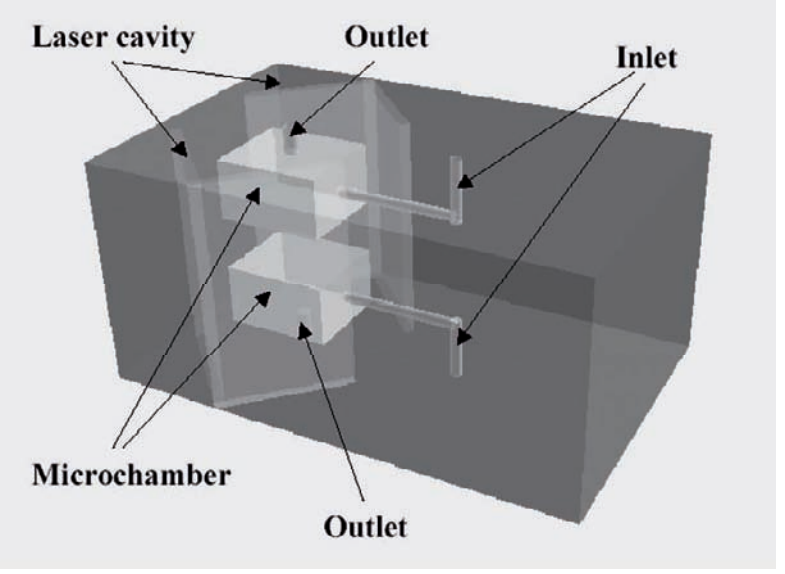

Figure 16. 3D schematic diagram of the dual-color microfluidic laser.

For fabrication of an "all-in-one" biosensor or a μ-TAS device that incorporates microfluidic circuitry with integrated microoptical networks, first, a microfluidic laser beam is coupled into an optical waveguide, and then, the waveguide brings light to a liquid sample in a microfluidic chamber to realize optical absorption spectroscopy or fluorescence

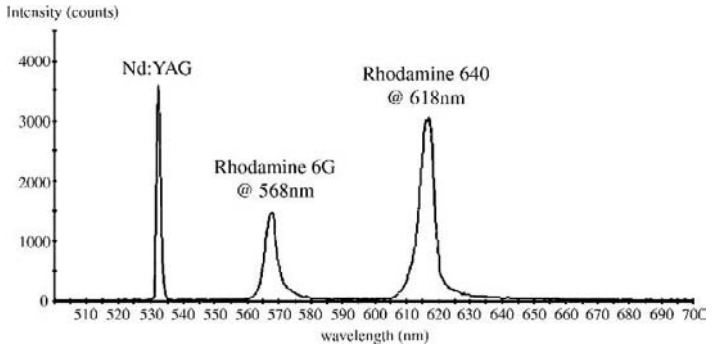

Figure 17. Measured spectrum of the dual-color laser using Rh6G (568 nm) Rhodamine 640 (618 nm) laser dyes as lasing media.

detection. Lastly, a second waveguide, which is connected to an optical spectrometer or a photodetector, collects the light transmitted from or emitted by the liquid sample for information acquisition. Although optical waveguides buried in the photosensitive glass have been achieved by refractive index modification using fs laser microprocessing (Cheng et al., 2003c), two main issues hamper the use of these waveguides for the above-mentioned biosensor application. First, the refractive index modification of the photosensitive glass is realized by the selective precipitation of silver nanoparticles. The silver nanoparticles not only change the refractive index, but also cause a significant optical loss due to light absorption, particularly in the visible range. Second, the fabrication techniques used to produce the buried waveguides and the internal hollow structures are incompatible; thus the waveguides must be written after the formation of the hollow structures. This two-step approach would require the highly accurate repositioning of the etched sample on the stage for the waveguide writing process, thereby increasing the number of manufacturing steps and the cost. To resolve these two issues, freestanding optical fibers in the glass chip were fabricated using the present technique (Cheng et al., 2005).

To fabricate the fiber, first we scanned the areas surrounding the fibers in the glass using the fs laser beam tightly focused by an objective lens with NA of 0.46. Based on the critical dose, a pulse energy of 525nJ/pulse (measured after the objective lens) and a scanning speed of 200μm/s were used throughout this experiment. After laser irradiation, the samples were baked and the etched in a 10% HF solution similarly to the fabrication of the other microcomponents described above. We then fabricated a structure composed of a freestanding fiber integrated with a 45° micromirror at the entrance of the fiber in the glass, as illustrated in Fig. 18 (a). In this case, the dark color region surrounding the free standing fiber was exposed with the fs laser beam and etched. The optical path of the coupling scheme is

indicated in Fig. 18 (a) by arrows. The 45° micromirror allows us to couple the light into the fiber from the side of the sample. Figure 18 (b) shows the optical micrograph of the micromirror and entrance of the fiber. The inset of Fig. 18 (b) (upper right corner) shows the cross-sectional shape of the fabricated fiber, which has dimensions of approximately 100μm×80μm (width×height). Coupling light into the fiber was obtained by focusing a He-Ne laser beam at the micromirror using the objective lens with NA of 0.46, as shown in Fig. 18 (c). The guided light was clearly observed at exit of the fiber. The total length of the fiber in Fig. 18 (c) was 8mm, which is sufficient for many microchip applications. The propagation loss of the fabricated fiber was evaluated to be approximately 0.7dB/cm.

The freestanding fibers can be easily incorporated into a microfluidic circuit for on-chip biophotonic applications. For this purpose, we fabricated a

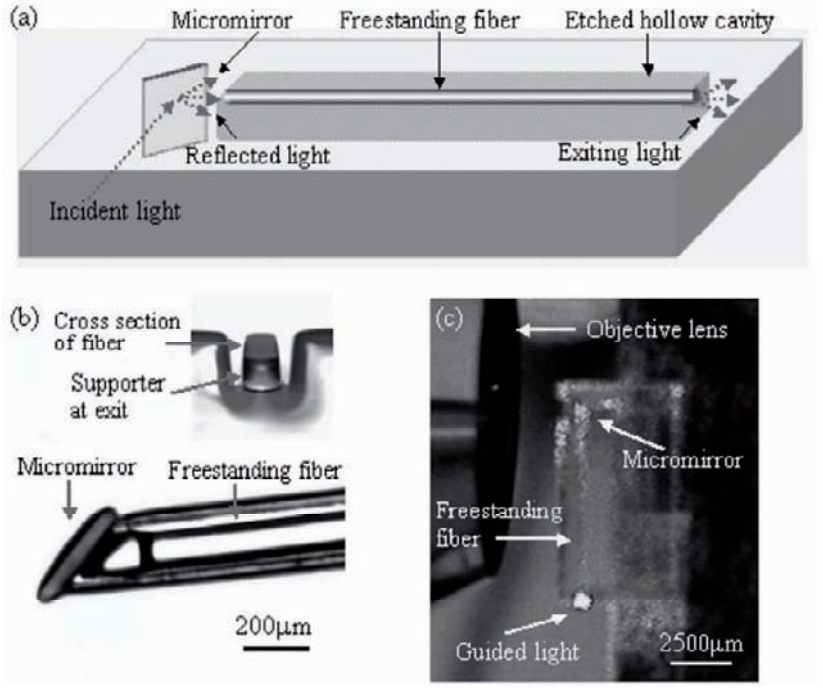

Figure 18. (a) 3D schematic drawing of a freestanding optical fiber integrated with a micromirror fabricated on a glass chip. Red arrows show the optical path of the coupling scheme. (b) Optical micrograph of the top view of the freestanding fiber and the micromirror. The inset (upper right corner) shows the cross section of the fabricated fiber. (c) Digital-camera-captured image of the side coupling of a He-Ne laser beam into the freestanding fiber through the micromirror.

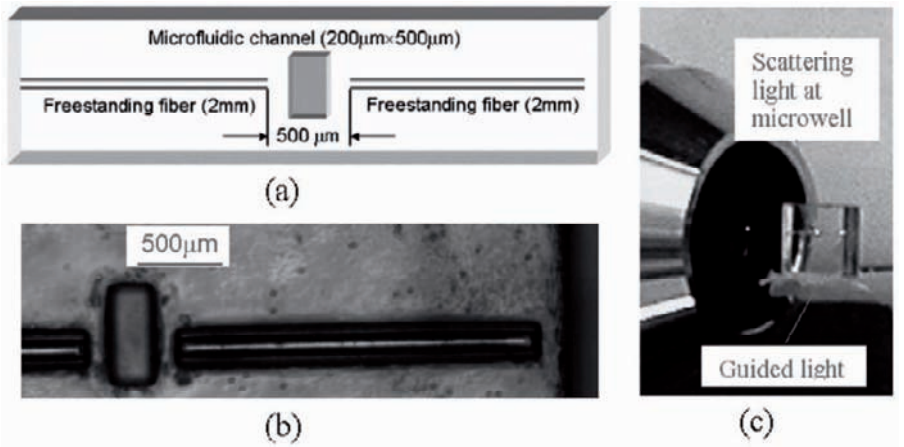

Figure 19. (a) 3D schematic drawing of two freestanding optical fibers intercepted by a microreservoir fabricated on a glass chip. (b) Optical micrograph of the structure. (c) Image of the guiding He-Ne light through the entire structure. Scattering light at microreservoir and the guided light at the exit facet of the second fiber are indicated by arrows.

structure that comprises two series of freestanding fibers intercepted by a microreservoir fabricated in the glass chip, as illustrated in Fig. 19 (a). Figure 19 (b) is the optical micrograph of a part of the fabricated microstructure. To demonstrate that the exiting light from the first fiber can still be effectively coupled into the second fiber, we focused the He-Ne laser beam into the entrance facet of the first fiber by the 20× objective lens. As shown in Fig. 19 (c), both scattering light at the microreservoir and the guided light at the end of the second fiber can clearly be seen. We then measured the coupling loss between the two fibers intercepted by the microreservoir which was approximately 1dB. We successfully demonstrated fluorescence detection from Rh6G using this structure.

10. Conclusions

We have demonstrated the feasibility of true 3D micromachining in the photosensitive glass by use of a fs laser operated at near-IR wavelength for lab-on-a-chip applications. Photoreaction mechanism study revealed that free electrons were generated in the glass for precipitation of Ag atoms by inter-band excitation through defect levels with a six-photon process. The photochemical reaction using the six-photon process would perform high throughput processing with high spatial resolution. Based on the examined process parameters and photoreaction mechanism, 3D microfluidic

structures were fabricated inside the glass. Mixing two kinds of aqueous solutions was successfully demonstrated using the fabricated microfluidic structure. Advanced irradiation methods using a slit or a crossed-beam irradiation have been developed for control of the aspect ratio of the cross-sectional shape of microchannels. Micromechanical components such as a microvalve integrated in the microfluidics were also fabricated and switching of flow direction of the reagents was demonstrated using the fabricated structure. For electrical control of the micromechanical components, selective metallization of the photosensitive glass was developed by the photochemical reaction of the fs laser in a Cu electroless plating solution. For optical analysis of reactants in the lab-on-a-chip devices, microoptical components, freestanding fibers and microlasers were integrated into the glass chip. Thus, we conclude that the present techniques are of great use for the manufacture of "all-in-one" lab-on-a-chip devices.

References

Burns M. A., Johnson B. N., Brahmasandra A. N., Handique K., Webster J. R., Krishnan M., Sammarco T. S., Man P. M., Jones D., Heldsinger D., Mastrangelo C. H., Burke D. T., 1998, An integrated nanoliter DNA analysis device, *Science* **282**:484-487, and the references therein.

Cheng Y., Sugioka K., Midorikawa K., Masuda M., Toyoda K., Kawach M., Shihoyama K., 2003a, Control of the cross-sectional shape of a hollow microchannel embedded in photostructurable glass by use of a femtosecond laser, *Opt. Lett*. **28**: 55-57.

Cheng Y., Sugioka K., Midorikawa K., Masuda M., Toyoda K., Kawachi M., Shihoyama K., 2003b, Three-dimensional micro-optical components embedded in photosensitive glass by a femtosecond laser, *Opt. Lett.* **28**:1144-1146.

Cheng Y., Sugioka K., Masuda M., Shihoyama K., Toyoda K., Midorikawa K., 2003c, Optical gratings embedded in photosensitive glass by photochemical reaction using a femtosecond laser, *Opt. Express* **11**:1809-1816.

Cheng Y., Sugioka K., Midorikawa K., 2004, Microfluidic laser embedded in glass by three-dimensional femtosecond laser microprocessing, *Opt. Lett*. **29**:2007-2007.

Cheng Y., Sugioka K., Midorikawa K., 2005a, Mixrofabrication of 3D hollow structure embedded in glass by femtosecond laser for Lab-on-a-chip applications, *Appl. Surf. Sci*. **248**:172-176.

Cheng Y., Sugioka K., Midorikawa K., 2005b, Freestanding optical fibers fabricated in a glass chip using femtosecond laser micromachining for lab-on-a-chip application, *Opt. Express* **13**:7225-7232.

Fuqua P. D., Janson S. W., Hansen W. W., Helvajian H., 1999, Fabrication of true 3D microstructures in glass/ceramic materials by pulsed UV laser volumetric exposure techniques, *Proc. SPIE* **3618**:213-220.

Fuqua P. D., Taylor D. P., Helvajian H., Hansen W. W., Abraham M. H., 2000, A UV direct-erite approach for formation of embedded structures in photostrcuturable glass-ceramics, *Matr. Res. Soc. Symp. Proc*. **624**:79-86.

Hansen W.W., Janson S. W., Helvajian H., 1997, Direct-write UV-laser microfabrication of 3D structures in lithium-aluminosilicate glass, *Proc. SPIE* **2991**:104-112.

Helvajian H., Fuqua P. D., Hansen W. W., Janson S., 2000, Nanosatellites and MEMS fabrication by laser microprocessing, *Proc. SPIE* **4088**:319-326.

Hongo T., Sugioka K., Niino H., Cheng Y., Masuda M., Miyamoto I., Takai H., Midorikawa K., 2005, Investigation of photoreaction mechanism of photosensitive glass by femtosecond laser, *J. Appl. Phys.* **97**:063517.

Ke K., Hasselbrink E., Hunt A. J., 2005, Nanofabrication with ultrafast lasers at critical intensity, *Proc. SPIE* Vol. **5714**:53-62.

Kim J., Berberoglu H., Xu X.. 2004, Fabrication of microstructures in photoetchable glass ceramics using excimer and femtosecond lasers, *J.Microlithogr. Microfabr. Microsyst*. **3**:478-485.

Kondo Y., Qui J., Mitsuyu T., Hirao K., Yoko T., 1999, Three-Dimensional Microdrilling of Glass by Multiphoton Process and Chemical Etching, *Jpn. J. Appl. Phys*. **38**:L1146-L1148 .

Li Y., Itoh K., Watanabe W., Yamada K., Kuroda D., Nishii J., Youngyuan J., 2001, Three-dimensional hole drilling of silica glass from the rear surface with femtosecond laser pulses, *Opt. Lett*. **26**:1912-1914.

Marcinkevicius A., Juodkazis S., Watanabe M., Miwa M., Matsuo S., Misawa H., 2001 Femtosecond laser-assisted three-dimensional microfabrication in silica, *Opt. Lett*. **26**:277-279.

Masuda M., Sugioka K., Cheng Y., Aoki N., Kawachi M., Shihoyama K., Toyoda K., Helvajian H., Midorikawa K., 2003, 3-D microstructuring inside photosensitive glass by femtosecond laser excitation, *Appl. Phys*. **A76**:857-860.

Masuda M., Sugioka K., Cheng Y., Hongo T., Shihoyama K., Toyoda K., Takai H., Miyamoto I., Midorikawa K., 2004, Direct fabrication of freely movable microplate inside photosensitive glass by femtosecond laser for lab-on-chip application, *Appl. Phys*. **A78**:1029-1032.

Moon H. J., Chough Y. T., An K., 2000, Cylindrical microcavity laser based on the evanescent-wave-coupled gain, *Phys. Rev. Lett*. **85**:3161-3614.

Poon A. W., Courvoisier F., and Chang R. K., 2001, Multimode resonances in square-shaped optical microcavities, *Opt. Lett*. **26**:632-634.

Scaffer C. B., Brodeur A., Garcia J. F., Mazur E., 2001, Micromachining bulk glass by use of femtosecond laser pulses with nanojoule energy, *Opt. Lett*. **26**:93-95.

Stookey S. D., 1953, Chemical machining of photosensitive glass, *Ind. Eng. Chem*. **45**, 115-118.

Sugioka K., Cheng Y., Masuda M., Midorikawa K., 2004, Fabrication of microreactors in photostructurable glass by 3D femtosecond laser direct write, *Proc. SPIE* Vol. **5339**:205-213.

Sugioka K., Cheng Y., Midorikawa K., 2005, Three-dimensional micromachining of glass using femtosecond laser for lab-on-a-chip device manufacture, *Appl. Phys*. **A81**:1-10.

Sugioka K., Hongo T., Takai H., Midorikawa K., 2005, Selective metallization of internal walls of hollow structures inside glass using femtosecond laser, *Appl. Phys. Lett*. **86**:171910.

Sugioka K., Cheng Y., Midorikawa K., 2006, Femtosecond laser microprocessing with three dimensionally isotropic spatial resolution using crossed-beam irradiation, *Opt. Lett*. **31**:208-210.

Yamada K., Watanabe W., Toma T., Itoh K., Nishii J., 2001, In situ observation of photoinduced refractive-index changes in filaments formed in glasses by femtosecond laser pulses, *Opt. Lett*. **26**:19-21.

PHOTO-ASSISTED PROCESSES FROM NANO SIZE COLLOID SOLS

AARON PELED* AND NINA MIRCHIN
Electrical and Electronics Department
Holon Academic Institute of Technology
52 Golomb St., Holon 58102, Israel

Abstract. This chapter describes the Photodeposition from Colloid Solutions (PDCS) of nano-size. In the introduction, the basic photodeposition processes and their current technological trends are described. In section (2) the PDCS basics are given and in Section (3) the microscopic observations. In sections (4) and (5) the significant controlling PDCS parameters are discussed and related to the experimental kinetic investigations. Section (6) describes the currently suggested theory of PDCS process.

Keywords: Photodeposition from colloid solutions (PDCS), nanosize colloid systems, photo-assisted processes

1. Introduction

Photo-assisted processes include today photodeposition (PD) of thin films, photo-electrochemical deposition and etching. Also photo-doping, laser ablation, laser writing and machining, chemical laser processing with lasers and photo-diagnostics, laser recrystallization for Thin Film Transistors (TFT), Pulsed Laser Deposition (PLD), and others [1]. Although Gas Phase Photodeposition processes (GPPD) and PLD [2], became the mainstream, stemming from the interest in microelectronics [3], Liquid Phase Photodeposition (LPPD) [4] was also investigated by various groups to develop photo-assisted processes in the more condensed phase. To a lesser extent solid phase photodeposition processes were sought, such as Laser Induced Forward Transfer (LIFT) [5], in which material is transferred to a substrate by the impact momentum of photons.

*Correspondence should be addressed to: peled@hait.ac.il

J.J. Dubowski and S. Tanev (eds.), Photon-based Nanoscience and Nanobiotechnology, 333–343.

Since the energy for initiating and driving these processes is obtained from light sources such as lasers, many choices are available during the deposition processes by varying irradiation parameters such as the wavelength, power, dose and pulse length, and by changing between pulsed and continuous wave excitation. The possibility of spatial localization of these processes by scanning and focusing the laser beam down to the optical resolving power of the system, or even below it by undercutting, is another remarkable feature of material processing by photodeposition [6]. Direct photonic driven deposition methods were used, for instance, to obtain microelectronic devices eliminating the multi-step lithography processing [7]. They were used to obtain insulating and semiconducting dielectric optical filters and waveguides for integrated optoelectronic devices [8]. Many papers have appeared since 1980, on photodeposition techniques from the gaseous phases [9]. Fewer deal with photodeposition techniques from liquid phases [10]. In particular, hydrosol systems became a subject of investigation for several colloid/solution combinations [11]. In this chapter we focus on the characteristics of liquid-phase nanosize colloid photodeposition (PDCS), its underlying physico-chemical principles and experimental results.

2. PDCS Systems

2.1. BASIC FEATURES

As in other photodeposition systems, a PDCS system incorporates three functions: light "harvesting" agents such as nano size colloid particles, which serve as photon absorbing centers, also known as chromophores, dissolved ions which decompose or react due to the electronic photo-excited state of the chromophores, and a substrate or other types of adsorbing sites. The chromophores may decompose, serve only as catalysts, be precipitated by photoredox or photo-oxidation reactions. They create solid state phases by agglomeration or direct adsorption on surfaces. We specify here the interactions between the ion source M^+, photoelectron e^- or photohole h^+, substrate/colloid used and photon beam properties such as wavelength λ and fluence F by the following detailed reaction scheme:

$$
\begin{array}{lcl}
Chromophore & \xrightarrow{\lambda(nm);F(W/cm^2)} & e^- + h^+ \\
M^+(solution) + e^- & \longrightarrow & \mathrm{M}^{(0)}\ \text{(metallic deposit)} \\
M^+(solution) + h^+ + H_2O & \longrightarrow & M_xO_y + H^+\ \text{(oxide deposit)} \\
\mathrm{H_2}O + 2h^+ & \longrightarrow & \tfrac{1}{2}O_2 + 2H^+
\end{array}
$$

2.2. SPECIFIC PDCS PROCESSES

One of the first photodeposition liquid phase processes investigated since 1975 used a metastable nanosize colloid hydrosol containing solvated Se^{4+} ions and elemental Se particles [6,10]. The process is described by the following photo-chemical equation:

$$\begin{pmatrix} Se^{(0)} - \text{colloid} \\ SeO_2 \\ SO_3^{2-} \text{ insolution} \end{pmatrix} Se^{4+}(aq) \xrightarrow[\text{Lasers, Discharge Lamps, } F_T = 10^{-2} - 10^{2}\ \frac{Joule}{cm^2}]{\lambda < 630 nm} Se^{(0)} \begin{pmatrix} \text{insulating substrates} \\ \text{PMMA, Mylar,} \\ \text{Glass, Quartz} \end{pmatrix}$$

This particular photodeposition system contains an aqueous reducing solution of SO_3^{2-} or similar reducing agents. The transport of photo-reduced material from the solution bulk to the adsorption sites is believed to be controlled by Brownian motion and the adsorption is thermally and photonically activated.

A binary photodeposition system, in which the colloid chromophore is a chalcogenide compound, i.e., of composition XS, where X is a metal and S is Sulphur was developed later. In one system [12], the CdS decomposes by UV light irradiation ($\lambda < 450$ nm) and elemental $Cd^{(0)}$ is precipitated in the solution and growing also as a thin film on plastic substrates according to the following scheme:

$$\begin{pmatrix} CdS \text{ colloids in} \\ CdSO_4 \text{ solution} \end{pmatrix} Cd^{2+}(aq) \xrightarrow[\text{UV - Fiber Lamp}]{\lambda < 450 \text{ nm}} Cd^{(0)} \begin{pmatrix} onto \text{ various} \\ \text{plastic substrates} \end{pmatrix}$$

$$Fluence = 100\ Joule / cm^2$$

In another chalcogenide system [13], Zn and ZnS were co-deposited from ZnS colloids according to the following photochemical equation:

$$\begin{pmatrix} ZnS \text{ colloids} \\ ZnSO_3 \text{ solution} \end{pmatrix} Zn^{2+}(aq) \xrightarrow[KrF \text{ Laser, f} = 1Hz, \tau_p = 10 ns, 60 mJ / pulse]{\lambda = 248 nm} ZnS / Zn^{(0)} \begin{pmatrix} \text{quartz} \\ \text{substrates} \end{pmatrix}$$

Another photodeposition method involved photo-electrolytical deposition of gold, Au, onto p-Si substrates [14].

$$(HAuC\ell_4 \text{ solution}) Au^{+}(aq) \xrightarrow[P = 1 mW]{\lambda = 633 nm} Au^{(0)} \quad (\text{substrate p - Si})$$

$$He \text{ - Ne Laser}$$

Recently we also investigated photodeposition from bio-organic materials using UV bleaching processes in chlorophyll solutions [15], similar to other works on organic and metallic liquid phase solutions [16]. The photochemical scheme of an Chlorophyll-α bleaching process is given by [15]:

$$Chlorophyll\text{-}\alpha + h\nu\,(UV) \rightarrow Pyrenes\ (localized\ deposits\ on\ plastic\ substrates)$$

In this process, the chromophore was *Chlorophyll-a* and UV photon energies with wavelengths below 340 nm were needed to activate the deposition process. Here, bio-organic material, are bleached by photolytic processes, and the resulting material is deposited on PMMA substrates [15].

3. Microscopic Observations of LPPD

The colloid liquid phase photodeposition processes start with a very fine nano-colloidal particles precipitation. This effect was termed Volume Photo-deposition (VP) [10]. A second effect which follows at a lower rate and accompanies VP, named Surface Photodeposition(SP)[10], consists of nanoparticles adsorption on substrates, windows, and on other suspended particles in the solution. The nanometer colloid particles in the irradiated solution grow radially outwards, while at the same time adsorption and aggregation processes on the substrates create continuous thin film or aggregates. In Fig.1, one may observe the details of the submonolayer photodeposition stages of a-Se films on PMMA[1,10]. In Fig. (1a) a SEM morphology of a-Se particles deposited on the substrates is shown. These particles come into contact as seen in Figs. (1b)-(1c) morphologies, when gaps fill up and a continuous film is created.

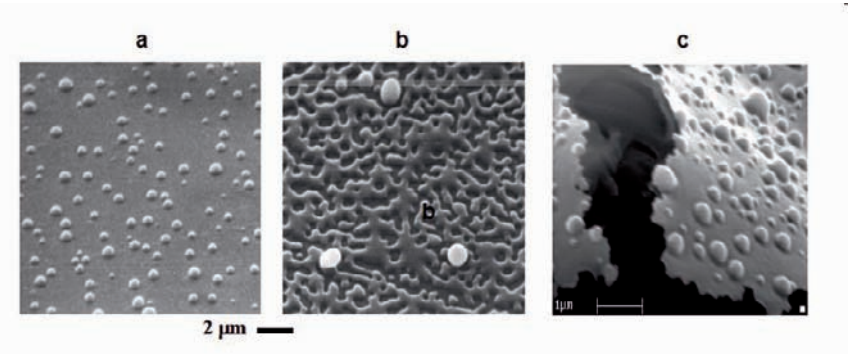

Figure 1. SEM micrographss of thin film sub - monolayer PD stages - (a) and (b); (c) compact layer split by heating to reveal the thickness of the compact layer, from ref. [1].

4. Photodeposition Parameters

The typical dynamics of an a-Se PD film thickness growth is shown in Fig. 2. For photodeposition of a-Se films, a logarithmic growth law was found [1,10]. The experimental film thickness ξ, see Fig. 2a., could be fitted to a logarithmic function, also called the Elovich equation:

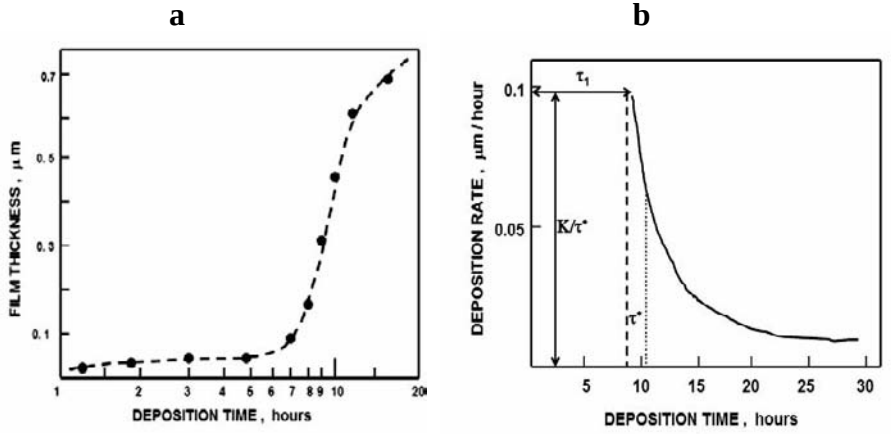

Figure 2. A typical photodeposition a-Se film thickness vs. time - curve (a), and growth rate - curve (b), from ref. [1]; K, τ_1, and τ^* are fitting constants, see text.

$$\xi(t) = K_{opt} \cdot \ell n\left(1 + \kappa \frac{t - \tau_1}{\tau *}\right) + \xi_1, \qquad (1)$$

and the film thickness growth rate given by the following equation:

$$\frac{d\xi(t)}{dt} = \frac{K_{sol}}{\tau *} \cdot \exp\left(-\frac{\xi(t) - \xi_1}{K_{opt}}\right), \qquad (2)$$

where τ_1 is the incubation time i.e., the period of time needed to form a compact film layer of thickness ξ_1. K_{sol}, K_{opt}, $\kappa = K_{sol}/K_{opt}$, τ^*, are fitting constants of the kinetic equation (1).

A division of the overall process into incubation, quasi-linear, and saturation range, can be made observing that the growing rate is changing with time in a wide range of 0-10 nm/sec for a-Se [10] to 0 100 nm/sec for CdS [12]. The parameter $\rho = K_{sol}/\tau^*$ in eqn. (2) can be identified as an unhampered photodeposition rate of film growth starting at $t = \tau_1$, which diminishes in time due to light absorption in the growing film when deposition is performed in the transmission mode. This parameter was called the Quasi Linear Deposition Rate(QLDR) [10]. The typical value of

K_{opt} = 90 nm can be compared with the a-Se film optical absorption inverse value, $1/\alpha$ ~ 60 nm at the excitation wavelength λ = 488 nm. Since $K_{opt} \sim 1/\alpha$, the Elovich equation constant K_{opt}, is related closely to the optical absorption constant of the depositing material.

The incubation period τ_1 is related to the threshold fluence value F_T for active photoablation and photoetching [1]. In experiments of a-Se photodeposition we identified the thickness value $\xi_1 = \xi(F_T)$ to the threshold value of F_T ~ 24 J/cm^2 [1], and thus:

$$\xi(F) - \xi_1 = K_F \cdot \ell n\left(\frac{F}{F_T}\right), \tag{3}$$

where K_F is a fitting constant whose value is close to the inverse of the optical absorption constant of the deposited film. This fluence threshold parameter is related to the Beer Lambert absorption law and accepted in this form in many works on polymer ablation such as Brannon et al., and Braun et al., [17].

Thus we suggested that many photo-adsorption and photo-ablation phenomena can be explained by a heterogeneous incubation process prevailing before the homogenous-active process starts.

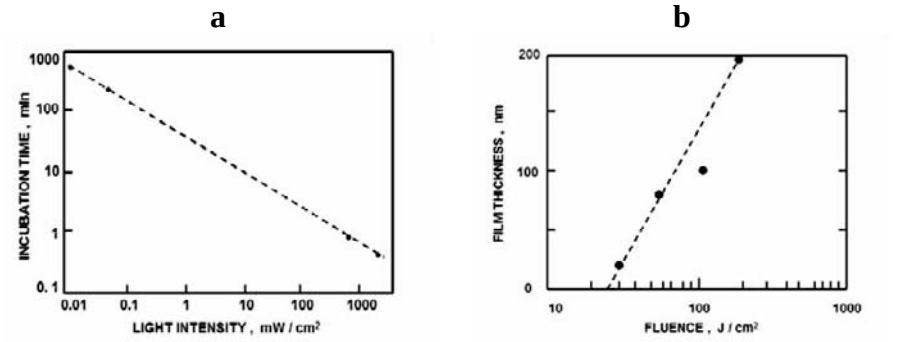

Figure 3. Incubation time τ_1 ,for various light intensities for a photon energy of 2.65 eV, at RT; b.) Film thickness vs. fluence giving an extrapolated threshold fluence at F_T = 24.2 (J·cm^{-2}), see ref. [1].

5. Photodeposition Controlling Parameters

Since the optical properties of the irradiated solution change in time, the spatio-temporal light intensity in the solution, $I(x,t)$, is a function combining the optical properties of the colloid solution and film layer:

$$I(x,t) = I_0(1-R)e^{-\alpha_1 \cdot \xi(t)} \cdot e^{-\int_0^x \alpha_2(x,t)dx}, \qquad (4)$$

where I_0 is the light intensity entering the photoreactor window, $\xi(t)$ is the deposited film thickness at time t, and α_1 and α_2 are the optical absorption constants of the growing film and the colloid solution, respectively. R is the reflectivity at the film/window interface.

The type of substrate material, its cleanliness, topographic structure and optical properties, all affect the incubation period τ_1 and also the final morphology of the photodeposited film. τ_1 depends strongly on the adsorption affinity A of the depositing material, with respect to the substrate. For the Se [10] and Cd [12] photodeposition processes the following trend governs these affinities:

$$A(\text{Glass}) < A(\text{Mylar}) < A(\text{PMMA}) < A(\text{Se or Cd}). \qquad (5)$$

The general functional dependence of QLDR is quite complicated due to its many processing variables. However, the photodeposition processes can be monitored one variable at a time, eventually building the $\rho(\lambda, I, T)$ dependencies in equation (6):

$$\rho(\lambda, I, T) = \rho_0 \cdot \exp\left(\frac{U(\lambda, I)}{kT^*}\right)\exp\left(-\frac{U(\lambda, I)}{kT}\right), \qquad (6)$$

where ρ_0 and T* are constants of the system with the physical insight discussed in [18]. In short, the process in this particular case is a combined photon and thermally activated process with a characteristic activation energy $\mathrm{U}(\lambda, \mathrm{I})$.

In the a-Se case, an Arrhenius thermal activation energy was found i.e., the QLDR has a form

$$\rho = \rho_0 \exp\left(-\frac{U_D}{kT}\right),$$

with typical activation energies in the range $\mathrm{U_D} \approx 0.5 - 1.0(\mathrm{eV})$. The low end value is typical of room or low temperature diffusive processes and the higher end involves photonic, non-thermal, high photon energy activation processes. The parameter T*, in particular, is of interest because it defines the temperature above which the photolytic activated process becomes less effective. This observation led to the suggestion of the so-called *compensation effect* [18], between photons and phonons. This effect is a physical realization that in photodeposition processes, the photonic and thermal processes compete and assist each other during the film growth.

Their relative contributions cross at a critical temperature T*, so called *compensation temperature*, which in a-Se is about 303K [18].

The spectral efficiency QY_{SP} can be defined simply by:

$$\mathrm{QY_{SP}} = \frac{\mathrm{M}}{\mathrm{I_0 \cdot \tau_d}}, \tag{7}$$

where M is the photodeposited mass, τ_d the period of film deposition, and I_0 the constant light intensity of wavelength λ, entering the liquid system. Equation (7) assumes that the process is linear in intensity and hence it applies only to the initial deposition time, i.e., using the QLDR concept for evaluating the intrinsic quantum yield of the process, ε:

$$\varepsilon = \rho / N_{\upsilon}\ , \tag{8}$$

where N_υ denotes the photons flux with energy $h\upsilon$ entering the liquid system. The experiments gave typically values of ~ 0.1 atoms/photon for a-Se and about 0.5 atoms/photon for CdS [10].

6. The Adsorption Brownian Model of Photodeposition

In both photolytic and pyrolitic processes, it is assumed that the absorption of photons occurs primarily by interaction with electrons which are raised to excited states. Then rapidly, in times of the order of 10^{-12} sec, the photons create ions, radicals, free electrons and also give some of their energy to heating the environment, i.e., the absorbing substrate or liquid media. These interactions cause either electron-photon excitations in the light absorbing chromophores [19] or create photo-excited radicals in the solution [10].

A phenomenological mechanism scheme of nano-particles diffusive-Brownian flow and absorption above an energy barrier located in the liquid boundary layer near the substrate is shown in Fig. (4).

Under simplifying assumptions [18], this phenomenological model yields an expression predicting the depositing particles flux density J_p (x,t) due to photoexcitation and diffusion by the following equation:

$$J_p = \frac{n^*(x,t) \cdot D}{X_{eff} \cdot \exp(U_0 / kT)}, \tag{15}$$

where X_{eff} is the particles depletion layer thickness in the solution close to the substrate and D is their diffusion constant. X_{eff} can be estimated from

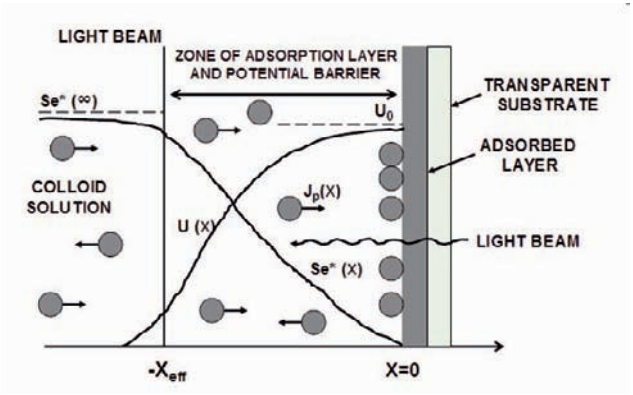

Figure 4. A conceptual mechanism of flow and absorption in photodeposition of a-Se , Ref [18].

the particles diffusion characteristic length in the solution $L = \sqrt{D\tau}$, which for selenium colloids is about 2.3 μm [10]. U_0 is the top of the potential barrier *U(x)* for the adsorbing excited particles, of concentration $n^*(x,t)$, which adsorb on the substrate. For nano-size colloid solutions, this potential barrier depends strongly on the electric fields existing in the colloid particle's double layer charge region. Experimentally, U_0 was resolved into a diffusive term and adsorption term with values ranging between 0.2 and 1.5 eV/atom depending upon parameters such as wavelength and light intensity [18].

7. Conclusions

In this chapter we have categorized and described the design, operation, parametric monitoring and theory underlying the liquid phase photodeposition processes in nanosize colloid systems. Although the principles of operation differ greatly for various types of systems and materials, some fundamental quantifying and processing variables have been defined towards the goal of setting comparable standards in this field.

References

1. A. Peled and N. Mirchin :"Liquid Phase Photodeposition Processes from Colloid Solutions", in A. Peled, Editor, "Photo-Excited Processes, Diagnostics and Applications", Chapter 9, Kluwer Academic Publishers, London 2003.
2. K.L. Saenger, "Pulsed laser deposition. I. A review of process characteristics and capabilities", Processing of Advanced Materials, **3** (1), 1-24, (1993); D.B. Chrisey,

G.K. Hubler (Editors), “Pulsed Laser Deposition of Thin Films", Wiley, New York, 1994.

3. T.H. Baum and P. B. Comita, "Laser-induced CVD of metals for microelectronics technology", Thin Sol. Films, **218**, 80-94, (1992).
4. M.R. Brook, K.I. Grandberg and G.A. Shafeev, "Kinetics of laser-induced Au pyrolytic deposition from the liquid phase", Appl. Phys. A, **52**, 78-81, (1991) ; A.M. Dhote, S.C. Patil, S.M. Kanetkar, S.A. Gangal and S.B. Ogale, "Metallization of glass/ceramic from solutions of organometallic compounds by laser induced pyrolisis", J. Mater. Res., **7**, (7), 1685-1689, (1992); Zs. Geretovski, T.Szorenyi, K. Bali and A. Toth, "Dependence of deposition kinetics on precursor concentration and writing speed in pyrolitic laser deposition from solution", Thin Sol. Films, **241**, 67-70, (1994).
5. J. Bohandy, B.F. Kim, F. J. Adrian and A.N. Jette, "Metal Deposition at 532 nm using laser transfer technique", J. Appl. Phys., **63** (4), 1158-1162 ,(1988); Z. Toth, T. Szorenyi and L. Toth, "Ar laser induced forward transfer(LIFT): a novel method for micrometer size surface patterning”, Appl. Surf. Sci., **69** (1-4), 317-320, (1993); H. Hidai, H. Tokura, "Direct laser writing of aluminum and copper on glass surfaces from metal powder", Appl. Surf. Sci., **174** (2), 118-124, (2001).
6. I. Baal-Zedaka, S. Hava, N. Mirchin, R. Margolin, M.Zagon, I. Lapsker, J. Azoulay, and A Peled, “Photodeposition of Optical Elements from Colloid Solutions", Colloids and Surfaces A: Physicochem. Eng. Aspects, **217**, 191-202, (2003).
7. C. Arnone, M. Rothschild, J. G. Black and D. J. Ehrlich, "Visible Laser photodeposition of chromium oxide films and single crystals", Appl. Phys. Lett**., 48** (15), 1018-1020, (1986); H. W. Lee and S.D. Allen, "High deposition rate laser direct writing of Al on Si", Appl. Phys. Lett., 59(19), 2087-2089, (1991); M. Meunier, R. Izquierdo, M. Tabbal, S. Envoy, P. Desjardins, M-H. Bernier, J. Bertomeu, N. Elyaagouby, M. Suys, E. Sacher and A. Yelon, "Laser induced deposition of tungsten and copper", Matls. Sci. And Eng. B **45**, 200-207,(1997).
8. V. Haruna, S. Yoshida, H. Toda and H. Nishihara, "Laser beam writing system for optical integrated circuits", Appl. Opt., **26** (21), 4587-4592, (1987); C. A . Sunil, Ye. Gouzhang, H. Gafney, "Photodeposition of Diffraction Gratings in Glass: A Comparison of Lithographic, Laser Writing and Holographic Deposition", Applied Spectroscopy, **54** (6), 869-877, (2000).
9. D. Bäuerle, "Laser processing and chemistry: recent developments", Appl. Surf. Sci., **186 (**1-4), 1-6 (2002).
10. A. Peled, "Review: State of the Art in Liquid Phase Photodeposition Processes and Applications (LPPD)", Lasers in Engineering, **6**, 41-79, (1997).
11. Y. Yonezawa, T. Sato, M. Ohno and H. Hada, "Photochemical formation of colloidal metals", J. Chem. Soc., Faraday Trans., **1** (83), 1559-1567, (1987); A. Peled, "Volume photodeposition process in a-Se hydrosols", Colloid Polym. Sci., 262, 718-820, (1984).
12. V. Weiss, A. Peled and A.A. Friesem, "Photodepositon of thin films from CdS colloid solutions", Thin Sol. Films, **218** (1), 193-201, (1992).
13. A. Peled, B. Dragnea, R. Alexandrescu, A. Andrei, "Laser Induced Photodeposition from ZnS Colloid Solutions", Appl. Surf. Sci., **86**, 538-542, (1995).
14. A.K. M. Braga, V. Baranauskas and A. Peled, "Laser induced photodeposition of gold upon p-silicon immersed in chloroauric acid solutions", Appl. Surf. Sci., **79/80**, 375-380, (1994).
15. A. Peled, Y. Dror, I. Baal-Zedaka, A. Porat, N. Mirchin, I. Lapsker, "Photobleaching and Photodeposition in a Chlorophyll Based Solution", Synthetic Metals, **115**, 167-171, (2000).

16. M.S. Paley, D. O. Frazier, H. Abdeldeyem, S. Armstrong and S. P. McManus, "Photodeposition of amorphous polydiacetylene films from monomer solutions onto transparent substrates", J. Amer. Chem. Soc., **117** (17), 4775-4780 , (1995); D. B. Wolfe, S.J. Oldenburg, S. L. Westcott, J.B.Jackson, M.S. Paley and N. Hallas, "Photodeposition of molecular layers on nanoparticle substrates", Langmuir, **15**, 2745-2748, (1999).
17. J.H. Brannon, D. Scholl and E. Kay, "Ultraviolet Photoablation of a plasma-synthesized fluorocarbon polymer", Appl. Phys., **A 52**, 160-166, (1991); A. Braun, K. Zimmer and F. Bigl, "The influence of ambient temperature on KrF laser ablation of polyimide in air", Appl. Surf. Sci., **154-155**, 73-77, (2000).
18. A. Peled, D. Naot and M. Perakh, "On the theory of photoadsorption kinetics of a-Se colloids: the thermal activation energy and compensation effect", Colloid Polym. Sci., **266**, 958-964, (1988).
19. Y. Yonezawa, T. Sato, M. Ohno and H. Hada, "Photochemical formation of colloidal metals", J. Chem. Soc., Faraday Trans., **1** (83), 1559-1567, (1987).

CONTROLLING THE SURFACE PLASMON RESONANCES IN METAL NANOPARTICLES BY LASER LIGHT

HASSAN OUACHA
Nanoarchitectonics Research Center (NARC)
National Institute of Advanced Industrial Science and Technology
AIST Tsukuba Central 5, 1-1-1 Higashi
Tsukuba, Ibaraki 305-8565, JAPAN
E-mail: hassan.ouacha@aist.go.jp

FRANK TRÄGER
Institut für Physik and Center for Interdisciplinary Nanostructure Science and Technology – CINSaT
Universität Kassel, Heinrich-Plett-Strasse 40
34132 Kassel, Germany

Abstract. In this study, we show that supported gold nanoparticles with a given well-defined shape can be produced by laser-assisted growth on substrates based on different materials. For this purpose, gold nanoparticles with average radii ranging from 1.5 to 13 nm, i.e., covering between 0.45 x 10^{16} and 5.6 x 10^{16} atoms/cm^2, were prepared at room temperature by self-assembly of atoms deposited on quartz and sapphire substrates. For analysis of the samples, the optical spectra of the particles were measured with p-polarized light and photon energies in the range of 1.3 to 3.1 eV. Irradiating the particles during growth with laser light of different wavelengths to stimulate surface plasmon excitation made it possible to stabilize mean axial ratios between 0.19 and 0.98. The impact of the laser fluence on the shape of the nanoparticles was also investigated and shows that the position of the surface plasmon resonance shifts to higher energies as the fluence rises. Optimum growth conditions to shape gold nanoparticles with axial ratios close to unity (spheres) with a relatively low laser fluence of 60 mJ/cm^2 have been found. The results of these experiments show that laser-assisted growth is a powerful technique to control the shape of nanoparticles of different materials on different substrates.

Keywords: Nanoparticles, laser-assisted growth, surface plasmon resonance, optical characterization

J.J. Dubowski and S. Tanev (eds.), Photon-based Nanoscience and Nanobiotechnology, 345–360.

1. Introduction

Nanotechnology is predicted to stimulate a series of industrial revolutions in the future, and is an emerging field of research and development dedicated to increasing the control over material structures of nanoscale size. These systems of reduced dimensions, such as metal nanoparticles (NPs), have been extensively investigated and have a variety of properties that make them attractive for technological applications. For example, their size-dependent reactivity and interaction with other atoms and molecules[1,2] make them suitable for the development of new biophysical sensors.[3,4] Furthermore, the chemical properties of metal NPs make them potential candidates for use as novel catalysts with optimized selectivity.[5,6] Other future applications of NPs include enhanced absorption of light in thin photodetectors and organic solar cells.[7,8]

Of particular interest have long been the optical properties of nanoparticles. The main feature of the optical extinction spectra of metal NPs is the excitation of plasmon polaritons, i.e., collective oscillations of the free electrons driven by the electromagnetic field. The surface plasmon resonances (SPR) can be used for a variety of optical applications such as waveguides.[9] Metal NPs with pronounced SPR can also serve as optical filters, which selectively block radiation in specific wavelength intervals and in integrated optical devices for ultrafast switching of light.[10,11] Recently, Alschinger[12] has described experiments in which the field enhancement by silver NPs that accompanies plasmon excitation has been exploited in confocal laser scanning microscopy. It is known that the center frequency, width and amplitude of SPR depend on the size, shape, and the chemical environment of NPs. Many studies of SPR in metal NPs have been reported earlier.[13-19]

Today, metal NPs of atomic species can be prepared using different growth techniques. For instance, N. Vandamme[20] has produced gold clusters by laser vaporization and deposited them at low kinetic energy (~ 0.4 eV/atom) on atomically flat substrates. Gas aggregation and ion sputtering, as production methods, have also been reported.[21] Furthermore, small Au-NPs were recently synthesized from a tetrachloroaurate complex ($AuCl_4$) solution.[22] Major drawbacks of most of these methods are, for example, that the particles may change shape during the deposition and that the chemical environment is often not well defined. We also mention that particles larger than about 20 nm can be prepared using lithographic techniques.[5]

Generation of NPs often results in a mixture of different sizes and shapes with broad distributions[9]; in particular, there is no control of the

shape in self-organized growth.[13] Therefore, an essential issue is to prepare NPs with predetermined shape and narrow size distributions. This does not only make them ideal for the applications mentioned above, but also permits correlation of their properties such as SPR frequencies to well-defined particle shapes and sizes. Therefore, efficient control of these two parameters is important. Here, these experiments are performed to prepare Au-NPs with predetermined shape independent of size. To the best of our knowledge, this is the first study of gold nanoparticles on quartz and sapphire substrates where the size and shape are manipulated by ns-laser pulses and their optical properties are exploited and characterized.

2. Experimental Set-up and Growth Procedure

2.1. EXPERIMENTAL SET-UP

The experimental set-up, as shown in Figure 1, consists of an ultrahigh vacuum (UHV) system with a load lock chamber, a transfer system, and a deposition chamber with a base pressure of $p = 5 \times 10^{-10}$ mbar. An electron beam evaporator serves to generate a beam of Au atoms, and a Xenon arc lamp combined with a monochromator to measure the optical spectra. The size of the quartz and sapphire substrates is 10 x 10 mm, the thickness being 0.5 mm. For laser treatment, a Nd:YAG laser system combined with a BBO-OPO (Barium-Betaborate Optical Parametric Oscillator) was used to shape the Au-NPs during laser-assisted growth. The pulse duration was about 5.5 ns at a repetition rate of 10 Hz.

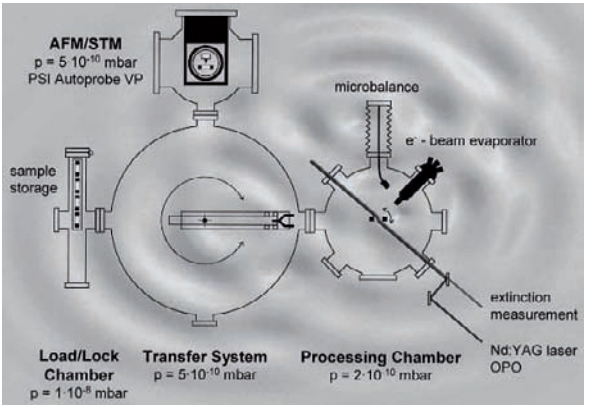

Figure 1. UHV system and experimental set-up.

The laser beam diameter on the sample was 2 ± 0.15 mm. The optical spectra were measured *in-situ* using p-polarized light with photon energies between 1.3 – 3.1 eV (400 – 954 nm). The angle of incidence was set to 45º with respect to the surface normal of the substrate. The Au-NPs were further characterized by atomic force microscopy (AFM) (Park Scientific, AutoProbe-CP) under ambient conditions and in non-contact mode. Silicon tips (Park Scientific, Ultralevers) were used to scan the Au-NPs.

2.2. GENERATION OF GOLD NANOPARTICLES

Au-NPs were prepared on quartz and sapphire substrates by deposition of atoms and subsequent surface diffusion and nucleation *via* Volmer-Weber growth. The surface coverage was determined by measuring the flux of Au atoms with a water-cooled quartz crystal microbalance. The flux typically amounted to 8×10^{14} atoms/cm^{2}min^{-1}, and Au coverages in the range of 0.45×10^{16} to 5.6×10^{16} atoms/cm^2 were obtained. It is known that particles generated by this method usually exhibit broad size and shape distributions[23] and have an oblate shape at sizes larger than about 1 nm. Furthermore, the size and shape are correlated to each other and, therefore, cannot be controlled independently.[13] This makes it difficult to prepare NPs with special sizes and shapes by such self-organized growth. To overcome this difficulty, a laser-assisted growth technique to generate Au-NPs with a well-defined, predetermined shape irrespective of size has been developed.[16] In the following, this method will be briefly described. The NPs are characterized by their short and long half-axes denoted by a and b, respectively. The quantity <a/b> is defined as the mean axial ratio and serves as a measure of the shape of the NPs. When an electromagnetic field is applied to a metal nanoparticle with a radius that is very small compared to the wavelength of the incident light, the conduction electrons are forced to collective oscillations. These oscillations as defined in the introduction, are called surface plasmon resonance. The result is the absorption of light by the nanoparticle at a specific wavelength. The energetic position, the width and the amplitude of the resonances depend on the dielectric function of the metal, the particle morphology, and the dielectric function of the surrounding. Figure 2 shows that when using p-polarized light, and for finite angle of incidence, the light can excite two modes of oscillations, (1,1) along the long axis and (1,0) along the short axis of the nanoparticle, whereas s-polarized light can only stimulate the (1,1) mode. The frequencies of both resonances depend solely on a/b (i.e., shape of the

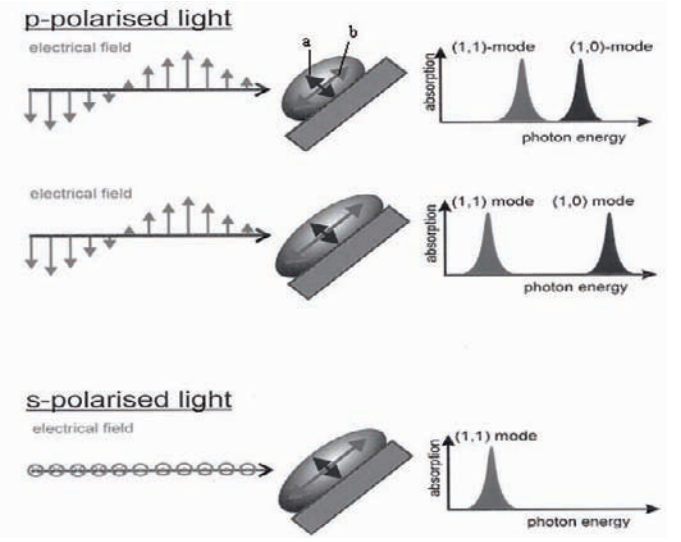

Figure 2. Schematic of metal nanoparticles adsorbed on surfaces and excitation of their surface plasmon resonances**.**

nanoparticle). For example, the (1,1) mode is red-shifted and (1,0) mode is blue-shifted if a/b decreases.

The shape control technique is illustrated in Figure 3. In natural growth, <a/b> drops off as the NPs grow in size and the energetic position of the SPR shifts to lower energy. To stabilize <a/b> at a given value, the Au-NPs are irradiated during growth with ns-laser pulses. The photon energy of the incident laser light is chosen in advance such that only NPs that have reached a certain axial ratio absorb light efficiently. The deposited photon energy is quickly converted into heat. As a result, evaporation and diffusion of atoms are stimulated. The competition between the two processes, i.e., growth of NPs with a decrease of <a/b> during deposition of Au atoms, and selective heating by laser irradiation with an increase of <a/b>, gives particles that have nearly the same axial ratio. In other words, the chosen photon energy constitutes a barrier that the NPs plasmon mode cannot pass. With this technique, NPs of different, predetermined shape can be fabricated using different wavelengths of the laser light during growth. Further details of this laser-assisted growth technique and the preparation procedures of NPs can be found elsewhere.[13,14,16,23]

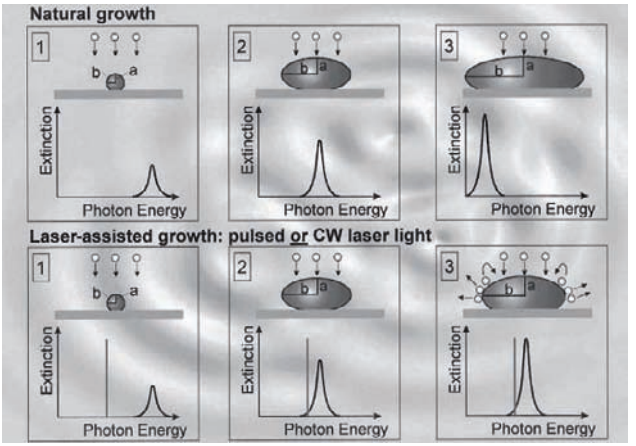

Figure 3. Schematic of the laser-based technique for the fabrication of nanoparticles with well-defined shape.

3. Results and Discussion

3.1. DETERMINATION OF THE MEAN PARTICLE RADIUS AND AXIAL RATIO

The Au-NPs were characterized by AFM in order to determine their number density on the substrate. Since the Au coverage is known, the average volume of the particles can be calculated which, in turn, gives the mean particle radius <R>. This quantity refers to spheres with the same volume as the actual oblate NPs. We found that the number density of the Au-NPs decreases from 16.8 x 10^{10} cm^{-2} to 7.41 x 10^{10} cm^{-2} for coverages of 0.91 x 10^{16} atoms/cm^2 to 4.39 x 10^{16} atoms/cm^2, respectively. This decrease is attributed to coalescence of the NPs as the coverage rises. This gives values of <R> between 1.5 nm and 13 nm for Au-NPs generated *without* laser-assisted growth. For laser-assisted growth, <R> cannot be determined simply from the number density of the particles and the deposited coverage since an unknown number of atoms is released from the particles by laser irradiation. In this case, we have determined the equivalent radii by theoretical modelling of the optical spectra for particles of different sizes and shapes and subsequently compared these to the measured spectra. Figure 4 shows an example of AFM measurements of Au-NPs on a quartz substrate at a coverage of 4.39 x 10_{16} atoms/cm_2,

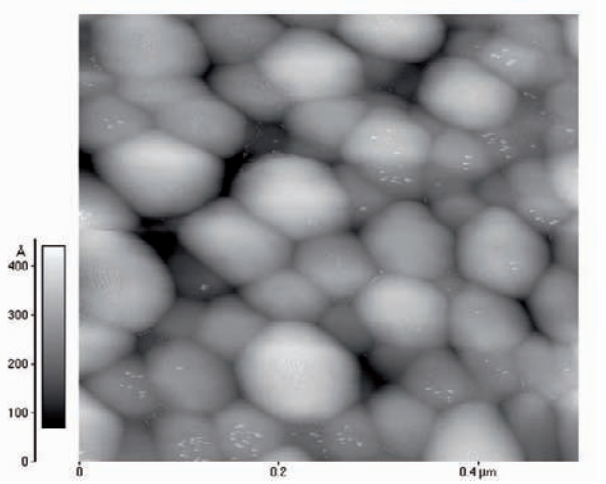

Figure 4. AFM image of Au nanoparticles prepared by laser-assisted growth on quartz substrate.

prepared with laser-assisted growth at a photon energy of E = 1.95 eV and a fluence of 60 mJ/cm^2.

We note that the shape of the NPs cannot be determined by AFM microscopy because of the large radius of curvature of the probe tip. The mean axial ratio <a/b> of the Au-NPs has been extracted from the position of the plasmon resonance peak by measuring the optical extinction spectra of the NPs. Theoretical modelling of the extinction cross-section with the quasistatic approximation[24] was used to derive the quantity <a/b>. We note that the position of the SPR peak in the size regime of 1 – 20 nm depends only on the shape, not on particle size.[9]

3.2. SHAPING AND OPTICAL PROPERTIES

3.2.1. *Au-NPs on Quartz Substrates*

Figure 5a presents the optical extinction as a function of photon energy for Au-NPs naturally grown on quartz substrates with coverages in the range of 0.45 x 10^{16} to 4.39 x 10^{16} atoms/cm^2. The position of the SPR peak, i.e., the (1,1) mode, is red-shifted with increasing coverage. This shift demonstrates that the Au-NPs become more and more oblate as their size rises, i.e., the axial ratio decreases.

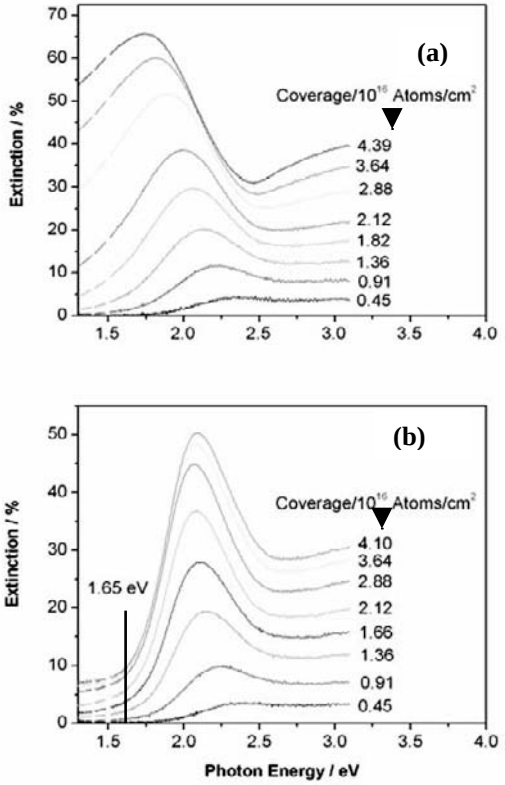

Figure 5. Optical extinction as a function of photon energy for Au nanoparticles grown on quartz substrates with different Au coverages given in Atoms/cm^2 (a) without and (b) with laser irradiation during growth. The photon energy and the fluence of the laser light were set to E = 1.65 eV and F = 60 mJ/cm^2, respectively.

To stabilize <a/b>, the laser-assisted growth technique as described above was used. For comparison, samples with the same coverage as in natural growth, Figure 5a, were prepared. Figure 5b shows the extinction spectra of Au-NPs irradiated during growth with laser light of a photon energy E = 1.65 eV, i.e., λ = 751.5 nm. The laser fluence was set to F = 60 mJ/cm^2. For coverages of 0.45 x 10^{16} atoms/cm^2 and 0.91 x 10^{16} atoms/cm^2, i.e., for relatively small particles, we do not observe any influence of the laser light on the growth process, and the surface plasmon resonances are located at the same photon energies as in Figure 5a. This is simply explained by the lack of overlap between the laser line and the extinction profiles of the small NPs. However, as the Au-NPs grow in size the extinction increases and, due to the interaction with the laser line, the position of the SPR remains constant at about 2.1 eV. This indicates that the

laser irradiation has indeed stabilized the shape of the Au-NPs, i.e., kept the axial ratio constant. In this case, <a/b> is 0.19.

An important advantage of the laser-assisted growth is that it is not restricted to certain shapes. Simply by tuning the photon energy of the laser light, one can choose different axial ratios. The influence of the applied photon energy on the axial ratio of Au-NPs is illustrated in Figure 6. The diagram shows the position of the plasmon peak and the mean axial ratio as a function of Au coverage, i.e., NPs size, grown without and with laser irradiation of different photon energies at a fixed fluence of F = 60 mJ/cm^2.

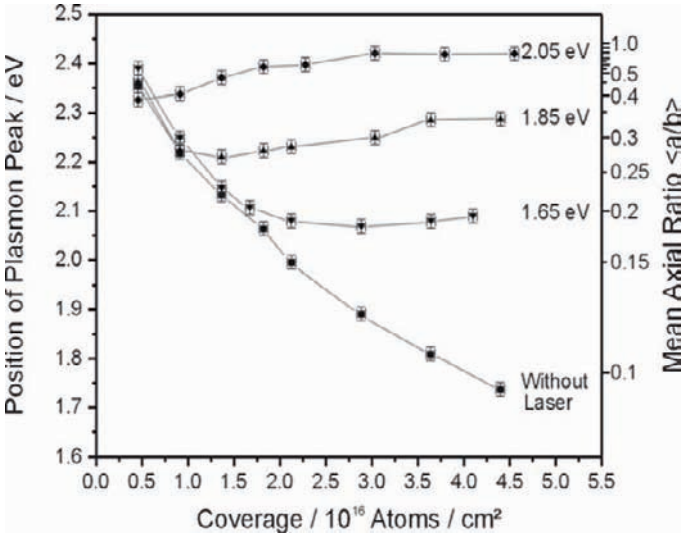

Figure 6. Position of plasmon peak and mean axial ration as a function of the Au coverage for Au nanoparticles grown on quartz substrates without and with laser irradiation of different photon energies. The fluence was set at F = 60 mJ/cm^2 for each photon energy.

As can be seen, Au-NPs with <a/b> = 0.19, 0.35 and 0.98 ± 0.10 have been fabricated by applying photon energies of E = 1.65 eV, 1.85 eV and 2.05 eV, respectively. For a coverage of 4.39 x 10^{16} atoms/cm^2, the final axial ratio of the NPs drops off from 0.98 (nearly spherical Au-NPs grown with a photon energy of 2.05 eV) to 0.09 (oblate Au-NPs grown without laser light). It is found that as the coverage reaches 1.66 x 10^{16} atoms/cm^2, the axial ratio of Au-NPs remains nearly constant at photon energies of 1.65 eV, 1.85 eV and 2.05 eV. Figure 6 also shows that as the photon energy increase, the laser line gets closer and closer to the absorption profile of smaller Au-NPs, and their overlap took place even at the start of the

growth. In the case of 2.05 eV, the interaction already starts at a coverage of only 1.0 x 10^{16} atoms/cm^2.

3.2.2. *Au-NPs on Sapphire Substrates*

In order to investigate the influence of the substrate material, we have also prepared Au-NPs on sapphire substrates. The results are presented in Figure 7, where the position of the plasmon resonance and the mean axial ratio are plotted as a function of the gold coverage without and with laser irradiation at photon energies of 1.65 eV, 1.85 eV and 2.05 eV.

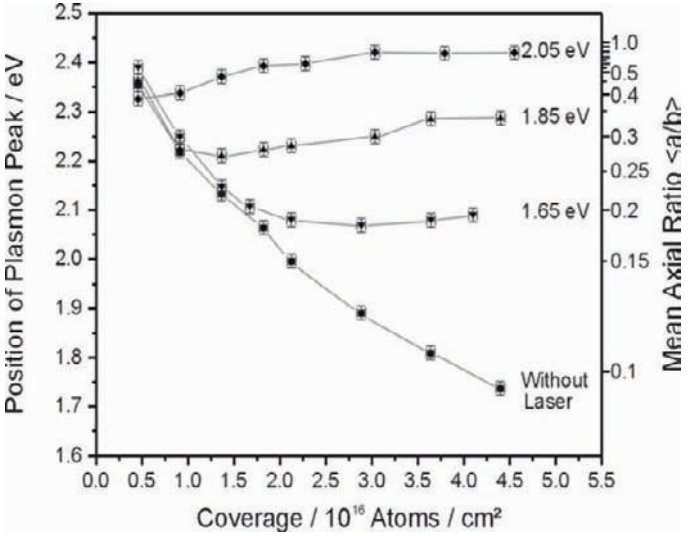

Figure 7. Position of plasmon peak and mean axial ration as a function of the Au coverage for Au nanoparticles grown on sapphire substrates without and with laser irradiation of different photon energies. The fluence was set at F = 60 mJ/cm^2 for each photon energy.

The laser fluence was chosen to be of the same order of magnitude as for the experiments with Au-NPs on quartz substrates (F = 55 ± 5 mJ/cm^2). In general, the results of laser-assisted growth of gold nanoparticles on sapphire are similar to those using quartz substrates.

3.2.3. *Comparison of Shaping Results*

In the following, the results obtained with sapphire and quartz substrates will be discussed in more detail. In both sets of experiments, the same photon energies were used for laser-assisted growth and, therefore, one would expect the plasmon resonances to be located at the same frequencies. This, however, does not agree with our experimental results. In fact, we find that the SPR of Au-NPs on quartz is blueshifted by 0.16 eV, 0.17 eV,

and 0.07 eV for laser irradiation with 1.65 eV, 1.85 eV and 2.05 eV, respectively, as compared to Au nanoparticles on sapphire. This blueshift can be explained by the different thermal conductivities of the used substrates, which have been measured to be 47 W/mK and 14.3 W/mK for sapphire and quartz, respectively.[25] The different thermal conductivities have a pronounced influence on the temperature rise of the nanoparticles since they determine the heat flux into the substrate.[23,26] Due to the smaller thermal conductivity of quartz, the heat remains for a longer time in vicinity of the NPs and their final temperature rise during laser irradiation is higher. Desorption and diffusion take place at higher rates as compared to Au-NPs on sapphire substrates. As a result, the NPs get more spherical and a blue shift occurs as seen in our measurements (Figure 6 and Figure 7). This behavior opens up the possibility of using substrates with low thermal conductivities as supports for Au-NPs to achieve high axial ratios (i.e., nearly spherical shape).

T. Wenzel[13] has used quartz surfaces to study the in situ determination of the shape of supported Ag-NPs grown without irradiation. It was found that Ag-NPs made at room temperature become more and more oblate during growth, with an axial ratio decreasing from unity to 0.4 in a coverage range 0.23×10^{16} - 1.15×10^{16} atoms/cm^2. Compared to our results, we have found an axial ratio of 0.32 for Au-NPs with approximately the same coverage of 0.91×10^{16} atoms/cm^2 grown on a quartz substrate without laser irradiation. In another investigation,[16] quartz substrates were also used for laser-assisted growth of Ag-NPs in a coverage range 0.23×10^{16} - 1.32×10^{16} atoms/cm^2. The applied photon energies of the laser light were 2.95 eV, 2.70 eV and 2.33 eV, which correspond to wavelengths of 420 nm, 460 nm and 532 nm, respectively. The fluence was kept constant at F = 50 mJ/cm^2, which is close to the fluence used in the present study (F = 60 mJ/cm^2). In the reported study,[16] the highest axial ratio was found to be around 0.64 for Ag-NPs prepared under irradiation with photon energy of 2.95 eV. In comparison to our results, the value of the axial ratios of 0.98 is found for approximately the same coverage of Au grown under irradiation with photon energy of 2.05 eV (see Figure 6). Furthermore, when using sapphire surfaces as substrates, Au-NPs get an axial ratio of around 0.6 when a laser irradiation with photon energy of 2.05 eV is used during growth (see Figure 7). From this investigation we can conclude that an adjustment to nearly any axial ration (i.e., shape) of the NPs can be achieved by choosing appropriate substrates and laser parameters.

Other types of substrates, such as mica, have been used as supports for Ag and Au-layers. In this study, M. Kawasaki[27] demonstrated that by irradiation of nanosecond laser pulses with a photon energy of 2.33 eV (i.e.,

λ = 532 nm) with relatively low laser fluence of typically ~50 mJ/cm , Ag- and Au-island films sputter-deposited on mica could be converted to a dense monolayer of spherical NPs 40-60 nm in average diameter without aggregation. Other investigations on the impact of laser irradiation on Au-NPs prepared in solutions have also been reported.[28-30]

3.2.4. *Impact of the Laser Fluence on the Stabilization of the Shape of the NPs*

We have also studied the effect of laser fluence on the shape of Au-NPs prepared on quartz and sapphire substrates.

Figure 8 displays the extinction spectra of Au-NPs prepared on quartz irradiated during growth with photon energy of 1.65 eV (i.e., λ = 751.5 nm). The laser fluence was set to a higher value of F = 153 mJ/cm^2. As the nanoparticles increase in size, the SPR position shifts to higher photon energies due to the increased heating. This impact of the laser fluence is displayed in Figure 9, where the position of the plasmon peak and the mean axial ratio are plotted as a function of Au coverage for NPs grown without and with irradiation of different laser fluences at a photon energy of 1.65 eV.

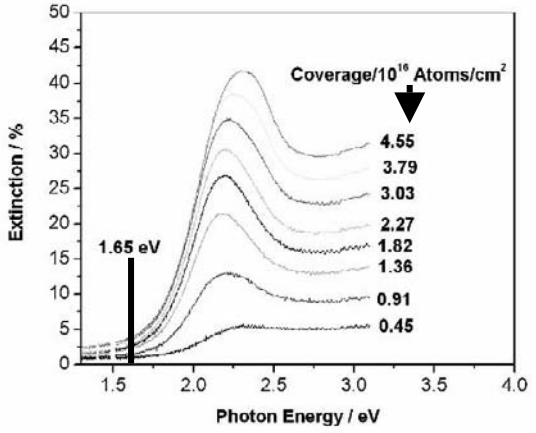

Figure 8. Optical extinction as a function of photon energy for Au nanoparticles grown on quartz substrates with different Au coverages given in Atoms/cm^2 with laser irradiation during growth. The photon energy and the fluence of the laser light were set to E = 1.65 eV and F = 153 mJ/cm^2, respectively.

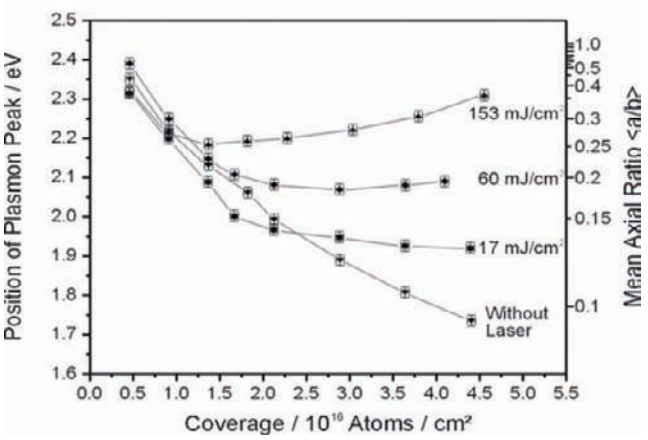

Figure 9. Position of plasmon peak and mean axial ratio as a function of the Au coverage for Au nanoparticles grown on quartz substrates without and with laser irradiation of different fluences. The photon energy of the laser was set at E = 1.65 eV for each fluence.

The axial ratio increases for the highest amounts of coverage from 0.09 to 0.38 as the laser fluence rises from F = 0 to 153mJ/cm^2. We attribute the increase of <a/b> with increasing fluence to self-diffusion and evaporation of atoms, processes that both tend to make the shape of the particles more and more similar to spheres.[31,32] At high fluences, there is no balance anymore between the decrease of the axial ratio, because of the deposition of atoms during growth, and the increase as a result of laser irradiation. In contrast, at low fluences of F = 17 mJ/cm^2 the temperature rise in the NPs is not high enough to prevent decrease of the axial ratio. Thus, variation of the fluence constitutes an additional parameter in preparing nanoparticles with predetermined combinations of sizes and shapes in the region forbidden in natural growth.

Similar to Figure 9, the SPR for Au-NPs grown on sapphire substrates does not remain constant, unless the appropriate laser parameters are chosen (Figure 10). Only for F = 55 ± 5mJ/ cm^2 the axial ratio remains constant at <a/b> = 0.15. This is comparable to the value of 0.19 for Au-NPs grown on quartz substrates irradiated with similar fluence of F = 60 ± 5mJ/ cm^2. At higher as well as at lower fluences, the axial ratio changes for the same reasons mentioned above.

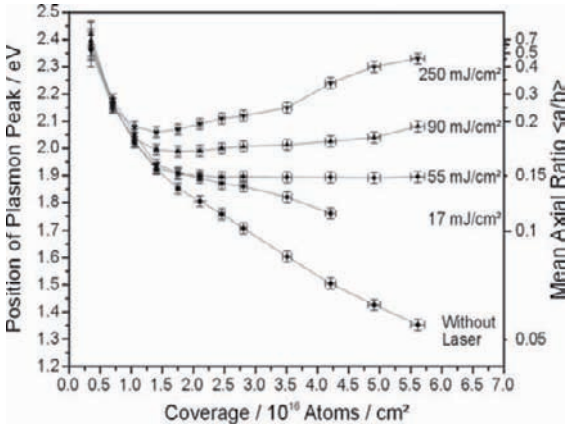

Figure 10. Position of plasmon peak and mean axial ration as a function of the Au coverage for Au nanoparticles grown on sapphire substrates without and with laser irradiation of different fluences. The photon energy of the laser light was set at E = 1.65 eV for each fluence.

The impact of the laser fluence on the shape of Au nanorods prepared by using an electrochemical method described previously by Yu[33], has been investigated earlier by Link[34] using fs - and ns-laser pulses. They found that at high laser fluence (~ 1 J/cm^2) Au-NPs fragment, and a melting of the nanorods into spherical NPs was observed when the laser energy is lowered. This is in agreement with our results as far as the use of low laser fluence is concerned. In our case, we can conclude that the best way to stabilize a constant axial ratio of Au-NPs is to apply relatively low laser fluences during growth, and higher values of <a/b> can be obtained when quartz substrates are used instead of sapphire.

4. Conclusions

Shaping of Au-NPs on quartz and sapphire substrates and their optical spectra have been studied at room temperature. NPs with average radii between 1.5 nm and 13 nm were prepared by deposition of Au atoms and subsequent surface diffusion and nucleation. The influence of the photon energy and of the fluence of the laser light on the shape of the NPs was investigated. Our experiments show that by applying photon energies of 1.65 eV, 1.85 eV and 2.05 eV during growth, axial ratios of 0.19, 0.35 and 0.98, respectively, for Au-NPs on quartz and of 0.15, 0.23 and 0.55,

respectively, for Au-NPs on sapphire can be fabricated. High axial ratios (close to unity) can be achieved with laser irradiation at a photon energy of around 2 eV and relatively low laser fluence of approximately 60 mJ/cm^2. We finally conclude that laser-assisted growth is a powerful method for controlling the shape of the Au-NPs irrespective of size.

Acknowledgements

The authors would like to thank Christian Hendrich and Frank Hubenthal for fruitful collaboration. Financial support by the EU network "Nano-Cluster" (grant number HPRN-CT-2002-00) is gratefully acknowledged.

References

1. A. Kudelski, B. Pettinger, Chem. Phys. Lett. **383**, 76 (2004).
2. I. V. Yudanov, K. M. Neyman, N. Rosch, Phys. Chem. Chem. Phys. **6**, 116 (2004).
3. H. Fissan, M. K. Kennedy, T. J. Krinke, F. E. Kruis, J. Nanopart. Res. **5**, 299 (2003).
4. Amanda J. Haes, Richard P. Van Duyne, J. Am. Chem. Soc. **124**, 10596 (2002).
5. G. A. Somorjai, Appl. Surf. Sci, **121/122**, 1 (1997).
6. S. Carrettin, P. McMorn, P. Johnston, K. Griffin, C. J. Kiely, G. A. Attard, G. J. Hutchings, Top. Catal. **27**, 131 (2004).
7. H. R. Stuart, D. G. Hall, Appl. Phys. Lett. **73**, 3815 (1998).
8. M. Westphalen, U. Kreibig, J. Rostalski, H. Lüth, D. Meissner, Solar Energy Mater. Solar Cells **61**, 97 (2000).
9. U. Kreibig, M. Vollmer: *Optical Properties of Metal Clusters* (Springer, Berlin 1995).
10. R. F. Haglund: *Optics of Small Particles, Interfaces and Surfaces*, ed. by E. Hummel, P. Wissmuth (CRC Press, Boca Raton 1996).
11. J. R. Krenn, H. Ditlbacher, G. Schider, A. Hohenau, A. Leitner, F. R. Aussenegg, Journal of Microscopy. **209**, 167 (2002).
12. M. Alschinger, M. Manik, F. Stietz, T. Vartanyan, F. Träger, Appl. Phys. B **76**, 771 (2003).
13. T. Wenzel, J. Bosbach, F. Stietz, F. Träger, Surf. Sci. **432**, 257 (1999).
14. J. Bosbach, D. Martin, F. Stietz, T. Wenzel, F. Träger, Eur. Phys. J. D **9**, 613 (1999).
15. J. Bosbach, D. Martin, F. Stietz, T. Wenzel, F. Träger, Appl. Phys. Lett. **74**, 2605 (1999).
16. T. Wenzel, J. Bosbach, A. Goldmann, F. Stietz, F. Träger, Appl. Phys. B **69**, 513 (1999).
17. C. Hendrich, J. Bosbach, F. Stietz, F. Hubenthal, T. Vartanyan, F. Träger, Appl. Phys. B **76**, 869 (2003).
18. T. Ziegler, C. Hendrich, F. Hubenthal, T. Vartanyan, F. Träger, Chem. Phys. Lett. **386**, 319 (2004).
19. T. Brandt, W. Hoheisel, A. Iline, F. Stietz, F. Träger, Appl. Phys. B. **65**, 793 (1997).
20. N. Vandamme, E. Janssens, F. Vanhoutte, P. Lievens, C. Van Haesendonck, J. Phys. Condens. Matter **15**, 2983 (2003).

21. W. D Schneider, H. V Roy, P. Fayet, F. Patthey, B. Delley, C. Massobrio: *Cluster Assembled Materials*, edited by K. Sattler, Materials Science Forum, Vol. **232** (Trans Tech, Switzerland, 1996).
22. S. Inasawa, M. Sugiyama, S. Koda, Japanese Journal of Applied Physics. **42**, 6705 (2003)
23. F. Stietz, Appl. Phys. A. **72**, 381 (2001).
24. Craig F. Bohren and Donald R. Huffman: *Absorption and Scattering of light by small Particles* (Wiley-Interscience Publication, USA 1983).
25. I. S. Grigoriev, E. Z. Meilikhov: *Handbook of physical quantities* (New York, CRC Press, 1995).
26. T. Vartanyan, J. Bosbach, F. Stietz, F. Träger, Appl. Phys. B **73**, 391 (2001).
27. M. Kawasaki, M. Hori, J. Phys. Chem. B **107**, 6760 (2003).
28. F. Mafuné, T. Kondow, Chem. Phys. Lett. **372**, 199 (2003).
29. K. Esumi, K. Hayakawa, T. Yoshimura, Journal of colloid and interface science. **268**, 501 (2003).
30. F. Mafuné, J. Kohno, Y. Takeda, T. Kondow, J. Phys. Chem. B. **107**, 12589 (2003).
31. M. Vollmer, F. Träger: *Physics and Chemistry of Small Clusters*, NATO ASI Series B 158, 499; ed. by P. Jena, B. K. Rao, S. N. Khanna (Plenum, New York, London 1987).
32. M. Vollmer, F. Träger, Surf. Sci. **187**, 445 (1987).
33. Y. Yu, S. Chang, C. Lee, C. R. C. Wang, J. Phys. Chem. B. **101**, 6661 (1997).
34. S. Link, C. Burda, B. Nikoobakht, M. A. El-Sayed, J. Phys. Chem. B. **104**, 6152 (2000).

A SUMMARY OF CANADIAN NANOMEDICINE RESEARCH FUNDING: STRENGTHS AND NEEDS

ERIC MARCOTTE*
Associate Director, Regenerative Medicine and Nanomedicine Initiative, Canadian Institutes of Health Research (CIHR), 160 Elgin St, 9th Floor, Ottawa, Ontario, Canada, K1A 0W9

RÉMI QUIRION
Scientific Director, Institute of Neurosciences, CIHR - Institute of Neurosciences, Mental Health and Addiction, Douglas Hospital Research Centre, McGill University, 6875 LaSalle Blvd. Verdun, Quebec, Canada, H4H1R3

*To whom correspondence should be addressed.

Abstract. The Canadian Institutes of Health Research (CIHR) has recently developed a major strategic initiative in the areas of regenerative medicine and nanomedicine. The present article presents a preliminary analysis of nanomedicine funding at CIHR (2000-2005), using a moderately stringent definition of nanomedicine.

Keywords: nanomedicine; nanohealth; regenerative medicine; CIHR; research funding

1. Introduction

The health benefits of nanotechnology have increasingly been recognized by scientists, economists, and the general public as one of the major potential impacts of this emerging field. Potential benefits span the whole range of health needs, from enhancing the basic understanding of cellular processes and function, to developing new and innovative ways to detect and treat disease.

1.1. BACKGROUND ON CIHR AND THE REGENERATIVE MEDICINE AND NANOMEDICINE INITIATIVE

CIHR was formed in June 2000, to replace the Medical Research Council of Canada and reorganize health research in Canada along the lines

J.J. Dubowski and S. Tanev (eds.), Photon-based Nanoscience and Nanobiotechnology, 361–370.

of 13 novel "virtual" CIHR institutes. These institutes are not physical entities, but virtual organizations aiming to support researchers located in universities, hospitals and research centres across Canada. Each institute is led by an internationally renowned expert, and aims to support trans-disciplinary, internationally competitive research, ranging from basic biomedical and clinical research to health systems and services, as well as the factors that affect the health of populations. Many of the institutes' strategic initiatives aim to promote genuine collaboration between experts not only from all disciplines of medical research but also from engineering, physical and natural sciences, law, ethics and social sciences, among others.

Regenerative medicine and nanomedicine were originally identified as key strategic priorities of the CIHR Institute of Neurosciences, Mental Health and Addiction (INMHA). These fields resonated with other CIHR Institutes, government agencies, and NGOs, and quickly grew into one of the key strategic initiatives of the organization, under the leadership of Rémi Quirion, Scientific Director of INMHA. The Regenerative Medicine and Nanomedicine Initiative (RMNI) is now one of the four large strategic initiatives of CIHR, and is a model of inter-agency collaboration.

1.2. CIHR DEFINITION OF NANOMEDICINE

Key to many definitions of nanotechnology is that phenomena and materials at the nanometer length scale have properties that are uniquely attributable to that scale length. This poses challenges for nanomedicine, as many biological structures and processes naturally occur at the nanometer length scale. Nanomedicine could be defined as the specialized biomedical measurement or intervention - at the nanometer scale - needed to treat disease or restore function. However, at present, CIHR broadly recognizes nanomedicine as the application of nanotechnology to health, embracing the four CIHR health research themes of biomedical, clinical, health systems and services, and population and public health.

There is great difficulty in accurately identifying Canadian nanomedicine research capabilities, due to the lack of a simple definition of nanomedicine. This understandable ambiguity is acknowledged through the intentional combination of regenerative medicine and nanomedicine into one initiative. Thus, research projects that may not meet a strict standard of nanomedicine can still be funded through this combined initiative. This perspective is meant to be inclusive of techniques and methodologies that may be relevant to nanomedicine, including mathematics, computational sciences, chemistry, physics, and engineering and applied sciences, among others. Also encouraged is research into the social, cultural and ethical impacts of these novel technologies.

This analysis marks our first attempt to quantify CIHR nanomedicine funding selectively, using moderately stringent criteria. This analysis formed part of a CIHR submission to the scientific assessment of Canadian research strengths in nanotechnology, led by the National Science Advisor to the Prime Minister in October, 2005. An international science review panel was presented with an overview of estimated Canadian nanotechnology funding using this data set and similar keyword searches of the other main federal funding databases including NSERC, CFI, and NRC. The final report of this panel was submitted the Prime Minister's Advisory Council on Science and Technology (PMACST), led by the Minister of Industry with additional input from Industry Canada.

The goal of the current analysis is to present an overview of some of the key areas of research in Canada that could unambiguously be considered as nanomedicine. It is not intended to be a comprehensive scan of all possible definitions of nanomedicine, or all areas of research eligible for funding through the regenerative medicine and nanomedicine initiative. Please see Appendix A and Section 2.1 for more details of the search parameters used for identifying nanomedicine applications in this analysis.

2. Breakdown of CIHR Nanomedicine Funding

At present, the majority of CIHR funding (approx. 70%) is administered through investigator-initiated, open competitions. These funds are not targeted to specific research areas. In addition, a number of strategic Requests for Applications (RFAs) with a nanomedicine component have been launched by CIHR in recent years. Funding estimates below refer to total CIHR expenditures, through both open and strategic competitions, and do not include external partner funds.

In Figure 1, note the large increase in nanomedicine-funded applications in recent years, despite a slowing in the growth of the total CIHR budget. This is due in large part to the successful launch of the Regenerative Medicine and Nanomedicine initiative, as well as other nanomedicine-related RFAs, beginning in the 2003-04 fiscal year. For FY2005-06, we are forecasting an estimated $11.2M in nanomedicine spending.

A subgroup analysis of funded nanomedicine applications is presented in Figure 2. Note that although all subgroups have received increasing funding in recent years, the greatest increases (as of FY2004-05) have occurred in the areas of basic and clinical imaging and technology development (currently approximately two thirds of total nanomedicine

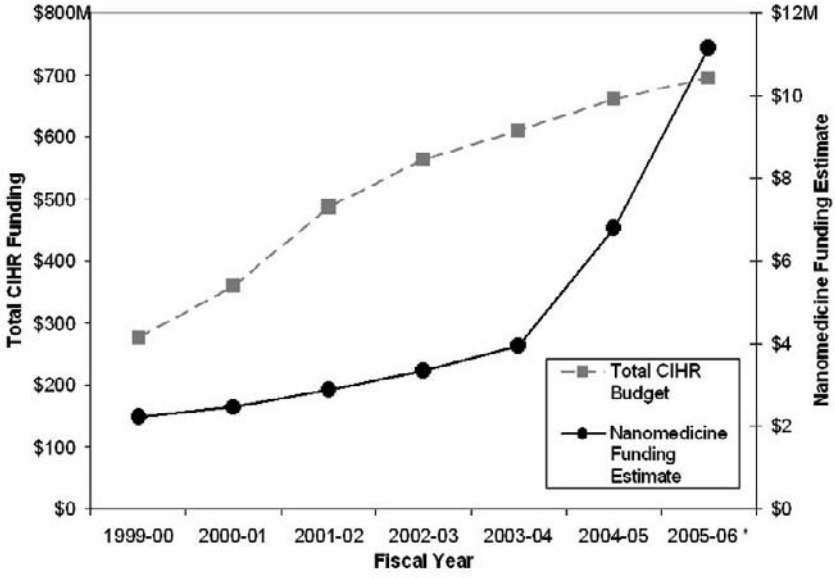

Figure 1. Total CIHR funding and estimated Nanomedicine funding over the past seven years. All funding numbers are in million CDN dollars.

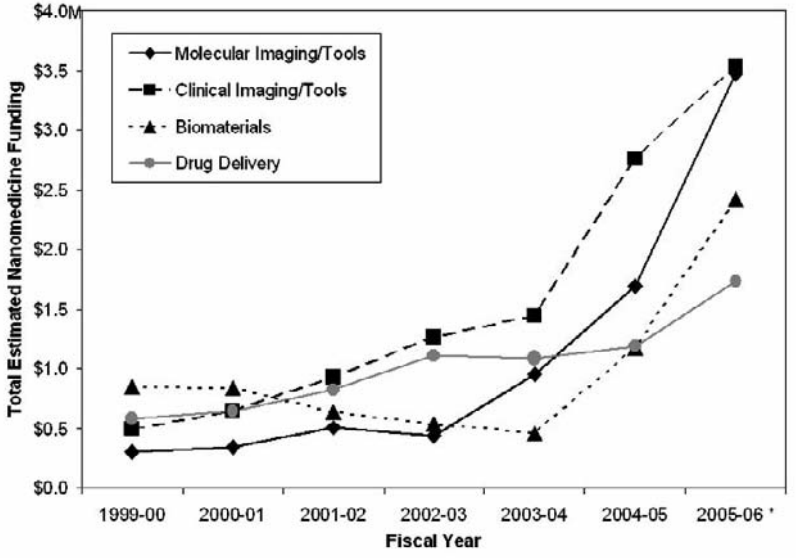

Figure 2. Subgroup analysis of estimated nanomedicine funding. All funding numbers are in million CDN dollars.

funding). This specific increase most likely reflects the increased awareness of the initiative in the physical science research community, and is a direct

result of the targeted workshops, publications, and RFAs promoted by CIHR.

2.1. STRENGTHS OF CANADIAN NANOMEDICINE RESEARCH

2.1.1. *Molecular Imaging and Technology/Tool Development*

Canada has considerable excellence in the area of cellular imaging and biophotonics. Included under this heading is research seeking to apply physical science tools to basic health science (e.g. AFM, STM, etc), as well as the *development* of new technologies (e.g. femtosecond lasers, microfluidics, etc.) and the refinement of existing tools (e.g. microscopy and optical imaging tools). Note that many novel optical imaging research projects (e.g. two-photon microscopy) are not captured by this current analysis, as they do not meet the strict criteria for nanomedicine. Nevertheless, these novel approaches are welcomed through the Regenerative Medicine and Nanomedicine initiative.

2.1.2. *Clinical Imaging and Tool Development*

There are large numbers of diagnostic/clinical imaging research groups located across Canada. Research projects included in this analysis involve the development of nanometer-scale contrast agents for MRI and PET, for example. Also included in this category is the development of femtosecond laser technology as “molecular scissors” for the clinical/surgical setting.

2.1.3. *Biomaterials*

Material science is a relative strength of the physical science community in Canada, and we have observed a strong increase in biomaterial applications in recent years. Specific applications include novel nanostructured surfaces and coatings for implants, 3-D matrices for stem cells, etc. Canada is also internationally recognized for its stem cell research, especially in the area of adult stem cells. Large research groups are located across the country, and are partially unified through a Network of Centres of Excellence. The close association of these diverse health and engineering research communities underscores the strategic decision to integrate nanomedicine and regenerative medicine funding.

2.1.4. *Drug Delivery*

Although Canada has world-expertise in several drug delivery fields, relatively little nanomedicine funding to date has been in this area. Small groups of research excellence are forming in nanoparticle delivery and novel gene delivery vectors. However, Canada’s leading drug delivery

research has been in the area of liposomes and microencapsulation. Note that most of this encapsulation research has been excluded from this analysis due to the near-microscale nature of the technology. A small number of liposome projects have been included due to their focus on the nanoscale structure of the liposome surface (i.e. "nanoimmunoliposomes").

2.2. ADDITIONAL CANADIAN ORGANIZATIONAL/STRUCTURAL STRENGTHS

2.2.1. *Strong Funding Support for Nanomedicine at CIHR*

The strong application pressure and quality of grant proposals have resulted in this initiative being named one of the four main large initiatives of CIHR. CIHR is thus committed to long-term support of nanomedicine research on an ongoing basis.

2.2.2. *Commitment to Multi-disciplinary Research*

The CIHR Team Grant programs have proven to be excellent vehicles for integrating research from the physical and applied domains to health. We have also observed a large increase in the number of applications with physical scientists as principal investigators.

2.2.3. *Close Inter-agency Collaboration*

CIHR has worked closely with other funding agencies (e.g. Natural Sciences and Engineering Research Council of Canada, National Research Council Canada, Canadian Space Agency), NGOs (e.g. Heart and Stroke Foundation Canada, Juvenile Diabetes Research Foundations International, etc.), government departments (e.g. Health Canada, Industry Canada, Environment Canada, etc.) and the Office of the National Science Advisor to the Prime Minister, among others, in developing its nanomedicine research agenda.

2.3. IDENTIFIED ISSUES AND NEEDS OF CANADIAN NANOMEDICINE RESEARCH

2.3.1. *Increased Funding for Research Teams*

Although CIHR has increased annual funding support for multi-disciplinary teams to $500K/yr for 5yrs in its latest Regenerative Medicine and Nanomedicine RFA, this amount is still considered insufficient to make a meaningful health impact, and is below internationally competitive levels.

2.3.2. *Commitment to Stable, Ongoing Funding*

Despite the success of strategic RFAs, researchers have expressed concerns about the stability and sustainability of targeted research programs. Long-term support for nanomedicine through an open grant competition process is required.

2.3.3. *Increased Funding for Bridging the Physical and Health Sciences More Generally*

Although CIHR has made commitments through this initiative and the Collaborative Health Research Projects (CHRP) with NSERC, total funding is clearly inadequate.

2.3.4. *Greater Investments in Research Training*

Given the unique needs of developing inter-disciplinary approaches to health, greater resources need to be placed behind the multi-disciplinary training of the next generation of scientists.

2.3.5. *Greater International Linkages*

Formation of international research teams should be encouraged, and the barriers to joint international Zfunding of teams need to be removed.

2.3.6. *Integration of Social Sciences Perspective*

Greater effort needs to be made to reach out and incorporate the social and cultural perspectives of health research, both at the funding agency and researcher team level.

2.3.7. *Commercialization Needs*

Translating new knowledge into beneficial outcomes for society is one of the main objectives of CIHR. The challenge for nanotechnology is may be particularly severe because most technologies will likely be developed through small start-up companies.

2.3.8. *Research to Support Regulatory and Health Policy Needs*

There is a general lack of dedicated research funds to support regulatory and policy research. This is particularly serious for nanotechnology, because the specific risks to health and the environment are unknown.

3. Conclusions

Despite the difficulties inherent with this sort of analysis, clusters of Canadian nanomedicine research strength can clearly be identified. But there are also broader fields of research where Canada has considerable expertise (e.g. stem cells, biophotonics, drug delivery, etc) that are only now making inroads into nanomedicine. These fields represent a large pool of experienced and talented researchers that may make a substantial impact to nanomedicine in the coming years.

CIHR has taken early steps in developing a strong integrated nanomedicine agenda through the Regenerative Medicine and Nanomedicine initiative. With our valued partners, we are fostering the creation of highly promising multi-disciplinary teams. Some of the expected health benefits from these current teams include improvements in patient function and quality of life, speed and accuracy of diagnosis and surgery, and reduced risks of adverse reactions. But we need to expand our support of these teams if they are to have a truly meaningful health impact and remain internationally competitive.

It is only by working together with all stakeholders that we can ensure that innovative health research in regenerative medicine and nanomedicine will be translated into a lasting impact on human health and productivity.

APPENDIX A. SEARCH CRITERIA FOR CIHR-FUNDED NANOMEDICINE GRANTS

Funded nanomedicine grants in the CIHR database were identified through a validated keyword search. Keywords were searched for under grant title, grant keyword, grant abstract (where available), and researcher expertise. Keywords included specific nanotechnology terms (e.g. atomic force microscop*, nano*) and more general terms (e.g. liposom*, biomedical imag*), to insure that all potentially relevant grants were captured by the search parameters. Search results were then validated by one of us (Eric Marcotte) for their adherence to a strict nanomedicine definition (examples described in this report). Of the nearly 400 resulting grant hits, only 115 were deemed relevant as "nanomedicine" for this analysis. Keywords:

aptamer
AFM
atomic force microscop*
biochip
biomedical imag*
cellular imag*
dendrimer
femtosecond
lab-on-a-chip
liposom*
medical imag*
MEMS
microfluidic*
molecular beam epitaxy
molecular comput*
molecular manufactur*
molecular elec*
molecular imag*
molecular switch
nano*
NEMS
optical imag*
optical tweezer
photonic*
quantum
scanning prob*
scanning tunnel*
self assem*

self-assem*
single electron*
sub-micro*
submicro*
STM
ultrafast
ultrafine

References

1. Canadian Institutes of Health Research (June, 2003); http://www.cihr-irsc.gc.ca/e/16044.html
2. Canadian Institutes of Health Research (June, 2005); http://www.cihr-irsc.gc.ca/e/28268.html
3. Canadian Institutes of Health Research (January, 2006); http://www.cihr-irsc.gc.ca/e/29542.html Stem Cell Network (January, 2006); http://www.stemcellnet.ca/
4. Stem Cell Network (January, 2006); http://www.stemcellnet.ca/e/
5. Quirion, R., 2002, A Canadian experiment: INMHA. How to link up the brain via a virtual institute, *Trends in Neuroscience*, **25**: 268-270.

Author Index